ABSTRACT

Title of Dissertation: INVESTIGATING STAR FORMATION FEEDBACK THROUGH GAS KINEMATICS IN NEARBY GALAXIES

Rebecca Chyba Levy
Doctor of Philosophy, 2021

Dissertation Directed by: Professor Alberto D. Bolatto
Department of Astronomy

Many stages of the stellar life cycle release energy and momentum into the surrounding interstellar medium within a galaxy. This feedback can have profound effects on the host galaxy. This thesis investigates the role of stellar feedback in star-forming galaxies in the local Universe through multiwavelength observations of gas kinematics.

First, I study extraplanar diffuse ionized gas (eDIG) which is thought to be produced by gas ejected from the midplane by repeated supernova explosions. By comparing molecular and ionized gas rotation curves derived from a sub-sample of intermediate inclination star-forming galaxies from the EDGE-CALIFA Survey, I find that $\sim$75% of my sample galaxies have smaller ionized gas rotation velocities than the molecular gas. I suggest and show that the lower ionized gas rotation velocity can be attributed to a significant contribution from eDIG in a thick disk which rotates more slowly than gas in the midplane. As a direct follow up to this study, I use a sample of edge-on galaxies selected from the CALIFA survey to directly

investigate the prevalence, properties, and kinematics of eDIG. I find that 60% of these galaxies show a decrease in the ionized gas rotation velocity as a function of height above the midplane. The ionization of the eDIG is dominated by star-forming complexes. These studies reveal the pervasiveness and importance of this phase in local star-forming galaxies.

Next, I study stellar feedback in the extreme environment of the nuclear starburst in the nearby galaxy NGC 253. Using ALMA observations with 0.5 pc resolution, I detect blueshifted absorption and redshifted emission (P-Cygni profiles) in multiple spectral lines towards three of the super star clusters (SSCs). This is direct evidence for outflows of dense molecular gas from these SSCs. Through a comparison of the outflow properties with predictions from simulations, I find that the outflows are most likely powered by dust-reprocessed radiation pressure or O-star stellar winds. The observed outflows will have very substantial effects on the clusters' evolution. Finally, I find that the arrangement of the SSCs may be morpho-kinematically consistent with a ring or crossing streams from the larger-scale gas flows which fuel the starburst.

INVESTIGATING STAR FORMATION FEEDBACK THROUGH GAS KINEMATICS IN NEARBY GALAXIES

by

Rebecca Chyba Levy

Dissertation submitted to the Faculty of the Graduate School of the
University of Maryland, College Park in partial fulfillment
of the requirements for the degree of
Doctor of Philosophy
2021

Advisory Committee:
Professor Alberto D. Bolatto, Chair/Advisor
Professor Stuart N. Vogel
Professor Sylvain Veilleux
Dr. Peter Teuben
Professor Adam K. Leroy, External Examiner
Professor Kara Hoffman, Dean's Representative

Preface

The research presented in Chapters 2, 3, and 4 of this dissertation has been previously published. Chapter 2 is presented with minimal changes since appearing in the Astrophysical Journal (ApJ) as *"The EDGE-CALIFA Survey: Molecular and Ionized Gas Kinematics in Nearby Galaxies"* (Levy et al., 2018). Chapter 3 is presented with minimal changes since appearing in ApJ as *"The EDGE-CALIFA Survey: Evidence for Pervasive Extraplanar Diffuse Ionized Gas in Nearby Edge-on Galaxies"* (Levy et al., 2019). Chapter 4 is presented with minimal changes since appearing in ApJ as *"Outflows from Super Star Clusters in the Central Starburst of NGC 253"* (Levy et al., 2021).

The material presented in Appendix D is a paper led by a high school student under my supervision that is currently under review at the Monthly Notices of the Royal Astronomical Society (MNRAS) as *"Cuspy Dark Matter Density Profiles in Massive Dwarf Galaxies"* (Cooke, Levy, et al., 2021). Though the student is the first author of this paper, I led the data processing, analysis, and presentation, wrote the vast majority of the text, and am the corresponding author of this submission. Therefore, I feel it merits a place in this thesis as the presentation of the research I led during my PhD. Aside from incorporating the appendix material into the main body, this work is presented with minimal changes from the version under review at MNRAS.

"Somewhere, something incredible is waiting to be known."

– Sharon Begley, *Seeking Other Worlds,* ***Newsweek***

Acknowledgments

I see this PhD thesis as not so much about this physical document, but rather about the forward-looking journey on which it has taken me. I am extraordinarily grateful to a number of people for enabling me to be the scientist and person I am today and for supporting me in the scientist and person I will become.

This PhD thesis would not have been possible without my advisor, Alberto Bolatto. Thank you for taking a chance on me and for all of the opportunities you have given me along the way. It's hard for me to fathom just how much you've taught me these past six years. Thank you for being a phenomenal advisor, mentor, advocate, colleague, and friend. I hope someday to be half the mentor you have been to me. I ardently look forward to our continued collaboration in the future!

I want to thank the rest of my thesis committee and research group — Stuart Vogel, Peter Teuben, Adam Leroy, Sylvain Veilleux, Kara Hoffman, Andy Harris, Laura Lenkić, Liz Tarantino, Vicente Villanueva, Rye Volpert, Jialu Li, and the LMA group — for their time and collaboration throughout my time at UMD. I also want to thank the members of the EDGE-CALIFA and "Starbursts" collaborations for all of the research guidance over the years. I also want to acknowledge my first research advisor, Dan Marrone, for setting me on this path as an undergraduate at the University of Arizona and for supporting me all along the way.

I want to thank *all* of the UMD Astronomy Department Staff, especially those with whom I worked most closely — John Cullinan, Olivia Dent, Barbara Hansborough, Dorinda Kimbrell, Susan Lehr, Eric McKenzie, Adrienne Newman, Mary Ann Phillips, and Mona Susanto — for making the administration end of things so easy for us. The work you do is of paramount importance, and I'm so grateful for your support and expertise. Thanks to Carrie Holt and Ginny Cunningham for being the best office mates ever. Finally, I want to thank *all* of the graduate students and *everyone* else in the UMD Department of Astronomy for your collaboration and friendship. I could not have asked for a better place and better people with whom to have spent the past six years.

It's hard to put into words the gratitude I have for my parents, Michele Chyba and Henry Levy, who instilled in me from a young age that education is of paramount importance. I am extremely privileged to have had a woman scientist role model from day one. Mom, you showed me that it could be done. I thank my dad for his curiosity and constant interest in science. I don't think it's an exaggeration that watching science and astronomy TV shows with you is a large reason why I'm writing this thesis today and pursuing my career in astronomy. Thank you doesn't seem enough for your lifelong support.

Next, I thank my partner, Will Roddy. Your love and support throughout this journey mean more to me than I can possibly put into words. Thank you for supporting me in big and small ways. Thanks for listening to me rant about my data cleaning problems and drone on about the intricacies of some random physical process. Thank you for moving across the country to be with me on this journey.

Thank you for reassuring me and believing in me at every step of the way. I love you to the greatest observable redshifts and back.

I also want to thank my brother and sister-in-law, Aaron and Kira Levy, and my niece Brynja Levy. The fall of 2020 was one of the hardest times of my life. Between the fear and isolation of a global pandemic, the underscored scourge of systemic racism, the uncertainty and insecurity of applying for postdoc positions, submitting a mammoth paper, and the most important and intensive observing proposal I had ever worked on, I was running a marathon on fumes. But, through it all, Brynja kept me going. The hope that your birth gave me and the promise that, soon, I would get to meet you was my motivation to push through. So, Aaron and Kira, in addition to your unwavering support and love, thank you for all the pictures and videos you send of Brynja and for having the most perfect little human.

I would also like to thank the Chyba, Levy, Roddy, and Mangas families for their love and support. I am very lucky to have you all in my life.

Finally, I gratefully acknowledge the Native and Indigenous Peoples across the globe on whose ancestral homelands we conduct research and gather.

Table of Contents

List of Tables

List of Figures

List of Abbreviations

Acronyms:

2MASS	2 Micron All Sky Survey
ACA	Atacama Compact Array (part of the Atacama Large Millimeter/submillimeter Array)
ADC	Asymmetric drift correction
AGB	Asymptotic giant branch
AGN	Active galactic nucleus
ALMA	Atacama Large Millimeter/submillimeter Array
B/D ratio	Bulge-to-disk ratio
CALIFA survey	Calar Alto Legacy Integral Field Area survey
CARMA	Combined Array for Millimeter Wave Astronomy
CASA	Common Astronomy Software Application
CDF	Cumulative distribution function
CDM	Cold dark matter
CIMF	Cluster initial mass function
CMF	Cluster mass function
CMZ	Central Molecular Zone
CNM	Cold neutral medium
DGDM survey	Dwarf Galaxy Dark Matter survey
DGR	Dust-to-gas ratio
DIG	Diffuse ionized gas
DR	Data release
EDGE survey	Extragalactic Database for Galaxy Evolution survey
eDIG	Extraplanar diffuse ionized gas
ETG	Early-type galaxy
EW	Equivalent width
FIR	Far infrared
FOV	Field of view
FWHM	Full-width-half-maximum
GBT	Green Bank Telescope
GC	Globular cluster
GMC	Giant molecular cloud
gNFW profile	Generalized Navarro-Frenk-White profile
HOLMES	Hot, old, low-mass evolved stars

HST	Hubble Space Telescope
HWHM	Half-width-half-maximum
IC	Index catalogue
IGM	Intergalactic medium
IFS	Integral field spectroscopy
IFU	Integral field unit
IILR	Inner inner Lindblad resonance
ILR	Inner Lindblad resonance
IMF	Initial mass function
IR	Infrared
IRAC	Infrared ARray Camera (onboard the Spitzer Space Telescope)
IRS	InfraRed Spectrograph (onboard the Spitzer Space Telescope)
JWST	James Webb Space Telescope
KDE	Kernel density estimator
KSS	Kinematic Sub-Sample
LEGUS	Legacy Extragalactic Ultraviolet Survey
LINER	Low-ionization nuclear emission-line region
LMC	Large Magellanic Cloud
LSRK	Kinematic local standard of rest
LTE	Local thermodynamic equilibrium
MaNGA survey	Mapping Nearby Galaxies at Apache Point Observatory survey
MAST	Mikulski Archive for Space Telescopes
MCMC	Markov Chain Monte Carlo
MGC	Morphological Galaxy Catalogue
MW	Milky Way
NEMO	Not Everybody Must Observe, a stellar dynamics toolbox
NFW profile	Navarro-Frenk-White profile
NGC	New general catalogue
ngVLA	Next Generation Very Large Array
NICMOS	Near Infrared Camera and Multi-Object Spectrometer (onboard the Hubble Space Telescope)
NIR	Near infrared
OILR	Outer inner Lindblad resonance
PA	Position angle
PAH	Polycyclic aromatic hydrocarbon
PDR	Photodissociation region (also sometimes called a photon-dominated region)

PPAK	Potsdam multi-aperture spectrophotometer fiber PAcK (at the Calar Alto 3.5 m Telescope)
PSF	Point spread function
PV	Position-velocity
rms	root-mean-square
RRL	Radio recombination line
SAMI survey	Sydney-Australian Astronomical Observatory Multi-object Integral field spectrograph survey
SB	Surface brightness
SDSS	Sloan Digital Sky Survey
SED	Spectral energy distribution
SFE	Star formation efficiency
SFH	Star formation history
SFMS	Star formation main sequence
SFR	Star formation rate
SIDM	Self-interacting dark matter
SN(e)	Supernova(e)
S/N	Signal-to-noise ratio
SNR	Signal-to-noise ratio
SOFIA	Stratospheric Observatory for Infrared Astronomy
SSC	Super star cluster
sSFR	Specific star formation rate
SSP	Simple stellar population
TIR	Total infrared
UGC	Uppsala General Catalogue
upGREAT	Upgraded German REceiver for Astronomy at Terahertz frequencies (onboard the Stratospheric Observatory for Infrared Astronomy)
UV	Ultraviolet
VLA	Very Large Array
WIM	Warm ionized medium
WISE	Wide-field Infrared Survey Explorer
WIYN	Wisconsin-Indiana-Yale-National Optical Astronomy Observatory telescope
WNM	Warm neutral medium
WR	Wolf-Rayet
ZAMS	Zero-age main sequence

Molecules, atoms, ions, and line transitions:

[CII]	Singly-ionized carbon emitting via a fine-structure transition at 1.9 THz (158 μm)
CO	Carbon monoxide
CS	Carbon monosulfide

H	Hydrogen
Hα	The n=3−2 electronic transition of hydrogen at 6562.68 Å
Hβ	The n=4−2 electronic transition of hydrogen at 4861.35 Å
Hγ	The n=5−2 electronic transition of hydrogen at 4340.47 Å
Hδ	The n=6−2 electronic transition of hydrogen at 4101.73 Å
HI	Neutral atomic hydrogen emitting via a spin-flip transition at 1420.41 MHz (21 cm)
HII	Singly-ionized hydrogen
H_2	Molecular hydrogen
HCN	Hydrogen cyanide
HCO^+	Formyl cation (formylium)
He	Helium
He^+	Ionized helium
N	Nitrogen
N^+	Ionized nitrogen
[NII]	The singly-ionized nitrogen emission line doublet at 6548 and 6583 Å
[OI]	Neutral oxygen emitting via fine-structure transition at 6300 Å
[OIII]	The doubly-ionized oxygen emission line at 5007 Å
Pa-α	The n=4−3 electronic transition of hydrogen at 1.87561 μm
S	Sulfur
S^+	Ionized sulfur
[SII]	The singly-ionized sulfur emission line doublet at 6717 and 6731 Å

Chapter 1: Introduction

"Don't shoot for the stars, we already know what's there.

Shoot for the space in between because that's where the real mystery lies."

– Dr. Vera Rubin

We live in a galaxy — a vast collection of stars, gas, dust, dark matter, planets, and beings. Our understanding of our place in our Galaxy and our Galaxy's place among the myriad of galaxies in the Universe has evolved dramatically over the millennia.

A complication of living in our Galaxy, the Milky Way (MW), is that we study it from within. To understand galaxies more broadly and the processes that shape and transform them, we must increase our sample size. The focus of this dissertation research is on nearby galaxies, those beyond our Local Group but within ∼100 Mpc (∼330 million light-years, $z \lesssim 0.025$). Galaxies in this vicinity span more than four orders-of-magnitude in stellar mass (M_*), more than seven orders-of-magnitude in star formation rate (SFR), and include examples of every morphological type. Figure 1.1 shows the SFMS for a sample of local galaxies from a review by Sánchez (2020), and we refer the reader to that paper for details on how the quantities shown in this figure were calculated.

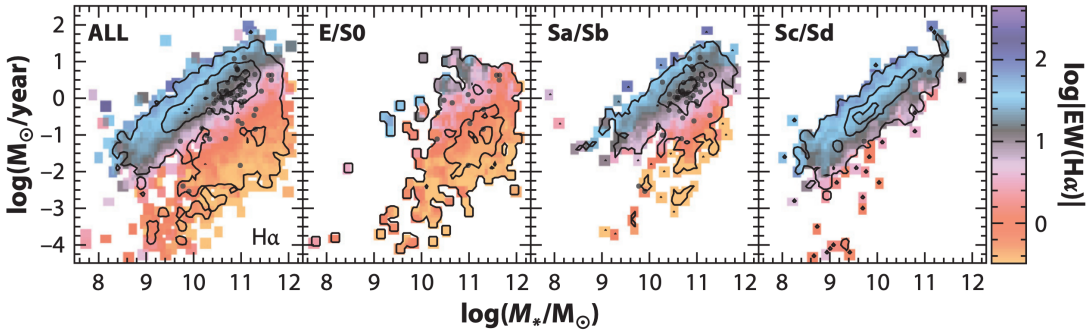

Figure 1.1: A plot of SFR versus M_* for local galaxies from Sánchez (2020). The first panel shows all of the galaxies in their sample. The next three panels show the samples split by morphological type. The galaxies are color coded by EW(Hα), an indicator of the ionization source. Star-forming galaxies — whether classified by their morphology or a high EW(Hα) form a line in this plot called the SFMS (e.g., last panel).

There are several populations of galaxies shown in Figure 1.1. Galaxies are not static in this diagram, and instead move around this parameter space as they grow, evolve, and interact. Galaxies which are still forming stars tend to form a line in this diagram, called the star forming main sequence (SFMS; e.g., Brinchmann et al., 2004; Whitaker et al., 2012; Renzini & Peng, 2015; Saintonge et al., 2017). The SFMS is most clearly seen in the right-most panel of Figure 1.1 which highlights the star-forming galaxies in the sample considered by Sánchez (2020). Star-forming galaxies tend to have blue optical colors, spiral-type morphologies, high cold gas fractions, and Hα equivalent widths (EW(Hα)) $>$ 6Å, meaning that the ionization is dominated by young OB-type stars with short lifetimes (e.g., Pozzetti et al., 2010; Sánchez et al., 2014; Lacerda et al., 2018). Galaxies well below this sequence are no longer forming stars and are referred to as "retired." These galaxies tend to have red optical colors, elliptical-type morphologies, low cold gas fractions, and EW(Hα)$<$ 6Å, meaning that the ionization is dominated by old stars (e.g., Faber

et al., 2007; Stasińska et al., 2008; Cid Fernandes et al., 2010; Lacerda et al., 2018). Between these galaxies is a transition region known as the "green valley" (e.g., Salim et al., 2007). Galaxies in this region are in the process of quenching, or shutting down their star formation activity, though precisely how this quenching proceeds is not definitively known and is the topic of current research (e.g., Colombo et al., 2020). There is also a population of galaxies that live above the SFMS, meaning they form more stars given their stellar masses than galaxies on the SFMS; these galaxies are know as "starbursts" (e.g., Weedman et al., 1981; Kennicutt & Evans, 2012). In many cases, the sites of the most intense star formation in these starburst galaxies are confined to the nucleus or circumnuclear rings.

The focus of this thesis will be on galaxies that are undergoing active star formation, and hence these galaxies will reside primarily along or above the SFMS at $z \sim 0$. Moreover, the galaxies considered here have metallicities consistent with solar metallicity.

The process of forming stars and the stellar life cycle impart energy and momentum into the surrounding galactic material called the interstellar medium (ISM). This so-called "feedback" can have important effects on the evolution of galaxies and helps regulate their growth over cosmic time. In these more distant galaxies, it is impossible to spatially resolve individual stars and difficult or impossible to resolve star clusters or supernova (SN) bubbles to determine the feedback they impart directly. Their effects, however, can be seen on the surrounding ISM, particularly by measuring how the kinematics of the ISM material are affected by this feedback.

This thesis investigates star formation feedback through measuring its effects

on the multiphase gas kinematics in the ISM of nearby galaxies. As a result, we have learned that stellar feedback has measurable and important effects in nearly all star forming galaxies in the local Universe.

In the remainder of this introductory section, I will briefly summarize the components and properties of the multiphase ISM relevant to this thesis (Section 1.1) and various modes and manifestations of stellar feedback (Section 1.2) as a function of environment. Finally, I will briefly review relevant technical aspects of radio interferometers and optical integral field spectroscopy (IFS) as they pertain to the data used in this thesis (Section 1.3).

Chapters 2 and 3 present the results of two published studies of a population of star-forming galaxies in the nearby Universe (Levy et al., 2018, 2019). By comparing the spatially-resolved kinematics of the molecular and ionized gas, I kinematically detect extraplanar diffuse ionized gas (eDIG) in the majority of the galaxies studied. This includes the first study of eDIG in a population of non-edge-on galaxies. eDIG is thought the be produced by repeated SN explosions. These studies show that eDIG and SN feedback are ubiquitous in star-forming galaxies.

In Chapter 4, I switch the focus to a single, starburst galaxy: NGC 253. This chapter presents a published study of the star star clusters (SSCs) powering the central starburst (Levy et al., 2021). I report the detection and characterization of stellar feedback-driven outflows from these SSCs seen in dense molecular gas tracers.

In Chapter 5, I investigate how the SSCs in the center of NGC 253 are related to the larger-scale gas flows fueling the nuclear starburst region. I find that the clusters may be morpho-kinematically consistent either with a nuclear ring or with

gas streams from the bar.

In Chapter 6, I briefly introduce future research directions building off of the work presented in this thesis.

1.1 The Multiphase ISM and its Tracers

The ISM is inherently multiphase (e.g., Field et al., 1969; McKee, 1995; Wolfire et al., 1995; Tielens, 2005; Draine, 2011; Tacconi et al., 2020). The gas exists in several phases* which are in pressure equilibrium with one another (e.g., Tielens, 2005). The different phases of the ISM can be traced by spectral observations of various ions, atoms, and molecules. These tracer particles are essential to our understanding of the ISM. The ability of a particle to trace a specific phase of the ISM is fundamentally related to its critical density ($n_{\rm crit}$) and radiative and collisional excitation properties. In the following background, I will focus on galaxies and the ISM at roughly solar metallicity, noting that the scenarios described here will differ at low metallicity (e.g., Bolatto et al., 2013b). In this section, I briefly summarize the properties and tracers of various phases of the ISM most relevant to this thesis, though I refer the reader to Draine (2011) for a review of all of the phases of the ISM.

1.1.1 The Molecular Medium

Stars form from cold ($T < 50$ K), dense ($n_{\rm H} > 10^3$ cm^{-3}) molecular gas (e.g., McKee & Ostriker, 2007; Draine, 2011, and references therein). Observations of

*The phase is described primarily by the temperature and density of the gas.

this phase are, therefore, crucial to understanding how stars form and affect their surroundings. The most abundant molecule in the Universe is molecular hydrogen (H_2). Because this molecule is symmetric, however, it does not have a permanent dipole and hence does not emit photons via dipolar rotational transitions (see e.g., Kennicutt & Evans, 2012; Bolatto et al., 2013b, for a brief review). The quadrupolar rotional transitions are weak and emit in the far-infrared (FIR), making them difficult to observe with current instruments. Moreover, the lowest quadrpolar transition has an energy of $E/k \approx 500$ K and is, therefore, only excited in relatively warm conditions (e.g., Dabrowski, 1984; Bolatto et al., 2013b). The lowest vibrational transition of H_2 occurs at $\lambda = 2.2$ μm with a corresponding energy of $E/k \sim 6500$ K. Thus the vibrational transitions of H_2 trace warm molecular gas, not the cold dense phrase from which stars form. The bulk component of the cold molecular gas is, therefore, almost completely invisible.

The second most abundant molecule is carbon monoxide ($^{12}C^{16}O$ hereafter CO). With a ground rotational transition of $E/k \approx 5.53$ K and a critical density of ~ 2200 cm^{-3}, the ground state rotational ($J = 1 - 0$) transition is easily excited in the conditions within molecular clouds (e.g., Draine, 2011; Bolatto et al., 2013b). Moreover, several of the low-J transitions of CO occur at submillimeter wavelengths, making them relatively easy to observe from the ground. Since the first observation of CO in the Galaxy by Wilson et al. (1970), it has become the main tracer of the molecular ISM. In Chapter 2, I will use CO $J = 1 - 0$ as the primary tracer of the bulk molecular gas in nearby galaxies.

The CO does not, however, perfectly trace the H_2. There are regions, par-

ticularly near the edges of molecular clouds or in photodisscoiation regions (PDRs; Hollenbach & Tielens 1997), where the carbon is primarily atomic or singly-ionized rather than in the CO molecule (e.g., van Dishoeck & Black, 1988). These regions still contain H_2 because it can self-shield (e.g., Draine, 2011; Bolatto et al., 2013b). This gas is often referred to as "CO-dark" molecular gas and is difficult to measure (e.g., Grenier et al., 2005; Bolatto et al., 2013b).

The molecular gas in a galaxy exists in several structures (in increasing order of density): diffuse molecular gas, (giant) molecular clouds, clumps, and cores. A few of these structures are illustrated in Figure 1.2. Clouds and filaments of neutral, atomic hydrogen (HI[†]) permeate the disks of star forming galaxies (e.g., Walter et al., 2008; Catinella et al., 2010; Peek et al., 2011). HI is found in two phases: a warm diffuse phase called the warm neutral medium (WNM; $T \lesssim 8000$ K, $n \sim 0.5$ cm^{-3}) and a colder denser phase called the cold neutral medium (CNM; $T \sim 70$ K, $n \sim 50$ cm^{-3}) (e.g., Dickey & Lockman, 1990; Wolfire et al., 1995; Heiles & Troland, 2003; Kalberla & Kerp, 2009). The CNM, however, is not sufficiently dense for stars to form directly from it, and observational trends between the surface densities of HI and the SFR show only very weak trends (e.g., Kennicutt, 1998). Instead, regions of WNM clouds collapse and cool, allowing CNM and molecular clouds to form (e.g., Vázquez-Semadeni et al., 2006).

Giant molecular clouds (GMCs) are hierarchical, self-gravitating objects con-

[†]The standard nomenclature of using roman numerals to specify the ionization state of an atom is used throughout this thesis. An atom followed by I is neutral (not ionized), whereas II refers to an atom which is singly-ionized, III refers to doubly-ionized, *et cetera*. Alternatively, an element symbol followed by ^{0} can also indicate that the atom is neutral (i.e., HI is the same as H^0). An atom (or molecule) followed by $^+$ indicates the atom is singly-ionized, $^{++}$ means doubly-ionized, *et cetera*. In this thesis, I will primarily use the roman numeral notation.

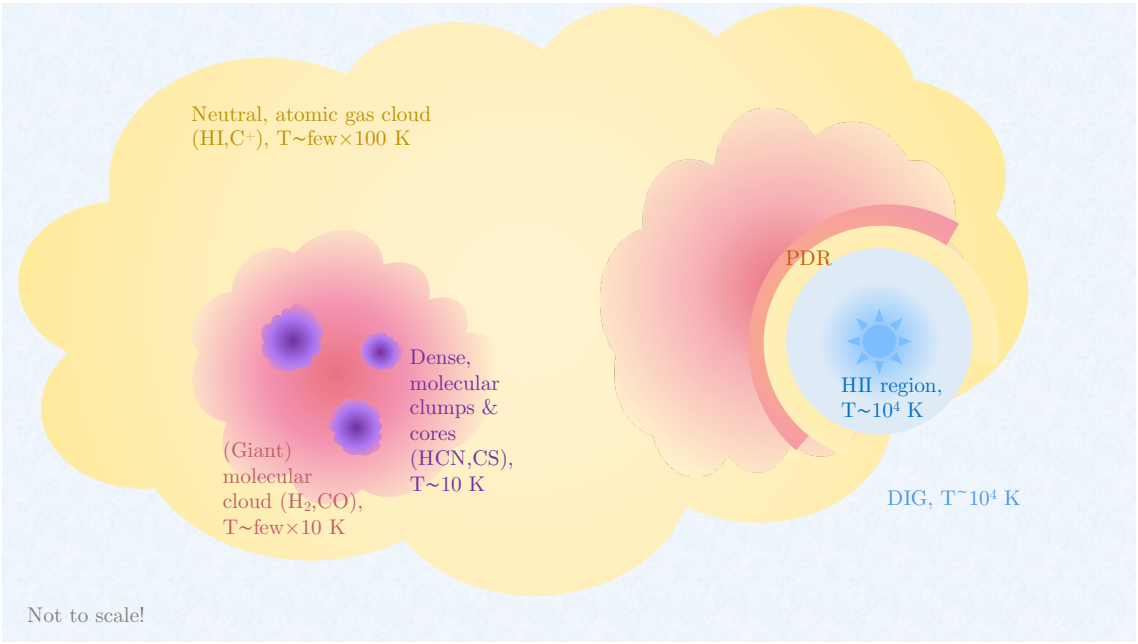

Figure 1.2: A schematic of a GMC and a PDR. The yellow regions show the cool neutral atomic gas (CNM), traced by HI and [CII], with temperatures of a few hundred K. Embedded within these atomic gas clouds are clouds of molecular gas (pink). As shown in the molecular cloud on the left, these clouds of molecular gas collapse under self-gravity and turbulence and fragment, such that the densest regions get denser. The densest regions form clumps and then cores (purple) where stars will eventually form. The right shows a cloud in which a massive star has formed. An HII region of ionized gas surround the massive star. Ionizing photons can leak out of the HII region, resulting in diffuse ionized gas (DIG) which permeates the galaxy. The HII region also impacts the natal molecular cloud, forming a PDR. Based in part on Pabst et al. (2019, Figure 3) and Draine (2011, Figure 31.2).

taining more than 10^4 $M_\odot$ of gas (e.g., McKee & Ostriker, 2007). The surrounding layers of atomic gas (and dust) shield the molecules from being dissociated by the interstellar UV radiation field (e.g., McKee & Ostriker, 2007). Guided by gravity, turbulence, and magnetic fields, high density regions within molecular clouds continue to fragment and collapse, forming even denser clumps (e.g., McKee & Ostriker, 2007). The densest regions of these clumps where the stars actually form are sometimes called cores. Because CO is easily excited, it is almost always optically thick (e.g., Bolatto et al., 2013b), and hence observations of CO cannot probe the very densest regions where stars are formed. Other molecules with higher critical densities, which therefore remain more optically thin, are necessary to trace these densest regions of molecular clouds. Low- to mid-J transitions of hydrogen cyanide (HCN), formylium (HCO^+), and carbon monosulfide (CS) are commonly used tracers of dense molecular gas. In their seminal paper, Gao & Solomon (2004) showed a strong correlation between the dense molecular gas (traced by HCN) and the SFR (see also Gallagher et al., 2018a,b). In addition, rarer molecular isotopologues[‡] are usually (but not always) optically thin; commonly used isotopologues include ^{13}CO, C^{18}O, and H^{13}CN, for example. Because they are less abundant than the main molecule, however, their emission is weak. For example, the abundances (which are directly related to the column density and hence the intensity of the observed emission) of ^{12}CO/^{13}CO and HCN/H^{13}CN depend primarily on the abundance ratio of ^{12}C/^{13}C, which is $\approx 45-70$ (e.g., van Dishoeck & Black, 1988; Bolatto et al., 2013b).

[‡]An isotopologue is where at least one of the elements in the molecule is an isotope, meaning that element has a different number of neutrons than the most common version of that element. Some common astrophysical examples of isotopes are ^{13}C instead of ^{12}C, ^{15}N instead of ^{14}N, and ^{18}O instead of ^{16}O.

$C^{18}O$ is even less abundant, with $C^{16}O/C^{18}O \sim 500$ (van Dishoeck & Black, 1988). In Chapter 4, I will primarily use observations of the CS $J = 7 - 6$ and $H^{13}CN$ $J = 4 - 3$ lines to trace the very dense molecular gas towards the still-forming sites of very massive "super" star clusters.

1.1.2 The Ionized Medium

Once a star is formed, it emits photons across the electromagnetic spectrum. Photons with energy above 13.6 eV ($\lambda = 912$ Å) can ionize HI, creating HII. Assuming a perfect blackbody, $> 10\%$ of the emitted photons will have energies > 13.6 eV for stars with temperatures $> 24,000$ K corresponding to to a B-type star (Figure 1.3). Even hotter O-type stars will fully ionize all of the H in the region. Other atoms, such as He, C[§], N, O, and S, may be singly- or more highly ionized (e.g., Osterbrock, 1989; Draine, 2011). Thus a massive star will rapidly ionized the region surrounding it within some radius, which is called an HII region. Because HII regions are photoionized by massive OB stars, which have very short lifetimes, they are tracers of recent ($t \sim 3 - 10$ Myr) star formation activity (e.g., Hao et al., 2011; Murphy et al., 2011; Kennicutt & Evans, 2012; Flores Velázquez et al., 2021).

Some of the main tracers of HII regions come from electronic transitions of hydrogen. Many transitions in the Balmer series (transitions to the $n = 2$ level), in particular, are used because they are bright and emit at optical wavelengths. The workhorse transition is Hα ($n = 3 - 2$) with a rest wavelength of 6562.68 Å.

[§]I note that singly-ionized carbon ([CII]) is a special case, since C can be singly-ionized in conditions present in the molecular, atomic, and ionized media (e.g., Madden et al., 1993; Heiles, 1994; Pineda et al., 2013).

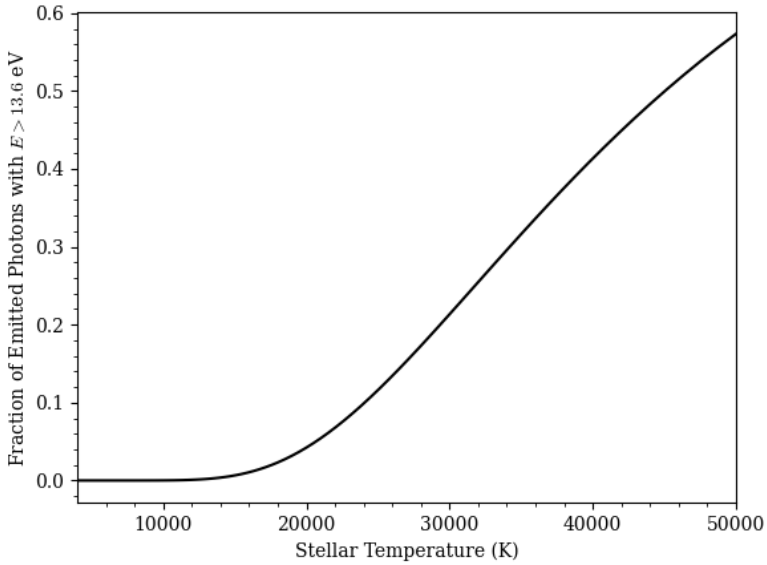

Figure 1.3: The fraction of ionizing ($E > 13.6$ eV) versus total emission from stars as a function of temperature assuming perfect Blackbody radiation.

Transitions in the Paschen series, such as Pa$-\alpha$ ($n = 4 - 3$) at 1.87 μm, are also frequently used. At longer wavelengths, radio recombination lines (RRLs) of hydrogen emitting at at frequencies above $\sim$ 10 GHz are used to trace ionized gas in HII regions and PDRs (e.g., Emig, 2021, and references therein).

In reality, HII regions leak. Ionizing photons to escape and permeate the galaxy up to $\sim$kpc distances from the leaking HII region by taking advantage of chimneys and lines-of-sight with little neutral gas created by past feedback (e.g., Reynolds et al., 2001; Madsen et al., 2006; Haffner et al., 2009). This produces a background of diffuse ($n \sim 0.1$ cm^{-3}) ionized gas (DIG), which is also called the warm ionized medium (WIM), as illustrated in Figure 1.2 (see e.g., Haffner et al., 2009, for a review). This component is a non-negligible fraction of the ionized gas in a galaxy, with a volume filling fraction of $\sim$0.25 and contributes $\gtrsim$50% of the Hα

luminosity (e.g., Reynolds, 1993; Veilleux et al., 1995; Zurita et al., 2000; Haffner et al., 2009; Poetrodjojo et al., 2019). The DIG is primarily traced by Hα, [NII], and [SII], as well as RRLs emitting from $\sim 0.3 - 10$ GHz (e.g., Haffner et al., 2009; Emig, 2021). It has elevated [SII]/Hα and [NII]/Hα ratios compared to HII regions, hinting at an additional ionization source beyond photons leaking from HII regions (e.g., Haffner et al., 2009, and references therein).

As discussed in the following section, DIG can also travel out of the disk midplane through channels along the minor axis cleared by SN explosions. This extraplanar DIG (eDIG) can exist in a quasi-steady state, forming a thick disk of ionized gas (e.g. Shapiro & Field, 1976; Bregman, 1980). eDIG at larger heights from the midplane rotates more slowly and is observed to "lag behind" the disk (e.g., Miller & Veilleux, 2003b; Barnabè et al., 2006; Heald et al., 2006a,b, 2007; Haffner et al., 2009; Marinacci et al., 2010, 2011; Bizyaev et al., 2017; Levy et al., 2019). This "lag" is a key characteristic of eDIG. In Chapters 2 and 3, I use observations of Hα and other ionized gas lines to kinematically identify and measure the properties of eDIG in a sample of nearby galaxies. The properties, observations, and modeling of (e)DIG will be discussed further in those chapters.

1.2 Stellar Feedback

Feedback describes the energy and momentum input into a system as a result of some physical process. In the context of this thesis, the process of forming stars and the stellar life cycle feeds back into the surrounding ISM and environment.

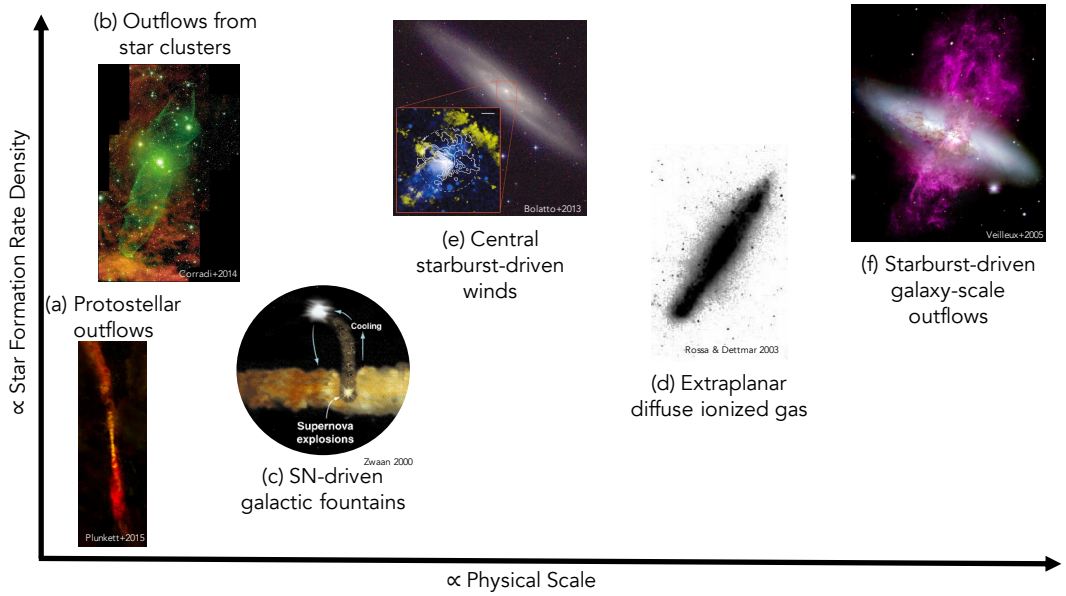

Figure 1.4: A schematic showing examples of observable manifestations of stellar feedback, relatively ordered by the physical scale over which they operate on the x-axis and the relative necessary star formation rate density on the y-axis. Examples are (a) protostellar outflows (image from Plunkett et al., 2015), (b) outflows from star clusters (image from Corradi et al., 2014), (c) SN-driven galactic chimneys and fountains (image from Zwaan, 2000), (d) extraplanar diffuse ionized gas (image from Rossa & Dettmar, 2003a), (e) central starburst-driven winds (image from Bolatto et al., 2013a), and (f) galaxy-scale starburst-driven outflows (image from Veilleux et al., 2005).

Active galactic nuclei (AGN) can also inject energy and momentum into the ISM, but this thesis focuses on stellar (or star formation) feedback.

Figure 1.4 shows several observable manifestations of stellar feedback, including protostellar outflows, outflows from clusters of stars, SN driven galactic fountains, central starburst-driven winds, extraplanar diffuse ionized gas, and galaxy-scale starburst-driven outflows. These examples are ordered along the abscissa by the relative physical scale over which each process operates or over which its effects are apparent. The ordinate shows the relative star formation rate density necessary for stellar feedback to result in the given manifestation.

On the smallest scales, bipolar outflows from the formation of protostars can disrupt their parent molecular clouds with jets spanning up to $\sim$ 10 pc in (projected) length (e.g., Bally, 2016, and panel (a) of Figure 1.4). At higher densities of star formation, a larger fraction of stars are formed in clusters (e.g., Lada & Lada, 2003; Kruijssen, 2012). Outflows from many protostars can combine to produce more massive, conglomerate outflows (e.g., Corradi et al., 2014, and panel (b) of Figure 1.4). In addition to (and more energetically important than) the combined effects of protostellar outflows, several processes during and after the main-sequence lifetimes of massive stars can also drive outflows from clusters. As we will discuss in Chapter 4, these mechanisms (such as stellar winds, radiation pressure, and SNe) can drive very massive outflows from "super" star clusters which can contain $\gtrsim$1000 O-type stars.

At the end of their stellar lifetimes, massive stars may explode as SNe, releasing huge amounts of energy and momentum into the surrounding material (e.g., Kim & Ostriker, 2015). If these SNe are clustered (in space and time), they may be able to punch holes in the disk midplane (e.g., Shapiro & Field, 1976; Bregman, 1980; Zwaan, 2000). This provides a low density channel (a "chimney") for gas and ionizing radiation to escape from the disk midplane into the halo. If the escape velocity of this material is relatively low or if other drag forces are important, it can "rain" back down on the disk as a galactic fountain (e.g., Shapiro & Field, 1976; Bregman, 1980; Zwaan, 2000, and panel (c) of Figure 1.4). Enough material is continually flowing into the galactic halo to support a thick extraplanar disk if the average surface density of star formation over the disk exceeds $\approx 1.4 \times 10^{-3}$ $M_\odot$ yr^{-1} kpc^{-2}

(Rossa & Dettmar, 2003a), where this limit is calculated within D_{25}, the diameter of the 25th mag arcsec^{-2} isophote. Such extraplanar thick disks have been observed in HI (e.g. Swaters et al., 1997; Fraternali et al., 2002, 2005; Zschaechner et al., 2015; Zschaechner & Rand, 2015), diffuse ionized gas (e.g., Dettmar, 1990; Rand et al., 1990; Rossa & Dettmar, 2003a,b; Miller & Veilleux, 2003a,b; Bizyaev et al., 2017; Levy et al., 2018, 2019, and panel (e) of Figure 1.4), and dust (e.g., Howk & Savage, 1997, 1999; Howk, 1999). The properties, kinematics, scale heights, ionization, and origin of eDIG will be discussed further in Chapters 2 and 3.

In galaxies undergoing a starburst, the sheer number and clustering of SNe can drive massive, multiphase winds and outflows perpendicular to the disk midplane (e.g., Veilleux et al., 2005, 2020). In Figure 1.4, we show two examples. Panel (e) shows the multiphase wind from the center of NGC 253 (e.g., Bolatto et al., 2013a) whereas panel (f) shows the larger galaxy-scale wind from M 82 (e.g., Veilleux et al., 2005). Whether the material in these winds escapes into the circumgalatic medium or rains back down in to the galaxy in a galactic fountain depends on the velocity of the outflow relative to the escape velocity of the galaxy and other drag forces (e.g., Veilleux et al., 2005, 2020; Martini et al., 2018). While these massive outflows rid the central regions of the galaxies of gas (negative feedback), material that rains back down onto the disk may fuel a future generation of star formation (positive feedback).

In this thesis, I will focus on eDIG (Chapters 2 and 3) and outflows from (super) star clusters (Chapter 4). I also explore how the star formation contained in the super stars clusters in the center of NGC 253 may be fueled by gas inflows from

the bar (Chapter 5). Future work related to starburst-driven winds and outflows are briefly described in Chapter 6. The relevant physical processes that can lead to each of these observable phenomena are described in the analysis presented in the aforementioned chapters. We refer the reader to reviews by Veilleux et al. (2005, 2020) and Zhang (2018) for a summaries of many of the possible mechanisms responsible for injecting energy and momentum from star formation into the ISM.

1.3 Interferometers and IFUs

Spectroscopy yields information about the intensity, velocity, and velocity dispersion of the tracer particle. By observing spectral lines with known rest-frequencies, the Doppler effect allows us to measure the velocity of the medium from which those spectral lines are emitted. The measured width of the spectral line is related to the dispersion of the velocity within the resolution element (modulo the intrinsic line shape set by the Heisenberg uncertainty principle and instrumental effects).

The key data presented in this thesis come from two categories of instrumentation. The submillimeter data come from two interferometers: the Combined Array for Millimeter wave Astronomy (CARMA; Chapters 2 and 3) and the Atacama Large Millimeter/submillimeter Array (ALMA; Chapters 4 and 5). The optical data used in Chapters 2 and 3 come from the PPaK integral field unit (IFU) on the Calar Alto Observatory 3.5 m telescope. Here I will briefly describe how these types of instruments work and the data products they generate.

1.3.1 Interferometers at Radio and Submillimeter Wavelengths

This section presents a top-level description of radio interferometers and imaging. For more detailed information, I point interested readers to excellent resources by Condon & Ransom (2016), Thompson et al. (2017), and the National Radio Astronomy Observatory Synthesis Imaging Workshops[¶] upon which the information in this section is heavily based.

1.3.1.1 Basics of Interferometry

The angular resolution of any telescope, θ is related to the wavelength of the observation (λ) and the diameter of the aperture (D): $\theta \approx \lambda/D$. This means that at long wavelengths, larger apertures are needed to obtain the same angular resolution as at shorter wavelengths. The 100 m Green Bank Telescope (GBT), for example, is the largest fully-steerable single-dish radio telescope in the world. The GBT is so large that the dish surface distorts under its own weight and must be modeled and corrected while observations are being taken. Although the GBT is an impressive feat of engineering, it can only reach angular resolutions of $\sim 5''$ at the highest frequencies it can observe[‖]. Other single-dish radio telescopes such as the Arecibo Observatory and the Five-hundred-meter Aperture Spherical Telescope are larger (with diameters of 300 m and 500 m respectively), but the field of view (FOV) over which they can observe is limited because they are not fully movable. Aside from the

[¶] `https://science.nrao.edu/science/meetings/2016/15th-synthesis-imaging-workshop/`

[‖] This is used as a motivating example, as the precise angular resolution also depends on the aperture efficiency and other factors.

technical challenges of building larger single-dish telescopes (fully-steerable or not), the cost in building and maintaining these facilities is immense and intractable. To push to sub-arcsecond angular resolution at radio and submillimeter wavelengths, another method must be used.

One solution to achieve higher angular resolution is to use an interferometer. The simplest interferometer consists of two receivers separated by a baseline length B. The angular resolution of an interferometer is set by the baseline length: $\theta \approx \lambda/B$. An interferometer, therefore, approximates a single-dish telescope with diameter B, but with many "holes" in the dish. In this way, an interferometer can achieve much higher angular resolutions than a standard single-dish telescope because the antennas can be moved far apart without needing to fill in the gaps. The sacrifice of these gaps, however, is reduced surface brightness sensitivity and other artifacts, which will be discussed later in this section.

A schematic of a two-element, quasi-monochromatic interferometer is shown in Figure 1.5, which is adapted from Condon & Ransom (2016). It is convenient to define a coordinate system relative to the antenna positions. The basis vectors of this coordinate system are typically called $\hat{u}$, $\hat{v}$, and $\hat{w}$, where $\hat{u}$ points east, $\hat{v}$ points north, and $\hat{w}$ is normal to the plane formed by $\hat{u}$ and $\hat{v}$ (called the uv-plane). The baseline between the antennas is a vector is this coordinate system ($\vec{b}$) where $B = |\vec{b}|$.

The separation between the antennas introduces a geometric time delay (τ_g) in the time-dependent signal received at each antenna. For a plane-parallel wave arriving at the antennas along a line of sight to the source $\hat{s}$, $\tau_g = \frac{\vec{b}\cdot\hat{s}}{c}$. For an

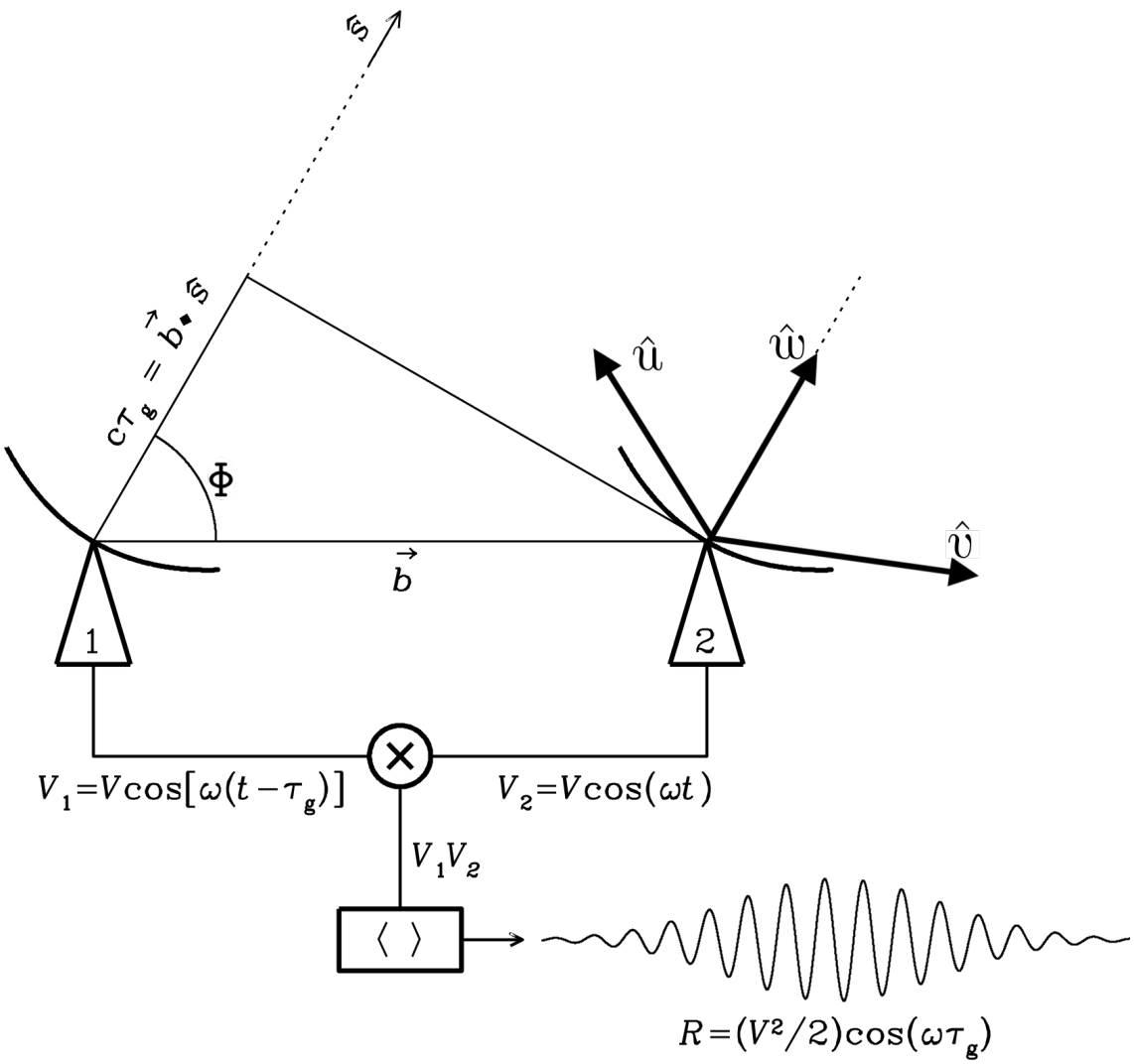

Figure 1.5: A schematic of a two-element quasi-monochromatic multiplying interferometer (adapted from Figure 3.41 of Condon & Ransom, 2016). The two antennas are separated by a baseline vector $\vec{b}$. This vector is a vector in (u, v, w) coordinates, which are illustrated above antenna 2 for the case of $\hat{w} \parallel \hat{s}$, where $\hat{s}$ is the line of sight to the source. A plane parallel wave arrives at the antennas along $\hat{s}$ with an angle Φ with respect to $\vec{b}$. The geometric time delay between the antennas is $\tau_g = \frac{\vec{b} \cdot \hat{s}}{c}$. The output voltage of the antennas is time-dependent (as given by V_1 and V_2), though the amplitudes V are the same. The correlator multiplies ($\otimes$) and time-averages ($\langle\ \rangle$) the signal from the antennas, yielding an output response R that only depends on the source flux density ($\propto V^2$), the time delay (τ_g), and the angular frequency at which the observation is taken ($\omega = 2\pi\nu$).

interferometer operating over a narrow range of frequencies (quasi-monochromatic), the output voltage from each antenna will be the same but offset in phase by τ_g.

The correlator combines the signal from the antennas. The output from the correlator is called the response, R. Because there is a time delay between the antennas, R is an interference pattern ("fringe") described by an amplitude and a phase, as illustrated in Figure 1.5. Moreover, R only depends on the time delay (τ_g), the angular frequency of the observation ($\omega = 2\pi\nu$), and the intrinsic source flux density ($I_\nu \propto V^2$).

In practice, there are a few ways for the correlator to combine the signal from the antennas. For a simple multiplying (cosine) correlator, such as the schematic in Figure 1.5, the signal from the antennas is multiplied and time-averaged. A cosine correlator works for point sources. For extended sources, which have both symmetric (even) and asymmetric (odd) components of their brightness distributions, a sine correlator must be added into the network following a 90° phase delay to recover the asymmetric components. It is convenient to treat sums of sines and cosines as a complex exponential, and hence a combined cosine and sine correlator is called a complex correlator. The complex correlator response is called a visibility, $\mathcal{V}$.

The visibilities produced from an interferometer with a complex correlator are measured in the (u, v, w) coordinate frame. The source brightness distribution as a function of frequency, I_ν, that we are trying to measure, however, is in the "image" plane (x, y). If $\hat{w} \parallel \hat{s}$ (as in Figure 1.5), then the visibilities in the uv-plane can be transformed into a brightness distribution in the image plane via a Fourier

transform:

$$I_\nu(x,y) = \int\int \mathcal{V}(u,v) e^{2\pi i(ux+vy)} du dv \tag{1.1}$$

(e.g. Condon & Ransom, 2016). By virtue of this relationship between the visibility and image planes, interferometers are spatial filters. Long baselines are sensitive to high spatial frequencies (high pass filters) and so only pick up on sharp structures in the source; short baselines, on the other hand, are sensitive to low spatial frequencies (low pass filter) and pick up smooth, more diffuse features in the source**. An extended astrophysical object—such as a galaxy or molecular cloud—contains information and signal on many spatial scales. Therefore, to properly sample and recover the source with an interferometer, antennas must be distributed such that the baseline pairs recover as many spatial scales as possible. For an interferometer with N antennas, there will be $N(N-1)/2$ antenna pairs and therefore $N(N-1)$ baselines or individual points in the uv-plane per integration time. Long observations also help populate the uv-plane, as shown in Figure 1.6, since the uv-plane rotates relative to the image plane with the Earth's rotation. The minimum spatial scale (the so-called zero-spacing) is always missing from an interferometric image since there is a minimum distance by which the antennas can be physically separated (roughly the dish diameter). This can be seen in Figure 1.6 as the hole in the center of the uv coverage. Therefore, interferometers always miss some of the large scale emission, and the flux in an interferometric image is always less than the intrinsic source flux (e.g., Bajaja & van Albada, 1979; Stanimirovic, 2002). In addition, the

**In the aphorismatic words of Professor Andy Harris, "Small is big, and big is small."

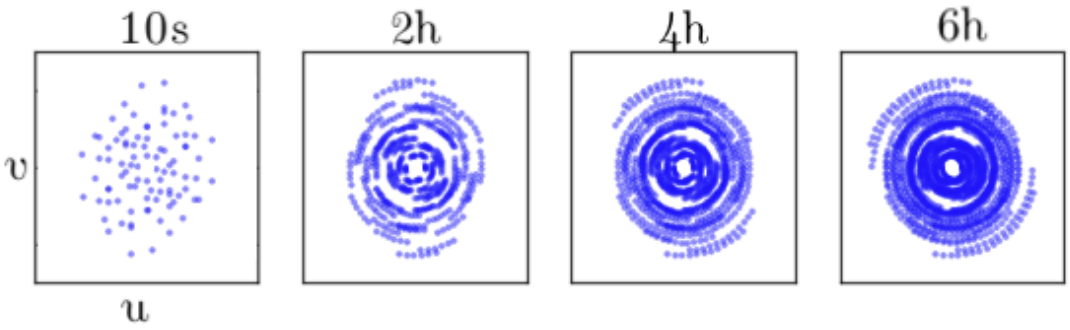

Figure 1.6: An example of the uv coverage for a 10-element interferometer, adapted from Avison & George (2013). Each blue point shows the uv location of one of the baselines. The panels show how the pattern rotates with the Earth's rotation over time, thus filling in the uv-plane. Better uv coverage results in better surface brightness sensitivity. This also illustrates the central hole in the uv coverage due to the missing short- and zero-spacings.

mean of an interferometric image is zero.

For interferometers with more than two elements, the signal from each pair of antennas must be multiplied and averaged with the correct relative time delay. Moreover, observations are rarely taken at a single frequency but over some wide bandwidth. For this reason, correlators for modern interferometers—such as ALMA which consists of 66 antennas and has an instantaneous bandwidth of 8 GHz—are supercomputers. The ALMA correlator can perform up to 1.7×10^{16} correlations per second (Escoffier et al., 2007).

1.3.1.2 Imaging and Deconvolution

When an interferometer measures the source brightness distribution, the source signal is convolved with the point spread function (PSF) of the interferometer ($s(x, y) \xrightarrow{\mathcal{F}} S(u, v)$, where $\xrightarrow{\mathcal{F}}$ denotes a Fourier transform). Therefore, when the visibilities are Fourier transformed to obtain the source image, the PSF pattern

is imprinted in the image. In other words, the "dirty image" ($I^D(x,y)$) produced by Equation 1.1 is the true image convolved with the PSF (often called the "dirty beam"): $\mathcal{V}(u,v)S(u,v) \xrightarrow{\mathcal{F}} I^D(x,y) = I(x,y) * s(x,y)$[††]. To accurately measure the intrinsic source brightness distribution $I(x,y)$, this PSF pattern should be removed.

This deconvolution process to remove the PSF from the dirty image is a non-linear and iterative process. For point sources and other simple, symmetric structures, this deconvolution can be performed in the visibility domain. For the complicated sources in this thesis, however, the deconvolution is done in the image plane.

The classic deconvolution algorithm is `clean` (e.g., Högbom, 1974). The basic idea of this algorithm—which remains the basis for many more modern algorithms—is to assume that $I(x,y)$ is a collection of point sources. This process is iterative and consists of an outer major cycle and an inner minor cycle. During the minor cycle, the algorithm finds the maximum pixel in the image. The value of this pixel is multiplied by $s(x,y)$ (with some gain $\ll 1$) and subtracted from the image. This version of the image with the "cleaned" components removed is the residual image. The amplitude and location of the cleaned component are stored in a (point source) model representation of the source. During the major cycle, the model image is Fourier transformed, and the model visibilties are subtracted from $\mathcal{V}(u,v)$. The residual visibilties are Fourier transformed back to form a new residual image. These major and minor cycles are repeated until some threshold is reached in the residual image, ensuring that $I(x,y)$ is recovered above some flux density level. The "clean

[††]All of these quantities are, in principle, a function of frequency ν, though here I have dropped that subscript for clarity.

beam" is an elliptical Gaussian fit to the main lobe of the PSF. The reported beam size usually refers to the major and minor axis full-width-half-maximum (FWHM) of this Gaussian ($\theta_{\rm maj}$ and $\theta_{\rm min}$), where the beam area $\Omega = \frac{\theta_{\rm maj}\theta_{\rm min}}{4\ln 2}$. The final "restored" image is made by convolving the model image containing the cleaned components with the clean beam and adding the residual image (which contains noise and structure below the specified threshold). For spectral data ($I_\nu(x,y)$) this process is repeated for each spectral channel along the frequency axis. In general, the PSF also changes as a function of frequency ($s_\nu(x,y)$). The final result of "cleaning" is an image of $I_\nu(x,y)$ (with noise) where the structure of the PSF is removed per frequency channel.

Other deconvolution and imaging methods exist besides the classic Hogbom `clean` algorithm. One such extension of the classic algorithm is "multiscale" clean (Cornwell, 2008), which is especially efficient for extended sources (e.g., Rich et al., 2008). While the classic Hogbom algorithm will work for extended sources, it can be slow as modeling an extended object as a collection of point sources is inefficient. In multiscale clean, multiple scalings of the PSF are removed from at the locations of the clean components. These `scales` are specified by the user. In this way, more extended emission is removed at each iteration owing to the (larger) scaled PSF.

1.3.2 Integral Field Spectroscopy

This section gives a top-level overview of integral field spectroscopy (IFS) and integral field units (IFU). For more detailed information, I point interested readers

to a review by Bershady (2009). For specifics of IFS galaxy studies, I point the reader to Appendix A of Sánchez (2020). Much of the information presented in this section is based on these references.

Integral field spectroscopy is a subset of "3D spectroscopy" in which spectral information is obtained simultaneously within some FOV visible to the telescope. This is in contrast to more classical slit spectroscopy, for example, where a spectrum is produced only over the region of the sky that lies within the slit. There are several types of IFS, but I will focus here on fiber-bundle IFS, since the CALIFA data used in this thesis are obtained with this method (e.g., Sánchez et al., 2012). In this method, which is illustrated schematically in Figure 1.7, a collection of spectroscopic fibers are used to link the telescope FOV to the spectrograph. First an array of microlenes guides the light from the telescope into each fiber and then onto the spectrograph's slit. The fibers are usually packed in a hexagonal pattern which allows for optimal dense packing of the round fibers. There will still be gaps between the fibers, however, which will result in gaps in the IFU's coverage of the FOV. A dither pattern can be used to fill in the gaps and completely sample the FOV. In the case of CALIFA, a three-point dither is used, meaning the same FOV is observed three times with a small pointing offset to fill the gaps between the fibers (Sánchez et al., 2012).

Once the spectra are observed with the IFU, there are a number of calibration steps which are described in detail by Sánchez et al. (2016b). These include the wavelength calibration (necessary to determine the correct scale of the spectral axis), correcting for fiber-to-fiber transmission, removing the sky spectrum, performing the

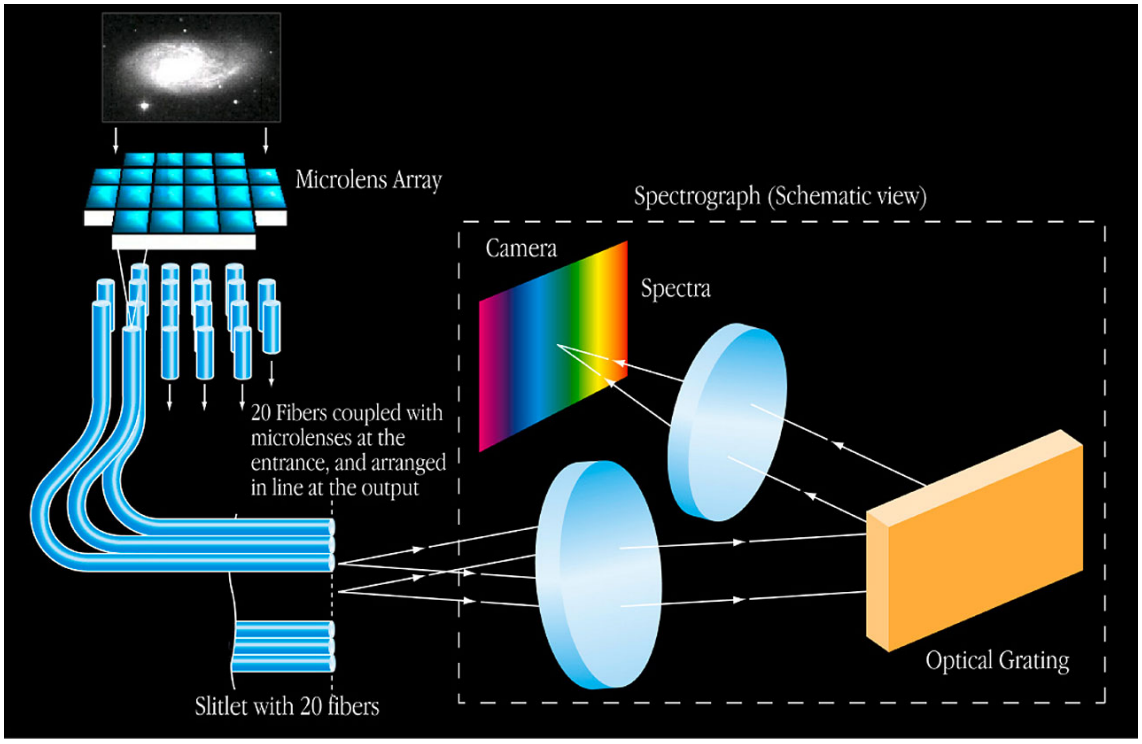

Figure 1.7: A schematic illustration of a fiber-bundle IFU. Image credit: European Southern Observatory.

flux calibration, and gridding the spectra such that the pixels are regularly sampled. The wavelength calibration for CALIFA will be described in more detail in Section 2.2.2. The post-calibration result from IFS is a 3D image with regular spatial and wavelength sampling, where each spatial pixel contains a spectrum at that location within the source.

1.3.3 3D Data Cubes and 2D Representations

The resulting data format from either IFS or a deconvolved interferometric image is a three-dimensional image called a "data cube," which has two spatial dimensions (x, y) and one spectral (frequency ν, wavelength λ, or velocity v[‡‡]) di-

[‡‡]Please see Appendix A.1 for conversions from frequency (or wavelength) to various velocity conventions. I note in particular that radio and optical astronomers use different velocity conven-

mension (e.g., Oosterloo, 1995). One way of thinking about a data cube is that it contains a 2D image of the source at every spectral channel. Another way is that a data cube contains a spectrum at every pixel. Sometimes, 2D spatial pixels are called "spaxels;" each spaxel in a data cube contains a spectrum. Individual volume elements within the data cube are called sometimes called "voxels." Each voxel in a data cube is usually a measure of the flux density I_ν. Radio data cubes often have data units of Jy beam^{-1}, whereas optical data cubes often have units of erg s^{-1} cm^{-2} Å^{-1} sr^{-1}.

Two-dimensional representations of the data can be derived by taking "moments" of the data cube around each spectral line of interest, where the n^{th} moment at each spaxel is defined as

$$\mathcal{M}_n(x,y) = \frac{1}{N}\sum_{i=1}^{N}\left[I(x,y,i) - \bar{I}(x,y)\right]^n \tag{1.2}$$

where $\bar{I}(x,y) = \frac{1}{N}\sum_{i=1}^{N} I(x,y,i)$ is the mean flux density and N is the number of channels along the spectral axis. The 0^{th} moment is the velocity-integrated intensity: $\mathcal{M}_0(x,y) = \Delta v \sum_{i=1}^{N} I(x,y,i)$. The 1^{st} moment is the intensity-weighted (mean) velocity: $\mathcal{M}_1(x,y) = \frac{\sum_{i=1}^{N} vI(x,y,i)}{\sum_{i=1}^{N} I(x,y,i)}$. The spectral line width can be calculated from the 2^{nd} moment: $\mathcal{M}_2(x,y) = \sqrt{\frac{\sum_{i=1}^{N}(v-\mathcal{M}_1)^2 I(x,y,i)}{\sum_{i=1}^{N} I(x,y,i)}}$.

The equivalent width (EW) of a spectral line is a normalized version of the line profile and is the width (usually in Å) of a boxcar line profile that has the same integrated flux and the true line profile: $\mathrm{EW}(x,y) = \int(1 - I_\lambda(x,y)/I_0(x,y))d\lambda$

tions.

where I_0 is the continuum level. For emission lines, the EW is formally negative, though the absolute value is used in practice.

For highly inclined systems, the spectral line profiles may become skewed, meaning that the mean velocity may underestimate the true velocity centroid. In this case, the "peak velocity" may be a better measure of the true velocity, where the peak velocity is the velocity of the channel corresponding to the peak intensity. The peak intensity is $I_{\rm peak}(x,y) = \max_i \left[I(x,y,i)\right]$. The spectral resolution of the peak velocity is limited by the channel width.

An alternate method to determine the 2D intensity, velocity, and linewidth is to fit the spectrum at each spaxel with a Gaussian line profile. This is especially useful when velocities of the atoms, ions, or molecules are due to thermal motions, in which case the Doppler broadened line profile shape is approximately Gaussian (e.g., Draine, 2011) and when there is only a single velocity component of the gas captured in the resolution element (PSF or beam). In this case, at each pixel, we can fit a Gaussian of the form:

$$\mathcal{G}(v) = I_{\rm peak} e^{-\frac{(v-v_0)^2}{2\sigma^2}} \tag{1.3}$$

where $I_{\rm peak}$ is the peak intensity, v_0 is the velocity centroid of the line, and σ is the Gaussian line width. Because a Gaussian is fit at every pixel, this results in 2D maps of the intensity $I_{\rm peak}(x,y)$, velocity $v_0(x,y)$, and linewidth $\sigma(x,y)$. Sometimes line widths from Gaussian fits are expressed in terms of the FWHM, where FWHM $\approx 2.355\sigma$. The integrated intensity can also be obtained from the Gaussian fit as

$I_{\rm peak}\sqrt{2\pi\sigma^2}$.

For the CALIFA IFS data, a few additional analysis steps are required to produce 2D images of the emission lines, as described by Sánchez et al. (2016b,c). First, the stellar contribution is removed from the spectra using models of a simple stellar population. This includes the stellar continuum as well as stellar emission and absorption lines. The spectral line intensity, velocity, and linewidth are then extracted using an optimal extraction method that is similar to the moment analysis described above but which is optimized for weak lines. This method will be described in more detail in Section 2.2.2.

Chapter 2: Extraplanar Diffuse Ionized Gas in Intermediate Inclination Galaxies

2.1 Introduction

Studying the molecular and ionized gas components of a galaxy gives powerful insights into various stages of star formation. The gas kinematics can reveal feedback mechanisms, such as inflows and outflows, and merger events which alter the star formation history (SFH) of the galaxy. The measurement of molecular kinematics of galaxies, as traced by ^{12}CO, has vastly improved in recent years due to the advent of interferometers which allow for high spatial and spectral resolution measurements. Similar advances have been made in the optical regime through the use of integral field units (IFUs). Studying the multiwavelength kinematic properties of nearby galaxies provides information about their formation, SFH, and evolution.

The multi-wavelength kinematics of disk galaxies have been compared in a number of case studies. Wong et al. (2004), Yim et al. (2014), and Frank et al. (2016) compare HI and CO kinematics and generally find good agreement between the rotation velocities of the atomic and molecular components. However, comparisons with the ionized gas often lead to different results. Most notably is NGC 891,

which shows vertical gradients in the rotation velocity ("lags") in HI of -10 – -20 $\mathrm{km\,s^{-1}\,kpc^{-1}}$ (Swaters et al., 1997; Fraternali et al., 2005) and in ionized gas of -15 $\mathrm{km\,s^{-1}\,kpc^{-1}}$(Heald et al., 2006a). Similar lags in Hα and HI are seen in NGC 5775 (Lee et al., 2001), where the CO and Hα rotation velocities agree in the midplane (Heald et al., 2006b). However, lags between the HI and Hα do not always agree (Fraternali et al., 2004, 2005; Zschaechner et al., 2015; Zschaechner & Rand, 2015). de Blok et al. (2016) study the CO, HI, and [CII] kinematics in ten nearby galaxies and find that the [CII] velocity is systematically larger than that of the CO or HI, although they attribute this is systematics in the data reduction and the low velocity resolution of the [CII] data. Simon et al. (2005) compare CO and Hα rotation curves in two disk galaxies: in NGC 5963, the CO and Hα velocities agree to within 1 $\mathrm{km\,s^{-1}}$, but the Hα in NGC 4605 shows systematically slower rotation than the CO by 4.8 $\mathrm{km\,s^{-1}}$. Clearly, comparisons among tracers of the different phases of the interstellar medium (ISM) are complicated. Large, homogeneous samples of galaxies in multiple tracers are needed to make headway towards understanding the causes and ubiquity of the kinematic differences between ISM phases.

Davis et al. (2013) studied the properties of 24 gas-rich early type galaxies from the ATLAS^{3D} survey by comparing the ionized, atomic, and molecular gas kinematics out to $\sim$0.5 R_e. They find that 80% of their sample show faster molecular gas rotation velocities than the ionized gas. The other 20% have the same molecular and ionized gas rotation velocities. They attribute these rotation velocity differences to the velocity dispersion of the ionized gas. Therefore, the dynamically cold molecular gas is a better tracer of the circular velocity than the ionized gas. Such a study has

yet to be carried out in a similar sample of star-forming disk galaxies.

One way to study the kinematics of a galaxy is through its rotation curve, the rotation velocity as a function of galactocentric radius. The velocity can be decomposed into rotational, radial, and higher order terms (e.g. Begeman, 1989; Schoenmakers, 1999; van de Ven & Fathi, 2010). High spatial resolution data are needed to construct robust rotation curves using this method. This high resolution data on a large sample of galaxies has been lacking, particularly for the molecular gas tracers. The CALIFA IFU survey (Sánchez et al., 2012) measured optical spectra of 667 nearby galaxies, providing spatially and spectrally resolved Hα velocities, as well as intensities, velocities, and velocity dispersions for many other ionized gas lines. The EDGE-CALIFA survey (EDGE, Bolatto et al., 2017), selected 126 galaxies from CALIFA and observed them in ^{12}CO($J = 1 - 0$) with the Combined Array for Millimeter Wave Astronomy (CARMA) at $\sim$4.5" resolution. Together, these surveys allow for the molecular and ionized gas kinematics of a statistical sample of nearby, star-forming galaxies to be analyzed. Using a sub-sample of 17 EDGE-CALIFA galaxies, this work constitutes the largest spatially resolved combined CO and Hα kinematic analysis to date for late-type galaxies.

Section 2.2 presents the EDGE, CALIFA, and ancillary data used for this study. The rotation curve fitting routine, procedure to determine the kinematic parameters from the EDGE CO data, and the sub-sample of galaxies used in this work are discussed in Section 2.3. Section 2.4 presents comparisons of the CO and Hα rotation curves. Potential explanations and interpretations of the results are presented in Section 2.5, including the results of the kinematic simulations, velocity

dispersions, and ionized gas line ratios. We present our conclusions and summary in Section 2.6. Throughout this paper, CO refers to $^{12}C^{16}O(J = 1 - 0)$.

2.2 Observations and Data Reduction

2.2.1 The EDGE-CALIFA Survey

The EDGE-CALIFA survey (Bolatto et al., 2017) measured CO in 126 nearby galaxies with CARMA in the D and E configurations. Full details of the survey, data reduction, and masking techniques are discussed in Bolatto et al. (2017), and we present a brief overview here. The EDGE galaxies were selected from the CALIFA sample (discussed in the following section) based on their infrared (IR) brightness and are biased toward higher star formation rates (SFRs) (see Figure 6 of Bolatto et al., 2017). A pilot study of 177 galaxies was observed with the CARMA E-array. From this sample, 126 galaxies selected for CO brightness were re-observed in the D-array. These 126 galaxies with combined D and E array data constitute the main EDGE sample*. The EDGE sample is the largest sample of galaxies with spatially resolved CO, with typical angular resolution of 4.5″ (corresponding to ∼1.5 kpc at the mean distance of the sample). Data cubes were produced with 20 $\mathrm{km\,s^{-1}}$ velocity channels. At each pixel in the cube, a Gaussian is fit to the CO line. Velocity-integrated intensity, mean velocity, velocity dispersion, and associated error maps are created from the Gaussian fits. Pixels with velocities that differ from their nearest (non-blanked) neighbors by more than 40 $\mathrm{km\,s^{-1}}$, generally caused

*The EDGE CO data cubes and moment maps for the main sample are publicly available and can be downloaded from `www.astro.umd.edu/EDGE`.

by fitting failures in low signal-to-noise data, are replaced with the median value of the neighbors. This replacement is rare and occurs for ∼0.5% of pixels in a given galaxy. Additional masking was applied to the CO maps where the Gaussian fitting introduced artifacts. This masking was based on signal to noise ratio (SNR) cut using the integrated intensity and associated error map. Pixels with SNR < 1 were blanked in the velocity field. Average CO velocity dispersions are derived and are listed in Table 2.1. A beam smearing correction is applied and is discussed in Appendix A.2.

2.2.2 The CALIFA Survey

The CALIFA survey (Sánchez et al., 2012) observed 667 nearby (z = 0.005–0.03) galaxies. Full details of the CALIFA observations are presented in Walcher et al. (2014) and other CALIFA papers, but we present a brief overview for completeness. CALIFA used the PPAK IFU on the 3.5m Calar Alto observatory with two spectral gratings. The low resolution grating (V500) covered wavelengths from 3745–7500 Å with 6.0 Å (FWHM) spectral resolution, corresponding a FWHM velocity resolution of 275 $\mathrm{km\,s^{-1}}$ at Hα. The moderate resolution grating (V1200) covered wavelengths from 3650–4840 Å with 2.3 Å (FWHM) spectral resolution, corresponding to a FWHM velocity resolution of 160 $\mathrm{km\,s^{-1}}$ at Hγ (Sánchez et al., 2016a). The V500 grating includes many bright emission lines, including Hα, Hβ, Hγ, Hδ, the [NII] doublet, and the [SII] doublet. The V1200 grating contains many stellar absorption features used to derive the stellar kinematics as well as a few ionized gas

emission lines, such as Hγ and Hδ. The typical spatial resolution of the CALIFA data are 2.5", corresponding to $\sim$0.8 kpc at the mean distance of the galaxies. The CALIFA galaxies were selected from the Sloan Digital Sky Survey (SDSS) DR7 to have angular isophotal diameters between 45" and 79.2" to make the best use of the PPAK field of view. The upper redshift limit was set so that all targeted emission lines were observable for all galaxies in both spectral set ups; the lower redshift limit was set so that the sample would not be dominated by dwarf galaxies. The data used for this study come from the final data release[†] (Sánchez et al., 2016a) and data products come from Pipe3D version 2.2 (Sánchez et al., 2016c,b) provided in the final form by the CALIFA Collaboration.

The wavelength calibration of the data is detailed in Sánchez et al. (2012) and Appendix A.5 of Husemann et al. (2013) and is crucial to extract accurate line velocities. The wavelength calibration data are used to resample the spectra to a linear wavelength grid and to homogenize the spectral resolution across the band (6.0 Å FWHM for V500 and 2.3 Å FWHM for V1200). The calibration is done using HeHgCd lamp exposures before and after each pointing using 16 lines for the V500 data and 11 lines for the V1200 data. The resulting accuracy of the wavelength calibration is $\sim$0.2–0.3 Å for the V500 data and $\sim$0.1–0.2 Å for the V1200 data. However, in our analysis of the V1200 data, we found errors in the wavelength calibration resulting from a bad line choice used to anchor the wavelength scale. This has been remedied in the current version of the data used here.

Once the data are calibrated, Pipe3D fits and removes the stellar continuum,

[†]The CALIFA data cubes are publicly available at `http://califa.caha.es`.

measures emission line fluxes, and produces two-dimensional data products for each emission line. Full details of Pipe3D and its application to the CALIFA data can be found in Sánchez et al. (2016c,b), and important details are reproduced here for completeness. The underlying stellar continuum is fit and subtracted to produce a continuum-subtracted or "emission line only" spectrum (Section 2 of Sánchez et al., 2016c). A Monte Carlo method is used to first determine the non-linear stellar kinematic properties and dust attenuation at each pixel in the cube. Next, the results of this non-linear fitting are fixed and the properties of the underlying stellar population are determined from a linear combination of simple stellar population (SSP) templates (see also Section 3.2 of Sánchez et al., 2016b). This model stellar spectrum is then subtracted from the CALIFA cube at each pixel to produce a continuum-subtracted cube. To determine the properties of the emission lines, Pipe3D uses a nonparametric fitting routine optimized for weaker emission lines ("flux_elines") which extracts only the line flux intensity, velocity, velocity dispersion, and equivalent width (see Section 3.6 of Sánchez et al. (2016b) for full details). Each emission line of interest is fit using a moment analysis similar to optimal extraction. The line centroid is first guessed based on the rest-wavelength of the line, and a wavelength range is defined based on the input guess for the line FWHM. A set of 50 spectra in this range are generated using a Monte Carlo method and each is fit by a Gaussian. At each step in the Monte Carlo loop, the integrated flux of the line is determined by a weighted average, where the weights follow a Gaussian distribution centered on the observed line centroid and the input line FWHM. With the integrated flux fixed, the velocity of the line centroid is determined. The line fluxes are not corrected for

extinction within Pipe3D so the desired extinction correction can be applied in the analysis. We do not apply an extinction correction since this would have a minimal effect on the line centroid used here. Additional masking was also applied to the CALIFA velocity fields using a SNR cut based on the integrated flux and error maps. Pixels with SNR < 3.5 were blanked.

The linewidths of the V500 data (which covers Hα) are dominated by the instrumental linewidth ($6.0\,\text{Å} \approx 275\,\text{km}\,\text{s}^{-1}$ at $\lambda(\text{H}\alpha) = 6562.68\,\text{Å}$), and hence reliable velocity dispersions are not available for the V500 data. The instrumental linewidth can be removed from the V1200 data ($2.3\,\text{Å} \approx 160\,\text{km}\,\text{s}^{-1}$ at $\lambda(\text{H}\gamma) = 4340.47\,\text{Å}$). To determine the H$\gamma$ linewidth, we start with the continuum-subtracted cube and isolate the Hγ line. We fit the Hγ line at each spaxel using a Gaussian, where the linewidth is given by the width of the Gaussian fit. Pixels with SNR < 3 are blanked. We convert the resulting maps from wavelength to velocity using the relativistic convention, producing maps of the velocity dispersions for each galaxy. Independently, Pipe3D does provide velocity dispersion maps derived from non-parametric fitting. The values in these maps, however, are frequently lower than the instrumental velocity dispersion over extended regions (a problem we do not find in our Gaussian fitting), and it is known that the pipeline systematically finds dispersions lower than obtained from Gaussian fitting (section 3.6 of Sánchez et al., 2016b).

We compare the velocity dispersions extracted from Pipe3D and our Gaussian fitting to non-parametric fitting done with NEMO (Teuben, 1995). In this fitting we find the linewidth at each spaxel using the `ccdmom mom=32` task. This finds the peak, locates the minima on either side of the peak, and takes a second moment over

those channels. Velocity dispersions from this method agree much better with the Gaussian fitting results than with the Pipe3D values, hence we adopt the Gaussian fitting results to determine the Hγ velocity dispersion.

Before using these velocity dispersion maps in our analysis (Section 2.5.5.1), we remove the instrumental velocity dispersion, and and model and remove the beam smearing effects (the latter is a small effect in the regions were we are interested in measuring the gas velocity dispersion). This procedure is discussed in Appendix A.2, and caveats are discussed further in Section 2.5.5.1. We regrid all CALIFA maps to the same grid as the corresponding EDGE map using the `Miriad` task `regrid` (Sault et al., 1995).

CALIFA also derived effective radius (R_e) measurements for all EDGE galaxies as described in Sánchez et al. (2014). These values are listed in Table A.3.

When comparing the velocity fields from the EDGE and CALIFA surveys, it is important to note that the velocities are derived using different velocity conventions: EDGE follows the radio convention, and CALIFA follows the optical convention. Because velocities in both surveys are referenced to zero, all velocities are converted to the relativistic velocity convention. In both the optical and radio conventions, the velocity scale is increasingly compressed at larger redshifts; typical systemic velocities in the EDGE-CALIFA sample are $\sim$4500 km s^{-1}. The relativistic convention does not suffer from this compression effect. Differences between these velocity conventions and conversions among them can be found in Appendix A.1. All velocities presented here are in the relativistic convention, unless otherwise noted.

2.2.3 Convolving to a Common Spatial Resolution

In order to accurately compare the CO and ionized gas velocity fields, the EDGE and CALIFA data cubes were convolved to the same angular resolution. The convolution was done using the `convol` task in `Miriad` (Sault et al., 1995), which uses a Gaussian kernel. The EDGE beam was first circularized by convolving to a value 5% larger than the beam major axis. The CALIFA point spread functions are circular (Sánchez et al., 2016a). The EDGE and CALIFA cubes were convolved to a final 6" resolution, corresponding to $\sim$2 kpc at the mean distance of the galaxies. Data products were reproduced as outlined in Sections 2.2.1 and 2.2.2. The CO and Hα velocity fields for NGC 2347 are shown in Figure 2.1. The rotation curves were derived as described in Section 2.3.1. There is excellent agreement between the native and convolved rotation curves for both CO and Hα, suggesting that while it is best to match physical resolution the convolution does not affect the results presented here.

2.2.4 GBT HI Data

The EDGE collaboration obtained HI spectra for 112 EDGE galaxies from the Robert C. Byrd Green Bank Telescope (GBT) in the 2015B semester as part of GBT/15B-287 (PI: D. Utomo). We defer detailed discussion of these data for a future paper (Wong et al. 2021, in preparation) and present a brief overview. Observations were taken using the VEGAS spectrometer with a 100 MHz bandwidth, 3.1 kHz (0.65 km s^{-1}) spectral resolution, and a 3-σ sensitivity of 0.51 mJy. On-source

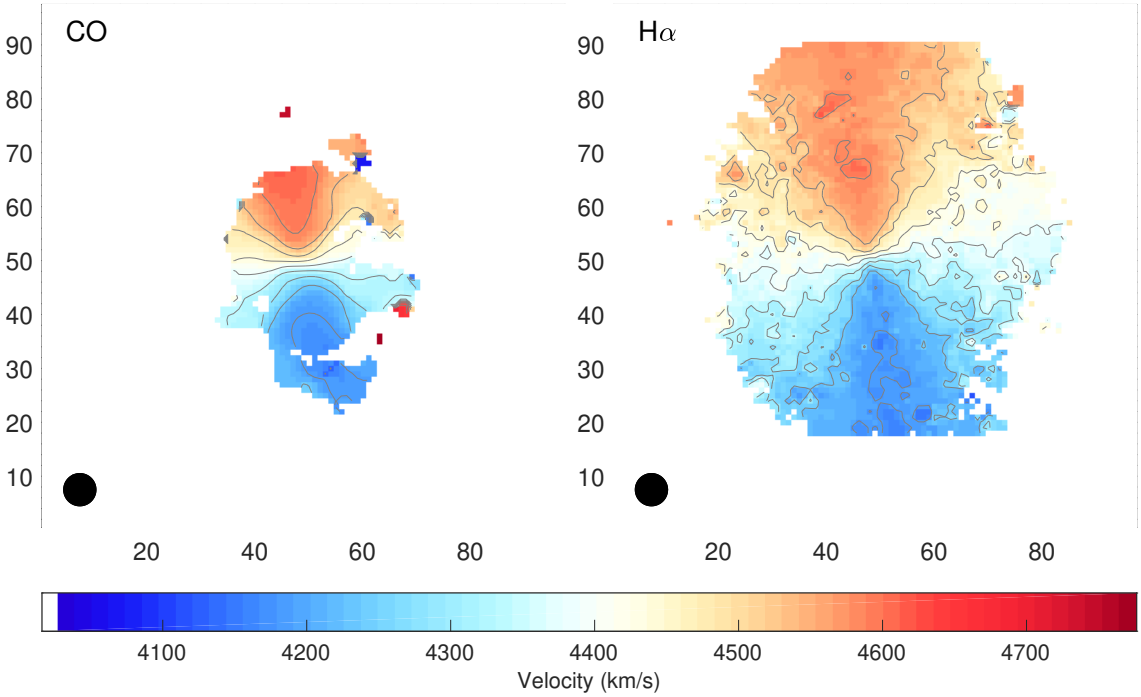

Figure 2.1: EDGE CO and CALIFA Hα velocity fields convolved to a 6" beam size for NGC 2347. Isovelocity contours are shown in 50 km s^{-1} increments out to $\pm$250 km s^{-1} from the systemic velocity. The circularized 6" beams are shown as the black circles.

integration time was 15 minutes for each galaxy. The GBT primary beam FWHM was 9' compared to the average EDGE $D_{25} = 1.6$', so the galaxies are spatially unresolved. Data were reduced using standard parameters in the observatory-provided GBTIDL package. A first or second order baseline was fit to a range of line-free channels spanning 300–500 km s^{-1} on either side of the signal range. The spectra were calibrated to a flux density scale assuming a gain of 2 K/Jy and a negligible coupling of the source size to the telescope beam. The widths containing 50% and 90% of the flux (W50 and W90 respectively) were derived from a Hanning smoothed spectrum to use as proxies for the maximum rotation velocity of the neutral atomic gas in these galaxies. These values are listed in Table 2.1, if available. The HI spectrum for NGC 2347 is shown in Figure 2.2, with the inclination corrected W50

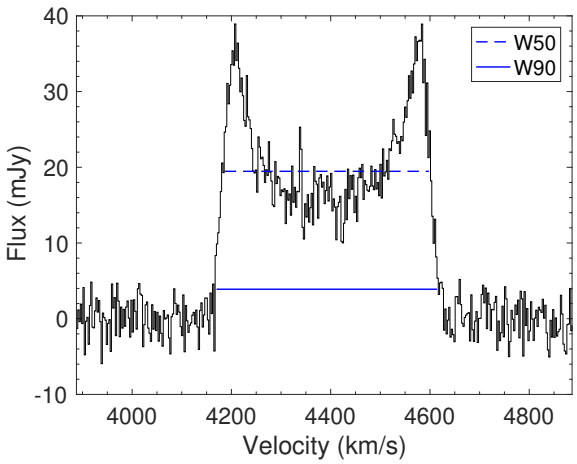

Figure 2.2: The HI spectrum from the GBT is shown for NGC 2347. The spectrum has been clipped to ± 500 km s^{-1} from the CO systemic velocity. The velocities here have been converted to the relativistic convention. Inclination corrected W50 and W90 values are indicated by the dashed and solid blue lines. For this work, the HI data are used as a comparison to the molecular and ionized gas rotation velocities.

and W90 values marked.

If HI data from GBT are not available, W50 values only were taken from Springob et al. (2005). Specifically, we use their W_C values which are W50 corrected for the instrumental and redshift effects. For this work, these data are used for only three galaxies and come from either the Green Bank 300 ft telescope (NGC 5480 and NGC 5633) or Arecibo (line feed system, UGC 9067). These values are also listed in Table 2.1.

In this work, we use the HI rotation velocities as point of comparison to the CO and Hα rotation velocities. We convert the W50 and W90 values to rotation velocities where V_{rot}=W/(2 sin i), where i is the galaxy's inclination as listed in Table A.3.

2.3 Data Analysis

2.3.1 Fitting CO Rotation Curves

Rotation curves were determined for each galaxy using a tilted ring method[‡] (Rogstad et al., 1974; Begeman, 1989), which has previously been applied to HI data (e.g Begeman, 1989; Schoenmakers, 1999; Fraternali et al., 2002; de Blok et al., 2008; Iorio et al., 2017), ionized gas data (e.g van de Ven & Fathi, 2010; Di Teodoro et al., 2016), CO data (e.g Wong et al., 2004; Frank et al., 2016), and recently [CII]158μm data in high redshift galaxies (Jones et al., 2017). Galaxies were deprojected (position angles and inclinations are listed in Table A.3) and divided into circular annuli. The radius of each annulus was determined such that the width was at least half a beam. The center position, inclination (i), and position angle (PA) are assumed the same for all annuli. The PA takes values between 0 and 360 degrees and increases counterclockwise, where PA = 0 indicates that the approaching side is oriented due north. The rotation ($V_{\rm rot}$), radial ($V_{\rm rad}$), and systemic ($V_{\rm sys}$) velocity components were determined in each ring using a first order harmonic decomposition of the form

$$V(r) = V_{\rm rot}(r)\cos\psi\sin i + V_{\rm rad}(r)\sin\psi\sin i + \Delta V_{\rm sys}(r) \tag{2.1}$$

where r is the galactocentric radius and ψ is the azimuthal angle in the plane of the disk (Begeman, 1989; Schoenmakers, 1999). Before fitting, the central systemic

[‡]We note that a python implementation of this rotation curve fitting routine has now been published by Cooke, Levy, et al., (2021) and is available at `https://github.com/rclevy/RotationCurveTiltedRings`.

velocity ($V_{\rm sys}^{\rm cen}$) was subtracted from the entire map, so that the fitted systemic component is $\Delta V_{\rm sys}(r) = V_{\rm sys}(r) - V_{\rm sys}^{\rm cen}$.

The initial values for the PAs and inclinations were chosen from photometric fits to outer optical isophotes (Falcón-Barroso et al., 2017). If values were not available from this method, they were taken from the HyperLeda database (Makarov et al., 2014). Initial central systemic velocity values ($V_{\rm sys}^{\rm cen}$) and center coordinates (RA and Dec) were taken from HyperLeda. The kinematic PAs were determined from the results of the ring fitting by minimizing $V_{\rm rad}$ at radii larger than twice the CO beam; an incorrect PA will produce a non-zero radial component. $V_{\rm sys}^{\rm cen}$ values were refined by minimizing $\Delta V_{\rm sys}$ at radii larger than twice the CO beam. The inclination is not as easily determined from kinematics; however, examining fits to individual annuli (rather than the rotation curve) can indicate whether the inclination is incorrect. Center offsets in RA and Dec ($\rm X_{off}$, $\rm Y_{off}$) were determined using a grid search method. At each point in the grid of $\rm X_{off}$ and $\rm Y_{off}$ values, a rotation curve was fit using that center. A constant was fit to the $\Delta V_{\rm sys}$ component, and the combination of $\rm X_{off}$ and $\rm Y_{off}$ resulting in the best fit was selected as the center. The value of $V_{\rm sys}^{\rm cen}$ was then adjusted as necessary to again minimize $\Delta V_{\rm sys}$. The sign of the offset is such that the correct center is ($x_{\rm cen}$, $y_{\rm cen}$) = (RA–$\rm X_{off}$, Dec–$\rm Y_{off}$). If a rotation curve could not be fit, either because there is little or no detected CO or because the velocity field is very disturbed, the parameter values were unchanged from the initial values. The final values of the geometric parameters can be found in Table A.3, including whether the PA, inclination, and $V_{\rm sys}^{\rm cen}$ values are derived from kinematics (this work), photometrically (Falcón-Barroso et al., 2017),

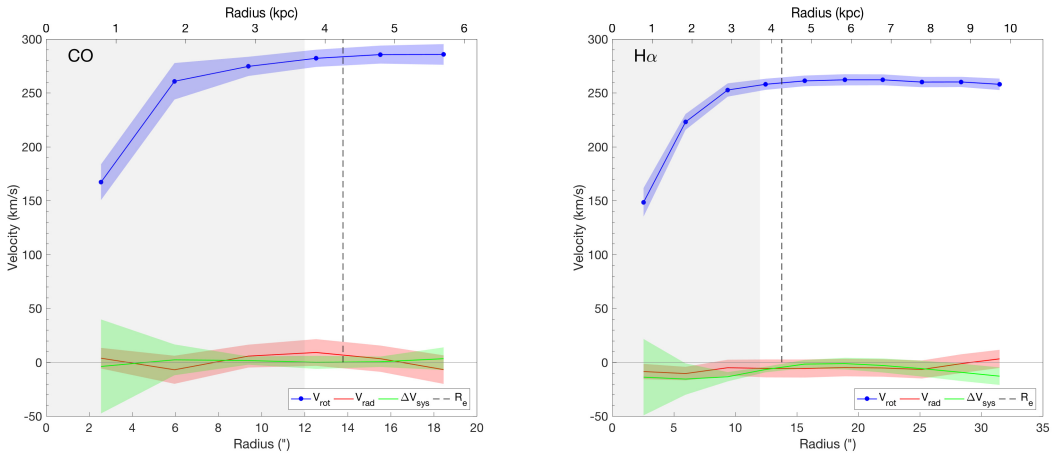

Figure 2.3: (Left) The CO rotation curve for NGC 2347, where $V_{\rm rot}$is shown in blue, $V_{\rm rad}$ in red, and $\Delta V_{\rm sys}$ in green. The colored shaded regions are the errors on the rotation curve from the Monte Carlo method. The gray shaded region shows the inner 2 beams where beam smearing can affect the rotation curve substantially. The black dashed line shows R_e (Table A.3). (Right) The Hα rotation curve for NGC 2347, where the colors of the curves are the same as in the left panel. In both cases, the $V_{\rm rad}$ and $\Delta V_{\rm sys}$ components are small and consistent with zero within the error ranges. The $V_{\rm rot}$components flatten at larger radii. Interestingly, $V_{\rm rot}$(Hα) is noticeably smaller than $V_{\rm rot}$(CO).

or from HyperLeda.

Errors on the rotation curve were determined using a Monte Carlo method in which the geometrical parameters were drawn randomly from a uniform distribution. The center position was allowed to vary by 1" in either direction, since over the whole EDGE sample, the average change in the CO (or Hα) center position from the original value is 0.7". The inclination is varied by 2°, which is the average difference between the final and initial inclinations over the whole EDGE sample. The PA was also allowed to vary by 2°, which is the median difference between the final and initial PAs over the whole EDGE sample. This allows typical uncertainties in the kinematic parameters to be reflected in the rotation curves. The shaded error regions shows the standard deviation of 1000 such rotation curves. The CO rotation

curve showing $V_{\rm rot}$, $V_{\rm rad}$, and $\Delta V_{\rm sys}$ for one galaxy is shown in Figure 2.3 (left).

We note this method to determine errors on the rotation curve differs from methods which use the differences between the approaching and receding sides of the galaxy, assuming that those differences are at the 2-σ level (e.g. Swaters, 1999; de Blok et al., 2008). Typical uncertainties on the CO rotation velocity are $\sim$3–10 km s^{-1} (1-σ). For the uncertainties stemming from the difference in rotation velocity between the approaching and receding sides to exceed the typical 1-σ uncertainties we find in our Monte Carlo method, rotation velocities of the approaching and receding sides would have to differ by 12–40 km s^{-1}. This seems unlikely, especially given that uncertainties on the rotation velocities derived from the differences between the approaching and receding sides presented by de Blok et al. (2008) are generally $\sim$10 km s^{-1}. Therefore, we conclude that the major source of uncertainty in deriving our rotation curves are uncertainties in the geometric parameters.

Due to the beam size of the EDGE data, the observed velocities are affected by beam smearing, especially in the centers of the galaxies (Bosma, 1978; Begeman, 1987). Leung et al. (2018) analyzed the effect of beam smearing in the EDGE sample and found that it is only significant in the inner portions of the galaxy ($\lesssim$0.5 R_e) where the velocity gradient is steep. For this study, we do not correct for beam smearing but rather exclude from the analysis points in the rotation curve within 2 beams from the center. The radius corresponding to twice the CO beam is referred to as $R_{\rm 2beam}$ throughout. The excluded central region is shown in gray in Figure 2.3. Excluding the center of the galaxy also minimizes any effects from a bulge or an active galactic nucleus (AGN).

Name	Morph (Type)	log(M$_*$) (M$_\odot$)	log(SFR) (M$_\odot$ yr^{-1})	d (Mpc)	D$_{25}$ (')	CO V$_{max}$ (km s^{-1})	ΔV (km s^{-1})	HI W50 (km s^{-1})	HI W90 (km s^{-1})	Σ_* (M$_\odot$ pc^{-2})	σ_{CO} (km s^{-1})	σ_{ADC} (km s^{-1})	$\sigma_{H\gamma}$ (km s^{-1})	[SII]/Hα	[NII]/Hα
IC1199	Sbc (3.7)	10.8	0.2	68.3	1.2	199.0±5.7	2.6±4.3	141.8	229.0	189.6	11.1±5.5	52.1±26.5	34.6±9.2	0.19±0.01	0.39±0.01
NGC2253	Sc (5.8)	10.8	0.5	51.2	1.4	174.2±7.9	1.1±7.7	211.0	243.9	205.6	9.2±2.5	24.9±37.2	28.0±3.4	0.17±0.01	0.37±0.01
NGC2347	Sb (3.1)	11.0	0.5	63.7	1.6	285.6±2.0	24.1±0.4	267.7	289.2	336.5	10.1±4.0	85.9±5.0	36.6±5.1	0.18±0.01	0.38±0.01
NGC2410	Sb (3.0)	11.0	0.5	67.5	2.2	227.2±5.9	15.3±5.1	247.3	267.3	198.6	17.6±7.5	67.7±16.5	38.2±12.1	0.20±0.01	0.47±0.04
NGC3815	Sab (2.0)	10.5	0.0	53.6	1.4	185.8±5.2	18.8±3.6	176.5	223.5	215.4	15.1±5.1	52.9±8.0	26.9±3.3	0.20±0.02	0.38±0.01
NGC4047	Sb (3.2)	10.9	0.6	49.1	1.5	216.3±2.2	14.3±0.5	220.3	243.2	296.6	9.5±2.4	63.2±9.5	29.5±3.7	0.16±0.01	0.35±0.01
NGC4644	Sb (3.1)	10.7	0.1	71.6	1.5	186.1±5.8	13.5±2.8	171.0	214.7	132.6	16.6±8.1	53.2±10.9	31.3±7.7	0.16±0.01	0.40±0.01
NGC4711	SBb (3.2)	10.6	0.1	58.8	1.2	142.8±10.5	5.8±0.9	167.3	185.2	121.1	10.0±4.4	47.9±37.2	32.9±7.7	0.18±0.01	0.36±0.01
NGC5016	SABb (4.4)	10.5	-0.0	36.9	1.6	178.4±0.8	17.7±8.7	187.2	199.1	248.9	11.3±5.6	56.4±11.0	26.6±3.8	0.16±0.01	0.38±0.01
NGC5480	Sc (5.0)	10.2	0.2	27.0	1.7	111.4±6.6	4.8±5.1	147.7	-	180.0	11.2±3.5	37.1±41.5	24.0±2.9	0.20±0.01	0.33±0.01
NGC5520	Sb (3.1)	10.1	-0.1	26.7	1.6	162.3±0.2	15.3±1.4	158.1	170.1	202.3	13.4±6.8	60.5±0.4	26.5±2.5	0.20±0.01	0.39±0.01
NGC5633	Sb (3.2)	10.4	0.2	33.4	1.1	187.5±9.4	9.1±2.9	200.6	-	396.0	11.3±2.5	53.3±23.4	25.1±1.8	0.17±0.01	0.37±0.01
NGC5980	Sbc (4.4)	10.8	0.7	59.4	1.6	216.3±4.4	8.2±4.8	219.4	248.6	214.8	12.3±2.3	52.5±24.0	34.3±3.8	0.17±0.01	0.41±0.01
UGC04132	Sbc (4.0)	10.9	1.0	75.4	1.2	238.5±11.4	16.3±8.0	255.6	291.5	206.5	15.8±3.9	79.4±40.0	33.1±4.3	0.20±0.01	0.40±0.01
UGC05111	Sbc (4.0)	10.8	0.6	98.2	1.5	216.2±11.9	9.1±4.4	-	-	154.4	15.4±3.6	52.2±33.5	-	0.23±0.02	0.41±0.02
UGC09067	Sab (2.0)	11.0	0.7	114.5	0.8	211.7±4.2	1.0±2.1	212.7	-	110.7	14.1±7.6	12.5±40.7	29.0±4.9	0.21±0.01	0.35±0.01
UGC10384	Sab (1.6)	10.3	0.7	71.8	1.2	187.4±8.1	14.2±7.0	180.7	200.9	74.5	18.9±6.2	45.0±12.9	35.4±2.7	0.21±0.01	0.35±0.02

The table lists relevant parameters for the KSS galaxies not already listed in Table A.3. The morphology and types are from HyperLeda and are listed in Bolatto et al. (2017). Values for M$_*$, SFR, distances (d), and the diameter of the 25th magnitude isophote (D$_{25}$) are taken from CALIFA and are also found in Bolatto et al. (2017). Errors on log(M$_*$) and log(SFR) are ±0.1 in the corresponding units. CO V$_{max}$ is the maximum CO rotation velocity, determined by the median of the CO RC at radii larger than twice the CO beam; the error is the standard deviation. ΔV is the median difference between CO and Hα RCs, as described in Section 2.4. HI W50 and W90 listed here are uncorrected for inclination. All values are taken from the GBT except for NGC 5480, NGC 5633, and UGC 9067 (see Section 2.2.4). Σ_* are averages of stellar surface density radial profiles from (Utomo et al., 2017). σ_{CO} are the velocity dispersions estimated from the beam-smearing corrected CO maps (Section 2.2.1). σ_{ADC} are the velocity dispersions estimated from the asymmetric drift correction (ADC; Section 2.5.5.2). $\sigma_{H\gamma}$ are the median velocity dispersions measured from the Hγ line; errors are the weighted standard deviations (Section 2.5.5.1). [SII]/Hα and [NII]/Hα are the median intensity ratios, where is error is the standard error Section (2.5.6).

Table 2.1: Parameters for the KSS

2.3.2 Fitting Ionized Gas Rotation Curves

The CALIFA data were fit using the methods described in in previous section and the same PA and inclination as the CO listed in Table A.3. In some cases, the Hα velocity contours are noticeably offset from the CO contours. CALIFA provides refinements to their astrometry in the headers of the data; however, these refinements are not large enough to account for some observed offsets. The CALIFA pipeline registers the RA and Dec for the center of the PPAK IFU to the corresponding center of the SDSS DR7 image (García-Benito et al., 2015). In DR2, 7% of the galaxies have registration offsets from SDSS >3″ (García-Benito et al., 2015). However, this registration process is known to fail in some cases. Indeed, in many of the galaxies for which we find offsets, this registration process has failed. Therefore, CALIFA centers were re-fit in the same way as the EDGE data, as described in Section 2.3.1. Because the V500 and V1200 data were taken on different days, the centers of the V500 and V1200 data were re-fit independently. For both the V500 and V1200 data, the average magnitude of the center offset is 0.9". The center offsets and $V_{\rm sys}^{\rm cen}$ values for the CALIFA data are presented in Table A.3. The Hα rotation curve for NGC 2347 is shown in Figure 2.3 (right).

2.3.3 The Kinematic Sub-Sample

Of the 126 EDGE galaxies, ≈100 have peak brightness temperatures $\geq 5\sigma$ (Bolatto et al., 2017). Reliable CO and Hα rotation curves could not, however, be derived for every detected EDGE galaxy. To best compare the CO and Hα rotation

curves, a sub-sample of galaxies for which reliable CO and Hα rotation curves could be derived is used for the remainder of the analysis (the Kinematic Sub-Sample or KSS). A reliable rotation curve has small $V_{\rm rad}$ and $\Delta V_{\rm sys}$ components at radii larger than $R_{\rm 2beam}$ (as in Figure 2.3). In the centers of galaxies, there may be radial motions due to bars and other effects, but these should not affect the larger radii we consider here. Ensuring that both the CO and Hα have small $V_{\rm rad}$ components validates our assumptions that the CO and Hα have the same PA and inclination and that the PA and inclination do not change much over the disk (i.e. there are no twists or warps). In addition to the criteria on the rotation curves, there are four galaxies (NGC 4676A, NGC 6314, UGC 3973, and UGC 10205) for which the observed CO velocity width may not be fully contained in the band (Bolatto et al., 2017). One galaxy (UGC 10043) has a known Hα outflow (López-Cobá et al., 2017). These galaxies are also excluded from the subsample. Finally, we exclude galaxies with inclinations larger than 75°. At large inclinations, the line profiles can become skewed and a Gaussian fit to the line profiles is not appropriate and can lead to systematic biases in the mean velocities. We will analyze the highly inclined galaxies in the following chapter (Chapter 3; Levy et al. 2019). Under these criteria, our sample size is reduced to 17 galaxies. Figure A.4 shows CO and Hα velocity fields and rotation curves for all galaxies in the KSS. Specific notes on each galaxy in the KSS can be found in Appendix A.3. Table 2.1 lists global quantities for the KSS not listed in Tables A.3 or A.3.

2.4 Results

Previous comparisons of molecular and ionized gas rotation velocities for individual galaxies show variations in agreement (e.g. Wong et al., 2004; Simon et al., 2005; Heald et al., 2006a; de Blok et al., 2016). Davis et al. (2013), for example, found that for 80% of their sample of 24 gas-rich early-type galaxies (ETGs) the ionized gas rotation velocities were lower than for the molecular gas. For a few of the star-forming disk galaxies in our KSS, the molecular and ionized gas rotation velocities agree within the errors, such as UGC 9067 shown in Figure 2.4 (left). The majority of our galaxies, however, have CO rotation velocities which are measurably higher than the Hα rotation velocities (such as for NGC 2347, shown in Figure 2.4 right). In no case is the Hα rotation velocity measurably higher than the CO. To quantify the differences between the CO and Hα rotation curves, the rotational component of the Hα rotation curve was linearly interpolated and resampled at the same radii as the CO rotation curve. V_{rot}(CO) and V_{rot}(Hα) are compared at radii larger than twice the convolved beam (R_{2beam}) to ensure that beam smearing is not affecting the results; the gray shaded regions in Figure 2.4 show the radii over which the rotation curves are compared. The differences between V_{rot}(CO) and V_{rot}(Hα) are shown in Figure 2.4 (purple points). The median of these differences (ΔV) was taken to determine an average velocity difference between the CO and Hα rotational velocities. The standard deviation of the difference at each radius ($\sigma_{\Delta V}$) is quoted as an error on ΔV. Galaxies have measurably different CO and Hα rotation velocities if $|\Delta V| > \sigma_{\Delta V}$ and are consistent if $|\Delta V| \leq \sigma_{\Delta V}$. Of the 17 galaxies in the

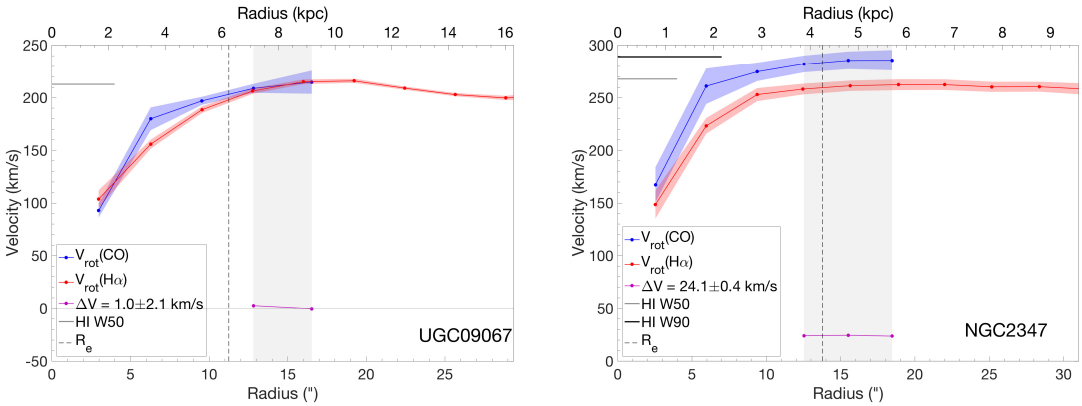

Figure 2.4: CO and Hα rotation curve comparisons for two galaxies. In both plots, V_{rot}(CO) is in blue and V_{rot}(Hα) is in red. The purple curves show the difference between the rotation curves at radii greater than R_{2beam} to the furthest CO extent. The median difference between V_{rot}(CO) and V_{rot}(Hα) (ΔV) is quoted and the error is the standard deviation. The solid gray and black lines show the inclination corrected V_{rot}(HI) values from W50 and W90 for comparison. The black dashed lines show R_e (Table A.3). (Left) UGC 9067 has CO and Hα rotation curves which are consistent within the error bars. (Right) NGC 2347 shows a difference of 24 km s^{-1} between the CO and Hα rotation curves. The HI rotation velocities tend to agree better with the CO rotation curve. Many galaxies in the KSS show ΔV which are larger than the errors on the rotation curves.

KSS, $77\%^{+23\%}_{-0\%}$ (13^{+4}_{-0}) show measurably higher CO rotation velocities than Hα, and the other $23\%^{+0\%}_{-23\%}$ (4^{+0}_{-4}) show consistent CO and Hα rotation velocities. This is remarkably similar to the ETG results of Davis et al. (2013).

To better understand the distribution of ΔV in the KSS, a kernel density estimator (KDE) was formed, where each galaxy is represented as a Gaussian with centroid $\mu = \Delta V$, $\sigma = \sigma_{\Delta V}$, and unit area. These Gaussians were summed and re-normalized to unit area. The resulting distribution is shown in Figure 2.5, showing that all galaxies in the KSS have $\Delta V > 0$. The median ΔV of the sample is 14 km s^{-1}.

We find no strong radial trends in ΔV, likely because the range of radii probed is relatively small. Over the 17 KSS galaxies, the median gradient in ΔV with radius

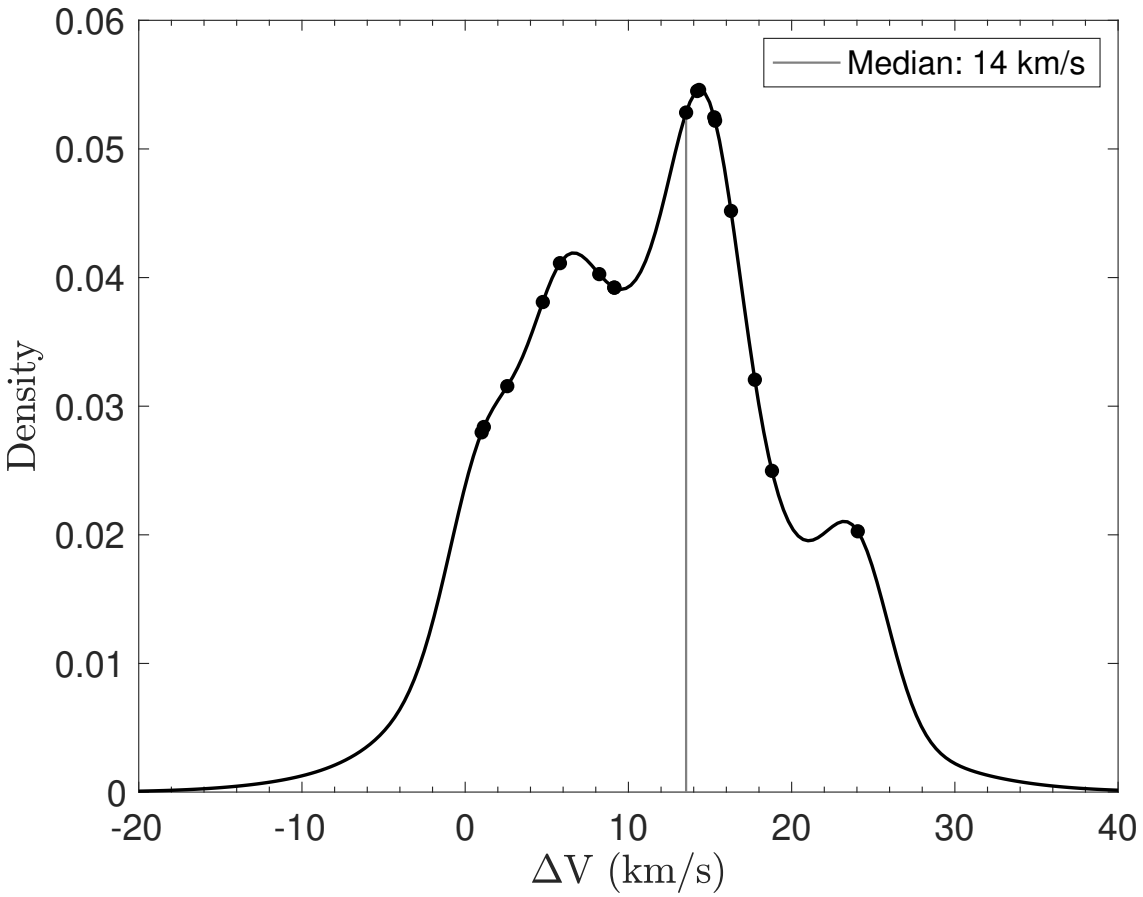

Figure 2.5: Kernel density estimator showing the distribution of ΔV (the median V_{rot}(CO)-V_{rot}(Hα)) in the KSS. Each galaxy is represented as a Gaussian with centroid $\mu = \Delta V$, $\sigma = \sigma_{\Delta V}$, and unit area. A minimum $\sigma_{\Delta V}$ of $2\,\mathrm{km\,s^{-1}}$ is imposed. The Gaussians are summed to produce a histogram and normalized to unit area. The circles indicate the peak of the Gaussian for each galaxy. All galaxies in the KSS have $\Delta V > 0$. The median ΔV is $14\,\mathrm{km\,s^{-1}}$.

is $-0.2 \pm 6.4\,\mathrm{km\,s^{-1}\,kpc^{-1}}$.

In addition to Hα, rotation curves were derived for other ionized lines available from CALIFA using the same method and parameters described in Section 2.3.2. These lines include Hβ, [OIII]λ5007, [NII]λ6548, [NII]λ6583, [SII]λ6717, and [SII]λ6731 from the V500 grating and Hγ from the V1200 grating. Rotation curves from these lines (as well as CO and Hα) are shown for NGC 2347 in Figure 2.6, where the colored shading indicates the errors on the rotation curves. Within these errors, the ionized gas rotation curves are consistent with one another, and below the CO rotation curve. Also shown are the W50 and W90 measurements from the HI data. These values straddle the CO rotation curve and both are larger than the ionized gas rotation velocities.

The low end of the ΔV values measured by Davis et al. (2013) are comparable to those we measure (Figure 2.7). Davis et al. (2013) also measure the luminosity weighted mean equivalent width (EW) of Hβ (a measure of the dominance of star formation). CALIFA provides maps of the EW(Hα), and we find the median EW(Hα) in the same region as where ΔV is calculated (excluding the inner 12" out to the furtherest CO extent). The error is the standard deviation of EWs divided by the square root of the number of beams over the region. As shown in Figure 2.7, there is a trend between the EW and ΔV. The EW(Hα) values we measure are larger than those measured by Davis et al. (2013). EWs > 14 Å trace star-forming complexes, and galaxies where the ionization is dominated by HII regions in the midplane tend to have larger EWs (Lacerda et al., 2018). This implies that the bulk of the ionized gas emission in our objects comes from the HII regions in midplane,

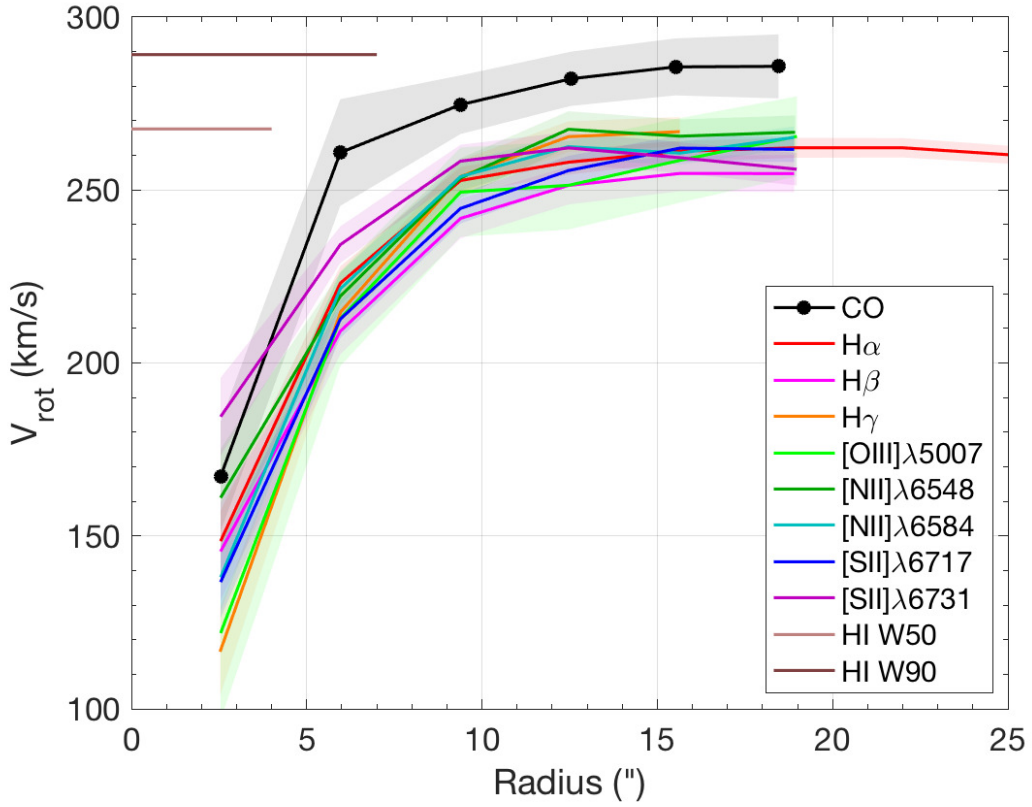

Figure 2.6: Rotation curves in several ionized gas lines are consistent with each other (using fixed geometric parameters listed in Table A.3). The figure shows an example for NGC 2347. For CO, the shaded region shows the error on the rotation curves from variations in the kinematic parameters using the Monte Carlo method described in Section 2.3.1. For all other curves, the shaded regions indicate the formal errors from the rotation curve fitting. The rotation curves from the ionized gas are consistent with one another and are all below the CO rotation curve. Ionized rotation curves other than Hα are truncated at the same radius as CO. The tan and brown horizontal lines show V_{rot}(HI) from W50 and W90 measurements, which tend to agree with the CO rotation velocity. Note that variations among the rotation curves are enhanced as the y-axis does not extend down to zero.

which naturally rotate at the same velocity as the molecular gas (since they represent recent episodes of star formation). Lacerda et al. (2018) also find that EWs < 3 Å trace regions of diffuse gas ionized by low-mass, evolved stars. These are prevalent in elliptical galaxies and bulges and can also be present above or below the midplane in spirals. EWs between these values are likely produced by a mixture of ionization processes.

This suggests a scenario where ionized gas caused by recent star formation (such as gas associated with HII regions), which is close to the galaxy midplane and has a small scale height, shares the rotation of the molecular gas from which the star formation arose. Ionized gas associated with older stellar populations or produced by cosmic rays (which typically have much larger scale heights), or possibly gas that has been shock-ionized (experiencing an injection of momentum that may drive it to large scale heights) or otherwise vertically transported may rotate at lower speeds.

This scenario is in agreement with the trend seen in Figure 2.7, in which the ETGs have lower EW(Hβ) and higher ΔV than the star-forming spirals studied here. It also agrees with studies that find vertical gradients in the rotation velocity of the ionized gas in some galaxies (e.g., Rand, 1997, 2000). As pointed out by a number of authors, however, the steady-state solution for a homogeneous barotropic fluid immersed in an axisymmetric potential does not allow for such vertical rotation velocity gradients (e.g., Barnabè et al., 2006; Marinacci et al., 2010). Having the ionized disks in equilibrium while maintaining such gradients may require an anisotropic velocity dispersion, similar to what may be expected for a galactic fountain (Marinacci et al., 2010).

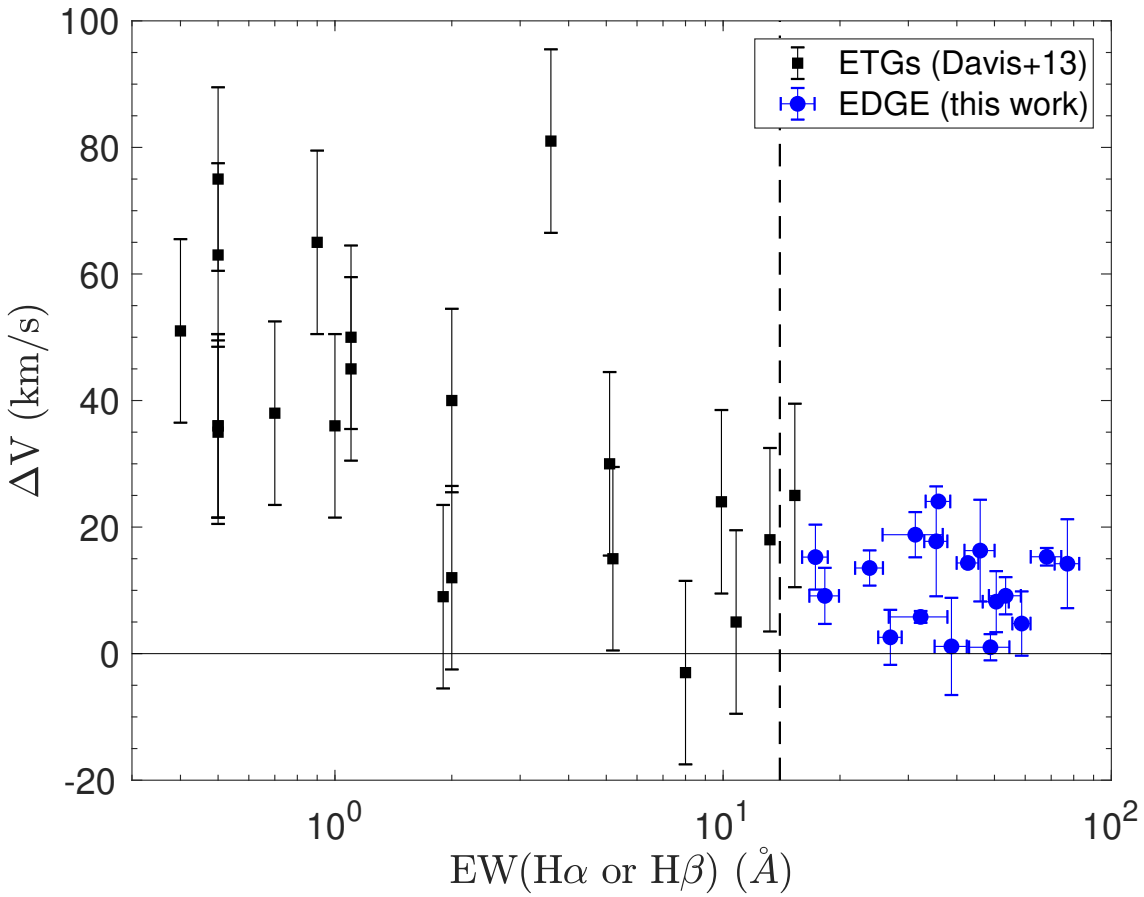

Figure 2.7: Equivalent width of the Hα or Hβ emission versus rotation velocity difference between the molecular and ionized gas, ΔV. The blue points are the KSS galaxies and use EW(Hα), and the black points are ETGs from Davis et al. (2013) who use the luminosity weighted mean EW(Hβ), excluding those which are counter-rotating. Error bars are not provided for the EW(Hβ) data. Our points are consistent with the low ΔV end of the ETGs. EWs > 14 Å (vertical dashed line) trace star formation (Lacerda et al., 2018), so it is not surprising that the star-forming disk galaxies used in this study have larger EWs than the ETGs use by Davis et al. (2013).

2.5 Discussion

The ubiquity and magnitude of the differences between the CO and Hα rotation velocities are striking. We propose that these differences could be due to the presence of significant extraplanar diffuse ionized gas (eDIG) in our KSS galaxies. In the following subsections, we give some background on previous eDIG detections, rule out scenarios other than eDIG that could produce this effect, and give support for eDIG in these systems from velocity dispersions and ionized gas line ratios. We also suggest that this thick, pressure supported disk would have a vertical gradient in the rotation velocity, with gas at higher latitudes rotating more slowly than gas in the midplane.

2.5.1 Previous Detections of Extraplanar Diffuse Ionized Gas

eDIG has been observed and discussed in the literature, and we highlight some results here for context. The importance of the warm ionized medium (WIM) as a significant fraction of the ISM in the Milky Way (MW) has been known for over four decades (e.g. Reynolds, 1971; Reynolds et al., 1973; Kulkarni & Heiles, 1987; Cox, 1989; McKee, 1990) and for over two decades in other galaxies (e.g. Dettmar, 1990; Rand et al., 1990; Rand, 1996; Hoopes et al., 1999; Rossa & Dettmar, 2003a,b). In particular, diffuse Hα can contribute >50% of the total Hα luminosity with large variations (Haffner et al., 2009, and references therein). In the MW, half of the HII is found more than 600 pc from the midplane (Reynolds, 1993). How such a large fraction of diffuse gas can be ionized at these large scale heights is debated, but it is

widely believed that leaky HII regions containing O-star clusters can produce WIM-like conditions out to large distances from the cluster and the midplane (by taking advantage of chimneys and lines-of-sight with little neutral gas created by past feedback, Reynolds et al., 2001; Madsen et al., 2006), although ionization sources with large penetration depths (such as cosmic rays) or re-accretion from the halo may also play a role.

Extraplanar HI exhibiting differential rotation has been detected in the MW (e.g. Levine et al., 2008) and in studies of individual galaxies (e.g. Swaters et al., 1997; Schaap et al., 2000; Chaves & Irwin, 2001; Fraternali et al., 2002, 2005; Zschaechner et al., 2015; Zschaechner & Rand, 2015; Vargas et al., 2017). Velocity gradients between the high latitude gas and the dynamically cold midplane are generally -10 – -30 $\mathrm{km\,s^{-1}\,kpc^{-1}}$ extending out to a few kpc, but there are large variations among and within individual galaxies.

Extraplanar Hα (i.e. eDIG) has also been found and studied in galaxies, primarily from photometry. In a recent study tracing the WIM in the spiral arms of the MW, Krishnarao et al. (2017) find an offset between the CO and Hα velocity centroids, although they do not interpret this offset as eDIG. Outside the MW, NGC 891 is the prototypical galaxy with bright eDIG extending up to 5.5 kpc from the midplane (Rand et al., 1990; Rand, 1997) and a vertical velocity gradient of -15 $\mathrm{km\,s^{-1}\,kpc^{-1}}$ (Heald et al., 2006a), in agreement with measurements of its extraplanar HI (Swaters et al., 1997; Fraternali et al., 2005). Boettcher et al. (2016) find that the thermal and turbulent velocity dispersions (11 $\mathrm{km\,s^{-1}}$ and 25 $\mathrm{km\,s^{-1}}$ respectively) are insufficient to support eDIG in hydrostatic equilibrium with a 1 kpc scale

height. NGC 5775 has observed HI loops and filaments with their rotation lagging the midplane (Lee et al., 2001) as well as Hα lags of -8 km s^{-1} kpc^{-1} detected up to 6–9 kpc from the midplane (Heald et al., 2006a; Rand, 2000). NGC 2403 has eDIG which lags the midplane by 80 km s^{-1} extending a few kpc above the midplane (Fraternali et al., 2004), in rough agreement with the lags observed in HI which extend 1–3 kpc from the midplane (Fraternali et al., 2002). Finally, eDIG has been observed in the face-on galaxy M 83 with a lag relative to the midplane of 70 km s^{-1} with a vertical scale height of 1 kpc (Boettcher et al., 2017). There is a range of eDIG velocity gradients and scale heights, and, moreover, HI and Hα vertical velocity gradients are not always similar or present (e.g. Zschaechner et al., 2015).

Apart from these case studies, there are several large photometric studies of eDIG independent of HI. Following the work of Rand (1996), Miller & Veilleux (2003a) and Rossa & Dettmar (2003a,b) performed larger photometric surveys of nearby edge-on spiral galaxies. Rossa & Dettmar (2003a,b) had a sample of 74 edge-on disks and found that 40.5% of the sample had eDIG extending 1–2 kpc from the midplane. In their sample of 17 galaxies, Miller & Veilleux (2003a) observe eDIG in all but one galaxy. Miller & Veilleux (2003b) did a spectroscopic follow up study of nine edge-on galaxies with observed eDIG and found vertical velocity gradients ranging from -30 to -70 km s^{-1} kpc^{-1}.

2.5.2 Comparison with Stellar Dynamical Modeling

The stellar circular velocity curve, which accounts for stellar velocity dispersion, should agree with the CO rotation curve if CO is a dynamically cold tracer. Leung et al. (2018) test three different dynamical models of the galaxy's potential to determine stellar circular velocity curves and compare these to CO rotation curves of 54 EDGE galaxies. Overall, they find agreement between the CO rotation curves and the three models to within 10% at 1 R_e. We defer to Leung et al. (2018) for a complete discussion of the details of the stellar modeling. The agreement between the stellar dynamical modeling and the CO rotation curves verifies that CO is indeed a dynamically cold tracer, indicating that the Hα is exhibiting anomalous behavior rather than the CO. Moreover, our measured CO velocity dispersions (Table 2.1) are small ($\sim$10 km s^{-1}), further indicating that the CO is dynamically cold.

2.5.3 An Inclined Disk

It is possible that the observed difference between the CO and ionized gas rotation velocities could be produced by the inclination of the disk; however, we find no correlation between ΔV and inclination, as shown in Figure 2.8. To determine a correlation, we calculate the Spearman rank correlation coefficient (r_s), which quantifies how well the relationship between the variables can be described by any monotonic function. Variables which are perfectly monotonically correlated will have $r_s = \pm 1$, assuming that there are no repeated values of either variable. The Spearman rank correlation coefficient does not, however, take the errors on the data

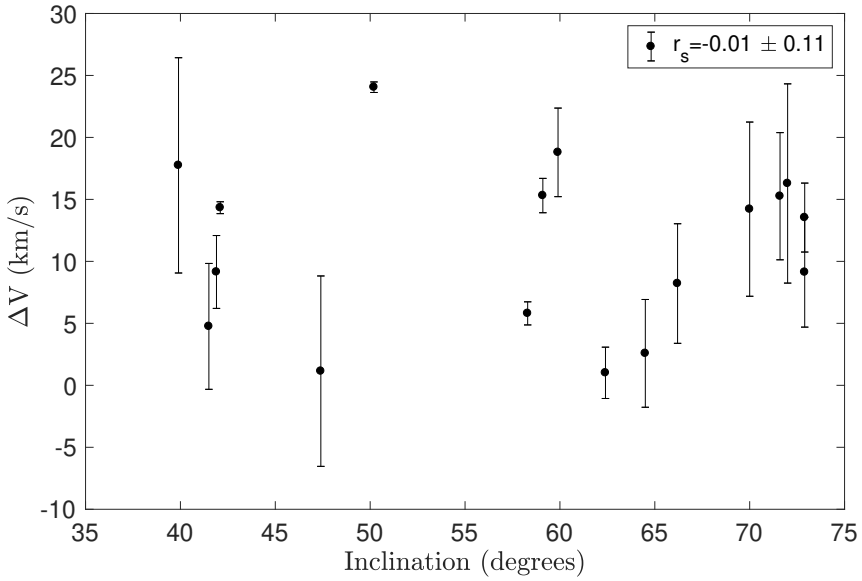

Figure 2.8: Lack of a trend between galaxy inclination and ΔV. The cause of the observed rotation velocity difference ΔV cannot be purely an inclination effect. The Spearman rank correlation coefficient (r_s) is consistent with 0.

into consideration. The errors on ΔV are especially important here. Therefore, we use a Monte Carlo method to determine the correlation coefficient over 1000 samples drawn from a uniform random distribution within the error ranges on each point. The error reported on r_s is the standard deviation of all 1000 r_s values. As shown in Figure 2.8, the difference between the CO and Hα rotation velocities is not a result of the inclination of the galaxy ($r_s = -0.01 \pm 0.11$).

We note that if the molecular and ionized gas disks had different inclinations, our assumption that they are the same could produce a ΔV. However, to produce only $\Delta V > 0$ would require that all ionized gas disks are less highly inclined (with respect to us) than the molecular gas disks, which for a sample of 17 galaxies is extremely unlikely. We can, therefore, rule out that the inclination affects the results in this way.

ΔV was also plotted against other global parameters of the galaxies, such

as stellar mass (M_*), SFR, specific SFR (sSFR $\equiv$ SFR/M_*), morphology, physical resolution, and CO V_{max}. There are no trends with any of these global parameters, and they are shown for completeness in Figure A.3 in Appendix A.3. As mentioned in Section 2.2.3, the lack of trend with physical resolution (Figure A.3 bottom left) justifies our choice to convolve to a common angular resolution rather than to a common physical resolution. These values and their sources are listed in Table 2.1. The lack of trends with these parameters agrees with Rossa & Dettmar (2003b), who also found no trends in the presence of eDIG with such global parameters.

2.5.4 Star Formation Rate Surface Density Threshold

In previous studies of eDIG, Rand (1996) and (Rossa & Dettmar, 2003a) find a possible trend in the amount of eDIG with the SFR per unit area ($\Sigma_{\rm SFR}$) as traced by the far infrared (FIR) luminosity ($L_{\rm FIR}$). The physical picture is that a minimum level of widespread star formation is needed to sustain a thick disk that covers the entire plane of the galaxy. Rossa & Dettmar (2003a) determine a threshold $\Sigma_{\rm SFR}$ above which they claim that an eDIG will be ubiquitous. This does not guarantee, however, that galaxies above this threshold will always have an eDIG or that galaxies below it cannot have eDIG. Rossa & Dettmar (2003a) define this threshold $\Sigma_{\rm SFR}$ as

$$\frac{L_{\rm FIR}}{D_{25}^2} = (3.2 \pm 0.5) \times 10^{40}\ {\rm erg\ s^{-1}\,kpc^{-2}} \tag{2.2}$$

where D_{25} is diameter of the 25th magnitude isophote. Catalán-Torrecilla et al. (2015) measure total IR (TIR, 8–1000 μm) luminosities ($L_{\rm TIR}$) for 272 CALIFA

galaxies, and $L_{\rm TIR}$ measurements are available for 15/17 KSS galaxies. The threshold defined by Rossa & Dettmar (2003a) can be converted to TIR by multiplying by 1.6 (Sanders & Mirabel, 1996) so

$$\frac{L_{\rm TIR}}{D_{25}^2} = (5.1 \pm 0.8) \times 10^{40}\ {\rm erg\ s^{-1}\,kpc^{-2}} \tag{2.3}$$

For the two galaxies without $L_{\rm TIR}$ measurements, we can estimate $L_{\rm TIR}$ from the SFR measured by CALIFA from extinction corrected Hα where

$$L_{\rm TIR} = \frac{1.6}{4.5 \times 10^{-44}} \left[\frac{\rm SFR}{M_\odot\ {\rm yr^{-1}}}\right] {\rm erg\ s^{-1}} \tag{2.4}$$

(Kennicutt, 1998) and the factor of 1.6 comes from converting from $L_{\rm FIR}$ to $L_{\rm TIR}$ (Sanders & Mirabel, 1996). Using measurements of D_{25} from HyperLeda (values are listed in Table 2.1), we compare the values of $L_{\rm TIR}/D_{25}^2$ for all KSS galaxies to the eDIG threshold (Equation 2.3) in Figure 2.9. We find that 94^{+6}_{-0}% of galaxies in the KSS have $L_{\rm TIR}/D_{25}^2$ greater than this threshold and should have eDIG based on this criterion.

If many galaxies have a thick ionized disk, this could underestimate the dynamical mass of the galaxy derived from the ionized gas rotation velocity. Because we find that the ionized gas rotates more slowly than the molecular gas in galaxies with large $\Sigma_{\rm SFR}$, this effect could be significant in local star-forming galaxies and even more so at higher redshifts where there is more star formation occurring on average.

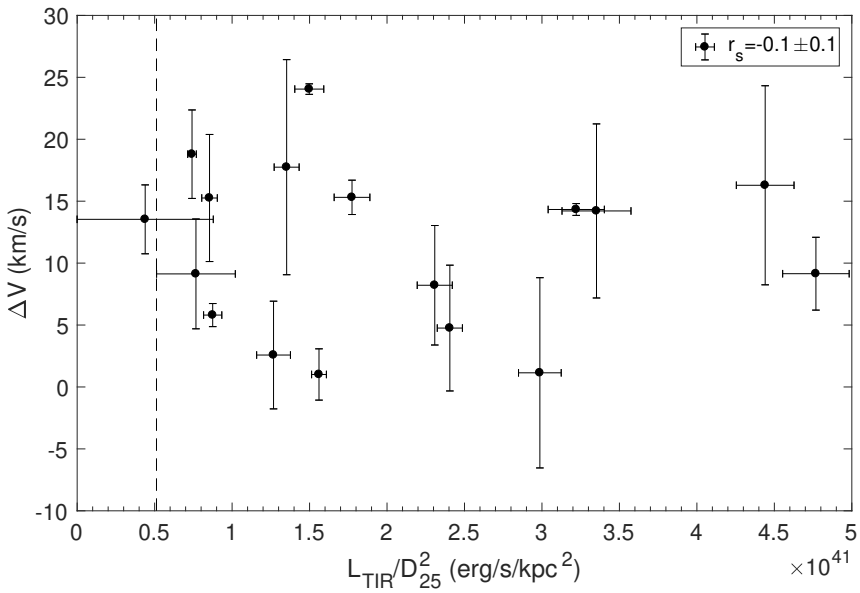

Figure 2.9: $L_{\rm TIR}/D_{25}^2$ versus ΔV for the KSS. The vertical dashed line shows the eDIG threshold from Rossa & Dettmar (2003a) of $L_{\rm TIR}/D_{25}^2 = 5.1 \times 10^{40}$ erg s^{-1} (Equation 2.3). We find that $> 90\%$ of our sample exceed this threshold, indicating the likely presence of eDIG in these systems. There is not, however, a trend between $L_{\rm TIR}/D_{25}^2$ and ΔV.

2.5.5 Ionized Gas Velocity Dispersion

The trends between the eDIG and the star-formation rate surface density discussed in Section 2.5.4 (e.g. Rand, 1996; Rossa & Dettmar, 2003a) are suggestive of star-formation feedback playing an important role in forming the eDIG. In order for ionized gas to remain above or below the disk midplane in a long-lived configuration, it must have sufficient velocity dispersion (or at least a vertical bulk motion). This effectively acts as as additional pressure term, allowing the gas to remain at larger scale heights. Therefore, we expect that galaxies with larger ionized gas velocity dispersions should have larger eDIG scale heights. Measuring the ionized gas velocity dispersion is, therefore, an important way to test these ideas.

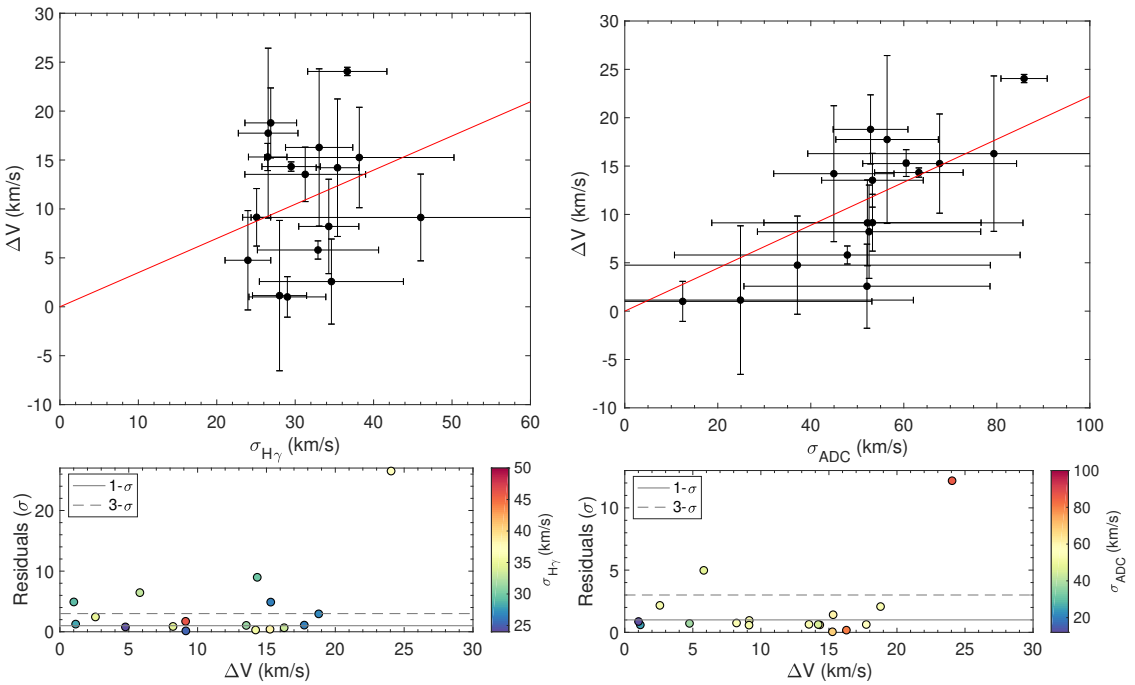

Figure 2.10: The left panel shows the trend between the velocity dispersion measured from the Hγ linewidth ($\sigma_{\mathrm{H}\gamma}$) and ΔV. Error bars reflect the propagated error. The red line is a linear fit to the data points. The lower panel shows the perpendicular distance of each point from the line in units of standard deviations plotted against ΔV. Points are color-coded by σ_{ADC}. The solid and gray dashed lines show 1- and 3-σ. 35% of the galaxies are within 1-σ of the best-fit line and 71% are within 3-σ. If there is an underlying correlation between $\sigma_{\mathrm{H}\gamma}$ and ΔV, it is weak. The right shows the same as the left but using the velocity dispersions inferred from the ADC (σ_{ADC}). The trend results from the form of the ADC used here (Equation 2.6). 71% of the galaxies are consistent with the best-fit line within 1-σ and 88% are consistent within 3-σ. In both bottom panels, the galaxy many σ away from the best-fit line is NGC 2347.

2.5.5.1 Hγ Velocity Dispersion Measurements

CALIFA data cannot, unfortunately, be used to accurately measure the Hα linewidth due to the low spectral resolution of the V500 grating employed (6.0 Å FWHM $\approx$ 275 km s^{-1} at Hα). CALIFA observes Hγ with the moderate-resolution V1200 grating (2.3 Å FWHM $\approx$ 160 km s^{-1} at Hγ), however, and those data can be used in principle to establish ionized gas velocity dispersions. Starting with the

continuum-subtracted cubes, we fit the Hγ line with a Gaussian at each spaxel where the width of the Gaussian corresponds to the velocity dispersion, as discussed in Section 2.2.2. The measured linewidth is the convolution of the instrumental response with the actual gas velocity dispersion, and has a small contribution from rotation smearing caused by the finite angular resolution. We apply a beam smearing correction which also accounts for the instrumental velocity dispersion. This method is described in detail in Appendix A.2. The accuracy of the resulting ionized gas velocity dispersion depends critically on the exact knowledge of the spectral resolution and response of the grating, because the instrumental velocity dispersion ($\sigma_{\rm inst} \approx 68\,{\rm km\,s^{-1}}$) is of the same order as the observed $\sigma_{\rm H\gamma}$ before removal: in other words, the spectral resolution of the V1200 observation is marginal for the purposes of measuring the velocity dispersion in these galaxies, and our results should be considered tentative. Inspection of the maps suggests that it is likely that the beam smearing-corrected $\sigma_{\rm H\gamma}$ values reported here are lower limits to the real ionized gas velocity dispersion, and we caution against over-interpretation of these values. We do not correct our $\sigma_{\rm H\gamma}$ for inclination and hence assume that the velocity dispersion is isotropic. As discussed in Section 2.4, anisotropic velocity dispersions may be required to maintain ionized gas disks with vertical gradients in the rotation velocity (Marinacci et al., 2010). With these caveats in mind, we calculate the average beam smearing-corrected Hγ velocity dispersion over the same region where ΔV is calculated. Velocity dispersions range from $\sim$25–45 ${\rm km\,s^{-1}}$ (Figure 2.10 left). The scale height of the disk (h) corresponding to a given isotropic velocity dispersion (σ)

is

$$h = \frac{\sigma^2}{\pi G \Sigma_*(r)} \tag{2.5}$$

(van der Kruit, 1988; Burkert et al., 2010). We use azimuthally averaged radial profiles of the stellar surface density (Σ_*) from Utomo et al. (2017) to find Σ_* over the same range of radii where ΔV is calculated (listed in Table 2.1). The scale heights corresponding to the observed $\sigma_{\mathrm{H}\gamma}$ are $\sim$0.1–1.3 kpc. Previous measurements of eDIG scale heights range from 1–2 kpc (Rossa & Dettmar, 2003a; Miller & Veilleux, 2003b; Fraternali et al., 2004) up to a few kpc above the disk (Rand, 2000, 1997; Miller & Veilleux, 2003a). Because our $\sigma_{\mathrm{H}\gamma}$ are likely lower limits, the scale heights may indeed be larger than we report here.

2.5.5.2 Velocity Dispersion Estimates from an Asymmetric Drift Correction

It is possible to infer the velocity dispersion needed to produce the observed ΔV using an asymmetric drift correction (ADC). Generally, an ADC is used to find V_{circ} given V_{rot}, σ, and $\Sigma_*(r)$; however, since $\mathrm{V_{rot}(CO)}$ traces V_{circ} (Section 2.5.2), we can invert the ADC to find σ instead, with $\mathrm{V_{rot}}$=$\mathrm{V_{rot}(H\alpha)}$. If we assume that the velocity dispersion is isotropic ($\sigma_r = \sigma_z = \sigma_\phi$), $\sigma(r)$ = constant, and $\Sigma_*(r) = 2\rho(r,z)h(z)$ (Binney & Tremaine, 2008), then

$$\sigma^2 = \frac{V_{\mathrm{circ}}^2 - V_{\mathrm{rot}}^2}{-d\ln\Sigma_*/d\ln r}. \tag{2.6}$$

We use azimuthally averaged radial profiles for $\Sigma_*(r)$ from Utomo et al. (2017) to find $d\ln\Sigma_*/d\ln r$. $V_{\rm circ}$, $V_{\rm rot}$, and $\Sigma_*(r)$ are averaged over the same radii as where ΔV is calculated; this excludes the central two beams (12"$\sim$4 kpc) where beam smearing or a bulge can affect the rotation curve. Velocity dispersions from the ADC method ($\sigma_{\rm ADC}$, Equation 2.6) range from $\sim$15–85 km s^{-1} in the KSS (Figure 2.10 right). There is an apparent trend with ΔV resulting from Equation 2.6. Using Equation 2.5, we find scale heights ranging from $\sim$0.1–2.0 kpc, again in rough agreement with previous measurements. For individual galaxies, the velocity dispersions and scale heights predicted from the ADC tend to be larger than those measured in the Hγ (Figure 2.11), but given the difficulty in the measurement the agreement is reasonable.

2.5.5.3 Trends between ΔV and the Velocity Dispersion

To explain the difference in rotation velocities observed between the molecular and ionized gas as resulting from the presence of eDIG, we would expect that galaxies with a larger ΔV should have larger velocity dispersions as well. There is a trend between ΔV and $\sigma_{\rm ADC}$ (Figure 2.10 right) stemming directly from the form of the ADC used (Equation 2.6). There is not, however, an immediately apparent relation between ΔV and $\sigma_{\rm H\gamma}$ (Figure 2.10 left). Because the errors on both ΔV and $\sigma_{\rm H\gamma}$ are large, however, there could be an underlying correlation. To assess whether an underlying correlation could exist, we fit a line to the data points (top panels of Figure 2.10). We then calculate the perpendicular distance of each point from

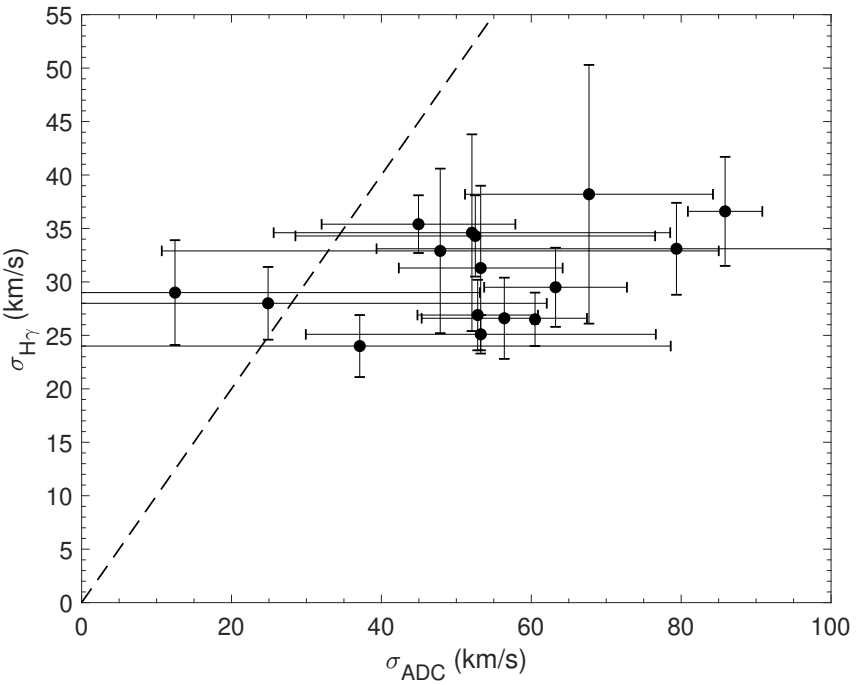

Figure 2.11: The velocity dispersions inferred from the ADC compared to those measured for the Hγ emission in each galaxy. The error bars reflect the statistical errors, measured from the standard deviation of the measurements in the annulus. The dashed line is one-to-one. The velocity dispersion $\sigma_{\mathrm{H}\gamma}$ is roughly comparable to those inferred from the σ_{ADC}; although $\sigma_{\mathrm{H}\gamma}$ tends to be smaller than σ_{ADC}this should not be over-interpreted given the difficulty of the measurement discussed in Section 2.5.5.1.

the line as well as the error on that distance accounting for the error bars on both quantities. From this, we determine the distance from the best-fit line in standard deviations (bottom panels of Figure 2.10). For the ADC, 71% of the galaxies are consistent with the best-fit line within 1-σ and 88% are consistent within 3-σ (Figure 2.10 left). This tight correlation again stems from the form of the ADC used, since $\sigma_{\rm ADC}$ depends explicitly on $\sqrt{V_{\rm rot}({\rm CO})^2 - V_{\rm rot}({\rm H}\alpha)^2}$ which is $\sim \sqrt{V_{\rm rot}\Delta V}$ (Equation 2.6). For $\sigma_{\rm H\gamma}$, however, only 35% of the galaxies are within 1-σ of the best-fit line and 71% are within 3-σ (Figure 2.10 left), so any underlying correlation between $\sigma_{\rm H\gamma}$ and ΔV is weak. Nonetheless, most of our galaxies have high enough velocity dispersions to support a thick ionized gas disk, and nearly all of our subsample have sufficient $\Sigma_{\rm SFR}$ (Figure 2.9).

2.5.6 [SII]/Hα and [NII]/Hα Ratios

The velocity dispersion is not the only tracer of eDIG. The ratios of [NII]λ6583/Hα ([NII]/Hα) and [SII]λ6717/Hα ([SII]/Hα) increase with distance from the midplane and are used to probe the ionization conditions of the WIM (e.g Miller & Veilleux, 2003a,b; Fraternali et al., 2004; Haffner et al., 2009). [SII]/Hα varies only slightly with temperature, whereas [NII]/Hα is used to trace variations in the excitation temperature of the gas (Haffner et al., 2009). From observations of the MW and a few other galaxies, [SII]/H$\alpha = 0.11 \pm 0.03$ and [NII]/H$\alpha \sim 0.25$ in the midplane (Madsen, 2004; Madsen et al., 2006), whereas [SII]/H$\alpha = 0.34 \pm 0.13$ and [NII]/H$\alpha \gtrsim 0.5$ in the eDIG (Blanc et al., 2009; Madsen, 2004). Observations of these ratios indicate

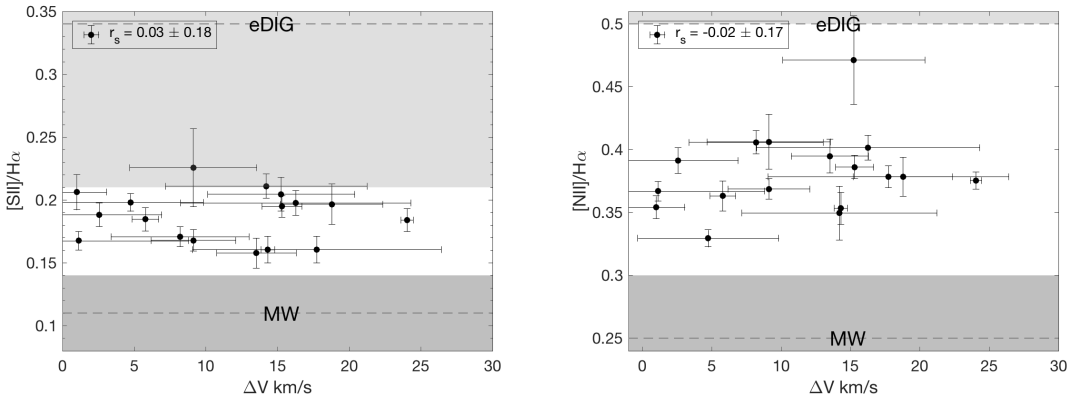

Figure 2.12: (Left) There is no trend between ΔV and [SII]/Hα, although the errors bars are large. All of our [SII]/Hα ratios are larger than for the MW (dark gray shaded region, [SII]/H$\alpha = 0.11 \pm 0.03$) but only a few fall within the observed range for the eDIG (light gray shaded region, [SII]/H$\alpha = 0.34 \pm 0.13$). The dashed gray lines show the median values for the MW and eDIG. (Right) There is no trend between [NII]/Hα and ΔV. As with [SII]/Hα, all of our measured ratios exceed those found in the plane of the MW (dark gray shaded region, [NII]/H$\alpha \sim 0.25$ where we have adopted a 20% error range) but are not as high as is generally observed in the eDIG (light gray shaded region, [NII]/H$\alpha \gtrsim 0.5$). The dashed gray lines show the median values for the MW and eDIG.

that there must be additional heating sources aside from photoionization from leaky HII regions to produce the WIM (Haffner et al., 2009, and references therein).

CALIFA provides Hα, [SII], and [NII] intensity maps for all galaxies. These were masked to cover the same radii as where ΔV is calculated. As shown in Figure 2.12, there are no trends between [SII]/Hα or [NII]/Hα with ΔV ($r_s = 0.03 \pm 0.18$ and $r_s = -0.02 \pm 0.17$ respectively). For both [SII]/Hα and [NII]/Hα, our ratios are all larger than for the plane of the MW but only a few fall within the observed range for the eDIG. This is perhaps not unexpected, since emission from the plane is mixed with emission from the eDIG which would systematically lower the observed ratios. This is an encouraging hint that the observed ΔV could be due to eDIG in a thick disk.

2.5.7 Kinematic Simulations

To further investigate how the disk's geometry affects the observed rotation curve, we perform a suite of kinematic simulations using NEMO. Disks are given different scale heights and vertical rotation velocity distributions as described in the follow subsections. The particle velocities are given by an input rotation curve which rises linearly from $r = 0 - 1$ units and is constant at $V_0 = 200\,\mathrm{km\,s^{-1}}$ from $r = 1 - 6$ units. The disk is then inclined and "observed" with a 1 unit beam. The velocity is derived by fitting the peak of the line at each point in the simulated data cube. $\mathrm{V_{rot}}(r)$ is averaged between $r = 1$ and $r = 5$ to give $\bar{V}$ in the flat part of the rotation curve. The error on $\bar{V}$ ($\sigma_{\bar{V}}$) is the standard deviation of $\mathrm{V_{rot}}(r)$. A simulated ΔV is computed by $V_0 - \bar{V}$, which is analogous to the ΔV defined previously (V_0 corresponds to $\mathrm{V_{rot}}$(CO) and $\bar{V}$ corresponds to the median $\mathrm{V_{rot}}(\mathrm{H}\alpha)$ in the outer part of the galaxy). We test four disk configurations, which are described below. To convert the scale heights to physical units (i.e. kpc), we use the turn-over radius (R_0) of the rotation curve (1 unit in the simulations) and find the average R_0 of the KSS Hα data. We fit the KSS Hα rotation curves with $V_{\mathrm{model}} = V_0(1 - e^{-R/R_0})$ (e.g. Boissier et al., 2003; Leroy et al., 2008) and fix V_0 to the value determined for that galaxy. The average R_0 over the sample is found, and the scaling is 1 unit = $1.77 \pm 0.25\,\mathrm{kpc}$. We note that the assumed beam in the simulations is 1 unit, which is nearly identical to the beam size of the observations (6" = 1.73 kpc at the average distance of the KSS galaxies).

2.5.7.1 Thin Disks

First, we create a thin disk of particles with scale height $h = 0$. The simulated ΔV as a function of inclination is shown in Figure 2.13 (top left). The resulting ΔV values are all very small and are insufficient to explain the offsets seen in Figure 2.5. We recover the input rotation curve to within $\sim$2 km s^{-1}. This $\sim$2 km s^{-1} offset is due to beam smearing. If a smaller beam is used, this offset disappears. So neither the inclination nor beam smearing of a thin disk can produce the observed ΔV.

2.5.7.2 Thick Disks

Using the same simulation set up described above, the initial disk can be given a scale height. The same input rotation curve is used at all heights, z, such that $\mathrm{V_{rot}}(r, z) = \mathrm{V_{rot}}(r, z = 0) = V_0$. Particles are distributed vertically using a Gaussian distribution where the FWHM is $2\sqrt{2 \ln 2}h$ (so the scale height above the midplane is h). ΔV is then calculated from these simulations as described previously. Figure 2.13 (top right) shows ΔV as a function of h, color-coded by inclination. There is only a trend for the highest inclinations, and even at these high inclinations, ΔV is not as large as many galaxies in the KSS. Therefore, a thick disk with $\mathrm{V_{rot}}(z) = V_0$ cannot cause the observed ΔV, except perhaps for very highly inclined galaxies. For intermediate inclinations, we recover the input rotation curve again to within the $\sim$2 km s^{-1} from beam smearing.

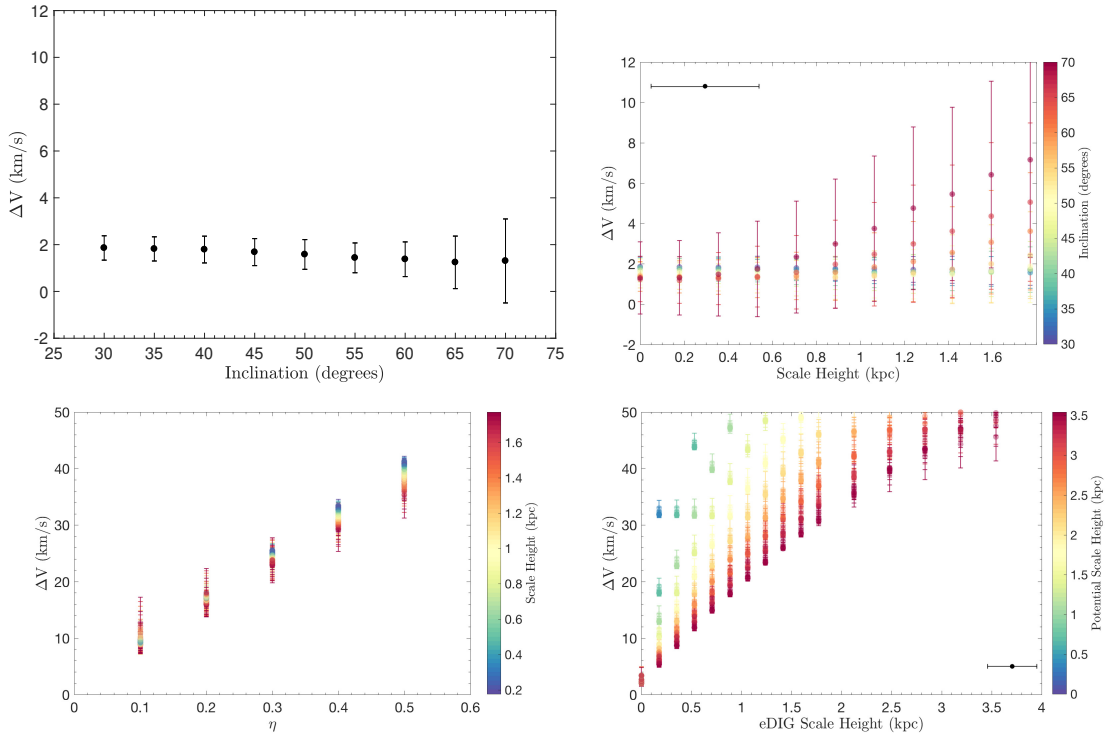

Figure 2.13: (Top left) From the simulations of thin inclined disks, the ΔV values are all very small, so inclination cannot explain the observed ΔV. The $\sim$2 km s^{-1} offset away from $\Delta V = 0$ is due entirely to beam smearing. (Top right) From the simulations of thick disks with no vertical rotation velocity gradient (i.e. $V_{rot}(z) = V_0$), there is no trend between ΔV and the scale height. There is only a trend for the most highly inclined galaxies (and the errors are large). So a thick disk without a vertical rotation velocity gradient cannot explain the ΔV measured in all systems. Again, the constant offset away from $\Delta V = 0$ is due entirely to beam smearing. The black point in the upper left corner shows the error on the scale height from the scaling between units in the simulation to kpc. Points are color-coded based on their inclination. (Bottom left) For a thick disk with a linear vertical rotation velocity gradient, there is a strong trend between the magnitude of the gradient (parameterized by η, see Equation 2.7) and ΔV, producing ΔV values comparable to those observed for $\eta \lesssim 0.3$. Points are color-coded based on the scale height. (Bottom right) Using the more realistic model with $V_{rot}(r, z)$ given by Equation 2.12 and $\rho_{eDIG}(z)$ given by Equation 2.13, we find that there is a strong trend between the eDIG scale height (h_{eDIG}) and ΔV. It is possible to produce ΔV in the range we observe (5–25 km s^{-1}) with $h_{eDIG} \lesssim 1.5$ kpc. There is also a trend with the scale height of the underlying potential (h_p, shown in the color-coding), but this trend is weaker. The black point in the lower right corner shows the error on the scale height from the scaling between units in the simulation to kpc.

2.5.7.3 Thick Disks with Vertical Rotation Velocity Gradients

We also test a thick disk with a vertical gradient in the rotation velocity. As mentioned in Section 2.5.1, vertical gradients in the rotation velocity have been observed in the extraplanar HI and eDIG of several galaxies. The physical rationale behind a vertical gradient in the rotation velocity is related to turbulent pressure support. Gas with larger velocity dispersions can be in pressure equilibrium at larger distances from the disk midplane. Material off the plane should have an orbit inclined with respect to the main disk enclosing the galactic center (like the stars); however, pressure support forces the gas to orbit parallel to the main disk. The gas further off the plane rotates more slowly than gas closer to the plane, creating the vertical gradient in the rotation velocity. First, we impose a linear vertical rotation velocity gradient parameterized by η where

$$V_{\rm rot}(z) = V_0\Big(1 - \eta\frac{z}{h}\Big). \tag{2.7}$$

As shown in Figure 2.13 (bottom left), there is a strong trend between η and ΔV. A linear vertical gradient in the rotation velocity can produce the observed values of ΔV for $\eta \lesssim 0.3$, meaning that at $z = h$, $\mathrm{V_{rot}} \gtrsim 0.7V_0$. For a given value of η, larger scale heights have less of an effect on ΔV, as seen from their shallower slope in Figure 2.13 (bottom left).

Next, we test a more realistic model for $\mathrm{V_{rot}}(z)$ than the linear vertical velocity gradient. The rotation velocity of material above the disk is governed by the poten-

tial. Here we assume that the rotation velocity in the disk midplane is constant (V_0) and, hence, the radial surface density profile, $\Sigma(r)$, is described by a Mestel disk (Mestel, 1963; Binney & Tremaine, 2008). We also assume that the vertical density distribution is exponential. Therefore, the total density distribution of material that dominates the potential has the form

$$\rho(r,z) = \frac{V_0^2}{2\pi G r h_p} e^{-|z|/h_p} \tag{2.8}$$

where h_p is the vertical scale height of the material that dominates the potential. The potential of a thin Mestel disk is

$$\phi(r) = -V_0^2 \ln\left(\frac{r}{r_{\max}}\right) \tag{2.9}$$

where $r_{\max}$ is the maximum extent of the disk (Binney & Tremaine, 2008). Therefore, the total potential is

$$\begin{aligned} \phi(r,z) &= \int \phi(r, z-z')\xi(z')dz' \\ &= -V_0^2 \ln\left(\frac{r}{r_{\max}}\right)\frac{1}{h_p}\int e^{-|z'|/h_p}dz' \\ &= V_0^2 \ln\left(\frac{r}{r_{\max}}\right)e^{-|z|/h_p} + c \end{aligned} \tag{2.10}$$

where the constant of integration (c) can be found by demanding that $\phi(r, z \to \infty) \to 0$. Therefore,

$$\phi(r,z) = V_0^2 \ln\left(\frac{r}{r_{\max}}\right)e^{-|z|/h_p}. \tag{2.11}$$

The rotation velocity from a potential is given by $V_{\rm rot}^2 = r\frac{\partial}{\partial r}\phi(r,z)$ (Binney & Tremaine, 2008) so from Equation 2.11

$$V_{\rm rot}(r,z) = V_0\sqrt{e^{-|z|/h_p}} \tag{2.12}$$

where the absolute value preserves the symmetry above and below the disk. The eDIG has its own density distribution and scale height ($h_{\rm eDIG}$) which are largely independent of the potential and determined mostly by the star formation activity. Although large ratios of $h_{\rm eDIG}/h_p$ are physically unlikely, here we treat these two scale heights as independent quantities. We can find the eDIG density as a function of z where the vertical density distribution is described by the hydrostatic Spitzer solution (Spitzer, 1942; Binney & Tremaine, 2008; Burkert et al., 2010):

$$\rho_{\rm eDIG}(r,z) = \rho_0 {\rm sech}^2\Big(\frac{z}{h_{\rm eDIG}}\Big) \tag{2.13}$$

where ρ_0 is the density in the midplane. We repeat the NEMO simulations as before, but using $\rm V_{rot}(r,z)$ given by Equation 2.12 (rather than Equation 2.7) and an eDIG density distribution give by Equation 2.13 (rather than a Gaussian). The results of this more realistic model are shown in Figure 2.13 (bottom right). There is a strong trend between $h_{\rm eDIG}$ and ΔV. There is also a secondary trend between h_p and ΔV. With this model, it is possible to reproduce the observed range of ΔV with $h_{\rm eDIG} \lesssim 1.5\,{\rm kpc}$. Using Equation 2.5 and the median Σ_* of the KSS at the radius where the measurements are done ($\approx 200\,{\rm M_\odot\,pc^{-2}}$), this implies a velocity

dispersion $\lesssim 60\,\mathrm{km\,s^{-1}}$, which agrees with the range of velocity dispersions inferred from the ADC and the measurements from Hγ.

2.5.8 Other Possible Explanations

In the previous subsections, we motivated our hypothesis that the observed difference between the molecular and ionized gas rotation velocities is due to eDIG in a thick disk with a vertical gradient in the rotation velocity. That is not, however, the only explanation. It is possible that we are instead measuring ionized gas velocities and velocity dispersions in the galactic bulge. To test this, we explore potential correlations between ΔV and measured the bulge-to-disk (B/D) luminosity ratios (Méndez-Abreu et al., 2017). Here, we use only results from the r-band since that overlaps with Hα. This is shown in the top panel of Figure 2.14 (left). To determine if there are any underlying correlations, we follow the same methodology as was done for the velocity dispersions discussed in Section 2.5.5.3. There is one galaxy with a large B/D ratio which is a clear outlier from the rest; this galaxy is NGC 2347 which has the largest ΔV in the subsample. It is excluded from the fitting of the linear regression. The bottom panel of Figure 2.14 (left) shows the distance of each galaxy from the best-fit line. For r-band, 33% of galaxies are consistent with the best-fit line within 1-σ and 67% are consistent within 3-σ. It is possible that the bulge could be affecting the measured rotation velocities and contributing to the measured ΔV. This affect is likely minimized, however, as ΔV is only measured at radii larger than R_{2beam} (12"$\sim$4 kpc). Méndez-Abreu et al. (2017) also measure

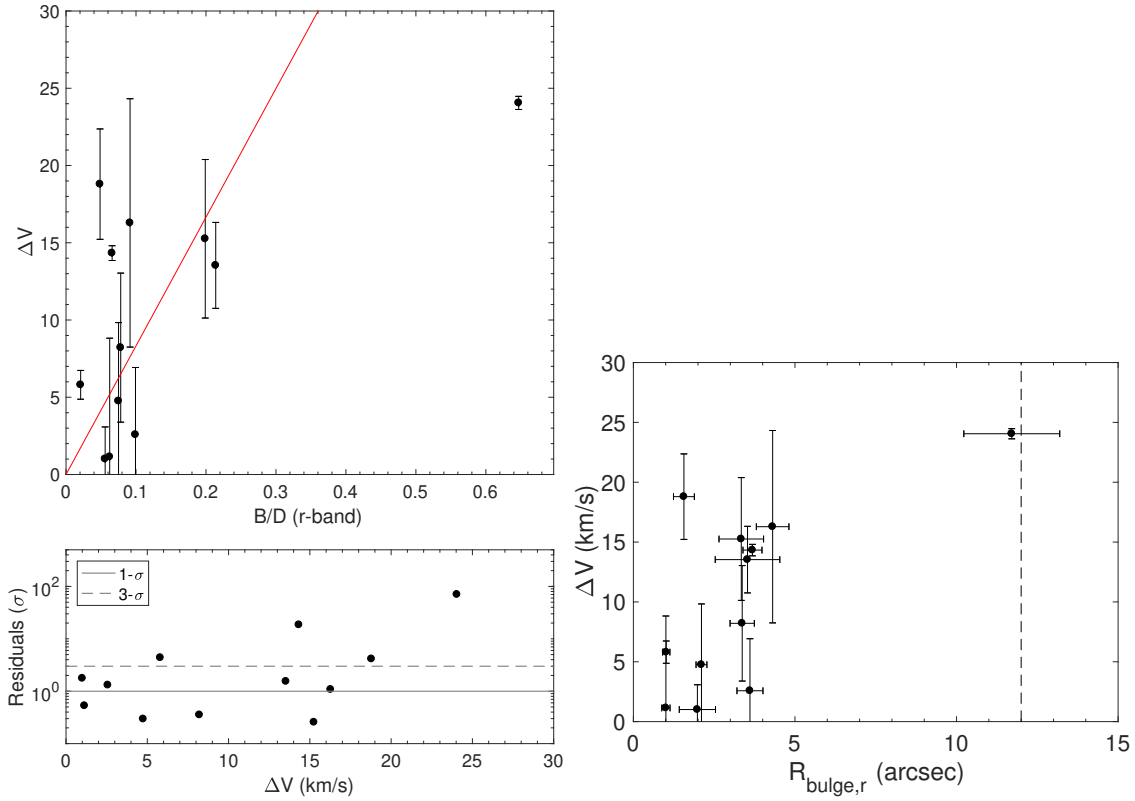

Figure 2.14: (Left) The trend between the B/D ratio and ΔV. B/D ratios are derived from Méndez-Abreu et al. (2017), who do not report errors on those values. The red line is a linear fit to the data points, excluding NGC 2347 whose B/D ratio is an outlier compared to the other galaxies used here. The bottom panel shows the perpendicular distance from the line for each point in units of standard deviations plotted against ΔV. The solid and gray dashed lines show 1- and 3-σ. For the r-band, 33% of the galaxies are consistent with the best-fit line within 1-σ and 67% are consistent within 3-σ. (Right) We also investigate the relationship between the effective radius of the bulge ($R_{\rm bulge}$) from Méndez-Abreu et al. (2017) and ΔV. All bulges (except NGC 2347) are much smaller than $R_{\rm 2beam}$ (vertical dashed line), so contamination from the bulge is likely small in these galaxies.

the effective bulge radius ($R_{\rm bulge}$). We plot $R_{\rm bulge}$ versus ΔV in Figure 2.14 (right). The dashed vertical line marks $R_{\rm 2beam}$, which is the smallest radius included when measuring ΔV. Bulge contamination is likely for NGC 2347 since $R_{\rm bulge} \approx R_{\rm 2beam}$, but the other galaxies in the sample have much smaller bulges so the likelihood of contamination from the bulge is lessened. The exact contributions of the bulge and eDIG to ΔV are difficult to disentangle in detail, however, and it is likely that both contribute to the measured ΔV at some level.

2.6 Summary

We present a kinematic analysis of the EDGE-CALIFA survey, combining high resolution CO maps from EDGE with CALIFA optical IFU data. Together, the CO and Hα kinematics can be compared in a statistical sample. We summarize our results as follows, indicating the relevant figures and/or tables:

1. Using a sub-sample of 17 galaxies from the EDGE-CALIFA survey where precise molecular gas rotation curves could be derived, we fit CO and Hα rotation curves using the same geometric parameters out to $\gtrsim 1$ R_e (Figure A.4).

2. In our sub-sample, we find that most galaxies ($\sim$75%) have CO rotation velocities which are measurably higher than the Hα rotation velocity in the outer part of the rotation curves. We refer to the median difference between the CO and Hα rotation velocity as ΔV. Measurable differences between CO and Hα rotation velocities range from 5–25 km s^{-1}, with a median value of 14 km s^{-1}

(Figure 2.5).

3. The rotation velocity differences between CO and Hα are not driven by inclination effects since we find no significant trend between the inclination and ΔV (Figure 2.8).

4. We suggest that these differences are caused by extraplanar diffuse ionized gas (eDIG) in these galaxies, which may constitute a thick, turbulent disk of ionized gas. Extraplanar ionized gas would be caused by stellar feedback, so we expect that galaxies with sufficient SFR per unit area ($\Sigma_{\rm SFR}$) would have extended thick ionized gas disks and that galaxies with smaller $\Sigma_{\rm SFR}$ might have patchy extraplanar ionized gas above HII regions (Rand, 1996; Rossa & Dettmar, 2003a). Indeed, the majority of the galaxies in the high-quality rotation curve sub-sample ($\sim$95%) have sufficient $\Sigma_{\rm SFR}$ to harbor eDIG (Figure 2.9). Because EDGE galaxies were selected from CALIFA based on their FIR brightness (Bolatto et al., 2017), it is not surprising that the majority of them are star-forming disk galaxies with large $\Sigma_{\rm SFR}$.

5. If galaxies frequently feature thick ionized gas disks, the effect described above would cause a systematic underestimate of galaxy dynamical masses derived from ionized gas rotation velocity. Because we find that the ionized gas rotates more slowly than the molecular gas in galaxies with large $\Sigma_{\rm SFR}$, this effect could be significant in local active star-forming galaxies and even more so at higher redshifts where star formation rates are much higher on average.

6. We measure ionized gas velocity dispersion using the Hγ line ($\sigma_{\rm H\gamma}$) as a proxy

for Hα, and compare them to predictions for the asymmetric drift correction (ADC), assuming velocity dispersion explains the observed difference in rotation velocities (Figure 2.10). For the ADC, we infer velocity dispersion which would support a thick ionized gas disk with scale height ranging from $\sim$0.1–2.0 kpc. The velocity dispersion measured from the Hγ is comparable but somewhat smaller than predicted from the ADC (Figure 2.11). The low spectral resolution of the data makes this measurement very difficult, so these results are tentative.

7. We find that [SII]/Hα and [NII]/Hα, which are tracers of the WIM, are elevated in these galaxies compared to typical values in the plane of the MW ([SII]/Hα=0.11, [NII]/H$\alpha\sim$0.25; Madsen, 2004; Madsen et al., 2006), but are not as large as typically found in the eDIG ([SII]/Hα=0.34, [NII]/H$\alpha\gtrsim$0.5; Blanc et al., 2009; Madsen, 2004). This is likely because emission from the midplane and eDIG are mixed together in these measurements (Figure 2.12).

8. We investigate the effect of disk geometry by performing a suite of kinematic simulations with NEMO. We find that neither a thin disk nor a thick disk without a vertical gradient in the rotation velocity can reproduce the observed ΔV (Figures 2.13 top). The observed ΔV can be reproduced with a vertical gradient in rotation velocity. For a linear vertical rotation velocity gradient, our results favor $\eta \equiv 1 - \frac{V_{\rm rot}(z=h)}{V_0} \lesssim 0.3$ (Figure 2.13 bottom left). For a more realistic vertical rotation velocity gradient, our results can be reproduced with an eDIG scale height $\lesssim$ 1.5 kpc corresponding to a velocity dispersion

$\lesssim 60\,\mathrm{km\,s^{-1}}$ (Figure 2.13 bottom right).

An ideal way to test for eDIG in these galaxies would be to directly measure the CO and Hα scale heights in a sample of edge-on disks and to correlate the Hα scale height with ΔV. Additionally, a systematic decrease in the Hα rotation velocity with distance from the midplane would be compelling evidence for our proposed model of a thick disk with a vertical velocity gradient. We carry out this analysis using the edge-on galaxies in the EDGE-CALIFA survey in the following chapter (Chapter 3; Levy et al., 2019).

Chapter 3: Extraplanar Diffuse Ionized Gas in Edge-on Galaxies

3.1 Introduction

The diffuse gas phases of the interstellar medium (ISM) are, by their very nature, harder to study than the denser phases. Nonetheless, they provide important windows into the evolution of galaxies. The diffuse ionized gas phase (frequently referred to as Warm Ionized Medium or WIM in the Milky Way and Diffuse Ionized Gas or DIG in other galaxies), in particular, has important connections to star formation activity and accretion history. A large fraction (perhaps the majority) of ionized gas in galaxies is found in this diffuse phase (e.g. Haffner et al., 2009). The existence of extraplanar diffuse ionized gas (eDIG) raises further questions about the formation and ionization of the DIG (e.g. Dettmar, 1990; Rand et al., 1990). The origin of the eDIG is debated; possible formation and ionization mechanisms include leaky HII regions (e.g. Haffner et al., 2009; Weber et al., 2019), star formation feedback in the form of galactic fountains (e.g. Shapiro & Field, 1976; Bregman, 1980), post-asymptotic giant branch (AGB) stars in the stellar thick disk (Flores-Fajardo et al., 2011; Lacerda et al., 2018), outflows (e.g. López-Cobá et al., 2019), accretion from the intergalactic medium (IGM) (e.g. Binney, 2005), or some combination of these processes. Properties of the eDIG, such as relation to the star formation rate

(SFR), diagnostic line ratios tracing temperature and density, connections to extraplanar HI, and kinematics can give insights into the formation and ionization of the eDIG and to the formation history of the galaxy itself.

Studies of eDIG in other galaxies are usually limited to edge-on systems, where the eDIG can be photometrically detected and separated from the disk. While there are large photometric studies of the eDIG (Miller & Veilleux, 2003a; Rossa & Dettmar, 2003a,b), obtaining high resolution optical spectra of an entire disk has been observationally expensive. The kinematics of the eDIG, however, have proven to be very interesting: the rotation velocity decreases with increasing height above the midplane of the galaxy (e.g. Rand, 2000; Miller & Veilleux, 2003b; Fraternali et al., 2004; Heald et al., 2006a; Bizyaev et al., 2017). This vertical gradient in the rotation velocity (referred to as "lag") is also seen in extraplanar HI (e.g. Swaters et al., 1997; Fraternali et al., 2002; Zschaechner et al., 2015; Zschaechner & Rand, 2015). The advent of integral field unit (IFU) spectroscopy has revolutionized our ability to obtain high spatial and spectral resolution spectra of many galaxies. IFU galaxy surveys — such as CALIFA (Sánchez et al., 2012, 2016a), MaNGA (Bundy et al., 2015), and SAMI (Croom et al., 2012; Bryant et al., 2015) — enable the study of the kinematics of the eDIG in much larger samples.

Using intermediate inclination star-forming disk galaxies drawn from the EDGE-CALIFA survey, Levy et al. (2018) find that the ionized gas (traced by Hα) rotates slower than the molecular gas for 75% of their subsample. They attribute this difference in rotation velocity to a significant contribution from eDIG to the Hα emission. In the midplane, the molecular and ionized gas should have the same rotation ve-

locity. But if the eDIG rotates more slowly at greater heights above the midplane, the line-of-sight ionized gas rotation velocity will be consequently lowered. Indirect support for this hypothesis includes measured star formation rate surface densities above the empirical threshold for existence of the eDIG (Rossa & Dettmar, 2003a), [SII]/Hα and [NII]/Hα ratios higher than observed in galaxy midplanes (e.g. Haffner et al., 2009), and inferred ionized gas velocity dispersions large enough to support a thick ionized gas disk (Burkert et al., 2010). The results of Levy et al. (2018) reinforce the idea that eDIG is ubiquitous in star-forming galaxies.

With intermediate inclination galaxies, however, eDIG scale heights and the decrease in rotation velocity as a function of height cannot be directly measured. We, therefore, extend the work of Levy et al. (2018) using a sample of edge-on CALIFA galaxies to directly measure these eDIG properties. We show below that the measured ionized gas scale heights that are consistent with previous measurements. We find too that the ionized gas rotation velocity decreases with height for $\sim$75% of the galaxies, and that the magnitude of this decrease (the lag) is also consistent with previous ionized gas lag measurements. We discuss how our results fit into the various eDIG formation scenarios. We also verify that the lags are indeed due to eDIG through analysis of the ionization properties, uniquely possible due to the large wavelength coverage of the CALIFA IFU survey. It appears that the eDIG is indeed a prominent component in star-forming galaxies, affecting the morphology and kinematics of these systems. This also complements studies of eDIG in edge-on galaxies done with MaNGA (Jones et al., 2017; Bizyaev et al., 2017) and SAMI (Ho et al., 2016), as well as studies of outflows in CALIFA (López-Cobá et al., 2017,

2019).

We summarize the observations and sample selection in Section 3.2. The method and results of fitting the ionized gas scale height are reported in Section 3.3. The kinematic analysis and results are presented in Section 3.4. Section 3.5 discusses how the eDIG could be formed and constraints placed on its origin from this analysis. Constraints on the source of the lagging extraplanar ionized gas are discussed in the context of the ionization in Section 3.6. The results of this work are summarized in Section 3.7.

3.2 Observations and Data Reduction

3.2.1 The CALIFA Survey

The CALIFA survey (Sánchez et al., 2012) observed 667 nearby (z = 0.005–0.03) galaxies as of the third data release (DR3). Full details of the CALIFA observations are presented in Sánchez et al. (2012), Husemann et al. (2013), Walcher et al. (2014), García-Benito et al. (2015), and Sánchez et al. (2016a), as well as in Levy et al. (2018). A brief overview is presented here for context. All CALIFA galaxies are drawn from the Sloan Digital Sky Survey (SDSS). CALIFA used the PPAK IFU on the 3.5m Calar Alto observatory with two spectral gratings. The low resolution grating (V500) used here covered wavelengths from 3745–7500 Å with 6.0 Å (FWHM) spectral resolution, corresponding to a FWHM velocity resolution of 275 $\mathrm{km\,s^{-1}}$ at Hα. The typical spatial resolution of the CALIFA PSF is 2.5", corresponding to $\sim$0.8 kpc at the mean distance of the galaxies. We note that the

CALIFA PSF is a Moffat profile, not a Gaussian. The data used for this study come from the DR3 main sample as well as an additional 147 galaxies from the extension sample (Sánchez et al., 2016a)*. These data are gridded with 1" pixels. As in Levy et al. (2018), the "flux_elines" data products are used (Sánchez et al., 2016c,b). Additional masking was also applied to the CALIFA velocity fields using a SNR cut based on the integrated flux and error maps. Pixels with Hα SNR $<$ 3.5 were blanked. Data products, such as line intensity and velocity maps, come from Pipe3D version 2.2 (Sánchez et al., 2016c,b) provided in the final form by the CALIFA Collaboration.

The Hα fluxes were corrected for extinction by applying the Calzetti et al. (2000) extinction correction using the provided dust attenuation maps (A_V) from CALIFA. However, because the galaxies used here are edge-on, this correction is insufficient in the midplane where the extinction is much higher. We discuss the impact of extinction on our results in Appendix B.1.

3.2.2 The EDGE-CALIFA Survey

The EDGE-CALIFA survey (Bolatto et al., 2017) measured CO in 126 nearby galaxies with CARMA in the D and E configurations. Full details of the survey, data reduction, and masking techniques are discussed in Bolatto et al. (2017), and we present a brief overview here. The EDGE galaxies were selected from the CALIFA sample based on their infrared (IR) brightness and are biased toward higher star formation rates (SFRs) (see Figure 6 of Bolatto et al., 2017). The EDGE sample

*The CALIFA data cubes are publicly available at `http://califa.caha.es`.

is the largest sample of galaxies with spatially resolved CO, with typical angular resolution of 4.5″ (corresponding to ∼1.5 kpc at the mean distance of the sample). Data cubes were produced with 20 km s^{-1} velocity channels. Data products used in this analysis are as described in Bolatto et al. (2017)[†], except for the velocity maps. At high inclinations, the lines can become skewed so that a first moment or Gaussian fit to determine the velocity centroid will underestimate the velocity in general. The CO velocity maps used here are the velocity of the line peak (moment=-3 in `Miriad`)[‡].

When comparing the velocity fields from the EDGE and CALIFA surveys, it is important to note that the velocities are derived using different velocity conventions: EDGE follows the radio convention, and CALIFA follows the optical convention. Because velocities in both surveys are referenced to zero, all velocities are converted to the relativistic velocity convention. In both the optical and radio conventions, the velocity scale is increasingly compressed at higher redshifts. Typical systemic velocities in the EDGE-CALIFA sample are ∼4500 km s^{-1}, so this compression is non-negligible. The relativistic convention does not suffer from this compression effect. Differences between these velocity conventions and conversions among them can be found in Section A.1. All velocities presented here are in the relativistic convention, unless otherwise noted.

[†]The EDGE CO data cubes and moment maps for the main sample are publicly available and can be downloaded from `www.astro.umd.edu/EDGE`.

[‡]We note that this does not affect the CALIFA velocity maps because of the large instrumental line width; the lines remain Gaussian for very highly inclined systems.

3.2.3 Selecting Edge-on Galaxies

For this study, it is important to select the most edge-on systems for analysis to avoid interpreting a deviation in inclination away from edge-on as a detection of eDIG from either the photometry or kinematics (see Appendix B.2 for a more detailed discussion of this effect). Starting with 814 galaxies from CALIFA DR3 and the extended sample (Sánchez et al., 2016a), we first find those with inclinations of 90° in HyperLEDA (Makarov et al., 2014). Inclinations in HyperLEDA are defined as

$$\sin^2 i = \frac{1 - 10^{-2 \log r_{25}}}{1 - 10^{-2 \log r_o}} \tag{3.1}$$

where i is the inclination, r_{25} is the axis ratio of the B-band 25th mag arcsec^{-2} isophote, and

$$\log r_o = \begin{cases} 0.43 + 0.0053t, & \text{for } -5 \leq t \leq 7 \\ 0.38, & \text{for } t > 7 \end{cases} \tag{3.2}$$

which accounts for intrinsic disk thickness based on the morphological type (t). This results in 156 galaxies with $i = 90°$. Because morphological types are highly uncertain in edge-on systems, we follow this step with a visual inspection of the SDSS images, confirming the edge-on nature of each galaxy (Gunn et al., 1998, 2006; Doi et al., 2010; Eisenstein et al., 2011; Alam et al., 2015). Dust lanes were used (if present) to visually confirm the edge-on nature of the galaxies; galaxies with dust lanes that were not centered in the midplane were excluded. If no dust lane was present, very thin systems were selected. Galaxies with visible spiral arms, bars, or

other features that hinted at them not being perfectly edge-on were discarded. The inclination classifications from the Morphological Galaxy Catalog (MGC; Vorontsov-Vel'Yaminov & Arkhipova, 1962) were also used to confirm the edge-on nature of the galaxies; all galaxies are classified as edge-on in the MGC. This restricted the sample to 54 galaxies. From there, galaxies with robust Hα maps and clear rotation were selected. From these criteria, we construct a sample of 25 high-fidelity edge-on CALIFA galaxies. Composite SDSS and CALIFA images are shown in Figure 3.1; the Hα flux maps shown in this image are not masked based on the Hα SNR. The subsample of galaxies used here and relevant physical parameters are listed in Table 3.1. Throughout, IC 480 will be used as an example.

Four of these galaxies have known ionized gas outflows (Notes O in Table 3.1; López-Cobá et al., 2017, 2019). We do not exclude these galaxies from further analysis and will discuss the impacts of outflows in Section 3.6.3. Five of the galaxies have extraplanar ionized gas but do not meet the criteria to have an outflow according to López-Cobá et al. (2019) (Notes E in Table 3.1). The selection criteria used here and by López-Cobá et al. (2019) differ due to the goals of each study, so that our samples of galaxies with eDIG are not identical. We use a more stringent inclination cut than López-Cobá et al. (2019), who select galaxies with $i > 70°$. Whereas our primary selection criteria are edge-on systems with robust, clearly rotating Hα, López-Cobá et al. (2019) further select only galaxies whose ionized gas line ratios increase with height off the midplane. To be selected as an outflow candidate (labeled O in Table 3.1), the Hα equivalent width must be greater than 3 Å and there must be some biconical morphology (López-Cobá et al., 2019). Galaxies that do not meet

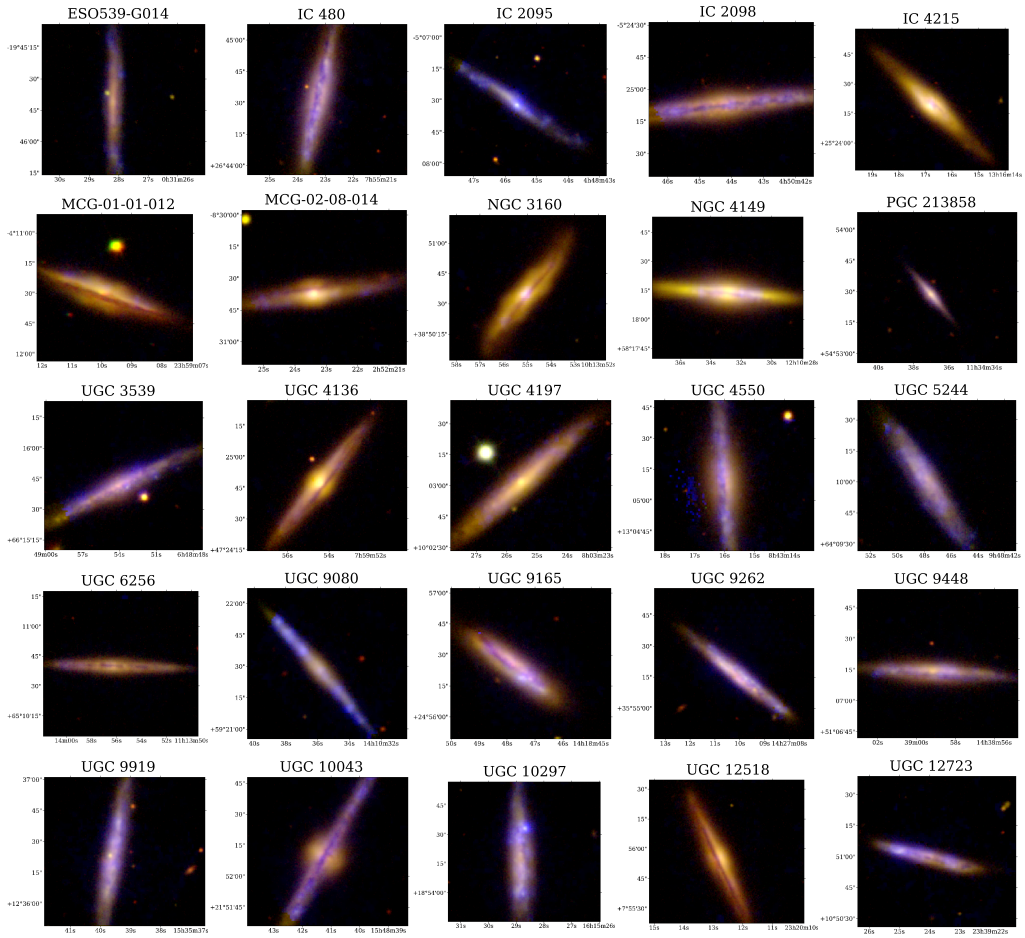

Figure 3.1: Composite images for the 25 edge-on CALIFA galaxies showing the SDSS r- and g-bands (red, green) and (non-masked) Hα flux from CALIFA (blue). The horizontal axes show J2000 right ascension and the vertical axes show J2000 declination. Images are cropped to the CALIFA field-of-view (74"×64"; Sánchez et al., 2012).

the additional outflow requirements are labeled as having eDIG, but not an outflow (labeled E in Table 3.1; López-Cobá et al., 2019). Three of the edge-on galaxies have robust CO measurements (IC 480, UGC 3539, and UGC 10043), and comparisons between the molecular and ionized gas for these galaxies will be discussed in Section 3.4.2.1.

3.3 Ionized Gas Scale Height Measurements

We determine the ionized gas scale height by fitting an exponential function to the Hα intensity maps. The fitting of the Hα intensity as a function of distance from the midplane is performed in single pixel (1") increments along the major axis; we refer to these increments (which are parallel to the rotation axis of the galaxy) as "radial bins". Independent scale heights are fit to the emission above and below the midplane. Before finding the scale height, the location of the midplane at each pixel along the major axis is determined by fitting a Gaussian to the Hα intensity along the minor axis (above and below the midplane); the centroid pixel is taken to be the location of the midplane and is used to divide emission above and below the midplane. To avoid being biased by the (much brighter) emission from HII regions in the midplane, we exclude the middle five pixels (the midplane and roughly one PSF FWHM above and below) from the fit. Fits for two radial bins in IC 480 are shown in Figure 3.2 (top). The reported Hα scale height is the exponential scale length. The PSF size is subtracted in quadrature from each fit to give an estimate of the scale height as a function of radius. We then interpolate the radial bins so that the spacing

Name	ID	R.A. (J2000 °)	Decl. (J2000 °)	Type	Notes	Distance (Mpc)	D_{25} (kpc)	PA (°)	V_{sys} ($km\,s^{-1}$)	W4 (mag)	SFR ($M_\odot\ yr^{-1}$)	$h(H\alpha)$ (kpc)	V(z=0) ($km\,s^{-1}$)	Lag ($km\,s^{-1}\,kpc^{-1}$)	ΔLag/Δr ($km\,s^{-1}\,kpc^{-2}$)
ESO539-G014	15	7.86771	-19.76127	Scd	...	102.21	52.87±3.14	88.9	6984	6.94 ± 0.10	$0.71^{+0.50}_{-0.12}$	1.10±0.80	$144.5^{+15.6}_{-15.7}$	$18.9^{+8.1}_{-8.0}$	$-3.4^{+0.2}_{-0.2}$
IC 480	159	118.84634	26.74287	Sbc	O	66.02	33.60±2.07	256.7	4545	3.97 ± 0.02	$4.58^{+3.21}_{-0.62}$	1.13±0.35	$138.5^{+15.6}_{-15.7}$	$18.6^{+8.4}_{-8.4}$	$-1.7^{+1.5}_{-1.5}$
IC 2095	141	72.19066	-5.12475	Sc	...	40.71	17.27±1.29	327.7	2820	...	...	0.60±0.26	$54.9^{+18.7}_{-18.7}$	$2.7^{+17.7}_{-17.5}$	$4.9^{+1.3}_{-1.3}$
IC 2098	142	72.68451	-5.41857	Sc	E	39.77	28.33±1.23	187.0	2776	4.57 ± 0.03	$0.95^{+0.66}_{-0.13}$	0.62±0.32	$91.8^{+16.1}_{-15.2}$	$-10.4^{+18.5}_{-17.4}$	$8.2^{+1.7}_{-4.9}$
IC 4215	615	199.07117	25.40582	Sab	...	55.46	25.04±1.75	131.2	3828	5.07 ± 0.04	$1.17^{+0.82}_{-0.16}$	1.64±0.58	$151.5^{+19.7}_{-18.9}$	$16.8^{+31.4}_{-29.8}$	$20.9^{+1.0}_{-14.5}$
MCG-01-01-012	936	359.79867	-4.19247	Sb	E	82.50	37.77±2.61	339.7	5657	5.59 ± 0.06	$1.60^{+1.12}_{-0.23}$	2.94±1.57	$158.8^{+30.0}_{-30.1}$	$14.9^{+20.0}_{-19.9}$	$1.3^{+2.1}_{-2.0}$
MCG-02-08-014	111	43.09772	-8.51057	Sab	...	71.80	37.22±2.23	188.2	4936	4.22 ± 0.02	$4.28^{+3.00}_{-0.58}$	0.92±0.35	$124.3^{+29.6}_{-29.7}$	$29.6^{+22.6}_{-22.6}$	$0.5^{+1.5}_{-1.5}$
NGC 3160	319	153.47951	38.84297	Sab	B	98.52	35.75±3.43	50.8	6689	4.72 ± 0.03	$5.09^{+3.57}_{-0.70}$	...	$192.0^{+47.3}_{-44.4}$	$-9.7^{+71.8}_{-19.6}$	$8.0^{+0.1}_{-2.3}$
NGC 4149	502	182.63695	58.30408	Sb	BE	43.76	17.45±1.57	174.8	3030	6.00 ± 0.09	$0.31^{+0.22}_{-0.05}$	0.83±0.25	$199.4^{+27.0}_{-22.2}$	$66.0^{+17.3}_{-21.1}$	$9.5^{+9.3}_{-3.8}$
PGC 213858	5033	173.65409	54.89121	Sab	...	83.13	14.44±2.83	310.9	5699	8.27 ± 0.14	$0.14^{+0.10}_{-0.03}$	...	$117.8^{+13.7}_{-13.8}$	$16.0^{+23.7}_{-23.4}$	$0.9^{+7.0}_{-6.0}$
UGC 3539	148	102.22453	66.26050	Sbc	BO	46.70	24.89±1.49	32.6	3231	4.47 ± 0.03	$1.45^{+1.01}_{-0.20}$	0.72±0.37	$117.2^{+13.1}_{-13.1}$	$14.8^{+6.7}_{-6.7}$	$1.9^{+2.4}_{-2.4}$
UGC 4136	168	119.97651	47.41340	Sa	...	95.86	44.29±3.04	51.1	6551	6.08 ± 0.07	$1.37^{+0.96}_{-0.20}$	1.22±1.05	$234.2^{+37.0}_{-37.5}$	$29.6^{+25.8}_{-26.0}$	$-2.7^{+0.5}_{-0.4}$
UGC 4197	174	120.85633	10.05058	Sb	...	65.56	32.84±2.23	41.8	4514	5.33 ± 0.04	$1.29^{+0.90}_{-0.18}$	0.58±0.35	$197.0^{+23.7}_{-32.4}$	$69.1^{+17.0}_{-32.0}$	$-0.6^{+1.6}_{-0.8}$
UGC 4550	218	130.81647	13.08536	Sb	E	29.36	18.01±0.92	94.6	2070	4.64 ± 0.03	$0.49^{+0.34}_{-0.07}$	0.47±0.30	$101.5^{+11.5}_{-11.7}$	$25.8^{+24.7}_{-24.7}$	$-8.8^{+6.4}_{-1.9}$
UGC 5244	297	147.20058	64.16847	Sc	...	43.33	18.99±1.41	122.3	3000	6.24 ± 0.07	$0.24^{+0.17}_{-0.04}$	0.68±0.38	$99.9^{+13.3}_{-13.5}$	$18.5^{+11.4}_{-11.4}$	$-3.1^{+1.4}_{-1.4}$
UGC 6256	383	168.48397	65.17769	Sc	...	47.80	17.07±1.59	357.7	3336	7.06 ± 0.11	$0.14^{+0.10}_{-0.02}$	1.03±0.52	$110.8^{+32.1}_{-27.3}$	$-2.8^{+62.3}_{-25.7}$	$4.2^{+2.6}_{-8.4}$
UGC 9080	713	212.64959	59.35802	Sc	...	43.58	15.63±1.44	130.4	3048	6.40 ± 0.08	$0.21^{+0.15}_{-0.03}$	0.69±0.30	$78.1^{+13.4}_{-13.5}$	$16.6^{+15.9}_{-15.9}$	$8.1^{+2.3}_{-2.6}$
UGC 9165	731	214.69920	24.94047	S0a	O	74.87	26.43±2.55	144.8	5199	3.47 ± 0.02	$9.33^{+6.54}_{-1.26}$	1.08±0.34	$160.4^{+13.4}_{-13.5}$	$14.1^{+5.0}_{-5.0}$	$2.2^{+0.6}_{-0.6}$
UGC 9262	747	216.79358	35.92219	Sbc	E	122.50	41.39±4.45	141.0	8318	4.04 ± 0.02	$14.70^{+10.30}_{-1.99}$	1.97±0.97	$200.1^{+24.2}_{-24.2}$	$16.8^{+5.0}_{-4.9}$	$-0.1^{+0.4}_{-0.4}$
UGC 9448	765	219.74656	51.12068	Sb	...	31.50	14.73±1.02	356.6	2188	6.12 ± 0.07	$0.14^{+0.10}_{-0.02}$	0.39±0.16	$96.2^{+17.2}_{-17.1}$	$19.8^{+25.7}_{-25.4}$	$-4.7^{+10.7}_{-1.4}$
UGC 9919	805	233.91577	12.60638	Sc	...	45.81	19.66±1.48	80.0	3170	5.30 ± 0.04	$0.64^{+0.45}_{-0.09}$	0.99±0.43	$107.2^{+12.2}_{-12.3}$	$15.7^{+14.2}_{-14.2}$	$5.3^{+1.5}_{-1.5}$
UGC 10043	811	237.17269	21.86980	Sbc	O	30.62	19.57±0.99	60.6	2128	4.39 ± 0.03	$0.66^{+0.47}_{-0.09}$	0.48±0.13	$104.5^{+15.9}_{-16.0}$	$22.6^{+18.4}_{-18.4}$	$-12.1^{+1.0}_{-0.5}$
UGC 10297	827	243.87017	18.90479	Sc	B	32.94	20.63±1.03	272.6	2287	5.60 ± 0.06	$0.25^{+0.18}_{-0.04}$	0.48±0.22	$91.3^{+10.0}_{-10.2}$	$24.6^{+8.0}_{-7.9}$	$3.5^{+1.7}_{-1.8}$
UGC 12518	910	350.05353	7.93222	Sb	...	55.31	22.68±1.78	295.1	3818	5.64 ± 0.06	$0.69^{+0.48}_{-0.10}$	...	$151.2^{+25.6}_{-25.7}$	$24.5^{+46.3}_{-45.6}$	$7.4^{+1.1}_{-13.4}$
UGC 12723	926	354.84994	10.84992	Sd	...	78.07	26.43±2.52	167.2	5359	5.07 ± 0.04	$2.32^{+1.63}_{-0.32}$	1.00±0.66	$98.8^{+31.1}_{-31.1}$	$6.7^{+17.9}_{-17.7}$	$1.6^{+1.1}_{-1.1}$

The table lists edge-on CALIFA galaxies, their CALIFA ID number, and their R.A. and Decl. from HyperLEDA (with offsets as needed).Morphological types and the diameter of isophote corresponding to 25 mag arcsec^{-2} (D_{25}) are from HyperLEDA. Notes denote whether this galaxy has a bar (B), ring (R), is part of a multiple (M) (all from HyperLEDA), has an outflow (O) (López-Cobá et al., 2019), or has extraplanar ionized gas (E) (López-Cobá et al., 2019). Distances, position angles (PA), and systemic velocities (V_{sys} are from CALIFA. W4 is the WISE W4 (22μm) Vega magnitude (see Section 3.5.2). SFR is the star formation rate calculated from the WISE W4 magnitudes (see Section 3.5.2). $h(H\alpha)$ is the measured Hα scale height (see Section 3.3). V(z=0) is the fitted rotation velocity in the midplane (see Section 3.4.2). $\Delta V/\Delta z$ is the vertical gradient in the rotation velocity (see Section 3.4.2). The 'lag' reported here is $-\Delta V/\Delta z$. ΔLag/Δr is the radial gradient in the lag (i.e. the change in lag as a function of radius; see Section 3.5.1). Uncertainties on $\Delta V/\Delta z$, V(z=0), and ΔLag/Δr reflect the 68% confidence interval determined from the posterior likelihood distributions.

Table 3.1: Parameters for the Edge-On CALIFA Galaxies

along the major axis is the PSF FWHM. The Hα scale height measurement at small galactocentric radii may be affected or dominated by a bulge or outflow as opposed to an eDIG disk. Méndez-Abreu et al. (2017) measure r-band bulge effective radii ($R_{e,bulge}$) for a subset of the CALIFA galaxies. Their photometric analysis excludes all highly inclined systems. Their sample of 404 galaxies is representative of the CALIFA sample as a whole, and we will assume their median $R_{e,bulge}$ is representative of our sample as well. Using the redshift of each galaxy and $H_0 = 70\,km\,s^{-1}\,Mpc^{-1}$ (Méndez-Abreu et al., 2017), the median $R_{e,bulge} = 1.05\,kpc$. We exclude radial bins with $r < 2\,R_{e,bulge} = 2.1\,kpc$ (gray regions in Figure 3.2 middle, bottom). We discuss the impact of bulge and outflow contamination on our results in Sections 3.6.2 and 3.6.3. The average scale height ($h(H\alpha)$) was found for each galaxy by averaging all radial bins above and below the midplane weighted inversely by the variance of each bin. The uncertainty ($\sigma_{h(H\alpha)}$) is the weighted standard deviation. These values are in Table 3.1. The Hα scale height as a function of radius is shown for IC 480 in Figure 3.2 (middle, bottom). We find that >88% of the subsample galaxies have a measurable eDIG scale height, where a measurable eDIG scale height has $h(H\alpha) > \sigma_{h(H\alpha)}$.

We investigate the distribution of Hα scale heights in this sample using a kernel density estimator (KDE). A KDE can be thought of as a histogram where the "bin width" is set by the uncertainty. Each $h(H\alpha)$ measurement is represented as a Gaussian, where the centroid is $h(H\alpha)$ and the width is set by the measurement uncertainty ($\sigma_{h(H\alpha)}$). The individual Gaussians are summed and normalized to unit area to produce the distribution of $h(H\alpha)$ as shown in Figure 3.3. Since the KDE

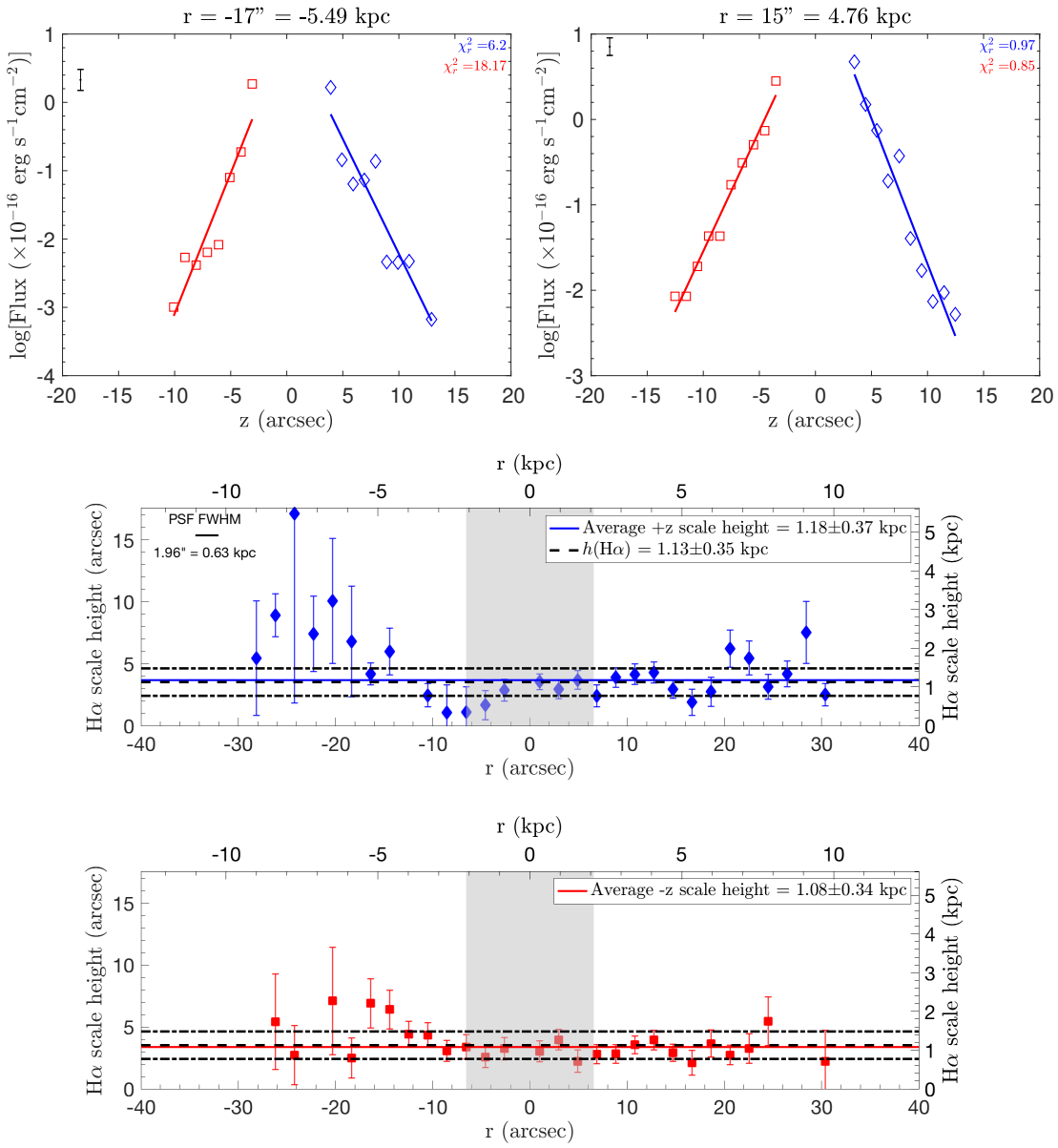

Figure 3.2: (Top left) The exponential fit to the Hα flux in IC 480 as a function of distance from the midplane (z) in one radial bin ($r = -17" = -5.49$ kpc). The open symbols show the flux measurements at each pixel above (blue diamonds) or below (red squares) the midplane. The solid lines show the exponential fits. The black error bars in the upper left corner show the typical uncertainty on the Hα flux measurements. Top right panels is the same as the top left but for $r = 15" = 4.76$ kpc. The two lower panels show the fitted exponential scale height of the Hα disk above (top; blue diamonds) and below (bottom; red squares) the midplane as a function of radius (r) for IC 480. The PSF FWHM has been removed in quadrature. The average scale height weighted by the uncertainties and corresponding weighted standard deviation are shown in the black dashed and dot-dashed lines. The gray shaded region shows the central radii excluded from the median (where $r < 2\,R_{e,bulge}$). The solid black line in the upper left corner shows the FWHM of the PSF.

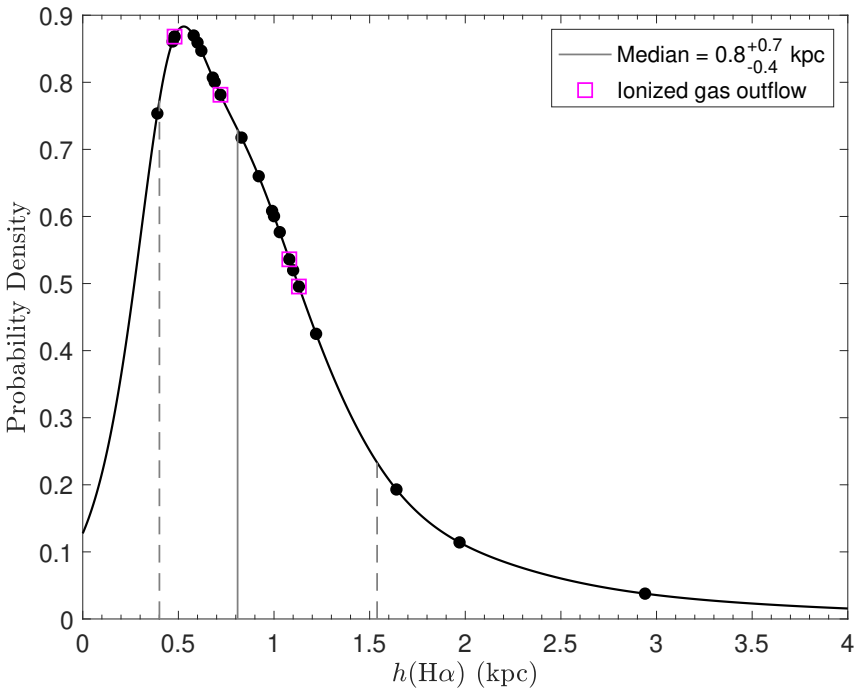

Figure 3.3: The distribution of h(Hα) all 25 galaxies. Individual galaxies are shown as the black points. Those galaxies with known ionized gas outflows are outlined with magenta squares (López-Cobá et al., 2017, 2019). The median h(Hα) for this sample of edge-on galaxies is $0.8^{+0.7}_{-0.4}$ kpc, with values ranging from 0.3–2.9 kpc.

is a probability distribution, the median of the distribution is where the cumulative distribution function is 0.5. We report this value as the median h(Hα) for the sample and find the inner 68% of the distribution in the same way. The median scale height of this sample is $0.8^{+0.7}_{-0.4}$ kpc. Values range from 0.3–2.9 kpc, and the distribution is peaked around 0.5 kpc. Galaxies with ionized gas outflows (López-Cobá et al., 2017, 2019) are shown in magenta in Figure 3.3; those galaxies reside around the median scale height rather than populating the high h(Hα) tail of the distribution. We investigate whether there are correlations between h(Hα) and any global galaxy property (such as stellar mass, star formation rate, star formation rate surface density, etc.; see Section 3.5.2) and find no trends with any parameter.

3.3.1 Previous eDIG Scale Height Measurements

We compare our eDIG scale heights to those previously measured in the literature. The most extensive sample of eDIG scale height measurements is from the MaNGA sample investigated by Bizyaev et al. (2017) who find a median Hα scale height of 1.2 ± 0.5 kpc over their sample of galaxies with detected eDIG. Miller & Veilleux (2003a) also measured eDIG scale heights in a large sample of galaxies. The used both one- and two-component exponential fits, where the latter represents a brighter quiescent eDIG phase as well as a fainter disturbed phase. The median scale height for the more extended (disturbed) eDIG phase over their sample of 16 galaxies is 2.3 ± 4.3 kpc[§]. If only a one-component exponential fit is used, the median scale height is 0.5 ± 0.9 kpc over the sample. We attempted to fit a two-component exponential model to our data, but the fits were poorly constrained because our data are not sensitive enough at large distances from the midplane. Levy et al. (2018) estimated the Hα scale height in their sample of intermediate-inclination EDGE-CALIFA galaxies using three methods: (1) from the Hγ velocity dispersion; (2) using an asymmetric drift correction to estimate for the Hα velocity dispersion and the implied scale height; (3) using a suite of kinematic simulations. We refer the reader to Sections 5.5 and 5.7 of Levy et al. (2018) for the specifics of each method. For all three methods, possible Hα scale heights were limited to $\lesssim 1.5$ kpc. Our observations of the edge-on galaxies in this subsample are well matched to this

[§]Miller & Veilleux (2003a) report the average scale height of their sample (4.3 kpc). An unweighted mean is easily biased by a few galaxies with large scale heights. We consider the median or weighted mean to be more representative of the sample as a whole.

limit in general. We compiled an extensive list of eDIG scale heights from a variety of sources, observations, and fitting techniques (Veilleux et al., 1995; Rand, 1997; Wang et al., 1997; Hoopes et al., 1999; Collins et al., 2000; Collins & Rand, 2001; Miller & Veilleux, 2003a; Rosado et al., 2013; Bizyaev et al., 2017). The median eDIG scale height from these various techniques is 1.0 ± 2.2 kpc. We conclude that our $h(\mathrm{H}\alpha)$ measurements are in good agreement with previous measurements of eDIG in nearby galaxies, although there is substantial scatter from galaxy to galaxy across all samples.

3.4 Ionized Gas Kinematics

3.4.1 Position-Velocity Diagrams

In order to compare the kinematics as a function of distance from the midplane, we construct position-velocity (PV) diagrams by taking cuts parallel to the major axis in single-pixel increments along the minor axis. The systemic velocity is subtracted (listed in Table 3.1). Pixels with SNR < 5 in either the Hα intensity or velocity maps are masked out. Although we refer to this quantity as $\mathrm{V_{rot}}$, it is likely that it includes contributions from non-rotational motions as well. None of the velocities have been corrected for inclination since we assume that all galaxies are perfectly edge on; we investigate the effects of extinction and inclination on our results in Appendices B.1 and B.2 respectively. Figure 3.4 shows the PV diagram for IC 480 color-coded by distance from the midplane. Distances are converted from angular to physical units using the distance to each galaxy listed in Table 3.1.

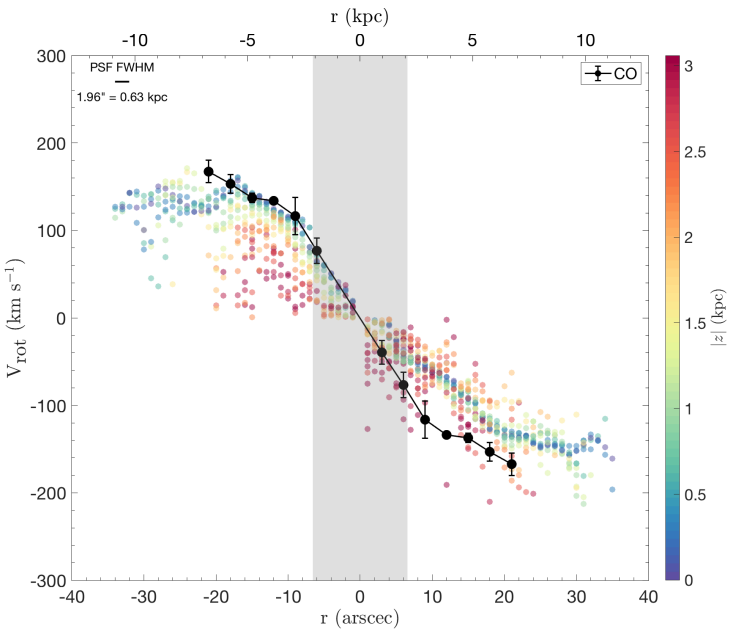

Figure 3.4: PV diagram for IC 480. The colored dots show the Hα emission color-coded by distance from the midplane. The gray shaded region shows radii $< 2\,R_{e,bulge}$. The Hα rotation velocity decreases with distance from the midplane. The black dots show the CO PV diagram (see Section 3.4.2.1). The solid black line in the upper left corner shows the FWHM of the PSF.

3.4.2 Vertical Gradients in Ionized Gas Rotation Velocity

Both the Hα velocity fields and PV diagrams show evidence for a decrease in V_{rot} with distance from the midplane (Figure 3.4). We can further quantify this decrease in terms of the vertical gradient in the rotation velocity ($\Delta V/\Delta z$) with units of $km\,s^{-1}\,kpc^{-1}$. The magnitude of $\Delta V/\Delta z$ is often referred to as the "lag" in the literature. From the PV diagrams, the rotation velocity at each height is averaged, excluding radii less than $2\,R_{e,bulge}$. This is shown in Figure 3.5. We fit a line using a Bayesian method, where the slope is $\Delta V/\Delta z$. We marginalize over the intercept of the line and calculate the 68% confidence interval from the posterior distribution of the slopes. The best fit line and confidence interval are also shown

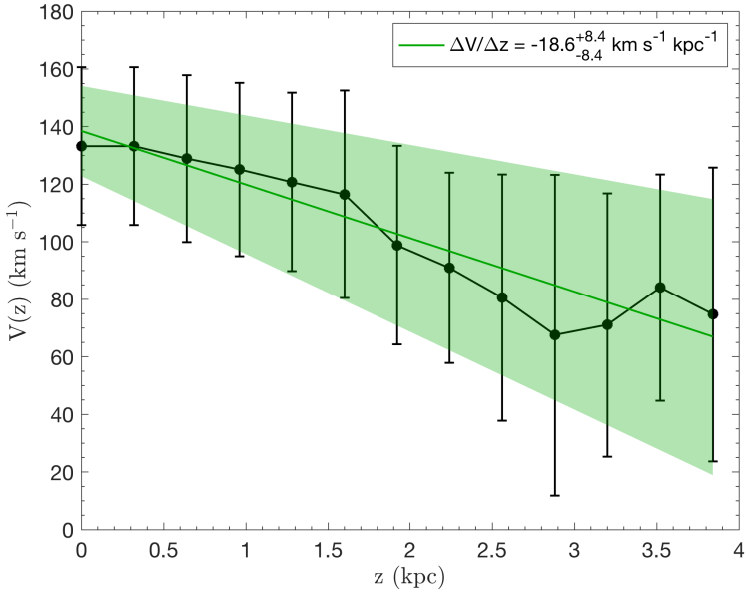

Figure 3.5: The Hα rotation velocity as a function of height for IC 480, calculated from the median of the position-velocity diagram (e.g., Figure 3.4) over all radii $> 2\,R_{e,bulge}$ at each height. There is a clear, nearly linear decrease in V_{rot} with increasing distance from the midplane. The green line is the best fit. The green shaded region shows the 68% confidence interval.

in Figure 3.5. We argue that extinction does not significantly bias the observed $\Delta V/\Delta z$ in Appendix B.1.

We investigate the distribution of $\Delta V/\Delta z$ over the sample. We find that 60% have measurable negative vertical gradients in the rotation velocity, where a measurable negative vertical gradient has $\Delta V/\Delta z + \sigma_{\Delta V/\Delta z,+} < 0$. The other 40% are consistent with no gradient. There are no galaxies for which the Hα rotation velocity increases with height within the uncertainties (i.e. where $\Delta V/\Delta z - \sigma_{\Delta V/\Delta z,-} > 0$). We can further investigate the distribution of $\Delta V/\Delta z$ using a KDE (Figure 3.6 top). The distribution of $\Delta V/\Delta z$ is strongly peaked around -20 km s^{-1} kpc^{-1} with values ranging from $[-70,\ 10]$ km s^{-1} kpc^{-1} and a median of -19^{+17}_{-26} km s^{-1} kpc^{-1}.

Extraplanar ionized gas which "lags" (i.e. rotates more slowly than) gas in

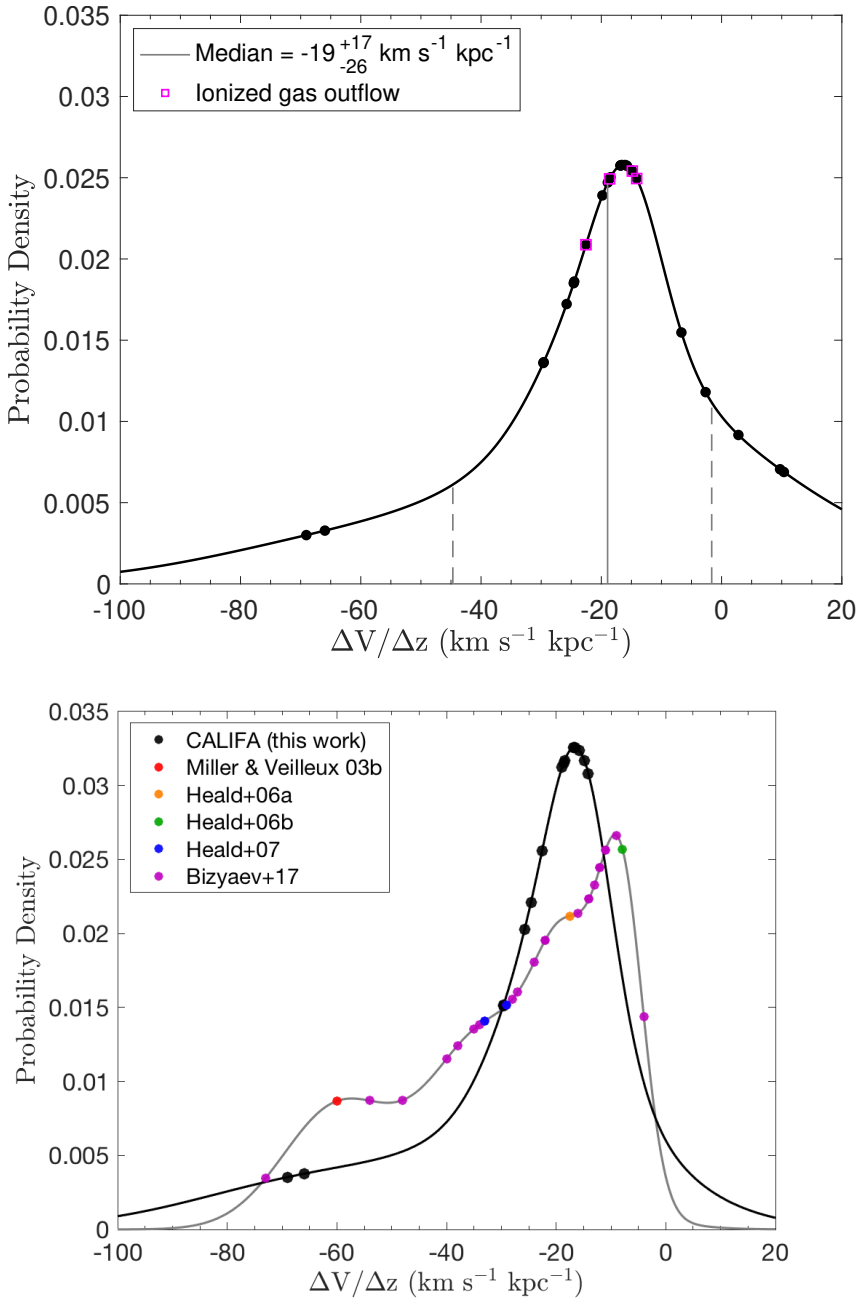

Figure 3.6: (Top) The KDE of $\Delta V/\Delta z$ for the 25 edge-on CALIFA galaxies. The median $\Delta V/\Delta z$ and inner 68% of the distribution are marked by the solid and dashed gray lines. Galaxies with ionized gas outflows are marked with a magenta square (López-Cobá et al., 2017, 2019). (Bottom) The KDE for the 17 CALIFA galaxies with significant lags (with respect to the measurement uncertainty, black) compared to the KDE of the literature values (gray) measured from Miller & Veilleux (2003b), Heald et al. (2006a,b, 2007), and Bizyaev et al. (2017). The median $\Delta V/\Delta z$ for the values pulled from the literature is -25^{+16}_{-28} km s^{-1} kpc^{-1} whereas the median for the CALIFA galaxies with lags is -21^{+12}_{-27} km s^{-1} kpc^{-1}.

the midplane has been observed in many systems, such as NGC 891 (Heald et al., 2006b), NGC 5775 (Heald et al., 2006a), NGC 4302 (Heald et al., 2007), NGC 2820 (Miller & Veilleux, 2003b), NGC 4013 (Miller & Veilleux, 2003b), and 25 galaxies from the MaNGA survey (Bizyaev et al., 2017)[¶]. We compare the distribution and magnitudes of lags from this sample to those compiled from the literature listed above. Figure 3.6 (top) shows the distribution for this sample of edge-on CALIFA galaxies. Because of our strict selection criteria (see Section 3.2.3), we have sufficient detections along the minor axis to measure lags in all galaxies, and can measure lags which are consistent with zero within the uncertainties. To better compare with the literature values — which only report lags where they are nonzero — we select the 17 galaxies in our subsample with significant nonzero lags given their uncertainties. Figure 3.6 (bottom) shows the distribution of $\Delta V/\Delta z$ for these galaxies with nonzero lags compared to the distribution of values from the literature listed above. Although our distribution is more peaked, the values from the literature also cluster between $\sim -40 - 0$ km s^{-1} kpc^{-1}. The median $\Delta V/\Delta z$ from the literature values is -25^{+16}_{-28} km s^{-1} kpc^{-1}, where the uncertainty is the inner 68% of the distribution. The median $\Delta V/\Delta z$ of the CALIFA galaxies with measurable lags is -21^{+12}_{-27} km s^{-1} kpc^{-1}. The full sample of 25 galaxies is used for the remainder of the analysis.

In particular, we highlight the results of a systematic study of lagging eDIG using observations from the MaNGA survey (Bundy et al., 2015). Bizyaev et al. (2017) find lagging extraplanar ionized gas in at least 37% of their sample of 67 edge-

[¶]Lagging extraplanar HI has also been observed in several systems, but we limit the discussion here to the ionized gas properties.

on galaxies (purple points in Figure 3.6 bottom) compared to the 60% of galaxies we find with lagging Hα in this study. The fraction of lagging eDIG they find is likely lower than in this study due to their selection criteria and their slightly coarser spatial resolution. In their sample, edge-on galaxies have no evidence of spiral arms in the SDSS images, a dust lane projected near the galaxy midplane in the SDSS images (if present), and no sign of interaction (Bizyaev et al., 2017). They make no selection based on the SNR of the Hα velocity fields for their sample of 67 edge-on galaxies. As a consequence—as Bizyaev et al. (2017) point out—they cannot determine whether the other 63% of the edge-on galaxies in their sample have lags or not. Because of our selection criteria (Section 3.2.3), however, we can distinguish between galaxies with and without lags for our entire sample. In other words, the subsample of 67 galaxies used by Bizyaev et al. (2017) includes all edge-on, non-interacting MaNGA galaxies. Our subsample of 25 galaxies includes all edge-on, non-interacting CALIFA galaxies with Hα measurements which are robust enough to allow for a lag measurement to be made. The lower spatial resolution of the MaNGA local sample ($\sim$1.5 kpc) compared to CALIFA ($\sim$ 0.8 kpc) also makes distinguishing extraplanar gas more difficult in the former. Therefore, the 37% of galaxies with lags that Bizyaev et al. (2017) do find is a lower limit.

We connect this result and those of Levy et al. (2018) and Davis et al. (2013) as being part of the same phenomenon. Levy et al. (2018) and Davis et al. (2013) found that the rotation velocity of the ionized gas is systematically lower than that of the molecular gas in intermediate inclination galaxies. Levy et al. (2018) argued that this was indeed due to eDIG with a vertical gradient in the rotation velocity.

Viewed at an intermediate inclination, velocities from eDIG at different heights average along the line of sight, producing a smaller net ionized gas rotation velocity. A similar averaging is likely occurring in the early-type galaxies studied by Davis et al. (2013), although the source of this more slowly-rotating ionized gas is likely due to the bulge rather than a layer of extraplanar gas. Neither Davis et al. (2013) nor Levy et al. (2018) find galaxies in which the ionized gas rotates faster than the molecular gas. Similarly, we find no galaxies in which the ionized gas rotation velocity increases with height above the midplane (given the uncertainties). We note that the fractions of galaxies found to have some form of more slowly-rotating ionized gas not associated with the thin gas disk are similar among these three studies: 77% of intermediate-inclination disk galaxies (Levy et al., 2018), 80% of gas-rich early-type galaxies, and 60% of edge-on disk galaxies show evidence of extraplanar ionized gas that rotates more slowly than the midplane. As there is evidence for lagging, extraplanar diffuse gas in a large fraction of galaxies in surveys of the local universe, understanding the origin and properties of this diffuse ionized gas is important. Moreover, investigating galaxies without lagging eDIG or those with negative lags (e.g. Péroux et al., 2019) may give insights into the unique evolutionary and star formation histories of these systems.

3.4.2.1 Comparisons with the Molecular Gas

There are three galaxies in this subsample that have robust CO detections from the EDGE-CALIFA survey (Bolatto et al., 2017): IC 480, UGC 3539, and

Galaxy	CO $\Delta V/\Delta z$ ($km\,s^{-1}\,kpc^{-1}$)	CO V(z=0) ($km\,s^{-1}$)	Max. Height[a] (kpc)
IC 480	$-1.5^{+28.5}_{-46.1}$	$136.3^{+11.0}_{-10.0}$	0.32
UGC 3539	$1.4^{+21.5}_{-23.1}$	$134.3^{+4.0}_{-4.0}$	0.23
UGC 10043	$-24.3^{+40.2}_{-41.0}$	$142.3^{+8.0}_{-10.0}$	0.30

[a] The is the maximum vertical extent probed by the CO data.

Table 3.2: CO Lags

UGC 10043. For their galaxy and kinematic parameters, we refer the reader to the tables in Bolatto et al. (2017) and Levy et al. (2018). All of these galaxies are candidates to host ionized gas outflows (López-Cobá et al., 2017, 2019). We repeat the analysis described in Sections 3.4.1 and 3.4.2 to derive PV diagrams and measure any lag in the CO velocity as a function of height. As shown in Table 3.2, the CO scale height can be measured only out to ∼0.3 kpc from the midplane (which is substantially smaller than the CO PSF) and the uncertainties on each point and the gradient are large. The maximum heights probed by the CO are much smaller than the Hα scale heights listed in Table 3.1. All three galaxies have CO lags consistent with zero, although this is limited by the small range of heights probed. Higher sensitivity and resolution data are needed for robust CO lag and scale height measurements.

3.4.2.2 Implications for Galaxy Dynamical Mass Measurements

Reiterating from Levy et al. (2018), the dynamical mass inferred from the ionized gas rotation velocity of a galaxy with lagging ionized gas will be systematically underestimated if left uncorrected. Although the midplane HII regions constitute the bulk of the ionized gas mass in a galaxy, more than half of the Hα luminosity

comes from the (e)DIG (e.g. Reynolds, 1993; Veilleux et al., 1995; Zurita et al., 2000; Poetrodjojo et al., 2019). This systematic underestimate of the dynamical mass will be worse in systems with smaller circular velocities and/or larger lags. For a galaxy with an eDIG scale height of 0.8 kpc (the median for this sample), a circular velocity of 200 $\mathrm{km\,s^{-1}}$, and a lag of 21 $\mathrm{km\,s^{-1}\,kpc^{-1}}$ (the median for this sample), the dynamical mass will be underestimated by ∼13%. This effect scales proportionally with the lag and eDIG scale height and inversely with the maximum rotation velocity.

A measurement of the ionized gas velocity dispersion is needed to correctly determine the circular velocity and dynamical mass (e.g. Iorio et al., 2017; Aquino-Ortíz et al., 2018; Leung et al., 2018). The low spectral resolution of CALIFA (275 $\mathrm{km\,s^{-1}}$ FWHM at $\lambda_{\mathrm{H}\alpha}$) makes determining the ionized gas velocity dispersion difficult, if not impossible, for this sample (see Levy et al., 2018). Since the presence of eDIG is presumably related to the star formation rate surface density (Rand, 1996; Rossa & Dettmar, 2003a), we would expect more eDIG in higher-redshift systems where SFRs are higher and galaxies are more compact on average. Moreover, since spatially-resolved galaxy studies at high redshift are difficult, inferring the presence of this lagging eDIG photometrically or kinematically will be difficult. Therefore, the potential to underestimate the dynamical masses of these high redshift systems using ionized gas rotation velocities is increased due to astrophysical and instrumental effects.

3.5 The Origin of Extraplanar Gas

Both internal and external origins of lagging extraplanar gas have been suggested and substantiated. For internal origins, stellar feedback from overpressured superbubbles driven by star formation activity can eject material through galactic fountains. The material does not have enough momentum to escape the galaxy, but settles into a thick ionized disk (e.g. Shapiro & Field, 1976; Bregman, 1980). Models of galactic fountain-produced extraplanar gas can reproduce the observed vertical gradients in the rotation velocity of extraplanar HI and Hα (Barnabè et al., 2006; Marinacci et al., 2010, 2011). For external origins, material is accreted from the IGM or corona, (e.g. Oort, 1970; Binney, 2005; Fraternali et al., 2005; Kaufmann et al., 2006). In simulations of accretion from the hot corona, gas is accreted cylindrically along the angular momentum axis, and vertical gradients in the rotation velocity agree with observed values (Kaufmann et al., 2006). In reality it is likely that both internal and external processes contribute (e.g. Kaufmann et al., 2006; Haffner et al., 2009; Combes, 2014). These various formation scenarios are summarized schematically in Figure 3.7.

3.5.1 Radial Variations in the Lag

Inferring the origin of the extraplanar gas directly from the data is difficult. The formation scenarios make different predictions for radial variations in the lag which can possibly be used to differentiate among them. If the extraplanar gas origin is internal to the galaxy, caused for example by galactic fountains, a decrease

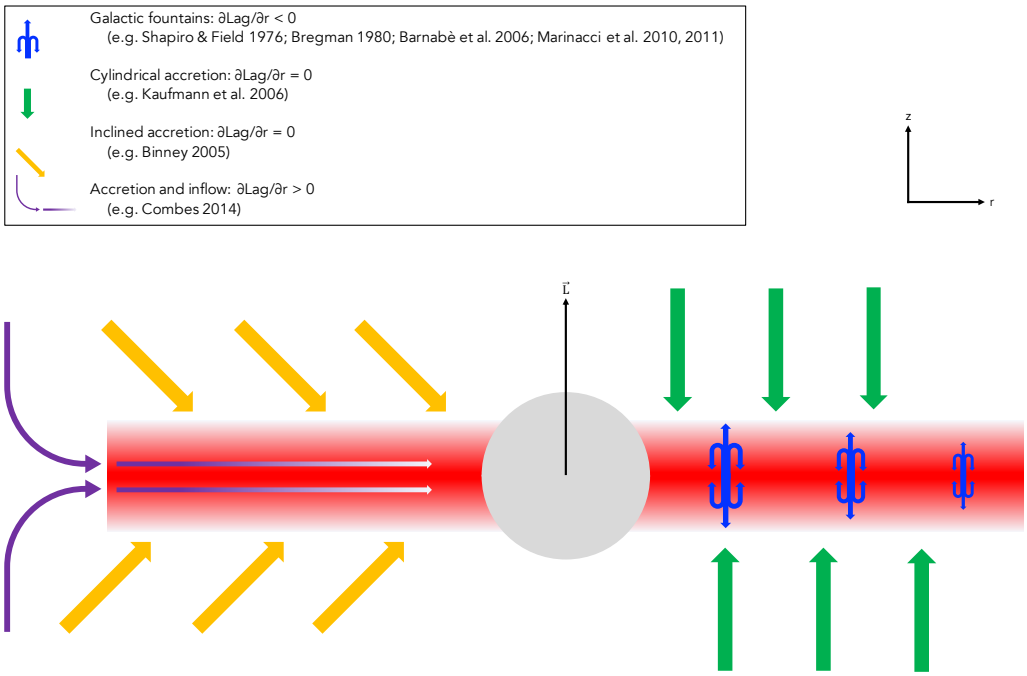

Figure 3.7: A cartoon diagram of the various formation mechanisms for extraplanar gas discussed in Section 3.5. A schematic edge-on disk galaxy is shown, where the midplane is solid red, the bulge is the gray circle, and the lagging extraplanar gas is shown as the red-to-white gradient. Galactic fountains are shown in the blue curved arrow clusters, where the size of the symbol is related to the magnitude of the lag produced (Shapiro & Field, 1976; Bregman, 1980; Barnabè et al., 2006; Marinacci et al., 2010, 2011). The green vertical arrows show cylindrical accretion from the corona (Kaufmann et al., 2006). Accretion which is inclined with respect to the angular momentum axis (vector labeled $\vec{L}$) is shown in the gold slanted arrows (Binney, 2005). Accretion at the outskirts and the resulting inflow are shown in the purple arrows, where the purple-to-white gradient shows the decreasing inflow velocity from the outskirts to center (Combes, 2014). The legend gives the expected behavior of the radial variation of the lag ($\partial \mathrm{Lag}/\partial r$) for each process (see Section 3.5.1 for details). As we discuss in Section 3.5.1, it is not as straightforward to infer the origin of the eDIG from the data using the sign of the radial gradient in the lag as implied in this figure.

(shallowing) of the lag with radius might be expected. Physically, for a centrally concentrated potential, gas at smaller radii will overcome a larger change in the potential to be ejected to the same height as gas at larger radii. As a result, gas at smaller radii will have a larger lag than gas at larger radii (for gas ejected to the same height at all radii; see Zschaechner et al., 2015). If the extraplanar gas is due to accretion instead of galactic fountains, simulations of cylindrical accretion parallel to the angular momentum axis do not show evidence for radial variations in the lag (see Figure 4 of Kaufmann et al., 2006). Even if gas is accreted with some inclination with respect to the angular momentum axis (Binney, 2005), no radial variation in the lag is expected. If, instead, cold material is accreted from streams in the outskirts of the galaxy (e.g. Combes, 2014), radial inflows are expected. If the radial inflow velocity increases with radius (i.e. is largest at the outskirts of the galaxy where the gas is being accreted), then larger lags at larger radii might be expected (i.e. a steepening of the lag with radius). These scenarios for the origin of the eDIG gas are shown schematically in Figure 3.7. As we will show in this section, however, determining the origin of the extraplanar gas from measurements of the radial lag gradient is not as straightforward as laid out here.

3.5.1.1 Radial Lag Gradients in the Edge-On CALIFA Galaxies

With the edge-on CALIFA sample, we can investigate radial trends in the measured eDIG lags. Following Section 3.4.2, we fit for the lag at each radial bin independently above and below the midplane. We find the median lag measurement

for each radius and fit a line where the slope is the radial variation in the lag (ΔLag/Δr). The distribution of ΔLag/Δr over the sample is shown in Figure 3.8 and values for individual galaxies are listed in Table 3.1. In our dataset, 36% of the galaxies are consistent with no radial variation in the lag within the uncertainties. There are six galaxies (24%) with lags that shallow with radius (significantly within the uncertainties) with a median $\Delta\text{Lag}/\Delta\text{r} = -3.2 \pm 4.2\,\text{km}\,\text{s}^{-1}\,\text{kpc}^{-2}$. As shown in Figure 3.8, the shallowing lags we find for the eDIG are comparable to shallowing HI lags (discussed in Section 3.5.1.3). There are ten galaxies (40%) with lags that steepen with radius (significantly given the uncertainties) with a median $\Delta\text{Lag}/\Delta\text{r} = 6.6 \pm 5.3\,\text{km}\,\text{s}^{-1}\,\text{kpc}^{-2}$. Unlike the systematically shallowing HI lags, the Hα lags shallow, steepening, and remain constant with radius. If the sign of the radial variation in the lag reflects the origin of the extraplanar gas, these results suggest a mix of internal and external origins for the eDIG.

3.5.1.2 Lags and Radial Lag Gradients Induced by a Thick-Disk Potential

The kinematics of the eDIG will be shaped by the potential, regardless of whether the extraplanar gas originated internally or externally to the system. We analytically investigate the anticipated lag and radial variation in the lag from a Miyamoto-Nagai potential which describes a three-dimensional axisymmetric potential of a disk galaxy with total mass M, radial disk scale length r_0, and vertical disk scale length z_0 (Miyamoto & Nagai, 1975). From this potential, we derive

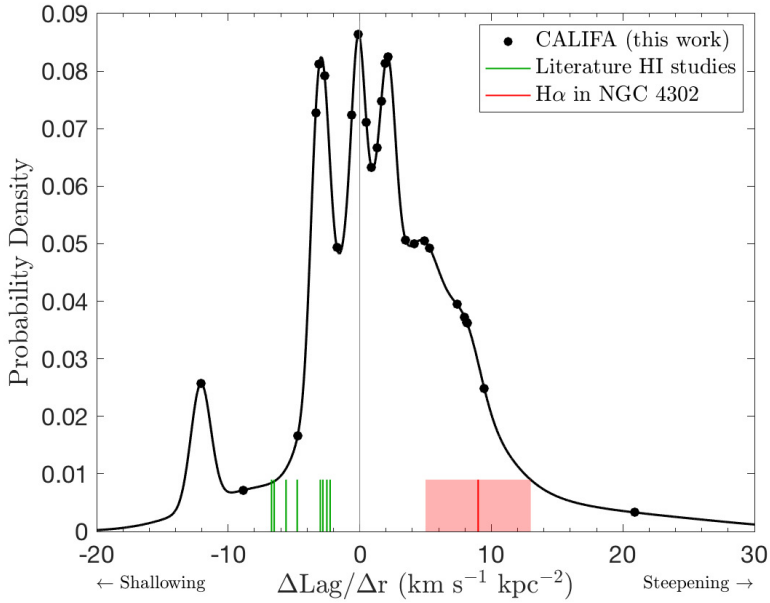

Figure 3.8: The distribution of radial variations in the lag (ΔLag/Δr) for the sample. We find no systematic shallowing (or steepening) of the lag with radius. The green line segments show radial lag variations from previous HI studies (see values and references in Table 3.3). The red line and shaded region show the Hα radial lag variation and uncertainty in NGC 4302 (Heald et al., 2007).

$V_{rot}(r, z)$, the lag $(-\partial V_{rot}(r, z)/\partial z)$, and the radial variation in the lag $(\partial \text{Lag}/\partial r \equiv -\partial[\partial V_{rot}(r, z)/\partial z]/\partial r)$. The full derivation and corresponding equations can be found in Appendix B.4. The analytic potential and resulting equations for the kinematics are agnostic to the origin of the extraplanar gas: the equations describe a disk with vertical scale height z_0 regardless of how the gas became extraplanar.

Figure 3.9 (top) shows the lag at $z = z_0$ as a function of r/r_0 (from Equation B.5) assuming $M = 10^{11}\,M_\odot$, $z_0 = 0.8$ kpc (the median $h(\text{H}\alpha)$ for this sample), and $r_0 = 3.3$ kpc (the median stellar scale length for the EDGE-CALIFA sample; Bolatto et al., 2017). The lag increases sharply for $r \lesssim 1\ r_0$, then decreases smoothly for $r \gtrsim 1\ r_0$. Figure 3.9 (bottom) shows $\partial \text{Lag}/\partial r$ as a function of r/r_0 (from Equation B.6). As in Figure 3.9 (top), the radial lag gradient steepens for $r \lesssim 1\ r_0$ and

shallows for $r \gtrsim 1\ r_0$. Therefore, the sign of the radial lag gradient (i.e. whether the lag shallows or steepens with radius) induced by the potential depends on the radius at which the measurement is made within the galaxy. This kinematic signature will be imprinted on top of any kinematic imprint relating to the origin of the extraplanar gas.

We can compare the analytic predictions from Equations B.5 and B.6 to the measured lag and ΔLag/Δr values. To find an average r/r_0 for each galaxy, we average the minimum and maximum radii used. The minimum radius is $2\,\mathrm{R_{e,bulge}}$; the maximum radius is assumed to be 30". Angular distances are converted to kpc using the distance to each galaxy listed in Table 3.1. We assume $r_0 = 3.3\,\mathrm{kpc}$ as before, which is the median stellar scale length of the EDGE-CALIFA sample (Bolatto et al., 2017). The measured lag and ΔLag/Δr values for each galaxy are shown as the blue dots in Figure 3.9. Given the assumptions, the ionized gas lags and ΔLag/Δr we measure for this sample (Table 3.1) are broadly consistent with our analytic expectation, although there is significant scatter. As shown in Figure 3.9, this may be due to the radial regime probed by the Hα data. Radial lag gradients with magnitudes comparable to those we measure are induced by the potential (Figure 3.9 bottom) regardless of the origin of the extraplanar gas. While large deviations from the analytic curve may reflect the origin of the extraplanar gas, the kinematic signature imprinted by the origin of the extraplanar gas is largely overwhelmed by the kinematics induced by the potential itself. Given the assumptions, we conclude that the majority of the radial lag gradient we measure is likely due to the potential and does not give much information about the origin of the eDIG.

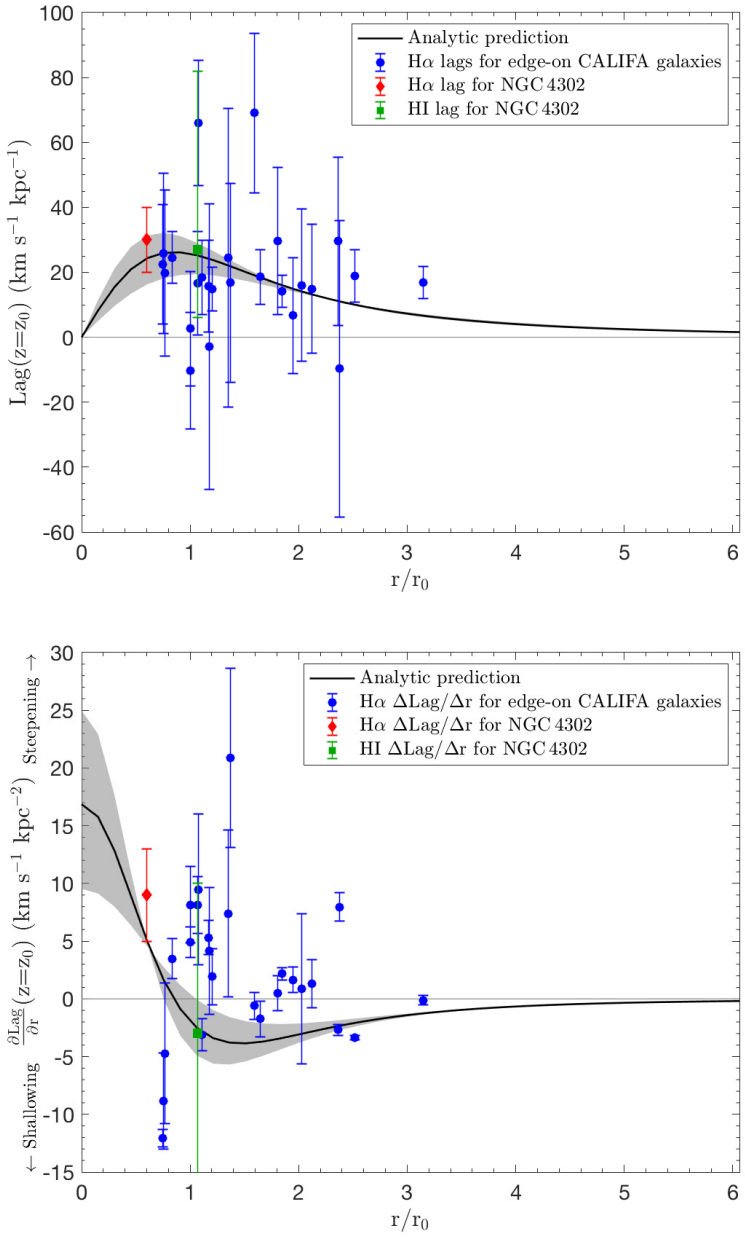

Figure 3.9: The analytic (top) lag (Equation B.5) and (bottom) $\partial \mathrm{Lag}/\partial r$ (Equation B.6) as a function of r/r_0 at $z = z_0$ for a Miyamoto-Nagai potential. The lag shallows with radius for $r \gtrsim r_0$. In both panels, the black curve shows the analytic prediction for $z_0 = 0.8\,\mathrm{kpc}$ (the median $h(\mathrm{H}\alpha)$ for this sample). The gray shaded region shows z_0 ranging from $0.3 - 1.5\,\mathrm{kpc}$, corresponding to the inner 68% around the median $h(\mathrm{H}\alpha)$ (Figure 3.3). The blue dots show the measurements of the (top) lag and (bottom) $\Delta\mathrm{Lag}/\Delta\mathrm{r}$ for each galaxy studied here. The red diamond shows the (top) lag ($30 \pm 10\,\mathrm{km\,s^{-1}\,kpc^{-1}}$) and (bottom) $\Delta\mathrm{Lag}/\Delta\mathrm{r}$ ($\sim 9 \pm 4\,\mathrm{km\,s^{-1}\,kpc^{-2}}$) for the ionized gas in NGC 4302 (Heald et al., 2007). The green square shows the (top) lag ($27^{+55}_{-21}\,\mathrm{km\,s^{-1}\,kpc^{-1}}$) and (bottom) $\Delta\mathrm{Lag}/\Delta\mathrm{r}$ ($-3^{+31}_{-13}\,\mathrm{km\,s^{-1}\,kpc^{-2}}$) for HI in NGC 4302 (Zschaechner et al., 2015). See Section 3.5.1 for details.

Galaxy	ΔLag/Δr ($\mathrm{km\,s^{-1}\,kpc^{-2}}$)	Ref
NGC 891	-2.5	(1)
MW	-6.7	(2)
NGC 4244	-2.25	(3)
NGC 4665	-5.6	(4)
NGC 5023	-2.8	(5)
NGC 3044	-4.75	(6)
NGC 4302	-3^{+31}_{-13}	(6)
NGC 4013	-6.5	(7)

(1) Oosterloo et al. (2007), (2) Marasco & Fraternali (2011), (3) Zschaechner et al. (2011), (4) Zschaechner et al. (2012), (5) Kamphuis et al. (2013), (6) Zschaechner et al. (2015), (7) Zschaechner & Rand (2015)

Table 3.3: HI Radial Lag Deviations from the Literature

3.5.1.3 Reassessing Previous Conclusions about the Origin of Extraplanar Gas Based on Radial Lag Variations

Measured changes in the lag as a function of radius (ΔLag/Δr) have been found for lagging HI in several galaxies (Table 3.3). Zschaechner et al. (2015) summarize many of these results, finding a systematic decrease in the lag with radius between $r \sim 0.5 - 1.0\ R_{25}$. Assuming $R_{25} = 3.2\ r_0$ (Persic & Salucci, 1991), HI lags tend to decrease between $r \sim 1.6 - 3.2\ r_0$. For the galaxies studied by Zschaechner et al. (2015), many galaxies are probed out to $1.5\ R_{25} \sim 4.8\ r_0$. This is in agreement with our analytic expectation (Figure 3.9), where lags induced by the potential tend to shallow with radius for $r \gtrsim 1\ r_0$. In light of this modeling, the interpretation by Zschaechner et al. (2015) that this shallowing of the lag with radius points toward an internal origin for the extraplanar HI is, therefore, not a clear-cut as they claim. We suggest that the majority of the shallowing of the lag with radius may be a result of the thick-disk potential which overwhelms any kinematic signature of the

origin of the extraplanar gas.

Large kinematic studies of extraplanar ionized gas (e.g. Bizyaev et al., 2017; Levy et al., 2018) have lacked the "radial resolution" necessary to investigate radial trends in eDIG lags. To highlight one particular example comparing HI and eDIG lags, we consider NGC 4302, studied in HI by Zschaechner et al. (2015) and in Hα by Heald et al. (2007). NGC 4302 is the only galaxy in the literature with measured radial variations in the Hα lag. On the approaching side of the galaxy, both the HI and Hα lags are constant with radius (although the Hα lag is much larger than the HI lag). On the receding side, however, the HI lag shallows slightly with radius whereas the Hα lag steepens by $\sim 36\,\mathrm{km\,s^{-1}\,kpc^{-1}}$ at $r = 4.25\,\mathrm{kpc} = 0.6\,r_0$ (assuming $r_0 = 7\,\mathrm{kpc}$; Heald et al., 2007), resulting in $\Delta\mathrm{Lag}/\Delta\mathrm{r} \sim 9 \pm 4\,\mathrm{km\,s^{-1}\,kpc^{-2}}$. These measurements for the receding side of NGC 4302 are overplotted in Figures 3.8 and 3.9. At the radii probed by each measurement, the steepening Hα lag and shallowing HI lags are completely reproduced by our analytic models (Figure 3.9). On the receding side of NGC 4302, at least, tension between internal and external origins of the extraplanar HI and Hα are alleviated by the potential dominating the kinematics. The difference in the kinematics between the approaching and receding sides of NGC 4302 are, however, still unresolved.

To conclude, measurements of radial variations in the lag cannot easily discriminate between an internal or external origin for the eDIG, as they are convolved with radial variations induced by the equilibrium potential. Perhaps large excursions from the analytic predictions could discriminate between an internal or external origin, but the uncertainties are large.

3.5.2 Trends with Galaxy Properties

The relationship between the eDIG and global galaxy properties can give insights into the origin of the extraplanar gas. If the eDIG is a result of star formation activity in the disk (i.e. an internal origin), then trends between the eDIG scale height and/or the lag with some measure of the star formation activity might be expected (e.g. Heald et al., 2007). To complicate matters, however, trends with the star formation activity may not be inconsistent with an external origin in a scenario where the accretion that creates the eDIG also powers the star formation. There is a relationship between the presence of eDIG and the SFR surface density ($\Sigma_{\rm SFR}$), where eDIG is ubiquitous for galaxies above a threshold $\Sigma_{\rm SFR}$ (Rand, 1996; Rossa & Dettmar, 2003a). From a sample of edge-on MaNGA galaxies, Bizyaev et al. (2017) find a trend between the Hα luminosity (a proxy for the SFR) and the eDIG scale height. Correlations between the magnitude of the lag and the star formation activity have yet to be found (Zschaechner et al., 2015; Bizyaev et al., 2017; Levy et al., 2018, and references therein). Levy et al. (2018) did not find strong correlations between the difference between the molecular and ionized gas rotation velocity and any other global galaxy property, similar to previous photometric eDIG studies (e.g. Rossa & Dettmar, 2003b) as well as studies of extraplanar HI (Zschaechner & Rand, 2015). Previous evidence is, therefore, suggestive of an internal origin but inconclusive.

We compare the measured lag to galaxy-wide properties, such as the Hα disk scale height (h(Hα)), morphology, stellar mass (M$_*$), SFR, specific SFR (sSFR $\equiv$ SFR/M$_*$),

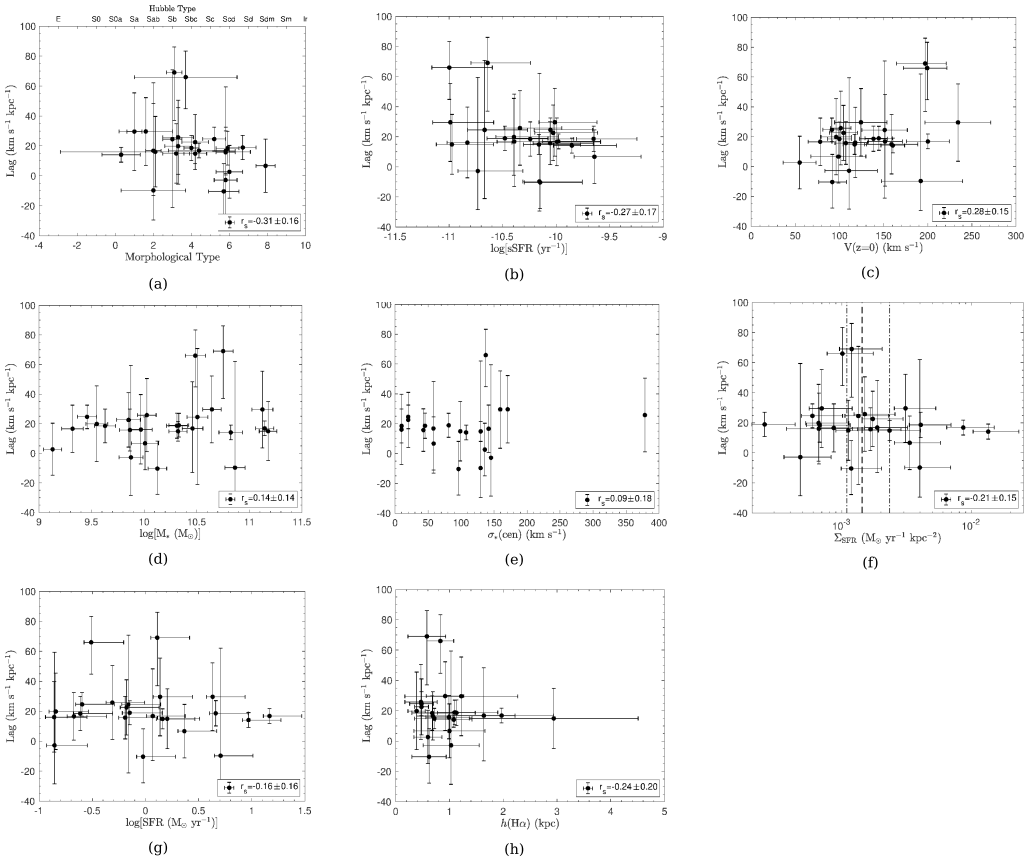

Figure 3.10: There are possible trends between the vertical gradient in the ionized gas rotation velocity (lag) and (top left) the morphology. We find no strong correlations between the measured ionized gas lag and the (top center) sSFR, (top right) rotation velocity in the midplane (V(z=0)), (middle left) stellar mass (M_*), (middle center) central stellar velocity dispersion (σ_*(cen)), (middle right) SFR surface density ($\Sigma_{\rm SFR} \equiv {\rm SFR}/{\rm D}_{25}^2$), (bottom left) SFR, or (bottom center) measured Hα scale height (h(Hα)). The vertical dashed and dot-dashed lines in (middle right) show the threshold $\Sigma_{\rm SFR}$ (and uncertainties) from Rossa & Dettmar (2003a).

average SFR surface density ($\Sigma_{\rm SFR} \equiv {\rm SFR}/{\rm D}_{25}^2$), central stellar velocity dispersion (σ_*(cen)), and V_{max}. Morphologies and D_{25} (the diameter of B-band isophote corresponding to 25 mag arcsec^{-2}) are from HyperLEDA; M_* and $\sigma_{*,\rm cen}$ are from CALIFA; $h(\alpha)$ measurements are described in Section 3.3; V(z=0) is the intercept of the fitted vertical velocity gradient (Section 3.4.2, Table 3.1). We derive the SFR (and hence sSFR and $\Sigma_{\rm SFR}$) from the WISE 22 μm (W4) AB magnitudes reported by Bitsakis et al. (2019) which use the apertures from Catalán-Torrecilla et al. (2015). We use the WISE W4 magnitudes to derive these quantities because extinction by dust in these edge-on systems renders the Hα extinction correction impossible, especially in the midplane. We find inconsistencies in the magnitudes reported by Bitsakis et al. (2019) stemming from an improper application of a scaling factor to account for systematics (described in a few sentences). To convert from the AB magnitudes in Bitsakis et al. (2019) to the Vega magnitudes listed in Table 3.1, a value of 7.220 should be subtracted[‖]. It is known that star-forming galaxies measured with WISE W4 are systematically brighter by $\sim 10\%$ than inferred from *Spitzer* IRS and 24 μm observations (Wright et al., 2010; Jarrett et al., 2013; Brown et al., 2014), and we apply this scaling factor of 1/1.1 to the W4 Vega magnitudes. The W4 magnitudes in Table 3.1 include this scaling factor. We then find the 22 μm luminosity using $L(22\,\mu{\rm m}) = \frac{\nu_{\rm W4}}{\Delta\nu_{\rm W4}} F_{\rm W4} \times 10^{-m_{\rm W4}/2.5} \times 4\pi d^2$, where $\nu_{\rm W4}$ is the W4 isophotal system frequency, $\Delta\nu_{\rm W4}$ is the W4 bandwidth, $F_{\rm W4}$ is the in-band flux (all given in Jarrett et al., 2011), $m_{\rm W4}$ is the W4 Vega magnitude, and d is the distance to the galaxy

[‖]This corrects for an older conversion between Vega and AB magnitudes used by Bitsakis et al. (2019) (6.604 instead of 6.620 (Jarrett et al., 2011)) and an improper application of a scaling factor to account for systematics so that $7.220 = 6.604 + (6.620 - 6.604/1.1)$

(both in Table 3.1). We then convert from L(22 μm) to SFR using the single-band linear calibrator without type-2 AGN developed by Catalán-Torrecilla et al. (2015). We list our values of SFR inferred from the W4 magnitudes in Table 3.1**. Finally, we use the values of M_* and D_{25} listed in Table 3.1 to find sSFR$\equiv$SFR/M_* and $\Sigma_{\rm SFR} \equiv {\rm SFR}/D_{25}^2$.

We investigate whether there is a trend between the parameters by using the Spearman rank correlation coefficient (r_s) which tests for any monotonic relationship between the two parameters. We estimate the uncertainty in r_s by using 1000 Monte Carlo iterations in which the values are allowed to randomly vary within the error bars, and r_s is computed for each iteration. The reported uncertainty on r_s is the standard deviation of the Monte Carlo iterations.

We find a weak inverse correlation between the lag and the morphology ($r_s = -0.31 \pm 0.16$) (Figure 3.10 top left). This is similar to the trends with axis ratio and Sérsic index found by Bizyaev et al. (2017) (with $r = 0.48$ and $r = 0.26$ respectively). We note, however, that determining the morphology, axis ratio, or Sérsic index for an edge-on system is very difficult. We find no evidence for a trend with any of the other parameters (Figure 3.10). The weak trends with sSFR, V(z=0), and $\Sigma_{\rm SFR}$ (classified by their non-zero correlation coefficients and uncertainties; Figure 3.10 top center, top right, middle right) are ultimately not significant. If the two galaxies with the largest lags are removed, none of the weak trends in Figure 3.10

**Catalán-Torrecilla et al. (2015) assume a Kroupa initial mass function (IMF) (Kroupa, 2001) when deriving their SFR calibrators. A Salpeter IMF (Salpeter, 1955) is assumed the EDGE and CALIFA surveys in general (Bolatto et al., 2017; Sánchez et al., 2016b). These different IMFs do not affect the results presented here, but this should be kept in mind when comparing the SFRs we derive here with other derivations of the SFR from the EDGE and CALIFA surveys.

(top center, top right, middle right) are significant. Bizyaev et al. (2017) found stronger trends between their lag measurements and V_{max} ($r = 0.55$), M_* ($r = 0.5$), and σ_*(cen) ($r = 0.55$). As pointed out by Bizyaev et al. (2017), a trend with the maximum rotation velocity (V_{max} or V(z=0)) is likely an observational effect, since larger amplitude lags are easier to find in systems with large V_{max}.

If the extraplanar gas indeed has an internal origin, we might expect a correlation between the lag and Σ_{SFR}. For gas ejected from the midplane through galactic fountains due to star formation activity, there should be some minimum level of widespread star formation (i.e. Σ_{SFR}) needed to sustain a thick disk that covers the entire plane of the galaxy (Rand, 1996). As in Levy et al. (2018), we find no such trend (Figure 3.10 middle right). From this idea of a minimum level of star formation activity, Rossa & Dettmar (2003a) define a threshold to have eDIG of $L_{FIR}/D_{25}^2 = (3.2 \pm 0.5) \times 10^{40}\,\mathrm{erg\,s^{-1}\,kpc^{-2}}$ (Rossa & Dettmar, 2003a), where L_{FIR} is the far infrared luminosity from 60 and 100 μm emission. We convert L_{FIR} to L_{TIR} (total infrared, $8 - 1000\mu$m) using a factor of 1.6 (Sanders & Mirabel, 1996) and then to a SFR using the single-band linear calibrator without type-2 AGN developed by Catalán-Torrecilla et al. (2015). The threshold to have eDIG is $\Sigma_{SFR} = 1.4^{+0.9}_{-0.3} \times 10^{-3}\,\mathrm{M_\odot\,yr^{-1}\,kpc^{-2}}$ (shown in Figure 3.10 middle right). We find that $46^{+42}_{-21}\%$ of galaxies in this subsample are above this threshold. We note that there are galaxies below this threshold with comparable lags to those above it (as indicated by the lack of trend).

The CALIFA data enable us to look for trends with properties of the stars—such as age, metallicity, and extinction—and to investigate the presence of vertical

gradients in these parameters. Because these properties are degenerate, they are difficult to interpret. We present the results of this analysis in Appendix B.3, but the interpretation is beyond the scope of this paper.

As mentioned in Section 3.3, we also test for trends between the eDIG scale height and the same global galaxy properties described here. We find no significant trends with any parameter.

3.5.3 Synthesis

Determining the origin of the lagging extraplanar gas is difficult. Gradients in the lag with radius do not provide a straightforward diagnostic of the origin of the eDIG gas. The kinematic signatures imprinted by the equilibrium gravitational potential will likely overwhelm those relating to the origin of the eDIG material. We find no strong trends between the lag and galaxy properties, similar to previous studies of lagging HI and eDIG (e.g. Zschaechner et al., 2015; Levy et al., 2018). We also do not find trends between the eDIG scale height and global galaxy properties. Therefore, although some evidence points toward an internal star formation-powered origin for the eDIG, it is possible that external inflows of gas may also contribute to the eDIG thickness.

3.6 The Ionization and Source of the Lagging Ionized Gas

Extraplanar ionized gas can be found in thick gas disks from ejected material, galaxy bulges, the stellar thick disk, or outflows. These various locations and sources for the eDIG will have different ionization and other properties. In the following

subsections, we attempt to place limits on the source of the extraplanar ionized gas in these galaxies.

It is generally thought that the eDIG is ionized primarily by leaky HII regions (see review by Haffner et al., 2009, and references therein). Additional ionization sources are required, however, to explain the increase of ionized gas line ratios ([SII]/Hα, [NII]/Hα, [OIII]/Hβ) with height above the midplane (e.g. Collins & Rand, 2001; Otte et al., 2001; Hoopes & Walterbos, 2003). Such additional ionization mechanisms could include shocks (Veilleux et al., 1995; Rand, 1998; Collins & Rand, 2001), turbulent mixing layers (Rand, 1998; Binette et al., 2009), magnetic reconnection (Reynolds et al., 1999; Hoffmann et al., 2012), cosmic rays (Wiener et al., 2013), photoelectric heating from small grains (Reynolds et al., 2001), or hot, old, low-mass evolved stars (HOLMES; Sokolowski & Bland-Hawthorn, 1991; Flores-Fajardo et al., 2011; Weber et al., 2019). For this paper, we will focus on ionization by HOLMES since we have the data in hand to constrain this mechanism, and many of the other processes are outside the scope of this paper. López-Cobá et al. (2019) studied ionization by shocks in the context of galactic outflows using CALIFA. HOLMES are commonly found in retired galaxies (galaxies which lie below the star-forming main sequence) and in the bulges and halos of disk galaxies and produce line ratios similar to low-ionization nuclear emission-line regions (LINERs) (Sarzi et al., 2010; Belfiore et al., 2016; Gomes et al., 2016; Lacerda et al., 2018). Recent ionization models of hot, young stars in the midplane of galaxies, however, can reproduce observed line ratios in the DIG indicating that additional ionization mechanisms may not be necessary (Weber et al., 2019).

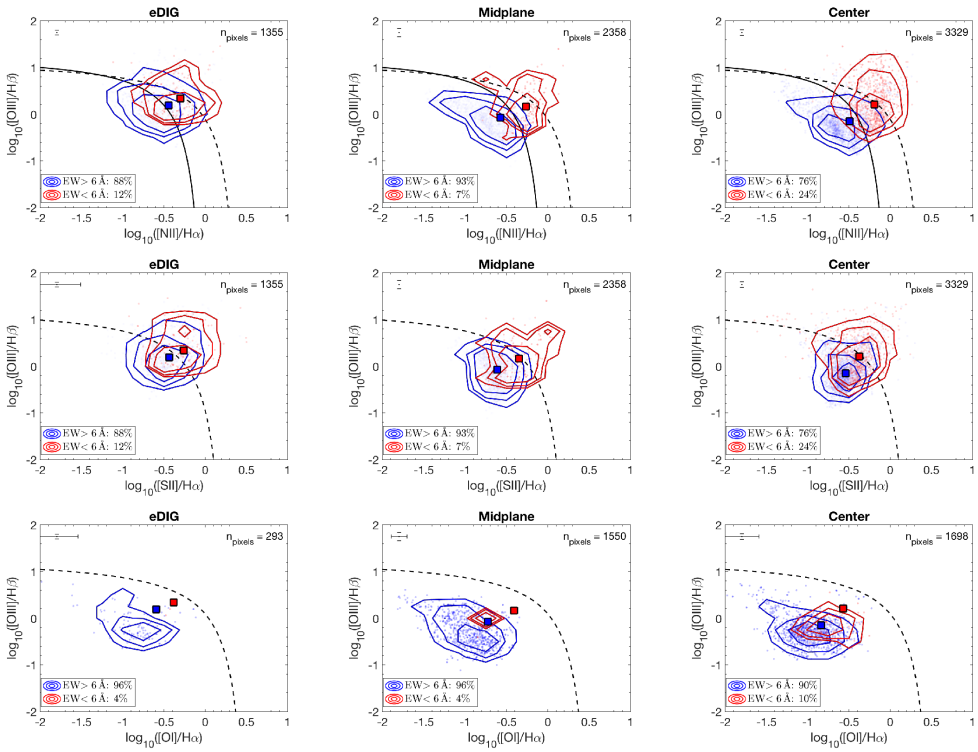

Figure 3.11: Diagnostic diagrams for all 25 edge-on galaxies color-coded in bins of EW(Hα) (Sánchez et al., 2014). The left column plots pixels in the eDIG (i.e. excluding the center and midplane), the middle columns shows pixels in the midplane, and the right column shows pixels in the center. The top row uses [NII]/Hα, the middle uses [SII]/Hα, and the bottom uses [OI]/Hα. Individual pixels are shown in the light points. Contours contain 50, 75, and 90% of the pixels in each group. The large square symbols show the median of each group. Demarcations from Kauffmann et al. (2003) and Kewley et al. (2001) are shown (solid and dashed black curves). The percent of pixels in each group are in the legend, and the number of pixels in each region is in the upper right corner. Typical uncertainties for the individual pixels are shown in the upper left corner. The eDIG is primarily ionized by star-forming regions, rather than by the bulge, HOLMES, or some other process. See Section 3.6 for details.

There are various diagnostic line-ratio diagrams used to investigate the ionization source of gas in galaxies. Here we will use [NII]/Hα, [SII]/Hα, and [OI]/Hα versus [OIII]/Hβ and the Hα equivalent width (EW(Hα)) to infer the ionization properties of the eDIG in this sample. Lacerda et al. (2018) find that regions where the ionization is dominated by star formation have EW(Hα) >14 Å, and those with EW(Hα) <3 Å are dominated by HOLMES. These separations are fairly conservative; above 14 Å and below 3 Å, ionization will be dominated by star formation or HOLMES respectively. It is interesting, however, to include in the interpretation of intermediate EW(Hα). Sánchez et al. (2014) find a division between clumpy HII regions and more diffuse gas at EW(Hα) = 6 Å. We adopt EW(Hα) = 6 Å as our nominal division between gas ionized by star forming HII regions and more diffuse gas ionized by other means (HOLMES, shocks, etc). Maps of EW(Hα) are calculated in Pipe3D for the CALIFA galaxies (Sánchez et al., 2016c,b). We divide the galaxies in this sample into three spatial regions: eDIG, midplane, and center. We define the eDIG region as pixels with $|z| > h(\mathrm{H}\alpha)$ and $r > 2\,\mathrm{R_{e,bulge}}$, the midplane region as pixels with $|z| < h(\mathrm{H}\alpha)$ and $r > 2\,\mathrm{R_{e,bulge}}$, and the center region as pixels with $r < 2\,\mathrm{R_{e,bulge}}$. The diagnostic diagrams for each region color-coded by the EW(Hα) categories proposed by Sánchez et al. (2014) are shown in Figure 3.11. Most of the eDIG is dominated by ionization from star-forming complexes ($\sim$ 90%; Figure 3.11). Only a small fraction is ionized by HOLMES ($\sim$ 10%). Although we do not analyze other ionization mechanisms (such as those mentioned in the introduction to this section), they must play a minor role since the eDIG ionization is dominated by star formation. A larger fraction of the midplane gas is ionized by star-forming

complexes ($\sim$ 95%), whereas a larger fraction of gas in the central regions is ionized by HOLMES ($\sim$20%) and the distributions extend further above the Kewley et al. (2001) and Kauffmann et al. (2003) demarcation curves. If the more conservative EW(Hα) bins defined by Lacerda et al. (2018) are used instead, only 3% of the eDIG is ionized by HOLMES, 66% by star-forming regions, and 31% by a mix of ionization processes (these groups are not well separated; see Lacerda et al., 2018). In the center, 8% is ionized by HOLMES and 45% by a mix of ionization processes. We discuss these results in the context of the source of the ionized gas lags (stellar thick disk, bulge, outflows, and WIM-like gas) in the following subsections.

3.6.1 Is the Ionized Gas Related to a Stellar Thick Disk?

It is possible that the lagging ionized gas at large heights off the midplane is associated with the stellar thick disk, rather than gas ejected from the midplane via star formation feedback. The stellar thick disk is known to rotate more slowly than the thin disk (e.g. Pasetto et al., 2012) and may have vertical gradients in the rotation velocity (e.g. Spagna et al., 2010). The ionization of gas in the stellar thick disk is thought to be dominated by HOLMES (Flores-Fajardo et al., 2011, although see Weber et al. 2019). However, for eDIG regions—where we measure lags—ionization by HOLMES contributes only a small fraction ($\sim$ 10%; Figure 3.11). Therefore, we conclude that we are likely not measuring lags due to ionized gas associated with the stellar thick disk.

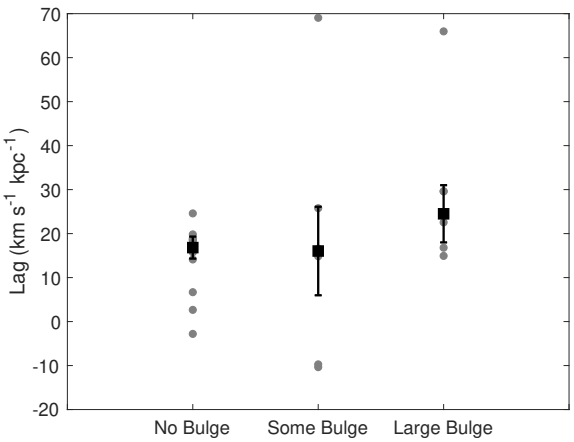

Figure 3.12: There is no significant trend between the measured lag and the by-eye bulge classification. Points for individual galaxies are shown in gray (without error bars for clarity). Medians (with standard errors) for each bulge classification are shown in black squares and are consistent across bulge classifications.

3.6.2 Contamination from a Bulge?

It is also possible that we are measuring lags due to gas in the bulge which has larger velocity dispersions and lower rotation velocities. Although we exclude pixels with $r < 2\,\mathrm{R_{e,bulge}}$ at all z, it is still possible that we are not masking all of the bulge emission.

Because these galaxies are edge-on, there are no measurements of the bulge fractions or effective radii (as was measured for the intermediately-inclined CALIFA galaxies by Méndez-Abreu et al., 2017). Making detailed decompositions of the bulges of these galaxies is out of the scope of this paper. Based on the SDSS images, we classified the galaxies into rough bulge groups by eye. As shown in Figure 3.12, there is no significant difference in lags measured for galaxies of different bulge classifications.

We do find a weak inverse correlation between the amplitude of the lag and the

Hubble type (Figure 3.10 top left). Earlier-type galaxies are more bulge-dominated and do seem to have larger lags, possibly indicating that the bulge is contributing to our measurement of the lags. We note, however, that the trend is not strong ($r_s = -0.31 \pm 0.16$) and that there are galaxies with lags $\sim 20\,\mathrm{km\,s^{-1}\,kpc^{-1}}$ across all Hubble types. We also note that morphological classifications for edge-on galaxies are highly uncertain.

Finally, the ionization of gas in the bulge would be dominated by HOLMES (Sarzi et al., 2010; Belfiore et al., 2016; Gomes et al., 2016). From the line ratio diagrams (Figure 3.11), we find that the fraction of the eDIG ionized by HOLMES is small ($\sim 10\%$). This fraction is higher and line ratios are more consistent with LINER-like emission in the center region where a bulge may dominate. We conclude that contamination from the bulge is not significantly affecting these results.

3.6.3 Contamination from Ionized Gas Outflows?

López-Cobá et al. (2019) analyzed the prevalence of outflows in edge-on CALIFA galaxies finding that 8% are candidates to host outflows. A further 13% present eDIG but do not meet their outflow criteria. There are four galaxies in our subsample which are outflow candidates and five which have eDIG according to López-Cobá et al. (2019) (Notes O and E in Table 3.1). We note that our selection criteria are different so that our subsamples contain different galaxies. While we exclude the centers of galaxies from our analysis which should mitigate the effects of any outflows present, it is possible that this masking is insufficient as outflows can extend

up to several kpcs towards the extraplanar regions. Therefore, the lags detected in these galaxies could be consequence of the presence of outflows.

To investigate the effect of outflows on our results, we mark outflow candidates in magenta in Figures 3.3 and 3.6 (top). Neither those galaxies with the largest Hα scale heights (Figure 3.3) nor those with the largest lags (Figure 3.6 top) are outflow candidates. We, therefore, conclude that outflows are not biasing our results in a significant way.

3.6.4 The Lagging Ionized Gas is WIM-like

Following the previous sections, we interpret the observed lagging extraplanar gas as a thick, turbulent eDIG layer, similar to the WIM in the MW, as opposed to gas associated with the bulge, stellar thick disk, or outflows. The majority of eDIG is ionized by star-forming regions (i.e. leaky HII regions) as opposed to some other ionization source (Figure 3.11). When two bins of EW(Hα) are used (following Sánchez et al., 2014), $\sim$90% the eDIG is ionized by star formation (Figure 3.11).

Several line ratios are used as diagnostics of eDIG, as they trace variations in temperature and density. The ratios of [NII]λ6583Å and [SII]λ6717Å to Hα are strong functions of temperature and also trace variations in abundance and ionization (see the review by Haffner et al., 2009). Previous studies show that [SII]/Hα and [NII]/Hα clearly increase with distance from the midplane in the eDIG, indicating a general increase in temperature with height and large variations in temperature and ionization fraction in the eDIG (e.g. Veilleux et al., 1995; Madsen et al., 2006;

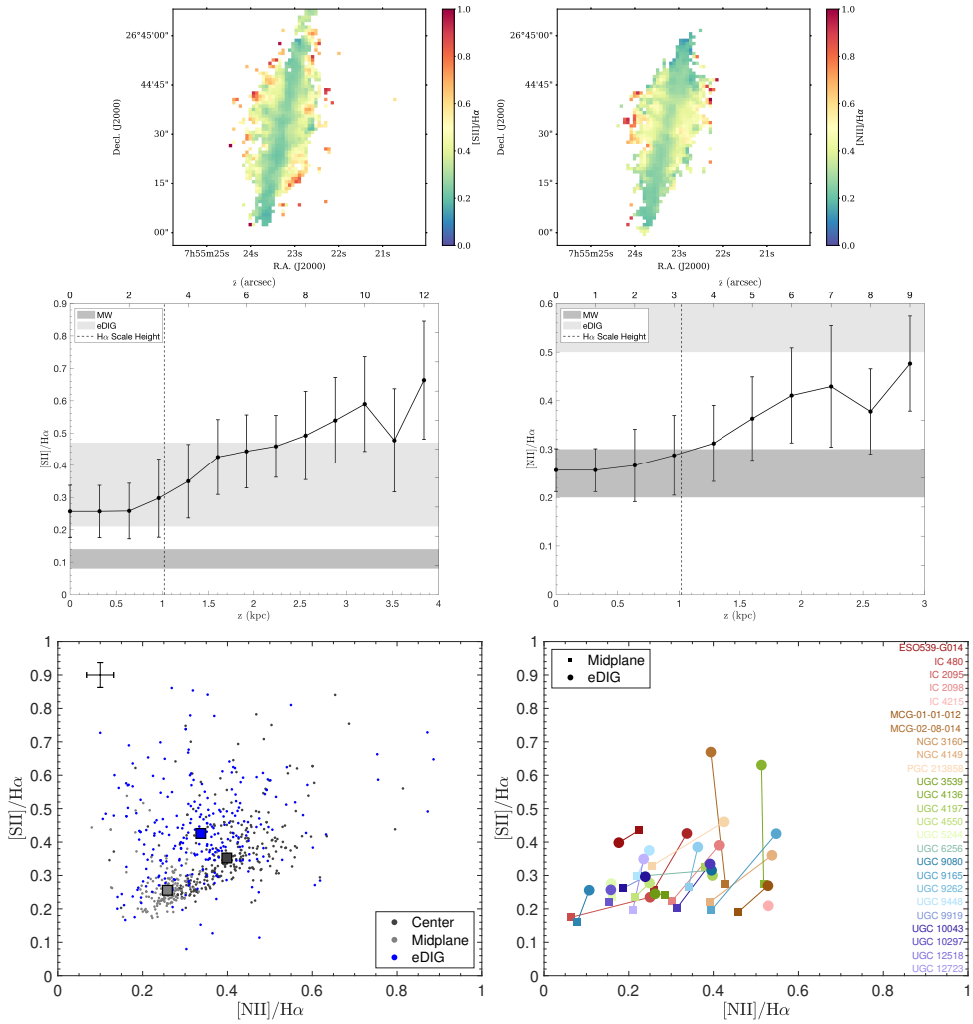

Figure 3.13: For IC 480, the spatial distribution of extinction-corrected (top left) [SII]/Hα and (top right) [NII]/Hα. Median line ratios increase as a function of height above the midplane (z), as shown for (middle left) [SII]/Hα and (middle right) [NII]/Hα. (Bottom left) The [NII]/Hα versus [SII]/Hα for pixels with EW(Hα) > 6 Å for IC 480. Points are separated by region in the galaxy. Representative error bars are shown in the upper left corner. Squares show the median of each region. As in the MW, the eDIG tends to have higher [SII]/Hα than the midplane (e.g. Haffner et al., 2009). (Bottom right) The median [NII]/Hα versus [SII]/Hα in the midplane (squares) and eDIG (circles) for all galaxies. Lines connect the midplane and eDIG points of the same galaxy (also shown in the colors). The eDIG of most galaxies has larger [SII]/Hα than the midplane.

Haffner et al., 2009; Ho et al., 2016; Jones et al., 2017). In the midplane of the MW and a few other galaxies, [SII]/H$\alpha = 0.11 \pm 0.03$ and [NII]/H$\alpha \sim 0.25$ (Madsen, 2004; Madsen et al., 2006), whereas [SII]/H$\alpha = 0.34 \pm 0.13$ and [NII]/H$\alpha \gtrsim 0.5$ in the eDIG (Blanc et al., 2009; Madsen, 2004). We note that some photoionization models of HOLMES have also been able to reproduce the observed line ratios (Flores-Fajardo et al., 2011), but other models of young, massive stars in the midplane can reproduce the observed line ratios and trends (e.g. Barnes et al., 2014; Weber et al., 2019). In a stacked analysis of MaNGA galaxies, Jones et al. (2017) find a potential transition in the heating source from HII regions to HOLMES, shocks, etc. at $\sim$6 kpc from the midplane based on the ratio of [OII]/Hα. Our observations do not probe out to these distances (Figures 3.13 middle), which is consistent with midplane HII regions dominating the ionization of these eDIG measurements.

CALIFA provides spatially-resolved maps of [SII] and [NII] at high SNR for the galaxies studied here. We mask pixels with [SII] and [NII] SNR < 3 and Hα SNR < 5. We correct each line for extinction using the Calzetti et al. (2000) extinction curve. We note that this extinction correction will be insufficient in the midplane of these edge-on galaxies. We also apply a SNR cut of 3 in the line ratio maps (Figure 3.13 top). To investigate trends in [SII]/Hα and [NII]/Hα with distance above the midplane, we take a radial average at each height (excluding radii $< 2\,R_{e,bulge}$). Indeed we find systematic increases in the line ratios with height above values found in the midplane (Figures 3.13 middle).

Studies of the WIM in the MW reveal significant spatial variations in temperature and ionization fraction (e.g. Haffner et al., 2009). These can be studied by

comparing the [SII]/Hα and [NII]/Hα line ratios. Because the excitation temperatures of [SII] and [NII] are similar, [SII]/[NII] is nearly independent of the electron temperature (T_e) (see equation 1 in Haffner et al., 2009). Variations in [SII]/[NII] trace variations in S^+/N^+, N/H, and S/H. The [NII]/Hα and [SII]/Hα line ratios primarily trace variations in T_e, although they are also sensitive to variations in the abundance of N or S (see equation 2 in Haffner et al., 2009). In the MW, Haffner et al. (2009) find that the WIM has larger [SII]/Hα ratios than regions near HII regions (see their Figure 2). We plot the [SII]/Hα line ratio against the [NII]/Hα line ratio for the eDIG, midplane, and center regions for each galaxy (Figure 3.13 bottom left). Figure 3.13 (bottom right) shows the median line ratios for the eDIG and midplane for each galaxy in this sample. Indeed for many galaxies in this subsample, the eDIG region has higher [SII]/Hα ratios than in the midplane or center indicating variations in the S^+/S or S/H ratios as is seen in the MW.

From this analysis of the line ratio and ionization diagnostics, we conclude that the eDIG in these galaxies is primarily ionized by photons escaping from HII regions in the midplane, similar to the WIM in the Galaxy (e.g. Haffner et al., 2009). We note that although the ionization is dominated by midplane HII regions, this analysis of the ionization does not constrain whether the extraplanar gas originated internal or external to the galaxy (as was investigated in Section 3.5).

3.6.5 Synthesis

To summarize this section, we investigate the source of the lagging ionized gas through the ionization properties. We consider four potential sources for the lagging

ionized gas: gas in the stellar thick disk, gas in the bulge, outflows, and gas in a thick disk ionized by star-forming regions in the midplane. From the diagnostic line ratio diagrams (Figure 3.11), we show that the line ratios and EW(Hα) are consistent with ionization by star-forming regions (i.e. leaky HII regions) dominating in the eDIG region. The fraction of ionization by HOLMES is small, unlike what is expected in the stellar thick disk (e.g. Flores-Fajardo et al., 2011; Lacerda et al., 2018) or bulge. We find no trend between the bulge fraction of these galaxies and the lag, again indicating that we are not being biased by incomplete masking of the bulge regions. We also rule out bias from outflows, as those galaxies with ionized gas outflows (López-Cobá et al., 2019) do not dominate the Hα scale height or lag distributions. Evidence for the lagging gas coming from an eDIG layer similar to the WIM in the MW is (1) ionization dominated by star-forming regions, (2) increasing [SII]/Hα and [NII]/Hα line ratios with height above the midplane which is characteristic of the eDIG, and (3) elevated [SII]/Hα versus [NII]/Hα in the eDIG region compared to the midplane.

3.7 Summary

We investigate the presence, properties, and kinematics of eDIG in a sample of 25 edge-on galaxies from the CALIFA survey. Much of the motivation for the study was an extension of the kinematic detection of eDIG in intermediate inclination EDGE-CALIFA galaxies by Levy et al. (2018). We summarize our main results below, indicating relevant figures and/or tables.

1. We measure exponential ionized gas scale heights ($h(\mathrm{H}\alpha)$) in ∼90% of this sample. We find $h(\mathrm{H}\alpha) = 0.3 - 2.9\,\mathrm{kpc}$, with a median $h(\mathrm{H}\alpha) = 0.8\,\mathrm{kpc}$ over the sample (Table 3.1, Figure 3.3). These values are consistent with previous measurements of eDIG scale heights (e.g. Rand, 1997; Wang et al., 1997; Hoopes et al., 1999; Collins et al., 2000; Collins & Rand, 2001; Miller & Veilleux, 2003a; Rosado et al., 2013; Bizyaev et al., 2017; Levy et al., 2018).

2. We investigate the rotation velocity ($\mathrm{V_{rot}}$) as a function of height above the midplane (z) by constructing Hα PV diagrams in vertical bins. By radially averaging, we find a systematic decrease in $\mathrm{V_{rot}}(z)$ in many of our sources (Figure 3.5). We use a linear fit to find the vertical gradient in the rotation velocity ($\Delta\mathrm{V}/\Delta z$, where the lag is -$\Delta\mathrm{V}/\Delta z$) (Table 3.1). We find significant lags in 60% of our galaxies with measurable lags ranging from 10–70 $\mathrm{km\,s^{-1}\,kpc^{-1}}$. There are no galaxies for which $\mathrm{V_{rot}}$ increases with z. This is consistent with previous measurements of ionized gas lags in the literature (Figure 3.6).

3. We investigate radial variations in the lag, which may indicate an internal origin of the eDIG material. We find no indication of systematic shallowing (or steepening) of the lag with radius as is often seen in HI (Figure 3.8, Table 3.1). Moreover, our analytic modeling indicates that radial variations in the lag are induced by the potential, regardless of the origin of the extraplanar gas (Figure 3.9). Disentangling this effect in order to use radial variations in the lag to deduce the origin of the extraplanar gas will be difficult.

4. There are no strong trends between $\Delta\mathrm{V}/\Delta z$ and global galaxy properties (Fig-

ure 3.10). There is potentially an inverse correlation between the lag and morphology ($r_s = -0.31$; Figure 3.10 top left), but morphologies for edge-on galaxies are very uncertain.

5. We use the ionization properties to discriminate among four potential sources for the lagging ionized gas: gas in the stellar thick disk, gas in the bulge, outflows, and extraplanar gas ionized by photons from star-forming regions. From the diagnostic line ratio diagrams, we show that the line ratios and EW(Hα) in the eDIG are consistent with ionization dominated by star-forming regions (Figure 3.11). The fraction of the eDIG ionized by HOLMES is small, unlike what is expected in the stellar thick disk or bulge. Evidence for an eDIG layer due to star formation is ionization dominated by star-forming regions (Figure 3.11), increasing [SII]/Hα and [NII]/Hα line ratios with height above the midplane (Figures 3.13 middle), and elevated [SII]/Hα versus [NII]/Hα in the eDIG region compared to the midplane (Figures 3.13 bottom). We can further rule out bulge contamination because there is no trend between the lag and bulge fraction (Figure 3.12). We also find no systematic influence from outflows on either h(Hα) or $\Delta V/\Delta z$ (Figures 3.3 and 3.6 top). We, therefore, conclude that the lags are indeed due to a thick, eDIG layer similar to the WIM in the MW.

To extend this work, it would be useful to measure the ionized gas velocity dispersions. It is thought that the increased velocity dispersion of the gas acts effectively as an additional pressure term so the gas can remain above or below the

midplane (e.g. Burkert et al., 2010; Marinacci et al., 2010). Due to the low spectral resolution of CALIFA, the ionized gas velocity dispersions cannot be measured. Higher spectral resolution observations of these galaxies are, therefore, necessary and will be discussed in Chapter 6. It is also extremely useful to have spatially resolved observations of a dynamically cold tracer (such as CO) to compare with the ionized gas. This would allow us to determine whether the molecular and ionized gas rotation velocities indeed agree in the midplane, to measure the thin disk scale height, and to measure the velocity dispersion in the dynamically cold component. All of these measurements will help contextualize the ionized gas results. The EDGE Survey provides CO measurements for three of the galaxies studied here, but deeper CO observations in more galaxies (and with better spatial resolution if possible) are necessary. Finally, the neutral atomic gas (HI) is also observed to lag the midplane in some systems (e.g. Oosterloo et al., 2007; Kamphuis et al., 2013; Zschaechner et al., 2011, 2012, 2015; Zschaechner & Rand, 2015). More spatially resolved HI measurements in systems with resolved ionized gas data will enable comparison between the neutral and ionized gas lags in a larger sample.

Chapter 4: Feedback from Super Star Clusters in the Nuclear Starburst of NGC253

4.1 Introduction

Many stages of the stellar life cycle inject energy and momentum into the surrounding medium. For young clusters of stars, this feedback can alter the properties of the cluster itself in addition to the host galaxy. Outflows from young clusters, in particular, remove gas that may have otherwise formed more stars, affecting the star formation efficiency (SFE) of the cluster. The gas clearing process can proceed through a number of physical mechanisms that are efficient over different density regimes and timescales, such as photoionization, radiation pressure, supernovae, and stellar winds. Outflows from forming massive clusters have been observed in the Large Magellanic Cloud (Nayak et al., 2019) and in the Antennae (Gilbert & Graham, 2007; Herrera & Boulanger, 2017).

At high levels of star formation, a larger fraction of stars form in clustered environments (Kruijssen, 2012; Johnson et al., 2016; Ginsburg & Kruijssen, 2018). The most extreme star forming environments can lead to massive ($M_* > 10^5$ $M_\odot$) and compact ($r \sim 1$ pc) so-called "super" star clusters (SSCs; e.g., Portegies Zwart

et al., 2010). Because they are often deeply embedded, observations of young SSCs in the process of forming are rare (e.g., Keto et al., 2005; Herrera & Boulanger, 2017; Oey et al., 2017; Turner et al., 2017; Leroy et al., 2018; Emig et al., 2020). Observations and simulations both indicate that SSCs should have high SFEs (e.g., Skinner & Ostriker, 2015; Oey et al., 2017; Turner et al., 2017; Krumholz et al., 2019; Lancaster et al., 2021a,b). Given these high SFEs, by what process(es) do these SSCs disperse their natal gas?

NGC 253 is an ideal target to study massive, clustered star formation in detail. It is one of the nearest (d$\sim$3.5 Mpc; Rekola et al., 2005) starburst galaxies forming stars at a rate of $\sim$2 $M_\odot$ yr^{-1} in the central kiloparsec (Bendo et al., 2015; Leroy et al., 2015). The star formation is concentrated in dense clumps, knots, and clouds of gas (Turner & Ho, 1985; Ulvestad & Antonucci, 1997; Paglione et al., 2004; Sakamoto et al., 2006, 2011; Bendo et al., 2015; Leroy et al., 2015; Ando et al., 2017). Recent high-resolution data from the Atacama Large Millimeter/submillimeter Array (ALMA) reveal at least 14 dusty, massive proto-SSCs (Leroy et al., 2018) at the heart of these larger dense gas structures. Moreover, the clusters themselves have radio recombination line (RRL) and radio continuum emission (Mills et al., 2021), further confirmation that these are young clusters.

However, even at the 1.9 pc (0.11″) resolution of the previous study by Leroy et al. (2018), the clusters, which have radii of $0.6 - 1.5$ pc, are only marginally resolved. Even higher resolution data are needed to spatially resolve these compact clusters to study the cluster-scale kinematics and feedback.

Here we present direct evidence for massive outflows from three forming SSCs

in the center of NGC 253 using new, very high resolution ($0.028'' \approx 0.48$ pc $\approx 10^5$ AU) data from ALMA at 350 GHz. These three clusters show blueshifted absorption and redshifted emission line profiles—P-Cygni profiles—in several lines. Our analysis shows that these profiles are a direct signature of massive outflows from these SSCs. We briefly describe the observations, data processing, and imaging in Section 4.2. We present measured properties of the outflows from three SSCs based on the line profiles and modeling in Section 4.3. We discuss the relevant timescales of the outflows and clusters in terms of their evolutionary stage, mechanisms to power the outflows, and comment on the specific case of SSC 5—which is the only cluster visible in the NIR—in Section 4.4. We summarize our findings in Section 4.5.

The analysis in this chapter will be focused on the three clusters with clear P-Cygni profiles: SSCs 4a, 5a, and 14. We will focus on results obtained from the CS $7-6$ and H^{13}CN $4-3$ lines for the following reasons. First, these lines show bright emission towards many of the SSCs and are detected at relatively high signal-to-noise ratio (SNR). Because of their high critical densities ($n_{\rm crit} \sim 3-5\times10^6\,{\rm cm}^{-3}$ and $n_{\rm crit} \sim 0.8-2\times10^7\,{\rm cm}^{-3}$ respectively; Shirley 2015) they probe gas that is more localized to the clusters themselves, lessening uncertainties introduced by the foreground gas correction (Section 4.2.4). In the case of H^{13}CN $4-3$, the ^{13}C/^{12}C isotopic ratio means this line is even less likely to be very optically thick. Although strong, the CO $3-2$ line shape is complicated because it has components from clouds along the line of sight that are not associated with the clusters. Though the HCN $4-3$ and HCO$^+$ $4-3$ lines are bright and also have high critical densities ($n_{\rm crit} \sim 0.9-3\times10^7\,{\rm cm}^{-3}$ and $n_{\rm crit} \sim 2-3.6\times10^6\,{\rm cm}^{-3}$ respectively; Shirley 2015),

they are more abundant and more optically thick than CS $7-6$ and $H^{13}CN$ $4-3$, and the absorption components in these lines suffer from saturation (i.e. absorption down to zero). This makes determining physical quantities of the outflows—which rely on the absorption depth to continuum ratio (Section 4.3)—difficult and uncertain. Therefore, we find that the CS $7-6$ and $H^{13}CN$ $4-3$ lines provide the best balance between bright lines with sufficient SNR, absorption features which do not suffer from saturation effects, and which probe gas localized to the clusters to minimize uncertainties from the foreground gas correction.

4.2 Observations, Data Processing, and Outflow Identification

Data for this project were taken with the Atacama Large Millimeter/submillimeter Array (ALMA) as part of project 2017.1.00433.S (P.I. A. Bolatto). We observed the central $16.64''$(280 pc) of NGC 253 at Band 7 ($\nu \sim 350$ GHz, $\lambda \sim 0.85$ μm) using the main 12-m array in the C43-9 configuration. This configuration resulted in baselines spanning from 113 m $-$ 13.9 km and hence a maximum recoverable scale of $0.38''$ (6.4 pc). The spectral setup is identical to our previous observations of this region (Leroy et al., 2018; Krieger et al., 2019, 2020b), spanning frequency ranges of $342.08-345.78$ GHz in the lower sideband and $353.95-357.66$ GHz in the upper sideband. Observations were taken on November $9-11$, 2017 with a total observing time of 5.7 hours of which 2.0 hours were on-source. The visibilities were pipeline calibrated using the Common Astronomy Software Application (CASA; McMullin et al. 2007) version 5.1.1-5 (L. Davis et al. in prep.). J0038-2459 was the phase

calibrator, and J0006-0623 was the bandpass and flux calibrator.

4.2.1 Imaging the Continuum

In this paper, we focus on the line profiles, specifically the CS $7-6$ and $H^{13}CN$ $4-3$ lines towards three of the SSCs. We will present the continuum data more fully in the following chapter. Some of the data are presented and used here, and we provide a brief summary.

To extract the 350 GHz continuum data, we flagged channels that may contain strong lines in the band, assuming a systemic velocity of $243\,\mathrm{km\,s^{-1}}$ (Koribalski et al., 2004). Lines included in the flagging are ^{12}CO $3-2$, HCN $4-3$, $H^{13}CN$ $4-3$, CS $7-6$, HCO^+ $4-3$, ^{29}SiO $8-7$, and ^{12}CO $3-2$ v=1 (though this line is not detected), and channels within ± 200 $\mathrm{km\,s^{-1}}$ of the rest frequencies of these lines were flagged. We imaged the line-flagged visibilities using the CASA version 5.4.1 `tclean` task with `specmode='mfs'`, `deconvolver='multiscale'`, `scales=[0,4,16,64]`, Briggs weighting with `robust=0.5`, and no *uv*-taper. The baseline was fit with a linear function (`nterms=2`) to account for any change in slope over the wide band. The continuum was cleaned down to a threshold of 27 $\mu\mathrm{Jy\,beam^{-1}}$, after which the residuals resembled noise. This map has a beam size of $0.024'' \times 0.016''$and a cell (pixel) size of $0.0046''$(0.078 pc), so that we place around 4 pixels across the minor axis of the beam. Finally, the map was convolved to a circular beam size of $0.028''$ (0.48 pc). The rms noise of the continuum image (away from emission) is 26 $\mu\mathrm{Jy\,beam^{-1}}$(0.3 K).

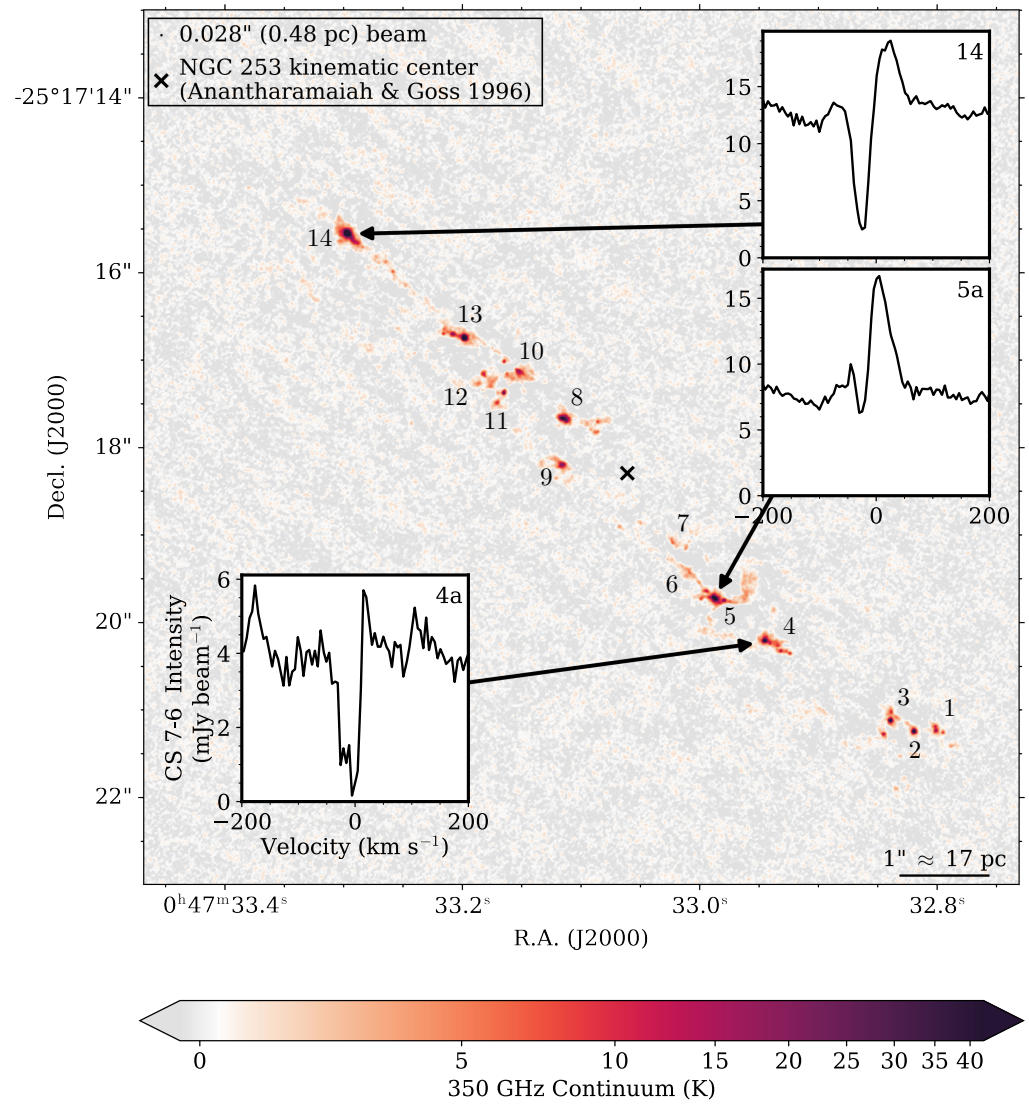

Figure 4.1: The 350 GHz dust continuum map covering the central 10″×10″(170 pc × 170 pc) of NGC 253 with an rms noise of 26 μJy beam^{-1}(0.3 K). The beam FWHM is shown in the upper left corner. The × marks the center of NGC 253 from ionized gas kinematics traced by radio recombination lines (Anantharamaiah & Goss, 1996). The 14 clusters identified by Leroy et al. (2018) are labeled. Despite the increased resolution most of the massive clusters identified by Leroy et al. (2018) persist, sometimes with a few lower-mass companion objects. The insets show the CS 7 − 6 spectra towards the three SSCs analyzed in this paper (SSCs 4a, 5a, and 14), highlighting the characteristic P-Cygni profiles indicative of outflows. These are the only clusters toward which we unambiguously identify blueshifted absorption signaling outflow activity.

From this high resolution 350 GHz continuum image (Figure 4.1), we identify approximately three dozen clumps of dust emission. These are co-spatial with the 14 proto-SSCs identified by Leroy et al. (2018), with many sources breaking apart into smaller clumps that likely represent individual clusters. We note that there is appreciable overlap in the spatial scales probed by these observations and those presented by Leroy et al. (2018). This means that the larger cluster sizes measured by Leroy et al. (2018) are due to the lower resolution, with the true cluster sizes better traced by these observations. We further verify this by computing the fluxes in the high resolution continuum image in the same apertures used by Leroy et al. (2018, see their Table 1). For SSCs 4, 5, and 14 (the focus of this analysis), we recover $> 80\%$ of the reported flux.

We follow the SSC naming convention of Leroy et al. (2018), adding letters to denote sub-clusters in decreasing order of brightness. For clusters that break apart, there is always a main, brightest cluster. For example, SSC 4 from Leroy et al. (2018) breaks apart into six dust clumps, where the peak intensity of SSC 4a is $>4\times$ that of any of the smaller clumps. For this paper, we will focus only on the primary clusters since those are the most massive, and smaller dust clumps may not be true clusters. We also remove SSC 6 from this analysis, as it is extended and more tenuous in the high resolution continuum map and so may not be a SSC. Leroy et al. (2018) also note that this clump is weak and may instead be a supernova remnant, which is further supported by a non-negligible synchrotron component to this cluster's spectral energy distribution (SED; Mills et al. 2021).

The position and orientation of each primary cluster is measured by fitting a

SSC Number	R.A. (J2000)	Decl. (J2000)	$r_{\mathrm{half-flux}}$ (pc)	V_{LSRK} (km s^{-1})
1a	$0^{\mathrm{h}}47^{\mathrm{m}}32.801^{\mathrm{s}}$	$-25°17'21.236''$	0.59	315
2	$0^{\mathrm{h}}47^{\mathrm{m}}32.819^{\mathrm{s}}$	$-25°17'21.247''$	0.19	305
3a	$0^{\mathrm{h}}47^{\mathrm{m}}32.839^{\mathrm{s}}$	$-25°17'21.122''$	0.47	302
4a	$0^{\mathrm{h}}47^{\mathrm{m}}32.945^{\mathrm{s}}$	$-25°17'20.209''$	0.50	251
5a	$0^{\mathrm{h}}47^{\mathrm{m}}32.987^{\mathrm{s}}$	$-25°17'19.725''$	0.76	215
7a	$0^{\mathrm{h}}47^{\mathrm{m}}33.022^{\mathrm{s}}$	$-25°17'19.086''$	0.59	270
8a	$0^{\mathrm{h}}47^{\mathrm{m}}33.115^{\mathrm{s}}$	$-25°17'17.668''$	1.20	295
9a	$0^{\mathrm{h}}47^{\mathrm{m}}33.116^{\mathrm{s}}$	$-25°17'18.200''$	0.46	155
10a	$0^{\mathrm{h}}47^{\mathrm{m}}33.152^{\mathrm{s}}$	$-25°17'17.134''$	1.32	280
11a	$0^{\mathrm{h}}47^{\mathrm{m}}33.165^{\mathrm{s}}$	$-25°17'17.376''$	0.13	145
12a	$0^{\mathrm{h}}47^{\mathrm{m}}33.182^{\mathrm{s}}$	$-25°17'17.165''$	1.29	160
13a	$0^{\mathrm{h}}47^{\mathrm{m}}33.198^{\mathrm{s}}$	$-25°17'16.750''$	0.36	245
14	$0^{\mathrm{h}}47^{\mathrm{m}}33.297^{\mathrm{s}}$	$-25°17'15.558''$	0.53	205

The cluster positions and sizes for the primary SSCs identified from the 350 GHz continuum image (Figure 4.1). We follow the cluster naming convention of Leroy et al. (2018). Clusters that break apart into multiple sub-clusters have an "a" added to their number. We remove SSC 6 as it is likely not a true cluster due to its morphology. Positions are determined by fitting a 2D Gaussian. $r_{\mathrm{half-flux}}$ is the half-flux radius determined from the radial profile. The beam (0.028" = 0.48 pc) has been deconvolved from the reported sizes. V_{LSRK} is the cluster systemic velocity (see Section 4.2.5). For SSCs 4a, 5a, and 14, the estimated uncertainty is ± 1 km s^{-1}. For the other clusters, estimated uncertainties are ± 5 km s^{-1}.

Table 4.1: Primary Cluster Positions and Sizes Measured from the 350 GHz Continuum Image

2D Gaussian to each cluster in the continuum image using `emcee` (Foreman-Mackey et al., 2013). The reported values are the medians of the marginalized posterior likelihood distributions (Table 4.1). As a non-parametric measurement of the cluster sizes, we compute the half-flux radius ($r_{\rm half-flux}$) for each cluster. Given the cluster positions and orientations from the 2D Gaussian fit, we construct elliptical annuli in steps of half the beam FWHM. The half-flux radius is the median of the cumulative flux distribution. We use this radius measurement as opposed to those from the 2D Gaussian fit because the cluster light profiles are not necessarily well described by a Gaussian, which will be discussed further in the following chapter. We deconvolve the beam from the radius measurements by removing half the beam FWHM from the half-flux radius in quadrature. The beam deconvolution will be treated more fully in the following chapter focusing on the continuum properties of the SSCs which will also include the lower resolution data.

4.2.2 Imaging the Lines

We image the CS $7-6$ and $H^{13}CN$ $4-3$ lines by selecting a 800 $\rm km\,s^{-1}$ window around the line center (rest frequencies of 342.883 GHz and 349.339 GHz respectively), assuming a systemic velocity of 243 $\rm km\,s^{-1}$ (Koribalski et al., 2004). We clean the lines of interest using `tclean` in CASA version 5.4.1 with `specmode='cube'`, `deconvolver='multiscale'`, `scales = [0]`, Briggs weighting with `robust = 0.5`, and no *uv*-taper. No clean mask was used. The baseline was fit with a linear function (`nterms=2`) to account for any change in slope over the wide band. The contin-

uum is not removed from the visibilities or the cleaned cubes. The cell (pixel) size is 0.0046″(0.078 pc), so that we place around 4 pixels across the minor axis of the beam. The final elliptical beam is 0.027″×0.019″. Finally, we convolve to a round 0.028″ (0.48 pc) beam. The rms noise is 0.5 mJy beam^{-1} (6.5 K) per 5 km s^{-1} channel. Figure 4.2 shows the peak intensity maps for CS $7-6$ and H^{13}CN $4-3$ within $\pm$200 km s^{-1} about the galaxy's systemic velocity to avoid possible contamination by other strong lines (especially by HC_3N in the case of H^{13}CN $4-3$).

4.2.3 Full-Band Spectra and Detected Lines

Though the analysis is focused on the CS $7-6$ and H^{13}CN $4-3$ lines, we also make a "dirty" cube covering the entire band and imaged area by running `tclean` with `niter=0`. This dirty cube has a cell (pixel) size of 0.02″ and an rms noise away from the emitting regions of 0.57 mJy beam^{-1} per 5 km s^{-1} channel. The synthesized beam is 0.05″×0.025″. The continuum is not removed from the visibilities or the dirty cube.

In Figure 4.3, we show the full band spectrum of SSCs 4a, 5a, and 14, extracted from the dirty cube and averaged over the FWHM continuum source size. There are several immediately striking features in these spectra. The brightest lines in SSCs 4a, 5a, and 14 show deep, blueshifted absorption features, extending down to ~ 0 mJy beam^{-1}, and redshifted emission. This line shape is commonly referred to as a P-Cygni profile — for the star in which it was first detected — and is indicative of outflows. As a comparison, we also show the spectrum of SSC 8a in Figure 4.3,

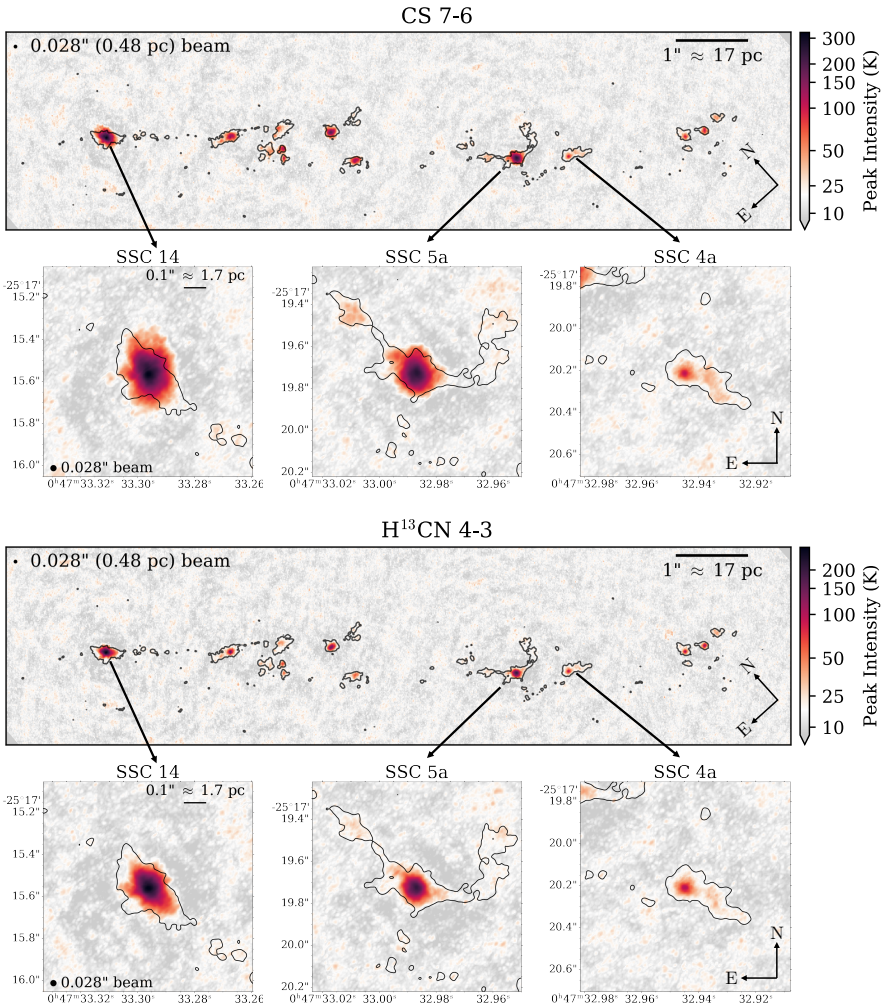

Figure 4.2: Peak intensity maps of CS $7-6$ (top group) and $H^{13}CN$ $4-3$ (bottom group) within ± 200 km s^{-1} of the galaxy systemic velocity to avoid contamination by other strong lines in the band. The top panels in each group have been rotated so the linear structure is horizontal, as indicated by the coordinate axes in the lower right corner. The contours show 5 times the rms noise level in the 350 GHz dust continuum shown in Figure 4.1 ($5\times$rms = 1.5 K), and so indicate the extent of the dust structures around the SSCs. The square plots show the peak intensity maps and dust continuum contours zoomed in to $1''$ (17 pc) square regions around SSCs 14, 5a, and 4a, highlighting the localized and spatially resolved emission towards these SSCs. These have not been rotated, as indicated by the coordinate axes in the lower right corner.

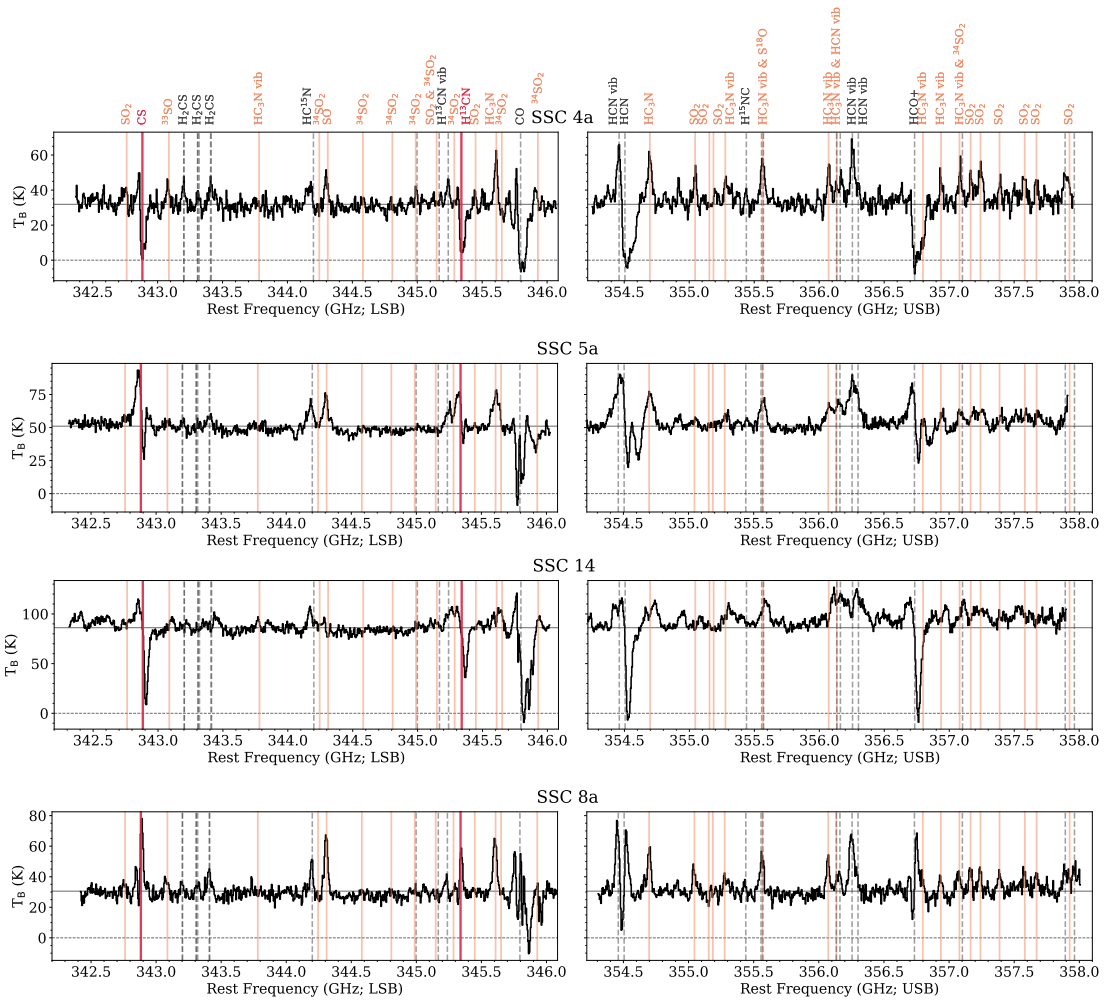

Figure 4.3: The full band spectra of SSCs 4a (top), 5a (top-middle), 14 (bottom-middle), and 8a (bottom). These spectra are averaged over the FWHM continuum source size and have been corrected for foreground gas (Section 4.2.4). The continuum has not been removed, and is shown by the solid horizontal gray lines. There are many spectral lines detected in these clusters, some of which are marked by the vertical lines and labels (where vib denotes a ro-vibrational transition; see also Krieger et al. 2020b). The main lines used in this study (CS $7-6$ and $H^{13}CN$ $4-3$) are marked in red (thick solid), lines used to determine the systemic velocity are in orange (thin solid), and other lines are in gray (dashed). The P-Cygni profile is seen in many lines in SSCs 4a, 5a, and 14. In some cases, the absorption is saturated (i.e. absorbed down to zero intensity shown by the horizontal gray dashed lines) especially in the brightest lines (such as CO $3-2$, HCN $4-3$, and HCO^+ $4-3$). The CO $3-2$ line profile is further complicated due to clouds along the line of sight. SSC 8a is shown as an example of bright source without evidence for outflows, though there may be a hint of inflows in CS $7-6$, $H^{13}CN$ $4-3$, and HCO^+ $4-3$.

which does not have these P-Cygni line shapes. We note that the CO $3-2$ line has a complicated structure, likely because it traces lower density gas than other detected lines ($n_{\rm crit} \sim 2 \times 10^4\,{\rm cm}^{-3}$; e.g., Turner et al., 2017) and so it arises in many places along the line of sight to the SSCs.

There are many detected lines in addition to the usual dense gas tracers. These include shock tracers such as SO $8-7$ and SO_2 lines and vibrationally excited HC_3N and HCN $4-3$, which are primarily excited through IR pumping (e.g. Ziurys & Turner, 1986; Krieger et al., 2020b). Many of these have been previously identified by Krieger et al. (2020b), some of which are marked in Figure 4.3.

4.2.4 Correcting for Foreground Gas

Because the SSCs are embedded in the nucleus of NGC 253, there is dense gas along the line of sight which may contribute to the observed spectra but is not associated with the SSCs themselves. This can be seen in the line channel maps around each SSC, shown in Figure 4.4 for CS $7-6$. This gas is most evident in SSCs 5a and 14, which both show changes in the gas morphology with velocity (relative to the cluster systemic velocity; see Section 4.2.5). The first panel of each set of channel maps shows the CO $3-2$ velocity field in the same region as a tracer of the bulk gas motions not associated with the clusters themselves. Because we are interested in the large scale gas motions, we smooth the CO $3-2$ velocity maps presented by Krieger et al. (2019) to $5\times$ the beam major axis ($5\times0.17'' = 0.85'' = 14.4$ pc). The velocities shown in Figure 4.4 are relative to the cluster systemic velocities. All

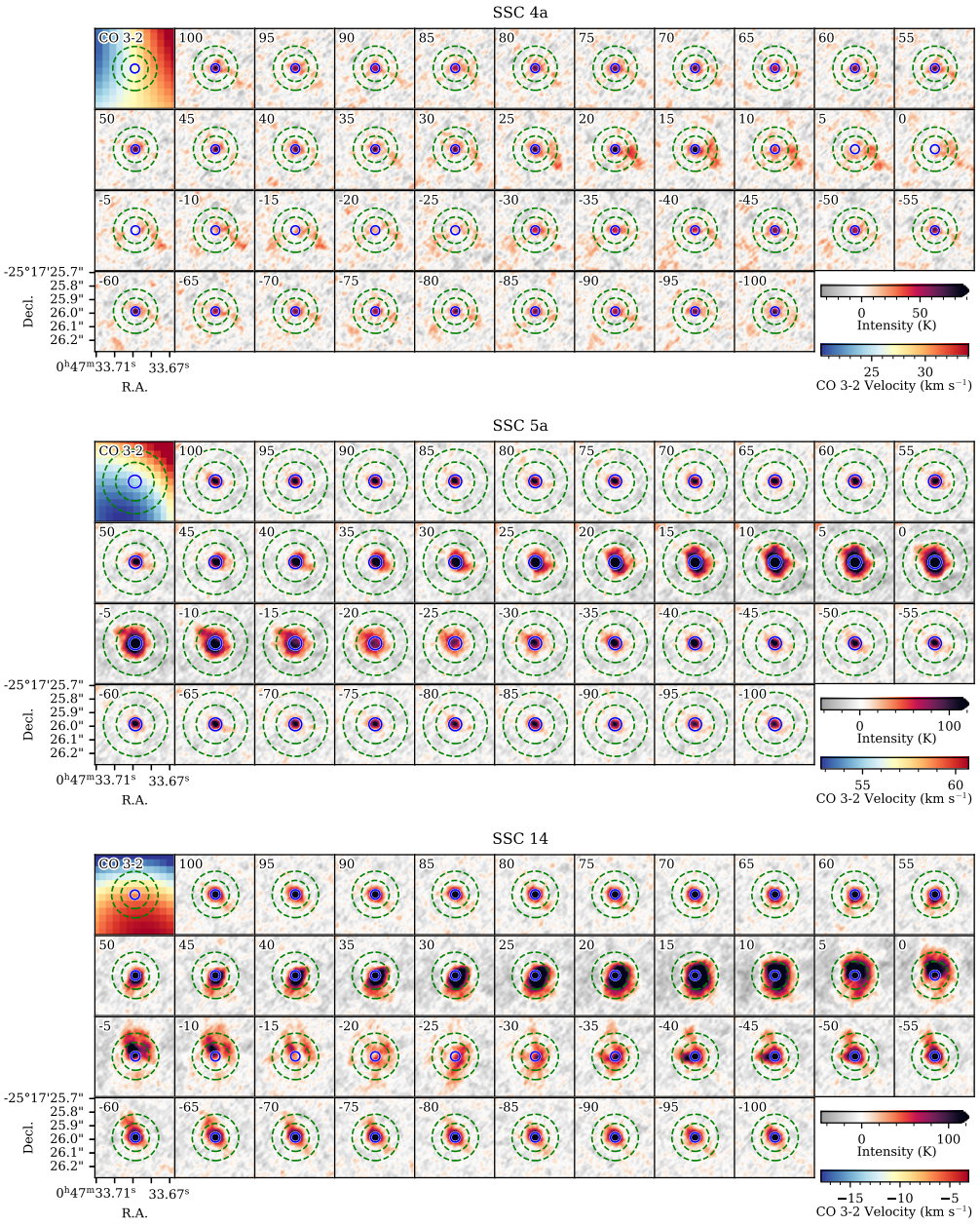

Figure 4.4: Channel maps around CS $7-6$ for SSCs 4a (top), 5a (middle), and 14 (bottom) in 10 pc $\times$ 10 pc regions. The continuum has not been removed. The first panel shows the smoothed CO $3-2$ velocity field in this region (Krieger et al., 2019), indicative of the large-scale bulk gas motions. The CO $3-2$ colorscale and the labeled CS $7-6$ velocity channels (in km s^{-1}) are relative to the cluster systemic velocity (Table 4.1). The solid blue circles show the continuum source sizes, and the dashed green annuli show the regions used for the foreground correction. The H^{13}CN $4-3$ channel maps are similar.

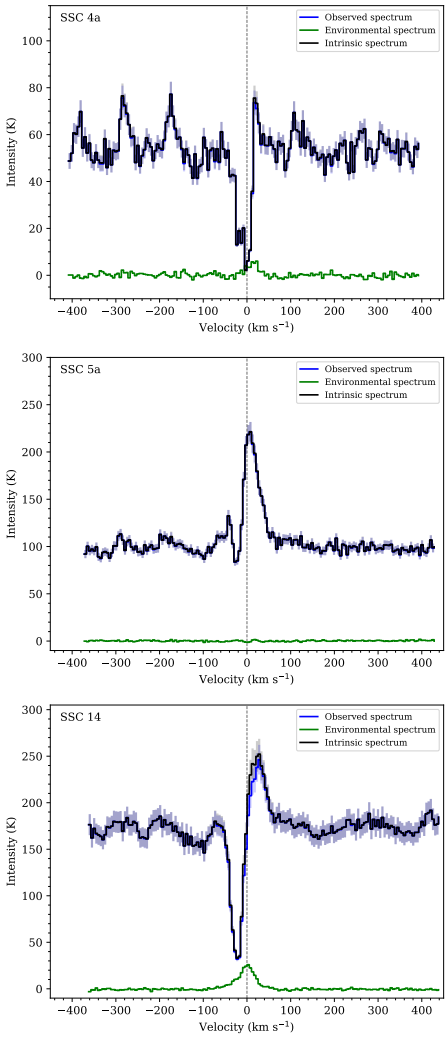

Figure 4.5: The CS $7-6$ spectra for SSCs 4a (top), 5a (middle), and 14 (bottom) averaged over the 350 GHz continuum source area (blue; corresponding to the blue ellipses in Figure 4.4), the foreground gas (green; corresponding to the green annuli in Figure 4.4), and the corrected, intrinsic CS $7-6$ spectrum accounting for the foreground gas (black). The blue shaded region around the observed spectrum reflects the standard deviation of the spectrum within the continuum source area. The gray shaded region around the intrinsic spectrum includes the propagated uncertainties from the assumed excitation temperature ($T_{ex} = 102 \pm 28$ K). See Section 4.2.4 for details of the foreground gas correction.

three clusters are located at different velocities compared to the bulk gas motions (i.e., CO $3-2$ velocity maps are not centered on zero). In the case of SSC 14, the distinct morphological evolution with velocity matches qualitatively with the CO $3-2$, though there is a velocity offset. It is difficult to know what fraction of this is associated with the clusters themselves or with dense gas in the environment of the clusters but not necessarily bound to them. Here, we will assume that all of the emission in the green annuli in Figure 4.4 is not bound to the clusters and should be corrected to obtain the intrinsic spectrum of the clusters. The spectrum of the environmental gas (T_{env}) is averaged in an annulus with an inner radius of $3\times$ the half-flux radius and an outer radius of $5\times$ the half-flux radius, as shown in Figure 4.4. This effectively assumes the environmental dense gas forms a uniform screen in between the cluster and our line of sight. This is unlikely to be the case and is one of the uncertainties of this correction.

We calculate the optical depth (τ_ν) of the environmental gas following Mangum & Shirley (2015). Combining their Equations 24 and 27, we have

$$\tau_\nu = -\ln\left[1 - \frac{kT_{env}}{h\nu}\left(\frac{1}{e^{h\nu/kT_{ex}}-1} - \frac{1}{e^{h\nu/kT_{bg}}-1}\right)^{-1}\right] \tag{4.1}$$

where the filling fraction is assumed to be unity, the excitation temperature (T_{ex}) is 102 ± 28 K and the background temperature (T_{bg}) is measured from the continuum level of the environmental spectrum (but is $\approx$ 0 K; Figure 4.5). The assumed value of T_{ex} is the average of the excitation temperatures found by Meier et al. (2015) over larger scales in the nucleus (74 K) and by Krieger et al. (2020b) for

regions more localized to the SSCs (130 K), since the true value of the excitation temperature of this dense gas near the clusters likely falls somewhere between these two measurements. The uncertainty reflects half of the difference of these two values.

We assume that half of the environmental emission comes from the foreground, so that the optical depth of the material along the line of sight in front of the cluster is $\tau_{\nu,\mathrm{fg}} = \tau_\nu/2$. We also assume that the environmental gas is colder than the gas in the cluster, so it will absorb emission from the cluster. We then derive the corrected (intrinsic) SSC spectra where

$$\begin{aligned} \mathrm{T_{obs}} &= \mathrm{T_{intrinsic}} e^{-\tau_{\nu,\mathrm{fg}}} + \mathrm{T_{env}} \left(1 - e^{-\tau_{\nu,\mathrm{fg}}}\right) \\ \Rightarrow \mathrm{T_{intrinsic}} &= e^{\tau_{\nu,\mathrm{fg}}} \left[\mathrm{T_{obs}} - \mathrm{T_{env}} \left(1 - e^{-\tau_{\nu,\mathrm{fg}}}\right)\right], \end{aligned} \tag{4.2}$$

where the second equation is a rearrangement of the first. The observed, environmental, and intrinsic spectra of CS $7-6$ for SSCs 4a, 5a, and 14 are shown in Figure 4.5. This process is repeated for $\mathrm{H^{13}CN}$ $4-3$ and the full-band spectra in Figure 4.3.

As discussed earlier, it is difficult to determine what fraction of the extended emission seen in the channel maps (Figure 4.4) is environmental or associated with the cluster. Moreover, our method for the foreground correction is quite simplistic, and there are uncertainties related to the fraction of gas that may be associated with the clusters, the geometry of the environmental material, and the assumed excitation temperature. As can be seen in Figure 4.5, however, the correction mostly affects the peak of the emission components. After the foreground correction, the emission peak

for SSC 14 increases by 7% (17 K), whereas the absorption trough only increases by 4.5% (1.5 K). There is no appreciable change in the spectra for SSCs 4a and 5a. The absorption features are, therefore, largely unaffected by this correction, and the derived properties of the outflow (presented in Sections 4.3.1 and 4.3.2) are robust. The intrinsic (corrected) spectra are used throughout the analysis of this paper.

4.2.5 Cluster Systemic Velocities

We constrain the systemic velocity of all of the detected clusters using the full-band spectra and the detected line list presented by Krieger et al. (2020b). Using the full-band spectrum for each cluster, we simultaneously fit each line in the line list using a series of Gaussians of the form

$$I(\nu) = I_{\rm cont} + \sum_{\rm line} I_{\rm line} \exp\left[\frac{-(\nu - \nu_{\rm line-rest})^2}{2\sigma^2_{\rm line}}\right] \tag{4.3}$$

where $I_{\rm cont}$ is the fitted continuum level over the whole spectrum, $I_{\rm line}$ is the fitted intensity of each line, $\nu_{\rm line-rest}$ is the fixed rest frequency of each line, $\sigma_{\rm line}$ is the fitted width of each line, and ν is the rest frequency of the observed spectrum which depends on the assumed systemic velocity. The primary lines used to determine the systemic velocity are marked in orange in Figure 4.3; these lines tend to have strong emission and simple line shapes. Other strong lines in the band (e.g., CO $3-2$, HCN $4-3$, HCO^+ $4-3$) tend to have complicated line shapes that make accurately determining the systemic velocity difficult. Due to the presence of lines with complicated shapes and line-blending, the cross-correlation of each full-band

spectrum and the multi-Gaussian fit is done by-eye. The systemic velocities of for all the clusters are listed in Table 4.1. The uncertainty is estimated to be ± 5 km s^{-1}. For SSCs 4a, 5a, and 14, the systemic velocities are further refined and confirmed using other lines in the cleaned CS $7-6$ and H^{13}CN $4-3$ cubes (Figure 4.6). Several of these lines — the vibrational transitions, in particular — have sharp peaks and are spatially localized to the clusters themselves. They, therefore, provide tighter constraints on the cluster systemic velocities. For SSCs 4a, 5a, and 14, we estimate that our cluster systemic velocities are accurate to ± 1 km s^{-1}.

4.2.6 Other Cluster Properties

In addition to cluster properties derived from these new 0.5 pc resolution data described in the previous subsections, we use stellar masses, total H_2 gas masses, and escape velocities of the clusters calculated by Leroy et al. (2018). Here we briefly describe how these quantities were derived. These quantities are reproduced in Table 4.2 for the three clusters which are the focus of this work.

4.2.6.1 Stellar Masses (M_*)

The stellar masses are calculated based on the 36 GHz image from the VLA convolved to 0.11″ (1.9 pc) resolution (Leroy et al., 2018; Gorski et al., 2017, 2019). At 36 GHz, the emission is assumed to be entirely due to free-free (Bremsstrahlung) emission. From the 36 GHz luminosity, Leroy et al. (2018) derived M_* for a zero-age main sequence (ZAMS) population with a standard initial mass function (IMF)

(see their Section 4.3.1 and Table 2). As described below, we consider additional sources of uncertainty beyond those described by Leroy et al. (2018). First, we assume that the primary clusters retain all of the stellar mass measured by Leroy et al. (2018), which may lead to an overestimate of M_* for those clusters that break apart. We estimate that this is at worst 50% in those cases (although the higher resolution data presented here shows a number of satellite structures, the original one remains dominant in most). Secondly, Leroy et al. (2018) estimate that there is a $\pm$20% systematic uncertainty due to assumptions about the Gaunt factor. Finally, Mills et al. (2021) measure M_* of these clusters at 5 pc resolution using hydrogen radio recombination lines (RRLs). These agree with the M_* estimated by Leroy et al. (2018) to within $\pm$0.3 dex on average. For SSCs 4a, 5a, and 14, the agreement is even better, and the RRL analysis finds M_* which differ by $+0.1$, -0.1, and -0.2 dex from those derived from the 36 GHz emissions, where $+$ ($-$) means the RRL measurements produce a larger (smaller) M_*. Included in the calculations by Mills et al. (2021) is the effect of a synchrotron component. If synchrotron contaminates the 36 GHz flux (which is assumed to be entirely free-free in the M_* calculation of Leroy et al. 2018), this would lead to an overestimate of M_*. There is negligible synchrotron emission in SSCs 4a, 5a, and 14, but this could affect the M_* of other clusters (especially SSCs 1a, 10a, 11a, and 12a; Mills et al. 2021). To determine the lower error bar on M_*, we take the largest of the above three sources of uncertainty for each cluster, where the uncertainty from the RRL measurements are included only if they yield a smaller M_*. To determine the upper error bars, we take the larger of the 20% systematic uncertainty and

RRL-measured M_* where they yield a larger M_*. In addition to these quantifiable uncertainties on M_*, there are unquantified uncertainties relating to ionizing photons absorbed by dust and evolution beyond the ZAMS, both of which would result in the reported stellar masses being underestimates (Leroy et al., 2018). While we do not attempt to calculate these unquantifiable uncertainties, we caution that they could be important. In this work, we use these stellar masses primarily to place the clusters in a mass-radius diagram and to evaluate the possible mechanisms powering the observed outflows.

4.2.6.2 Total H_2 Gas Mass ($M_{H_2,tot}$)

The cluster gas masses are based on the 350 GHz image from ALMA at 0.11″ (1.9 pc) resolution (Leroy et al., 2018). At 350 GHz, the majority of the emission is due to thermal dust emission, though there may be a small level of free-free contamination. Leroy et al. (2018) quantify this free-free contamination and correct the measured 350 GHz fluxes to determine a more accurate flux due to thermal dust emission (see their Section 4.1 and Table 1). Assuming a dust temperature of 130 K, dust-to-gas ratio of 1:100, and a dust mass absorption coefficient of 1.9 cm^2 g^{-1}, Leroy et al. (2018) calculate the total H_2 mass of the clusters. Uncertainties are $\sim$0.4−0.5 dex, with these measurements likely biased low due to assumptions about the dust temperature, dust-to-gas ratio, and the dust opacity. See their Section 4.3.3 and Table 2 for more details. In this work, we consider these to be the total gas masses of the clusters, including gas still bound within the cluster and outflowing

from it.

4.2.6.3 Escape Velocity (V_{escape})

Leroy et al. (2018) calculate the escape velocity from the clusters using their measured stellar and gas masses and their measured sizes from Gaussian fits to the 0.11″ (1.9 pc) resolution 350 GHz image. Uncertainties are dominated by those from M_* and $M_{H_2,tot}$. See Section 4.3.6 and Table 2 of Leroy et al. (2018) for more details. In this work, we use these escape velocities to compare against the outflow velocities we measure to place constraints on whether the outflowing material will escape the cluster.

4.2.7 Outflow Candidates

We analyze the spectra towards all of the clusters (primary or otherwise) identified in the high resolution continuum data (Figure 4.1) in search of spectral outflow signatures. We determine our final list of outflow candidates based on robust detections of blueshifted absorption and redshifted emission in the CS $7-6$ and $H^{13}CN$ $4-3$ lines. We present SSCs 4a, 5a, and 14 as our conservative list of detected P-Cygni profiles indicative of outflows. The CS $7-6$ and $H^{13}CN$ $4-3$ spectra towards SSCs 4a, 5a, and 14 are shown in Figure 4.6, which are from the cleaned line cubes (Section 4.2.2) and have been corrected for foreground gas (Section 4.2.4).

While other SSCs show absorption features, these are not due to outflowing material as the absorption occurs at the line center. Absorption at the line center

is likely due to self-absorption of the cold material surrounding the cluster against the embedded continuum source(s). Redshifted absorption would be indicative of material inflowing towards the cluster; a hint of inflow is perhaps seen towards SSC 8a (Figure 4.3, especially the CS $7-6$, HCN $4-3$ and HCO^+ $4-3$ lines). Blueshifted absorption, on the other hand, means that the cold foreground material is outflowing from the cluster. For this analysis, we are focused on the blueshifted absorption indicative of outflows.

We also verify that these absorption features are not induced by the spatial filtering by the interferometer. Due to the incomplete sampling of the Fourier plane and the lack of short spacings, emission on larger scales is filtered out and cannot be properly deconvolved, causing an increase in the RMS of the data at the velocities where bright extended emission would be present. This problem manifests itself as negative "bowls" around bright emission, but also as negative features that have velocity structure. While this mainly affects the continuum (which is not removed from these data), it can also induce false absorption features in the affected velocity range. This can be seen, for example, in the CO $3-2$ lines in Figure 4.3, where the absorption profiles are very complex. Our choice to focus on CS $7-6$ and $H^{13}CN$ $4-3$ mitigates this problem, as these transitions require high densities to be excited and are hence fairly localized to the clusters themselves, with not much of an extended component. As shown in Figure 4.5 the environmental CS $7-6$ spectra around the SSCs are either flat or show the line in emission; the $H^{13}CN$ $4-3$ spectra show similar profiles. Therefore, we conclude that the CS $7-6$ and $H^{13}CN$ $4-3$ absorption features are not a result of the spatial filtering by the interferometer,

although it may contribute to uncertainties at the 10% level.

A careful measurement of the cluster systemic velocities (Section 4.2.5) is critical to determine whether the absorption is blueshifted with respect to the cluster or not. Critically, for a few clusters (e.g., SSCs 3a and 13a) there are pathological combinations of absorption at the line center coupled with strong vibrationally excited lines in emission at the redshifted edge of the absorption feature, which together could masquerade as P-Cygni profiles. We identify other line candidates present in the spectra around CS $7-6$ and $H^{13}CN$ $4-3$ using the line list presented by Krieger et al. (2020b) as well as Splatalogue*, which are listed in the shaded yellow regions in Figure 4.6. It is outside the scope of this paper to verify precisely which other lines are present in the spectra, so we present them simply as possible candidates (or combinations of candidates) which confuse the CS $7-6$ and $H^{13}CN$ $4-3$ spectra. This line blending can lead to false detections of P-Cygni profiles. For example, $H^{13}CN$ $4-3$ $v_2=1$ is located 100 MHz (≈ 88 km s^{-1}) red-ward of $H^{13}CN$ $4-3$, as can be seen in the right column of Figure 4.6. Similarly, HCN $4-3$ $v_2=1$ is located only 45 MHz (≈ 38 km s^{-1}) red-ward of HCN $4-3$. Given the broad line profiles (in emission and absorption), these lines can easily blend together to produce a facsimile of a P-Cygni profile. A careful measurement of the cluster systemic velocities (using other lines with simpler profiles), cross-referencing with the line list presented by Krieger et al. (2020b), and further verification using Splatalogue reveals that these are not true P-Cygni profiles. It is also worth noting that there is an emission feature (likely $OS^{18}O$, an SO_2 isotopologue) seen in the CS

* https://www.cv.nrao.edu/php/splat/advanced.php

$7-6$ absorption trough of SSC 4a (upper left panel of Figure 4.6).

That we detect outflows from SSCs 4a, 5a, and 14 is in large part due to our ability to spatially resolve the individual clusters, since the spectral signatures of the outflows are localized roughly to the central half-flux radius of the clusters. In retrospect, there are indications of these outflows in the CS $7-6$ and $H^{13}CN$ $4-3$ line profiles presented by Leroy et al. (2018, see their Figure 3) in SSCs 4 and 14. The much weaker outflow in SSC 5a is not apparent in these lower resolution data where the clusters are only marginally resolved. There are also kinematic offsets between HCN $4-3$ and H40α measurements towards these clusters which are consistent with the effects of these outflows at lower resolution (Mills et al., 2021).

4.2.8 Internal Cluster Kinematics

Briefly here, we investigate whether SSCs 4a, 5a, and 14 exhibit signs of internal rotation. Observational detections of rotation in star and globular clusters in the Milky Way are mixed (e.g. Kamann et al., 2019; Cordoni et al., 2020), though simulations predict that massive star clusters (> 1000 $M_\odot$) should have appreciable rotation (Mapelli, 2017).

We investigate the internal kinematics by constructing position-velocity (PV) diagrams over a range of angles as well as peak-velocity and intensity-weighted velocity (moment 1) maps around each of the clusters. While we see no clear signs of internal rotation, the absorption hinders this analysis significantly as it affects the (effective) intensity weighting of the peak- and intensity-weighted velocity (moment

1) maps. It similarly confuses the interpretation of the PV diagrams. Therefore, we cannot claim that the SSCs are not rotating, only that, given the presence of absorption, we see no clear evidence for rotation. We also check clusters without absorption or outflow signatures, and also find no evidence of rotation.

4.3 Results

Using ALMA data at 350 GHz at 1.9 pc resolution, Leroy et al. (2018) identified 14 marginally-resolved clumps of dust emission whose properties are consistent with forming SSCs. In our new 0.5 pc resolution data, many of these SSCs fragment substantially such that there is a bright, massive primary cluster surrounded by smaller satellite clusters (Figure 4.1). From the 0.5 pc resolution 350 GHz dust continuum image (Figure 4.1), we identify roughly three dozen clumps of dust emission. We spectrally identify candidate outflows towards three SSCs: SSCs 4a, 5a, and 14 (where the appended "a" denotes the primary cluster of the fragmented group). The locations of these clusters within the nucleus of NGC 253 are shown in Figure 4.1, where the insets show the CS $7-6$ line profiles towards these three clusters. In each of these SSCs, we see evidence for blueshifted absorption and redshifted emission in many lines (Figure 4.3), but we focus on the CS $7-6$ and $H^{13}CN$ $4-3$ lines (Figure 4.6) which provide the best balance between bright lines with sufficient SNR, absorption features which do not suffer from saturation effects, and which probe gas localized to the clusters. This line shape—blueshifted absorption and redshifted emission—is commonly referred to as a P-Cygni profile and is indicative of outflows.

We take two approaches to derive the physical properties of the outflows in each cluster. First, we fit the absorption component of the line profiles to measure the outflow velocity, column density, mass, mass outflow rate, momentum, etc (Section 4.3.1). Second, we model line profiles of the CS $7-6$ and $H^{13}CN$ $4-3$ spectra towards each cluster with the goal of constraining the outflow opening angles and orientations to the line of sight (Section 4.3.2). While the primary goal of the line profile modeling is to constrain the outflow geometry, it also provides a measurement of the outflow velocity, column density, mass, mass outflow rate, etc. We compare common parameters of these methods in Section 4.3.3 and discuss our recommended values in Section 4.3.4.

4.3.1 Outflow Properties from Absorption Line Fits

For a first estimate, we measure the outflow velocities, column densities, gas masses, and momentum of each outflow by fitting the profiles of $H^{13}CN$ $4-3$ and CS $7-6$ with a two-component Gaussian (blue dashed curves in Figure 4.6). We exclude the portions of the spectra that may be contaminated by other lines, as marked by the yellow shaded regions in Figure 4.6. The fit to the absorption feature yields the velocity at the maximum absorption ($V_{max-abs}$), or the velocity at which the bulk of the material is outflowing. We define the maximum outflow velocity as 2σ from the average velocity ($V_{max,out} \equiv V_{max-abs} + 2\frac{\Delta V_{out,FWHM}}{2.355}$), which means that 95% of the material traced by CS $7-6$ and $H^{13}CN$ $4-3$ has an outflow velocity slower than $V_{max,out}$ (for a truly Gaussian line). Given the mean outflow velocity and the cluster

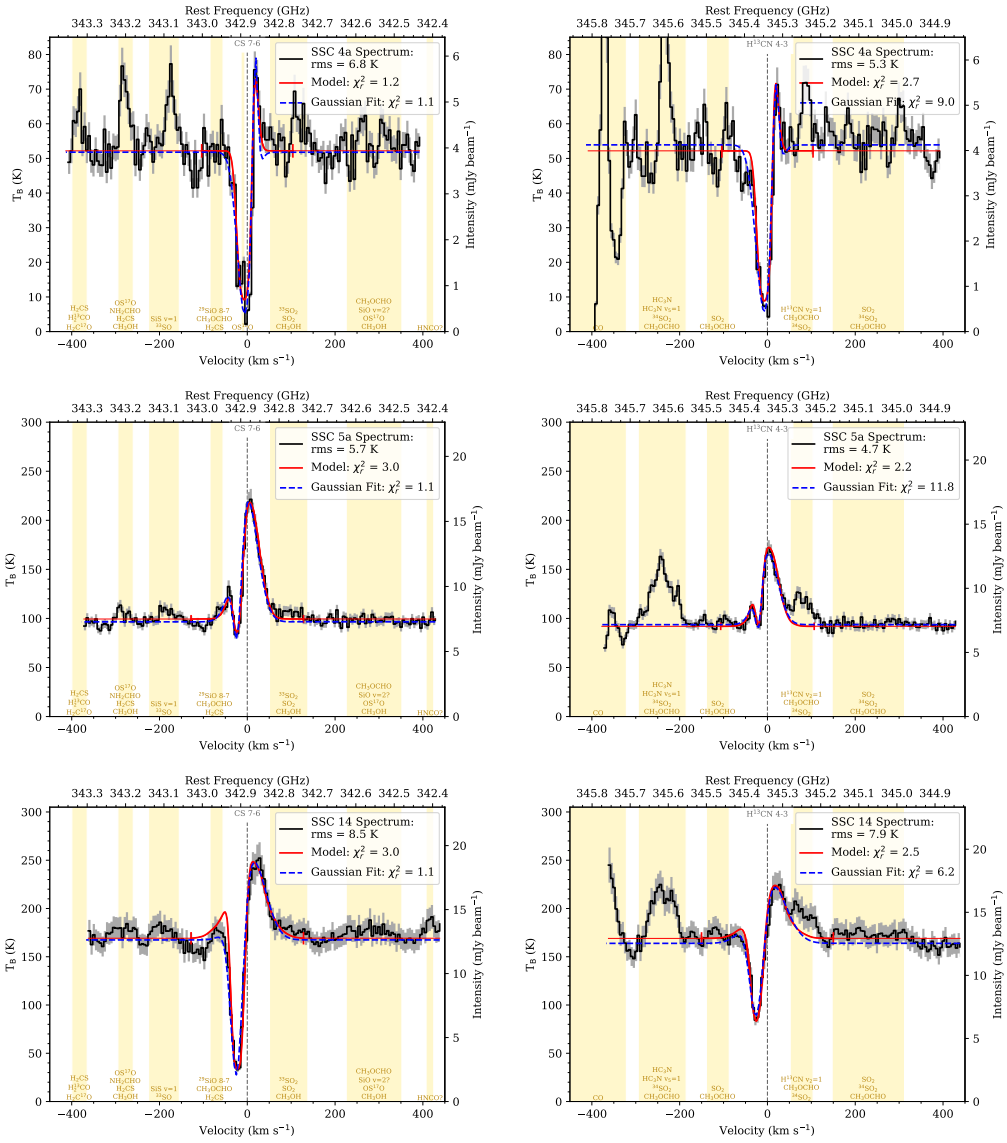

Figure 4.6: The CS $7-6$ (left) and $H^{13}CN$ $4-3$ (right) spectra for SSCs 4a (top), 5a (middle), and 14 (bottom). The yellow shaded regions show where other lines may contaminate the spectrum. Possible candidate lines are listed at the bottom of the yellow shaded regions. The dashed blue curves show the two-component Gaussian fit to the profile (Section 4.3.1). The solid red curves show the best-fitting spherical outflow models (Section 4.3.2). The vertical red line segments shows the range of velocities actually modeled, the red curve outside of these vertical line segments is an extrapolation.

		SSC 4a		SSC 5a		SSC 14	
Quantity	Unit	CS 7 − 6	$H^{13}CN$ 4 − 3	CS 7 − 6	$H^{13}CN$ 4 − 3	CS 7 − 6	$H^{13}CN$ 4 − 3
$\log_{10}(M_{H_2,tot})$ [a]	$\log_{10}(M_\odot)$	5.1		5.3		5.7	
$\log_{10}(M_*)$ [b]	$\log_{10}(M_\odot)$	5.0		5.4		5.5	
V_{escape} [c]	km s^{-1}	22.0		33.2		45.5	
τ [d]		2.3	2.3	0.2	0.0	1.8	0.6
$V_{max-abs}$ [e]	km s^{-1}	6	6	22	20	24	24
$V_{out,max}$ [f]	km s^{-1}	40	46	42	34	51	56
$\Delta V_{out,FWHM}$ [g]	km s^{-1}	40	46	24	17	32	38
$\log_{10}(t_{cross})$ [h]	$\log_{10}$(yr)	5.0	5.0	4.5	4.6	4.4	4.4
$\log_{10}(N_{H_2,out})$ [i]	$\log_{10}(cm^{-2})$	23.9	25.3	22.7	23.2	23.7	24.6
$\log_{10}(M_{H_2,out})$ [j]	$\log_{10}(M_\odot)$	4.7	6.1	3.8	4.3	4.6	5.5
$\log_{10}(M_{H_2,out}/M_{H_2,tot})$ [k]		-0.4	1.0	-1.5	-1.0	-1.1	-0.2
$\log_{10}(M_{H_2,out}/M_*)$ [k]		-0.3	1.1	-1.6	-1.1	-0.9	-0.0
$\log_{10}(\dot{M}_{H_2,out})$ [l]	$\log_{10}(M_\odot\ yr^{-1})$	-0.3	1.1	-0.7	-0.3	0.2	1.1
$\log_{10}(t_{remove-gas})$ [m]	$\log_{10}$(yr)	5.4	4.0	6.0	5.6	5.5	4.6
$\log_{10}(p_r/M_*)$ [n]	$\log_{10}$(km s^{-1})	0.7	2.1	0.0	0.5	0.7	1.6
$\log_{10}(E_{kin})$ [o]	$\log_{10}$(erg)	49.2	50.6	49.6	49.9	50.4	51.3

Values (aside from the top three) are derived from fits to the absorption component of the line profiles. See Section 4.3.1 and Appendix C.1 for details on how these values were calculated. [a]The cluster gas mass measured from the dust continuum and assuming a gas-to-dust ratio of 100 (Leroy et al., 2018). Uncertainties are ∼0.4−0.5 dex, with these measurements likely biased low due to assumptions about the dust temperature, dust-to-gas ratio, and the dust opacity. See Section 4.2.6 for a detailed discussion of how these values were calculated. [b]The cluster zero age main sequence (ZAMS) stellar mass measured from the 36 GHz free-free emission (Leroy et al., 2018). See Section 4.2.6 for a detailed discussion of the uncertainties on these stellar masses. [c]The escape velocity from the cluster (Leroy et al., 2018). Uncertainties are dominated by those from the gas and stellar masses. See Section 4.2.6 for a detailed discussion of how these values were calculated. [d]The optical depth in the outflow calculated from the absorption to continuum ratio (Eq. C.4). [e]The velocity where the absorption is maximized, corresponding to the velocity at which the bulk of the material traced by CS 7 − 6 and $H^{13}CN$ 4 − 3 is outflowing. [f]The maximum outflow velocity, defined as 2σ from the mean outflow velocity (Eq. C.3). For a Gaussian line, this means that 95% of the dense material has an outflow velocity slower than $V_{max,out}$. [g]The FWHM line width from the Gaussian fit to the absorption feature. [h]The gas crossing time, or the time it would take a parcel of gas to travel from the center of the cluster to r_{SSC} at $V_{max-abs}$ (Eq. C.2). [i]The H_2 column density in the outflow derived from τ (Eqs. C.5−C.9). This calculation assumes LTE with an excitation temperature of 130 ± 56 K and abundances of CS 7 − 6 and $H^{13}CN$ 4 − 3 relative to H_2 from Martín et al. (2006). The abundances may vary by an order-of-magnitude on these small scales, so all quantities which depend on the column density are limited to order-of-magnitude precision. The blueshifted outflow component only probes the portion of the outflow on the approaching side, so the values are multiplied by 2 to account for the receding side of the outflow, assuming it is identical to the approaching side. Uncertainties are ±1 dex. [j]The H_2 mass in the outflow derived from $N_{H_2,out}$ and the projected cluster size (Eq. C.10). This calculation and others which depend on it assume the outflow is spherical, which is supported by the results of our modeling (Section 4.3.2). Uncertainties are ±1 dex. [k]The H_2 mass in the outflow compared to the total gas or stellar mass in the cluster. Uncertainties are ±1 dex. [l]The mass outflow rate derived over one crossing time (Eq. C.11). Uncertainties are ±1 dex. [m]The gas removal time, or the time it would take for the current mass outflow rate to expel all of the cluster gas mass ($M_{H_2,tot}$) from the clusters (Eq. C.12). Uncertainties are ±1 dex. [n]The radial momentum carried by the outflow per unit stellar mass, which also assumes the outflow is spherical (Eq. C.13). Uncertainties are ±1 dex. [o]The kinetic energy of the outflow calculated from $M_{H_2,out}$ and $V_{max-abs}$ (Eq. C.14). Uncertainties are ±1 dex.

Table 4.2: Cluster and Outflow Properties from Absorption Line Fits

size, we calculate the crossing time, or the time for a parcel of gas to travel from the center of the cluster to the edge ($t_{cross} \equiv r_{SSC}/V_{max-abs}$), where r_{SSC} is equivalent to the half-flux radius (Table 4.1). From the fitted absorption to continuum intensity ratio, we derive the optical depth and hence the column density in absorption. We convert from the column density of the molecule to H_2 ($N_{H_2,out}$) using abundances from Martín et al. (2006). From the column density and projected size (Table 4.1), we estimate the H_2 mass in the outflow ($M_{H_2,out}$) assuming the outflow is spherical. Constraints on the opening angle of the outflows derived from modeling of the line profiles are discussed in Section 4.3.2 and show that the outflows must be nearly spherical. Given the mass, crossing time, and mean outflow velocity, we calculate the mass outflow rate ($\dot{M}_{H_2,out}$), the gas removal timescale ($t_{remove-gas}$), the radial momentum injected per unit stellar mass in the cluster (p_r/M_*), and the kinetic energy of the outflow (E_{kin}). Further details and equations used to derive these quantities are presented in Appendix C.1. The outflow parameters derived from the absorption profile fits are reported in Table 4.2.

The clusters have outflows with maximum velocities ($V_{max,out}$) of $\sim 40-50$ $km\,s^{-1}$. For all three SSCs with outflows, $V_{max,out}$ is larger than the escape velocity (V_{escape}; reproduced in Table 4.2 from Leroy et al. 2018 and see also Section 4.2.6). The bulk of the material traced by CS $7-6$ and $H^{13}CN$ $4-3$, however, has velocities less than V_{escape} (as traced by $V_{max-abs}$). For SSCs 4a, 5a, and 14, 20%, 7%, and 7% of the outflowing material has velocities larger than the escape velocity and will be able to escape from the cluster. Gas which is outflowing with velocities below V_{escape} may be reaccreted by the cluster. The gas crossing time (t_{cross}) is $\sim$few$\times 10^4$

years, which is a lower limit on the age of the outflow. These timescales and the possibility of reaccretion will be discussed further in Section 4.4.1.

The masses in the outflows are large. The molecular hydrogen column densities and masses derived from $H^{13}CN$ $4-3$ are larger than those derived from CS $7-6$ in all cases. One possibility is that CS $7-6$ is more optically thick than $H^{13}CN$ $4-3$, which may be supported by the depth of the absorption in SSC 4a, but this cannot explain the discrepancy in SSC 5a. A more likely possibility is that the relative molecular abundances we assume are not correct for these small, extreme regions. We adopt molecular abundances for $H^{13}CN$ and CS with respect to H_2 of $[H^{13}CN]/[H_2] = (1.2 \pm 0.2) \times 10^{-10}$ and $[CS]/[H_2] = (5.0 \pm 0.6) \times 10^{-9}$ from a study of the the center of NGC 253 at 14–19″ ($\sim 240 - 320$ pc) resolution by Martín et al. (2006), where the brackets refer to the abundance of that species. Adopting these abundances on the parsec scales of our clusters, however, is highly uncertain. Observations of envelopes around high-mass young stellar objects in the Milky Way, for example, reveal order-of-magnitude variations in the abundances of molecules, especially nitrogen and sulfur bearing species (van Dishoeck & Blake, 1998, and references therein). The impact of the uncertainty on the fractional molecular abundances is that they translate into order-of-magnitude accuracy for the H_2 column density measurements, as well as the subsequent calculations which depend on the column density, as reported in Table 4.2. In the following subsection we discuss in more detail what we know about chemical abundances and their variation: our conclusion is that the masses derived from $H^{13}CN$ $4-3$ are likely more accurate.

4.3.1.1 Fractional Abundance Variations

To resolve the discrepancies between our abundance-dependent measurements ($N_{H_2,out}$, $M_{H_2,out}$, $\dot{M}_{H_2,out}$, and $t_{remove-gas}$) from CS $7-6$ and $H^{13}CN$ $4-3$ would require that either $[CS]/[H_2]$ is enhanced and/or $[H^{13}CN]/[H_2]$ is reduced in these clusters compared to the values measured by Martín et al. (2006). In the case of CS, modeling by Charnley (1997) shows that $[CS]/[H_2]$ varies from $\sim 10^{-10} - 10^{-8}$ depending on age, O_2 abundance, and temperature, with CS being most abundant after $\sim 10^4$ years, at low O_2 abundance, and at low temperatures (T$\sim$100 K) though the trend with temperature is not monotonic. Estimates of the kinetic temperatures of the (marginally resolved) clusters vary from $\sim 200 - 300$ K (Rico-Villas et al., 2020). At $\sim 10^5$ years (the ZAMS ages of these clusters; Rico-Villas et al. 2020) and a temperature of 300 K, Charnley (1997) find $[CS]/[H_2] \sim 4 \times 10^{-9}$ depending on the assumed temperature and O_2 abundance, very close to our assumed ratio of $(5.0 \pm 0.6) \times 10^{-9}$ measured by Martín et al. (2006). From CS, SO, and SO_2 line ratios towards these clusters, Krieger et al. (2020b) suggest that $[CS]/[H_2]$ may be enhanced by a factor of 2−3 from the values measured by Martín et al. (2006). For SSCs 5a and 14, an enhancement of $[CS]/[H_2]$ by a factor of 2−3 brings our abundance-dependent measurements into much better agreement with those derived from $H^{13}CN$ $4-3$, but this is not sufficient for SSC 4a. The gas in SSC 4a is likely more optically thick than in SSCs 5a and 14, as seen in the absorption to lower temperatures ($\sim$ 7 K), which could help explain the lingering discrepancy in this cluster.

In the case of $[H^{13}CN]/[H_2]$, Colzi et al. (2018) find that chemical evolution does not affect nitrogen fractionation, so the main driver of a different $[H^{13}CN]/[H_2]$ in these SSCs would be due to changes in the $^{12}C/^{13}C$ ratio. If there is less ^{13}C in these clusters compared to the environment, then $[H^{13}CN]/[H_2]$ may be lower. Towards these clusters, Krieger et al. (2020b) find hints that $^{12}C/^{13}C$ may be on the high side of the assumed ratio of 40 ± 20 (Martín et al., 2010, 2019; Henkel et al., 2014; Tang et al., 2019). If the the ^{12}C abundance remains the same, this suggests that reductions in ^{13}C and hence $[H^{13}CN]/[H_2]$ are possible. To bring our abundance-dependent measurements from $H^{13}CN$ $4-3$ into agreement with the lower values derived from CS $7-6$ would imply $^{12}C/^{13}C \gtrsim 300$, much larger than even the highest ratios measured in NGC 253 (Martín et al., 2010) while keeping ^{12}C fixed. Changing $[H^{13}CN]/[H_2]$, therefore, likely plays a minor role in remedying the differences in our abundance-dependant quantities.

If, therefore, the discrepancy between our abundance-dependent quantities measured from CS $7-6$ and $H^{13}CN$ $4-3$ is due to a change in the abundances of those species, the effect is likely driven by CS which is enhanced relative to our assumed $[CS]/[H_2]$ with perhaps a small contribution from reduced $[H^{13}CN]/[H_2]$. As a result, the abundance-dependant quantities derived from $H^{13}CN$ $4-3$ are likely more accurate. In the values presented here and in the following section, we adopt the abundances measured by Martín et al. (2006) and maintain the conservative order-of-magnitude uncertainties on these quantities.

4.3.2 Outflow Properties from Line Profile Modeling

The short gas crossing times, large outflow masses, and outflow mass rates (Table 4.2) suggest the outflow activity in these objects cannot be sustained for a long time. From this standpoint, it is reasonable that we detect outflows in $\lesssim$10% of the SSCs, so it is possible that we are indeed catching a small fraction of the SSCs in this short-lived phase. The analysis in Section 4.3.1, however, implicitly assumes that the outflows are spherical. Another possibility, however, is that the outflows are biconical with a more-or-less narrow opening angle. In that case the outflows from the three clusters we identify are serendipitously pointed close enough to the line of sight to make them detectable. If the observed outflows are not spherical, geometric correction factors will need to be applied to the measured quantities in Table 4.2, and more outflows could exist that we do not detect because their geometry is unfavorable.

In order to determine whether the observed outflows are spherical or biconical and how they are oriented with respect to the line of sight, we build a simple radiative transfer model to model the spectrum through the outflow[†]. We consider spherical and biconical outflows, where the opening angle (θ) and orientation to the line of sight (Ψ) of the biconical outflows can be varied. Opening angles are defined as the full-angle for one hemisphere; the maximum opening angle is $\theta = 180°$, corresponding to a sphere. Technical details and equations are presented in Appendix C.2, but we summarize the basic scheme here. We construct a four-

[†]The code and best-fit input parameter files are available at `https://github.com/rclevy/ModelSSCOutflows`.

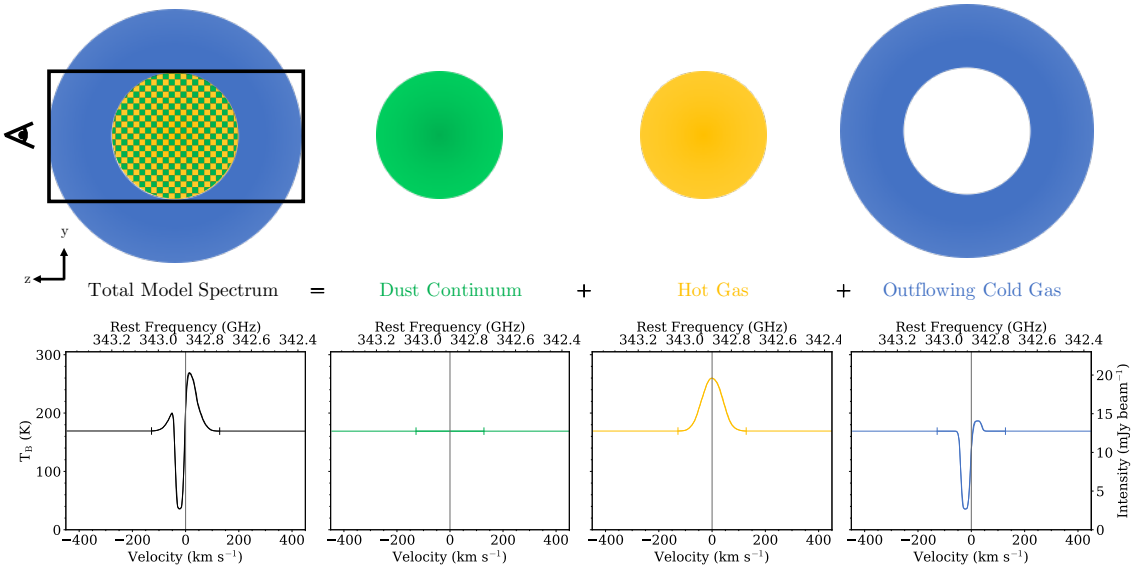

Figure 4.7: A 2D schematic showing the three physical components of the model at a slice through the box at $x = 0$ and their spectral contributions. The black rectangle shows the slice of the field of view used to calculate the final spectrum. A representative spectrum for each component is shown below the corresponding 2D schematic. CS $7-6$ towards SSC 14 is used here as an example. The thicker curves bounded by the vertical line segments show the velocity range modeled, whereas the thin curves outside are an extrapolation. The hot gas and cold outflowing gas spectra include the dust continuum component so that the absorption due to the outflowing components is visible.

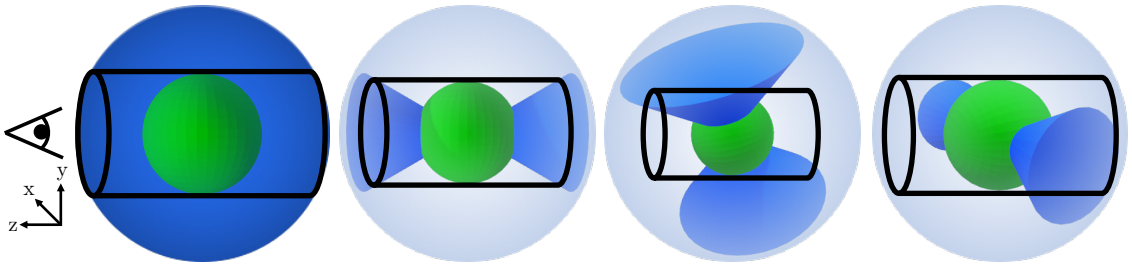

Figure 4.8: 3D schematics of (from left to right) a spherical ($\theta = 180°$) outflow, a biconical ($\theta = 60°$) outflow pointed along the line of sight, and biconical ($\theta = 90°$ and $\theta = 45°$) outflows that are inclined to the line of sight ($\Psi = 95°$ and $\Psi = 60°$). The green central sphere includes both the dust continuum and hot gas components and has $r = r_{\rm SSC}$. The dark blue outer shell or cones show the outflowing gas. The light blue component shows the ambient gas between the outflow cones. The black cylinder shows the line of sight and field of view over which the model spectrum is integrated and averaged, which has $r = r_{\rm SSC}$ (in the xy-plane) and spans $4 \times r_{\rm SSC}$ along the z-axis.

		SSC 4a		SSC 5a		SSC 14	
Quantity	Unit	CS 7 – 6	$H^{13}CN$ 4 – 3	CS 7 – 6	$H^{13}CN$ 4 – 3	CS 7 – 6	$H^{13}CN$ 4 – 3
$V_{max-abs}$ *,a	km s^{-1}	7	7	25	22	25	28
$\Delta V_{out,FWHM}$ *,b	km s^{-1}	25	25	20	15	20	25
$V_{out,max}$ c	km s^{-1}	28	28	42	35	42	49
$\log_{10}(t_{cross})$ d	$\log_{10}$(yr)	4.9	4.9	4.5	4.6	4.4	4.3
$\Delta V_{hot,FWHM}$ *,b	km s^{-1}	10	10	50	50	80	85
T_{out} *,e	K	7	7	25	20	35	40
T_{hot} *,f	K	900	900	800	800	800	800
T_{cont} *,g	K	105	105	200	185	340	340
$\log_{10}(n_{out})$ *,h	$\log_{10}(cm^{-3})$	7.8	7.5	5.5	5.9	6.2	6.8
$\log_{10}(n_{hot})$ *,h	$\log_{10}(cm^{-3})$	8.6	9.9	8.8	9.8	8.8	10.0
$\log_{10}(\tau_{cont,max})$ *,i		-1.3	-1.3	-1.3	-1.3	-1.3	-1.3
$\log_{10}(N_{H_2,out})$ j	$\log_{10}(cm^{-2})$	25.4	25.1	23.2	23.7	24.0	24.5
$\log_{10}(M_{H_2,out})$ j	$\log_{10}(M_\odot)$	6.3	6.0	4.4	4.9	5.3	5.4
$\log_{10}(\dot{M}_{H_2,out})$ j	$\log_{10}(M_\odot\ yr^{-1})$	1.4	1.1	-0.1	0.3	0.9	1.1
$\log_{10}(t_{remove-gas})$ j	$\log_{10}$(yr)	3.7	4.0	5.4	5.0	4.8	4.6

The input and output or derived parameters for the best-fitting spherical outflow models. See Section 4.3.2 and Appendix C.2 for details. *Best-fit input parameters to the model. The uncertainties listed below are reflective of the grid of tested parameters. [a]The outflow velocity, which is assumed constant. Uncertainties are ±1 km s^{-1}. [b]The FWHM velocity dispersion of the given component. Uncertainties are ±2 km s^{-1}. [c]The maximum outflow velocity defined as $V_{max-abs} + 2\frac{\Delta V_{out,FWHM}}{2.355}$. Propagated uncertainties are ±2 km s^{-1}. [d]The gas crossing time defined as $\frac{r_{SSC}}{V_{max-abs}}$. Propagated uncertainties are 4% for SSCs 14 and 5 and 14% for SSC 4a. [e]The gas temperature in the outflow at the line peak, which is constant spatially. Uncertainties are ±2 K. [f]The gas temperature in the hot component at the line peak, which is constant spatially. Uncertainties are ±25 K. [g]The continuum temperature, which is constant spatially and spectrally. Uncertainties are ±5 K. [h]The log of the peak H_2 number density for the given component. Uncertainties are ±0.25 dex. [i]The peak optical depth of the continuum component. Uncertainties are ±0.025. [j]Uncertainties are ±1 dex due to the molecular abundance ratios relative to H_2.

Table 4.3: Line Profile Modeling Input Parameters and Calculated Values

dimensional box (x, y, z, ν), where radii are measured in spherical coordinates from the center of the box. We define the measured cluster radius such that $r_{SSC} = r_{half-flux}$ (Table 4.1). The simulated box is scaled to $4\times r_{SSC}$ in each spatial dimension (x, y, z) to fully encompass the line emission (e.g. Figure 4.4) especially since the geometry along the line of sight (z-axis) is unknown. The velocity axis is scaled based on the input outflow velocity and velocity dispersion, so that the velocity resolution is optimized over the velocities relevant for the cluster and outflow; this is described more fully in Appendix C.2. Three physical components are required to adequately model the CS 7 – 6 and $H^{13}CN$ 4 – 3 spectra, as shown in Figures 4.7 and 4.8. These components and the input parameters for each are described below. The input parameters are denoted with * in Table 4.3, which lists input parameter values that yield the best model fits. Radial profiles of these components and the input parameters are summarized in Figure C.2 in Appendix C.2.

1. Dust continuum component: Shown in green in Figures 4.7 and 4.8, this component is a sphere with $r = r_{\rm SSC}$ and a constant (in space and frequency) temperature ($T_{\rm cont}$). The optical depth in a single cell is a maximum ($\tau_{\rm cont,max}$) at the center, then decreases like a Gaussian with FWHM $= 2 \times r_{\rm SSC}$. In other words, the FWHM of the dust continuum optical depth profile matches the diameter of the 350 GHz continuum source. The temperature and optical depth are set to zero for $r > r_{\rm SSC}$.

2. Hot gas: Shown in yellow in Figure 4.7 (and encompassed within the green sphere in Figure 4.8), this spherical component is required to reproduce the strong emission component of the P-Cygni profiles. This component is defined by an input hot gas temperature ($T_{\rm hot}$), a H_2 volume density ($n_{\rm hot}$) for the central ($r = 0$) pixel, and a velocity dispersion ($\Delta V_{\rm hot,FWHM}$). $T_{\rm hot}$ is constant (spatially) for $r \leq r_{\rm SSC}$, and is set to zero outside. The density falls off $\propto r^{-2}$ from the center and is set to zero for $r > r_{\rm SSC}$. The line is centered on zero velocity along the frequency axis, and the Gaussian linewidth is given by $\Delta V_{\rm hot,FWHM}$. Using the equations in Appendix C.2, this produces a spectrum at every pixel in the box.

3. Cold, outflowing gas: Shown in blue in Figures 4.7 and 4.8, this is the outflow component which produces the absorption features. This component is defined by an input gas temperature ($T_{\rm out}$), a H_2 volume density ($n_{\rm out}$) at the cluster boundary ($r = r_{\rm SSC}$), a constant outflow velocity ($V_{\rm out}$), a velocity dispersion ($\Delta V_{\rm out,FWHM}$), an opening angle (θ), and an orientation to the line of sight

(Ψ). The gas temperature is constant (spatially) within this component. The density is a maximum at $r = r_{\rm SSC}$ and decreases $\propto r^{-2}$ until the edges of the box; the density is set to zero inside the cluster ($r < r_{\rm SSC}$). In the spectral dimension, the line has a centroid velocity given by $V_{\rm out}$ and a FWHM linewidth of $\Delta V_{\rm out,FWHM}$. Using the equations in Appendix C.2, this produces a spectrum at every pixel in the box. Since the outflow velocity is constant and the density $\propto r^{-2}$, the outflow conserves mass, energy, and momentum. To create a biconical outflow with the input opening angle (θ), the velocity of the pixels outside the outflow cones is set to zero. This creates an ambient gas component (shown in light blue in Figure 4.8), which has the same temperature, density, and velocity dispersion properties as the outflowing gas (but with $V_{\rm out} = 0$). The box is then rotated to the input orientation from the line of sight (Ψ).

Together, these three components are integrated from the back of the box forward (e.g. along the $-z$-axis in Figures 4.7 and 4.8). To obtain the final spectrum, only pixels within a cylinder along the line of sight with $r = r_{\rm SSC}$ are integrated (shown as the black cylinder in Figure 4.8) to best compare with the measured spectra which are extracted only over an area corresponding to the continuum source half-flux radius. We adjust the input parameters component-by-component to find the model spectrum that best matches the observed CS $7-6$ and $H^{13}CN$ $4-3$ spectra for SSCs 4a, 5a, and 14. There are degeneracies among input parameters, which are described below and in Appendix C.2. These best-fit models are shown

in red in Figure 4.6, and the best-fit parameters for CS $7-6$ and $H^{13}CN$ $4-3$ are listed in Table 4.3. For all spectra and sources, the spherical model provides the best fit, implying that the opening angles of the outflows need to be broad to explain the observed line profiles. A wide opening angle is in agreement with recent magneto-hydrodynamic (MHD) simulations, which show that cluster outflows are asymmetric and chaotic, but still wide-angle in general and regardless of the precise feedback mechanism (e.g., Skinner & Ostriker, 2015; Kim et al., 2018; He et al., 2019; Geen et al., 2021; Lancaster et al., 2021a,b). From these best fit models, we also calculate the H_2 column density and mass in the outflows, which are also listed in Table 4.3.

We tested models with a fourth physical component representing a fast outflowing component. This was mainly motivated by SSC 14 and the mismatch between the spectrum and model at the blue-ward edge of the absorption feature for both CS $7-6$ and $H^{13}CN$ $4-3$ (Figure 4.6). In the model, this component is otherwise identical to the "slow" outflow component described above but with a larger outflow velocity and velocity dispersion and a different maximum H_2 volume. While including this component did marginally improve the fits — especially for SSC 14 — the improvement was not enough to justify the additional three parameters introduced into the model.

Our model assumes a constant outflow velocity and r^{-2} density profile to conserve mass, energy, and momentum in the outflow. In reality, a constant outflow velocity is unlikely to be precisely the case, due to turbulence within the outflow itself (e.g., Raskutti et al., 2017) and because the outflow may decelerate as it

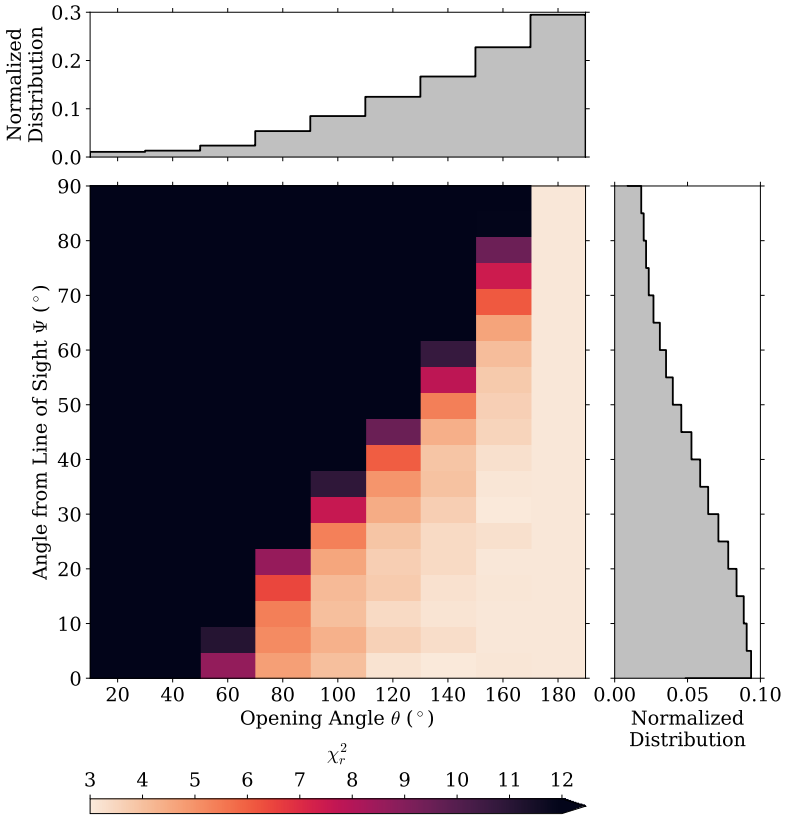

Figure 4.9: A heatmap showing the reduced chi-squared (χ^2_r) values for models with varying opening angles (θ) and orientations from the line of sight (Ψ) for the same input parameters as listed in Table 4.3 for CS $7-6$ in SSC 14. The gray histograms show the marginalized distributions for θ (top) and Ψ (right), normalized to unit area. This shows that the outflow opening angles must be wide and/or closely aligned with the line of sight.

encounters the surrounding medium. From the data, we investigate the location of the absorption trough around and across the sources. We see no strong evidence for systematic velocity shifts around or across SSCs 4a, 5a, or 14.

There are ranges of opening angles (θ) and orientations (Ψ) which are degenerate and will produce similar output spectra. To investigate how well we can constrain θ and Ψ, we run a grid of models with the same input parameters as in Table 4.2 with varying θ in steps of 20° and Ψ in steps of 5°. The results for CS $7-6$ in SSC 14 are displayed in Figure 4.9, which shows that wide outflows and/or

those pointed close to the line of sight are strongly favored. Wide angle outflows from clusters are in agreement with results of numerical simulations as mentioned previously. Though the outflows in simulations are clumpy and highly non-uniform, they cover nearly 4π steradians and hence approach the spherical limit of our simple modeling. Narrow and/or off-axis opening angles substantially increase the required input density in s our models and result in unphysical solutions for the outflowing mass. In any case, we cannot pin down the precise opening angle and/or line of sight orientation from this modeling, but we place limits on them that suggest the dearth of clusters with observed outflows is not a selection bias due to geometrical effects. It is possible that we miss outflows if the dense gas is very optically thick and therefore obscures underlying outflow signatures (e.g., Aalto et al., 2019). We could also miss weak outflows below our detection limit of sensitivity and cluster mass.

4.3.3 Comparing the Two Methods

The two methods of measuring the outflow properties described have calculated quantities in common. In Figure 4.10, we compare the velocity where the absorption is maximum ($V_{max-abs}$), the FWHM of the absorption feature ($\Delta V_{out,FWHM}$), the maximum outflow velocity ($V_{out,max}$), the gas crossing time (t_{cross}), the H_2 column density in the outflow ($N_{H_2,out}$), the H_2 mass in the outflow ($M_{H_2,out}$), the mass outflow rate ($\dot{M}_{H_2,out}$), and the time to remove all of the gas mass of the cluster at the current $\dot{M}_{H_2,out}$ ($t_{remove-gas}$). The equations used to calculate these parameters

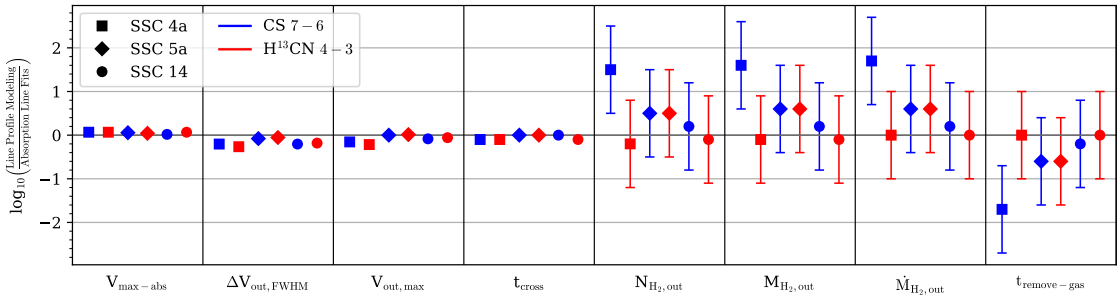

Figure 4.10: A comparison of common quantities measured from the absorption line fits (Section 4.3.1) and the line profile modeling (Section 4.3.2). Each bin (separated by black vertical lines) shows one quantity listed in Tables 4.2 and 4.3. Within the bins, points are artificially offset along the horizontal axis for clarity. The different symbols show the three SSCs and the colors show quantities derived from the two spectral lines, as defined in the legend. The vertical axis shows the logarithm of the ratio of the quantities from each method, such that each major tick mark corresponds to an order of magnitude. The error bars for the first four quantities are negligible; the errorbars on the last four quantities reflect the order-of-magnitude uncertainty on the abundance ratio of the molecule with respect to H_2.

are given in Appendices C.1 and C.2 for the absorption line fits and line profile modeling respectively. The vertical axis of Figure 4.10 shows the logarithm of the ratio of the quantities derived from each method; each major tick mark and horizontal gridline corresponds to an order of magnitude difference. In general, there is good agreement between the two methods for the quantities which depend on the velocity of the outflow s ($V_{max-abs}$, $\Delta V_{out,FWHM}$, $V_{out,max}$, and t_{cross}). The uncertainties in Figure 4.10 reflect the order-of-magnitude adopted uncertainties around the abundance ratios, as discussed in Section 4.3.1.

Given the uncertainties the agreement between the absorption line fits and the line profile modeling is good, especially for $H^{13}CN$ $4-3$. A notable exception is for CS $7-6$ in SSC 4a, where the line profile modeling yields 1.5 dex larger H_2 columns and masses than derived from the absorption line fits. This is likely because the CS $7-6$ absorption in SSC 4a is the most saturated (i.e., the closest

to zero). For the absorption line fits, this renders a more uncertain optical depth (from the absorption to continuum ratio) as small changes in the absorption depth leads to large changes in the optical depth and hence the column density. For the line profile modeling, the depth of the absorption depends on the assumed gas temperature and H_2 volume density in the outflow. The bottom of the absorption trough sets an upper limit on the assumed gas temperature in the outflow (T_{out}); in the modeling, the temperature of the absorption trough cannot be lower than the assumed T_{out}. In the case of SSC 4a, this temperature is low ($\sim$ 7 K), well below the temperature needed to excite the $J = 7$ level of CS of 66 K (Schöier et al., 2005)[‡]. As a result, the H_2 density in the outflow must be increased, leading to a large outflowing mass. We assume a constant temperature in the outflowing gas, whereas a temperature gradient is likely needed to produce this absorption depth. Because the other sources and lines have shallower absorption depths, they do not suffer from this effect. Other strong lines—HCN $4-3$ and HCO^+ $4-3$—shown in Figure 4.3 also suffer from this saturation, which is why they are not the focus of this analysis. We, therefore, suggest that the column density, mass, and mass outflow rate from the modeling are overestimated in the case of CS $7-6$ in SSC 4a. This effect is not seen in the absorption line fitting because the absorption to continuum ratio is used to infer the optical depth, but an excitation temperature of 130 K is assumed to derive the level populations (Appendix C.1). In the line profile modeling, the input gas temperature (7 K in the case of CS $7-6$ in SSC 4a) is used

[‡]This information was retrieved from the Leiden Atomic and Molecular Database (LAMDA) on 2020-10-30.

to derive the level populations instead (Appendix C.2). Discrepancies between the two methods are also seen in both lines towards SSC 5a, though they are not as extreme as for SSC 4a. The discrepancies in SSC 5a cannot, however, be explained by saturation. The same abundance ratios are used for both methods and these enter into the calculations in the same way, so this discrepancy cannot be remedied by changing [CS]/[H_2].

4.3.4 Recommended Values

Given the number of assumptions of the line profile modeling and the parameter covariances, we suggest that the outflow properties from the absorption line fits presented in Table 4.2 are more reliable and should be adopted. The assumption of spherical outflows in computing those numbers is substantiated by the modeling, which strongly favors wide outflows (Figure 4.9). It is encouraging that the line profile modeling generally finds similar values for the outflowing mass, but there are cases where the model likely overestimates the outflowing mass (e.g., SSC 4a). Both sets of measurements are limited in the same way by the uncertainty on the molecular abundances with respect the H_2. As discussed in Section 4.3.1.1, discrepancies between quantities derived from CS $7-6$ and $H^{13}CN$ $4-3$ may be driven primarily by changes in [CS]/[H_2] relative to the assumed abundance, so that quantities derived from $H^{13}CN$ $4-3$ may be more reliable. Studies, such as the ALMA Comprehensive High-Resolution Extragalactic Molecular Inventory (ALCHEMI)[§], that measure abundances at higher spatial resolution than currently available in

[§]`https://alchemi.nrao.edu`

these extreme environments may improve the accuracy of our column density, mass, mass outflow rate, and gas removal timescale estimates.

4.4 Discussion

The existence of outflows in SSCs 4a, 5a, and 14 suggests these clusters may be in a different evolutionary stage compared to the other SSCs in the starburst. In the following section, we investigate the relationship between various timescales relevant to the clusters (4.4.1) and possible outflow mechanisms (4.4.2). We also investigate SSC 5a in more detail, as it is the only cluster visible in the NIR and shows evidence for a shell of dense gas surrounding it (4.4.3).

4.4.1 Timescales, Ages, and Evolutionary Stages

There are several timescales and ages calculated from this and previous analyses for these clusters, which we summarize here and list in Table 4.4:

4.4.1.1 ZAMS Age ($t_{ZAMS-age}$)

Rico-Villas et al. (2020) uses the ratio of the luminosity in protostars to that of ionizing zero-age main sequence (ZAMS) stars to estimate the ages of the clusters ($t_{ZAMS-age}$), finding that SSC 4a is $\sim 10^{4.95}$ yrs old, SSC 5a is $\gtrsim 10^{5}$ yrs old, and SSC 14 is $\sim 10^{4.88}$ yrs old (Table 4.4). These measurements are based on the same 36 GHz emission used by Leroy et al. (2018) to calculate the stellar masses. The stellar masses and ages associated with the ionizing photon rates derived from the ZAMS

SSC Number	$\log_{10}(t_{ZAMS-age})$ [a]	$\log_{10}(t_{ff})$ [b]	$t_{ZAMS-age}/t_{ff}$	$\log_{10}(t_{cross})$ [c]	$\log_{10}(t_{remove-gas})$ [d]	$\log_{10}(t_{dep})$ [e]
4a	4.95	4.9	1.1	5.0	4.3±0.7	6.6
5a	$\gtrsim 5$	4.7	$\gtrsim$2.0	4.6	5.5±0.4	6.4
14	4.88	4.5	2.4	4.4	4.9±0.4	6.8

For details, see the discussion in Section 4.4.1. [a]The age of the cluster since the zero-age main sequence ($t_{ZAMS-age}$) calculated by the ratio of the luminosity in proto-stars to that in ZAMS stars from Rico-Villas et al. (2020). [b]The free-fall time (t_{ff}) calculated by Leroy et al. (2018). For SSC 4a, the value for SSC 4 is used because SSC 4a is the dominant component of the SSC 4 complex. The uncertainty introduced by this assumption is likely minor compared to other uncertainties which are $\sim 0.4 - 0.5$ dex (c.f. Table 2 of Leroy et al., 2018). [c]The time for gas to travel from the center of the cluster to the radius of the continuum source (r_{SSC}) at the typical outflow velocity ($V_{max-abs}$). This timescale (t_{cross}) is a proxy for the age of the outflow. For each SSC, this is the average of the values in Table 4.2 and 4.3. [d]The time for the entire gas mass of the cluster (from Leroy et al., 2018) to be depleted at the current $\dot{M}_{H_2,outflow}$. For each SSC, this is the average of the values in Table 4.2 and 4.3. Uncertainties reported in the table are the standard deviations of the mean values from Table 4.2 and the values in Table 4.3. Propagated systematic uncertainties (due to the uncertainty in the molecular abundances) are 0.4 dex. [e]The gas depletion timescale, defined as $t_{dep} \equiv \frac{M_{H_2,tot}}{SFR_{36\ GHz}}$. For SSC 4a, the gas mass for SSC 4 is used because SSC 4a is the dominant component of the SSC 4 complex.

Table 4.4: A comparison of relevant cluster timescales and ages

assumption may be underestimated if the cluster stellar population has evolved beyond the ZAMS stage, or if some fraction of the ionizing photons are absorbed by dust. These three SSCs have negligable synchrontron components of their SEDs, so synchrotron contamination of the 36 GHz emission is a small effect. These ages are, therefore, likely lower limits on the true "age" of the cluster.

4.4.1.2 Cluster Formation Timescales

Given the $t_{ZAMS-age}$ and free-fall times (t_{ff}) calculated by Leroy et al. (2018), we can try to place the clusters in a relative evolutionary sequence. An important caveat is that Leroy et al. (2018) estimated t_{ff} based on the marginally resolved data. With these spatially resolved data, the radii of the clusters decreased (e.g., Figure 4.11), meaning that these values of t_{ff} may be overestimated. SSCs 4a, 5a, and 14 have $t_{ZAMS-age}/t_{ff} = 1.1$, $\gtrsim$2.0, and 2.4 respectively (Table 4.4). Modeling by Skinner & Ostriker (2015) suggests that gas is actively collapsing to form stars on timescales $\sim 1-2t_{ff}$, the typical timescale for cluster formation is $\sim 5t_{ff}$, and the gas is completely dispersed by $\sim 8t_{ff}$. These clusters should be nearing the end of the period of active gas collapse. SSC 5a may possibly be transitioning to the initial stages of gas dispersal, especially because it is the only cluster visible in the NIR (Section 4.4.3), though the gas dispersal has not yet finished because we still see evidence for an outflow. It is important to note, however, that these evolutionary stages are not clear-cut divisions, as gas accretion can continue while the cluster is forming and while outflows are present, and that the $t_{ZAMS-age}$ are likely lower

limits on the cluster ages. Moreover, the possibility that expelled gas is reaccreted onto the clusters may mean that this cluster formation sequence is more cyclic.

4.4.1.3 Crossing Time (t_{cross})

The crossing times (t_{cross}) we report in Tables 4.2 and 4.3 are short: $10^{4.5-5.2}$ years. Similarly short crossing times are also seen in a SSC candidate in the Large Magellanic Cloud ($\sim 10^{4.8}$ yr; Nayak et al., 2019) and in simulations (e.g., Lancaster et al., 2021a,b). At least one crossing-time has passed since the outflows turned on, as P-Cygni line profiles are detected out to $\gtrsim r_{SSC}$. If the outflows are present beyond r_{SSC}, they are increasingly difficult to detect in absorption away from the continuum source. Therefore, this timescale places a lower limit on the age of the outflow.

4.4.1.4 Gas Removal Time ($t_{remove-gas}$)

The gas removal times ($t_{remove-gas}$) are longer in general than the crossing or free-fall times, though the uncertainties on $t_{remove-gas}$ are large. The average $t_{remove-gas} \sim 10^{5.0\pm0.6}$ years, where the uncertainty is the standard deviation of the mean $t_{remove-gas}$ for each SSC and line. The gas removal times are $\gtrsim t_{ZAMS-age}$, except for SSC 4a. Assuming a constant mass outflow rate, this would imply that there is still gas in the clusters to be removed, though a constant mass outflow rate is unlikely (e.g. Kim et al., 2018). This timescale also assumes that none of the expelled gas is reaccreted later on. Given that the bulk of the gas has outflow

velocities below the escape velocity (Section 4.3.1), reaccretion of material is a likely scenario.

4.4.1.5 Gas Depletion Timescale (t_{dep})

This timescale is the duration of future star formation, assuming a constant SFR for each cluster and no mass loss: $t_{dep} \equiv M_{H_2,tot}/SFR$ where $M_{H_2,tot}$ is from Leroy et al. (2018). The SFRs we use are also from Leroy et al. (2018) and are based on the measured 36 GHz fluxes which trace the free-free emission from each cluster (Gorski et al., 2017, 2019). This estimate of t_{dep} based on the SFR assumes continuous star formation (over $\sim$ 10 Myr; Murphy et al. 2011), whereas we would expect the actual star formation in these clusters to be bursty. These are the longest timescales for each cluster listed in Table 4.4. s Compared to the clusters' $t_{ZAMS-age}$, this may suggest that the clusters are early in their star formation process and that there is plenty of fuel to form new stars and for the clusters to continue grow. This assumes, however, that all of the molecular gas remains in the cluster. The current gas removal times of the outflows ($t_{remove-gas}$) are much shorter than t_{dep}, indicating that these outflows will substantially affect the cluster's star formation efficiency (SFE). The possibility that gas is reaccreted by the cluster will affect the available gas reservoir for future star formation.

That we detect outflows only in three sources, or $\sim$8% of the three dozen SSCs in the center of NGC 253 (Figure 4.1), gives credence to the idea that this outflowing phase must be short-lived. It is unlikely that we miss many sources with outflows

due to their orientation and geometry because the modeling presented in Section 4.3.2 as well as simulations (e.g., Geen et al., 2021) suggest that the outflows are wide. We could, however, be missing outflows if the outer layers of dense gas are very optically thick, which could obscure the outflows (e.g., Aalto et al., 2019) or if there are weak outflows below our sensitivity or cluster mass detection limits. Given that it is expected that the SSCs begin disrupting their natal clouds after $\sim 10^{5-6}$ years (Johnson et al., 2015) and taking $t_{cross} = 10^{4.5}$ years as the lower limit on the age of the outflow, we would expect to find outflows in at least $3 - 30\%$ of SSCs, which agrees well with our detection rate of 8%. This percentile range is a lower limit because t_{cross} is the minimum possible age of the outflow and there could be additional outflows below our detection limit, though they would be weak. This also assumes that the clusters formed at the same time, which is also unlikely.

In general the chemistry-based age sequences presented by Krieger et al. (2020b) lead to different relative cluster ages than the dynamical progression presented here, which are also different from the ZAMS age sequence of Rico-Villas et al. (2020). It is important to keep in mind, however, that the oldest clusters are not necessarily the most evolved, and vice versa. Using HCN/HC_3N as a relative age tracer, Krieger et al. (2020b) suggest that SSCs 4 and 14 are in the younger half of the SSCs studied while SSC 5 is among the oldest. An age sequence using the chemistry of sulfur bearing molecules suggests instead that SSCs 5 and 14 are younger whereas SSC 4 is older (Krieger et al., 2020b). This is in disagreement with the age progression suggested by Rico-Villas et al. (2020), who suggest an inside out formation with SSCs 4−12 being the oldest and SSCs 1−3, 13, and 14 being the youngest. The

detections of outflows towards SSCs 4a, 5a, and 14 would suggest that they are the most evolved clusters in the young burst, in the simplest model where the clusters completely and finally clear their gas at the end of their formation periods. As described in the following section, SSC 5a may be among the most evolved clusters, as it is the only one of these clusters visible in the NIR. Krieger et al. (2020b) also find the lowest dense gas ratios in SSC 5a, suggesting that it has expelled and/or heated and dissociated much of its natal molecular gas. Given the gas-rich environment surrounding these clusters, however, it is possible that other clusters are older and more evolved, but have reaccreted gas from the surrounding medium or that was not completely expelled. Given that the mean velocities of the outflows in SSCs 4a, 5a, and 14 are less than the escape velocities, this is perhaps a likely scenario.

4.4.2 Outflow Mechanics

There are a handful of feedback mechanisms relevant for setting the SFE of star clusters. These include proto-stellar outflows, supernovae, photoionization, UV (direct) radiation pressure, dust-reprocessed (indirect) radiation pressure, and stellar winds. Each of these processes is efficient in driving outflows for different cluster masses, radii, and ages. One way to visualize this is through a mass-radius diagram (e.g., Fall et al., 2010; Krumholz et al., 2019), as shown in Figure 4.11. There is a locus where none of the feedback mechanisms considered by Krumholz et al. (2019) are efficient, and so clusters with those masses and radii should grow with high SFEs. An important caveat of this figure is that there are other parameters relevant

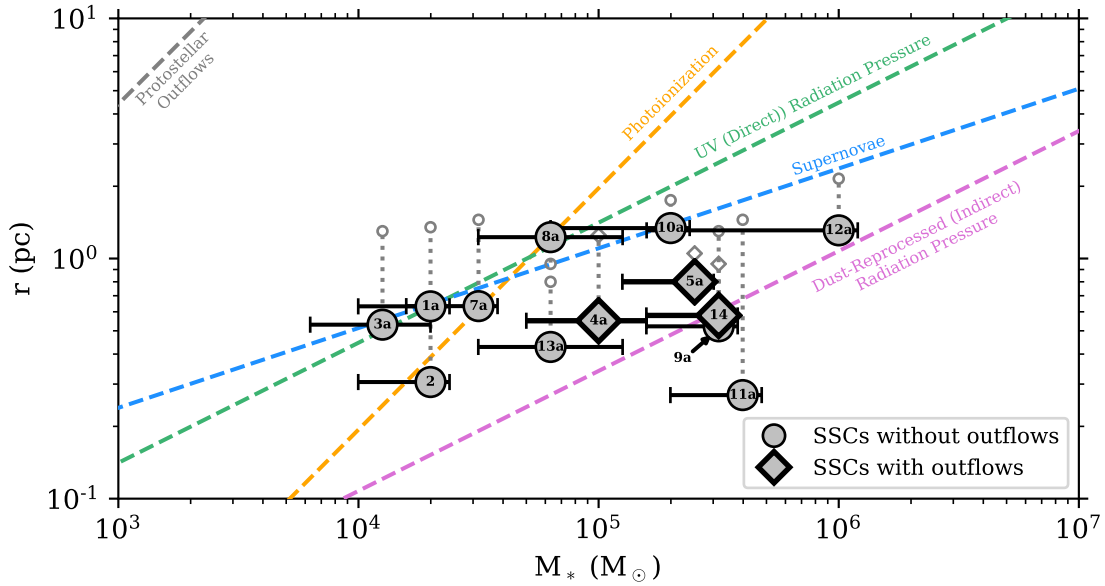

Figure 4.11: The cluster mass-radius diagram, adapted from Figure 12 of Krumholz et al. (2019). The colored shaded regions bounded by dashed lines show the regions of this parameter space where the corresponding feedback mechanism is efficient. There is a locus where none of these feedback mechanisms are expected to be efficient, resulting in high star formation efficiencies. The circles show the primary SSCs in NGC 253 without evidence for outflows, and the diamonds show those with outflows. The cluster stellar masses (M_*) are from Leroy et al. (2018). The error bars include differences with measurements from RRLs (Mills et al., 2021), systematics due to assumptions about the Gaunt factor, and conservative estimates of the effects of the clusters resolving into multiple smaller clusters. Not shown are unquantified uncertainties related to absorption of ionizing photons by dust and evolution beyond the ZAMS, both of which would result in higher values of M_* than reported. See Section 4.2.6 for details on the calculation of the error bars. The radii are our measured 350 GHz half-flux radii (Table 4.1), which are smaller than the radii previously measured by Leroy et al. (2018) (gray open symbols in the same style as in the legend) due to the increase in the spatial resolution of these observations. The change in radius is shown by the vertical gray dotted lines connecting the symbols. Notably, the SSCs with outflows lie within or near the locus where feedback is expected to be inefficient.

to whether a feedback mechanism is efficient, such as the momentum carried by each mechanism and the timescales over which it operates, which are not shown in this representation.

We show in Figure 4.11 the primary SSCs in NGC 253, where SSCs without outflows are shown as circles and those with outflows are shown as diamonds. The radii are our measured half-flux radii listed in Table 4.1. Because of the factor of 4 improvement in the linear spatial resolution with respect to the observations reported by Leroy et al. (2018), the radii of these clusters are smaller than reported by Leroy et al. (2018). As a result, the clusters are systematically shifted down in Figure 4.11 as shown by the vertical dotted gray lines. The stellar masses are taken from Leroy et al. (2018), as described in Section 4.2.6. We note, in particular, that the reported stellar masses may be underestimated (beyond the error bars) due to uncertainties about dust absorption and evolution beyond the ZAMS.

Many of the SSCs in NGC 253 fall inside the white area of inefficient feedback in Figure 4.11, which suggests that none of those mechanisms may be efficient for these clusters. The detection of outflows in SSCs 4a, 5a, and 14, however, means there is direct evidence of strong feedback. The H_2 masses in the outflows are significant compared to the total mass in the cluster itself (Table 4.2). From the previous section (and quantified in Table 4.4), the gas removal times ($t_{remove-gas}$) based on the current mass outflow rates are much shorter than the timescale for future star formation (t_{dep}). Comparison of these timescales implies that the outflows will remove the molecular gas faster than it would otherwise be used up by star formation. Note that these timescales assume either a constant mass outflow rate or a constant

star formation rate, respectively, neither of which is likely to be the case in reality. Moreover, $t_{remove-gas}$ assumes there is no new infall replenishing the reservoir, and t_{dep} assumes no molecular gas is removed. Nevertheless, the outflows will have a non-negligible effect on the reservoir of gas available to the cluster to form stars and hence on the cluster's SFE.

What mechanism, then, is powering these outflows, given that SSCs 4a and 5a lie in the locus where no mechanism is expected to be efficient and SSC 14 is near a boundary? We explore four plausible mechanisms shown in Figure 4.11 below (excluding proto-stellar outflows which are only important for much lower mass clusters; e.g., Guszejnov et al., 2021). We also consider winds from high mass stars which may be important for clusters of these masses and ages (e.g., Gilbert & Graham, 2007; Agertz et al., 2013; Geen et al., 2015; Lancaster et al., 2021a,b). In addition to their location in the mass-radius diagram (a re-framing of their surface densities), we also compare the momentum expected to be carried by each of these processes and the timescales over which they operate to the values estimated for these clusters. It is also possible that a synergistic combination of mechanisms is at work (e.g., Rahner et al., 2017, 2019). These potential scenarios are discussed in the reminder of this section.

4.4.2.1 Supernovae

These clusters are young ($\sim 10^5$ years; Rico-Villas et al., 2020), and so it is not expected that many, if any, supernovae have exploded since it typically takes $\sim$3

Myr before the first supernova explosion s (e.g., Zapartas et al., 2017). Moreover, the expected cloud lifetimes in a dense starburst like NGC 253 are expected to be shorter than 3 Myr (e.g., Murray et al., 2010), meaning that clouds would be disrupted before supernova feedback would be important. The gas removal times estimated for these outflows are $\ll$ 3 Myr in all cases (Table 4.4), supporting the idea that the clusters are too young for supernovae. Even with the large uncertainties, the radial momentum we measure in their outflows (Table 4.2) is an order of magnitude or more lower than expected for supernova-driven outflows ($1000 - 3000$ km s^{-1}; e.g. Kim & Ostriker, 2015; Kim et al., 2017a). Finally, Mills et al. (2021) construct millimeter spectral energy distributions of these SSCs at 5 pc resolution and find that all three of these sources have negligible synchrotron components, further ruling out supernovae as the mechanism driving the cluster outflows.

4.4.2.2 Photoionization

Photoionization can remove a substantial amount of gas from a cluster, depending primarily on the density of the cluster (e.g., Kim et al., 2018; He et al., 2019; Geen et al., 2021, 2020; Dinnbier & Walch, 2020). He et al. (2019) study the effects of photoionization on massive star clusters, finding that photoionization is most efficient at suppressing star formation in lower density clusters. Similarly, Dinnbier & Walch (2020) find that photoionization (and winds) are inefficient at clearing the natal gas from clusters with masses $> 5 \times 10^3$ M$_\odot$, unless they form with a high SFE. Though simulating different size and mass scales, Dinnbier &

Walch (2020) and Geen et al. (2020, 2021) find that feedback by photoionization is most important at the outer layers of the cloud or HII region. Kim et al. (2018) find that the momentum carried by a photoionization-driven outflow decreases with increasing cluster surface density. Assuming that the dense gas we measure follows the trends for the neutral gas simulated by Kim et al. (2018) and that the trends continue to these higher surface densities, the radial momentum per unit mass from photoionization should be very small ($p_r/M_* \lesssim 1$ km s^{-1}) for the molecular gas surface densities of SSCs 4a, 5a, and 14 of $\Sigma_{H_2} \sim 10^{4.2-4.9}$ M$_\odot$ pc^{-2} (Leroy et al., 2018). Using the stellar masses and radii, we can calculate the estimated ionized gas masses and momentum (using Equations 3, 4, and 11 of Leroy et al., 2018) and assuming $V_{ion} = 15$ km s^{-1} (as below), finding the $p_{ion}/M_* \approx 0.13,\ 0.15,$ and 0.08 km s^{-1} for SSCs 4a, 5a, and 14. We note that the ionizing photon rates estimated by Leroy et al. (2018) for these sources are consistent with a new analysis by Mills et al. (2021). These estimated momenta based on the ionizing photons are much smaller than the measured values of $p_r/M_* \approx\ 5-126,\ 1-3,$ and $5-40$ km s^{-1} (Table 4.2).

Krumholz et al. (2019) parameterize the effect of photoionizaion in terms of the ionized gas sound speed ($c_{s,ion}$) and the cluster escape velocity (V_{esc}), such that photoionization will be efficient when $c_{s,ion} > V_{esc}$. It is thought that the photoionization will be efficient for clusters with $V_{esc} \approx c_{s,ion} \leq 10$ km s^{-1}. Figure 4.11 and Krumholz et al. (2019) assume $V_{esc} \approx c_{s,ion} = 15$ km s^{-1}. The escape velocities of SSCs 4a, 5a, and 14 are approximately 23, 34, and 50 km s^{-1}, respectively. This suggests photoionization could be important for SSC 4a, but the escape velocities of SSCs 5a and 14 are likely too large for this mechanism to be efficient. This is in

agreement with the qualitative results of simulations discussed above.

Therefore, feedback from photoionization likely plays a minor role in driving these outflows as these clusters are dense and hence their escape velocities are too large for photoionization to efficiently drive outflows.

4.4.2.3 UV (Direct) Radiation Pressure

There are many studies that investigate the role of UV (direct) radiation pressure in driving outflows and expelling gas from a molecular cloud or HII region (e.g., Kim et al., 2016, 2017b, 2018, 2019; Raskutti et al., 2017; Crocker et al., 2018a,b; Barnes et al., 2020; Dinnbier & Walch, 2020). In general, many of these studies find that UV radiation pressure can play an important — if not dominant — role in expelling gas from a cluster, especially for low surface density clouds (e.g., Skinner & Ostriker, 2015; Raskutti et al., 2017). Using a numerical radiation hydrodynamic approach, Raskutti et al. (2017) study the effects of radiation pressure from non-ionizing UV photons on massive star forming clouds, finding that over a cloud's lifetime $\gtrsim 50\%$ of the UV photons escape through low-opacity channels induced by turbulence and hence do not contribute to radiation pressure-driven outflows. An important caveat is that the clouds simulated by Raskutti et al. (2017) are larger in size and so have lower densities than the clusters in NGC 253. Raskutti et al. (2017) find that the mean outflow velocity of their radiation-pressure driven outflows is $\sim 1.5 - 2.5$ V_{esc}, independent of cloud surface density. For the clusters in NGC 253, this translates to expected mean outflow velocities of $\sim 33 - 114$ km s^{-1},

faster than the observed mean velocities of $6-28$ km s^{-1}. The radial momentum per unit stellar mass (p_r/M_*) of SSCs 4a, 5a, and 14 are an order of magnitude or more less than measured by Raskutti et al. (2017) for clouds of roughly the same initial mass, though the clusters in NGC 253 are denser than the simulated clouds. In contrast, the clusters in NGC 253 have slightly larger radial momenta per unit outflowing mass (p_r/M_{out}). This means that the clusters in NGC 253 have less outflowing mass relative to their stellar masses than the simulated clusters, though this could also be due to the difference in cloud densities.

Simulations of feedback from photoionization and UV radiation pressure by Kim et al. (2018) find $t_{dep} \sim 2.5$ Myr for their densest clouds ($\Sigma_{neutral} = 10^3$ M$_\odot$ pc^{-2}). Our clusters, which have $\Sigma_{H_2} \sim 10^{4.4-5.3}$ M$_\odot$ pc^{-2} (Leroy et al., 2018), have $t_{dep}= 2.5-6.3$ Myr, whereas extrapolation of the Kim et al. (2018) calculations would result in lower values of t_{dep} if the trends continue to these higher densities. Kim et al. (2018) also find relatively constant outflow velocity of ~ 8 km s^{-1}, approximately independent of surface density in the neutral phase. This is similar to the mean outflow velocities of the dense gas traced by CS $7-6$ or H^{13}CN $4-3$ for SSC 4a ($\approx$7 km s^{-1}), but lower than those for SSCs 5a and 14 ($\approx$ 22 and 25 km s^{-1}, respectively). In terms of momentum, according to Equation 18 in Kim et al. (2018), an outflow driven by photoionization and UV radiation pressure would have a momentum per unit stellar mass of ~ 1 km s^{-1} at the surface densities observed in our clusters. This is about an order of magnitude lower than the p_r/M_* measured for dense gas traced by CS $7-6$ or H^{13}CN $4-3$ in these clusters (though our uncertainties are large). s An important caveat to this is that the clusters in

NGC 253 are denser than those simulated by Kim et al. (2018). Additionally, these simulations probe the neutral outflowing phase whereas our observations probe the outflowing dense molecular gas.

The efficiency of UV radiation pressure can be parameterized in terms of the surface mass density of the cluster (Σ) compared to the the outward force of radiation pressure. Skinner & Ostriker (2015) and Krumholz et al. (2019) define a critical surface density, $\Sigma_{\rm DR} = \frac{\Psi}{4\pi {\rm Gc}}$ where Ψ is the light-to-mass ratio, below which UV radiation pressure becomes important. A population of ZAMS stars that fully samples a Chabrier (2003) IMF has $\Psi \approx 1100$ L$_\odot$ M$_\odot{}^{-1}$ (e.g. Fall et al., 2010; Kim et al., 2016; Crocker et al., 2018a), resulting in $\Sigma_{\rm DR} \approx 340$ M$_\odot$ pc^{-2}. Models and simulations show that UV radiation is only effective for surface densities $\Sigma \lesssim 10\,\Sigma_{\rm DR}$ because turbulence will introduce low-column sight-lines that allow the radiation to escape (e.g. Thompson & Krumholz, 2016; Grudić et al., 2018; Krumholz et al., 2019). The value of $\Sigma_{\rm DR}$ depends principally and linearly on the assumed light-to-mass ratio and hence on the IMF. SSCs 4a, 5a, and 14 are all well below this boundary shown in green in Figure 4.11, meaning that a significantly top-heavy IMF resulting in a much higher value of Ψ is required for these outflows to be powered solely by UV radiation pressure. A top-heavy IMF has been suggested in other massive or super star clusters (e.g. Turner et al., 2017; Schneider et al., 2018). Turner et al. (2017) find a top-heavy IMF in a SSC in NGC 5253 with $\Psi \approx 2000$ L$_\odot$ M$_\odot^{-1}$. However, an unphysically large light-to-mass ratio $\sim 10,000$ L$_\odot$ M$_\odot^{-1}$ is needed for UV radiation to explain the feedback in SSCs 4a, 5a, and 14.

It is, therefore, unlikely that UV (direct) radiation pressure is the dominant

mechanism responsible for driving the outflows in SSCs 4a, 5a, and 14.

4.4.2.4 Dust-Reprocessed (Indirect) Radiation Pressure

Given the large dust columns in these SSCs, dust-reprocessed (indirect) radiation pressure is a promising mechanism to power the outflows. In a study of massive star clusters in the Milky Way's Central Molecular Zone, Barnes et al. (2020) find that indirect radiation pressure is important at early times (< 1 Myr). Similarly, Olivier et al. (2021) find that dust-reprocessed radiation pressure is the dominant feedback mechanism in ultra compact HII regions in the Milky Way. Moreover, given the possible underestimate of the stellar masses due to absorption of ionizing photons by dust or evolution beyond the ZAMS (which are not reflected in the error bars in Figure 4.11), indirect radiation pressure is a plausible mechanism to drive the observed outflows.

Whether the dust-reprocessed radiation pressure can drive an outflow fundamentally depends on the balance between the outward force of the radiation pressure and the inward force of gravity (i.e. the Eddington ratio, $f_{\rm Edd}$). This depends on the dust opacity and the input luminosity from the cluster, which can be parameterized by the light-to-mass ratio of the assumed IMF. The dust opacity (κ_d) quantifies a dust grain's ability to absorb infrared radiation. As explored by Semenov et al. (2003), this quantity varies with temperature, dust composition, grain shape, grain size distribution, and the opacity model. For example, grains in dense molecular clouds exhibit larger κ_d than those in the diffuse ISM, which is thought to be due

to the growth of mantles (e.g., Ossenkopf & Henning, 1994). Given the high density and intense radiation environment in these clusters, the dust opacity may be quite different than found in Galactic regions, though we have no precise observational constraints on how much κ_d can vary in these environments. Often times, a dust-to-gas ratio (DGR) is assumed to convert the dust opacity to the opacity in the gas, and the standard Solar Neighborhood value is DGR = 0.01. Finally, the light-to-mass ratio (Ψ) depends on the assumed IMF, where a top-heavy IMF will have a larger value of Ψ. Top-heavy IMFs have been claimed in massive clusters with $\Psi \sim 2000$ $L_\odot$ $M_\odot^{-1}$ (e.g., Turner et al., 2017; Schneider et al., 2018) compared to either a Kroupa (2001) or Chabrier (2003) IMF which have $\Psi = 883$ $L_\odot$ $M_\odot^{-1}$ and $\Psi = 1100$ $L_\odot$ $M_\odot^{-1}$ respectively. Models also find that the IMFs of globular cluster progenitors — thought to be SSCs — are more top-heavy with increasing density and decreasing metallicity (Marks et al., 2012). For clusters with the stellar masses and densities of those in NGC 253 (Leroy et al., 2018), we would expect a typical high-mass IMF slope. Towards constraining the nature of the IMF in these clusters, Mills et al. (2021) measure the fraction of ionized helium towards these SSCs using H and He radio recombination lines at 5 pc resolution. This ratio is expected to be somewhat dependent on the IMF, as a top-heavy IMF will result in more massive stars capable of ionizing He. Mills et al. (2021) measure mass-weighted He^+ fractions which are consistent with He^+ fractions found in HII regions in the center of the Milky Way (e.g., Mezger & Smith, 1976; de Pree et al., 1996; Lang et al., 1997) which is not thought to have a globally top-heavy IMF (e.g., Löckmann et al., 2010) though there are individual clusters which do seem to favor a top-heavy IMF (e.g.,

Lu et al., 2013). While the measured He^+ fractions do not completely rule out the possibility of a top-heavy IMF (it is unclear precisely how much the He^+ fraction changes with the IMF), it is unlikely that the IMF in these clusters is extremely top-heavy.

Below we describe two approaches taken by simulations in determining the efficiency of dust-reprocessed radiation pressure in driving outflows, and discuss how adjustments to the s fiducial assumptions on κ_d, DGR, and Ψ may help explain the outflows observed in SSCs 4a, 5a, and 14.

Numerical simulations of dust-reprocessed radiation pressure by Skinner & Ostriker (2015) assume that the dust opacity (κ_d) is constant with temperature (and hence distance from the UV source). Skinner & Ostriker (2015) find:

$$f_{\rm Edd} = 0.68 \left(\frac{\rm DGR}{0.01}\right) \left(\frac{\kappa_d}{0.1\ {\rm cm^2\ g^{-1}}}\right) \left(\frac{\Psi}{883\ {\rm L_\odot\ M_\odot^{-1}}}\right) \tag{4.4}$$

where we have explicitly included the dependence on the dust-to-gas ratio (DGR). For the fiducial values of DGR and Ψ, Skinner & Ostriker (2015) find $f_{\rm Edd} > 1$ only for $\kappa_d > 0.15$ cm^2 g^{-1}, which is unphysically large for Solar Neighborhood-like dust properties (typically 0.03 cm^2 g^{-1}; Semenov et al. 2003). If, however, the dust is different in these environments than in the Solar Neighborhood, κ_d could be larger, though we have no observational constraints to evaluate this. Assuming Solar Neighborhood-like dust and a Kroupa (2001) IMF, we can achieve $f_{\rm Edd} > 1$ if DGR > 0.05. Although the center of NGC 253 is known to have a super-solar metallicity ($Z = 2.2 Z_\odot$; Davis et al. 2013) and the clusters may be even more dust-

rich (Turner et al., 2015; Consiglio et al., 2016), a DGR > 0.05 seems quite high. Turning instead to the possibility of a top-heavy IMF, Equation 4.4 yields $f_{\rm Edd} > 1$ for $\Psi > 4300$ $L_\odot$ $M_\odot^{-1}$ (for Solar Neighborhood-like values of κ_d and DGR,), which is much more top-heavy than has been found in other SSCs (e.g., Turner et al., 2017). Given that Mills et al. (2021) do not find strong evidence for an increased He^+ fraction in these clusters, a very top-heavy IMF is unlikely. Finally, Skinner & Ostriker (2015) note that for clustered sources of UV photons — almost certainly the case in the SSCs in NGC 253 — there can be appreciable cancellation of the radiation pressure terms from each source, so that the net momentum to drive a cluster-scale outflow will be lower, independent of increases in the DGR, κ_d, or Ψ. Therefore, while there may be some combination of increased κ_d, DGR, and Ψ that enables dust-reprocessed radiation pressure to efficiently drive outflows in these clusters, it is unclear how much internal cancellation will affect the net momentum.

Crocker et al. (2018a) take a slightly different approach to study the efficiency of dust-reprocessed radiation pressure. s Modeling of the Rosseland mean opacity by Semenov et al. (2003) found $\kappa_d \propto T^2$ for $T < 100$ K. Crocker et al. (2018a) convert this temperature dependence into a radial dependence from the central source of UV photons, introducing a gradient in κ_d. This has the effect of boosting the effective dust opacity for clusters that are very dense, allowing for outflows to be driven more easily compared to Skinner & Ostriker (2015). Secondly, this allows Crocker et al.

(2018a) to express their $f_{\rm Edd}$ in terms of a critical surface density:

$$\Sigma_{*,\rm IR} = \left(1.3 \times 10^5 \ {\rm M}_\odot \ {\rm pc}^{-2}\right) \times \left(\frac{\kappa_d}{0.03 \ {\rm cm}^2 \ {\rm g}^{-1}}\right)^{-1} \left(\frac{\Psi}{1100 \ {\rm L}_\odot \ {\rm M}_\odot{}^{-1}}\right)^{-1} \left(\frac{\rm DGR}{0.01}\right)^{-1} \tag{4.5}$$

where we have again explicitly shown the dependence on the DGR. The dashed pink boundary in Figure 4.11 assumes the fiducial values of κ_d, Ψ, and DGR. While SSC 14 lies on this boundary, SSCs 4a and 5a fall above it, suggesting that dust-reprocessed radiation-pressure is not sufficient for driving outflows in these clusters.

Note, however, that there are considerable uncertainties in this picture. The cluster stellar masses may be underestimated if appreciable ionizing photons are absorbed by dust or if the stellar population is evolved beyond the ZAMS. Therefore, they may be closer to the region where dust-reprocessed radiation pressure is efficient than shown in Figure 4.11. Moreover, we do not fully understand the properties of dust in these conditions. As discussed above, the DGR in their surrounding gas may be $\gtrsim 0.022$ given the observed super-solar metallicity in the center of NGC 253 (Davis et al., 2013) and the high density conditions in the starburst molecular gas, which may favor dust formation. Assuming DGR $= 0.022$ in Equation 4.5, moves the $\Sigma_{*,\rm IR}$ boundary up to encompass SSCs 4a and 5a. This difference compared to the results of Skinner & Ostriker (2015) comes from the assumed temperature dependence in κ_d, which provides a boosted dust opacity for very compact sources. This itself is very uncertain, since the dust models are designed for proto-planetary disks, and the growth of κ_d with T saturates at $T \sim 100$ K (see Semenov et al.,

2003). Considering changes to the IMF using the fiducial value of κ_d and the DGR would require $\Psi \gtrsim 3000$ $L_\odot$ $M_\odot^{-1}$ to explain SSCs 4a and 5a, or 1.5× more top-heavy than the IMF in NGC 5253 (Turner et al., 2017). Even with the boost in κ_d, there would still be cancellations in the radiation pressure due to clustered UV sources, although these cancellations may not be as severe as in the constant κ_d case.

Therefore, it is possible that dust-reprocessed (indirect) radiation pressure could drive the outflows observed in SSCs 4a, 5a, and 14, though this hinges critically on the behavior of the dust opacity (κ_d) for which there are no observational constraints in these extreme environments. A likely elevated dust-to-gas ratio (DGR) in these sources helps, but cancellations from clustered UV sources hinders the efficiency with which dust-reprocessed radiation pressure can drive outflows. Therefore, whether dust-reprocessed radiation plays a dominant role in powering the outflows observed from SSCs 4a, 5a, and 14 is an open question.

4.4.2.5 Winds from High Mass Stars

Given the stellar masses of these clusters ($M_* = 10^{5.0-5.5}$ $M_\odot$), we would expect $\gtrsim 1000 - 3000$ O stars in each cluster, assuming a Kroupa (2001) IMF. It has been suggested that outflows from young, massive SSCs in the Antennae are driven by a combination of O and Wolf Rayet (WR) stellar winds (Gilbert & Graham, 2007), although other possible mechanisms are not evaluated. The combined power of the winds from these massive stars could, therefore, play an important role in powering the outflows from the clusters in NGC 253.

It has been suggested that winds from WR stars significantly impact how a cluster clears its natal gas, as they impart $\sim 10\times$ the energy of O-star winds over a shorter period of time (e.g., Sokal et al., 2016). The mass-loss rates of WR stars are metallicity dependent, with higher mass loss rates at higher metallicity for both carbon- and nitrogen-rich WR stars (Vink & de Koter, 2005). Because WR stars are evolved O-stars, it is thought that they should not contribute much towards the cluster feedback until after $\sim 3-4$ Myr, when other processes such as supernovae are becoming important and when much of the natal gas has already been dispersed. In an observational study of massive embedded clusters, however, Sokal et al. (2016) find that WR winds are important even at earlier stages, though the clusters they study all have ages >1 Myr. Moreover, they find that clusters without WR stars tend to stay embedded longer than those with WR stars, indicating that WR winds may accelerate the gas-clearing stage.

It is unclear, however, whether the clusters in NGC 253 harbor WR stars yet, given their very young ages ($t_{ZAMS-age} \approx 0.1$ Myr). There is evidence of a WR population towards SSC 5 — perhaps the most evolved cluster — but higher spatial and spectral resolution observations are needed to confirm this (Kornei & McCrady, 2009; Davidge, 2016). There is a known WR X-ray binary in NGC 253, but it is outside of the nuclear region studied here by ~ 250 pc in projection (Maccarone et al., 2014). Given the young ages of these clusters, it is unlikely that there are many, if any, WR stars present in these clusters, especially SSCs 4a and 14. Once a portion of the O star population evolves into WR stars, however, their winds could potentially strongly contribute to driving outflows.

Simulations of stellar wind feedback on the clearing of a cluster's natal gas have mixed conclusions. Some simulations show that stellar winds are important at early times in a cluster's life, especially for clearing the natal dense gas before supernovae start occurring at around 3 Myr (e.g., Agertz et al., 2013; Geen et al., 2015, 2020, 2021). s Given that the clusters in NGC 253 are substantially younger than this ($t_{ZAMS-age} \approx 0.1$ Myr), stellar winds may play a prominent role in driving the outflows we observe from these SSCs. Other simulations, however, find that stellar winds are most effective after 3 Myr (Calura et al., 2015). There are also simulations that find that stellar winds (and photoionization) alone cannot expel the natal gas for massive ($> 5 \times 10^3$ $M_\odot$) clusters at any time point unless they form with a SFE $\equiv M_*/(M_{gas} + M_*) > 1/3$ (Dinnbier & Walch, 2020).

In the absence of gas cooling, stellar winds can impart momentum into the surrounding material typically $p_r/M_* \approx 50 - 65$ km s^{-1} (Weaver et al., 1977), assuming a wind luminosity of 10^{34} erg s^{-1} (Starburst99; Leitherer et al., 1999), the ages of these clusters to be $\approx 10^5$ yrs (Rico-Villas et al., 2020), and $n_H = 10^5$ cm^{-3}. These estimates are on the high side of our observed range of $p_r/M_* \approx 5 - 126,\ 1 - 3,$ and $5 - 40$ km s^{-1} for SSCs 4a, 5a, and 14 respectively (Table 4.2), and are fairly insensitive to the assumed average gas density (an order of magnitude in n_H results in a factor of ≈ 1.5 change in the expected momentum).

If the gas can cool, however, the momentum imparted will be substantially lower, and this is especially relevant in the large ambient densities found near these SSCs (e.g., Silich et al., 2004; Palouš et al., 2014; Wünsch et al., 2017; Lochhaas & Thompson, 2017; El-Badry et al., 2019; Gray et al., 2019; Lancaster et al., 2021a,b).

An outflow stalled by cooling has been claimed in a SSC in NGC 5253 (Cohen et al., 2018). Nonetheless, recent simulations by Lancaster et al. (2021a,b) find that although cooling is important for the gas densities in the central starburst of NGC 253, the momentum imparted with significant cooling still provides a modest enhancement over a momentum-conserving wind. The computed enhancement factor (α_p) is sufficient to power outflows even with efficient cooling (with $\alpha_p \approx 1-4$ assuming a normal IMF and solar metallicity). For the typical ages of these SSCs (~ 0.1 Myr), Lancaster et al. (2021a,b) predict a momentum injection of $p_r/M_* \approx 0.8$ km s^{-1}, lower than momenta measured for SSCs 4a, 5a, and 14 of $p_r/M_* \approx 5-126,\ 1-3,$ and $5-40$ km s^{-1} (Table 4.2). Given the predicted shell velocity from Lancaster et al. (2021a,b), we can estimate the value of α_p implied by the observed outflows:

$$\alpha_p = \left(\frac{V_{max-abs}}{2.0 \text{ km s}^{-1}}\right)^2 \left(\frac{M_{H_2,out}}{M_*}\right) \left(\frac{r_{SSC}}{1 \text{ pc}}\right)^{-1}. \quad (4.6)$$

For the measured outflow properties of SSCs 4a, 5a, and 14, this suggests $\alpha_p \approx 9-227,\ 4-10,$ and $34-272$ respectively (using the parameters in Tables 4.1 and 4.2) compared to $\alpha_p \approx 1-4$ from the simulations. For all SSCs, our values of M_* may be underestimated (Section 4.2.6), reducing the values of α_p inferred from Equation 4.6. A top-heavy IMF could provide up to a factor of 4 enhancement in the strength of the wind (Lancaster et al., 2021a,b). As described in the Section 4.4.2.4, we do not expect the IMF in these clusters to be particularly top-heavy (e.g., Marks et al., 2012; Mills et al., 2021), although this possibility cannot be ruled out

entirely. The wind strength can also be enhanced if the metallicity is super-solar, as is likely the case for these clusters (Davis et al., 2013; Turner et al., 2015; Consiglio et al., 2016).

Given the uncertainties in our measured masses, the IMF, and the metallicity, it is possible that the outflow in 5a is powered by stellar winds. Given the concerns about saturation in SSC 4a, the outflowing mass may be overestimated and so our inferred α_p from Equation 4.6 may also be overestimated, meaning that the outflow from SSC 4a may also be driven (at least in part) by stellar winds. The outflow from SSC 14, on the other hand, is unlikely to be solely by stellar winds.

Therefore, O star winds are unlikely to be driving the outflow observed towards SSC 14 in NGC 253, although it is possible they play a role in driving the current outflows in SSCs 4a and 5a, especially if the current stellar masses of these clusters are underestimated and if the metallicities are super-solar. The O star populations in these clusters are likely too young to host many WR stars, except perhaps in the case of SSC 5a, so the effect of WR star winds is likely negligible at this stage in the SSCs evolution.

4.4.2.6 Summary: What Mechanisms Power the Outflows?

To summarize the above exploration of possible feedback mechanisms, we find that the outflows from SSCs 4a, 5a, and 14 are difficult to explain, though they are likely powered by a combination of dust-reprocessed radiation pressure and stellar winds. All three clusters are too young for supernovae to have exploded and too

dense for photoionization or UV (direct) radiation pressure to be efficient. Whether dust-reprocessed radiation pressure is efficient depends on the properties of the dust opacity (κ_d), for which there are virtually no constraints in extreme environments like these SSCs, and likely requires some combination of a higher dust opacity, an increased dust-to-gas-ratio, and a top-heavy IMF, all of which are currently poorly constrained in these clusters. Moreover, clustered UV sources within the SSCs can have the effect of cancelling out the radiation pressure terms from other sources (Skinner & Ostriker, 2015), reducing the net momentum to drive a cluster-scale outflow. In the case of stellar winds, cooling is expected to be important for these clusters. Although recent simulations find that even in the presence of strong cooling O star stellar winds may be sufficient to power outflows (Lancaster et al., 2021a,b), we find that the expected momentum is insufficient to explain the observed properties of the outflows in SSC 14 and possibly in SSC 4a. For SSC 14, the outflows are likely dominated by dust-reprocessed radiation pressure, whereas the outflow in SSC 5a may be dominated by stellar winds. For SSC 4a, the deep absorption renders the outflowing mass estimate especially uncertain and likely overestimated, so we can only say that the outflow in that cluster is likely a combination of dust-reprocessed radiation pressure and stellar winds. Therefore, the precise mechanism(s) powering these outflows remains uncertain.

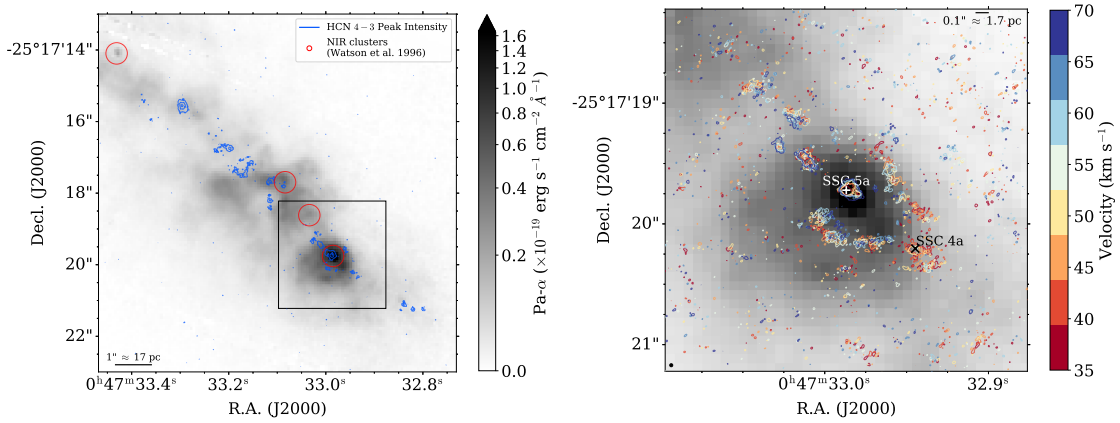

Figure 4.12: (Left) The *HST* Pa-α image. The blue contours show the ALMA HCN $4-3$ peak intensity at 2, 5, and 10$\times$ the rms of the peak intensity image. The red circles show the NIR clusters identified by Watson et al. (1996), where the size of the circle reflects their $0.3''$ positional uncertainty. Only one of the primary clusters (SSC 5a) corresponds to the previously identified NIR clusters. (Right) The *HST* Pa-α image centered on SSC 5a (white plus sign) over the $3''\times3''$ black square from the left panel. There is an asymmetry in the Pa-α emission, which Kornei & McCrady (2009) posit may be due to an outflow. The contours show the HCN $4-3$ emission in selected the velocity channels relative to the systemic velocity of SSC 5a (Table 4.2) showing a shell-like structure with a velocity gradient across the shell. The contours are drawn at 3$\times$ the rms of the HCN $4-3$ cube. The location of SSC 4a is also marked for context (black cross). The asymmetry in the Pa-α emission does not align with the HCN $4-3$ shell. This shell of HCN $4-3$ may be the signature of an earlier (stronger) outflow phase from SSC 5a.

4.4.3 SSC 5a and *HST* NIR Clusters

Several clusters and one SSC have been previously identified in the center of NGC 253 based on *HST* near-infrared (NIR) images (Watson et al., 1996; Kornei & McCrady, 2009), with the NIR-detected SSC corresponding to SSC 5 (Leroy et al., 2018). To be able to see the NIR emission, the cluster must have dispersed much of its natal gas and dust or it aligns with a serendipitous hole in the extinction screen. If the presence of NIR emission at this cluster location is from gas clearing, this implies that the cluster must be older than the other, highly extincted clusters. As shown in Figure 4.6, we see evidence for a weak outflow in the dense gas tracers from this cluster, which may be the tail-end of this gas dispersal process from the timescale arguments in Section 4.4.1. The measured mass outflow rate and momentum injection are also lower than for SSCs 4a and 14. It is important to note, however, that SSC 5a still has a high overall gas fraction ($M_{H_2,tot}/M_*$) of 0.8, though it is not as high as SSCs 4a and 14 (1.3 and 1.6, respectively).

Further support for this picture comes from the discovery of a shell near SSC 5a in HCN $4-3$ as shown in Figure 4.12. This feature is too faint to be seen in CS $7-6$ or $H^{13}CN$ $4-3$ at this resolution. The shell is visible from $\sim 35-70$ km s^{-1} relative to the cluster systemic velocity (Table 4.1) and has a projected radius of ~ 6 pc, though it is not perfectly centered on SSC 5a. Using these projected velocities, this implies an age of $\sim 8-16\times10^4$ years. At its largest extent, the shell reaches the location of SSC 4a (in projection) which also has a dense gas outflow. This shell-like structure is not seen around any other SSCs.

Kornei & McCrady (2009) note that the Pa-α emission around SSC 5a is asymmetric (Figure 4.12) and could be indicative of an outflow. We investigate how this asymmetric geometry corresponds to the observed shell in HCN $4-3$. There are systematic offsets between the location of SSC 5a in the ALMA data, the NIR clusters identified in the *HST* NICMOS data by Watson et al. (1996), and the F187N and F190N *HST* NICMOS data used by Kornei & McCrady (2009). Leroy et al. (2018) corrected the positions of the Watson et al. (1996) NIR clusters by $\Delta\alpha,\ \Delta\delta = +0.32'',\ -0.5''$, so that the NIR cluster corresponding to SSC 5a has $\alpha,\ \delta = 00^{\rm h}47^{\rm m}32.985^{\rm s},\ -25°17^{\rm m}19.76^{\rm s}$ (J2000). The positions of the F187N and F190N mosaics[¶] were corrected by matching the locations of the NIR clusters identified by Watson et al. (1996). A linear shift of $\Delta\alpha,\ \Delta\delta = +1.48'',\ -0.85''$ brings the *HST* images into agreement with the NIR clusters and the ALMA datasets. Figure 4.12 shows the Pa-α (F187N-F190N) image around SSC 5a with the HCN $4-3$ contours overlaid. The expanding HCN $4-3$ shell is not particularly aligned with the asymmetry seen in the Pa-α emission, though it does seem to align with the north-western edge.

It is therefore possible that this shell is a previous (stronger) version of the outflow detected spectrally in this work. The shell age of $\sim 10^5$ years is in good agreement with the minimum ZAMS age and the end of the period of active gas accretion (Section 4.4.1). It is unlikely that the outflow is due to a supernova explosion both because synchrotron emission is a negligible component of SSC 5's

[¶]These calibrated and reduced *HST* NICMOS (NIC2) images were downloaded from the Mikulski Archive for Space Telescopes (MAST) database from M. Rieke's August 1998 program with exposure times of ≈384 s. The mosaic tiles were stitched together using the `reproject` package in Astropy.

spectral energy distribution (Mills et al., 2021) and because the current momentum injection is well below what is expected from supernovae (e.g. Kim & Ostriker, 2015; Kim et al., 2017a).

4.5 Summary

The central starburst in NGC 253 harbors over a dozen massive ($M_* \gtrsim 10^5$ $M_\odot$) and extremely young SSCs which are still very rich in gas and likely in the process of formation (Leroy et al., 2018; Mills et al., 2021). Using high resolution ($\theta \approx 0.028''$, equivalent to 0.48 pc) data from ALMA we study the 350 GHz (0.85 mm) spectra of these objects. We summarize our main results below, indicating the relevant figures and/or tables.

1. We observe P-Cygni line profiles — indicative of outflowing gas — in three super star clusters in the center of NGC 253, sources 4a, 5a, and 14 (c.f., Table 4.1). These line profiles can be seen in the full-band spectra in many lines (Figure 4.3), and particularly cleanly in the CS $7-6$ and $H^{13}CN$ $4-3$ lines which are the focus of this analysis (Figures 4.1 and 4.6). Among these clusters, 5a is notable for being the only one of the massive clusters that is observable in the near IR (Figure 4.12), suggesting it has cleared much of its surrounding gas.

2. By fitting the absorption line profiles (Figure 4.6), we measure outflow velocities, column densities, masses, and mass outflow rates (Table 4.2). The outflow crossing times — a lower limit on the outflow age — are short ($\sim$ few $\times 10^4$

yr), suggesting we are witnessing a short-lived phase. The outflowing mass in these objects is a non-negligible fraction of the total gas or stellar mass.

3. To place limits on the opening angles and line of sight orientations of the outflows we construct a simple radiative transfer model aiming at reproducing the observed P-Cygni profiles in CS 7−6 and $H^{13}CN$ 4−3 (Figures 4.7 and 4.8). By varying the input temperatures, densities, velocities, and velocity dispersion of each component as well as the opening angle and orientation of the outflow component, we find that very wide opening angle models best reproduce the observed P-Cygni profiles (Figure 4.6). While we cannot precisely determine the opening angle for each cluster, the outflows must be almost spherical, although somewhat smaller opening angles are acceptable if the outflows are pointed almost perfectly along the line of sight (Figure 4.9). This modeling also provides measurements of the outflow velocity, column density, masses, and mass outflow rates (Table 4.3). In general, these two sets of measurements agree, given the large uncertainties (Figure 4.10).

4. We compare measurements of the ZAMS age (Rico-Villas et al., 2020) to the gas free-fall time (Leroy et al., 2018), outflow crossing time, gas removal time implied by the mass outflow rate, and the gas depletion time (Table 4.4). These estimates are consistent with the SSCs still being in a period of active gas collapse, though SSC 5a could be past this phase. The gas removal timescale (assuming a constant mass outflow rate) is about an order of magnitude smaller than the gas depletion time due to star formation, showing that

the outflows will have a substantial effect on the star formation efficiency of these SSCs. Reaccretion of gas that was expelled by the outflows is perhaps a likely scenario, which complicates the interpretation of the clusters' evolutionary sequences.

5. Given our measured velocities, masses, radii, surface densities, and momentum per unit stellar mass, we investigate the mechanisms responsible for driving the observed outflows. Possibilities are supernovae, photoionization, UV (direct) radiation pressure, dust-reprocessed (indirect) radiation pressure, and O star stellar winds. While none of these mechanisms completely explains the observations, the two explanations that are potentially in play are dust-reprocessed radiation pressure and stellar winds. It is possible that the outflows are powered by a combination of both mechanisms, with the feedback in SSC 14 dominated by dust-reprocessed radiation pressure and the feedback in SSC 5a dominated by stellar winds (Figure 4.11, Section 4.4.2).

6. We report the discovery of an expanding shell (seen in HCN $4-3$) around SSC 5a with $r \sim 6$ pc (Figure 4.12). As mentioned above, SSC 5a is the only cluster visible in the near IR, which coupled with it having only a lower limits on the ZAMS age suggests that SSC 5a is the most evolved cluster. SSC 5a also has the weakest P-Cygni profile among the three detected and the smallest current mass outflow rate. Given its velocity and size, the shell is $\sim 10^5$ yrs old, in good agreement with the minimum ZAMS age of the cluster and estimates of the end of the period of active gas collapse (Table 4.4). It

is thus likely that the expanding shell is a remnant from the earlier stages of the gas clearing phase when the outflow was stronger. It is unlikely that this shell was created by a past supernova explosion as synchrotron emission is a negligible component of this cluster's spectral energy distribution on 5 pc scales (Mills et al., 2021).

While the SSCs in the heart of NGC 253 constitute a very young population of clusters, there is evidence for differing evolutionary stages among them. A major step towards better characterizing these clusters is better measurements of their stellar masses. Current stellar mass estimates use the 36 GHz continuum emission — assuming that it is all due to free-free emission — to calculate the ionizing photon rate and hence the stellar mass (Leroy et al., 2018). Due to the enormous extinctions towards these clusters, it is not feasible to use traditional optical and near IR recombination lines as tracers of the ionized gas. High resolution hydrogen radio recombination lines (RRLs) offer direct probes of the ionizing photon rate and hence the stellar mass, and are uninhibited by dust extinction (Emig et al. 2020 in NGC 4945, Mills et al. 2021 in NGC 253). In the near future, *James Webb Space Telescope* observations may allow us to independently establish stellar masses, radiation fields, and ages by accessing mid IR spectral line indicators. This will be discussed further in Chapter 6. In the next decade, the combination of sensitivity and exquisite resolution of the Next Generation Very Large Array (ngVLA) may make studies at this high resolution possible for galaxies out to the Virgo cluster and beyond.

Chapter 5: The Morpho-Kinematic Architecture of Super Star Clusters in the Center of NGC 253

5.1 Introduction

Nuclear starburst regions in galaxies are thought to be triggered by inflows of cold gas to their centers. These gas inflows can be fueled by a strong bar or by a merger or tidal interaction. In the case of a barred system, the bar efficiently funnels gas toward to center and gas may collect in the locations of resonances or families of orbits forming a nuclear ring (e.g., Contopoulos & Mertzanides, 1977; Contopoulos & Grosbol, 1989; Binney et al., 1991; Athanassoula, 1992a,b; Buta & Combes, 1996; Knapen, 1999; Pérez-Ramírez et al., 2000; Regan & Teuben, 2003; Kormendy & Kennicutt, 2004). The inflowing gas may not, however, collect in these resonances, instead flowing deeper into the center forming a spiral or disk-like arrangement (e.g., Shlosman et al., 1989, 1990). These collections of gas undergo shocks, causing them to collapse and form stars more efficiently than elsewhere in the disk, for example, leading to a nuclear starburst.

In the case of the nearby galaxy NGC 253, a strong bar fuels the nuclear starburst (e.g., Sorai et al., 2000; Paglione et al., 2004). As a result of the inflowing

gas along the bar, the central kiloparsec of the galaxy is forming stars at a rate of ~ 2 $M_\odot$ yr^{-1} (e.g., Bendo et al., 2015; Leroy et al., 2015). The nuclear region hosts a number of massive, dense molecular clouds (e.g., Sakamoto et al., 2011; Leroy et al., 2015), radio continuum sources (likely HII regions and supernova remnants; Turner & Ho, 1985; Watson et al., 1996; Ulvestad & Antonucci, 1997; Kornei & McCrady, 2009), and masers (e.g., Gorski et al., 2017, 2019). The overwhelming majority ($\sim 100\%$) of the star formation in the nuclear starburst is concentrated in massive forming super star clusters (SSCs; Ando et al. 2017; Leroy et al. 2018; Mills et al. 2021). The SSCs have stellar masses $\approx 10^{4.0-6.0}$ $M_\odot$ and gas masses $\approx 10^{3.6-5.7}$ $M_\odot$ (Leroy et al., 2018; Mills et al., 2021). At the resolution of these studies, however, multiple SSCs are blended together, as revealed by very high (0.5 pc) resolution data of this regions which is able to resolve > 2 dozen compact clumps of dust emission (Levy et al., 2021). Determining the stellar masses of these individual, resolved SSCs will give a better estimate of their stellar masses and allow us to study the cluster mass function (CMF).

From high resolution images of the SSCs taken using the Atacama Large Millimeter/submillimeter Array (ALMA), the SSCs are arranged in a thin, linear structure (Ando et al., 2017; Leroy et al., 2018; Levy et al., 2021; Mills et al., 2021). The position angle (PA) of this structure is similar to that of the galactic disk and differs from the major axis of the bar (e.g., Sorai et al., 2000). Dust and molecular gas observations reveal that the SSCs are embedded with a background and connected by streams of material (e.g., Leroy et al., 2018; Levy et al., 2021; Mills et al., 2021). This thin structure is ~ 200 pc in length and resembles a scaled-up version of the

Milky Way (MW) Central Molecular Zone (CMZ; Sakamoto et al., 2011).

How is this thin, nearly linear structure containing the SSCs connected to the bar, which presumably supplies it with its molecular fuel? Is this structure an edge-on nuclear ring resulting from the bar resonances? A promising hint in this direction is that the location of the inner inner Lindblad resonance (IILR) — where gas is expected to concentrate — is located at a radius of ≈ 240 pc from the center (Sorai et al., 2000), of the same order as the SSC structure. While Paglione et al. (2004) find weaker evidence of an ILR than Sorai et al. (2000), they do find that the dense molecular gas in the center is consistent with the locations of x_2 orbits (see e.g., their Figure 11). The x_2 orbits are expected to lie between the outer ILR (OILR) and IILR and are oriented perpendicular to the bar major axis (e.g., Contopoulos & Grosbol, 1989; Buta & Combes, 1996).

Given the nearly edge-on inclination of NGC 253 and the SSC structure, inferring a connection with the bar and constraining the geometry of the SSC structure from the 2D morphology alone is nearly impossible. In this study, we will use new, combined resolution images of the dust continuum emission in the center of NGC 253 covering a wide range of spatial scales, allowing us to simultaneously resolve the compact SSCs and the more diffuse extended emission. We will combine the information with the systemic velocities of the clusters measured from very high resolution spectral line data (Levy et al., 2021, Chapter 4). This velocity information adds a third dimension to the data, allowing us to better constrain the morpho-kinematic architecture of the SSCs and their connection to the larger scale gas flows in this galaxy.

This chapter is organized as follows. We describe the observations and data processing steps in Section 5.2. This includes how the data were imaged (Section 5.2.1), the identification of dust emission associated with the southwest (SW) streamer of the molecular outflow (Section 5.2.2), and the identification of the clusters in the continuum (Section 5.2.3). The methods used to measure the cluster sizes and properties are described in Section 5.3. We discuss the CMF in Section 5.4. In Section 5.5, we qualitatively compare the arrangement and kinematic structure of the clusters to a ring and crossing streams. We summarize our findings in Section 5.6.

5.2 Observations and Data Processing

Data for this project were taken with ALMA as part of projects 2015.1.00274.S and 2017.1.00433.S (P.I. A. Bolatto). We observed the central 16.64″ (280 pc) of NGC 253 at Band 7 ($\nu \sim 350\,\mathrm{GHz}$, $\lambda \sim 0.85\ \mu\mathrm{m}$) using the main 12-m array in the C43-4, C43-6, and C43-9 configurations and the 7-m (ACA) array. These configurations resulted in baselines spanning from 8.85 m − 13.9 km and hence a maximum recoverable scale of 12.4″ 210 pc). The spectral setup spans frequency ranges of $342.08 - 345.78$ GHz in the lower sideband and $353.95 - 357.66$ GHz in the upper sideband. The visibilities were pipeline calibrated (L. Davis et al. in prep.) using the Common Astronomy Software Application (CASA; McMullin et al. 2007). More information on these observations has been published previously (Leroy et al., 2018; Krieger et al., 2019, 2020b; Levy et al., 2021, Chapter 4).

To extract the 350 GHz continuum data, we flagged channels that may contain strong lines in the band, assuming a systemic velocity of 243 $\mathrm{km\,s^{-1}}$ (Koribalski et al., 2004). Lines included in the flagging are ^{12}CO $3-2$, HCN $4-3$, H^{13}CN $4-3$, CS $7-6$, HCO^{+} $4-3$, and ^{29}SiO $8-7$, and channels within ± 200 $\mathrm{km\,s^{-1}}$ of the rest frequencies of these lines were flagged.

5.2.1 Imaging the Multi-Configuration Data Sets

In this work, we make two different combinations of the multi-configuration data sets. First, we combine the ACA data and three 12-m configurations together to make what we will refer to as the "12m+ACA map." The objective of this map is to recover the most extended dust continuum emission in the nuclear region. We also make a second multi-configuration data set using only the three 12-m configurations, which we will refer to the "12m map." The objective of this data set is to recover the dust emission associated with the clusters. The calibrated visibilities were combined for imaging using the `concat` task in CASA. We spectrally averaged the combined measurement set to have 10 channels per sideband, so that each channel covers ~ 40 MHz.

Since the 12m+ACA and 12m maps have different objectives, we used different deconvolution strategies to produce the final images, which we describe below. All of the visibilities were imaged using the CASA version 5.4.1 `tclean` task.

5.2.1.1 Imaging the 12m+ACA Data

We imaged the central 48″×48″ of the line-flagged, channel averaged, combined 12m+ACA visibilities interactively using `tclean`. Since we are interested in the more extended dust continuum emission, we choose a coarser cell (pixel) size of 0.04″ than was used to image the high resolution continuum in Chapter 4. In all iterations, we used `specmode='mfs'`, `deconvolver='multiscale'`, Briggs weighting with `robust=0.5`, and no primary beam correction. The baseline was fit with a linear function (`nterms=2`) to account for any change in slope over the bandpass. The "dirty" image (`niter=0`) is shown in Figure 5.1 (top) for the inner 20″×20″. The dirty map had a FWHM Gaussian beam size of 0.110″×0.095″. This image is convolved to a circular 0.15″ beam, to match the resolution of the cleaned, tapered image described below.

Before cleaning the extended emission, it was necessary to carefully clean the point source-like clusters, otherwise the algorithm had a tendency to over-subtract these regions leaving deep negative bowls. We cleaned the emission from the clusters using `scales=[0]` and interactively controlling the threshold and number of iterations to avoid over-cleaning. We cleaned the point sources until they were no longer point-like in the residual map and so that the extended residual emission near the point sources was similar to the larger scale emission in the map.

Due to the range of spatial scales covered by these combined data sets, the algorithm tends to favor small scales, making cleaning the extended emission time consuming. Since, for the 12m+ACA map, we are interested in the larger scale more

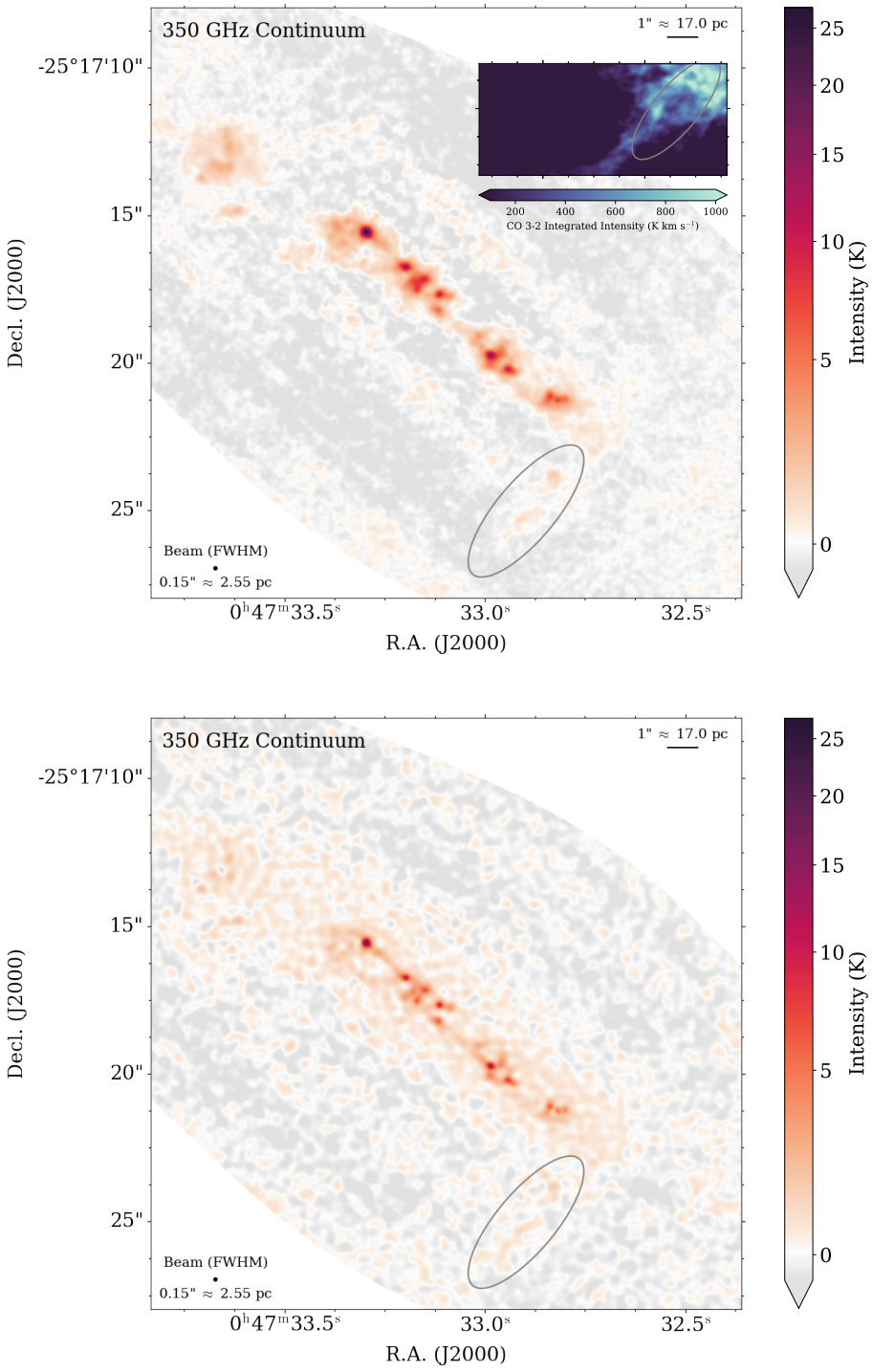

Figure 5.1: The 350 GHz 12m+ACA dust continuum emission in the central 20″ (340 pc) of NGC 253, made by combining three 12-m configurations and one 7-m (ACA) configuration. The top image shows the dirty map and the bottom shows the cleaned map as described in Section 5.2.1.1. The SW streamer seen in CO $3-2$ by Krieger et al. (2019) is shown in the inset in the top panel. The gray ellipses show the region used to estimate the gas mass in the SW streamer based on these dust measurements (see Section 5.2.2).

diffuse emission, we used a uv-taper of 0.2″, `scales=[0,8,16]`, `smallscalebias=0` which gives equal weight to all scales to more efficiently clean the map. We used a circular 0.15″ restoring beam. To avoid over-cleaning, we reduced the gain of each major cycle to 0.05 and interactively lowered the threshold. We interactively cleaned the map until the residuals stopped changing. The final cleaned 12m+ACA map is shown in Figure 5.1 (bottom), which has an rms in regions away from emission of 0.7 mJy beam^{-1} (0.3 K).

5.2.1.2 Imaging the 12m Data

We imaged the central 48″×48″ of the line-flagged, channel averaged, combined 12m visibilities interactively using `tclean`. Since we are interested in the dust continuum emission associated with the clusters, we use a different imaging strategy from the one described above. We use a cell (pixel) size of 0.0046″, the same as was used for the high resolution continuum map (Section 4.2.1) which is shown for comparison in Figure 5.2 (top). In all iterations, we used `specmode='mfs'`, `deconvolver='multiscale'`, Briggs weighting with `robust=0.5`, and no primary beam correction. The baseline was fit with a linear function (`nterms=2`) to account for any change in slope over the bandpass.

As with the 12m+ACA map, before cleaning the extended emission, it was necessary to carefully clean the point source-like clusters, otherwise the algorithm had a tendency to over-subtract these regions leaving deep negative bowls. We cleaned the emission from the clusters using `scales=[0]` and interactively control-

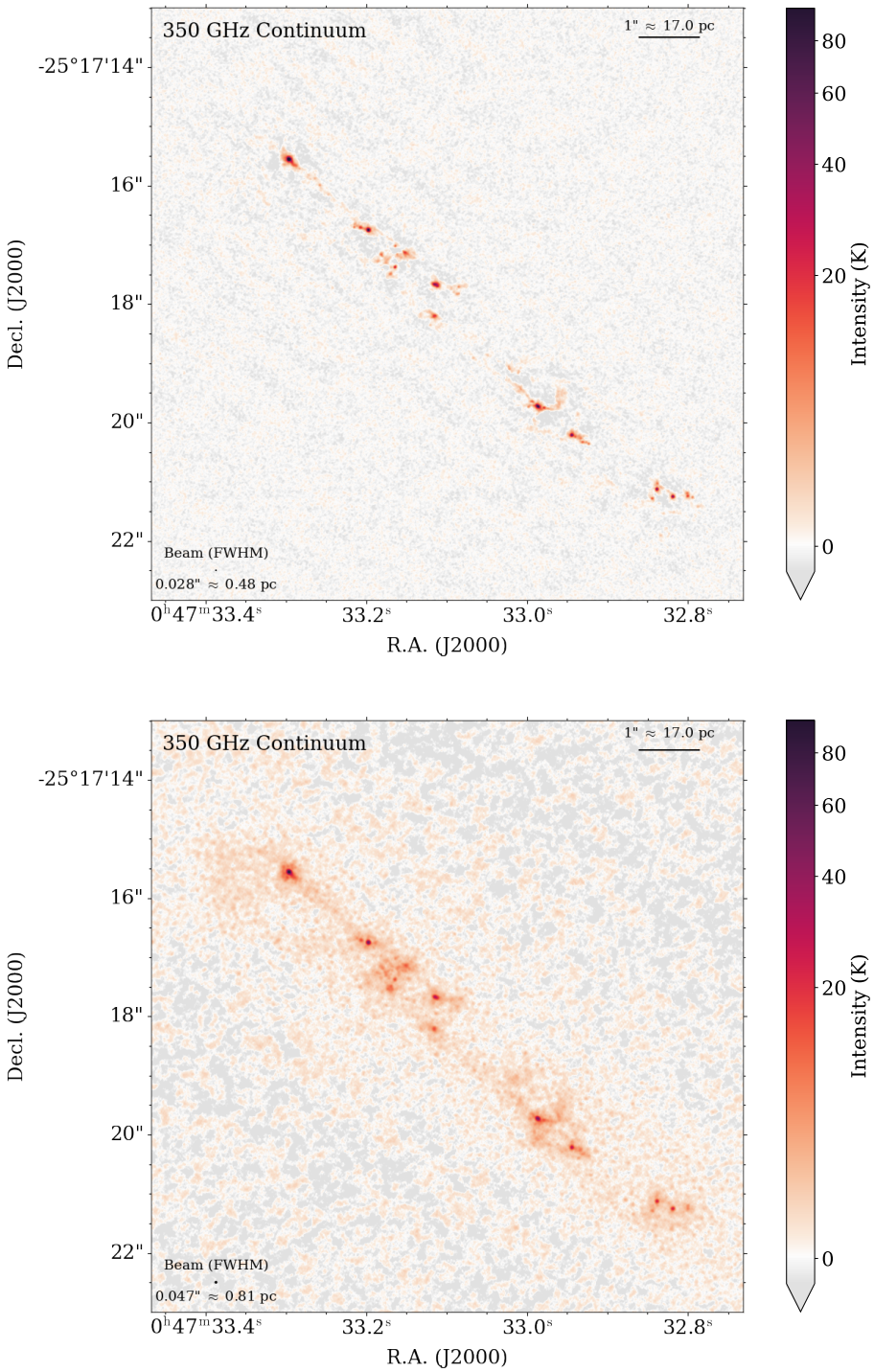

Figure 5.2: (Top) The 350 GHz dust continuum image in the central 10″ of NGC 253 using only the highest resolution (0.028″) data from Levy et al. (2021, Chapter 4). (Bottom) The dust continuum image made combining the three 12-m configurations, which has a final resolution of 0.047″. The cleaning has been optimized for the cluster-scales, as described in Section 5.2.1.2.

ling the threshold and number of iterations to avoid over-cleaning. We cleaned the point sources until they were no longer point-like and so that the emission in those regions was similar to the larger scale emission in the map.

Once the point sources were removed, we carefully cleaned the more extended emission, starting from large scales and moving to smaller ones. For each iteration, we used `smallscalebias=0` and no *uv*-taper. We first started with `scales=[16,32,64]` (corresponding to ≈0.07″, 0.15″, and 0.30″). We interactively cleaned these scales until the maximum residual and cleaned flux no longer changed significantly. We then added `scales=[8]` (≈0.04″) to the existing scales and continued to clean interactively as before. After this scale was cleaned, the overall residuals resembled noise. The map had a FWHM Gaussian beam size of 0.045″×0.041″. We convolved the image to a circular 0.0475″ beam. The final cleaned 12m map is shown in Figure 5.2 (bottom), which has an rms in regions away from emission of 0.2 mJy beam^{-1} (0.8 K).

5.2.2 SW Streamer Seen in Dust Continuum Emission

In Figure 5.1, we detect the SW streamer in 350 GHz dust continuum emission for the first time. We compare the location to the CO 3−2 from Krieger et al. (2019). We integrate their CO 3 − 2 cube from 185 − 285 km s^{-1} where the SW streamer is visible, and we show this integrated intensity map in the upper right corner of the top panel of Figure 5.1. We highlight the SW streamer in the dust continuum data in the gray ellipses in Figure 5.1 and show its corresponding location in the

CO $3-2$ inset map. The dust continuum emission appears to correspond to holes in the CO emission in the SW streamer.

We estimate the flux of dust emission in the SW streamer using the 12m+ACA maps within the ellipse shown in Figure 5.1 (bottom). The flux in this region is $\approx 440 \pm 20$ mJy. We convert this flux to an estimated gas mass, assuming a gas-to-dust ratio of 100 and a dust temperature of 130 K, following Leroy et al. (2018). This conversion yields a gas mass in the SW streamer based on the dust continuum emission of $\sim 10^{6.5}$ $M_{\odot}$. Walter et al. (2017) find a minimum mass of the SW streamer of $\sim 10^{6}$ $M_{\odot}$. Therefore, this dust-based estimate of the molecular gas mass in the SW streamer is consistent with other measurements (see also Bolatto et al., 2013a; Zschaechner et al., 2018; Krieger et al., 2019).

5.2.3 Identifying the Continuum Sources

From the high resolution continuum data, many of the candidate SSCs identified by Leroy et al. (2018) break apart into smaller structures (Figure 5.2 top; Levy et al. 2021). We find more than three dozen dust clumps by-eye. The SSCs identified by Leroy et al. (2018) remain the largest and brightest structures. We, therefore, follow the SSC nomenclature of Leroy et al. (2018), but add letters to sources that break apart in order of decreasing brightness, as described in Chapter 4. We use the dust clumps identified from the high resolution continuum map as a prior to identify and measure the properties of the clusters in the multi-configuration map (Figure 5.2 bottom). We robustly identify 33 clumps of dust emission. Some of the

very small sources previously identified in the high resolution image are no longer visible in the combined 12m map due to the slightly lower resolution and extended emission.

5.3 Cluster Size and Flux Measurements

In Chapter 4, we reported cluster positions and sizes based on the high resolution continuum image. The sizes reported there were based on the half-flux radii, derived from radial profiles. Because we now have continuum images with short spacings, we can recover more of the extended flux associated with the clusters. We, therefore, re-measure the cluster sizes using the 12m map (Figure 5.2 bottom) in two ways as described below.

5.3.1 2D Gaussian Fits and Flux Measurements

As a first approach to measure the sizes, we fit the continuum intensity map with a 2D rotated elliptical Gaussian function of the form

$$I_{\rm model}(x, y | I_{\rm peak}, x_o, y_o, \sigma_x, \sigma_y, \theta, I_o) = I_{\rm peak} e^{-\frac{1}{2}\left\{\left[\frac{(x-x_o)\cos\theta-(y-y_o)\sin\theta)}{\sigma_x}\right]^2+\left[\frac{(x-x_o)\sin\theta+(y-y_o)\cos\theta)}{\sigma_y}\right]^2\right\}} + I_o \quad (5.1)$$

where $I_{\rm peak}$ is the peak intensity, x_o and y_o are the center position (corresponding to RA and Decl.), θ is the orientation of the elliptical Gaussian, σ_x and σ_y are the widths of the Gaussian along the major and minor axes, and I_o is a constant offset since the clusters are embedded within a diffuse background of emission.

For some of the weaker clusters, the seven parameter fit above does not converge. We instead use a "constrained" cylindrically symmetric three parameter fit of the form

$$I_{\rm model}(x, y|I_{\rm peak}, \sigma, I_o) = I_{\rm peak} e^{-\frac{1}{2}\left[\frac{(x-x_o)^2+(y-y_o)^2}{\sigma^2}\right]} + I_o \tag{5.2}$$

where the center position ($x_o,\ y_o$) is fixed.

Before fitting, we mask out other sources in the images. This is especially important for clusters in crowded fields. We mask out primary clusters based on their half-flux radii ($r_{\rm half-flux}$) measured from the high resolution data (see Table 4.1), removing pixels within $2\times r_{\rm half-flux}$ from the cluster centers. For subclusters, we remove pixels within 1.5× the beam half-width-half-maximum (HWHM) from the cluster centers.

We implement the fitting using an affine invariant Markov Chain Monte Carlo (MCMC) method (`emcee`; Foreman-Mackey et al., 2013) to draw samples of the parameters. We use the reduced χ^2 statistic (χ^2_r) between the data and the model as our likelihood function. We use 500 walkers and 300 steps. After $\sim$ 75 steps, the MCMC has forgotten the initial conditions; we discard the initial 150 steps to be conservative.

The best-fitting parameters are given by the median of the marginalized posterior parameter distributions. The uncertainties are given by the 16$^{\rm th}$ and 84$^{\rm th}$ percentiles, which is equivalent to 1-σ for a Gaussian distribution. We show the posterior distributions and FWHM ellipses for two clusters (one fit using Equation

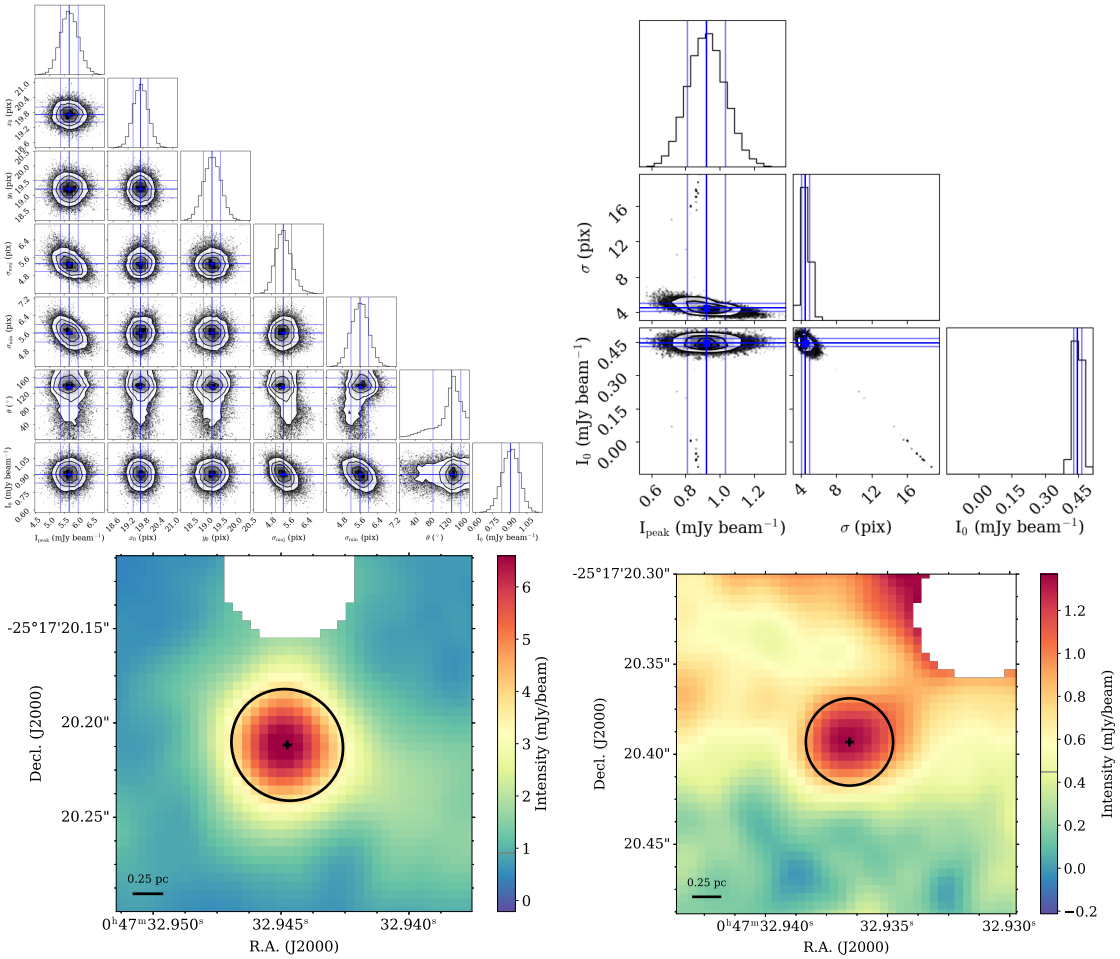

Figure 5.3: The 2D Gaussian fitting posteriors (top) and maps (bottom) for SSCs 4a (left) and 4d (right). Cluster 4a is fit with the full seven parameter model in Equation 5.1, whereas SSC 4d is fit with the constrained three parameter model in Equation 5.2. In the plots of the posteriors, the dark blue lines show the medians of the marginalized posterior distributions; the light blue lines show the 16$^{\text{th}}$ and 84$^{\text{th}}$ percentiles. The bottom row shows the masked continuum maps. The + shows the center position, and the ellipse shows the FWHM size and orientation. The gray horizontal mark on the colorbar shows the constant offset (I_o).

SSC Number	R.A. (J2000)	Decl. (J2000)	$I_{\rm peak}$ (K)	FWHM$_{\rm maj}$ (pc)	FWHM$_{\rm min}$ (pc)	PA[a] (deg)	I_o (K)	Flux (mJy)	Fit Type
1a	$0^{\rm h}47^{\rm m}32.801^{\rm s}$	$-25°17'21.242''$	$5.6^{+0.6}_{-0.5}$	$1.13^{+0.17}_{-0.14}$	$1.25^{+0.24}_{-0.19}$	$36.6^{+30.0}_{-52.8}$	$2.8^{+0.2}_{-0.2}$	$5.5^{+1.2}_{-1.0}$	full
1b	$0^{\rm h}47^{\rm m}32.801^{\rm s}$	$-25°17'21.197''$	$4.6^{+0.7}_{-0.6}$	$0.81^{+0.10}_{-0.10}$	$0.81^{+0.10}_{-0.10}$	—	$2.8^{+0.1}_{-0.1}$	$2.1^{+0.4}_{-0.4}$	constrained
2	$0^{\rm h}47^{\rm m}32.819^{\rm s}$	$-25°17'21.248''$	$22.0^{+0.9}_{-0.9}$	$0.99^{+0.05}_{-0.06}$	$0.93^{+0.06}_{-0.04}$	$24.6^{+46.2}_{-21.0}$	$2.7^{+0.1}_{-0.1}$	$14.1^{+0.7}_{-0.6}$	full
3a	$0^{\rm h}47^{\rm m}32.839^{\rm s}$	$-25°17'21.122''$	$21.0^{+1.2}_{-1.2}$	$0.93^{+0.09}_{-0.10}$	$0.89^{+0.09}_{-0.07}$	$30.5^{+49.4}_{-31.2}$	$3.7^{+0.2}_{-0.2}$	$12.2^{+1.0}_{-0.9}$	full
3b	$0^{\rm h}47^{\rm m}32.845^{\rm s}$	$-25°17'21.285''$	$6.2^{+0.6}_{-0.6}$	$0.88^{+0.07}_{-0.07}$	$0.88^{+0.07}_{-0.07}$	—	$3.0^{+0.1}_{-0.1}$	$3.3^{+0.4}_{-0.4}$	constrained
4a	$0^{\rm h}47^{\rm m}32.945^{\rm s}$	$-25°17'20.212''$	$25.1^{+1.4}_{-1.4}$	$0.98^{+0.07}_{-0.06}$	$1.03^{+0.07}_{-0.08}$	$43.7^{+23.7}_{-48.9}$	$4.0^{+0.3}_{-0.3}$	$17.6^{+1.3}_{-1.3}$	full
4b	$0^{\rm h}47^{\rm m}32.934^{\rm s}$	$-25°17'20.259''$	$5.8^{+0.7}_{-0.6}$	$1.32^{+0.20}_{-0.17}$	$1.32^{+0.20}_{-0.17}$	—	$3.7^{+0.3}_{-0.3}$	$6.9^{+1.8}_{-1.3}$	constrained
4c	$0^{\rm h}47^{\rm m}32.932^{\rm s}$	$-25°17'20.327''$	$4.4^{+0.6}_{-0.6}$	$1.10^{+0.15}_{-0.13}$	$1.10^{+0.15}_{-0.13}$	—	$3.5^{+0.2}_{-0.2}$	$3.7^{+0.9}_{-0.7}$	constrained
4d	$0^{\rm h}47^{\rm m}32.937^{\rm s}$	$-25°17'20.398''$	$4.1^{+0.5}_{-0.5}$	$0.82^{+0.08}_{-0.07}$	$0.82^{+0.08}_{-0.07}$	—	$2.0^{+0.1}_{-0.1}$	$1.9^{+0.3}_{-0.3}$	constrained
4e	$0^{\rm h}47^{\rm m}32.945^{\rm s}$	$-25°17'20.126''$	$3.9^{+0.8}_{-0.6}$	$1.09^{+0.14}_{-0.15}$	$1.09^{+0.14}_{-0.15}$	—	$3.5^{+0.2}_{-0.2}$	$3.1^{+0.7}_{-0.8}$	constrained
4f	$0^{\rm h}47^{\rm m}32.924^{\rm s}$	$-25°17'20.354''$	$2.9^{+0.4}_{-0.3}$	$1.30^{+0.18}_{-0.15}$	$1.30^{+0.18}_{-0.15}$	—	$2.1^{+0.1}_{-0.2}$	$3.3^{+0.8}_{-0.6}$	constrained
5a	$0^{\rm h}47^{\rm m}32.987^{\rm s}$	$-25°17'19.727''$	$46.3^{+1.9}_{-1.9}$	$0.89^{+0.04}_{-0.04}$	$1.23^{+0.06}_{-0.05}$	$40.1^{+4.8}_{-5.1}$	$5.4^{+0.3}_{-0.3}$	$35.5^{+1.8}_{-1.8}$	full
5b	$0^{\rm h}47^{\rm m}32.980^{\rm s}$	$-25°17'19.756''$	$7.4^{+1.0}_{-0.9}$	$1.62^{+0.40}_{-0.29}$	$1.62^{+0.40}_{-0.29}$	—	$5.5^{+0.6}_{-0.9}$	$12.4^{+5.4}_{-3.5}$	constrained
5c	$0^{\rm h}47^{\rm m}32.994^{\rm s}$	$-25°17'19.655''$	$3.8^{+31.3}_{-1.1}$	$1.38^{+1.49}_{-1.32}$	$1.38^{+1.49}_{-1.32}$	—	$4.7^{+0.6}_{-1.5}$	$4.0^{+9.3}_{-3.8}$	constrained
5d	$0^{\rm h}47^{\rm m}32.997^{\rm s}$	$-25°17'19.734''$	$3.7^{+1.6}_{-1.0}$	$0.84^{+0.23}_{-0.23}$	$0.84^{+0.23}_{-0.23}$	—	$4.2^{+0.2}_{-0.2}$	$1.8^{+0.7}_{-0.8}$	constrained
6	$0^{\rm h}47^{\rm m}33.010^{\rm s}$	$-25°17'19.395''$	$2.8^{+0.4}_{-0.3}$	$1.29^{+0.19}_{-0.16}$	$1.29^{+0.19}_{-0.16}$	—	$2.1^{+0.1}_{-0.1}$	$3.2^{+0.8}_{-0.6}$	constrained
7a	$0^{\rm h}47^{\rm m}33.014^{\rm s}$	$-25°17'19.015''$	$2.6^{+0.4}_{-0.4}$	$1.13^{+0.16}_{-0.14}$	$1.13^{+0.16}_{-0.14}$	—	$2.3^{+0.1}_{-0.1}$	$2.3^{+0.5}_{-0.5}$	constrained
8a	$0^{\rm h}47^{\rm m}33.114^{\rm s}$	$-25°17'17.675''$	$27.4^{+1.0}_{-1.0}$	$1.00^{+0.05}_{-0.04}$	$1.48^{+0.06}_{-0.06}$	$25.8^{+4.9}_{-4.3}$	$3.8^{+0.2}_{-0.2}$	$28.2^{+1.4}_{-1.3}$	full
8b	$0^{\rm h}47^{\rm m}33.083^{\rm s}$	$-25°17'17.707''$	$3.3^{+0.4}_{-0.4}$	$1.10^{+0.12}_{-0.11}$	$1.10^{+0.12}_{-0.11}$	—	$2.1^{+0.1}_{-0.1}$	$2.8^{+0.5}_{-0.4}$	constrained
8c	$0^{\rm h}47^{\rm m}33.087^{\rm s}$	$-25°17'17.828''$	$2.3^{+0.5}_{-0.4}$	$1.06^{+0.20}_{-0.17}$	$1.06^{+0.20}_{-0.17}$	—	$2.5^{+0.1}_{-0.1}$	$1.7^{+0.6}_{-0.4}$	constrained
9a	$0^{\rm h}47^{\rm m}33.116^{\rm s}$	$-25°17'18.211''$	$12.0^{+0.8}_{-0.7}$	$1.12^{+0.08}_{-0.08}$	$1.45^{+0.14}_{-0.13}$	$40.3^{+9.1}_{-9.6}$	$3.1^{+0.3}_{-0.3}$	$13.5^{+1.6}_{-1.4}$	full
10a	$0^{\rm h}47^{\rm m}33.151^{\rm s}$	$-25°17'17.149''$	$8.2^{+0.9}_{-0.8}$	$1.37^{+0.34}_{-0.24}$	$1.38^{+0.28}_{-0.21}$	$37.4^{+37.5}_{-46.1}$	$4.9^{+0.4}_{-0.5}$	$10.5^{+3.2}_{-2.1}$	full
10b	$0^{\rm h}47^{\rm m}33.164^{\rm s}$	$-25°17'17.018''$	$4.8^{+0.6}_{-0.6}$	$0.86^{+0.09}_{-0.08}$	$0.86^{+0.09}_{-0.08}$	—	$3.0^{+0.1}_{-0.1}$	$2.5^{+0.4}_{-0.4}$	constrained
11a	$0^{\rm h}47^{\rm m}33.165^{\rm s}$	$-25°17'17.376''$	$12.3^{+0.9}_{-0.9}$	$0.91^{+0.09}_{-0.09}$	$0.76^{+0.07}_{-0.06}$	$30.4^{+19.8}_{-16.1}$	$3.7^{+0.2}_{-0.2}$	$6.0^{+0.6}_{-0.5}$	full
11b	$0^{\rm h}47^{\rm m}33.170^{\rm s}$	$-25°17'17.491''$	$8.3^{+1.0}_{-0.9}$	$0.86^{+0.09}_{-0.08}$	$0.86^{+0.09}_{-0.08}$	—	$4.5^{+0.2}_{-0.2}$	$4.2^{+0.7}_{-0.6}$	constrained
11c	$0^{\rm h}47^{\rm m}33.174^{\rm s}$	$-25°17'17.530''$	$7.6^{+0.7}_{-0.7}$	$1.14^{+0.11}_{-0.10}$	$1.14^{+0.11}_{-0.10}$	—	$3.7^{+0.2}_{-0.2}$	$6.9^{+1.2}_{-1.0}$	constrained
11d	$0^{\rm h}47^{\rm m}33.170^{\rm s}$	$-25°17'17.550''$	$7.5^{+0.6}_{-0.6}$	$1.37^{+0.16}_{-0.13}$	$1.37^{+0.16}_{-0.13}$	—	$3.4^{+0.3}_{-0.3}$	$9.7^{+2.0}_{-1.6}$	constrained
12a	$0^{\rm h}47^{\rm m}33.180^{\rm s}$	$-25°17'17.177''$	$5.6^{+0.7}_{-0.7}$	$0.92^{+0.15}_{-0.13}$	$2.16^{+0.28}_{-0.31}$	$49.8^{+5.7}_{-5.3}$	$3.0^{+0.4}_{-0.5}$	$6.0^{+1.4}_{-1.1}$	full
12b	$0^{\rm h}47^{\rm m}33.186^{\rm s}$	$-25°17'17.268''$	$2.9^{+0.7}_{-0.6}$	$0.84^{+0.30}_{-0.19}$	$1.50^{+0.54}_{-0.44}$	$24.9^{+17.6}_{-13.8}$	$3.5^{+0.2}_{-0.2}$	$2.4^{+0.9}_{-0.7}$	full
13a	$0^{\rm h}47^{\rm m}33.198^{\rm s}$	$-25°17'16.750''$	$50.5^{+2.3}_{-2.4}$	$0.90^{+0.06}_{-0.05}$	$0.93^{+0.06}_{-0.06}$	$44.3^{+29.6}_{-62.6}$	$5.0^{+0.5}_{-0.5}$	$29.6^{+1.7}_{-1.6}$	full
13b	$0^{\rm h}47^{\rm m}33.207^{\rm s}$	$-25°17'16.712''$	$10.6^{+1.4}_{-1.7}$	$0.82^{+0.11}_{-0.08}$	$1.01^{+0.40}_{-0.15}$	$36.2^{+20.0}_{-14.1}$	$4.7^{+0.2}_{-0.3}$	$6.2^{+1.6}_{-0.8}$	full
13c	$0^{\rm h}47^{\rm m}33.212^{\rm s}$	$-25°17'16.678''$	$3.9^{+0.5}_{-0.5}$	$1.47^{+0.32}_{-0.22}$	$1.47^{+0.32}_{-0.22}$	—	$3.0^{+0.3}_{-0.3}$	$5.6^{+2.1}_{-1.3}$	constrained
14	$0^{\rm h}47^{\rm m}33.297^{\rm s}$	$-25°17'15.560''$	$85.1^{+3.2}_{-3.2}$	$0.88^{+0.03}_{-0.03}$	$1.08^{+0.04}_{-0.05}$	$41.8^{+6.7}_{-7.0}$	$9.0^{+0.4}_{-0.5}$	$56.2^{+2.4}_{-2.4}$	full

See Section 5.3.1 for details. [a] The PA reported in this table is measured counterclockwise from north.

Table 5.1: SSC Parameters from the 2D Gaussian Fitting

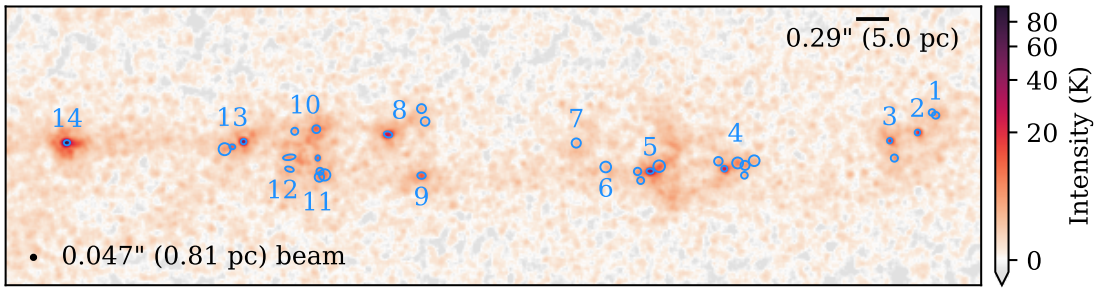

Figure 5.4: The continuum sizes of the SSCs over the high resolution combined 350 GHz continuum map. The map has been rotated counterclockwise by 42° so that the SSC structure is horizontal. The blue ellipses show the fitted FWHM sizes from the 2D Gaussian fits (Section 5.3.1). The cluster groups are labeled following the nomenclature of Leroy et al. (2018).

5.1 and one using Equation 5.2) in Figure 5.3. The best-fitting parameters for all the clusters are given in Table 5.1. We show the fitted FWHM sizes for all of the clusters in Figure 5.4.

We measure the 350 GHz flux of each cluster above the background level from the 2D Gaussian fit (Table 5.1). We use the MCMC samples to generate flux measurements and find the median and 16$^{\text{th}}$ and 84$^{\text{th}}$ percentiles. We compare the fluxes we measure to those reported by Leroy et al. (2018) in two ways, because we measure subclusters associated with the main clusters. We first compare the flux we calculate in only our primary clusters, which is likely an underestimate of the flux reported by Leroy et al. (2018) since their measurements may include our subclusters. We also sum all the flux measured for all of the subclusters of a given association. This is likely an overestimate of the flux reported by Leroy et al. (2018) since their measurements likely do not include all of the subclusters. As shown in Figure 5.5, the ratio of our measurements scatter around unity, but the scatter is large.

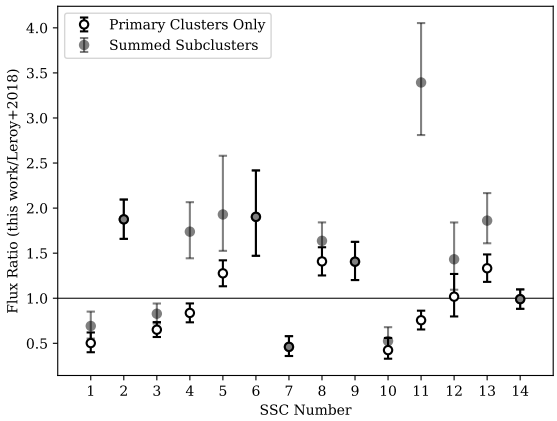

Figure 5.5: A comparison of the fluxes we measure for these SSCs compared to those measured by Leroy et al. (2018). We compare their fluxes to those measured for only the primary clusters in each group (black open circles) as well as for the summed flux of all the subclusters in a group (gray shaded symbols). On average, our fluxes are consistent, though the scatter is large.

5.3.2 Radial Profiles

We construct radial profiles for each cluster. Before extracting the radial profiles, we mask the images in the same way as for the 2D Gaussian fitting. We remove the background level determined from the 2D Gaussian fitting (I_o, Table 5.1). We use concentric circular annuli centered on the R.A. and Decl. from the 2D Gaussian fitting (Table 5.1). The width of the annuli is the beam HWHM (0.024″ = 0.40 pc) and the last ring has a radius of 3× the beam FWHM (3 × 0.0475″ = 2.4 pc). We measure the median intensity in each annulus, which is shown in Figure 5.6 for SSC 14; the uncertainty is the standard error in each annulus.

From the radial profiles, we calculate the cumulative flux distribution and measure $r_{\rm half-flux}$, the radius that contains half of the maximum cumulative flux. We show this radius over the continuum image and compare it to the FWHM measured from the Gaussian fitting for SSC 14 in Figure 5.4 (bottom left). All of the $r_{\rm half-flux}$

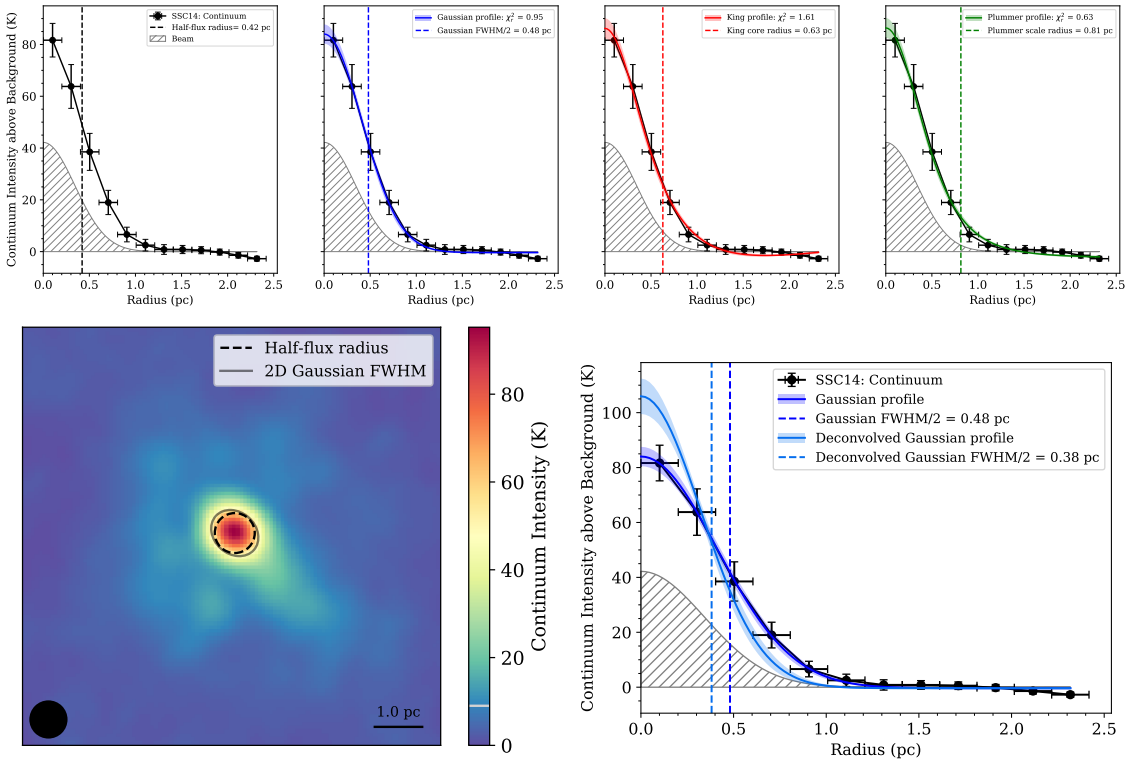

Figure 5.6: (Top) The extracted radial profile of SSC 14 with the background level from the 2D Gaussian fitting removed (black points). The gray hatched regions show the Gaussian beam with arbitrary vertical scaling. The colored fits in each panel show the best-fitting Gaussian, King, and Plummer profiles. The dashed vertical lines show the characteristic cluster radii from each model. (Bottom left) The continuum intensity map of SSC 14, with $r_{\rm half-flux}$ and the FWHM size from the 2D Gaussian fitting overplotted. The black circle in the lower left corner shows the beam FWHM. The light gray horizontal mark in the colorbar indicated the background level from the 2D Gaussian fitting. (Bottom right) The beam-deconvolved (intrinsic) Gaussian radial profile for SSC 14 (light blue). Other curves are the same as in the top center-left panel.

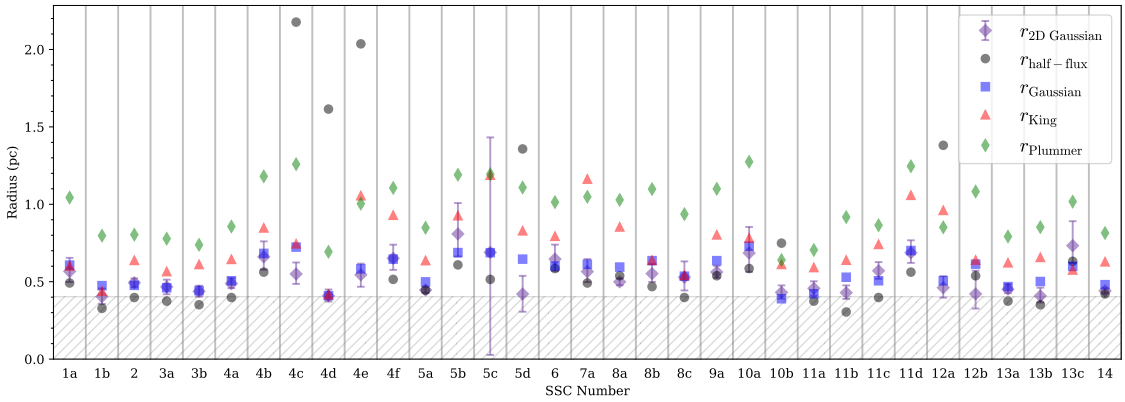

Figure 5.7: A comparison of the cluster radii measurements from the 2D Gaussian fitting (Section 5.3.1; Table 5.1) and the radial profile fitting (Section 5.3.2; Table 5.2). The gray hatched region shows radii smaller than the beam HWHM; radius measurements in this region may be unreliable. In general, $r_{\rm half-flux}$ (black circles) and $r_{\rm Gaussian}$ (blue squares) agree well with $r_{\rm 2D\ Gaussian}$ (purple rhombuses), whereas $r_{\rm King}$ (red triangles) and $r_{\rm Plummer}$ (green diamonds) tend to produce somewhat larger radii (see Section 5.3.2).

measurements are listed in Table 5.2. In Figure 5.7, we compare these half-flux radii measurements (black circles) to those measured from the 2D Gaussian fitting (purple rhombuses). In general there is good agreement between these two measurements of the cluster radii. For those clusters that have large discrepancies, this is due poor $r_{\rm half-flux}$ measurements, likely due to contamination from the background or other nearby clusters.

We model the cluster radial profiles with three different functions: 1) a Gaussian, 2) a King (1962) profile, and 3) a Plummer (1911) profile. We use a Gaussian of the form

$$\mathrm{SB}(r) = ae^{-\frac{r^2}{2\sigma^2}} + c \tag{5.3}$$

to model the radial surface brightness (SB) profile of the clusters. We also include a constant offset (c) since the clusters sit in a diffuse background of dust emission.

SSC Number	$r_{\rm half-flux}$ [a] (pc)	$r_{\rm Gaussian}$ [b] (pc)	$r_{\rm Gaussian,\ deconv}$ [c] (pc)	$r_{\rm King}$ [d] (pc)	$r_{\rm Plummer}$ [e] (pc)
1a	0.49	0.61	0.53	0.60	1.04
1b	0.33	0.47	0.37	0.44	0.80
2	0.40	0.48	0.38	0.64	0.80
3a	0.37	0.46	0.36	0.57	0.78
3b	0.35	0.44	0.33	0.61	0.74
4a	0.40	0.51	0.41	0.64	0.86
4b	0.56	0.68	0.62	0.85	1.18
4c	2.18	0.72	0.66	0.74	1.26
4d	1.62	0.41	0.29	0.41	0.69
4e	2.04	0.58	0.50	1.06	1.00
4f	0.51	0.65	0.58	0.93	1.11
5a	0.44	0.50	0.40	0.64	0.85
5b	0.61	0.69	0.62	0.93	1.19
5c	0.51	0.69	0.62	1.19	1.19
5d	1.36	0.65	0.58	0.83	1.11
6	0.59	0.60	0.53	0.79	1.01
7a	0.49	0.61	0.54	1.16	1.05
8a	0.54	0.59	0.52	0.85	1.03
8b	0.47	0.64	0.56	0.64	1.10
8c	0.40	0.54	0.45	0.54	0.94
9a	0.54	0.64	0.56	0.80	1.10
10a	0.59	0.73	0.67	0.78	1.27
10b	0.75	0.39	0.26	0.61	0.64
11a	0.37	0.42	0.30	0.59	0.70
11b	0.30	0.53	0.44	0.64	0.92
11c	0.40	0.51	0.41	0.74	0.86
11d	0.56	0.70	0.64	1.06	1.25
12a	1.38	0.51	0.41	0.96	0.85
12b	0.54	0.61	0.54	0.64	1.08
13a	0.37	0.47	0.37	0.62	0.79
13b	0.35	0.50	0.41	0.66	0.85
13c	0.63	0.60	0.52	0.58	1.02
14	0.42	0.48	0.38	0.63	0.81

See Section 5.3.2 for details. [a] The radius containing half the cumulative flux based on the radial profile. [b] Half the FWHM of the Gaussian fit to the radial profile. [c] The same as [b] but with the beam HWHM removed in quadrature. [d] The King core radius. [e] The Plummer scale length.

Table 5.2: SSC Parameters from the Radial Profile Fitting

We define $r_{\rm Gaussian}$ as the HWHM ($\equiv \frac{2.355\sigma}{2}$). The King profile has the form

$$\mathrm{SB}(r) = k\left\{\left[1+\left(\frac{r}{r_c}\right)^2\right]^{-1/2} - \left[1+\left(\frac{r_t}{r_c}\right)^2\right]^{-1/2}\right\}^2 + c \tag{5.4}$$

and was developed to describe the SB of globular clusters, which have a core radius (r_c) and a tidal radius (r_t) induced by the tidal interactions as with their host galaxy (King, 1962). We test the King profile as a model for these SSCs to approximate a core+envelope SB distribution. We define $r_{\rm King} \equiv r_c$. We also test a Plummer profile of the form

$$\mathrm{SB}(r) = \frac{3a}{4\pi b}\left[1+\left(\frac{r}{b}\right)^2\right]^{-5/2} + c \tag{5.5}$$

where b is the Plummer scale length (Binney & Tremaine, 2008, Eq. 2.44b). The Plummer profile described a spherical system with a constant density near the center, but that decreases to zero at infinity, and it was also developed to model the profiles of globular clusters. We define $r_{\rm Plummer} \equiv b$.

An example of these three models fit to the cluster radial profile is shown for SSC 14 in Figure 5.6 (top right three panels). All three functions provide similar quality fits to all of the cluster radial profiles. We compare the radius measurements from all of our fitting methods (2D Gaussian and the half-flux, Gaussian, King, and Plummer fits to the radial profiles) in Figure 5.7. In general, $r_{\rm 2D\ Gaussian}$, $r_{\rm half-flux}$, and $r_{\rm Gaussian}$ agree well with one another, whereas $r_{\rm King}$ and $r_{\rm Plummer}$ tend to be larger. We note, however, that these radii are not all measured in the same way. By definition, $r_{\rm 2D\ Gaussian}$, $r_{\rm half-flux}$, and $r_{\rm Gaussian}$ measure the radius that encloses

half of the flux and should, therefore, result in very similar radius measurements. In cases where $r_{\rm half-flux}$ measurements are poor and result in large values (e.g., SSCs 4c, 4d, 4e, 5d, 12a), $r_{\rm Gaussian}$ and $r_{\rm 2D\ Gaussian}$ tend to agree. $r_{\rm King}$ and $r_{\rm Plummer}$, on the other hand, are scale radii defined for those functions and do not correspond to some fraction of the flux. Therefore, the disagreement between $r_{\rm King}$ and $r_{\rm Plummer}$ and the other radius measurements does not indicate that these fits are poor, just that they are different definitions of the radius.

We deconvolve the beam size from $r_{\rm Gaussian}$ by removing the (Gaussian) beam HWHM in quadrature. We produce deconvolved Gaussian radial profiles using the deconvolved radii and conserving the flux. An example of the deconvolved Gaussian radial profile is shown for SSC 14 in Figure 5.6 (bottom right). We report the deconvolved cluster radii in Table 5.2 and we show the distribution of intrinsic cluster radii in Figure 5.8. Our intrinsic radii cover a narrow range of radii from $0.25 - 0.70$ pc.

We compare our measured cluster radii to those measured from the Legacy Extragalactic UV Survey (LEGUS) survey by Brown & Gnedin (2021). These clusters are identified in 31 nearby galaxies in five bands from the near-UV to near-IR. Brown & Gnedin (2021) measure the intrinsic stellar half-light (effective) radii of the young star clusters in these galaxies from the "white light" (i.e. combined 5-filter) images. From their cluster catalog*, we select clusters with reliable radius and mass measurements, ages ≤ 2 Myr, and stellar masses $\geq 10^4$ $M_\odot$; see Brown & Gnedin (2021) for the definitions of these quantities. We show a kernel density estimator

*https://www.gillenbrown.com/LEGUS-sizes

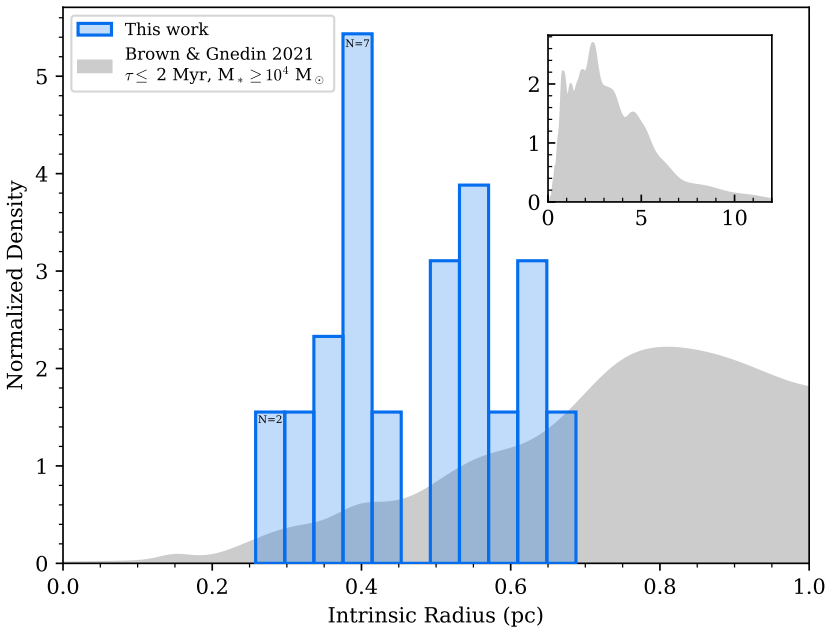

Figure 5.8: The light blue histogram shows the distribution of the intrinsic SSC radii, measured from the beam-deconvolved Gaussian fit to the radial profile. The histogram is normalized to unit area. The number in the highest and lowest bins show the number of clusters in these bins. The gray KDE shows the distribution of star cluster intrinsic effective radii measured in LEGUS galaxies normalized to unit area over the plotted radius range (Brown & Gnedin, 2021). We select clusters with ages < 2 Myr and stellar masses $> 10^4$ M$_\odot$ to be most comparable to our sample of very young, massive clusters. The inset shows the full distribution of the LEGUS radii with the same selection criteria, which peaks around radii of $2 - 3$ pc.

(KDE) of the LEGUS cluster radii in gray in Figure 5.8, where the inset shows the KDE over their full radius range. The LEGUS clusters tend to be larger than the SSCs studied here. The peak in the LEGUS radius distribution for clusters with the above selection criteria is between $2 - 3$ pc.

It is perhaps not unexpected that the clusters identified by Brown & Gnedin (2021) are larger. The radii we measure for the clusters in NGC 253 correspond to the size of the dust (and molecular gas) envelopes, whereas the radii measured for the LEGUS clusters come from the stellar light. The clusters in NGC 253 are still in the process of forming (Leroy et al., 2018) and are, therefore, still very compact. Since

the LEGUS clusters are older than the SSCs in this work and are no longer (deeply) embedded in their natal molecular clouds, it is possible that the stellar light would extend to larger radii than the compact dust emission from the SSCs. Simulations of star cluster evolution show an increase in the radius with age due primarily to stellar mass loss (e.g., Portegies Zwart et al., 2010, and references therein).

5.4 The Cluster Mass Function

From the fluxes we measure based on the 2D Gaussian fits (Section 5.3.1, Table 5.1), we construct the cluster flux density function, which is shown in Figure 5.9 (top). This is essentially a cumulative distribution function (CDF), where the ordinate counts the number of clusters with flux densities larger than the value on the abscissa. The horizontal error bars come from the uncertainties on the measured fluxes. To determine the vertical error bars, we use a Monte Carlo, allowing the measured fluxes to vary uniformly within their uncertainties. This can change the ordering of the flux densities and hence the CDF. We perform 100 trials of the Monte Carlo, and report the standard deviation of the CDF for each point over those trials as the vertical error bars.

In addition to the flux density, we are interested in the cluster stellar mass (M_*) function (CMF). We estimate M_* from our flux density (F_{350}) measurements as follows. We first convert F_{350} to a luminosity density (L_{350}) where $L_{350} = 4\pi d^2 F_{350}$, where d is the distance to the galaxy (3.5 Mpc; Rekola et al. 2005). We then estimate the free-free continuum luminosity ($L_{\rm ff}$) using the free-free contamination fractions

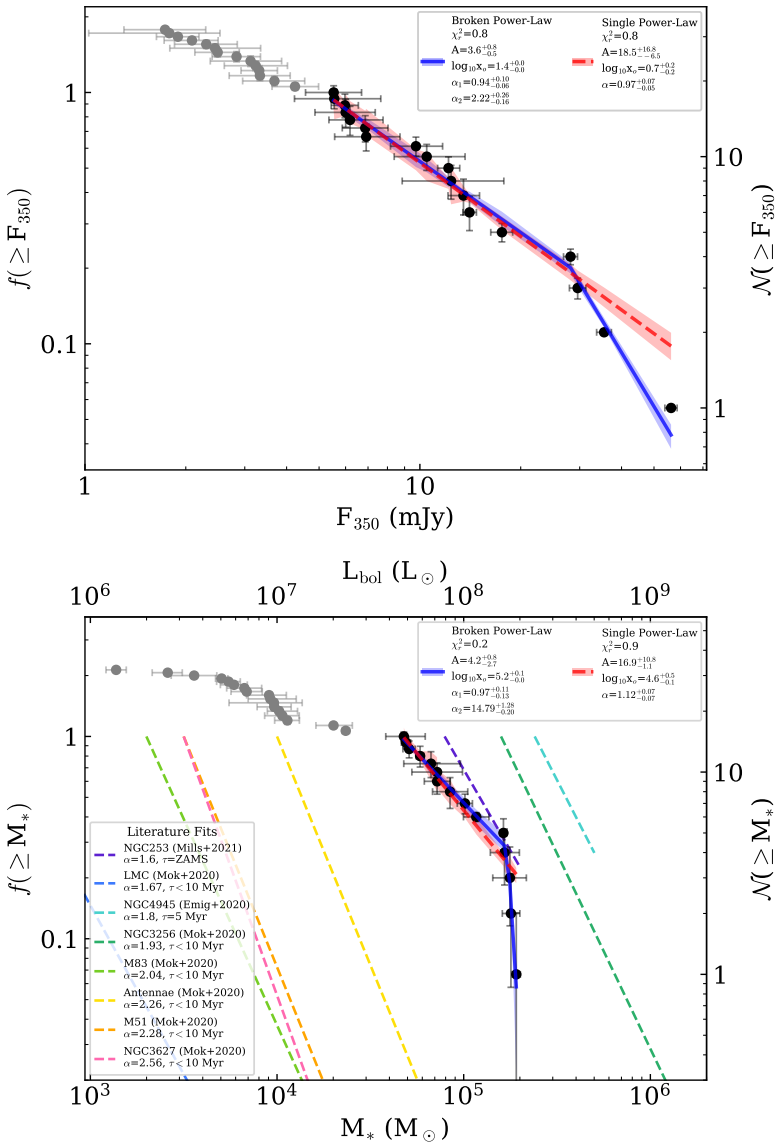

Figure 5.9: The cluster flux density (top) and stellar mass (bottom) functions. The right y-axis shows the number of clusters whereas the left y-axis shows the fraction of clusters with reliable measurements. The gray shaded regions and gray points show our estimate of confusion; measurements in this region are likely underestimated beyond the uncertainties. We fit the distributions with a broken power law (blue solid lines) and a single power law (red dashed lines). See Section 5.4 for details on the uncertainty calculations and the fitting. In the bottom panel, we compare to literature values from Mills et al. (2021), Emig et al. (2020), and Mok et al. (2020), where we have scaled their power law fits based on their reported minimum reliable masses. The top x-axis shows the corresponding bolometric luminosity, assuming a ZAMS mass-to-light ratio of 1000 $L_\odot\,M_\odot{}^{-1}$ (Leitherer et al., 1999; Leroy et al., 2018).

($f_{\rm ff}$) from Leroy et al. (2018, Table 1). For the subclusters, we assume the same $f_{\rm ff}$ as the main cluster. From there, we estimate the ionizing photon rate (Q_0) where

$$\left[\frac{Q_0}{\rm s^{-1}}\right] = 6.3 \times 10^{25} \left[\frac{T_e}{10^4\ \rm K}\right]^{-0.45} \left[\frac{\nu}{\rm GHz}\right]^{0.1} \left[\frac{L_{\rm ff}}{\rm erg\ s^{-1}\ Hz^{-1}}\right] \tag{5.6}$$

(Murphy et al., 2011, Equation 10), assuming $T_e = 10^4$ K, optically thin emission, and no absorption of the ionizing photons by dust. Finally, we convert Q_0 to $\rm M_*$ based on Starburst99 simulations of a 10^6 $\rm M_\odot$ zero age main sequence (ZAMS) cluster where

$$\rm M_* \sim \frac{Q_0}{4 \times 10^{46}}\ M_\odot \tag{5.7}$$

(Leitherer et al., 1999; Leroy et al., 2018; Mills et al., 2021). We can also estimate the bolometric luminosity ($\rm L_{bol}$) from this stellar mass, assuming a mass-to-light ratio for a ZAMS cluster of 1000 $\rm L_\odot\, M_\odot{}^{-1}$ (Leitherer et al., 1999; Leroy et al., 2018). To obtain the uncertainties on $\rm M_*$, we propagate the uncertainties on our flux measurements as well as the uncertainties on $f_{\rm ff}$ reported by Leroy et al. (2018). We caution that these uncertainties are likely to be substantially underestimated given the assumptions about $f_{\rm ff}$, T_e, the optical depth, the lack of dust absorption, the age of the burst (assumed ZAMS), and the conversion from Q_0 to $\rm M_*$ (Equation 5.7). We construct the CMF in the same way as for the flux density, and we repeat the Monte Carlo analysis to obtain the vertical error bars. The CMF is shown in Figure 5.9 (bottom).

Both distributions appear to follow a broken power law. This break could

be due to incompleteness or at the low flux end of the distribution (e.g., Emig et al., 2020). The SSC identification is done by-eye based on the high resolution continuum image (Figure 5.2 top). The 2D Gaussian fitting is performed on the 12m combined image (Figure 5.2 bottom) at the locations of the SSCs identified from the high resolution image, as long as they are still apparent in the lower resolution, 12m combined image. The major uncertainty matching the SSCs between these images are from the "speckles" seen in the 12m combined continuum image (Figure 5.2 bottom). These speckles arise in the imaging by modeling a extended emission as Gaussians matched to the beam size, and they can resemble small, compact clusters. We, therefore, use these speckles as our test particles to evaluate the completeness and confusion of our SSC flux density and mass functions. We choose a representative speckle in the image and measure its size and flux from the 2D Gaussian fitting as described in Section 5.3.1. We convert this flux to a stellar mass as described above. We find that a typical speckle has a flux of $\approx 2.4 \pm 0.3$ mJy and hence an inferred stellar mass of $\approx 10^{4.1 \pm 3.2}$ $M_{\odot}$. We show the upper uncertainty bounds as the gray shaded regions in Figure 5.9. Clusters with fluxes or masses near or below this limit are likely more uncertain than represented by the error bars and we are likely missing SSCs in this flux and mass regime. This range corresponds especially well to the break seen in the CMF.

We fit the cluster flux density and mass functions using a broken power law of

the form

$$f(x) = \begin{cases} A\left(\frac{x}{x_0}\right)^{-\alpha_1}; x < x_0, \\ A\left(\frac{x}{x_0}\right)^{-\alpha_2}; x > x_0, \end{cases} \tag{5.8}$$

which is implemented using `BrokenPowerLaw1D` from Astropy. As a comparison, we also fit the cluster flux density function with a single power law of the form

$$f(x) = A\left(\frac{x}{x_0}\right)^{-\alpha} \tag{5.9}$$

which is implemented using `PowerLaw1D` from Astropy.

We obtain the uncertainties on the fitted parameters using the same Monte Carlo approach described above. As the flux density or mass points are allowed the vary within their uncertainties, we re-fit Equation 5.8 at each iteration. The uncertainties listed in Figure 5.9 reflect the 16^{th} and 84^{th} percentiles of the parameter distributions after the Monte Carlo. The same strategy is used to obtain the uncertainty regions on the model curves, shown in the shaded regions in Figure 5.9.

We find a CMF slope of 1.12 ± 0.07 from our single power law fit. We compare our CMF to several previous studies, which are shown as the colored dashed curves in Figure 5.9 (bottom). These are single power law fits to star clusters in NGC 253 (Mills et al., 2021), NGC 4945 (Emig et al., 2020), the Large Magellanic Cloud (LMC), M 83, M 51, and NGC 3627 (Mok et al., 2020). The power-laws are only computed between the upper and lower mass ranges reported in the respective studies. The fits are ordered by increasing slope in the legend. The study of the SSCs in NGC 253 by Mills et al. (2021) is an especially important comparison. They use

an independent ALMA dataset at 5 pc resolution targeting the radio recombination line (RRL) emission towards these clusters. RRL measurements provide a relatively unbiased measurement of the ionizing photon rate, which they then convert to a stellar mass using Equation 5.7. We find a somewhat shallower slope than Mills et al. (2021), but caution that a single power law fit could easily be steeper given the very steep slope for the most massive clusters. Compared to the other galaxies, NGC 253 has the shallowest CMF slope. An important caveat of this plot is that the position along the horizontal axis depends on the assumed age of the cluster, as older clusters have larger stellar masses (e.g., Leitherer et al., 1999). For this work, we assume a ZAMS (e.g., Equation 5.7), which is also assumed by Mills et al. (2021). Emig et al. (2020) use a similar method as Mills et al. (2021) in the nuclear starburst of NGC 4945; this starburst is more evolved than NGC 253, however, so they adopt an age of 5 Myr for their calculation. For the galaxies considered by Mok et al. (2020), they use ages < 10 Myr in their analysis.

It is tempting to try to connect the CMF to the cluster initial mass function (CIMF) and hence to the stellar initial mass function (IMF; e.g., Portegies Zwart et al., 2010). The very young clusters in NGC 253 may provide the best opportunity to derive the CIMF, given that they must still be younger than 3 Myr and possibly younger than 1 Myr (Leroy et al., 2018; Rico-Villas et al., 2020; Levy et al., 2021; Mills et al., 2021). More robust measurements of the stellar masses on these resolved cluster scales and better estimates of the cluster ages are needed, however, before this can be attempted. We will discuss two sets of approved future observations that may enable this in Chapter 6.

5.5 The Morpho-Kinematic Architecture of the SSCs

The quasi-linear arrangement of the SSCs in the center of NGC 253 is striking (e.g., Figures 5.1, 5.2, 5.4). In projection, this structure measures ~ 155 pc $\times$ 15 pc in diameter with a major axis position angle (PA) of $\approx 48°$ east-of-north. This axis ratio of ~ 10 may suggest that the structure is intrinsically very thin. On the other hand, if the structure is intrinsically a circular ring, it would be inclined to our line of sight by $\sim 57°$. Using CO observations at 35 pc resolution, Leroy et al. (2015) measure the geometry of the GMC structures in which these SSCs are embedded. They build 3D models of the GMC geometry as a disk, a linear bar-like arrangement, and a hybrid model. They find that the hybrid model provides the best fit to the data, where the inner $\sim 100 - 150$ pc (diameter) is more disk-like and regions beyond this extending out to $\sim 850 - 1400$ pc (diameter) have a more linear structure. They find that the maximum vertical thickness of the GMC structure is < 100 pc for the molecular gas traced by CO and < 55 pc for the denser molecular gas. Our measurement of the minor axis width of the SSC structure sets a maximum vertical extent of < 15 pc, similar to the vertical extent of the MW CMZ (e.g., Kruijssen et al., 2015; Shin et al., 2017).

The galactic disk of NGC 253 is nearly edge-on, with an inclination of $\approx 78°$ and a PA of $\approx 50°$ (e.g., Pence, 1980; Westmoquette et al., 2011), as can be seen in the NIR image of the galaxy shown in Figure 5.10 (left). The bar also has an inclination of $\approx 78°$ but has a PA of 68° (Scoville et al., 1985; Sorai et al., 2000). The quasi-linear arrangement of SSCs has approximately the same PA as the galaxy

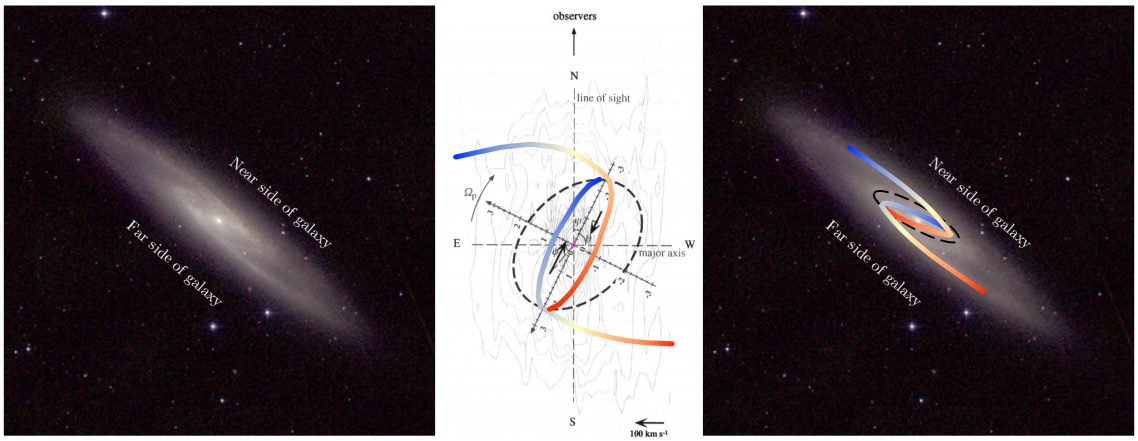

Figure 5.10: (Left) A 2MASS JHK image of NGC 253 (Jarrett et al., 2003), showing the strong bar. North is up and east is left. The near side of the galaxy is to the northwest, and the far side is to the southeast. (Center) A schematic of the deprojected spiral arm and bar inflows in the center of NGC 253 adapted from Figure 18 of Sorai et al. (2000). We have schematically color coded the spiral arms and bar inflows according to the bulk gas line of sight velocities. The dashed black ellipse shows the 2 kpc ring. We note, however, that Sorai et al. (2000) use a distance (d) to NGC 253 of 2.5 Mpc (Davidge et al., 1991; Mauersberger et al., 1996), whereas we adopt 3.5 Mpc (Rekola et al., 2005). The magenta box shows the central 10″ (120 pc for d = 2.5 Mpc, 170 pc for d = 3.5 Mpc) encompassing the SSCs (e.g., Figure 5.11). (Right) The same 2MASS image as the left panel, with the schematics of the spiral arm and bar kinematics overplotted for context.

disk and is offset from the PA of the bar.

To further orient ourselves with respect to the larger scale spiral arms and bar structures, we show an adaptation of a schematic from Sorai et al. (2000) in Figure 5.10 (middle). This schematic shows the deprojected orientation of the spiral arms, bar, and 2 kpc ring. We have color coded the spiral arms and bar based on the relative line of sight velocities, where the observer is at the top of the image. For scale, the magenta square shows 10″ (170 pc), the same field of view over which the clusters are visible. In the right panel of Figure 5.10, we reproject these color-coded structures back onto the NIR image. The near side of the galaxy is to the northwest and the far side is toward the southeast (e.g., Sakamoto et al., 2006).

Due to the strong bar and gas inflows to the nucleus (e.g., Sorai et al., 2000; Paglione et al., 2004), it is interesting to determine how the SSCs are arranged with respect to the bar orbits. Due to the nearly edge-on inclination, constraining arrangement purely from the cluster locations is difficult. A similar challenge is faced in studying the MW CMZ, where the massive star forming regions are viewed nearly edge-on and thought to be arranged as spirals, streams with either open or closed orbits, or a ring (e.g., Sofue, 1995; Sawada et al., 2004; Molinari et al., 2011; Krumholz & Kruijssen, 2015; Kruijssen et al., 2015; Henshaw et al., 2016; Ridley et al., 2017; Tress et al., 2020). Henshaw et al. (2016) provide an excellent review and testing of these models in the CMZ, and their Figures 18 and 19 show examples of these arrangements in position-position and position-velocity space. Without knowledge of how the SSC structure is dynamically linked to the bar (or not), it is impossible to tell whether the SSC structure is tilted in the same manner as the galaxy disk (i.e., where the near side of the disk to towards the northwest).

We can, however, use the kinematic information from the cluster velocity measurements presented in Chapter 4 (Table 4.1; Levy et al. 2021) together with the morphology to constrain the cluster arrangement. This approach has also been applied to the CMZ (e.g., Krumholz & Kruijssen, 2015; Kruijssen et al., 2015; Sormani & Barnes, 2019; Tress et al., 2020). Rather than the bulk gas kinematics, however, we will use the SSCs themselves as tracer particles of the gas flows in the nuclear region.

In Figure 5.11 (top right), we show a version of the 12m continuum image where the color scale has been stretched. The circles show the locations and systemic

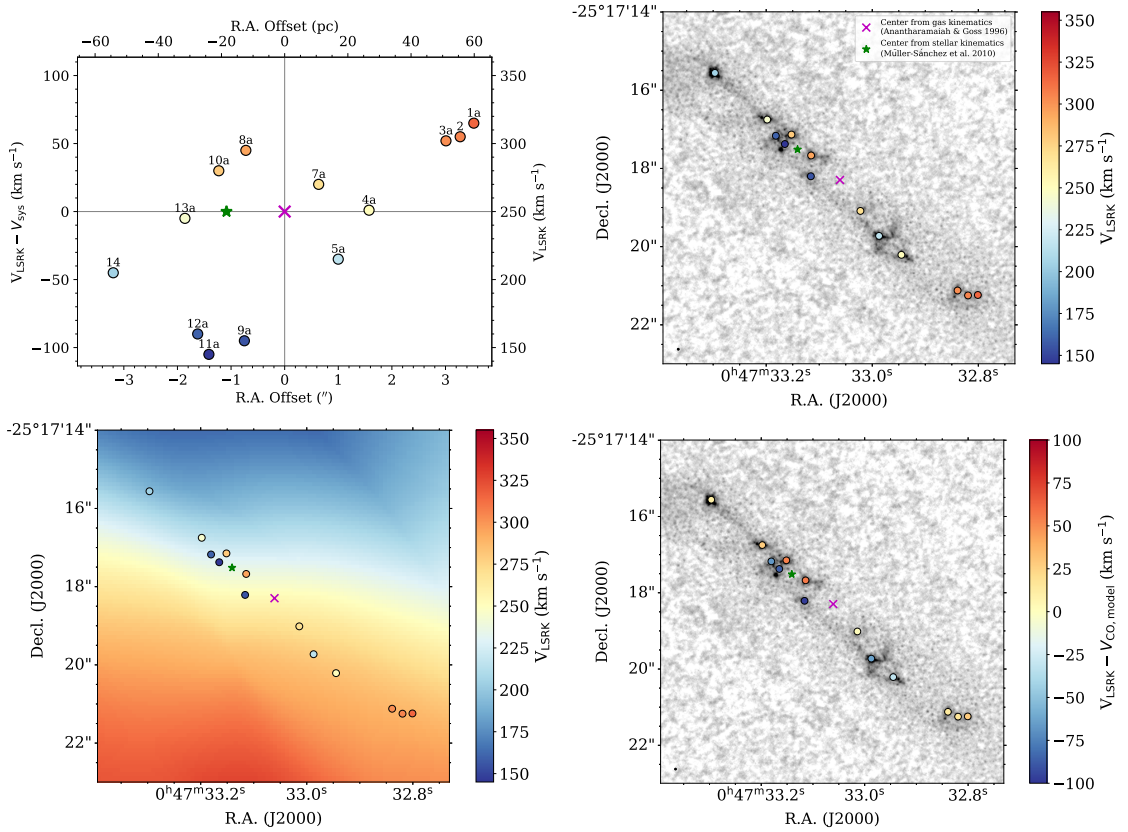

Figure 5.11: (Top left) A position-velocity diagram of the SSC systemic velocities values for the primary clusters (Table 4.1). The horizontal axis shows the R.A. offset from the center measured from gas kinematics (Anantharamaiah & Goss, 1996, magenta ×). The stellar kinematic center is also shown (Müller-Sánchez et al., 2010, green star). The points are color coded by the systemic velocity of the cluster (V_{LSRK}). (Top right) The background image shows the 12m continuum image. The circles show the locations and systemic velocities of the primary clusters. Two measurements of the center of NGC 253 are marked in the green star (based on stellar kinematics; Müller-Sánchez et al. 2010) and in the magenta × (based on ionized gas kinematics; Anantharamaiah & Goss 1996). The colorbar is centered on the systemic velocity of the galaxy (250 km s^{-1}). (Bottom left) The background image shows the model velocity map from Krieger et al. (2019) based on CO $1-0$ data with a beam size of $1.85'' \times 1.32''$. This model represents the bulk gas motions from galactic rotation and the bar. The cluster positions and systemic velocities are shown as in the previous panel. (Bottom right) The same as the top right, but where the SSCs are color coded by their V_{pec}, removing the velocity contribution from the galactic rotation and non-circular bar motions.

velocities of the primary clusters. The systemic velocities were measured by Levy et al. (2021) using a multi-Gaussian fit to many spectral lines detected towards these clusters (see Section 4.2.5). The uncertainties on the SSC systemic velocities are better than ± 5 km s^{-1} (Section 4.2.5). The velocity color scale is centered on the systemic velocity of the galaxy (250 km s^{-1}; Müller-Sánchez et al., 2010; Krieger et al., 2019, 2020a).

The precise center of NGC 253 is not known, because its central supermassive black hole has not been definitively identified. In Figure 5.11, we show two measurements of the center. The first is measured using ionized gas kinematics (Anantharamaiah & Goss, 1996, magenta $\times$) and the second is measured from stellar kinematics (Müller-Sánchez et al., 2010, green star). In Figure 5.11 (top left) we show a position-velocity (PV) diagram of the clusters. The x-axis is the offset in R.A. from the ionized gas kinematic center (Anantharamaiah & Goss, 1996). The y-axis and color coding scale match the color coding of the top right panel.

Krieger et al. (2019) measured the velocity field of the central $\sim$ 850 pc of NGC 253 at 2 pc spatial resolution traced by CO $1-0$, $2-1$, and $3-2$. The CO traces the bulk motions of the gas, reflecting the galactic rotation, non-circular motions from the bar, and the large-scale outflow. They also fit a kinematic model of the galactic rotation and non-circular bar motions using CO $1-0$ data. In Figure 5.11 (bottom left), we show the CO $1-0$ model velocity map in the central $\sim$ 170 pc. The positions and systemic velocities of the primary SSCs are marked. Some of the cluster systemic velocities agree well with the bulk gas motions (e.g., SSCs 1, 2, 3 in the lower right and SSC 14 in the upper left) whereas others have

large velocity offsets. To further investigate this, we remove the contributions from the bulk gas components by extracting the modeled CO $1-0$ velocity centered on the SSC positions and measuring the median velocity in a circular aperture with a radius equal to $2 \times r_{\rm Gaussian}$. We refer to the SSC velocities with the bulk gas motions removed as the peculiar velocities ($V_{\rm pec}$). As shown in Figure 5.11 (bottom right), $V_{\rm pec}$ can be large. Intriguingly, the southeast clusters tend to be blueshifted whereas the northwest clusters tend to be redshifted. Sorai et al. (2000) find maximum non-circular motions of the molecular gas in the bar of $\approx 70 - 130$ km s^{-1} in the rest frame of the bar. The $V_{\rm pec}$ we measure are approximately in the rest frame of the bar. Some of the measured $V_{\rm pec}$ values are consistent with these measurements, though many of the clusters have smaller $V_{\rm pec}$.

Below, we consider whether the clusters are morpho-kinematically consistent with a circumnuclear ring or crossing streams inflowing from the larger-scale bar. These are not the only possible arrangements, and quantitative comparisons with dynamical models are needed to constrain the arrangement more robustly.

5.5.1 SSCs as a Circumnuclear Ring with Closed Orbits

One possible configuration for the SSCs is in a circumnuclear starburst ring, as suggested by the GMC modeling done by Leroy et al. (2015). This ring could either be flat or have a vertical twist (e.g., Molinari et al., 2011). In either case, the orbits along the ring are closed.

In Figure 5.12, we also show a schematic of a two possible ring-like architec-

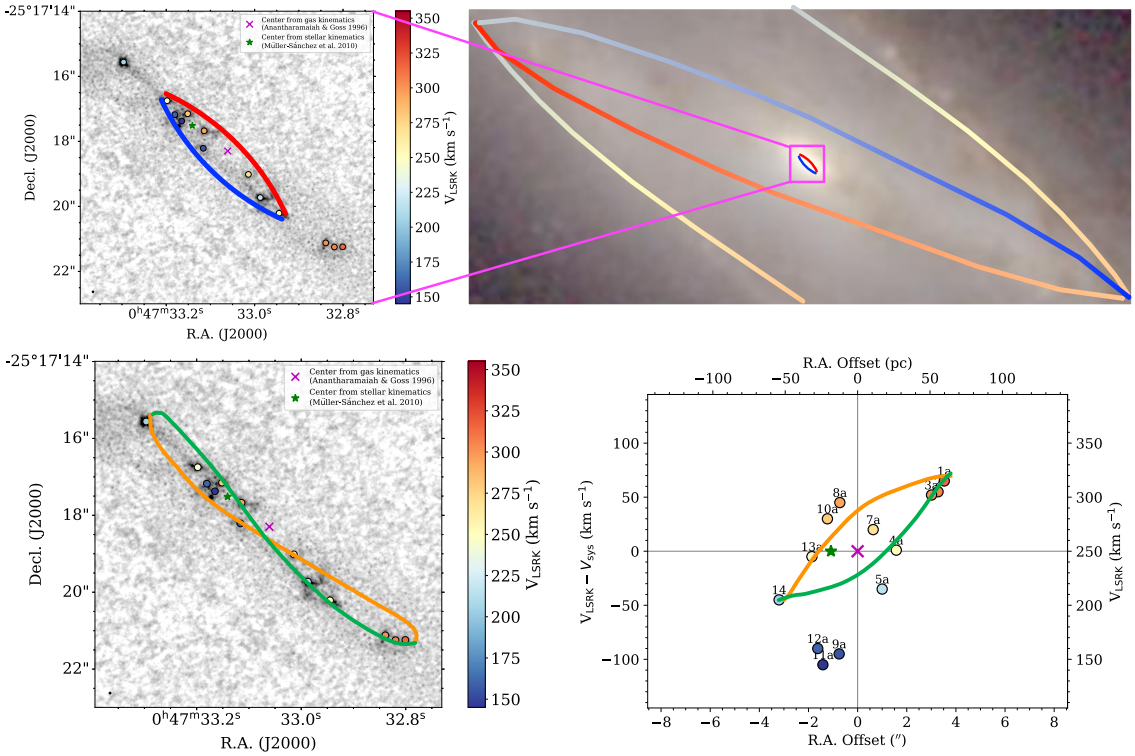

Figure 5.12: (Top Left) The same as Figure 5.11 (top right), with a schematic of a possible ring-like structure centered near the galaxy center measured by Anantharamaiah & Goss (1996) over plotted. The ring is color coded based on the cluster systemic velocities. (Top Right) A zoom in on the bar schematic shown in Figure 5.10 (right). The magenta square shows the size of the left panel (10″ = 170 pc). The ring-like structure from the left panel is also shown to scale with the other structures. (Bottom left) A different twisted ring-like model, based on the closed stream orbits of Molinari et al. (2011) and adapted from Henshaw et al. (2016). This model has been schematically placed over the SSCs. The green (orange) tracks would be on the front (back) side in this model. (Bottom right) The PV diagram of the twisted ring model from Henshaw et al. (2016) schematically placed on the SSC PV diagram. The kinematic agreement between the SSCs and this model is not perfect, though more detailed and quantitative comparisons are necessary.

tures. This ring may be centered on the galactic center from ionized gas kinematics (Anantharamaiah & Goss, 1996). For the flat ring, following the cluster systemic and peculiar velocities, the southeast side of the ring would be blueshifted and the northwest side would be redshifted (Figure 5.12 top left). The far (near) side of the galactic disk in to the southeast (northwest), as marked in Figure 5.10. Therefore, if the ring follows the same orientation as the disk, this may indicate that the ring is shrinking, though there is no guarantee that the ring has the same alignment as the disk. We caution against over-interpretation here, as this could also be a projection effect and requires a more quantitative comparison.

In Figure 5.12 (right) we show this ring in the context of the larger scale spiral arms and bar based on the schematic by Sorai et al. (2000) and shown in Figure 5.10. It is unclear precisely how this ring would connect to the bar without more quantitative dynamical modeling. In the CMZ of the MW, dynamical models by Krumholz & Kruijssen (2015) and Tress et al. (2020) find that the far (near) side of the bar end would connect to the near (far) side of the ring (see e.g., Figures 22 and 26 of Tress et al. 2020). Observationally, Sormani & Barnes (2019) find that the far side of the bar is increasingly blue shifted, but that the velocity decreases as the gas approaches the CMZ (and vice versa for the near side of the bar; see their Figure 1). If a similar model applies to the center of NGC 253, this could explain why the V_{pec} values we measure for the SSCs are smaller in general than the molecular gas velocities measured along the bar by Sorai et al. (2000).

Another possible ring-like arrangement would be a closed elliptical orbit or a twisted ring (Molinari et al., 2011). In the case of the CMZ, this configuration

is thought to follow the x_2 orbits and the twisted shaped is induced by a vertical oscillation. We show a schematic of a possible twisted ring-like architecture in Figure 5.12 (bottom left), which is adapted from Molinari et al. (2011) and Henshaw et al. (2016). The green (orange) segments indicate the front (back) of the ring in projection for a configuration like the CMZ. Without quantitative modeling, it is unclear whether this alignment is correct for the SSCs in NGC 253. In the bottom right panel of Figure 5.12, we compare the PV diagram of a twisted ring-like orbit to the SSCs (adapted from Henshaw et al., 2016). We have matched the orientation of the segments based on the bottom left panel. Without doing a proper fit, the kinematics of a twisted stream do not agree with the SSC kinematics particularly well. We caution against over interpretation here, as these comparisons have only been done schematically and qualitatively here.

Any of the possible arrangements with closed orbits are problematic, however, because orbits are expected to be open for extended gas structures. As pointed out by Kruijssen et al. (2015) and others for the MW CMZ, because the mass distribution in the CMZ is extended, closed orbits are only possible if the potential is not axisymmetric at these scales. The structural modeling by Leroy et al. (2015) suggests that there are asymmetries on larger scales (as is also expected for the CMZ). Their best fitting structural model, however, is axisymmetric on the $100-150$ pc scales we study here, though their data are not particularly constraining on these scales due to the 35 pc resolution. Therefore, since we know the SSCs are embedded in larger-scale gas structures (e.g., Sakamoto et al., 2011; Leroy et al., 2015; Krieger et al., 2019, 2020b,a), it is more likely that the SSC orbits will be

open, which we discuss in the following section. While we cannot definitively say that the SSCs form a circumnuclear ring without more quantitative comparisons to dynamical models, a ring-like architecture may be plausible.

5.5.2 SSCs as Crossing Streams with Open Orbits

Another possibility is that all of the SSCs are embedded in streams stemming from the bar-ends. Several of these kinds of models have been proposed for the CMZ in the MW (e.g., Sofue, 1995; Sawada et al., 2004; Kruijssen et al., 2015; Henshaw et al., 2016; Ridley et al., 2017). We show a schematic representation of possible configurations of gas streams with open orbits in Figure 5.13. In the top left panel, we show an example of spiral-like streams, such as those proposed in the MW CMZ (Sofue, 1995; Sawada et al., 2004; Ridley et al., 2017). We color code the schematic stream lines to roughly match the SSC systemic velocities. In the top right panel, we show these streams in the context of the larger scale spiral arms and bar based on the schematic by Sorai et al. (2000) and shown in Figure 5.10. It is unclear precisely how these streams would connect to the bar without more quantitative dynamical modeling.

Kruijssen et al. (2015) develop a model of the MW CMZ that consists of crossing streams that form a ring-like structure. Unlike the closed ring model, this stream model is open and Sagittarius A* (Sgr A*) is located at one of the foci of the eccentric orbits. We compare the PV diagram for the cluster systemic values to this orbital model for the CMZ (see Figure 4 of Kruijssen et al. 2015) in the bottom

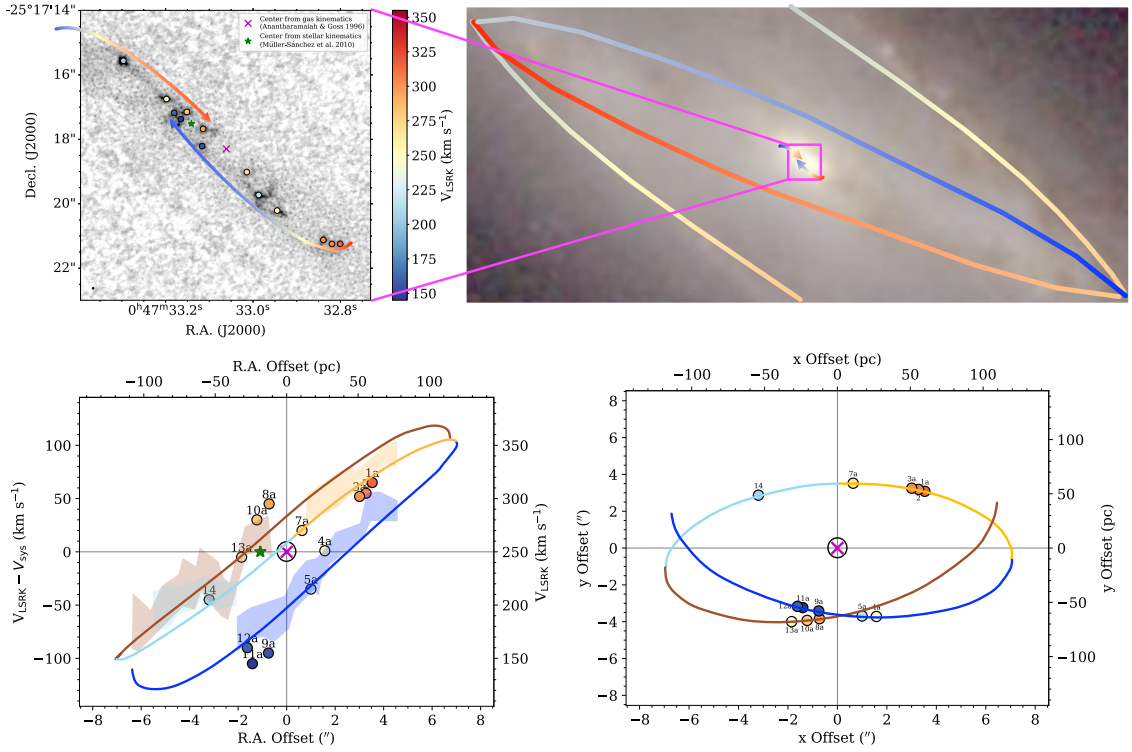

Figure 5.13: (Top left) The same as Figure 5.11 (top) but with schematic spiral-like stream-lines overplotted, where the colorscale of the stream lines is intended to reflect the trends in the systemic velocities of the SSCs. This schematic is more centered on the center from stellar kinematics measured by Müller-Sánchez et al. (2010). (Top right) A zoom in on the bar schematic shown in Figure 5.10 (right). The magenta square shows the size of the left panel (10″ = 170 pc). The stream lines from the left panel are shown to scale. (Bottom left) The SSC PV diagram as in Figure 5.11 with the PV diagram of the orbital model for the MW CMZ by Kruijssen et al. (2015) overlaid (see their Figure 4). The four different colored curves correspond to the four streams in the model. The color shaded regions show the uncertainty range for the data Kruijssen et al. (2015) used to derive the CMZ model. The CMZ model was scaled to the same physical size and velocity and shifted such that the center from ionized gas kinematics corresponds to the location of Sgr A* (black circle). The model is reflected across the velocity axis and the colors of the streams are adjusted accordingly. (Bottom right) The top-down view of the streams implied by the Kruijssen et al. (2015) model (see their Figure 6). Colors and symbols are the same as the bottom left panel. SSCs are assigned to a y-position based on their closest stream segment in the PV diagram, with SSC 4a having the most uncertain stream assignment.

left panel Figure 5.13. For this rough comparison, we scaled the CMZ model PV diagram to the same physical and velocity scale as in NGC 253. We then shifted the model such that the center from ionized gas kinematics corresponds to the "true" center of NGC 253; for the MW, the center is the location of Sgr A*. We also reflected the model across the velocity axis and adjusted the coloring of the curves accordingly. Given this rough comparison, the stream model agrees overall with the SSC PV diagram.

Given this arrangement, we show the corresponding top-down view of these streams based on the model by Kruijssen et al. (2015) in Figure 5.13 (bottom right; see their Figure 6), accounting for the necessary reflection of the model across the velocity axis. In this top-down view, the horizontal axis is the offset from the center along the major axis of the structure. We measure this using the 2D distance of the clusters (in R.A. and Decl.) from the ionized gas kinematic center. The vertical axis is along the line of sight in the case of the MW. This direction is almost into the page in the case of NGC 253, and we therefore have no constrains on this coordinate from the observations. We assign the clusters locations along the stream lines based on their closet stream line in the PV diagram (Figure 5.13 bottom left). The most uncertain assignment is SSC 4a, which lays between the dark blue and yellow streams. We have tentatively assigned it to the blue (front) stream because it is closer to that stream in the PV diagram and is within the uncertainties on the data Kruijssen et al. (2015) used to derive the CMZ model. Its systemic velocity, however, may be more consistent with the yellow (back) stream.

We caution that given the high inclination of these SSCs, it is unclear how

unique this solution is. There are many possible stream lines that could be drawn through the SSCs. Aside from the edge-on nature of the data, the rosette pattern traced out by the orbits in the model by Kruijssen et al. (2015) (e.g., Figure 5.13 bottom right) rotates with time (Tress et al., 2020), and so it is not clear that this particular portion of the rosette is favored over another segment. Finally, there are disagreements between this model and observations of the CMZ (e.g., Henshaw et al., 2016; Ridley et al., 2017; Sormani et al., 2019).

Therefore, while we cannot definitively say that the SSCs trace out crossing orbits without more quantitative comparisons to these models, this kind of architecture seems plausible.

5.6 Summary

The SSCs in the center of NGC 253 are bright continuum sources at 350 GHz, which primarily traces thermal emission from warm dust (e.g., Leroy et al., 2018; Levy et al., 2021). Here, we combine ALMA data from three 12-m configurations and the 7-m array to construct maps of the dust emission covering scales from $0.028''-12.4''$ (0.48 pc−210 pc). This enables us to measure the compact dust emission associated with the clusters themselves as well as the more diffuse emission in which they are embedded (Figures 5.1 and 5.2). We summarize our main results below, indicating the relevant figures and/or tables.

1. For the first time, we detect the galaxy-scale outflow in dust continuum emission. As shown in Figure 5.1, we find dust emission along the SW streamer,

co-located with CO emission. We estimate that the SW streamer has a molecular gas mass of $\sim 10^{6.5}$ $M_{\odot}$, consistent with other measurements.

2. We measure the sizes of the SSCs in two ways. First, we fit the dust continuum maps of each SSC with a 2D Gaussian to measure the positions, sizes, and fluxes (Figure 5.4, Table 5.1). Next, we construct radial profiles for each cluster. As a non-parametric measurement of the cluster sizes, we measure the half-flux radius, or the radius that contains half of the cumulative flux of the cluster. We also fit the radial profiles using Gaussian, King, and Plummer models. In general, the three models provide equally good fits (Figure 5.6). Using the Gaussian fit to the radial profile, we deconvolve the Gaussian beam from the size measurements to provide beam-deconvolved cluster sizes (Figures 5.6 and 5.8).

3. From the flux and size measurements, we construct the cluster flux density and stellar mass functions (Figure 5.9). Our CMF slope agrees with an independent study of the SSCs in NGC 253 by Mills et al. (2021).

4. From the positions and systemic velocities of the SSCs, we investigate whether the clusters are morpho-kinematically consistent with a circumnuclear ring with closed orbits (e.g., Molinari et al., 2011; Krumholz & Kruijssen, 2015; Tress et al., 2020) or streams with open orbits (e.g., Sofue, 1995; Sawada et al., 2004; Kruijssen et al., 2015; Ridley et al., 2017). We find compelling evidence that the cluster positions and velocities may be consistent with either architecture (Figures 5.11, 5.12, and 5.13), though a model with open orbits

may be more physical. Quantitative comparisons with these and other models are necessary, however, to definitively constrain the SSC architecture.

Models of circumnuclear rings and streams make predictions for the relative ages of the clusters. In a ring scenario, it is thought that the youngest clusters are found at (or slightly downstream of) the contact points with the streams from the bar (e.g., Regan & Teuben, 2003; Böker et al., 2008; Mazzuca et al., 2008). Shocks at these intersections can trigger the collapse of molecular clouds. As the forming clusters move along the ring, they age. This is known as the "pearls-on-a-string" model (Böker et al., 2008). This picture will be more complicated if there are multiple entry points along the stream as the orbit precesses (e.g., Tress et al., 2020). Similarly in the case of the crossing streams models, close passages with other streams can trigger the gas to collapse and form stars (Kruijssen et al., 2015). Alternatively, it is possible that the ring becomes unstable to gravitational collapse due to turbulence. In this scenario, no age gradient is expected as either the clusters have approximately the same age or the ages are randomly distributed along the ring. This is known as the "popcorn" model (Böker et al., 2008). While there are estimates of the (relative) SSC ages in NGC 253 (Rico-Villas et al., 2020; Krieger et al., 2020b; Levy et al., 2021, see Section 4.4.1), they do not agree with one another. In the future, approved observations with the *James Webb Space Telescope* (JWST) may help constrain the ionizing radiation field of these clusters and hence provide the most robust measurements of the cluster ages. These ages and the age progressions may be able to help distinguish among the morph-kinematic models

for the SSC architecture. These JWST data are discussed further in Chapter 6.

Chapter 6: Future Work

The work presented in this thesis is the beginning rather than an endpoint. Below I outline a few future directions based on the research presented in the previous chapters.

6.1 Measurements of Ionized Gas Velocity Dispersions in eDIG

The advent of IFU spectroscopy has allowed for the kinematics of extraplanar diffuse ionized gas (eDIG) to be measured and studied in large samples of galaxies such as MaNGA (Bizyaev et al., 2017) and CALIFA (Levy et al., 2018, 2019, e.g., Chapters 2 and 3). However, a comprehensive study of eDIG from these and other IFU surveys is limited by the spectral resolution of the instruments. In order to support a thick, lagging disk of ionized gas, the velocity dispersion must be higher than in the midplane (e.g., Veilleux et al., 1995). Measurements of the velocity dispersion are, therefore, the final key observation to fully study and characterize the kinematics of the eDIG in these galaxies.

As a next step building off of this thesis, I will propose for new observations of the 42 galaxies used in my previous eDIG studies (Chapters 2 and 3 Levy et al., 2018, 2019) to measure the ionized gas velocity dispersions directly. I plan to apply

for time on the WIYN 3.5-m telescope on Kitt Peak to use the SparsePAK IFU (Bershady et al., 2004), which is designed to study galaxy kinematics. The WIYN 3.5-m telescope is in the same hemisphere and the same size as the telescope used for the CALIFA survey, so it is well-matched for this project. The major strength of SparsePAK is the increase in spectral resolution ($R \approx 10,000$, a FWHM velocity resolution of 30 km s^{-1}) which is sufficient for a robust velocity dispersion measurement.

The variable dust optical depth with height may complicate these measurements. As the dust optical depth decreases away from the midplane, we will be able to measure larger columns of the eDIG material and material at a larger range of rotation velocities (see e.g., Figure B.1). This will also broaden the measured linewidth, independent of whether the lines in the eDIG are intrinsically broader. We will model disks with variable dust optical depths as a function of height (e.g., with NEMO) to estimate the magnitude of this effect on the linewidths we measure.

6.2 Ionized Gas toward the Super Star Clusters in NGC 253

Our previous ALMA observations presented in Chapters 4 and 5 reveal more than two dozen compact dust structures that have the hallmarks of super star clusters (SSCs) in the process of forming (Leroy et al., 2018; Levy et al., 2021). We used several techniques to estimate their stellar masses, including a very high resolution VLA 36 GHz image which allowed us to estimate their stellar masses from free-free emission (Gorski et al., 2017, 2019; Leroy et al., 2018). These clusters range from

$\log(M_*/M_\odot)$=4.1−6.0. About 30% of the ionizing photons in the burst are generated by these sources, even before accounting for any absorption by dust, and they explain ∼20% of the bolometric emission (Leroy et al., 2018). The ionizing photon rates and stellar masses estimated from the 36 GHz continuum VLA observations are uncertain, however, due to absorption by dust and possible synchrotron contamination. Moreover, the current 36 GHz VLA observations have a resolution of 1.6 pc, close to the limit of the VLA's capabilities at these frequencies, which only marginally resolves the largest clusters.

To measure precise ionizing photon rates and stellar masses for these objects, we must use another method. Because the extinction toward these SSCs is immense (Leroy et al., 2018), observing the ionizing flux at optical wavelengths is impossible. Highly spatially resolved radio recombination lines (RRLs) can be used to constrain the stellar mass and radiation fields associated with these massive stellar clusters as they are unaffected by dust extinction (e.g., Roelfsema & Goss, 1992; Emig et al., 2020; Emig, 2021). Recently, this method was successfully employed to measure accurate ionizing photon rates and stellar masses of SSCs in another starburst galaxy (Emig et al., 2020). In NGC 253, very deep ALMA observations reveal H40α emission towards many of the SSCs (Mills et al., 2021), though the clusters are unresolved at the 5 pc resolution of that study.

I am the PI of an A-ranked ALMA proposal to observe RRLs at high resolution towards the SSCs in the nuclear starburst of NGC 253. Observations will be taken at two resolutions, matching those of our previous studies presented by Leroy et al. (2018, 0.1" = 1.9 pc) and Levy et al. (2021, 0.028" = 0.5 pc). The data for this

project have been partially observed and delivered and are a top priority to complete once ALMA operations resume. From early, low resolution data, the SSCs are clearly detected in the H27α RRL. Using these data, and following the methodology of Emig et al. (2020) and Mills et al. (2021), I will directly measure the ionizing photon flux and synchrotron emission in these objects. At the 0.5 pc resolution of these data, I will be able to measure the sizes and structure of the HII regions associated with these SSCs. From these, we can compare against their dust and dense gas properties to better constrain the evolutionary stages of the clusters. Using the high spectral resolution, we can also search for signs of feedback and outflows in the ionized gas, especially in those sources where molecular outflow signatures were found (Chapter 4; Levy et al., 2021).

6.3 Ages and Radiation Fields of the Super Star Cluster Populations in NGC 253 and M 82

When the *James Webb Space Telescope* (JWST) launches soon, its capabilities are sure to revolutionize our understanding of the Universe. In particular, its instruments allow for high spatial and spectral observations at mid-IR (MIR) wavelengths for the first time. I am a co-I on an approved Cycle 1 JWST proposal to observe the archetypal starburst galaxies NGC 253 and M 82. The goals of this project are primarily two-fold. The first is to obtain NIR and MIR imaging of the galaxy-scale outflows and centers of both galaxies. The filters we have selected will target warm (shocked) molecular gas and polycyclic aromatic hydrocarbon (PAH)

emission tracing the dust at unprecedented spatial resolution and sensitivity.

The second goal is to obtain MIR spectroscopy from $\approx 5 - 28$ μm of the super star clusters in the centers of both NGC 253 and M 82. From these observations, we will be able to constrain the radiation field strength near the clusters and measure their stellar masses more accurately than previously possible. Related to this thesis, we will also search for signs of radiative and mechanical feedback from the clusters, both from the spectral line profiles and spatially from the high resolution NIR and MIR images.

Appendix A: Appendices for Chapter 2

A.1 Velocity Conventions

When converting from frequency (or wavelength) to a velocity via the Doppler formula, the radio and optical communities use different conventions as approximations to the full relativistic conversion. The optical convention is

$$\frac{V_{\rm opt}}{c} = \frac{\lambda - \lambda_o}{\lambda_o} \equiv z, \tag{A.1}$$

the radio convention is

$$\frac{V_{\rm radio}}{c} = \frac{\nu_o - \nu}{\nu_o} = \frac{z}{1+z}, \tag{A.2}$$

and the relativistic convention is

$$\frac{V_{\rm rel}}{c} = \frac{\nu_o^2 - \nu^2}{\nu_o^2 + \nu^2}. \tag{A.3}$$

Therefore, combining Equations A.1 and A.2, a velocity measured in the optical convention ($V_{\rm opt}$) can be converted to the radio convention ($V_{\rm radio}$) where

$$V_{\rm radio} = \frac{V_{\rm opt}}{1 + \frac{V_{\rm opt}}{c}}. \tag{A.4}$$

A galaxy with a rotation speed measured in the optical convention ($V^{\rm rot}_{\rm opt}$) will result in a radio rotation speed ($V^{\rm rot}_{\rm radio}$), where

$$V^{\rm rot}_{\rm radio} = \frac{V_{\rm opt} + V^{\rm rot}_{\rm opt}}{1 + \frac{V_{\rm opt} + V^{\rm rot}_{\rm opt}}{c}} - \frac{V_{\rm opt}}{1 + \frac{V_{\rm opt}}{c}} \approx \frac{V^{\rm rot}_{\rm opt}}{1 + \frac{2V_{\rm opt}}{c}} \tag{A.5}$$

to first order. The rotation velocity in the optical convention is larger than in the radio convention. As an example, for a galaxy with $V_{\rm opt} = 4500\,{\rm km\,s^{-1}}$ and $V^{\rm rot}_{\rm opt} = 250\,{\rm km\,s^{-1}}$ (similar to the CALIFA galaxies), $V^{\rm rot}_{\rm radio} = 243\,{\rm km\,s^{-1}}$, so the rotation velocity in the radio convention is smaller than in the optical convention. For the velocity differences measured from the CO and Hα rotation curves, this discrepancy is not negligible. To avoid this, maps should be converted to the same convention.

Both the radio and optical convention scales become increasingly compressed at higher redshifts (large systemic velocities), but the relativistic convention does not suffer from this compression. Both EDGE and CALIFA reference to zero velocity, so typical velocities are a few thousand ${\rm km\,s^{-1}}$. Conversions to relativistic from radio or optical by combining Equations A.2 or A.1, respectively, with Equation A.3, where

$$\frac{V_{\rm rel}}{c} = \frac{(\frac{V_{\rm opt}}{c} + 1)^2 - 1}{(\frac{V_{\rm opt}}{c} + 1)^2 + 1} \tag{A.6}$$

and

$$\frac{V_{\rm rel}}{c} = \frac{1 - (1 - \frac{V_{\rm radio}}{c})^2}{1 + (1 - \frac{V_{\rm radio}}{c})^2}. \tag{A.7}$$

For a rotational velocity measured in the relativistic frame ($V^{\rm rot}_{\rm rel}$), the corresponding

$V_{\rm opt}^{\rm rot}$ and and $V_{\rm radio}^{\rm rot}$ are

$$V_{\rm opt}^{\rm rot} = \frac{V_{\rm rel}^{\rm rot}}{1 - \frac{V_{\rm rel}}{c}} \tag{A.8}$$

$$V_{\rm radio}^{\rm rot} = \frac{V_{\rm rel}^{\rm rot}}{1 + \frac{V_{\rm rel}}{c}}. \tag{A.9}$$

For a galaxy with $V_{\rm opt} = 4500\,{\rm km\,s^{-1}}$, this results in $V_{\rm rel} = 4466\,{\rm km\,s^{-1}}$ (Equation A.6) and $V_{\rm radio} = 4433\,{\rm km\,s^{-1}}$ (Equation A.4). For a $V_{\rm opt}^{\rm rot} = 250\,{\rm km\,s^{-1}}$, this results in $V_{\rm rel}^{\rm rot} = 246\,{\rm km\,s^{-1}}$ (Equation A.8) and $V_{\rm radio}^{\rm rot} = 242\,{\rm km\,s^{-1}}$ (Equation A.9).

Therefore, to avoid the effects of different velocity conventions and compression, all EDGE and CALIFA velocity fields are converted to the relativistic convention using Equations A.7 and A.6 respectively. All velocities are reported in this convention unless otherwise noted.

A.2 Beam Smearing Correction

In order to accurately measure the CO and Hγ velocity dispersions, a beam smearing correction must be applied to the data cubes. As the beam size increases, rotation velocities from different radii can be blended into the linewidth. To correct for this effect, we fit a rotation-only model to the CO and Hα rotation curves and construct model rotation velocity fields. The smooth model rotation curve for each galaxy was constructed using the "Universal Rotation Curve" (hereafter referred to

as a Persic Profile) from Persic et al. (1996) which is given by

$$V_{\rm Persic}(x) = V(R_{\rm opt})\Bigg\{\Big[0.72 + 0.44\log(L_B/L_{B*})\Big]\frac{1.97x^{1.22}}{(x^2+0.78^2)^{1.43}} + 1.6\exp\Big[-0.6(L_B/L_{B*})\Big]\frac{x^2}{x^2+1.5^2(L_B/L_{B*})^{0.4}}\Bigg\}^{1/2} \ {\rm km\ s^{-1}} \tag{A.10}$$

where $x = R/R_{\rm opt}$. Persic et al. (1996) use $\log L_{B*} = 10.4$, where $L_{B*} = 6 \times 10^{10} h_{50}^{-2}\ L_{B\odot}$ (Persic & Salucci, 1991) with $h = 0.75$; we also adopt this value of L_{B*}. $R_{\rm opt}$ is the optical radius. The Persic Profile was fit to $V_{\rm rot}$ using a non-linear least squares fit with $V(R_{\rm opt})$, L_B, and $R_{\rm opt}$ left as parameters to be fit which are listed in Table A.1. Model velocity fields were derived from the Persic Profile fits using a linear interpolation and rotated and inclined based on the PA and inclination of the corresponding galaxy.

Using the rotation-only model velocity fields, we construct data cubes to simulate the effects of beam smearing. For the CO data, the channel width and spectral resolution are both $20\,{\rm km\,s^{-1}}$. For each spaxel in the simulated CO data cube, a line is placed at the channel corresponding to the model rotation velocity of that pixel. The amplitude of the line is given by the value of the CO data cube at that voxel. The linewidth is a single $20\,{\rm km\,s^{-1}}$ channel. All other channels in that spaxel have zero amplitude. For the Hγ however, the channel width is 0.7 Å ($48.4\,{\rm km\,s^{-1}}$) and the spectral resolution (FWHM) is 2.3 Å ($159.0\,{\rm km\,s^{-1}}$). Therefore, at each spaxel in the simulated Hγ cube, a Gaussian line is placed at the channel corresponding to the model rotation velocity at that pixel. The FWHM of the Gaussian line is 2.3 Å. The amplitude of the line is given by the value of the Hγ data cube at that

Name	CO V(R_{opt}) ($km\,s^{-1}$)	CO L_B ($\times 10^8$ $L_{B\odot}$)	CO R_{opt} ($''$)	Hα V(R_{opt}) ($km\,s^{-1}$)	Hα L_B ($\times 10^8$ $L_{B\odot}$)	Hα R_{opt} ($''$)
IC1199	168.7	2.8	7.2	181.7	8.8	14.4
NGC2253	145.9	1.7	6.3	146.6	2.0	10.5
NGC2347	233.5	4.5	4.9	211.0	7.5	5.4
NGC2410	198.8	2.5	10.9	175.1	9.8	4.3
NGC3815	167.0	10.0	10.7	147.3	2.1	9.3
NGC4047	174.8	10.0	6.4	177.9	10.0	10.1
NGC4644	164.7	1.7	10.0	144.6	3.3	9.9
NGC4711	131.1	9.4	12.6	138.4	10.0	16.1
NGC5016	161.9	9.5	13.5	166.1	10.0	18.0
NGC5480	90.7	9.9	6.7	110.3	10.0	18.6
NGC5520	133.7	10.0	5.7	117.7	5.9	5.8
NGC5633	165.2	10.0	11.3	148.4	2.9	9.6
NGC5980	181.6	2.9	7.8	184.1	3.4	13.1
UGC04132	199.8	10.0	10.7	207.2	10.0	15.5
UGC05111	197.1	3.8	15.5	203.1	5.4	19.9
UGC09067	185.8	2.1	8.0	169.9	7.4	7.7
UGC10384	171.0	3.2	12.7	147.6	2.8	10.8

$V(R_{opt})$, L_B, and R_{opt} for CO and Hα are the parameters from the Persic Profile fitting (Equation A.10).

Table A.1: Parameters for the Persic Profile Fits

voxel. These simulated data cubes are then convolved to the corresponding CO or Hγ beam size using the `convol` task in `Miriad`. Model velocity dispersion maps (sigmas, not FWHM) are created using the `moment` task in `Miriad`, which quantify the velocity dispersion due to beam smearing. These model velocity dispersion maps are removed in quadrature from the corresponding CO or Hγ velocity dispersion maps, yielding a beam smearing corrected velocity dispersion map. Since the simulated data cubes incorporate the instrumental linewidth, removing the simulated velocity dispersion map also corrects for the instrumental linewidth. The beam smearing corrected velocity dispersion maps are then masked to the same region where ΔV is calculated, which excludes the centers where the beam smearing corrections are large. Figure A.1 shows the stages of the beam smearing correction for both CO (a)

and Hγ (b) for NGC 2347. We note that after this masking, the difference between the beam smearing correction applied here and simply removing the instrumental linewidth in quadrature is $\sim$2 km s^{-1} over the whole KSS sample. Each CO and Hγ velocity dispersion map has a corresponding error map. The weighted average CO or Hγ velocity dispersion for each galaxy is

$$\langle\sigma\rangle = \frac{\Sigma(\sigma_i/\delta^2_{\sigma_i})}{\Sigma(1/\delta^2_{\sigma_i})} \tag{A.11}$$

where σ_i is the velocity dispersion and δ_{σ_i} is the error on the velocity dispersion at each pixel. The error on $\langle\sigma\rangle$ is the weighted standard deviation given by

$$\sigma_{\langle\sigma\rangle} = \sqrt{\frac{N}{\Sigma(1/\delta^2_{\sigma_i})}}. \tag{A.12}$$

The resulting beam smearing corrected average CO and Hγ velocity dispersions are listed in Table 2.1. A comparison of the CO and Hγ velocity dispersions is shown in Figure A.2 for the KSS galaxies. We note that previous measurements of CO velocity dispersions from HERACLES in bright GMCs are $\sim$ 7 km s^{-1} but increase to $\sim$ 12 km s^{-1} if a larger beam is used which encompasses more diffuse CO (Mogotsi et al., 2016). The EDGE data are at $\sim$kpc resolution and would encompass diffuse CO as well as denser GMCs, and the values we derive are consistent with these results.

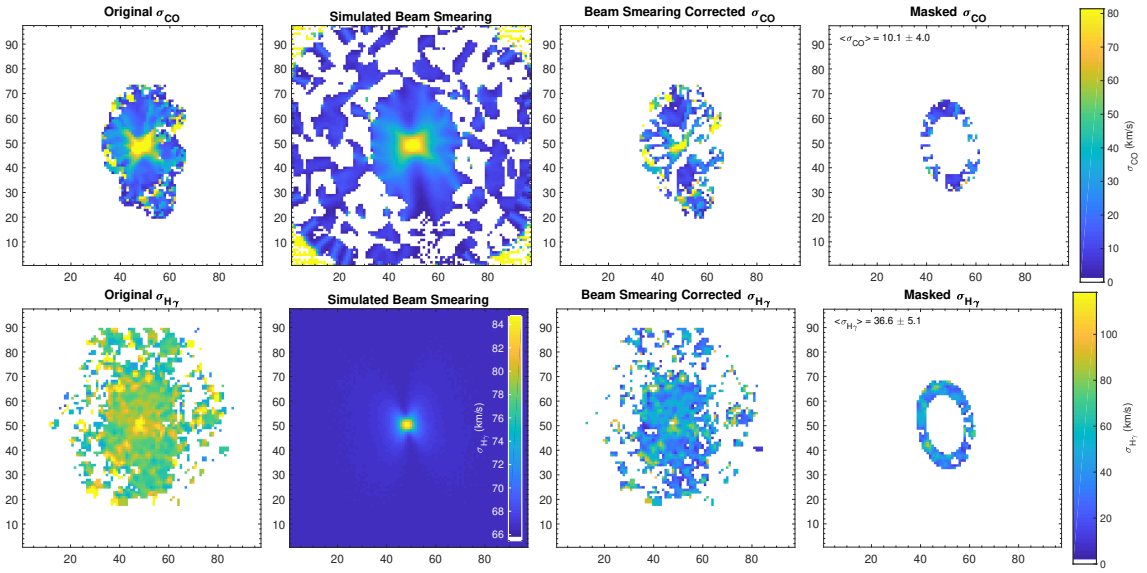

Figure A.1: The progression of the beam smearing correction for (top) CO and (bottom) Hγ for NGC 2347. From left to right, the panels show the original velocity dispersion map, the simulated velocity dispersion due to beam smearing, the beam smearing corrected velocity dispersion, and the masked beam smearing corrected velocity dispersion. All panels are normalized to the color scales shown to the right, except for the Hγ simulated beam smearing whose color scale is shown in the inset. White patches in the right two columns are where the simulated beam smearing is larger than the original velocity dispersion and are imaginary when removed in quadrature. These points are discarded for the analysis.

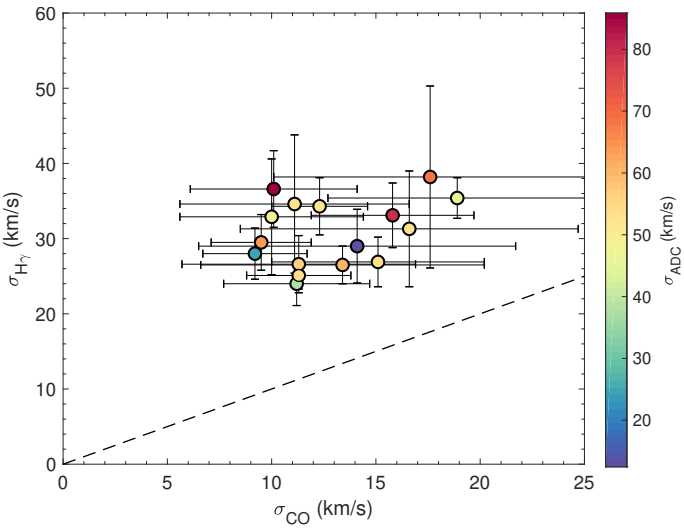

Figure A.2: The beam smearing corrected CO and Hγ velocity dispersions for the KSS galaxies. Points are color-coded by the velocity dispersion inferred from the ADC. The dashed line is one-to-one.

A.3 Galaxy-by-Galaxy Data, Figures, and Descriptions

Kinematic parameters used for the EDGE and CALIFA data for all 126 galaxies are listed in Tables A.3 and A.3 respectively. If kinematic parameters could not be fit, values were taken from outer isophote photometry (Falcón-Barroso et al., 2017) or from HyperLeda. Previous work to determine kinematic position angles in a subset of the CALIFA galaxies has also been carried out by García-Lorenzo et al. (2015) and Barrera-Ballesteros et al. (2014, 2015). More details are in the table captions. The lack of trends with global parameters discussed in Section 2.5.3 are shown in Figure A.3. CO and Hα velocity fields and rotation curves are shown for each galaxy in the KSS in Figure A.4. Below we provide brief comments on each galaxy in the KSS.

IC 1199 — This galaxy's CO velocity field is somewhat patchy due to the SN masking; however, its CO rotation curve is excellent, having radial and systemic components near zero. The Hα rotation curve is interesting, as it flattens until $\sim$13" then rises to meet the CO rotation curve. The Hα rotation curve generally has small radial and systemic components, although there is some non-zero radial component where the Hα rotation curve flattens which may explain the disagreement between the CO and Hα rotation curves in this region. The Hα systemic velocity is non-zero in the center, but since that region is excluded this will not affect the results. Neither the HI W50 nor W90 agree with the CO or Hα rotation curves well.

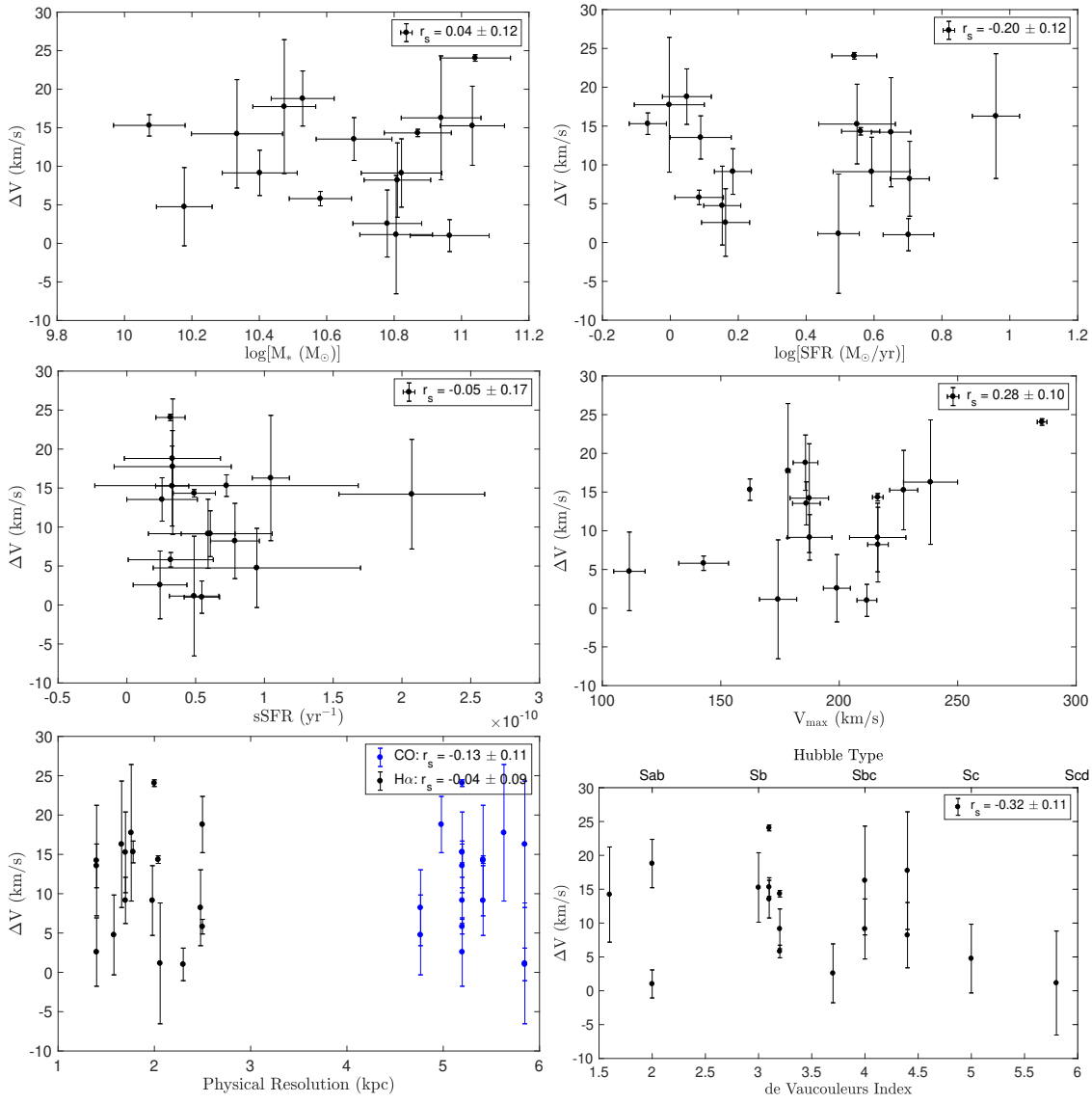

Figure A.3: There are no trends between ΔV and (top left) M_*, (top right) SFR, (middle left) sSFR, (middle right) CO V_{max}, (bottom left) physical resolution of the native (unconvolved) CO (blue) and Hα (black) data, and (bottom right) morphology. The Spearman rank correlation coefficients (r_s) are shown in the top right of each panel. de Vaucouleurs indexes are taken from HyperLeda. The lack of trend with physical resolution in particular justifies our choice to convolve to a common angular resolution rather than to a common physical resolution.

NGC 2253 — This galaxy's CO rotation curve is excellent, although there is a small trend in the radial component over the region of comparison. Its Hα rotation curve has large radial and systemic components in the center, but they are near zero over the comparison region. The CO and Hα rotation components cross, and the CO V_{rot} continues to rise despite the flattened Hα. Both the HI W50 and W90 are larger than the CO and Hα V_{rot}.

NGC 2347 — This galaxy is used as an example throughout this work. Overall, its CO and Hα rotation curves are excellent, and the ΔV is large and much greater than the errors on the rotation curves. Although there is a bump in the CO radial component in the comparison region, it likely cannot account for the ΔV. The HI W50 and W90 straddle the CO V_{rot}, potentially indicating that the Hα scale height in this galaxy is larger than the HI, which is closer to the CO scale height. This galaxy has a reported ring structure (Bolatto et al., 2017). It is also potentially an AGN candidate, based on its [OIII]/Hβ and [NII]/Hα ratios. However, since the central 12" ($\sim$4 kpc) are excluded from analysis, any AGN contamination should be minimal. This galaxy has a large bulge at redder optical wavelengths, with a bulge-to-disk ratio of 0.3 in g-band, 0.7 in r-band, and 1.1 in i-band and an average bulge effective radius of 3.5 ± 0.5 kpc (Méndez-Abreu et al., 2017), so bulge contamination is possible.

NGC 2410 — Although this galaxy does exhibit non-zero CO and Hα radial and systemic components over the comparison region, the components all track one

another so their effects on ΔV should be minimal. There is a kinematic twist visible in the Hα velocity field, which is likely responsible for the varying Hα radial component. This feature is less obvious in the CO velocity field. This galaxy has a bar, as listed in Bolatto et al. (2017), which is the likely source of this twist. Both the HI W50 and W90 are higher than the CO V_{rot}.

NGC 3815 — Although this galaxy has non-zero radial and systemic components over the comparison region, they track each other so the effect on ΔV should be minimal. The CO and Hα systemic components are near zero. At large radii, the Hα $V_{rot}$is consistent with the HI W50, whereas the W90 is much larger than both the CO and Hα V_{rot}.

NGC 4047 — This galaxy has excellent CO and Hα rotation curves and velocity fields. At large radii, the HI W50 appears to be consistent with the Hα V_{rot} and potentially the CO V_{rot}. The W90 is much larger.

NGC 4644 — The galaxy has excellent CO and Hα rotation curves, with small radial and systemic components overall. Interestingly, this galaxy is listed as having a bar and being a merger (Bolatto et al., 2017), although there are no obvious signs of either from the velocity fields or rotation curves. The HI W50 tends to agree with the Hα V_{rot}.

NGC 4711 — This galaxy has a warp in the center, as seen in the Hα velocity field and rotation component of the rotation curve. It is listed as having a bar (Bolatto

et al., 2017), which likely accounts for these features. These are not seen in the CO velocity field or rotation curve. Although both the CO and Hα have non-zero radial components in the comparison region, they track each other closely so their effect on ΔV is likely small. Neither the CO nor Hα rotation curve flattens over the radii probed, so it is unclear whether the HI W50 or W90 agree with either.

NGC 5016 — The $V_{\rm rad}$ and $V_{\rm sys}$ components for CO and Hα are nearly zero over the comparison region, although they deviate at small and large radii. This galaxy has a bar (Bolatto et al., 2017), although it is not obvious from either velocity field. The HI W50 and W90 are more consistent with $\rm V_{rot}$(CO), at least over the comparison region.

NGC 5480 — Neither the CO nor Hα rotation curve for this galaxy flattens out to large radii. It has small radial and systemic components over the comparison region, although there is a decreasing trend in the both of these components in Hα. HI data is taken from Springob et al. (2005) using the Green Bank 300 ft telescope.

NGC 5520 — The difference between the CO and Hα rotation velocity is striking in this galaxy. The radial and systemic components are all consistent with zero. The Hα rotation curve flattens quickly. The HI data agree well with the CO rotation velocity.

NGC 5633 — The CO and Hα rotation velocities are remarkably similar and only begin to deviate in the comparison region. Although there are trends in the radial

and systemic components in the center, they are near zero over the radii of interest. This galaxy in known to have a ring structure (Bolatto et al., 2017). HI data is taken from Springob et al. (2005) using the Green Bank 300 ft telescope.

NGC 5980 — This galaxy's CO rotation curve flattens, whereas the Hα rotation curve continues to rise slightly. Although the radial and systemic components dip in the center, they are near zero over the radii of interest. There is a kinematic twist visible in both the CO and Hα velocity fields, which likely causes the dip in the radial and systemic components. The HI W50 is close to V_{rot}(CO), but the W90 is higher.

UGC 4132 — There is an interesting dip in the Hα rotation curve that is not visible in the CO rotation curve. There is a slight trend in the Hα radial and systemic components. The HI W50 is close to the CO rotational velocity, but the W90 is substantially larger.

UGC 5111 — The CO and Hα velocity fields look different near the major axis; in the Hα velocity fields there are thin regions of high velocities whereas these larger velocities are not as concentrated along the major axis in the CO velocity field. The radial and systemic components are small over all radii. There is not HI data available for this galaxy from either our GBT observations or from Springob et al. (2005).

UGC 9067 — The galaxy's CO and Hα rotation velocities are nearly identical. Both the CO and Hα radial components are increasing over the comparison region but have the same values. HI data is taken from Springob et al. (2005) using the Arecibo telescope (line feed system).

UGC 10384 — This galaxy has small radial and systemic components over the region of interest, although there are small deviations at small and large radii. The rotation components are identical at small radii, but diverge as the Hα rotation curve flattens while the CO rotation curve continues to rise. The HI W50 and W90 are more consistent with the CO rotation velocity than the Hα.

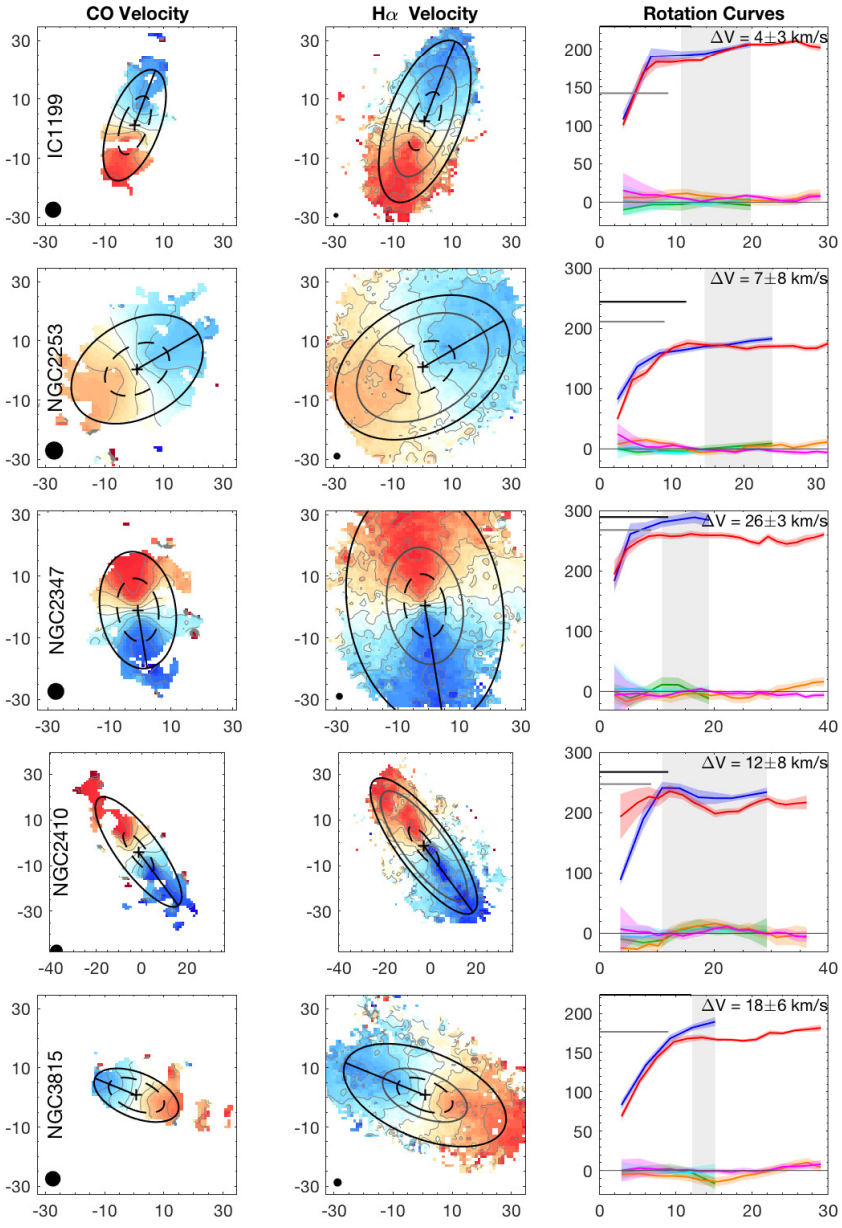
CO Velocity
Hα Velocity
Rotation Curves
IC1199
NGC2253
NGC2347
NGC2410
NGC3815
ΔV = 4±3 km/s
ΔV = 7±8 km/s
ΔV = 26±3 km/s
ΔV = 12±8 km/s
ΔV = 18±6 km/s

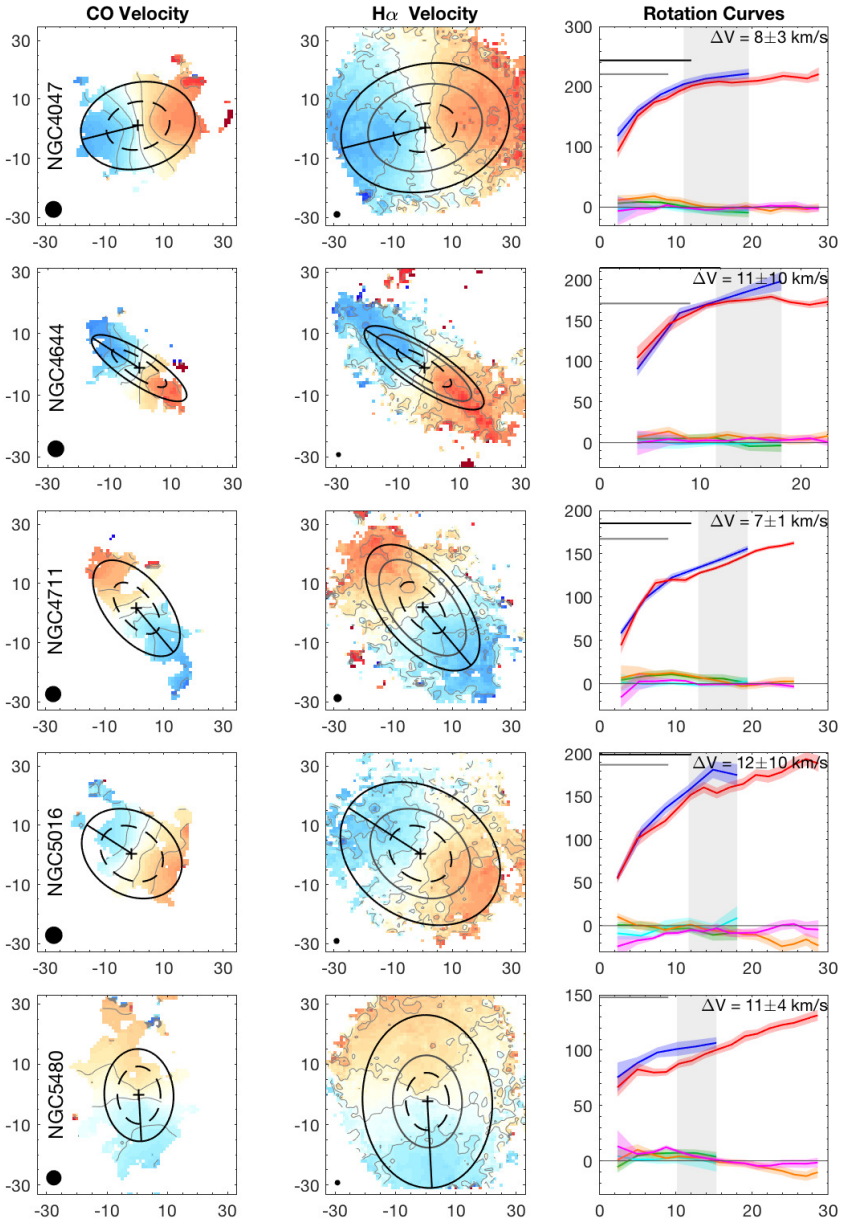
CO Velocity
Hα Velocity
Rotation Curves
NGC4047
NGC4644
NGC4711
NGC5016
NGC5480
ΔV = 8±3 km/s
ΔV = 11±10 km/s
ΔV = 7±1 km/s
ΔV = 12±10 km/s
ΔV = 11±4 km/s

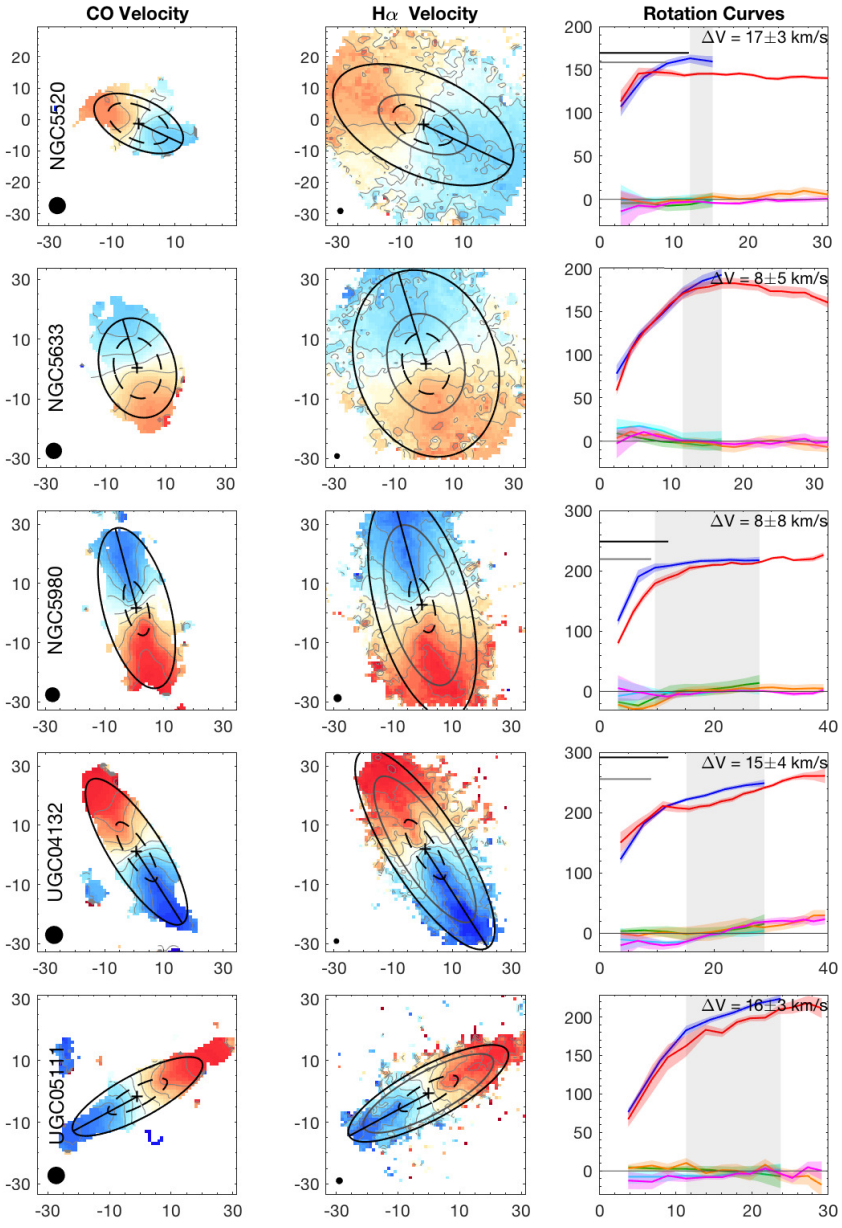
CO Velocity
Hα Velocity
Rotation Curves
NGC5520
NGC5633
NGC5980
UGC04132
UGC05111
ΔV = 17±3 km/s
ΔV = 8±5 km/s
ΔV = 8±8 km/s
ΔV = 15±4 km/s
ΔV = 16±3 km/s

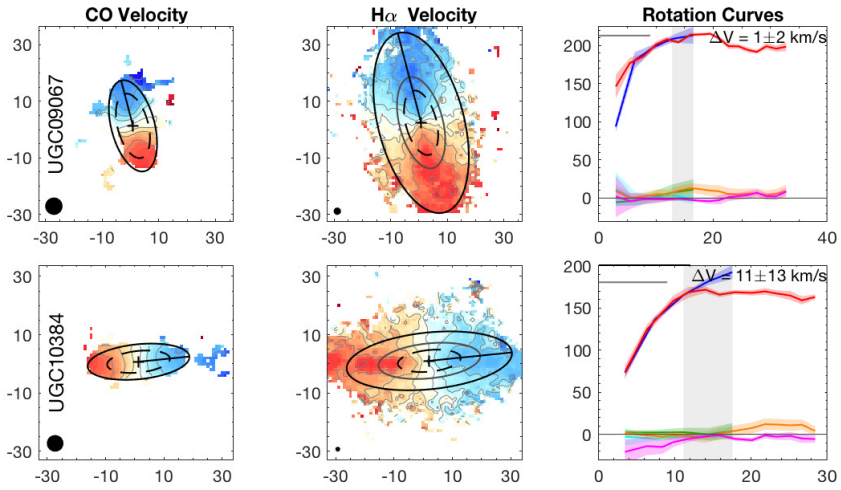

Figure A.4: The left column shows the CO velocity fields for the KSS galaxies. The color scale spans $\pm 300\,\mathrm{km\,s^{-1}}$, with negative velocities showing the approaching side in blue. Isovelocity contours are shown in gray spanning $\pm 300\,\mathrm{km\,s^{-1}}$ in $50\,\mathrm{km\,s^{-1}}$ increments. The values on the x- and y-axes show the offset in arcsec from the center position. The solid black circle shows the 6" beam size. The cross marks the kinematic center of the galaxy. The black line shows the semimajor axis. The black solid ellipse shows the orientation, and the size corresponds to the outermost ring in the rotation curve. The dashed ellipse indicates twice the CO beam; points within this ellipse are excluded from the rotation curve comparison due to possible beam smearing. The center column shows the Hα velocity fields. The color scale also spans $\pm 300\,\mathrm{km\,s^{-1}}$. The solid black circle shows the 6" beam size, the cross marks the kinematic center of the galaxy, and the solid black line shows the semimajor axis. The solid black ellipse shows the orientation, and the size corresponds to the outermost ring in the Hα rotation curve. The gray ellipse shows the outermost CO ring (the same as the black ellipse in the CO velocity panels). The right column shows the CO and Hα rotation curves. The x-axis is galactocentric radius ($''$) and the y-axis is velocity ($\mathrm{km\,s^{-1}}$). The colored curves show CO $V_{\rm rot}$ (blue), $V_{\rm rad}$ (green), and $V_{\rm sys}$ (cyan), and Hα $V_{\rm rot}$ (red), $V_{\rm rad}$ (orange), and $V_{\rm sys}$ (magenta). The colored shaded regions around the curves show the errors on the rotation curve components from the Monte Carlo analysis. The gray shaded region shows the radii over which the CO and Hα rotation curves are compared, where the inner radius is twice the CO beam size and the outer radius is the furthest CO extent. The ΔV in the upper right corner is the median difference between the CO and Hα $V_{\rm rot}$ over the gray region, and the error is the standard deviation of the differences at each radius. The thin solid gray line marks $V = 0$. The gray and black horizontal line segments show the HI rotation velocity from W50 and W90, respectively. All HI data have been corrected for inclination, using the values in Table A.3.

Name	RA	Dec	PA	Inc	V_{sys}	X_{off}	Y_{off}	PA Flag	Inc Flag	V_{sys} Flag
	(J2000)	(J2000)	(°)	(°)	($km\,s^{-1}$)	(″)	(″)			
ARP220	233.73900	23.50270	337.7	29.7	5247	0.0	0.0	P	P	C
IC0480	118.84665	26.74280	167.9	76.6	4595	0.0	0.0	P	P	C
IC0540	142.54290	7.90259	350.0	68.3	2022	0.0	0.0	P	P	C
IC0944	207.87900	14.09200	105.7	75.0	6907	0.0	0.0	P	C	C
IC1151	239.63550	17.44150	203.9	68.0	2192	0.0	0.0	C	P	C
IC1199	242.64300	10.04010	339.3	64.5	4686	0.6	1.1	C	P	C
IC1683	20.66190	34.43700	15.6	54.8	4820	0.0	0.0	P	C	C
IC2247	123.99615	23.19960	328.5	77.7	4254	0.0	0.0	P	P	C
IC2487	142.53840	20.09090	162.9	77.9	4310	0.0	0.0	P	P	C
IC4566	234.17550	43.53940	145.0	53.9	5537	0.0	0.0	C	P	C
IC5376	0.33233	34.52570	3.4	71.6	4979	0.0	0.0	P	P	C
NGC0444	18.95685	31.08020	158.7	74.9	4776	0.0	0.0	P	P	H
NGC0447	18.90660	33.06760	227.0	29.1	5552	0.8	0.8	C	P	C
NGC0477	20.33475	40.48820	140.0	60.0	5796	0.0	0.0	C	P	C
NGC0496	20.79810	33.52890	36.5	57.0	5958	-0.4	1.6	C	P	C
NGC0523	21.33660	34.02500	277.2	71.6	4760	0.0	0.0	C	P	C
NGC0528	21.38985	33.67150	57.7	61.1	4638	-3.0	1.8	P	P	H
NGC0551	21.91935	37.18290	315.0	64.2	5141	0.0	0.0	C	P	C
NGC1167	45.42660	35.20570	87.5	39.5	4797	-6.5	3.5	C	P	C
NGC2253	100.92420	65.20620	300.0	47.4	3545	0.0	0.0	C	P	C
NGC2347	109.01625	64.71080	189.1	50.2	4387	2.5	1.9	P	P	C
NGC2410	113.75940	32.82210	216.6	71.6	4642	0.0	0.0	C	P	C
NGC2480	119.29350	23.77980	343.1	55.4	2287	0.0	0.0	C	P	C
NGC2486	119.48535	25.16080	92.9	55.6	4569	0.0	0.0	P	P	H
NGC2487	119.58540	25.14920	117.5	31.4	4795	0.0	0.0	C	P	C
NGC2623	129.60000	25.75410	255.0	45.6	5454	0.0	0.0	C	P	C
NGC2639	130.90845	50.20540	314.3	49.5	3162	-1.4	0.6	C	P	C
NGC2730	135.56580	16.83830	260.8	27.7	3802	0.0	0.0	P	P	C
NGC2880	142.39410	62.49060	322.9	49.9	1530	0.0	0.0	P	P	H
NGC2906	143.02605	8.44159	262.0	55.7	2133	0.0	0.0	C	P	C
NGC2916	143.73990	21.70520	199.9	49.9	3620	0.0	0.0	P	P	C
NGC2918	143.93355	31.70550	75.1	46.1	6569	0.0	0.0	P	P	H
NGC3303	159.25050	18.13570	159.6	60.5	6040	0.0	0.0	P	P	H
NGC3381	162.10350	34.71140	333.1	30.8	1625	0.0	0.0	C	P	H
NGC3687	172.00200	29.51100	326.0	19.6	2497	0.0	0.0	C	P	H
NGC3811	175.32000	47.69080	351.5	39.9	3073	-2.6	0.1	P	P	C
NGC3815	175.41300	24.80040	67.8	59.9	3686	3.0	0.1	P	P	C
NGC3994	179.40300	32.27730	188.1	59.5	3097	2.4	1.6	P	P	C
NGC4047	180.71100	48.63620	104.0	42.1	3419	0.5	0.0	C	P	C
NGC4149	182.63700	58.30410	85.0	66.2	3050	-0.5	-0.9	C	P	C
NGC4185	183.34200	28.51100	344.4	48.2	3874	0.0	0.0	P	P	C
NGC4210	183.81600	65.98540	277.7	40.9	2714	0.0	0.0	P	P	C
NGC4211NED02	183.90600	28.16960	25.0	30.0	6605	0.0	0.0	C	C	C
NGC4470	187.40700	7.82390	349.5	47.5	2338	0.0	0.0	C	P	C
NGC4644	190.67850	55.14550	57.0	72.9	4915	-3.2	-0.1	P	P	C
NGC4676A	191.54250	30.73210	185.3	50.0	6541	-2.1	-0.8	C	C	C
NGC4711	192.19050	35.33270	220.0	58.3	4044	3.0	0.6	C	P	C
NGC4961	196.44900	27.73390	100.0	46.6	2521	-2.2	0.4	C	P	C
NGC5000	197.44800	28.90680	31.3	20.0	5557	0.0	0.0	C	C	C
NGC5016	198.02850	24.09500	57.4	39.9	2588	-0.1	-0.6	P	P	C
NGC5056	199.05150	30.95020	178.0	61.4	5544	-1.0	1.0	C	L	C
NGC5205	202.51500	62.51150	169.0	49.8	1762	0.0	0.0	P	P	C
NGC5218	203.04300	62.76780	236.4	30.1	2888	0.0	0.0	C	P	C
NGC5394	209.64000	37.45350	189.3	70.2	3431	0.0	0.0	C	P	C
NGC5406	210.08400	38.91540	111.4	45.0	5350	0.0	0.0	P	P	C
NGC5480	211.59000	50.72510	183.0	41.5	1879	-0.9	-0.4	C	L	C

Continued on next page

Name	RA	Dec	PA	Inc	V_{sys}	X_{off}	Y_{off}	PA Flag	Inc Flag	V_{sys} Flag
	(J2000)	(J2000)	(°)	(°)	($km\,s^{-1}$)	($''$)	($''$)			
NGC5485	211.79700	55.00160	74.5	47.2	1893	2.0	-0.6	C	P	H
NGC5520	213.09450	50.34850	245.1	59.1	1870	1.1	0.4	C	P	C
NGC5614	216.03150	34.85890	270.0	35.9	3859	0.0	0.0	C	P	C
NGC5633	216.86850	46.14640	16.9	41.9	2319	0.0	0.0	P	P	C
NGC5657	217.68150	29.18070	349.0	68.3	3860	2.1	0.2	C	P	C
NGC5682	218.68800	48.66950	310.6	76.3	2242	-0.9	1.7	C	P	H
NGC5732	220.16250	38.63770	43.2	58.4	3723	-2.0	-0.2	P	P	C
NGC5784	223.56900	42.55780	255.0	45.0	5427	-2.1	0.6	C	C	C
NGC5876	227.38200	54.50650	51.4	65.9	3240	-0.1	0.6	P	P	H
NGC5908	229.18050	55.40940	153.0	77.0	3294	0.0	0.0	C	C	C
NGC5930	231.53250	41.67610	155.0	45.0	2637	2.2	0.1	C	C	C
NGC5934	232.05300	42.92990	5.0	55.0	5566	0.0	0.0	C	C	C
NGC5947	232.65300	42.71720	248.6	32.2	5898	-0.9	0.1	C	P	C
NGC5953	233.63550	15.19380	48.3	26.0	1988	-1.0	0.4	C	C	C
NGC5980	235.37700	15.78760	15.0	66.2	4060	-1.0	1.0	L	P	C
NGC6004	237.59400	18.93920	272.3	37.3	3818	3.2	1.1	C	P	C
NGC6021	239.37750	15.95600	157.1	43.4	4673	1.7	-0.1	P	P	H
NGC6027	239.80200	20.76330	231.4	30.9	4338	0.0	0.0	P	P	H
NGC6060	241.46700	21.48490	102.0	64.3	4416	-1.2	-0.2	P	P	C
NGC6063	241.80450	7.97887	331.6	56.2	2807	0.0	0.0	C	P	H
NGC6081	243.23700	9.86703	308.2	65.6	4978	0.0	0.0	P	P	H
NGC6125	244.79850	57.98410	4.8	16.9	4522	0.0	0.0	P	P	H
NGC6146	246.29250	40.89260	78.3	40.7	8693	0.0	0.0	C	P	H
NGC6155	246.53400	48.36680	130.0	44.7	2418	3.0	3.0	C	P	C
NGC6168	247.83750	20.18550	111.1	76.6	2540	0.0	0.0	L	P	C
NGC6186	248.60700	21.54090	64.6	71.2	2940	-3.0	0.5	C	L	C
NGC6301	257.13600	42.33900	288.5	52.8	8222	0.0	0.0	P	P	C
NGC6310	256.98900	60.99010	69.9	73.7	3459	0.0	0.0	P	P	C
NGC6314	258.16200	23.27020	356.0	57.7	6551	-2.2	0.0	C	P	C
NGC6361	259.67100	60.60810	46.8	75.0	3791	0.0	0.0	C	C	C
NGC6394	262.59000	59.63990	237.4	60.0	8453	0.0	0.0	C	C	C
NGC6478	267.15900	51.15720	29.2	73.4	6756	0.0	0.0	C	C	C
NGC7738	356.00850	0.51671	234.7	65.6	6682	0.0	0.0	C	P	C
NGC7819	1.10206	31.47200	270.3	54.0	4918	0.0	0.0	C	P	C
UGC00809	18.96615	33.81070	18.6	78.9	4171	0.0	0.0	C	P	C
UGC03253	79.92345	84.05250	267.7	58.3	4040	0.0	0.0	P	P	H
UGC03539	102.22470	66.26130	302.9	72.1	3278	0.0	0.0	C	P	C
UGC03969	115.30965	27.61410	134.3	70.0	8029	0.0	0.0	P	C	C
UGC03973	115.63560	49.80980	143.8	39.1	6594	0.5	-1.8	C	P	C
UGC04029	117.07920	34.33220	63.5	77.6	4389	0.0	0.0	C	P	C
UGC04132	119.80425	32.91490	212.6	72.0	5151	0.0	-0.8	C	P	C
UGC04280	123.63885	54.79950	183.7	71.5	3500	0.0	0.0	P	P	C
UGC04461	128.34450	52.53230	222.8	70.1	4941	0.0	0.0	C	P	C
UGC05108	143.85960	29.81260	136.1	66.1	8015	0.0	0.0	C	P	C
UGC05111	144.21855	66.78840	118.3	72.9	6660	2.0	-1.0	C	P	C
UGC05244	147.20070	64.16800	32.8	77.9	2974	0.0	0.0	P	P	H
UGC05359	149.71530	19.21500	94.5	72.3	8344	-0.9	0.8	C	P	C
UGC05498NED01	153.01500	23.08540	61.8	81.0	6250	0.0	0.0	C	C	H
UGC05598	155.55900	20.58940	215.6	74.8	5591	0.0	0.0	P	P	C
UGC06312	169.50000	7.84466	224.6	68.7	6266	0.0	0.0	C	P	H
UGC07012	180.51300	29.84810	184.1	60.5	3052	0.0	0.0	C	P	H
UGC08107	194.91600	53.34130	228.2	71.4	8201	0.0	0.0	C	P	C
UGC08250	197.58450	32.48260	11.7	76.2	5169	0.0	0.0	C	P	H
UGC08267	197.79750	43.72650	223.0	75.4	7159	-1.0	0.0	C	P	C
UGC09067	212.68950	15.20920	14.6	62.4	7740	0.0	0.0	C	P	C
UGC09476	220.38300	44.51270	307.0	48.5	3243	0.0	0.0	C	P	C
UGC09537	222.11100	34.99800	135.7	72.0	8662	0.0	0.0	C	C	C
UGC09542	222.25500	42.46400	214.3	72.7	5417	2.1	-1.9	P	P	C

Continued on next page

Name	RA (J2000)	Dec (J2000)	PA (°)	Inc (°)	V_{sys} ($km\,s^{-1}$)	X_{off} (″)	Y_{off} (″)	PA Flag	Inc Flag	V_{sys} Flag
UGC09665	225.38550	48.31980	138.2	74.0	2561	0.0	0.0	P	P	C
UGC09759	227.67000	55.35040	49.7	66.8	3394	3.6	-2.1	P	P	C
UGC09873	232.46100	42.62900	129.0	75.3	5575	0.0	0.0	C	P	C
UGC09892	233.21700	41.19140	101.0	72.2	5591	0.0	0.0	P	P	C
UGC09919	233.91450	12.60630	349.2	77.9	3160	0.0	0.0	P	P	C
UGC10043	237.17250	21.86950	327.8	90.0	2154	-2.4	-0.6	C	L	C
UGC10123	239.76150	51.30460	231.6	70.0	3738	3.6	-0.4	C	C	C
UGC10205	241.66800	30.09900	128.6	51.7	6491	0.0	0.0	C	P	C
UGC10331	244.33800	59.32010	140.8	76.2	4415	0.0	0.0	P	P	H
UGC10380	246.45750	16.57610	288.2	77.9	8624	0.0	0.0	P	P	C
UGC10384	246.69450	11.58020	275.8	70.0	4927	0.0	0.0	C	C	C
UGC10710	256.71900	43.12210	329.5	69.6	8228	0.0	0.0	L	P	C

The table lists the geometric parameters used for the EDGE data for each galaxy. RA and Dec values are taken from Bolatto et al. (2017). The V_{sys} values are reported in the relativistic convention. PA Flag, Inc Flag, and V_{sys} Flag indicate whether those respective values were derived from CO kinematic fits (C) or Hα kinematic fits (H) done in this work, from photometric fits to the outer isophotes (P, Falcón-Barroso et al., 2017), or from HyperLeda (L).

Table A.2: Geometric Parameters for the EDGE Data

Name	R_e (″)	V500 V_{sys} ($km\,s^{-1}$)	V500 X_{off} (″)	V500 Y_{off} (″)	V1200 V_{sys} ($km\,s^{-1}$)	V1200 X_{off} (″)	V1200 Y_{off} (″)
ARP220	12.7	5294	0.0	0.0	5247	0.0	0.0
IC0480	11.5	4553	0.0	0.0	4518	0.0	0.0
IC0540	14.9	2050	0.0	0.0	2043	0.0	0.0
IC0944	9.8	6854	0.2	2.5	6805	-2.5	3.4
IC1151	19.3	2122	0.0	0.0	2114	0.0	0.0
IC1199	18.8	4636	0.0	2.5	4625	0.3	3.0
IC1683	10.0	4787	-3.4	1.4	4704	-3.0	3.4
IC2247	16.3	4218	0.4	0.6	4188	0.0	0.0
IC2487	16.8	4281	0.0	0.0	4250	0.0	0.0
IC4566	13.2	5504	1.2	0.1	5453	1.2	0.1
IC5376	11.6	4944	0.0	0.0	4903	0.0	0.0
NGC0444	17.4	4776	-4.0	2.6	4738	-4.0	2.6
NGC0447	18.6	5489	0.8	0.8	5439	0.8	0.8
NGC0477	18.6	5794	0.0	0.0	5738	0.0	0.0
NGC0496	16.5	5966	-3.0	3.0	5898	0.4	2.1
NGC0523	8.1	4719	0.0	0.0	4682	0.0	0.0
NGC0528	9.0	4638	-3.7	0.7	4602	-3.7	0.7
NGC0551	14.4	5106	0.0	0.0	5091	-0.9	1.6
NGC1167	21.6	4875	-6.6	2.3	4835	-6.6	2.3
NGC2253	4.1	3530	2.4	0.6	3540	1.1	2.1
NGC2347	13.8	4383	3.6	3.3	4373	1.9	3.6
NGC2410	17.9	4650	1.6	2.6	4648	0.9	0.9
NGC2480	10.8	2305	0.0	0.0	2296	0.0	0.0
NGC2486	13.0	4569	0.0	0.0	4534	0.0	0.0
NGC2487	18.8	4808	0.0	0.0	4769	0.0	0.0
NGC2623	11.9	5440	2.5	0.5	5391	2.5	0.5
NGC2639	13.4	3157	-1.1	-2.6	3142	1.9	2.3
NGC2730	14.6	3773	0.0	0.0	3749	0.0	0.0
NGC2880	13.7	1530	0.0	0.0	1526	0.0	0.0
NGC2906	15.2	2142	1.6	0.5	2140	-0.1	2.1
NGC2916	20.6	3664	0.0	0.0	3642	0.0	0.0
NGC2918	9.3	6569	-0.6	2.4	6497	-0.6	2.4

Continued on next page

Name	R_e ($''$)	V500 V_{sys} (km s^{-1})	V500 X_{off} ($''$)	V500 Y_{off} ($''$)	V1200 V_{sys} (km s^{-1})	V1200 X_{off} ($''$)	V1200 Y_{off} ($''$)
NGC3303	9.2	6040	0.0	0.0	5979	0.0	0.0
NGC3381	14.8	1625	0.0	0.0	1621	0.0	0.0
NGC3687	15.4	2497	3.2	0.1	2487	3.2	0.1
NGC3811	14.7	3061	-2.6	0.1	3071	-1.0	0.0
NGC3815	8.8	3690	3.0	0.1	3648	1.6	2.1
NGC3994	7.1	3089	3.2	1.0	3055	1.6	1.5
NGC4047	14.8	3376	1.2	-0.7	3396	0.9	2.0
NGC4149	11.5	3042	-0.5	-0.9	3027	-0.5	-0.9
NGC4185	22.6	3831	0.0	0.0	3807	0.0	0.0
NGC4210	16.9	2689	2.6	3.1	2687	-1.4	2.1
NGC4211NED02	14.0	6555	0.0	0.0	6483	0.0	0.0
NGC4470	11.5	2319	3.2	0.5	2310	3.2	0.5
NGC4644	14.3	4889	-1.2	0.0	4885	-2.9	-0.9
NGC4676A	13.5	6518	-2.1	-0.8	6447	-2.1	-0.8
NGC4711	12.3	4044	4.0	0.8	4007	2.5	0.0
NGC4961	9.7	2528	-2.2	0.4	2517	-2.2	0.4
NGC5000	10.2	5505	0.0	0.0	5454	0.0	0.0
NGC5016	15.3	2539	-0.1	-0.6	2586	-1.9	0.5
NGC5056	13.8	5530	-1.5	1.0	5453	-0.4	0.9
NGC5205	16.4	1743	0.0	0.0	1738	0.0	0.0
NGC5218	12.3	2855	0.0	0.0	2841	0.0	0.0
NGC5394	16.8	3404	0.0	0.0	3385	0.0	0.0
NGC5406	14.9	5313	0.0	0.0	5331	-0.8	0.9
NGC5480	17.4	1851	-0.9	-2.5	1908	-3.5	-0.3
NGC5485	21.8	1893	2.0	-0.6	1887	2.0	-0.6
NGC5520	11.9	1852	3.0	0.0	1893	1.8	1.1
NGC5614	15.7	3824	3.4	-0.6	3800	3.4	-0.6
NGC5633	12.9	2295	0.0	1.5	2290	3.1	1.8
NGC5657	11.6	3861	3.1	-0.5	3836	3.1	-0.5
NGC5682	19.6	2242	0.0	1.1	2234	0.0	1.1
NGC5732	12.3	3703	-1.0	-0.6	3680	-1.0	-0.6
NGC5784	11.9	5420	-0.4	2.5	5307	-2.4	-0.4
NGC5876	15.1	3240	1.0	0.5	3222	1.0	0.5
NGC5908	14.6	3258	1.0	-0.3	3240	1.0	-0.3
NGC5930	14.4	2590	3.4	-0.1	2579	3.4	-0.1
NGC5934	6.7	5556	2.5	-1.2	5505	2.5	-1.2
NGC5947	10.5	5863	-3.2	2.4	5811	-3.2	-0.1
NGC5953	9.1	1967	0.1	0.0	1961	0.1	0.0
NGC5980	12.6	4049	0.0	2.0	4021	-0.9	0.3
NGC6004	20.4	3781	4.4	0.8	3757	4.4	0.8
NGC6021	8.5	4673	2.6	-0.4	4637	2.6	-0.4
NGC6027	10.8	4338	0.0	0.0	4307	0.0	0.0
NGC6060	20.2	4337	0.0	0.0	4306	0.0	0.0
NGC6063	17.8	2807	0.0	0.0	2794	0.0	0.0
NGC6081	10.4	4978	0.0	0.0	4937	0.0	0.0
NGC6125	15.4	4522	0.0	0.0	4488	0.0	0.0
NGC6146	11.0	8693	0.0	0.0	8567	0.0	0.0
NGC6155	13.5	2381	4.0	1.0	2396	-1.4	0.4
NGC6168	16.3	2505	0.0	0.0	2495	0.0	0.0
NGC6186	12.7	2910	-3.0	0.5	2896	-3.0	0.5
NGC6301	20.0	8221	3.5	-0.8	8118	2.0	-0.5
NGC6310	15.8	3377	0.0	0.0	3358	0.0	0.0
NGC6314	8.7	6493	-2.2	0.0	6423	-2.2	0.0
NGC6361	15.4	3759	0.0	0.0	3714	3.3	-2.4
NGC6394	9.0	8387	0.0	0.0	8261	-0.6	0.5
NGC6478	17.4	6735	0.0	0.0	6659	0.0	0.0
NGC7738	11.5	6642	0.0	0.0	6568	0.0	0.0
NGC7819	15.0	4898	0.0	0.0	4858	0.0	0.0

Continued on next page

Name	R_e ($''$)	V500 V_{sys} ($km\,s^{-1}$)	V500 X_{off} ($''$)	V500 Y_{off} ($''$)	V1200 V_{sys} ($km\,s^{-1}$)	V1200 X_{off} ($''$)	V1200 Y_{off} ($''$)
UGC00809	11.0	4143	-3.0	1.0	4114	0.0	0.0
UGC03253	12.7	4040	0.0	0.0	4013	0.0	0.0
UGC03539	13.7	3244	2.8	4.6	3250	-1.4	3.3
UGC03969	11.2	8001	0.0	0.0	7896	-2.4	-0.5
UGC03973	9.9	6551	0.5	-1.8	6479	0.5	-1.8
UGC04029	15.0	4367	0.0	0.0	4335	0.0	0.0
UGC04132	13.2	5158	0.0	0.0	5105	0.2	0.6
UGC04280	11.2	3485	0.0	0.0	3465	0.0	0.0
UGC04461	11.9	4954	0.0	0.0	4913	0.0	0.0
UGC05108	9.6	7987	-1.0	1.0	7881	0.0	0.0
UGC05111	12.7	6657	0.0	0.0	6557	3.4	-1.3
UGC05244	12.6	2974	-0.5	-5.0	2959	-2.0	-4.0
UGC05359	12.4	8332	0.0	0.0	8226	-0.4	1.5
UGC05498NED01	10.5	6250	0.0	0.0	6185	0.0	0.0
UGC05598	11.4	5601	0.0	0.0	5549	0.0	0.0
UGC06312	12.8	6266	0.0	0.0	6201	0.0	0.0
UGC07012	11.9	3052	0.0	0.0	3036	0.0	0.0
UGC08107	17.7	8199	0.0	0.0	8139	-0.4	2.5
UGC08250	11.8	5169	0.0	0.0	5124	0.0	0.0
UGC08267	10.5	7102	-0.4	0.3	7018	-0.4	0.3
UGC09067	11.3	7733	0.1	1.1	7661	1.0	0.0
UGC09476	15.5	3201	0.0	0.0	3184	0.0	0.0
UGC09537	15.8	8653	0.0	0.0	8528	0.0	0.0
UGC09542	12.9	5399	1.2	-0.4	5350	1.2	-0.4
UGC09665	11.6	2511	0.0	0.0	2500	0.0	0.0
UGC09759	13.5	3397	3.6	-2.1	3378	3.6	-2.1
UGC09873	14.8	5533	0.0	0.0	5482	0.0	0.0
UGC09892	13.7	5582	0.0	0.0	5530	0.0	0.0
UGC09919	13.1	3167	0.0	0.0	3150	0.0	0.0
UGC10043	24.6	2128	-0.5	-1.0	2120	-1.5	-1.0
UGC10123	11.0	3701	4.8	-0.5	3709	3.6	-0.4
UGC10205	14.0	6445	0.0	0.0	6376	0.0	0.0
UGC10331	15.4	4415	0.0	0.0	4382	0.0	0.0
UGC10380	12.8	8592	0.0	0.0	8469	0.0	0.0
UGC10384	9.3	4891	-0.8	0.3	4886	0.4	-0.6
UGC10710	12.0	8184	0.2	-0.2	8072	0.2	-0.2

The table lists the geometric parameters used for the CALIFA data for each galaxy, which are not already reported in Table A.3. R_e values are derived from growth curves fit to SDSS r-band images and are provided by the CALIFA team. V500 parameters were determined from kinematic fits to Hα, and V1200 parameters were determined from kinematic fits to Hγ. The V_{sys} values are reported in the relativistic convention.

Table A.3: Geometric Parameters for the CALIFA Data

Appendix B: Appendices for Chapter 3

B.1 Extinction Effects

While the Hα flux maps are extinction corrected, this correction is insufficient for the midplanes of the edge-on systems analyzed here. Extinction will be less severe away from the disk midplane, but it is nevertheless difficult to correct for. We investigate the effect of extinction on our results in two ways. First, we perform simulations to investigate the effects of extinction on the shape of the rotation curves. We create a thin disk with an input rotation curves which rises linearly and then flattens at some turnover radius (first panel in Figure B.1 left and the black curve in Figure B.1 right). Part of the disk is obscured above some level of extinction along the line of sight. This is shown in Figure B.1 (left), where the observer is in the plane of the page looking up into the disk, where the percent of the disk area extincted by dust is quoted above the panels. We then measure the rotation curve by taking a PV cut along the major axis. As shown in Figure B.1 (right), as the extinction increases, the rotation curve becomes more linear, approaching solid-body rotation. This result has been known for decades (e.g. Goad & Roberts, 1981; Bosma et al., 1992), but bears repeating here. In the context of this paper, ionized gas rotation velocities may be underestimated in the midplane from this

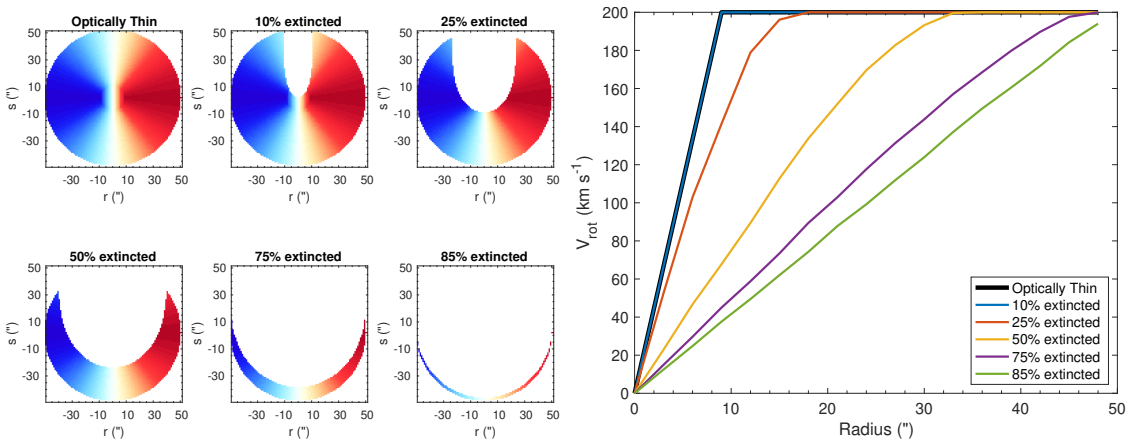

Figure B.1: (Left) Our simulated velocity fields with different amounts of dust extinction along the line of sight (quoted as the percent of the disk area extincted). The observer is in the plane of the page looking up. The color-scale ranges from -200–200 $\mathrm{km\,s^{-1}}$. (Right) The rotation curves resulting from the simulated velocity fields above. With increasing extinction, the rotation curves becomes more linear rather than flattening.

effect. With increasing distance from the midplane, however, the extinction will be less and the true rotation velocity can be recovered. Since our measured vertical gradients in the rotation velocity extend a few kpc from the midplane and still show this linear decrease in the rotation velocity, we do not expect that extinction is greatly affecting our measured gradients.

We investigate our previous claim that the extinction drops with distance from the midplane directly. Using the same method as described in Section 3.4.2, we determine the vertical gradient in the extinction ($\Delta A_V/\Delta z$). This is the extinction determined from the stellar population synthesis modeling (see Sánchez et al., 2016c,b), and it is degenerate with the stellar age and metallicity. We find that the extinction decreases with distance from the midplane for $76\%^{+12\%}_{-32\%}$ of galaxies. We list the values of $\Delta A_V/\Delta z$ and $A_V(z=0)$ in Table B.1. $A_V(z=0)$ and $\Delta A_V/\Delta z$ are inversely correlated (Figure B.2 top left), such that the galaxies with the largest

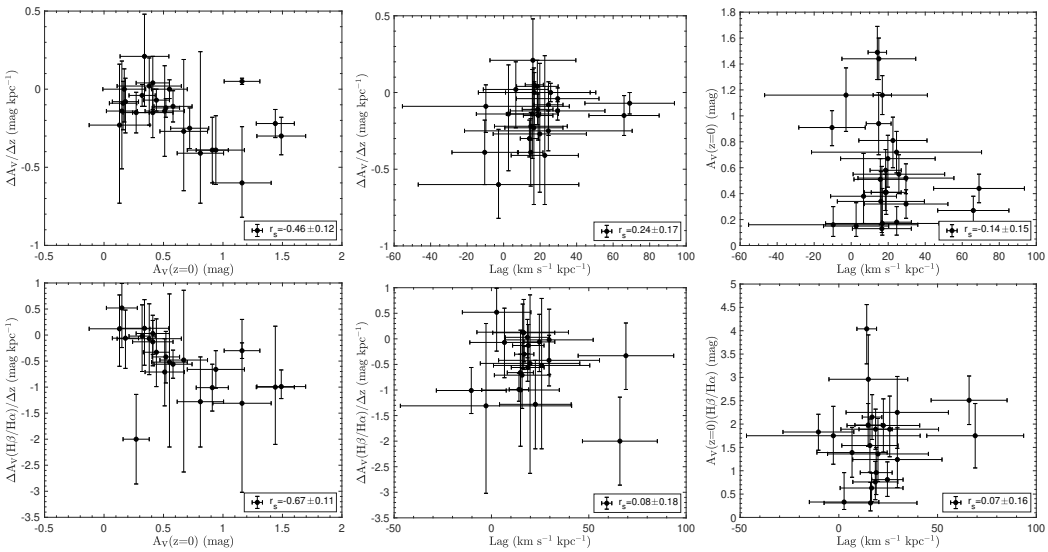

Figure B.2: (Top left) $\Delta A_V/\Delta z$ and $A_V(z = 0)$ (extinctions measured from the stellar population synthesis modeling) are correlated, where the galaxies with the highest extinctions decrease the most as a function of height. Neither $\Delta A_V/\Delta z$ (top center) nor $A_V(z = 0)$ (top rigth) are correlated with the measured velocity lag, indicating that the measurement of the lag is not affected significantly by extinction. The bottom row is the same as the top row, but the extinctions are determined from the Balmer Decrement.

extinctions in the midplane decrease the most as a function of distance. By $z = 1$, most galaxies have $A_V < 0.5$ mag. Away from the midplane, extinction will play a diminished role. The measured lag is not correlated with either $\Delta A_V/\Delta z$ or $A_V(z = 0)$ (Figures B.2 top center, top right), again indicating that extinction is not significantly biasing our lag measurements.

Because the extinction from the stellar population synthesis modeling is affected by stellar age and metallicity, we also investigate trends with the extinction derived from the Balmer decrement, assuming Case B recombination and an intrinsic ratio of $I(H\alpha)/I(H\beta) = 2.86$ (Osterbrock, 1989). We find vertical gradients in the extinction from the Balmer decrement ($\Delta A_V/\Delta z(H\beta/H\alpha)$) and the extinction in the midplane ($A_V(z = 0)(H\beta/H\alpha)$) in the same way as before. Although

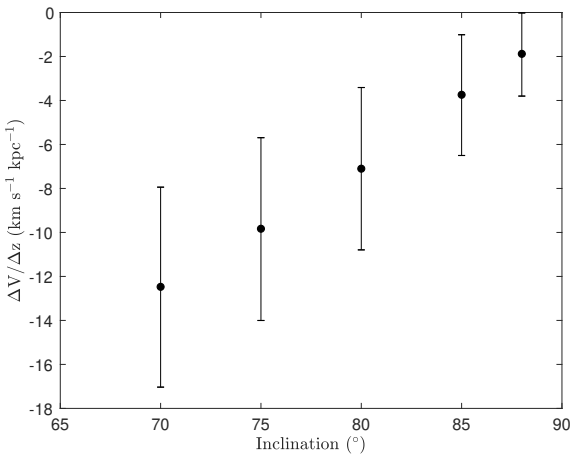

Figure B.3: For a simulated thin disk, we measure the lag induced by an inclination $< 90°$.

$A_V(z = 0)(H\beta/H\alpha) > A_V(z = 0)$ in general, we find the same general trends as with the extinctions derived from the stellar population synthesis modeling (Figures B.2 bottom). The measured lag is not correlated with $\Delta A_V/\Delta z(H\beta/H\alpha)$ or $A_V(z = 0)(H\beta/H\alpha)$ (Figures B.2 bottom center, bottom right), confirming indicating that extinction is not significantly biasing our lag measurements.

B.2 Inclination Effects

If the galaxies used in this study are not perfectly edge-on, then the measured ionized gas scale height will be a combination of gas above the midplane and in the disk. Moreover, the lag measurements will also be a combination of more slowly rotation gas in the eDIG and gas at different radii in the disk. This is why our selection criteria for edge-on galaxies are fairly restrictive (Section 3.2.3). Previous analysis and modeling has shown that the photometric vertical scale height increases by 20% if the inclination deviates from 90° by 5° (de Grijs et al., 1997). We investigate the effect of inclination on the measured lag. We simulate thin disks (that would not

have an intrinsic lag) given an input rotation curve that rises linearly until 1.77 kpc (based on Levy et al., 2018) and is then constant with $V_{rot} = 200\,km\,s^{-1}$. We then incline the disk and measure the vertical gradient in the rotation velocity as before (see Section 3.4.2) assuming that the simulated galaxy is edge-on. We show the measured vertical gradients in the rotation velocity as a function of the true inclination in Figure B.3. Because the simulated disks are thin and have no intrinsic lag, all of the resulting measured lag is due to measuring gas in the midplane due to the inclination. If the inclination deviates from 90° by 5°, the induced lag is $\tilde{4}\,km\,s^{-1}\,kpc^{-1}$, but larger deviations can produce appreciable lags. Our selection criteria are fairly stringent to minimize this effect, and the resulting sample consist of galaxies that are very edge-on (see Section 3.2.3 and Figure 3.1).

B.3 Vertical Gradients in Other Galaxy Properties

In addition to vertical gradients in the rotation velocity, we also investigate vertical gradients in other spatially resolved galaxy properties from CALIFA. Such properties include the stellar age and metallicity, nebular extinction (A_v), and extinction from the Balmer decrement ($A_v(H\beta/H\alpha)$). The stellar age and metallicity and A_v come from the stellar population synthesis done by the CALIFA collaboration (for details on the derivation of these maps, see Sánchez et al., 2016c,b). The extinction based on the Balmer decrement is calculated from the Hα and Hβ emission line flux maps following Domínguez et al. (2013) (which assumes Case B recombination (Osterbrock, 1989) and a Calzetti et al. (2000) extinction curve). These

Name	ΔAge/Δz ($\mathrm{dex\,kpc^{-1}}$)	Age(z=0) (log[yr])	Δ[Z/H]/Δz ($\mathrm{dex\,kpc^{-1}}$)	[Z/H](z=0) (log[$\mathrm{Z_\odot}$])	$\Delta\mathrm{A_v}/\Delta$z ($\mathrm{dex\,kpc^{-1}}$)	$\mathrm{A_v}$(z=0) (mag)	$\Delta\mathrm{A_v}(\mathrm{H}\beta/\mathrm{H}\alpha)/\Delta$z ($\mathrm{dex\,kpc^{-1}}$)	$\mathrm{A_v}(\mathrm{H}\beta/\mathrm{H}\alpha)$(z=0) (mag)
ESO539-G014	$-0.10^{+0.09}_{-0.09}$	$9.09^{+0.22}_{-0.22}$	$0.011^{+0.036}_{-0.036}$	$-0.243^{+0.088}_{-0.090}$	$-0.15^{+0.15}_{-0.16}$	$0.41^{+0.17}_{-0.17}$	$-0.13^{+0.41}_{-0.46}$	$0.96^{+0.54}_{-0.47}$
IC 480	$-0.05^{+0.07}_{-0.07}$	$8.93^{+0.10}_{-0.11}$	$0.065^{+0.039}_{-0.039}$	$-0.393^{+0.062}_{-0.066}$	$-0.11^{+0.10}_{-0.10}$	$0.58^{+0.16}_{-0.16}$	$-0.56^{+0.27}_{-0.27}$	$1.89^{+0.43}_{-0.43}$
IC 2095	$-0.01^{+0.42}_{-0.42}$	$8.31^{+0.28}_{-0.29}$	$0.001^{+0.114}_{-0.115}$	$-0.199^{+0.068}_{-0.068}$	$-0.14^{+0.32}_{-0.37}$	$0.15^{+0.18}_{-0.08}$	$0.52^{+0.47}_{-0.76}$	$0.33^{+0.63}_{-0.16}$
IC 2098	$0.05^{+0.12}_{-0.13}$	$8.90^{+0.11}_{-0.11}$	$0.087^{+0.059}_{-0.077}$	$-0.299^{+0.082}_{-0.070}$	$-0.39^{+0.21}_{-0.21}$	$0.91^{+0.13}_{-0.14}$	$-1.01^{+0.45}_{-0.45}$	$1.83^{+0.38}_{-0.39}$
IC 4215	$-0.20^{+0.17}_{-0.12}$	$9.72^{+0.15}_{-0.25}$	$0.032^{+0.053}_{-0.054}$	$-0.175^{+0.082}_{-0.084}$	$0.00^{+0.13}_{-0.21}$	$0.17^{+0.27}_{-0.09}$	...	...
MCG-01-01-012	$-0.02^{+0.07}_{-0.07}$	$9.18^{+0.13}_{-0.13}$	$-0.001^{+0.042}_{-0.043}$	$-0.103^{+0.114}_{-0.116}$	$-0.22^{+0.09}_{-0.09}$	$1.44^{+0.16}_{-0.16}$	$-1.00^{+1.17}_{-1.10}$	$2.96^{+0.95}_{-1.02}$
MCG-02-08-014	$-0.08^{+0.08}_{-0.08}$	$9.51^{+0.10}_{-0.11}$	$0.054^{+0.049}_{-0.050}$	$-0.261^{+0.078}_{-0.080}$	$-0.04^{+0.07}_{-0.07}$	$0.32^{+0.11}_{-0.11}$	$-0.02^{+0.60}_{-0.68}$	$1.24^{+0.68}_{-0.60}$
NGC 3160	$-0.12^{+0.04}_{-0.04}$	$9.71^{+0.10}_{-0.10}$	$-0.005^{+0.020}_{-0.020}$	$-0.025^{+0.052}_{-0.056}$	$-0.09^{+0.14}_{-0.17}$	$0.16^{+0.14}_{-0.09}$	...	...
NGC 4149	$-0.05^{+0.08}_{-0.08}$	$9.32^{+0.10}_{-0.11}$	$-0.013^{+0.046}_{-0.047}$	$-0.123^{+0.066}_{-0.070}$	$-0.15^{+0.13}_{-0.13}$	$0.27^{+0.11}_{-0.11}$	$-2.00^{+0.86}_{-0.86}$	$2.51^{+0.52}_{-0.52}$
PGC 213858	$-0.05^{+0.29}_{-0.29}$	$8.82^{+0.30}_{-0.30}$	$0.080^{+0.065}_{-0.100}$	$-0.169^{+0.106}_{-0.084}$	$0.21^{+0.27}_{-0.32}$	$0.34^{+0.23}_{-0.18}$	$0.13^{+0.55}_{-0.71}$	$0.31^{+0.44}_{-0.17}$
UGC 3539	$-0.10^{+0.17}_{-0.18}$	$8.93^{+0.17}_{-0.18}$	$0.094^{+0.054}_{-0.067}$	$-0.385^{+0.106}_{-0.088}$	$-0.39^{+0.22}_{-0.22}$	$0.94^{+0.24}_{-0.24}$	$-0.66^{+0.36}_{-0.36}$	$1.98^{+0.46}_{-0.46}$
UGC 4136	$-0.05^{+0.06}_{-0.06}$	$9.67^{+0.13}_{-0.14}$	$-0.015^{+0.034}_{-0.034}$	$-0.093^{+0.070}_{-0.072}$	$-0.12^{+0.06}_{-0.06}$	$0.52^{+0.11}_{-0.12}$	$-0.42^{+0.49}_{-0.50}$	$2.25^{+0.77}_{-0.77}$
UGC 4197	$-0.18^{+0.07}_{-0.07}$	$9.50^{+0.14}_{-0.15}$	$0.024^{+0.024}_{-0.024}$	$-0.151^{+0.068}_{-0.068}$	$-0.07^{+0.07}_{-0.07}$	$0.44^{+0.11}_{-0.11}$	$-0.33^{+0.64}_{-0.66}$	$1.75^{+0.69}_{-0.69}$
UGC 4550	$0.21^{+0.07}_{-0.07}$	$8.58^{+0.14}_{-0.14}$	$-0.002^{+0.033}_{-0.033}$	$-0.269^{+0.074}_{-0.076}$	$-0.00^{+0.06}_{-0.06}$	$0.55^{+0.15}_{-0.15}$	$-0.52^{+1.31}_{-1.63}$	$1.89^{+0.71}_{-0.59}$
UGC 5244	$-0.26^{+0.12}_{-0.13}$	$8.77^{+0.13}_{-0.13}$	$0.007^{+0.073}_{-0.073}$	$-0.373^{+0.088}_{-0.092}$	$0.04^{+0.17}_{-0.17}$	$0.41^{+0.14}_{-0.14}$	$0.03^{+0.35}_{-0.40}$	$0.76^{+0.44}_{-0.38}$
UGC 6256	$-0.06^{+0.32}_{-0.32}$	$8.93^{+0.28}_{-0.28}$	$0.014^{+0.089}_{-0.095}$	$-0.269^{+0.096}_{-0.094}$	$-0.60^{+0.36}_{-0.22}$	$1.16^{+0.21}_{-0.28}$	$-1.31^{+1.61}_{-1.71}$	$1.75^{+0.63}_{-0.61}$
UGC 9080	$-0.08^{+0.57}_{-0.50}$	$8.24^{+0.32}_{-0.35}$	$0.165^{+0.008}_{-0.239}$	$-0.309^{+0.094}_{-0.086}$	$-0.23^{+0.39}_{-0.50}$	$0.13^{+0.48}_{-0.03}$	$0.12^{+0.65}_{-0.72}$	$0.63^{+0.32}_{-0.29}$
UGC 9165	$-0.11^{+0.10}_{-0.10}$	$9.14^{+0.18}_{-0.18}$	$0.027^{+0.034}_{-0.034}$	$-0.293^{+0.066}_{-0.066}$	$-0.30^{+0.12}_{-0.12}$	$1.49^{+0.20}_{-0.21}$	$-0.99^{+0.32}_{-0.23}$	$4.04^{+0.52}_{-0.75}$
UGC 9262	$0.04^{+0.01}_{-0.01}$	$8.96^{+0.08}_{-0.08}$	$0.013^{+0.009}_{-0.009}$	$-0.209^{+0.054}_{-0.054}$	$0.05^{+0.02}_{-0.02}$	$1.16^{+0.15}_{-0.15}$	$-0.30^{+0.15}_{-0.15}$	$2.15^{+0.48}_{-0.48}$
UGC 9448	$0.21^{+0.31}_{-0.32}$	$8.83^{+0.17}_{-0.17}$	$-0.018^{+0.121}_{-0.104}$	$-0.331^{+0.072}_{-0.078}$	$-0.27^{+0.46}_{-0.38}$	$0.67^{+0.18}_{-0.22}$	$-0.48^{+1.34}_{-2.15}$	$1.36^{+0.76}_{-0.59}$
UGC 9919	$0.12^{+0.26}_{-0.26}$	$8.44^{+0.21}_{-0.21}$	$0.022^{+0.094}_{-0.108}$	$-0.365^{+0.114}_{-0.106}$	$-0.14^{+0.29}_{-0.29}$	$0.51^{+0.16}_{-0.17}$	$-0.71^{+0.64}_{-0.65}$	$1.54^{+0.57}_{-0.57}$
UGC 10043	$0.04^{+0.29}_{-0.29}$	$8.65^{+0.11}_{-0.12}$	$0.130^{+0.031}_{-0.157}$	$-0.375^{+0.074}_{-0.060}$	$-0.41^{+0.65}_{-0.32}$	$0.81^{+0.18}_{-0.21}$	$-1.28^{+0.86}_{-0.87}$	$1.97^{+0.57}_{-0.57}$
UGC 10297	$0.08^{+0.16}_{-0.16}$	$8.79^{+0.13}_{-0.13}$	$0.044^{+0.089}_{-0.134}$	$-0.349^{+0.090}_{-0.080}$	$-0.08^{+0.15}_{-0.20}$	$0.18^{+0.12}_{-0.10}$	$-0.06^{+0.54}_{-0.58}$	$0.81^{+0.38}_{-0.36}$
UGC 12518	$-0.21^{+0.13}_{-0.13}$	$9.70^{+0.11}_{-0.12}$	$-0.056^{+0.057}_{-0.055}$	$-0.037^{+0.074}_{-0.076}$	$-0.25^{+0.13}_{-0.13}$	$0.72^{+0.16}_{-0.16}$	...	...
UGC 12723	$-0.16^{+0.19}_{-0.19}$	$8.79^{+0.30}_{-0.30}$	$0.061^{+0.053}_{-0.054}$	$-0.297^{+0.092}_{-0.092}$	$0.02^{+0.18}_{-0.25}$	$0.38^{+0.33}_{-0.21}$	$-0.07^{+0.67}_{-0.69}$	$1.39^{+0.54}_{-0.53}$

Measured vertical gradients and midplane values for the stellar age, stellar metallicity ([Z/H]), nebular extinction ($\mathrm{A_v}$), and extinction from the Balmer decrement ($\mathrm{A_v}(\mathrm{H}\beta/\mathrm{H}\alpha)$). See Appendix B.3 for more details.

Table B.1: Measured Gradients for Other Galaxy Properties

parameters are not independent from one another due to degeneracies between age, color, extinction, and metallicity when modeling the spectra. Attempting to disentangle these degeneracies is beyond the scope of this paper. We, nevertheless, fit vertical gradients in these quantities using the same method as described in Section 3.4.2 and present the gradients and fitted midplane values in Table B.1. We do discuss the results based on the nebular extinction in the previous section as they relate to the effect of extinction on our results.

B.4 Analytic Derivation of the Lag and Radial Variation in the Lag

In Section 3.5.1, we investigate radial variations in the lag in the context of the origin of the eDIG. We begin our analytic derivation assuming a Miyamoto-Nagai potential:

$$\phi(r,z) = \frac{GM}{\left\{r^2 + \left[r_0 + \left(z^2 + z_0^2\right)^{1/2}\right]^2\right\}^{1/2}} \tag{B.1}$$

where M is the total mass of the galaxy and r_0 and z_0 are the radial and vertical scale lengths (Miyamoto & Nagai, 1975). This potential assumes that baryons in the disk dominate the potential (a maximal disk) and ignores the dark matter contribution. This assumption is likely valid at small radii (where $r \ll r_s$, where r_s is the dark matter scale length), but may break down further out in the disk. Studies of the Milky Way's dark matter halo suggest $r_s \sim 20\,\mathrm{kpc}$ (Hooper, 2017), whereas our Hα measurements probe out to $\lesssim 10\,\mathrm{kpc}$. The rotation velocity for the potential in

Equation B.1 is

$$\mathrm{V_{rot}}(r,z) = \frac{(GM)^{1/2} r}{\left\{ r^2 + \left[r_0 + \left(z^2 + z_0^2 \right)^{1/2} \right]^2 \right\}^{3/4}} \tag{B.2}$$

where $\mathrm{V_{rot}^2} = r\frac{\partial \phi(r,z)}{\partial r}$ (e.g. Binney & Tremaine, 2008). The vertical gradient in $\mathrm{V_{rot}}$ is then

$$\mathrm{Lag} \equiv \frac{-\partial \mathrm{V_{rot}}}{\partial z} = \frac{3(GM)^{1/2} r z \left[r_0 + \left(z^2 + z_0^2 \right)^{1/2} \right]}{2\left(z^2 + z_0^2 \right)^{1/2} \left\{ r^2 + \left[r_0 + \left(z^2 + z_0^2 \right)^{1/2} \right]^2 \right\}^{7/4}}. \tag{B.3}$$

The radial variation in the lag ($\partial \mathrm{Lag}/\partial r$) is

$$\frac{\partial \mathrm{Lag}}{\partial r} \equiv \frac{-\partial(\partial \mathrm{V_{rot}}/\partial z)}{\partial r} = \frac{3z(GM)^{1/2} \left[r_0 + \left(z^2 + z_0^2 \right)^{1/2} \right] \left[2r_0^2 + 4r_0 \left(z^2 + z_0^2 \right)^{1/2} + 2z_0 - 5r^2 + 2z^2 \right]}{4\left(z^2 + z_0^2 \right)^{1/2} \left[r_0^2 + 2r_0 \left(z^2 + z_0^2 \right)^{1/2} + z_0 + r^2 + z^2 \right]^{11/4}}. \tag{B.4}$$

For simplicity, we evaluate Equations B.3 and B.4 at $z = z_0$, so that

$$\mathrm{Lag}|_{z=z_0} = \frac{-\partial \mathrm{V_{rot}}}{\partial z}\Big|_{z=z_0} = \frac{3\sqrt{GM}\left(r_0 + \sqrt{2} z_0 \right) r}{2\sqrt{2}\left[r^2 + \left(r_0 + \sqrt{2} z_0 \right)^2 \right]^{7/4}} \tag{B.5}$$

and

$$\frac{\partial \mathrm{Lag}}{\partial r}\Big|_{z=z_0} = \frac{-\partial(\partial \mathrm{V_{rot}}/\partial z)}{\partial r}\Big|_{z=z_0} = \frac{3\sqrt{GM}\left(r_0 + \sqrt{2} z_0 \right)\left(2r_0 + 4\sqrt{2} r_0 z_0 + 4z_0 - 5r^2 \right)}{4\sqrt{2}\left(r^2 + r_0^2 + 2\sqrt{2} r_0 z_0 + 2z_0^2 \right)^{11/4}}. \tag{B.6}$$

Figure 3.9 shows Equations B.5 and B.6 as a function of r/r_0.

Appendix C: Appendices for Chapter 4

C.1 Measuring Outflow Properties from Fitting the Absorption Features

For each outflow candidate SSC, we measure important outflow properties based on the $H^{13}CN$ $4-3$ and CS $7-6$ spectra (Section 4.3.1, Table 4.2). Below, we explain how each of these properties is calculated. First, we fit the foreground-removed (Section 4.2.4) $H^{13}CN$ $4-3$ and CS $7-6$ spectra with a two-component Gaussian of the form

$$I(V) = I_{max-emis} e^{-(V-V_{max-emis})^2/2\sigma^2_{emis}} + I_{max-abs} e^{-(V-V_{max-abs})^2/2\sigma^2_{abs}} + I_{cont} \quad \text{(C.1)}$$

with terms to fit the emission, absorption, and continuum components respectively. These fits are shown in Figure 4.6 as the blue dashed curves. We define the outflow crossing time, which the time it takes a gas parcel to travel from the center of the cluster to r_{SSC} (half the major axis FWHM sizes listed in Table 4.1) moving at the

typical outflow velocity ($V_{max-abs}$) as

$$t_{cross} = \frac{r_{SSC}}{V_{max-abs}}. \tag{C.2}$$

This is a lower limit to the outflow age, assuming a constant outflow velocity, since the outflows are observed out to at least r_{SSC} and could be present at larger distances from the cluster. The maximum outflow velocity is defined as

$$V_{out,max} \equiv V_{max-abs} + 2\sigma_{abs}. \tag{C.3}$$

We determine the optical depth of the center of the absorption feature where

$$\tau_{max-abs} = -\ln\left(\frac{I_{max-abs}}{I_{cont}}\right). \tag{C.4}$$

From there, we calculate the column density in the *lower* state of each molecule following Mangum & Shirley (2015)

$$N_\ell = 16\pi\sqrt{2\ln 2}\left(\frac{\nu_{u\ell}}{c}\right)^2 \sigma_{abs} \frac{\tau_{max-abs}}{A_{u\ell}} \left[e^{h\nu_{u\ell}/kT_{ex}} + 1\right]^{-1} \tag{C.5}$$

(combining their equations 29, A1, and A7), where $\nu_{u\ell}$ is the frequency of the transition, c is the speed of light, $A_{u\ell}$ is the Einstein A coefficient for the transition, and T_{ex} is the excitation temperature. By replacing T_ℓ with T_{ex}, we are assuming LTE, which we will assume throughout. We assume $T_{ex} = 130 \pm 56$ K, which is the excitation temperatures found in these clusters (Krieger et al., 2020b). The uncer-

tainty is the difference between this value and the excitation temperature measured at lower resolution (74 K; Meier et al., 2015). Our assumption on T_{ex} is a major source of uncertainty in these calculations. We then calculate the column density in the upper state

$$N_u = N_\ell \frac{g_u}{g_\ell} e^{-h\nu_{u\ell}/kT_{ex}} \tag{C.6}$$

(e.g. equation 6 of Mangum & Shirley, 2015, assuming the upper and lower states have the same density distribution along the line of sight). The total column density of each molecule (e.g. of all energy levels) is

$$N_{mol} = \frac{N_u}{g_u} Z e^{h\nu_{u\ell}/kT_{ex}} \tag{C.7}$$

(e.g. equation 31 Mangum & Shirley, 2015), where Z is the partition function calculated assuming LTE

$$Z = \sum_i g_i e^{-E_i/kT_{ex}} \tag{C.8}$$

where g_i and E_i are the degeneracy and excitation energy of each level i. We calculate Z assuming LTE up to $i = 19$ for CS and $i = 16$ for $H^{13}CN$*. To convert from the column density of each molecule to the column density of H_2 in the outflow ($N_{H_2,out}$), we need to know the abundance ratio of each molecule with respect to H_2:

$$N_{H_2,out} = 2 \frac{[H_2]}{[mol]} N_{mol} \tag{C.9}$$

*Level population data are from `https://www.astro.umd.edu/rareas/lma/lgm/properties/cs.pdf` for CS and `https://www.astro.umd.edu/rareas/lma/lgm/properties/h13cn.pdf` for $H^{13}CN$.

where the factor of 2 accounts for the redshifted outflowing material, assuming it is the same as the blueshifted component. The abundance ratios vary with environment, so we use those calculated in the center of NGC 253 by Martín et al. (2006), where $[CS]/[H_2] = 5.0 \times 10^{-9}$ and $[H^{13}CN]/[H_2] = 1.2 \times 10^{-10}$. The assumed abundance ratio is another large source of uncertainty in our measurements and can vary substantially by environment (e.g. van Dishoeck & Blake, 1998, and references therein). We take an order-of-magnitude uncertainty on the abundance fractions, which limits subsequent calculations to order-of-magnitude precision as well (see the discussion in Section 4.3.1.1).

To calculate the H_2 mass along the line of sight,

$$M_{H_2,out} = 4\Sigma_{H_2,out}A = 4m_{H_2}N_{H_2,out}A \tag{C.10}$$

where m_{H_2} is the mass of a hydrogen molecule, A is the area of the source measured from the continuum (Table 4.2), and the factor of 4 converts the projected area to a sphere.

From the mass in the outflow and the crossing time, we calculate the mass outflow rate ($\dot{M}_{H_2,out}$) where

$$\dot{M}_{H_2,out} = \frac{M_{H_2,out}}{t_{cross}}. \tag{C.11}$$

From the total gas mass of the cluster (Leroy et al., 2018) and the mass outflow rate, we calculate the gas-removal time, or the time it would take to expel all of the

gas in the cluster at the current mass outflow rate:

$$t_{remove-gas} = \frac{M_{H_2,tot}}{\dot{M}_{H_2,out}}. \tag{C.12}$$

The timescale assumes that the mass outflow rate is constant with time, which is likely not the case (e.g. Kim et al., 2018). The momentum injected into the environment normalized by the stellar mass (M_*) by the outflow is

$$\frac{p_r}{M_*} = \frac{\sqrt{3}V_{max-abs}M_{H_2,out}}{M_*} \tag{C.13}$$

assuming spherical symmetry (Leroy et al., 2018). We assume the SSC stellar masses reported by Leroy et al. (2018), and the uncertainties in these M_* measurements are discussed in Section 4.2.6. The kinetic energy in the outflow is

$$E_k = \frac{1}{2}M_{H_2,out}V^2_{max-abs}. \tag{C.14}$$

Values calculated using CS $7-6$ and $H^{13}CN$ $4-3$ for each outflow candidate are listed in Table 4.2 along with the propagated uncertainties.

C.2 Outflow Modeling Details

We perform simple radiative transfer modeling of the source with varying outflow geometries and input physical parameters to constrain the outflow opening angles and orientations as described in Section 4.3.2.

To set up the model, we define a three-dimensional grid that is 65 ($= 2^6$+1) pixels in each dimension; we refer to this grid as the simulated box. The physical scale of the box is such that the length of each size is $4 \times r_{\rm SSC}$, or twice the diameter of the SSC to be modeled. Every pixel in the box is given a fourth dimension, corresponding to the spectral axis (in terms of frequency or velocity, which we use interchangeably here). The spectral axis has 129 ($= 2^7 + 1$) channels. The velocity range of the spectral axis and hence the spectral resolution of the model is defined adaptively for each model to maximize the number of channels over the emission and absorption features. The spectral axis is centered on zero velocity (the rest frequency of the line to be modeled) and spans $\pm 4\sqrt{\rm V_{max-abs}^2 + \Delta V_{out,FWHM}^2}$, where $\rm V_{max-abs}$ and $\rm \Delta V_{out,FWHM}$ are the outflow velocity and FWHM outflow velocity dispersion input into the model. This is done to optimize the velocity resolution over the velocities relevant for the cluster and outflow as opposed to picking a fixed velocity range. This is shown most clearly in Figure 4.7, where the portions of the spectra within the vertical line segments show the velocities actually modeled and the thin lines are extrapolations.

Once the four-dimensional box is defined, the three physical components representing the cluster and outflow are constructed. It is helpful to define coordinates related to the simulated box in cartesian coordinates, whereas coordinates pertaining to the cluster and outflow are in spherical coordinates, as shown in Figure C.1. As described in Section 4.3.2, the three components of the system are:

1. Dust continuum component: Shown in green in Figures 4.7, 4.8, C.1, and

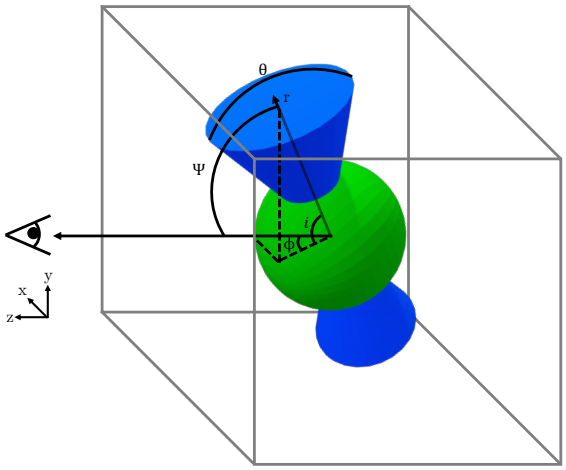

Figure C.1: An example outflow, in the style of Figure 4.8; for clarity, the ambient gas is not shown. The simulated box is shown in gray. The orientation angle definitions are marked, where θ is the outflow opening angle and Ψ is the orientation angle to the line of sight measured from the center of the outflow cone with components i and ϕ to the x- and y-axis respectively.

C.2 this component is a sphere with $r = r_{\rm SSC}$ and a constant (in space and velocity) temperature ($\rm T_{cont}$). The optical depth is a maximum ($\tau_{\rm cont,max}$) at the center, then decreases like a Gaussian with FWHM $= 2 \times r_{\rm SSC}$, so that the continuum source is semi-transparent. The temperature and optical depth are set to zero for $r > r_{\rm SSC}$.

2. Hot gas: Shown in yellow in Figures 4.7 and C.2 (and encompassed within the green sphere in Figures 4.8 and C.1), this spherical component is required to reproduce the strong emission component of the P-Cygni profiles. This component has a hot gas temperature ($\rm T_{hot}$), a central $\rm H_2$ volume density ($\rm n_{hot}$), and a velocity dispersion ($\Delta \rm V_{hot,FWHM}$). $\rm T_{hot}$ is constant (spatially) for $r \leq r_{\rm SSC}$, and is set to zero outside. The density falls off $\propto r^{-2}$ from the center, and is set to zero for $r > r_{\rm SSC}$. The line is centered on zero velocity along the spectral axis, and the Gaussian linewidth is given by $\Delta \rm V_{hot,FWHM}/2.355$.

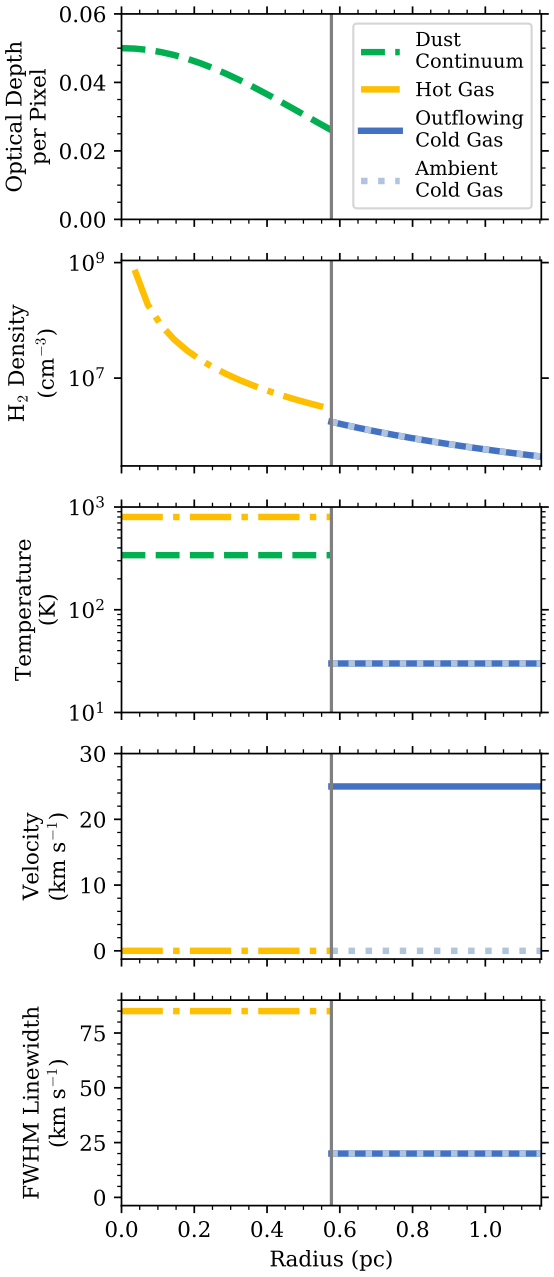

Figure C.2: Radial profiles of the input parameters to the modeling for the dust continuum (green dashed), hot gas (gold dash-dotted), outflowing cold gas (blue solid), and the ambient cold gas (light blue dotted) as described in Section 4.3.2. For the dust continuum, the optical depth per pixel is specified, whereas for the other components, the H_2 density per pixel is specified. For the ambient cold gas, input parameters are identical to the outflowing cold gas except for the velocity. Cold gas inside the outflow cones has the properties of the outflowing cold gas, whereas cold gas outside the outflow cones has the properties of the ambient cold gas. The vertical gray line marks $r_{\rm SSC}$ which is the boundary between the cluster (e.g. continuum and hot gas components) and the cold gas components (outflowing or ambient). These input parameters are scaled to the best-fit spherical model for the CS $7-6$ line in SSC 14 (Table 4.3).

3. Cold, outflowing gas: Shown in dark blue in Figures 4.7, 4.8, C.1, and C.2 this is the outflow component which produces the absorption features. This component is defined by a gas temperature (T_{out}), a maximum H_2 volume density (n_{out}), a constant outflow velocity (V_{out}), a velocity dispersion ($\Delta V_{out,FWHM}$), and opening angle (θ), and an orientation to the line of sight (Ψ). The gas temperature is constant (spatially) within this component and is set to zero for $r < r_{SSC}$. The density is a maximum at $r = r_{SSC}$ and deceases $\propto r^{-2}$ until the edges of the box; the density is set to zero for $r < r_{SSC}$. The line is centered on along the frequency axis at $V_{outflow}$, and the Gaussian linewidth is given by $\Delta V_{out,FWHM}$. Since the outflow velocity is constant and the density $\propto r^{-2}$, the outflow conserves energy and momentum. The outflow cones are masked to the given opening angle (θ) and rotated to the given orientation from the line of sight (Ψ) (Figure C.1). For outflows with $\theta < 180°$, the outflowing gas component outside the outflow cones is replaced by an ambient gas component (shown in light blue in Figures 4.8 and C.2), which has the same properties as the outflowing gas but with $V_{out} = 0$. We refer to these together simply as the "cold" component.

The optical depths of the hot and cold (outflowing and ambient) gas are needed at every pixel and as a function of frequency ($\tau_{\nu,hot}$ and $\tau_{\nu,outflow}$ respectively) for the radiative transfer. For simplicity in the following equations, we will drop the "hot" and "cold" subscripts since the calculations are the same for both components.

First, we calculate the intrinsic line shape assuming Doppler broadening is dominant

$$\phi_\nu = \frac{1}{\sqrt{\pi}\nu_{u\ell}} \frac{c}{b} e^{-V^2/b^2} \tag{C.15}$$

where $b \equiv \sqrt{2}\sigma_V = \frac{\Delta V_{\rm FWHM}}{2\sqrt{\ln 2}}$, $\nu_{u\ell}$ is the rest frequency of the transition being modeled, and V is the velocity along the spectral axis (with $V = 0$ corresponding to $\nu = \nu_{u\ell}$) and where $\int \phi_\nu d\nu = 1$ (Draine, 2011). The absorption cross section is

$$\sigma_{\ell u}(\nu) = \frac{g_u}{g_\ell} \frac{c^2}{8\pi\nu_{u\ell}^2} A_{u\ell} \phi_\nu \tag{C.16}$$

where g_u and g_ℓ are the upper and lower level degeneracies and $A_{u\ell}$ is the Einstein A value of the transition (Draine, 2011). Given the H_2 number density at every pixel ($\mathrm{n_{H_2}}(x, y, z)$), the number density in the lower state of the modeled transition is

$$n_\ell(x, y, z) = \frac{[\mathrm{mol}]}{[\mathrm{H_2}]} \frac{g_\ell}{Z} e^{-T_\ell/T} \mathrm{n_{H_2}}(x, y, z) \tag{C.17}$$

where $\frac{[\mathrm{mol}]}{[\mathrm{H_2}]}$ is the fractional abundance of the molecule being modeled with respect to H_2, Z is the partition function (Equation C.8), $T_\ell \equiv E_\ell/k$ is the excitation energy of the lower energy state, and T is the input temperature of the gas. The absorption coefficient is then

$$\kappa_\nu(x, y, z) = n_\ell(x, y, z)\sigma_{\ell u}(\nu) \left(1 - e^{-k\nu/kT}\right) \tag{C.18}$$

(Draine, 2011). Finally, the optical depth of each pixel and as a function of frequency

is

$$\Delta\tau_\nu(x,y,z) = \kappa_\nu(x,y,z)\Delta z \tag{C.19}$$

where Δz is the size of each pixel in the z direction (though in this simulation the pixels are equal size in all spatial dimensions).

For each component—now also including the continuum component— the intensity (expressed in Rayleigh-Jeans brightness temperature units) at every pixel and as a function of frequency is

$$\Delta T_\nu(x,y,z) = T\left[1 - e^{-\Delta\tau_\nu(x,y,z)}\right]. \tag{C.20}$$

We perform the radiative transfer along the line of sight from the back of the box to the front (e.g. along the $+z$-axis):

$$T_\nu(x,y,z_i) = T_\nu(x,y,z_{i+1})e^{-\sum_{\rm comp}\Delta\tau_\nu(x,y,z_i)} + \sum_{\rm comp}\Delta T_\nu(x,y,z_i) \tag{C.21}$$

where z_i denotes an individual step along the z-axis and $\sum_{\rm comp}$ means a sum over the dust continuum, hot gas, and cold (outflowing and ambient) gas components.

The observed spectra are averaged over the FWHM continuum source size. To best compare with the observed spectra, we mask the simulated box of $T_\nu(x,y,z)$ to a cylinder along the z-axis with $r = r_{\rm SSC}$ as shown in Figure 4.8, setting pixels outside this region equal to zero. The final modeled spectrum is

$$T_\nu = \frac{1}{N_{\rm pix}}\sum_{x,y} T_\nu(x,y,z=z_{\rm max}) \tag{C.22}$$

where $z = z_{\rm max}$ denotes the slice (in the xy plane) at the front of the box and $N_{\rm pix}$ is the number of non-masked pixels in that slice. The best-fitting modeled spectra are shown in red in Figure 4.6.

There are degeneracies between input parameters. The observed continuum level is a combination of the intrinsic continuum temperature ($\rm T_{cont}$) and the continuum optical depth ($\tau_{\rm cont}$); a higher $\tau_{\rm cont}$ with a lower $\rm T_{cont}$ can produce the same fit as a lower $\tau_{\rm cont}$ with a higher $\rm T_{cont}$. The temperature and density of the hot gas component ($\rm T_{hot}$ and $\rm n_{hot}$) are linked in a similar way. More, a lower $\tau_{\rm cont}$ means less of the hot gas and redshifted outflow are attenuated, and so lower $\rm T_{hot}$ and $\rm n_{hot}$ values are required. These degeneracies, especially with regards to the density, lead to a very uncertain total mass for the modeled cluster. The outflow parameters, however, are more robust. The gas temperature in the outflow ($\rm T_{out}$) is linked to the density in the outflow ($\rm n_{out}$), but are not as degenerate as for the hot gas component for the following reason. For absorption, the minimum modeled brightness temperature cannot be less than the given $\rm T_{out}$, even for an arbitrarily high density. That is, in order to match the models with the observations, the observed temperature at maximum absorption sets the maximum possible $\rm T_{out}$ in the model. For these reasons, though we report all input parameters for the best-fitting models, we only report derived parameters for the outflow in Table 4.3.

Appendix D: Cuspy Dark Matter Density Profiles in Massive Dwarf Galaxies

D.1 Introduction

Dwarf galaxies have proven to be important laboratories to test principles of current dark energy and cold dark matter cosmology (ΛCDM), despite their difficulty to observe (e.g. Bullock & Boylan-Kolchin, 2017). Historically, one of the most important problems of the ΛCDM paradigm is the core-cusp problem (e.g., Flores & Primack, 1994; Moore, 1994). Cosmological simulations of cold dark matter predict a cusp-like dark matter density distribution near the centre, meaning the density has a power-law slope (β) between 1 and 1.5 (e.g. Navarro et al., 1996b; Moore et al., 1999)*. The most well-known form of this density distribution is the Navarro-Frenk-White (NFW) profile (Navarro et al., 1996b). Observational studies of dwarf galaxies, however, show that central density profiles range from flat core-like distributions ($\beta \approx 0$) to the cusp-like profiles expected from dark matter-only simulations (see e.g. de Blok et al., 2001a,b; de Blok & Bosma, 2002; Simon et al., 2005; Oh et al., 2011, 2015; Adams et al., 2014; Relatores et al., 2019a,b). This

*In some of the literature, the power-law slope is denoted as α, where $\alpha \equiv -\beta$. Here we use β throughout for consistency.

discrepancy between observations and simulations is called the core-cusp problem (e.g. Flores & Primack, 1994; Moore, 1994; Bullock & Boylan-Kolchin, 2017).

There are, in principle, two possible solutions to this problem, which have been summarized in a recent review by Bullock & Boylan-Kolchin (2017). First, dark matter could behave differently than assumed under the ΛCDM model. For example, if dark matter could interact with itself (so-called self-interacting dark matter or SIDM), the transfer of energy between dark matter particles would soften the density profiles, alleviating the core-cusp problem (e.g. Spergel & Steinhardt, 2000; Vogelsberger et al., 2012; Peter et al., 2013; Fry et al., 2015; Elbert et al., 2015; Cyr-Racine et al., 2016; Vogelsberger et al., 2016; Kaplinghat et al., 2020; Leung et al., 2021). An important test for SIDM comes from galaxy clusters, where the upper-limit on the SIDM cross section is marginally consistent with the lower limit needed to alleviate the core-cusp problem, suggesting that SIDM models are unlikely to be a solution to the core-cusp problem (Bullock & Boylan-Kolchin, 2017). As pointed out by Bullock & Boylan-Kolchin (2017), warm dark matter models produce the same density distributions as CDM and are therefore not a solution to the core-cusp problem.

A solution within the ΛCDM paradigm is that baryonic physics and feedback impact the dark matter distribution in a galaxy. This feedback, especially from supernovae, can redistribute mass in a galaxy, reshaping the potential and hence the dark matter density distribution. This feedback will be most efficient in the centres of dwarf galaxies, where the dark matter density and star formation rate surface densities are highest. Numerical simulations, including feedback, find that

the peak core-formation occurs in galaxies with $M_* \simeq 10^{8-9}$ $M_\odot$ (e.g. Navarro et al., 1996a; Governato et al., 2012; Pontzen & Governato, 2014; Di Cintio et al., 2014; Chan et al., 2015; Tollet et al., 2016; Fitts et al., 2017; Hopkins et al., 2018; Lazar et al., 2020; Macciò et al., 2020). At smaller masses, the star formation rates are too low for the resulting stellar feedback to significantly alter the density distribution. At larger masses, the gravitational potential is too deep for stellar feedback to significantly redistribute the dark matter into a core-like profile.

In this study, we build upon the set of observed inner dark matter density slopes using new observations of a sample of six galaxies from the Dwarf Galaxy Dark Matter (DGDM) survey (Truong et al., 2017). Using new ^{12}CO $J = 1-0$ (CO) observations from ALMA and *Spitzer* 4.5 μm data as tracers of the total potential and stellar component, we kinematically decompose the dark matter density profiles to measure the inner dark matter density slopes (β^*).

This work closely follows that of Relatores et al. (2019a,b, hereafter R19a and R19b), who measured β^* from another DGDM survey sub-sample using Hα observations to trace the total potential. The β^* values derived by R19b agree with other CO data points from CARMA (Truong et al., 2017). Specifically, R19b find that one third of the inner slopes were consistent with the NFW profile, while the rest were more core-like than the NFW profile predicts.

From our sample of six dwarf galaxies, we find cusp-like inner dark matter density distributions ($\langle\beta^*\rangle = 1.0$ with a standard deviation of ± 0.3 among the measurements). This agrees with predictions from simulations (that include stellar feedback) in this stellar mass range of $10^{9.3-9.7}$ $M_\odot$ (e.g., Tollet et al., 2016; Mac-

ciò et al., 2020; Lazar et al., 2020). These simulations find that cores can only be maintained through accretion, mergers, and/or outflows from stellar feedback which disturb the potential. We, therefore, conclude that these dwarfs are likely too massive for stellar feedback to effectively alter the dark matter distributions. Some of the β^* values that we measure are even steeper than predicted by the simulations for galaxies with this range of stellar masses.

This study is organized as follows. We describe the CO data used for this study and the data reduction in Section D.2. Section D.3 describes the method used to derive the CO rotation curves. The determination of the stellar components, decomposition of the dark matter density profiles, and measurement of β^* are presented in Section D.4. Our results and robustness tests are described in Section D.5. Implications of our results are discussed in Section D.6. We summarize our conclusions in Section D.7.

D.2 Observations and Data Reduction

The initial galaxy selection for the DGDM survey is described by Truong et al. (2017), who observed these galaxies in ^{12}CO $J = 1 - 0$ (CO) with the Combined Array For Millimeter-wave Astronomy (CARMA). Of the initially selected 26 galaxies, 14 were robustly detected in CO with CARMA. Of these, 13 were followed up with new and more sensitive CO observations using the Atacama Large Millimeter/submillimeter Array (ALMA) as part of project number 2015.1.00820.S (PI L. Blitz). These 13 galaxies were chosen to be bright and extended in the WISE 22 μm

Name	Beam FWHM (arcsec)	rms Noise (mJy beam^{-1} (mK))	CASA Cal. Version
NGC1035*	2.90	4.2 (46)	4.5.1
NGC4310	2.40	4.1 (65)	4.5.3
NGC4451*	2.80	4.2 (49)	4.5.1
NGC4701	2.80	4.3 (50)	4.5.1
NGC5692*	2.85	4.7 (53)	4.5.1
NGC6106*	2.40	3.4 (54)	4.5.2

Galaxies marked with * overlap with R19a and R19b. The FWHM of the synthesized, circularized Gaussian beam is given. The rms noise per 2 km s^{-1} channel is reported for the cleaned cube for regions with SNR > 3 based on the peak intensity in mJy beam^{-1} and mK (parentheses). CASA Cal. Version lists the version of CASA used for calibration. All of the visibilities were imaged with CASA version 5.7.2-4.

Table D.1: CO Data Cube Parameters

band (W4), to have substantial IRAS 100 μm flux, and to be far enough south to be visible to ALMA. These galaxies were observed in Band 3 in the C36-1 configuration with baselines ranging from $15 - 640$ m and a maximum recoverable scale of $\approx 21''$ ($\sim$ 2 kpc). Mosaics of a few pointings were used for galaxies with large angular extents on the sky (e.g., NGC 1035 and NGC 6106). This configuration results in $\sim 2''$ ($\sim$ 200 pc) resolution that is well matched to the Hα data from the Palomar Cosmic Web Imager presented by R19a.

The visibilities were calibrated and flagged by the observatory using the Common Astronomy Software Application (CASA; McMullin et al., 2007) version listed in Table D.1. The data were imaged using `tclean` in CASA version 5.7.2-4 with `decolvolver='hogbom'`, `specmode='cube'`, Briggs weighting with `robust=0.5`, and no *uv*-taper. The baseline was fit with a linear function (`nterms=2`) to account for

any change in slope over the band. The imaging was performed on the three-dimensional RA-Dec-velocity images, where each spatial pixel (spaxel) contains a spectrum. These images were cleaned until the residuals were consistent with the root-mean-square (rms) noise levels given in in Table D.1. The final images all have a velocity resolution of 2 $\mathrm{km\,s^{-1}}$, and we convolved the images to a circular beam, which is listed in Table D.1. The rms noise per channel reported in Table D.1 is calculated where the SNR > 3 based on the peak intensity maps (described in the following paragraph).

Moment maps (peak intensity, velocity, linewidth) were produced by fitting each pixel of the CO images with a Gaussian. Error maps are also produced based on the statistical uncertainties in the Gaussian fitting. Fits that do not converge are blanked. Isolated blanked pixels (i.e., where none of the neighbouring values is blanked) are replaced with the median value of the neighbours. Pixels in the CO intensity, velocity, and velocity dispersion maps with SNR < 3 based on the peak intensity and associated error maps are masked out. The CO peak intensity, velocity, and full-width-half-maximum (FWHM) linewidth maps are shown in Figure D.1. All velocities presented in this work have been converted to the relativistic velocity frame (see e.g., Appendix A.1 for details and conversions.).

Of the 13 galaxies observed with ALMA, three galaxies (NGC 853, NGC 1012, NGC 4376) have insufficient signal to produce a velocity field even before our SNR mask is applied. Our SNR mask excludes three more galaxies (NGC 4150, NGC 4396, UGC 8516). Finally, we exclude NGC 4632. This galaxy is in a group with NGC 4666 (a large starburst galaxy), NGC 4668, and two other smaller dwarf galaxies (Garcia,

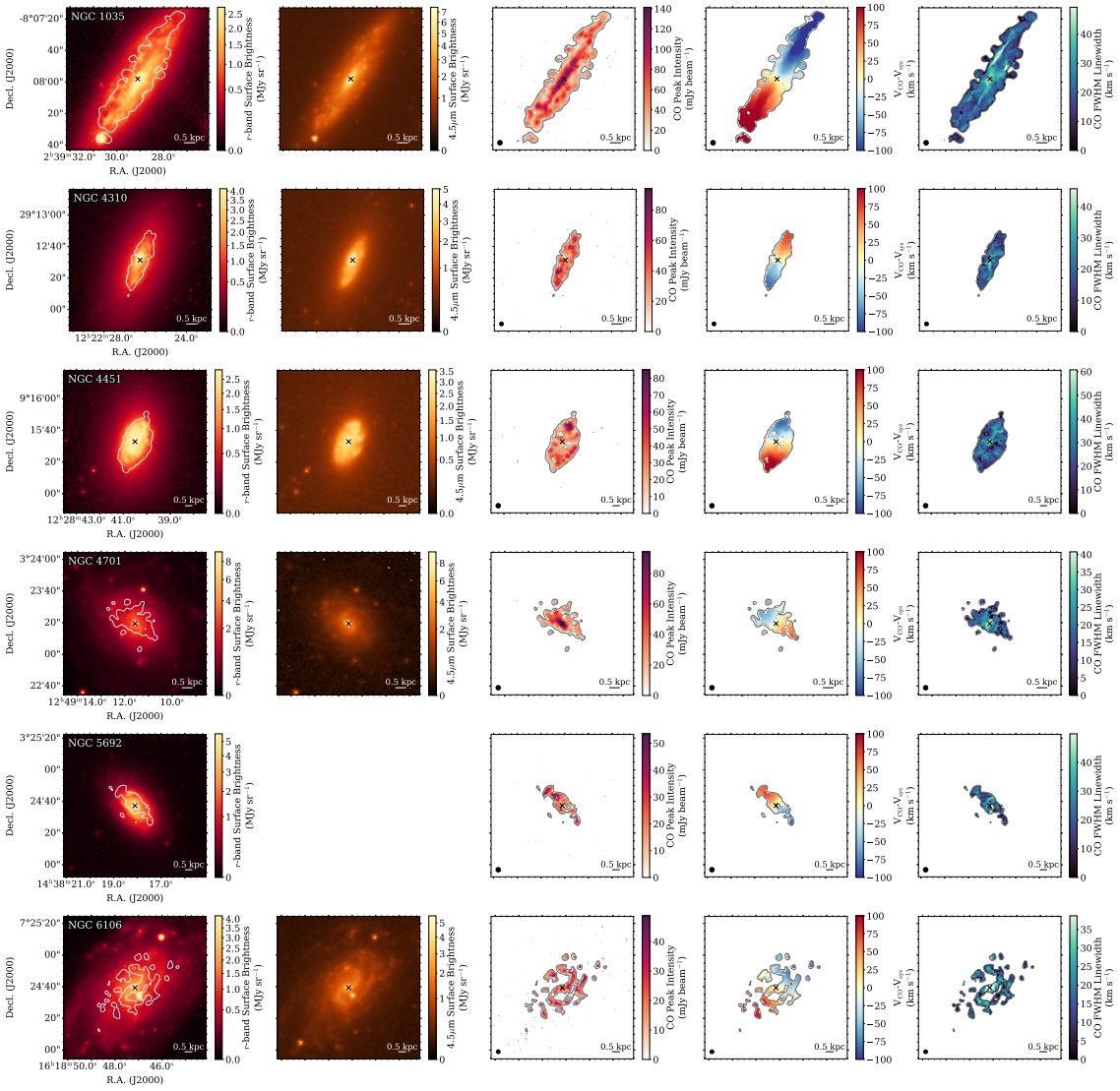

Figure D.1: The six galaxies studied here, showing (from left to right) their PS1 r-band images, *Spitzer* 4.5 μm images, the CO peak intensity, the CO velocity, and the CO FWHM linewidth. There is no *Spitzer* image for NGC 5692. Each image is cropped to 1.5′ on a side. The crosses show the location of the kinematic centre (Table D.2). The white or grey contours show SNR = 3 based on the CO peak intensity. The CO maps are masked to this level. The black ellipses in the lower left corners of the CO images show the FWHM beam sizes.

1993; Walter et al., 2004), though our ALMA observations only cover NGC 4632. The CO in NGC 4632 follows the spiral arms, with the northern spiral arm being much more prominent. A single prominent spiral arm can be a sign of a past interaction (e.g., Oh et al., 2008a), which is possible for this galaxy given its known group membership. We, therefore, exclude this galaxy from the sample as the presence of other close, large galaxies and the hints of tidal interaction may affect the kinematics and dark matter halo of this system. Our final sample consists of six galaxies (NGC 1035, NGC 4310, NGC 4451, NGC 4701, NGC 5692, NGC 6106), shown in Figure D.1 and listed in Table D.1.

These ALMA observations cover antenna spacings from $15 - 640$ m, and will miss some of the flux on scales larger than $\approx 21''$. Lower-sensitivity CARMA data of these galaxies taken in the C, D, and E configurations (antenna spacings from $7.5 - 373$ m) recover scales up to $\sim 40''$ (Truong et al., 2017). Importantly for our study, we are interested in the CO kinematics, as opposed to robust CO fluxes or molecular gas masses. As a test of the effects of the missing short spacings on the CO kinematics, we combined the ALMA and CARMA images using the `immerge` task in `Miriad` (Sault et al., 1995). We derived the velocity fields from these combined images in the same way as described above. The resulting combined velocity fields show no significant differences with the ALMA-only velocity fields. We therefore proceed using only the ALMA data in our analysis.

In addition to the CO data, we will use *Spitzer* IRAC 4.5μm (Channel 2) maps from the Spitzer Survey of Stellar Structure in Galaxies (S4G; Sheth et al., 2010;

Name	R.A. (J2000 hours)	Decl. (J2000 deg)	Distance (Mpc)	V_{sys} ($km\,s^{-1}$)	PA (deg)	Inc (deg)	R_{max} (kpc)	log $M_{dyn}(R_{max})$ (log $M_\odot$)	σ_V ($km\,s^{-1}$)
NGC1035	$2^h39^m29.1^s$	$-8°07'58.2''$	16 (a)	1224	142	72	2.9	10.0 ± 0.1	20.6 ± 7.8
NGC4310	$12^h22^m26.3^s$	$+29°12'31.1''$	16 (b)	927	335	71	1.6	9.5 ± 0.1	19.0 ± 5.8
NGC4451	$12^h28^m40.5^s$	$+9°15'32.5''$	26 (a)	849	178	49	2.2	10.0 ± 0.1	25.3 ± 7.8
NGC4701	$12^h49^m11.6^s$	$+3°23'19.0''$	17 (b)	725	230	49	1.5	9.4 ± 0.1	17.1 ± 6.4
NGC5692	$14^h38^m18.1^s$	$+3°24'37.1''$	25 (b)	1605	36	53	1.7	9.5 ± 0.1	21.6 ± 8.4
NGC6106	$16^h18^m47.2^s$	$+7°24'39.3''$	24 (a)	1465	143	59	3.3	10.0 ± 0.1	18.1 ± 8.7

R.A. and Decl. list the best fit center. The distance is from (a) Tully et al. (2013) where available or (b) HyperLEDA otherwise (see Section D.2). V_{sys} is in the relativistic velocity frame. The PA is measured E of N to the receding side of the major axis. $M_{dyn}(R_{max})$ is the dynamical mass measured from the CO rotation curve at radius R_{max}. σ_V is the median FWHM velocity dispersion, uncorrected for beam smearing; the uncertainty is the standard deviation.

Table D.2: Parameters from Rotation Curve Fitting

Muñoz-Mateos et al., 2013; Querejeta et al., 2015) to trace the stars[†]. *Spitzer* IRAC data are not available for NGC 5692. We instead use r-band images from the 3π Steradian Survey on the PAN-STARRS1 (PS1) telescope (Chambers et al., 2016)[‡]. PS1 r-band and *Spitzer* 4.5 μm images are shown for these galaxies in Figure D.1.

Distances to these galaxies are taken from two sources. Three of our galaxies have Tully-Fisher distances reported by Tully et al. (2013). For the other three, we use the distances from the `modbest` column in the HyperLEDA catalogue (Makarov et al., 2014)[§]. These distances are reported in Table D.2.

D.3 Derivation of CO Rotation Curves

We derive the CO rotation curves using a first order harmonic decomposition:

$$V(r) = \mathrm{V_{rot}}(r)\cos\phi\sin i + \mathrm{V_{rad}}(r)\sin\phi\sin i + \Delta\mathrm{V_{sys}}(r) \tag{D.1}$$

which fits for the rotation ($\mathrm{V_{rot}}$), radial ($\mathrm{V_{rad}}$), and systemic ($\Delta\mathrm{V_{sys}}$) components, where r is the galactocentric radius, ϕ is the azimuthal angle in the plane of the disk, and i is the inclination and is assumed the same for all rings (e.g. Begeman, 1989). Before fitting, the central systemic velocity ($\mathrm{V_{sys}}$) is subtracted from the map, such that the fitted systemic component ($\Delta\mathrm{V_{sys}}$) describes the deviation from this value. We extract the rotation velocities in concentric rings using a new Python

[†]These images were downloaded directly from the NASA/IPAC Infrared Science Archive: `https://irsa.ipac.caltech.edu`.

[‡]This image was downloaded directly from the PS1 Image Cutout Server: `https://ps1images.stsci.edu/cgi-bin/ps1cutouts`.

[§]`http://leda.univ-lyon1.fr/`

implementation[¶] of the original MATLAB code developed by Bolatto et al. (2002) and used by Simon et al. (2003, 2005). Levy et al. (2018) modified the ring spacing algorithm so that rings are spaced in half-beam-width increments or contain at least 30 pixels per ring, whichever is larger.

The initial values for the kinematic parameters (centre, position angle (PA), inclination, systemic velocity) were taken from Truong et al. (2017), but were adjusted as needed. The PA takes values between 0° and 360°, where PA = 0° indicates that the receding side is oriented north, and increases counterclockwise (east of north). We modify the centre position of each galaxy to minimize the ΔV_{sys} component at small radii, as offsets from the correct centre induce sharp deviations from zero in this component very near the centre. We then adjust the systemic velocity value (V_{sys}) such that $\Delta V_{sys} \approx 0$. The PA is modified such that $V_{rad} \approx 0$ throughout the galaxy, as an incorrect PA will induce a constant offset in V_{rad}. The inclination was adjusted based on the harmonic fits in each ring, where an incorrect inclination can result in flat-topped or peaked harmonic models whose shapes do not match the data. Our CO rotation curves are shown in Figure D.2, and the final values of the kinematic parameters are listed in Table D.2.

We determine the uncertainty on the rotation curves as follows. First, we calculate the rms scatter between the model and data in each annulus. Next, we account for the systematic uncertainties related to the input geometric parameters using a Monte Carlo method. In each realisation, the centre position is allowed to

[¶]The Python implementation of the rotation curve fitting code is publicly available at `https://github.com/rclevy/RotationCurveTiltedRings`.

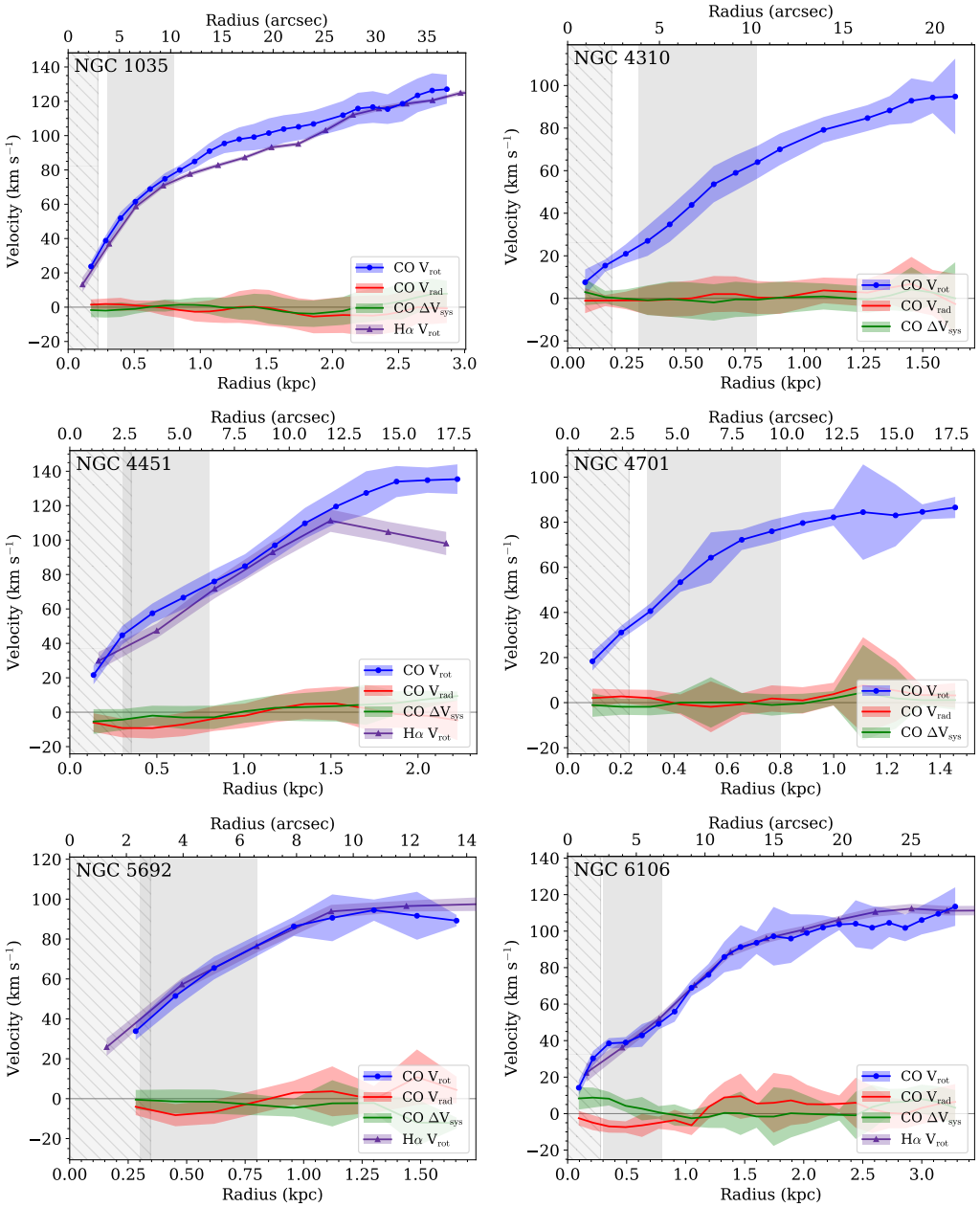

Figure D.2: CO rotation curves for the six galaxies studied here using the parameters in Table D.2. The fits use a first order harmonic decomposition (Equation D.1), where V_{rot} is shown in blue, V_{rad} in red, and ΔV_{sys} in green. The uncertainties (shaded regions) reflect both the rms scatter from the fits in each ring and systematic uncertainties in the kinematic parameters (see Section D.3 for details). The grey hatched region shows twice the beam HWHM, indicating radii over which the CO measurements may be most affected by beam smearing. The solid grey region shows the range of radii over which β^* will be calculated. The purple curves show the Hα rotation curve derived by R19b, where available. The uncertainties on the Hα rotation curves reflect the statistical fitting errors and do not account for the larger systematic uncertainties. In general, the CO and Hα rotation curves agree well; see Section D.3.1 for notes on individual galaxies.

vary uniformly by $\pm 0.4''$, the position angle by $\pm 5°$, and inclination by $\pm 4°$ from the best-fitting kinematic parameters in Table D.2. These values come from the median differences in the centre position, PA, and inclination used here compared to those kinematically derived by R19a. We use 50 trials; the uncertainty is the standard deviation of the results of these trials. To obtain the total uncertainty on each component, we add the rms errors and the standard deviations of the Monte Carlo trials in quadrature, shown in the shaded regions in Figure D.2.

The central regions of the rotation curve will be affected by beam smearing (e.g., Warner et al., 1973; Bosma, 1978; Begeman, 1987; Teuben, 2002; Leung et al., 2018). Beam smearing has the effect of artificially lowering the rotation velocity and increasing the velocity dispersion. This effect is worst in the central regions where the rotation curve rises sharply and for highly inclined systems (e.g., Leung et al., 2018). For our sample, the effect of beam smearing can be most clearly seen in the linewidth map of NGC 1035 (upper right-most panel of Figure D.1), which shows the characteristic $\times$ pattern induced by this effect (e.g., Teuben, 2002). For this analysis, we do not correct for beam smearing. In Figure D.2, the grey hatched regions show twice the beam half-width-half-maximum (HWHM), indicating the radii most affected by beam smearing. As discussed in the following section, the inner slope of the dark matter density profile is calculated from $0.3 - 0.8$ kpc. There is only minimal overlap between this radius range and where the effects of beam smearing will be most apparent, so we conclude that beam smearing will not significantly affect the results presented here.

In order to use CO as the tracer of the total galaxy potential, it must be

dynamically cold. To verify this, we find the median CO velocity dispersion for each galaxy (uncorrected for beam smearing), which are listed in Table D.2. The velocity dispersions are quite low and the galaxies have $\frac{V_{rot}}{\sigma_V} > 4$, which both indicate that the CO is dynamically cold in these galaxies. As a further check, we account for the velocity dispersion using an asymmetric drift correction (ADC; e.g., Binney & Tremaine, 2008) and the stellar surface brightness profiles derived in Section D.4.1. The ADC only increases the rotation velocity by at most 3 $\mathrm{km\,s^{-1}}$, which is well within the uncertainties on the rotation curves. We also compare our CO rotation curves to the Hα rotation curves from R19b where possible (Figure D.2). The CO and Hα rotation curves show good agreement, as was also found by comparing the Hα and CARMA CO data (R19a; R19b). Therefore, we are confident that the CO in these galaxies is dynamically cold and a robust tracer of the total potential. We calculate the dynamical mass (M_{dyn}) at the measured maximum radius of our CO rotation curve (R_{max}). Our measurement of M_{dyn} is a lower limit on the true dynamical mass of these galaxies since the rotation curves generally continue to rise as they approach R_{max}.

D.3.1 Notes on Individual Galaxies

Here, we briefly provide notes on each galaxy in this sample. All morphological information is taken from the HyperLEDA catalogue.

NGC 1035 — This spiral galaxy is the most highly inclined of the subsample. Its CO V_{rot} lies systematically above the Hα V_{rot} derived by R19a, but the shapes of

the rotation curves agree well. The shape of the rotation curve is most important for determining the slope of the dark matter. The amplitude depends on the inclination, though, for this galaxy, we use the same inclination as R19a, so this cannot explain the offset.

NGC 4310 — This galaxy is classified as intermediate between a lenticular and spiral galaxy. From the optical and 4.5 μm data (Figure D.1), there appears to be a dust lane. The CO traces the extent of the bright optical and NIR emission. Kinematically, this is a very well-behaved galaxy, with only a small systemic component in the centre.

NGC 4451 — This spiral galaxy was also observed in Hα, though its mass model was graded as low-quality (R19b). There is a significant offset between the CO and Hα rotation velocities at large radii and the Hα rotation velocity is slightly lower than that of the CO overall, which may be due to irregular ionized gas kinematics in the outer regions of this galaxy. In the inner regions, the slopes of the rotation curves agree well. We use a slightly larger inclination compared to R19a (49° compared to their 45.1°), but this does not completely explain the small offset between the CO and Hα rotation curves at radii less than 1.5 kpc.

NGC 4701 — This spiral galaxy shows no evidence for a bar, though the spiral arms are prominent and strong towards the centre. CO is mainly detected on the blueshifted side of the galaxy. This is not due to a tuning error, but rather due to less signal on the redshifted side of the galaxy.

NGC 5692 — This spiral galaxy has no evidence for a bar. The agreement between the rotation curves derived from the CO and Hα is better than 3 km s^{-1} on average. We use nearly the same inclination as R19a (53° compared to their 52.4°). There is no *Spitzer* IRAC data available for this galaxy, so r-band data are used to measure the stellar components instead.

NGC 6106 — The spiral galaxy has strong spiral arms, and the CO detections are concentrated in the spiral arms. There is no reported bar, though the spiral arms in the centre may contribute to the non-zero radial velocity component seen in the CO rotation curve fits. This is the largest galaxy in the sample, in terms of angular and physical CO extent. We use a slightly higher inclination of 59° compared to R19a who found 53.4°. The agreement between the CO and Hα rotation curves is excellent, though there appears to be a slight increase in the CO velocity at very small radii that is not seen in the Hα, though this may be explained by the finer radial sampling of the CO data.

D.4 Determining the Dark Matter Density Profiles

Our method for decomposing the contributions of the various tracers to the total rotation curve follows that of R19b. To summarize, we can determine the dark matter rotation curve, $V_{\rm DM}(r)$, knowing the rotation curve of the total potential, $V_{\rm tot}(r)$, and the contributions from the stars, $V_*(r)$, atomic gas, $V_{\rm atomic}(r)$, and

molecular gas, $V_{\rm mol}(r)$:

$$V_{\rm tot}(r)^2 = V_{\rm DM}(r)^2 + V_*(r)^2 + V_{\rm atomic}(r)^2 + V_{\rm mol}(r)^2. \quad \text{(D.2)}$$

$V_*(r)$ is calculated from *Spitzer* 4.5μm or r-band photometric data (Section D.4.1). The contributions of the atomic and molecular gas components are negligible compared to the stars and dark matter (Section D.4.2). We include these components when available from R19b, otherwise their contributions are set to zero. We use the CO rotation curves derived here as our measurement of $\rm V_{tot}(r)$. As described in Section D.3, the measured CO velocity dispersions are low (Table D.2), even without a correction for beam smearing, meaning that the CO is a robust, dynamically cold tracer of the total potential.

Therefore, having measured the total potential, the stellar component, and the contributions from the atomic and molecular components where available, we can solve for the contribution from the dark matter. As we describe in Section D.4.3, we use a forward-modelling approach to measure the dark matter component. From the best-fitting dark matter density profile, we compute β^*, the slope of the dark matter density profile from $0.3 - 0.8$ kpc (R19b).

D.4.1 Stellar Mass and Velocity Profiles

We derive the stellar rotation curves starting from the *Spitzer* IRAC 4.5μm maps (Figure D.1). As discussed by R19a and R19b, the 4.5μm data are preferred since they more closely trace the stellar mass distribution than the r-band data.

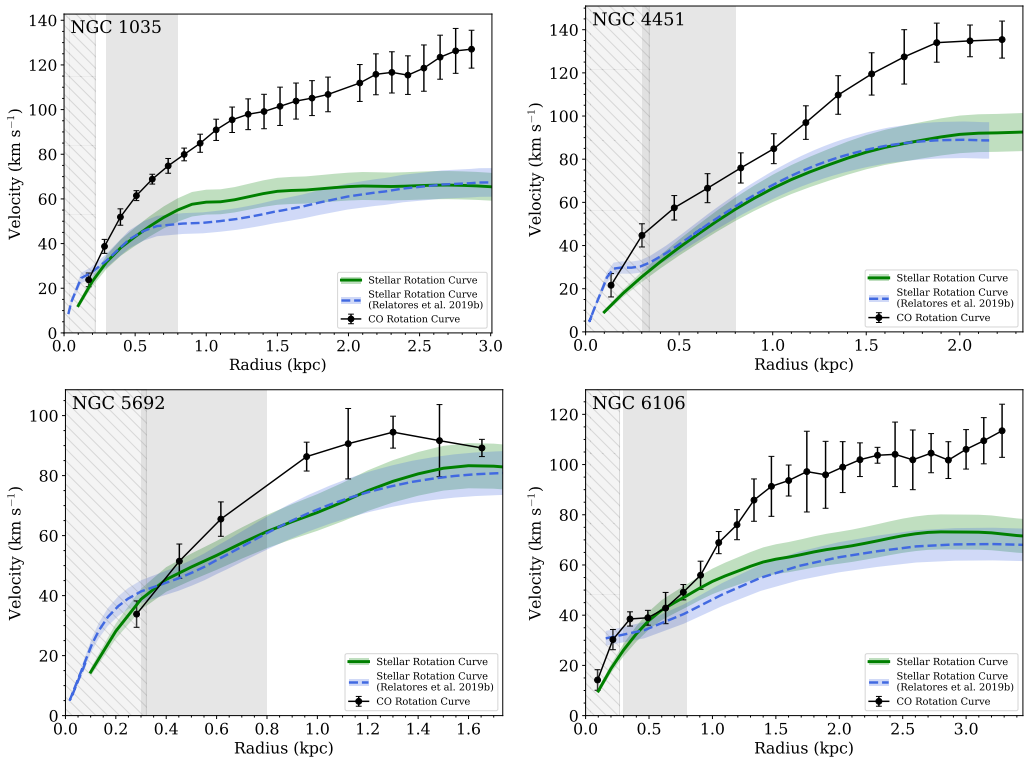

Figure D.3: A comparison of the stellar rotation curves derived as described in Section D.4.1 (green) compared to those derived by R19b (blue dashed). We also show the CO rotation curves (black) which trace the total potential. In general, the agreement between these methods is good, especially in the radial regime where β^* will be calculated (grey shaded region). The grey hatched region shows twice the CO beam HWHM, indicating the central regions in which the CO rotation velocities may be affected by beam smearing.

Using the geometric parameters listed in Table D.2, the 4.5μm maps were divided into annuli centred on the centre of the galaxy. For radii that overlap with the CO rotation curves, the radial binning matches that of the CO. For radii beyond the CO extent, the annuli are 5 pixels wide and extend out to a radius $R_{max,*}$ (listed in Table D.3). The cumulative stellar mass profiles do not continue to rise substantially at $R_{max,*}$, so stellar masses calculated at this radius encompass nearly all of the stellar mass of the galaxies. The surface brightness was summed in each annulus and converted to a luminosity. To convert to solar luminosities, we find the luminosity of the Sun at 4.5 μm using the IRAC Channel 2 zero-point (0 Vega mag = 179.7 Jy; Reach et al., 2005) and the absolute magnitude of the Sun at 4.5 μm ($M_{\odot}^{4.5}$ = 3.27 Vega mag; Oh et al., 2008b). This yields $L_{\nu,\odot}^{4.5} = 1.06 \times 10^{18}$ erg s^{-1} Hz^{-1} or $\nu L_{\nu,\odot}^{4.5} = 7.05 \times 10^{31}$ erg s^{-1} = 0.018 $L_{\odot}$. To convert to mass, we assume a constant mass-to-light ratio (Υ_*) from stellar population synthesis models reported by R19b (see their Table 1). For those galaxies that do not overlap with R19b's sample, we take their average $\Upsilon_* = 0.21 \pm 0.04$. We report the Υ_* value used in this work in Table D.3.

Spitzer IRAC 4.5 μm data are not available for NGC 5692. Like R19b, we instead use r-band images from PS1 (Figure D.1) and employ the same method as described above to calculate the surface brightness profiles. The filters on PS1 are quite similar to the corresponding Sloan Digital Sky Survey (SDSS) filters (Tonry et al., 2012). The absolute magnitude of the Sun is 4.65 AB magnitudes in the SDSS r-band (Willmer, 2018), and the effective central wavelength of the PS1 r-band filter is 617 nm (Tonry et al., 2012). This yields $L_{\nu,\odot}^{r} = 5.99 \times 10^{18}$ erg s^{-1} Hz^{-1}

or $\nu L^r_{\nu,\odot} = 2.91 \times 10^{33}$ erg s^{-1} $= 0.746\ L_\odot$. To convert to mass, we use the r-band Υ_* from stellar population synthesis models derived by R19b ($\Upsilon_* = 0.83 \pm 0.15$; see their Table 1 and our Table D.3).

We use NEMO (Teuben, 1995) to determine the rotation velocity due to the stellar mass from the extracted surface brightness profiles. We assume that the stars are in a thin disk. In reality, the stars are likely in an oblate spheroid distribution. However, the axis ratio of stellar distributions tend to be small (e.g., Kregel et al., 2002), and all of the galaxies used here are classified as spirals. For their modelling, R19b assume an oblate spheroid with $c/a = 0.14$ motivated by observations. Where possible, we compare our derived stellar rotation curves (assuming a thin disk) to those derived by R19b (Figure D.3). In general, the agreement (both in terms of shape and amplitude) are good, especially over the range of radii where β^* will be calculated. The stellar rotation curves derived by R19b tend to be higher than ours in the centres, which may be due to our coarser binning. The uncertainty on the stellar rotation curve is propagated from the uncertainty on Υ_*. The total stellar masses of the galaxies in our sample (listed in Table D.3) agree with those measured by R19b within the uncertainties, where available.

If the stellar component of the rotation velocity is higher than that of the CO, we fix V_* at those radii to a maximal disk (i.e. where the stellar component accounts for the total potential). We increase the uncertainty on the stellar rotation velocity in these bins by adding the velocity difference to the existing uncertainty in quadrature. The first five bins in NGC 4701 and the first bin in NGC 5692 are affected by this change.

D.4.2 Atomic and Molecular Gas Components

For the four galaxies that overlap with R19b, we also include contributions from the atomic and molecular gas in the decomposition. We refer the reader to that paper for a detailed discussion of how these components were measured. We do not include uncertainties on the atomic and molecular components for this analysis (nor are they given by R19b). For the other two galaxies, however, we assume that these components are a negligible contribution to the mass. As we will discuss in Section D.5.1, including or excluding these components does not affect the final results.

D.4.3 Decomposing the Dark Matter Component

Knowing the contributions from the stars (and atomic and molecular gas, if available) and the total potential, we can derive the dark matter density profile, following Equation D.2. We take a forward-modelling approach, generating trials of the dark matter density profile and minimizing the difference between the model total rotation curve and that observed from the CO as described below.

We must assume some parameterized form for the dark matter density profile. We use a generalised Navarro-Frenk-White (gNFW; Zhao 1996) profile of the form

$$\rho_{\rm DM}(r) = \frac{\rho_o}{(r/r_s)^{\beta}(1 + r/r_s)^{3-\beta}} \tag{D.3}$$

where r_s is the scale radius, ρ_o is the characteristic density, and β sets the slope as

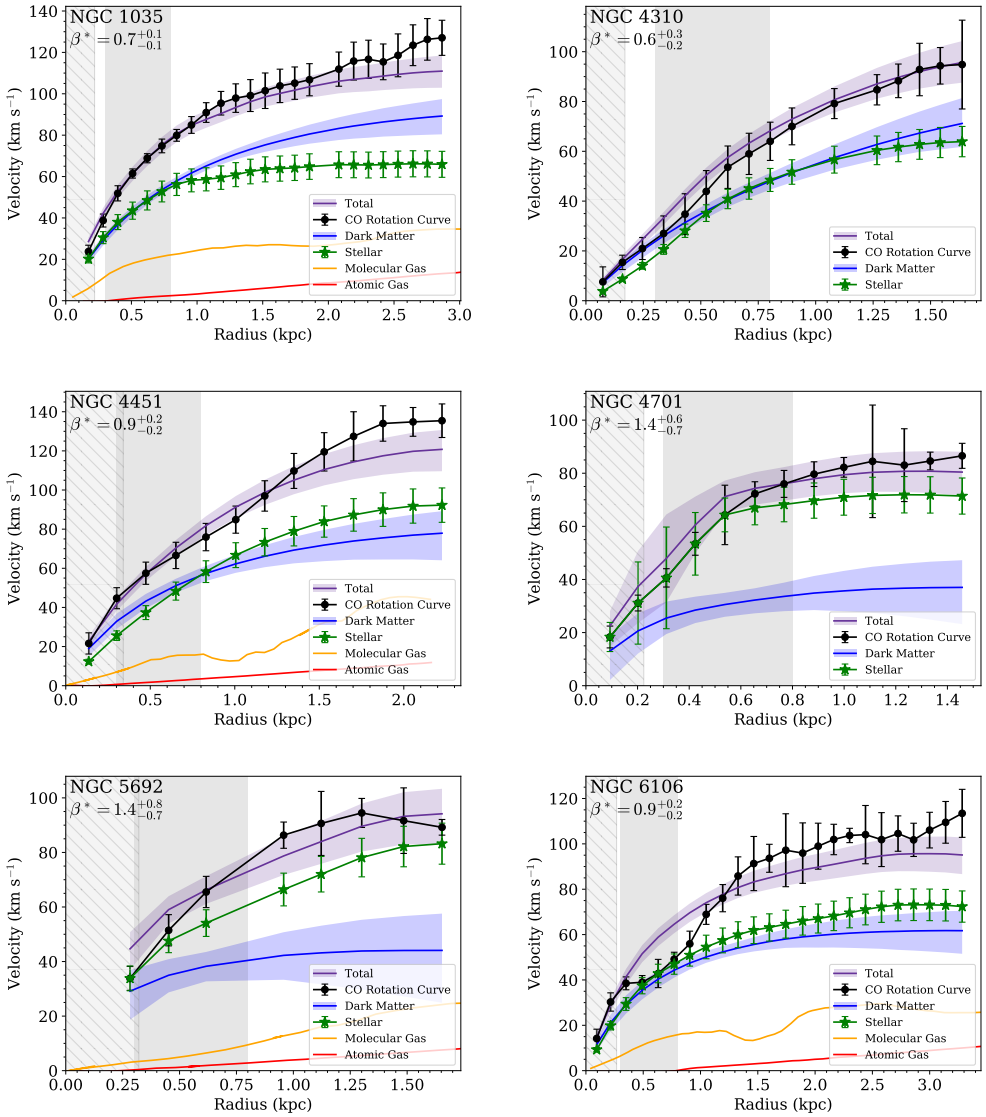

Figure D.4: The results of the rotation curve decomposition. The CO rotation curve is shown as the black dots (Section D.3), the stellar rotation curve in the green stars (Section D.4.1, and the atomic and molecular components (if available) in red and orange (Section D.4.2). The blue curves and shaded regions show the dark matter component, and the purple curves and shaded regions show the total modelled rotation curves of all the components (Equation D.2), which should closely match the CO. The grey hatched region shows twice the CO beam HWHM, indicating the central regions which may be affected by beam smearing. The grey shaded region shows the radii over which β^* is calculated (Equation D.7), and the best-fitting β^* values are listed in the upper left corners.

Name	Υ_*	$R_{max,*}$ (kpc)	$\log M_*(< R_{max,*})$ ($\log M_\odot$)	R_{vir} (kpc)	1−2% R_{vir} (kpc)	$\log M_{200}$ ($\log M_\odot$)	c_{200}	β^*
NGC 1035	0.21±0.04	6.0	9.5	76^{+49}_{-18}	$0.8^{+1.3}_{-0.6}$−$1.5^{+2.5}_{-1.2}$	$11.4^{+2.2}_{-0.3}$	27^{+24}_{-11}	$0.7^{+0.1}_{-0.1}$
NGC 4310	0.21±0.04	6.2	9.3	76^{+75}_{-26}	$0.8^{+1.5}_{-0.5}$−$1.5^{+3.0}_{-1.0}$	$11.4^{+3.8}_{-0.3}$	22^{+29}_{-13}	$0.6^{+0.3}_{-0.2}$
NGC 4451	0.21±0.04	9.7	9.7	88^{+47}_{-13}	$0.9^{+1.4}_{-0.8}$−$1.8^{+2.7}_{-1.5}$	$11.5^{+1.9}_{-0.2}$	38^{+38}_{-16}	$0.9^{+0.2}_{-0.2}$
NGC 4701	0.21±0.04	6.5	9.4	58^{+48}_{-7}	$0.6^{+1.1}_{-0.5}$−$1.2^{+2.1}_{-1.0}$	$10.9^{+5.0}_{-0.2}$	54^{+121}_{-28}	$1.4^{+0.6}_{-0.7}$
NGC 5692	0.83±0.15	4.8	9.3	70^{+52}_{-7}	$0.7^{+1.2}_{-0.6}$−$1.4^{+2.4}_{-1.3}$	$11.1^{+4.4}_{-0.1}$	62^{+152}_{-30}	$1.4^{+0.8}_{-0.7}$
NGC 6106	0.21±0.04	8.9	9.7	67^{+41}_{-11}	$0.7^{+1.1}_{-0.6}$−$1.3^{+2.2}_{-1.1}$	$11.2^{+2.3}_{-0.2}$	34^{+36}_{-15}	$0.9^{+0.2}_{-0.2}$

Υ_* is the mass-to-light ratio assumed here reproduced from the stellar population synthesis model results presented by R19b. M_* is the total stellar mass within a radius $R_{max,*}$ from the fitting described in Section D.4.1; uncertainties are ±0.1 dex. R_{vir} is the virial radius derived from the best-fitting total density profile, at which the density is 200× the critical density. Uncertainties are propagated from the uncertainties on the total density profile. M_{200} is the mass contained within $R_{200} \equiv R_{vir}$. Uncertainties are propagated from R_{vir}. c_{200} is the concentration parameter, defined as R_{200}/r_s. Uncertainties are propagated from R_{vir} and r_s. β_* is the inner slope of the dark matter density profile, as defined in Equation D.7.

Table D.3: Fitted Stellar and Dark Matter Density Parameters

$r \to 0$. Setting $\beta = 1$ recovers the original NFW profile.

We transform this density profile into its corresponding rotation curve, $V_{\rm DM}(r)$, where

$$V(r)^2 = \frac{4\pi G}{r} \int_0^r \imath^2 \rho(\imath) d\imath \tag{D.4}$$

(e.g. Binney & Tremaine, 2008).

We use an affine invariant Markov Chain Monte Carlo (MCMC) method (`emcee`; Foreman-Mackey et al., 2013) to draw samples of ρ_o, r_s, and β to generate trials of the dark matter density and associated rotation curve (Equations D.3 and D.4). The uniform priors on these values are set such that $0 < \frac{\rho_o}{\rm M_\odot\ pc^{-3}} < 1.0$, $0 < \frac{r_s}{\rm kpc} < 10$, and $0 < \beta < 2.5$.

We then calculate the model rotation curve of the total potential for each trial using Equation D.2.

Our log-likelihood function, which minimizes the difference between the observed CO rotation curve and the model, is given by

$$\log \mathcal{L} = \frac{-1}{2} \sum_i \frac{\left(\sqrt{V_{{\rm CO},i}^2 - V_{*,i}^2 - V_{{\rm atomic},i}^2 - V_{{\rm mol},i}^2} - V_{{\rm DM},i}\right)^2}{\sigma_i^2}. \tag{D.5}$$

where

$$\sigma_i^2 = \frac{V_{{\rm CO},i}^2 \sigma_{V_{{\rm CO},i}}^2 + V_{*,i}^2 \sigma_{V_{*,i}}^2}{V_{{\rm CO},i}^2 - V_{*,i}^2 - V_{{\rm atomic},i}^2 - V_{{\rm mol},i}^2} \tag{D.6}$$

where $\sigma_{V_{{\rm CO},i}}$ and $\sigma_{V_{*,i}}$ are the uncertainties on the CO and stellar rotation curves[‖].

We initialize the MCMC with $\rho_o = 0.5\ {\rm M_\odot\ pc^{-3}}$, r_s equivalent to the maximum

[‖] We note that in cases where $V_{{\rm atomic},i} = V_{{\rm mol},i} = 0$ and where $V_{*,i} = V_{{\rm CO},i}$ (e.g., the first five radii in NGC 4701), $\sigma_i \to \infty$. However, because σ_i is in the denominator of our likelihood function (Equation D.5) and because for no galaxy does this situation occur at all i, $\log \mathcal{L}$ will be finite.

Name	ρ_o ($M_\odot$ pc^{-3})	r_s (kpc)	β
NGC 1035	$0.245^{+0.264}_{-0.137}$	$2.8^{+1.7}_{-1.0}$	$0.3^{+0.2}_{-0.2}$
NGC 4310	$0.195^{+0.149}_{-0.083}$	$3.5^{+3.1}_{-1.6}$	$0.1^{+0.2}_{-0.1}$
NGC 4451	$0.272^{+0.324}_{-0.164}$	$2.3^{+1.9}_{-0.9}$	$0.4^{+0.3}_{-0.3}$
NGC 4701	$0.218^{+0.442}_{-0.143}$	$1.1^{+2.2}_{-0.5}$	$0.5^{+0.8}_{-0.4}$
NGC 5692	$0.272^{+0.390}_{-0.183}$	$1.1^{+2.6}_{-0.5}$	$0.6^{+0.9}_{-0.5}$
NGC 6106	$0.229^{+0.327}_{-0.143}$	$1.9^{+1.6}_{-0.8}$	$0.3^{+0.3}_{-0.2}$

The density normalisation (ρ_o), radial scale length (r_s), and power-law index (β) are the three fitted parameters in the gNFW profile (Equation D.3). The uncertainties are the 68 per cent confidence intervals of the marginalized posterior distributions (Figure D.5). See Section D.4 for details.

Table D.4: Fitted Dark Matter Density Parameters

radius in the CO rotation curve, $\beta = 0.5$, and use 100 walkers for 300 steps. Samples of the parameters are drawn linearly between these bounds set by the priors. By examining the chains, the MCMC has forgotten the initial conditions after 50 steps. To be conservative, we discard the initial 100 steps.

The best-fitting parameters are given by the median of the marginalized posterior parameter distributions. The uncertainties are given by the 16$^{\text{th}}$ and 84 $^{\text{th}}$ percentiles, which is equivalent to 1-σ for a Gaussian distribution. These best-fitting parameters are given in Table D.4, and the posterior distributions are shown in Figure D.5. The best-fitting rotation curve decompositions are shown in Figure D.4.

We are interested in the inner slope of the dark matter density profile. Following R19b, we define "inner" as radii from $0.3 - 0.8$ kpc and denote the slope in this radial range as β^*:

$$\beta^* \equiv -\frac{\log\left(\frac{\rho_{\rm DM}(0.8\ \rm kpc)}{\rho_{\rm DM}(0.3\ \rm kpc)}\right)}{\log\left(\frac{0.8\ \rm kpc}{0.3\ \rm kpc}\right)}. \tag{D.7}$$

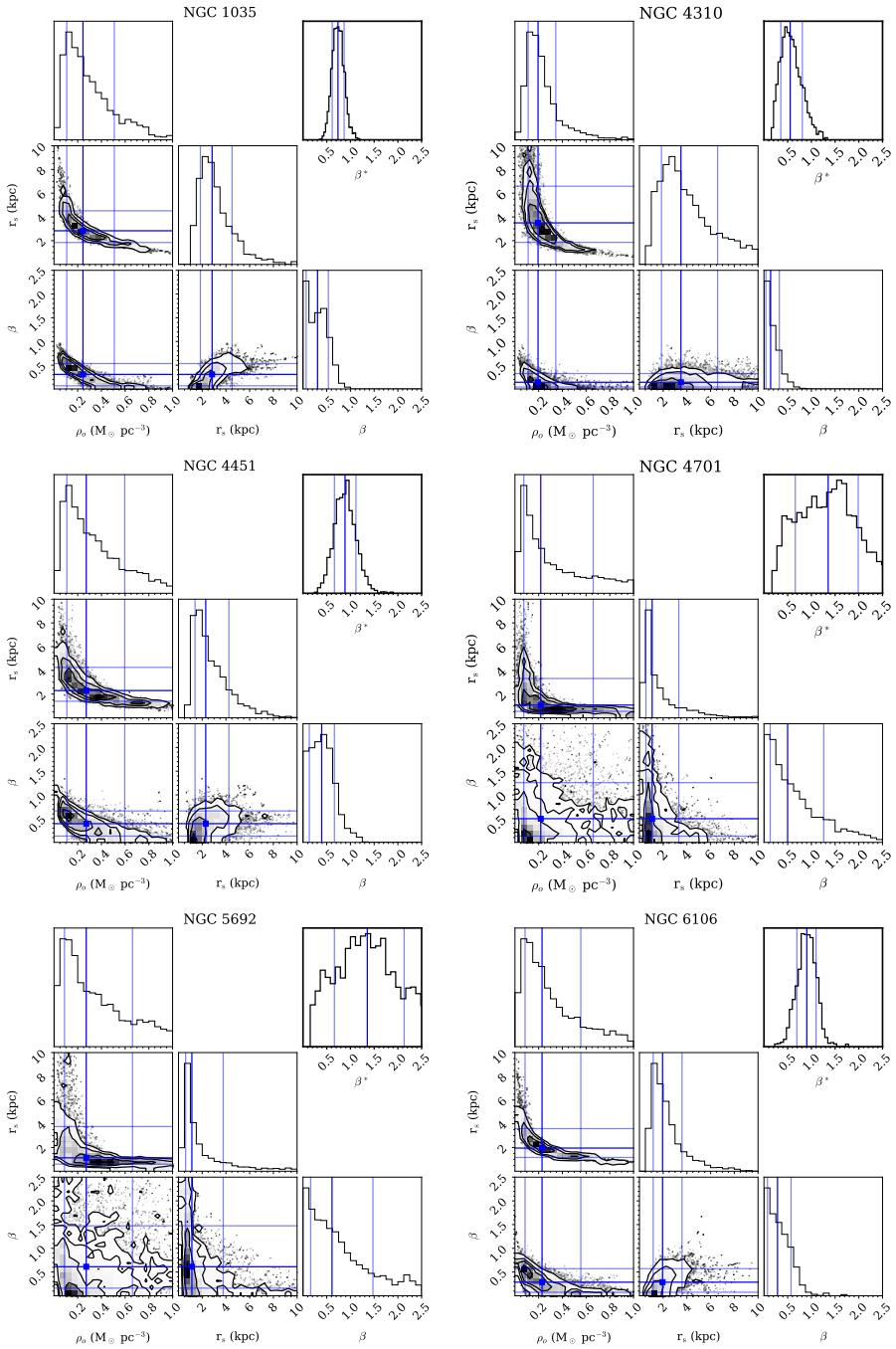

Figure D.5: The posterior distributions for ρ_o, r_s, and β in the gNFW dark matter profile given in Equation D.3 are shown in these corner plots. The plots in the upper right corner of each panel with thick outlines show the resulting distribution of β^*. The dark blue lines show the median and the light blue lines show the 16^{th} and 84^{th} percentiles of the marginalized posterior likelihood distributions.

We calculate β^* at each step in the MCMC chain. The best-fitting value of β^* is given by the median of the distribution and the quoted uncertainties are the $16^{\rm th}$ and $84^{\rm th}$ percentiles (upper right corner panels of Figure D.5). While some of the posterior distributions of the fitted gnFW parameters are wide, the value of β^* is relatively insensitive to the precise individual values of ρ_o, r_s, and β. Rather, it is the combination of these parameters yielding the dark matter density distribution that determines the value of β^*. Our final values of β^* and uncertainties are reported in Table D.3.

Simulations primarily define the inner dark matter density slope from $1-2\%$ of the virial radius ($\rm R_{vir}$). It is often convenient to define $\rm R_{vir} \equiv R_{200}$, where $\rm R_{200}$ is the radius at which the density is 200 times the critical density ($\rho_{\rm crit}$; e.g. Bullock & Boylan-Kolchin, 2017). We refer to this density as ρ_{200} ($\equiv 200\rho_{\rm crit}$). The mass enclosed within $\rm R_{200}$ is $\rm M_{200}$. Assuming a local Universe value of $H_0 = 73.2$ km s^{-1} Mpc^{-1} (Riess et al., 2021; Di Valentino et al., 2021) yields $\rho_{\rm crit} = 148.7$ $\rm M_\odot$ kpc^{-3}. We extrapolate our best-fitting density profile for the total potential to estimate $\rm R_{vir}$ ($\equiv \rm R_{200}$) and $\rm M_{200}$ (Table D.3). Given the uncertainties on the total density profile, we estimate the uncertainty on $\rm R_{vir}$ and hence $\rm M_{200}$. We find that $0.3-0.8$ kpc corresponds to $0.3-1.6\%$ of $\rm R_{vir}$ for these galaxies. Said another way, $1-2\%$ of $\rm R_{vir}$ corresponds to $0.6-1.8$ kpc for these galaxies (Table D.3). Accounting for the uncertainties on $\rm R_{vir}$, the $1-2\%$ of $\rm R_{vir}$ spans a range of $0.1-5.0$ kpc. Therefore, our definition of β^* tends to probe smaller physical radii in these galaxies than the definition used in many simulations. This will be discussed further in Section 4.4 when we compare our results to simulations.

We also compute the central concentration (c_{200}) implied by our measurements, where $c_{200} \equiv \frac{R_{200}}{r_s} \equiv \frac{R_{vir}}{r_s}$ (e.g., Dutton & Macciò, 2014; Newman et al., 2015). We report our values of c_{200} in Table D.3, where the uncertainties are substantial and propagated from the uncertainties on R_{vir} (Table D.3) and r_s (Table D.4). We compare with R19b where possible,** and we agree well within the uncertainties, except for NGC 5692 for which we have the largest uncertainty.

D.5 Results

We are interested in measuring the inner slope of the dark matter density distribution for our sample of dwarf galaxies. We define "inner" as from $0.3-0.8$ kpc and denote the slope in this radial range as β^* (Equation D.7). We use the CO rotation curves that we derive here (Figure D.2; Section D.3) as a robust tracer of the total potential. We use an MCMC method to construct model dark matter density profiles, assuming a gNFW form (Equation D.3). By including the stellar component (Section D.4.1), we minimize the difference between the CO rotation curve and our model of the total potential (including the stars and dark matter; Section D.4). We measure β^* from the fitted dark matter density profiles (Figure D.4). We find no trends between the value of β^* and galaxy parameters such as inclination, distance, R_{max}, R_{vir}, M_{dyn}, or M_*.

For these six galaxies, we find β^* values that are on average consistent with cuspy dark matter density profiles ($\langle\beta^*\rangle = 1.0$ with a standard deviation of ± 0.3;

**Though R19b do not report c_{200} directly, it is related to β and c_{-2}, which they report in their Table 4, where $c_{200} = c_{-2}(2-\beta)$. c_{-2} is the concentration measured at the radius at which $\rho \propto r^{-2}$ locally. See Newman et al. (2015) and R19b for more details.

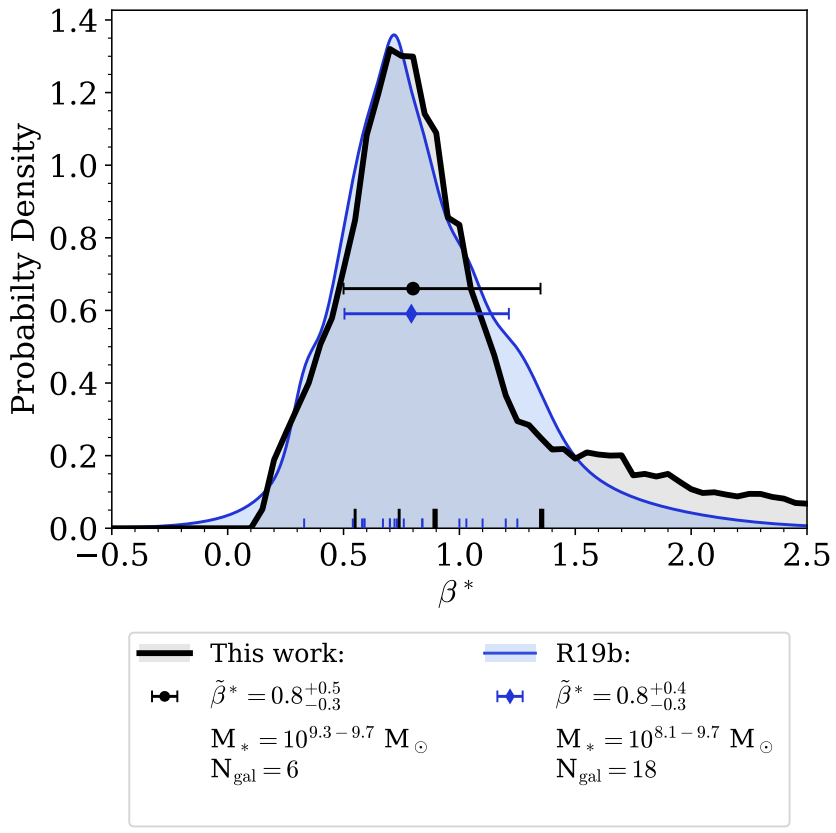

Figure D.6: A KDE showing the distribution of β^* values we measure in this study (black curve). The black tick marks at the bottom show the individual β^* values. The black dot shows the median of the distribution ($\tilde{\beta}_*$); the error bars show the 16^{th} and 84^{th} percentiles. The blue KDE, tick marks, diamond, and error bars show the same quantities but for the galaxies studied by R19b with reliable mass decompositions. The legend also notes the number of galaxies in each KDE and the stellar mass range covered by those galaxies.

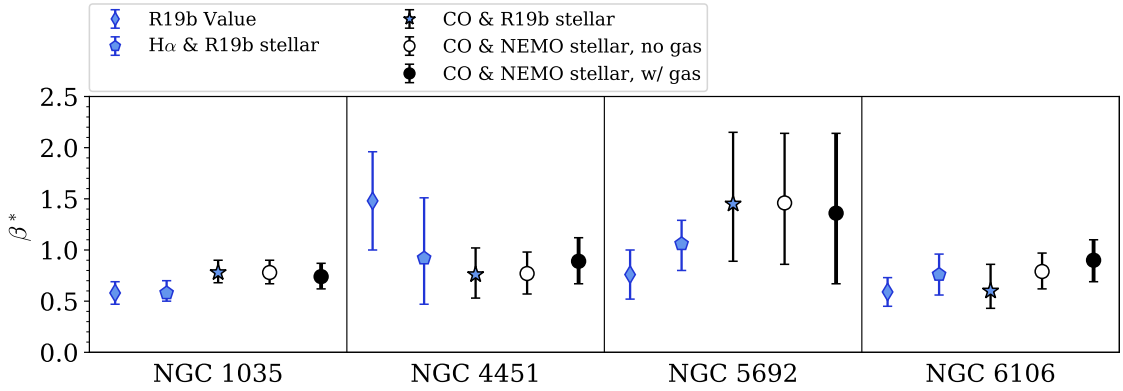

Figure D.7: A comparison of the β^* values derived for different sets of assumptions as described in Section D.5.1 for the galaxies that overlap with R19b. The blue diamonds show the values derived by R19b. The blue pentagons show the β^* we derive using Hα rotation curves to trace the total potential (R19a), the stellar rotation curves from R19b, and including the atomic and molecular components as a check on the accuracy of our decomposition method. The blue filled stars show the results when using our CO rotation curves to trace the total potential, the stellar rotation curves from R19b, and including the atomic and molecular components. The circles show the values of β^* derived using our CO rotation curves to trace the total potential, the stellar rotation curves we derive using NEMO (Section D.4.1), and either excluding (open) or including (filled) the atomic and molecular components. Within each galaxy bin, points are artificially offset along the horizontal axis for clarity. In general, we do not find significant differences in the values of β^* derived for each set of assumptions given the uncertainties.

Table D.3). We show the distribution of our β^* values in black in Figure D.6 as a kernel density estimator (KDE). We make this KDE by summing the posterior distributions of β^* for each galaxy (Figure D.5) and renormalising to unit area. The median of this distribution is $\tilde{\beta}_* = 0.8^{+0.5}_{-0.3}$, where the lower and upper uncertainties correspond to the 16$^{\rm th}$ and 84$^{\rm th}$ percentiles of the distribution (1-σ for a Gaussian distribution). By our KDE construction, this quoted uncertainty reflects both the measurement uncertainties and the galaxy-to-galaxy scatter (though counted in a different way than the standard deviation of the best values). We note in particular that the high-slope end of our distribution is driven by one galaxy with large uncertainties (NGC 5692). The average and scatter derived from Table D.3 ($\langle\beta^*\rangle = 1.0$ with standard deviation of ± 0.3) reflect only the galaxy-to-galaxy scatter in the best-fitting β^* values.

We compare the distribution of our β^* measurements to those from R19b. A KDE of their values is shown in blue in Figure D.6. For this KDE, we represent each of their measurements as a Gaussian, where the width is set by their measurement uncertainties (see their Table 3, grades 1 and 2). The individual Gaussians are summed and normalised to unit area. We find excellent agreement in the distribution of slopes with our measurements of those of R19b ($\tilde{\beta}_* = 0.8^{+0.4}_{-0.3}$, where the lower and upper uncertainties correspond to the 16$^{\rm th}$ and 84$^{\rm th}$ percentiles of the distribution). In comparing these distributions, it is important to keep in mind that our sample only includes six galaxies, whereas R19b have 18 galaxies.

D.5.1 Checks on the Method and Assumptions

Below we describe several tests we performed to check the robustness of our modelling and results to various assumptions. We show the resulting values of β^* for these different tests in Figures D.7 and D.8. For the discussion in Section 4.4, we will adopt the values of β^* we derive using our CO and stellar rotation curves, including the atomic and molecular gas components where available, as reported in Table D.3. In general, we do not find significant differences in the values of β^* derived for each set of assumptions given the uncertainties.

D.5.1.1 Decomposition Method

As a check on our decomposition method, we measure β^* using the Hα rotation curves from R19a as a tracer of the total potential and the stellar rotation curves from R19b to most closely reproduce their results. Any differences in these values compared to those presented by R19b will be due to our fitting method, as the assumptions about the total and stellar potentials and the form of the dark matter density are the same.

As shown in Figure D.7, the results of this test (blue pentagons) are in good agreement with the values reported by R19b (blue diamonds), meaning that our fitting routine will not introduce biases in the measurement of β^*. The most discrepant galaxies are NGC 4451 and NGC 5692, though they are still consistent within the uncertainties. We note that the errorbars on the blue pentagons are related to the uncertainties on the Hα and stellar rotation curves. In the case of the Hα rotation

curves, the uncertainties are reflective of the formal fitting uncertainties (R19a) and, therefore, do not include larger sources of systematic uncertainty.

D.5.1.2 CO v. Hα as Tracers of the Total Potential

A difference between this analysis and that presented by R19b is that we use CO to trace the total potential while they use Hα. As discussed in Section D.3 (and by R19b), there is good agreement in general between the CO and Hα rotation curves (Figure D.2). For the Hα, this indicates that it is indeed a dynamically cold tracer. The low velocity dispersions of the CO (Table D.2) confirm that it is also dynamically cold.

We compare the values of β^* we derive using the CO rotation curves (blue stars) with those derived using Hα by R19b (blue pentagons) in Figure D.7, using the stellar rotation curves derived by R19b to purely test the effect of the different tracers of the total potential. Given the uncertainties, the β^* measurements from CO and Hα are in excellent agreement with one another.

D.5.1.3 Stellar Rotation Curve Derivation

As described in Section D.4.1, while we use the same photometric data to measure the stellar components as R19b, we derive the stellar light profiles and rotation curves using different methods and assumptions. As shown in Figure D.3, the agreement between our derived stellar rotation curves is quite good in general.

In Figure D.7, we compare the values of β^* derived using our stellar rotation

curves (black filled circles) and those from R19b (blue stars), with all other variables the same. These values are in excellent agreement within the uncertainties. Therefore, our calculation of the stellar rotation velocities assuming a thin disk will not greatly affect the results.

D.5.1.4 Excluding the Atomic and Molecular Components

We do not have information about the atomic and molecular components readily available for two of the galaxies in this sample. We test whether the measured β^* values are biased by not including the atomic and molecular gas in the mass decomposition. We repeat the decomposition to determine β^* with and without this gas data for the four galaxies that overlap between our sample and the R19b sample, using the CO data to trace the total potential and using our stellar rotation curves from NEMO. The β^* values with (filled circles) and without (open circles) the gas are compared directly in Figure D.7. For all galaxies, the derived β^* values are consistent well within the uncertainties. We, therefore, conclude that excluding the atomic and molecular gas data from the decomposition will not significantly affect the results.

D.5.1.5 Assumed Functional Form of the Dark Matter Density Profile

In addition to the gNFW profile in Equation D.3, we also tried a single power-law of the form

$$\rho_{\rm DM}(r) = Ar^{-\beta} \tag{D.8}$$

since our CO observations tend to probe small radii close to the centre and the three parameter fits shown in Figure D.5 appear under-constrained. The posteriors of the power-law fits are good and, in general, better constrained than the three parameter gNFW fits. The resulting power-law model rotation curves, however, tend to continue rising whereas the CO rotation curves tracing the total potential flatten. This suggests that while the CO observations tend to probe close to the galaxy centres, they do reach the radial range where a second power-law slope may be important. This is most evident for NGC 6106, which has the largest R_{max} in the sample. The power-law fit continues to rise, producing a steeper dark matter slope in the centre, resulting in the slightly larger values of β^* compared to the gNFW, all else being equal. We directly compare the derived values of β^* in Figure D.8. For the same assumptions about the gas content and stellar profiles used, the β^* values from the power-law and gNFW dark matter density profiles are consistent within the uncertainties.

These tests show that while the precise values for the gNFW dark matter density profile parameters may be under-constrained, their combination and hence the derivation of β^* is fairly robust. R19b also found that β^* itself is better constrained than the individual gNFW parameters. We, therefore, adopt the β^* values from the more physically motivated gNFW profile in the discussion.

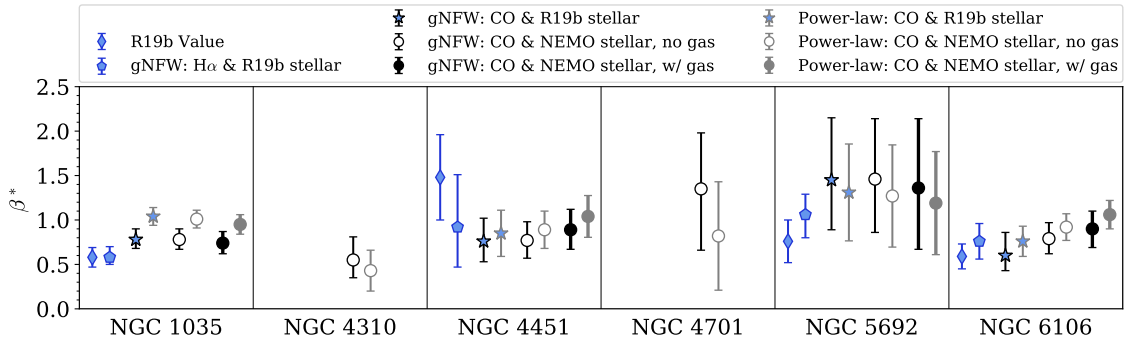

Figure D.8: A comparison of the β^* values derived for different forms of the dark matter density profiles, in the style of Figure D.7. The blue diamonds show the values derived by R19b. The blue pentagons show the β^* we derive using Hα rotation curves to trace the total potential (R19a), the stellar rotation curves from R19b, including the atomic and molecular components, and using a gNFW profile as a check on the accuracy of our decomposition method. The blue filled stars show the results when using our CO rotation curves to trace the total potential, the stellar rotation curves from R19b, and including the atomic and molecular components. The circles show the values of β^* derived using our CO rotation curves to trace the total potential, the stellar rotation curves we derive using NEMO (Section D.4.1), and either excluding (open) or including (filled) the atomic and molecular components. The symbols outlined in black show the results using a gNFW profile (Equation D.3), and symbols outlined in grey show the results using a power-law profile (Equation D.8). In general, the β^* values from the power-law fits agree with those from the gNFW within the uncertainties. Within each galaxy bin, points are artificially offset along the horizontal axis for clarity.

D.6 Discussion

D.6.1 Comparison to Previous Observational Studies

We compare our measurements of the inner dark matter density slope to other observational studies of dwarf galaxies as a function of the stellar mass of the galaxy (Figure D.9 top). These observational studies span a range of tracers and methodologies, as described briefly here. There is no overlap between our sample of galaxies and those from Simon et al. (2005), Oh et al. (2011, 2015), Adams et al. (2014), Collins et al. (2021), or Leung et al. (2021). In Figure D.9, we have tried to use similar colours for studies with similar methodologies, as described below.

Simon et al. (2005) use a combination of Hα and CO data (where available) in five galaxies to measure β^*. The rotation curves were extracted using the same method as described in Section D.3, and they fit their stellar rotation curves using a similar method to the one used here (Section D.4.1). They measure their dark matter slopes from a power-law fit to the full dark matter rotation curves which extend out to $2-5$ kpc from the centre. Assuming a fiducial $R_{vir} \sim 100$ kpc, these data probe $\sim 2-5\%$ of R_{vir}. This is corresponds to somewhat farther out in the dark matter halo than probed by our measurements which probe $\sim 0.3-1.6\%$ of R_{vir} (see Section D.4).

Adams et al. (2014) use integral field measurements, which trace the kinematics of the stars and ionized gas in a sample of six dwarf galaxies. They extract their circular velocity curves using dynamical modeling of both the stars and ionized gas.

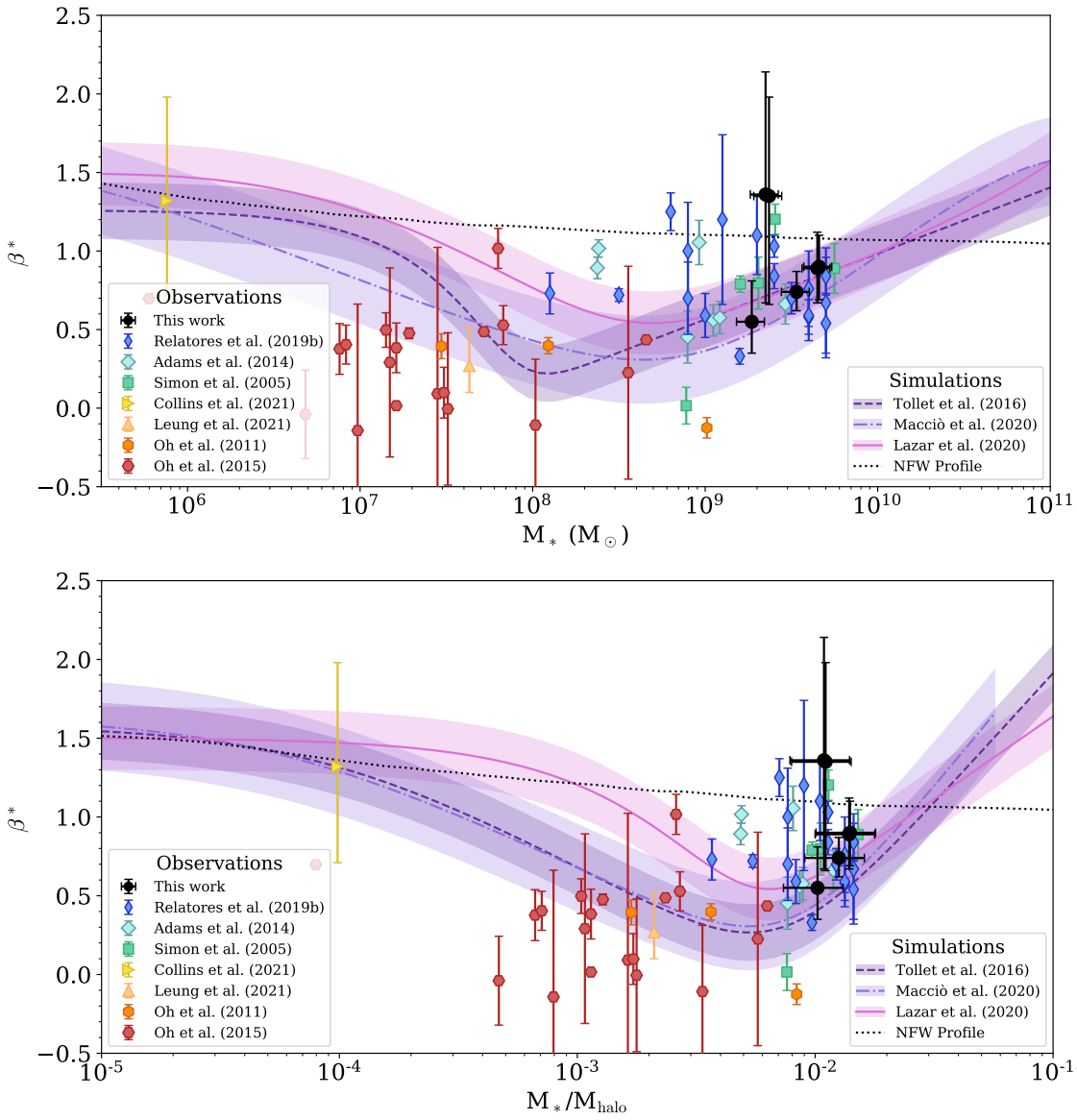

Figure D.9: The inner dark matter density slope (β^*) as a function of stellar mass (top) and the ratio of stellar mass to halo mass (bottom). The points derived here are shown in the black circles. The horizontal error bars on our points reflect the uncertainty in our stellar mass measurements (top) or the scatter in the assumed stellar mass-halo mass relation (bottom). We compare with other observational studies (colored symbols; Simon et al., 2005; Oh et al., 2011, 2015; Adams et al., 2014; Relatores et al., 2019b; Collins et al., 2021; Leung et al., 2021) and simulations (shaded curves; Tollet et al., 2016; Lazar et al., 2020; Macciò et al., 2020). The black dotted line shows the expectation from an NFW profile. Cores have $\beta^* \sim 0$ and cusps have $\beta^* \gtrsim 1$. Our measurements are in good agreement with previous measurements at similar M_* and M_*/M_{halo}, given the scatter and uncertainties. Galaxies in this range of M_* and M_*/M_{halo} tend to have cuspy dark matter density profiles.

As described by R19b, we use their gNFW fits to calculate β^* following Equation D.7.

Oh et al. (2011, 2015) use HI data from the THINGS and LITTLE THINGS surveys to trace the galaxy potentials and *Spitzer* 3.6 μm data to remove the stellar contributions. They derive their rotation curves using a tilted ring model and apply an asymmetric drift correction to their data. Their method of deriving the stellar mass profiles is similar to ours, but using the 3.6 μm data. For their mass models, they use both a NFW profile (which produces a cusp) and a pseudo-isothermal model (which produces a core), finding that the pseudo-isothermal profiles are a better fit to their observations. They measure the inner slope of their dark matter density profiles by fitting a power-law at radii smaller than a "break" radius, which is the radius where the slope changes most rapidly. This "break" radius changes for each galaxy, but is $\lesssim 1$ kpc, so we are measuring β^* over a similar range of radii.

As discussed previously, R19b use Hα measurements to trace the total potential of the galaxies and *Spitzer* 4.5 μm data to trace the stellar components. They obtain their stellar profiles using a multi-Gaussian expansion method, as opposed to our method of extracting the stellar light in concentric annuli. We base our decomposition method on theirs and adopt their definition of β^*. Figure D.7 shows the comparison of our β^* measurements to theirs for the five common galaxies.

Collins et al. (2021) study the dark matter in a single low mass galaxy, Andromeda XXI. They find that the dark matter is under-dense compared to results from abundance matching in ΛCDM, perhaps due to extreme tidal stripping or repeated tidal shocks. They probe the potential using the dynamics of 77 individual

stars. We use their derived dark matter density profile to measure β^* following Equation D.7. The uncertainties on β^* are propagated from the 68% confidence intervals on their dark matter density.

Leung et al. (2021) use HI data and stellar dynamical modelling to constrain the dark matter distribution in the dwarf irregular galaxy WLM. They use a gNFW profile, but also allow for flattening of the dark matter distribution, finding a prolate geometry is favoured. Their reported best-fitting value of the dark matter density slope is β in the gNFW profile (not β^*; Eq. D.3). To best compare with our measurements, we use their value of the dark matter slope for a spherical dark matter distribution including the gas and stars ($0.27^{+0.25}_{-0.17}$) which agrees within the uncertainty with their best-fitting slope allowing the dark matter geometry to vary.

From the observations, there is a general trend of lower mass galaxies exhibiting core-like inner dark matter density profiles with slopes ($\beta^* \sim 0$; Figure D.9 top), though this trend is driven by the results of Oh et al. (2011, 2015) and supported by Leung et al. (2021), which employed a different density profile methodology than the studies of larger dwarfs. The two galaxies with $M_* < 10^6$ $M_\odot$ may suggest that β^* increases at lower stellar mass, but these measurements are very uncertain. Higher mass galaxies—like those in this study—tend to have cuspy dark matter density slopes ($\beta^* \gtrsim 0.5$), but the scatter is large. In general, our measurements of β^* agree well with other observations at similar stellar masses (Figure D.9 top).

D.6.2 Comparison to Simulations

We also compare our measurements to those from simulations (Figure D.9) as a function of both the stellar mass and the ratio of the stellar mass to the halo mass (M_*/M_{halo}). The curves show the results from the FIRE (Lazar et al., 2020) and NIHAO (Tollet et al., 2016; Macciò et al., 2020) simulations. The simulations measure β^* from $1-2\%$ of R_{vir}.

We convert the curve presented by Lazar et al. (2020) in terms of M_*/M_{halo} to M_* using their stellar mass-halo mass relation (see their Figure 1). We use this same relation to convert the observations from M_* to M_*/M_{halo}. The horizontal errorbars on our points in the bottom panel of Figure D.9 include the scatter in the stellar mass-halo mass relation in addition to the uncertainties on the stellar mass measurements.

The above simulations predict a stellar mass range ($M_* \sim 10^{7.5-9.5}$ $M_\odot$) where feedback is efficient in softening the dark matter density profile in the centres of galaxies. In reality, this trend depends on M_*/M_{halo} and evolves with time (e.g., Di Cintio et al., 2014; Tollet et al., 2016). For example, Tollet et al. (2016) find that all galaxies begin with cuspy profiles. For low mass galaxies, Tollet et al. (2016) find that the central regions evolve passively once star formation has finished, and so they retain their cuspy profiles until $z = 0$. Other groups, however, find that very low mass systems can retain core-like profiles due to late-time minor mergers (Orkney et al., 2021) or starburst phases (Read et al., 2016). For galaxies of intermediate M_*/M_{halo}, the amount of gas is rapidly changing due to inflow, accretion of satellites,

mergers, and star formation-driven outflows. As a result, the potential undergoes rapid changes and the centre of mass of the gas changes with respect to the dark matter, both of which help develop and maintain the core-like density profile (Tollet et al., 2016). For the most massive galaxies, cores may form due to accretion and stellar feedback, resulting in rapid changes in M_*/M_{halo} in the central regions as for the intermediate-mass systems. However, Tollet et al. (2016) find that the net result for these higher mass galaxies is that gas flows inward towards the centre, triggering more star formation and hence increasing the stellar mass relative to the halo mass in the centre. As the potential well deepens due to the gas inflows, feedback-driven outflows become less important in terms of expelling mass. As a result of the deepened central potential, dark matter becomes concentrated at the centre and hence the cuspy profile is restored. There is some evidence from simulations that Milky Way mass galaxies ($M_* \approx 10^{10-11}$ $M_\odot$, $M_{halo} \sim 10^{12}$ $M_\odot$) can retain small ($0.5 - 2$ kpc) cores, which are maintained by stellar feedback (Chan et al., 2015; Lazar et al., 2020). Outflows from active galactic nuclei can also soften the cuspy profile in the most massive galaxies ($M_{halo} > 10^{12}$ $M_\odot$), though the slopes are still within the cusp-like regime (Macciò et al., 2020).

The galaxies in this study have $M_* = 10^{8.9-9.7}$ $M_\odot$. Assuming a stellar mass-halo mass relation like Lazar et al. (2020) implies $M_{halo} \approx 10^{11.0-11.5}$ $M_\odot$. Therefore, for these relatively massive dwarfs at $z = 0$, we would expect to find more cuspy dark matter profiles, which we quantitatively confirm with these measurements.

Observations of dwarf galaxies at similar stellar masses also show a wide range of dark matter density slopes (Figure D.7). It is thought that these differences

stem from real galaxy-to-galaxy variations, rather than from measurement errors or noise. We find no clear trends between β^* and galaxy properties such as M_*, M_{dyn}, or R_{vir}. Similarly, R19b find no trends between β^* and the galaxy effective radius and stellar surface density in the inner kpc of the galaxy. Some recent simulations also confirm or reproduce this observed diversity in the dark matter density profiles at fixed stellar mass (e.g., Oman et al., 2015, 2019; Kamada et al., 2017; Santos-Santos et al., 2018, 2020; Orkney et al., 2021).

As discussed in Section D.4.3, our definition of β^* probes smaller radii than the simulations. The simulations measure the slope of the dark matter density profile from radii between $1-2\%$ of R_{vir}, which we report in Table D.3. However, our adopted definition of β^* (Equation D.7) covers a fixed radial range from $0.3-0.8$ kpc, which corresponds to $\sim 0.3-1.6\%$ of R_{vir} for these galaxies. In an effort to best compare with simulations, we also compute $\beta_{1-2\%\ R_{vir}}$, given our estimates of R_{vir} and its uncertainties in Table D.3. Like β^*, $\beta_{1-2\%\ R_{vir}}$ is calculated at every step in the MCMC chain during the decomposition, and hence β^* and $\beta_{1-2\%\ R_{vir}}$ are calculated for the same dark matter density profile at each step and any differences between them will reflect only the differences in the definitions of β^* and $\beta_{1-2\%\ R_{vir}}$. The uncertainty on $\beta_{1-2\%\ R_{vir}}$ also incorporates the uncertainty on R_{vir}. We compare our measurements to the simulations in Figure D.10. The top panel compares the KDEs of β^* and $\beta_{1-2\%\ R_{vir}}$, which are the sums of the posterior distributions over all of the galaxies normalised to unit area. The distribution of $\beta_{1-2\%\ R_{vir}}$ is shifted towards steeper slopes than the distribution of β^*.

When the measured dark matter density slope is parametrized by β^*, most

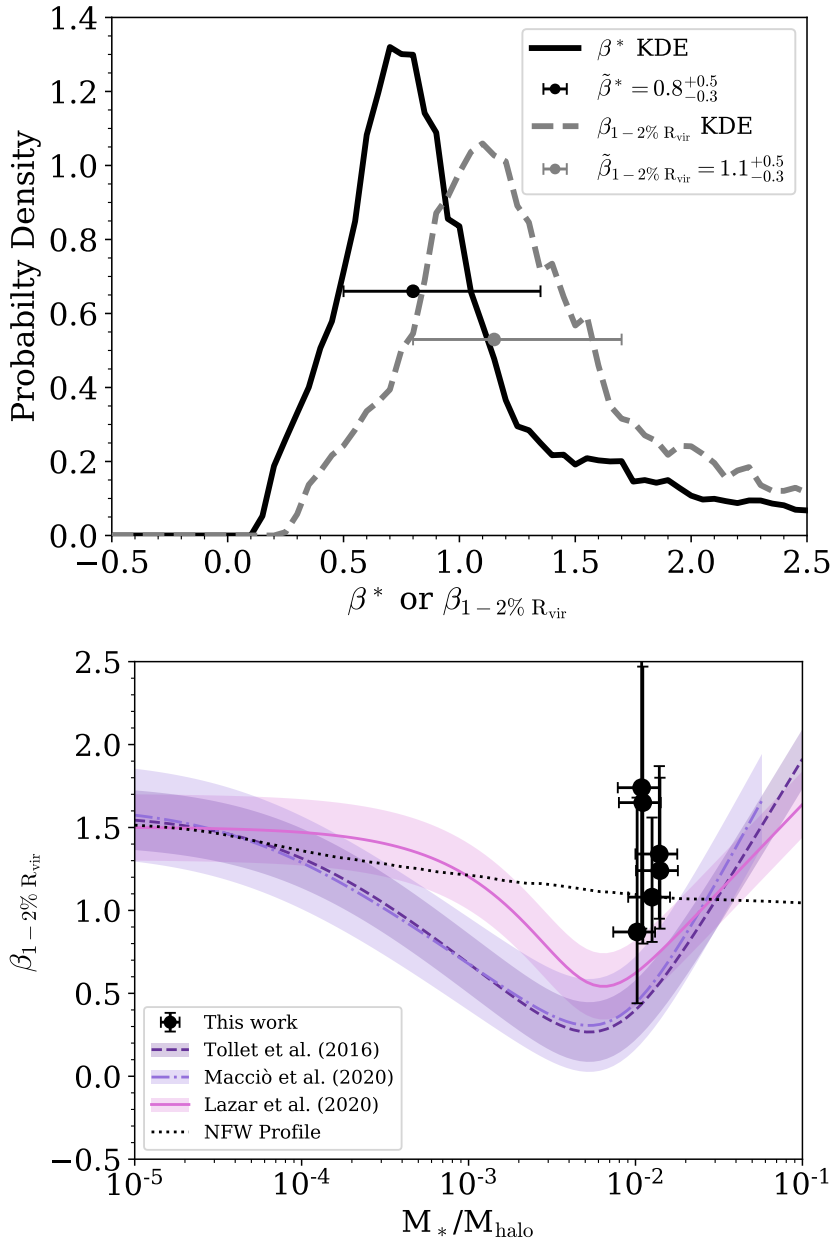

Figure D.10: Top: KDEs comparing the inner slope of the dark matter density profile as parametrized by β^* (black solid) or $\beta_{1-2\%\ R_{vir}}$ (grey dashed). The black and grey dots show the median of each distribution; the error bars show the 16th and 84th percentiles. The β^* KDE is the same as in Figure D.6. The dark matter slopes parametrized by $\beta_{1-2\%\ R_{vir}}$ are steeper than β^* in general. Bottom: We compare the simulations with our measurements of $\beta_{1-2\%\ R_{vir}}$ as a function of M_*/M_{halo} to most closely compare to the quantities measured by the simulations. The trends are similar to those seen in Figure D.9 (bottom), but the measured values of $\beta_{1-2\%\ R_{vir}}$ tend to be steeper than predicted by simulations.

of our measured points agree with the predictions from simulations and those that are steeper have larger uncertainties (Figure D.9). Observations at similar M_* and M_*/M_{halo} show a similar distribution of β^*, though the scatter is large (see also Figure D.6). If we instead use $\beta_{1-2\%\ R_{vir}}$ as our parametrization of the inner dark matter density slope—which is the value reported by the simulations—we find that most of our galaxies have steeper dark matter density profiles than predicted by the simulations (Figure D.10 bottom). Therefore, in this most equal comparison, our observations tend to have cuspier dark matter profiles than predicted by simulations that include stellar feedback.

As described above, one way for a galaxy to restore a cuspy profile is through gas inflow which triggers a burst of star formation. This both deepens the potential well, causing dark matter to concentrate in the centre of the galaxy, and increases the stellar mass of the centre relative to the halo mass. One possible explanation for the more cuspy profiles observed in these (and other) galaxies is that these galaxies had stronger gas inflows towards the centre than predicted by the simulations, resulting in more centrally concentrated dark matter at the centres. An alternate possibility is that the simulations over-predict the strength or frequency of accretion, merger, and/or outflow events for galaxies in this stellar mass range. As described by Tollet et al. (2016), these feedback events stir up the potential, allowing the dark matter distribution to be shallower and maintaining a core-like central profile. If there were less frequent or intense accretion or outflows, the dip in the β^* curves from simulations shown in Figure D.9 (peak in Figure D.10 bottom) would be both shallower and narrower. It is also possible that both effects are at work, or that

there are other factors responsible for this population of galaxies with cuspy profiles given their M_* and M_*/M_{halo}.

D.7 Summary

We have investigated the inner slope of the dark matter density distribution (β^*) using observations of six nearby spiral dwarf galaxies. We summarize our results below.

1. Using new CO observations from ALMA, we measure the CO rotation curves of these galaxies, which provide a dynamically cold tracer of the total potential (Section D.3, Figure D.2). We find excellent agreement between the CO and Hα rotation curves in most (but not all) galaxies, where both are available.

2. We decompose the dark matter rotation curve and density profile using an MCMC method, knowing the total potential and the contribution from the stars (Section D.4, Figure D.4). From these, we measure β^*, finding $\langle\beta^*\rangle = 1.0$ with a standard deviation of ± 0.3 among the best-fitting β^* values for galaxies in this sample (Table D.3). Considering the full posterior distributions of β^*, the median β^* for this sample is $\tilde{\beta}_* = 0.8^{+0.5}_{-0.3}$, where the lower and upper uncertainties correspond to the 16^{th} and 84^{th} percentiles of the distribution (Figure D.6).

3. We find that the relatively massive dwarf galaxies ($M_* = 10^{9.3-9.7}$ $M_\odot$) in this study show cuspier dark matter distributions than lower mass dwarf galaxies, in agreement with other observations at similar M_* and M_*/M_{halo}(Figures D.6

and D.9).

4. When we compare our measurements of β^* to the simulations, most of our measurements agree with them and those that are more discrepant have large uncertainties (Figure D.9). These simulations, however, measure $\beta_{1-2\%\ R_{vir}}$ whereas β^* is defined over a fixed radial range ($0.3 - 0.8$ kpc). To most accurately compare our measurements with the simulations, we calculate $\beta_{1-2\%\ R_{vir}}$ for our galaxies. The inner dark matter density slopes parametrized by $\beta_{1-2\%\ R_{vir}}$ are steeper than β^*, meaning that our galaxies have steeper slopes on average than predicted by the simulations including stellar feedback (Figure D.10).

5. The inner slopes of the dark matter density profiles we measure tend to be steeper than predicted by simulations. This may signal that these galaxies have undergone a stronger gas inflow than implemented in the simulations, that the simulations overpredict the frequency of accretion/merger/outflow events, or that a combination of these or other effects are at work.

Analyses such as these are often limited by the sensitivity needed to probe out to large radii in faint, often gas-poor dwarf galaxies. Future facilities, especially the Next Generation Very Large Array, will transform our ability to measure gas kinematics in dwarf galaxies. Owing to its increased sensitivity and angular resolution and the ability to observe both CO and HI, we can trace the rotation curves out to larger radii more robustly. The increased spatial resolution will allow for more accurate measurements in the centres, precisely in the range of radii where β^* is measured. Finally, the combination of the increased resolution and sensitivity will

allow us to probe lower mass and more distant systems to better understand how the dark matter distributions change over time and as a function of environment.

Appendix E: Facilities and Software used in this Thesis

E.1 Facilities

1. ALMA
2. Calar Alto Observatory 3.5 m/PPAK
3. CARMA
4. GBT
5. HST/NICMOS
6. Pan-STARRS1
7. SDSS
8. Spitzer/IRAC
9. WISE

E.2 Software

1. APLpy (Robitaille & Bressert, 2012)
2. Astropy (Astropy Collaboration et al., 2018)
3. CASA (McMullin et al., 2007)

4. corner (Foreman-Mackey, 2016)
5. emcee (Foreman-Mackey et al., 2013)
6. FitTiltedRings (Cooke, Levy, et al., 2021)*
7. MatPlotLib (Caswell et al., 2020)
8. Miriad (Sault et al., 1995)
9. ModelSSCOutflows (Levy et al., 2021)†
10. NEMO (Teuben, 1995)
11. NumPy (Harris et al., 2020)
12. pandas (Reback et al., 2020)
13. photutils (Bradley et al., 2021)
14. Pipe3D (Sánchez et al., 2016c,b)
15. SciPy (Virtanen et al., 2020)
16. seaborn (Waskom et al., 2014)
17. Starburst99 (Leitherer et al., 1999)

*`https://github.com/rclevy/RotationCurveTiltedRings`
†https://github.com/rclevy/ModelSSCOutflows

Bibliography

Aalto, S., Muller, S., König, S., Falstad, N., Mangum, J., Sakamoto, K., Privon, G. C., Gallagher, J., Combes, F., García-Burillo, S., Martín, S., Viti, S., van der Werf, P., Evans, A. S., Black, J. H., Varenius, E., Beswick, R., Fuller, G., Henkel, C., Kohno, K., Alatalo, K., Mühle, S. The hidden heart of the luminous infrared galaxy IC 860. I. A molecular inflow feeding opaque, extreme nuclear activity A&A. 2019. 627 A147.

Adams, J. J., Simon, J. D., Fabricius, M. H., van den Bosch, R. C. E., Barentine, J. C., Bender, R., Gebhardt, K., Hill, G. J., Murphy, J. D., Swaters, R. A., Thomas, J., van de Ven, G. Dwarf Galaxy Dark Matter Density Profiles Inferred from Stellar and Gas Kinematics ApJ. 2014. 789, 1 63.

Agertz, O., Kravtsov, A. V., Leitner, S. N., Gnedin, N. Y. Toward a Complete Accounting of Energy and Momentum from Stellar Feedback in Galaxy Formation Simulations ApJ. 2013. 770, 1 25.

Alam, S., Albareti, F. D., Allende Prieto, C., Anders, F., Anderson, S. F., Anderton, T., Andrews, B. H., Armengaud, E., Aubourg, É., Bailey, S., al., et. The Eleventh and Twelfth Data Releases of the Sloan Digital Sky Survey: Final Data from SDSS-III ApJS. 2015. 219 12.

Anantharamaiah, K. R., Goss, W. M. Orthogonal Rotating Gaseous Disks near the Nucleus of NGC 253 ApJL. 1996. 466 L13.

Ando, R., Nakanishi, K., Kohno, K., Izumi, T., Martín, S., Harada, N., Takano, S., Kuno, N., Nakai, N., Sugai, H., Sorai, K., Tosaki, T., Matsubayashi, K., Nakajima, T., Nishimura, Y., Tamura, Y. Diverse Nuclear Star-forming Activities in the Heart of NGC 253 Resolved with 10-pc-scale ALMA Images ApJ. 2017. 849, 2 81.

Aquino-Ortíz, E., Valenzuela, O., Sánchez, S. F., Hernández-Toledo, H., Ávila-Reese, V., van de Ven, G., Rodríguez-Puebla, A., Zhu, L., Mancillas, B., Cano-Díaz, M., García-Benito, R. Kinematic scaling relations of CALIFA galaxies: A dynamical mass proxy for galaxies across the Hubble sequence MNRAS. 2018. 479 2133–2146.

Astropy Collaboration, , Price-Whelan, A. M., Sipőcz, B. M., Günther, H. M., Lim, P. L., Crawford, S. M., Conseil, S., Shupe, D. L., Craig, M. W., Dencheva, N., Ginsburg, A., VanderPlas, J. T., Bradley, L. D., Pérez-Suárez, D., de Val-Borro, M., Aldcroft, T. L., Cruz, K. L., Robitaille, T. P., Tollerud, E. J., Ardelean, C., Babej, T., Bach, Y. P., Bachetti, M., Bakanov, A. V., Bamford, S. P., Barentsen, G., Barmby, P., Baumbach, A., Berry, K. L., Biscani, F., Boquien, M., Bostroem, K. A., Bouma, L. G., Brammer, G. B., Bray, E. M., Breytenbach, H., Buddelmeijer, H., Burke, D. J., Calderone, G., Cano Rodríguez, J. L., Cara, M., Cardoso, J. V. M., Cheedella, S., Copin, Y., Corrales, L., Crichton, D., D'Avella, D., Deil, C., Depagne, É., Dietrich, J. P., Donath, A., Droettboom, M., Earl, N., Erben, T., Fabbro, S., Ferreira, L. A., Finethy, T., Fox, R. T., Garrison, L. H., Gibbons, S. L. J., Goldstein, D. A., Gommers, R., Greco, J. P., Greenfield, P., Groener, A. M., Grollier, F., Hagen, A., Hirst, P., Homeier, D., Horton, A. J., Hosseinzadeh, G., Hu, L., Hunkeler, J. S., Ivezić, Ž., Jain, A., Jenness, T., Kanarek, G., Kendrew, S., Kern, N. S., Kerzendorf, W. E., Khvalko, A., King, J., Kirkby, D., Kulkarni, A. M., Kumar, A., Lee, A., Lenz, D., Littlefair, S. P., Ma, Z., Macleod, D. M., Mastropietro, M., McCully, C., Montagnac, S., Morris, B. M., Mueller, M., Mumford, S. J., Muna, D., Murphy, N. A., Nelson, S., Nguyen, G. H., Ninan, J. P., Nöthe, M., Ogaz, S., Oh, S., Parejko, J. K., Parley, N., Pascual, S., Patil, R., Patil, A. A., Plunkett, A. L., Prochaska, J. X., Rastogi, T., Reddy Janga, V., Sabater, J., Sakurikar, P., Seifert, M., Sherbert, L. E., Sherwood-Taylor, H., Shih, A. Y., Sick, J., Silbiger, M. T., Singanamalla, S., Singer, L. P., Sladen, P. H., Sooley, K. A., Sornarajah, S., Streicher, O., Teuben, P., Thomas, S. W., Tremblay, G. R., Turner, J. E. H., Terrón, V., van Kerkwijk, M. H., de la Vega, A., Watkins, L. L., Weaver, B. A., Whitmore, J. B., Woillez, J., Zabalza, V., Astropy Contributors, . The Astropy Project: Building an Open-science Project and Status of the v2.0 Core Package AJ. 2018. 156, 3 123.

Athanassoula, E. Morphology of bar orbits. MNRAS. 1992a. 259 328–344.

Athanassoula, E. The existence and shapes of dust lanes in galactic bars. MNRAS. 1992b. 259 345–364.

Avison, A., George, S. J. A graphical tool for demonstrating the techniques of radio interferometry European Journal of Physics. 2013. 34, 1 7.

Bajaja, E., van Albada, G. D. Complementing aperture synthesis radio data by short spacing components from single dish observations. A&A. 1979. 75, 1-2 251–254.

Bally, J. Protostellar Outflows ARA&A. 2016. 54 491–528.

Barnabè, M., Ciotti, L., Fraternali, F., Sancisi, R. Hydrostatic models for the rotation of extra-planar gas in disk galaxies A&A. 2006. 446 61–69.

Barnes, A. T., Longmore, S. N., Dale, J. E., Krumholz, M. R., Kruijssen, J. M. D., Bigiel, F. Which feedback mechanisms dominate in the high-pressure environment of the central molecular zone? MNRAS. 2020. 498, 4 4906–4923.

Barnes, J. E., Wood, K., Hill, A. S., Haffner, L. M. Photoionization and heating of a supernova-driven turbulent interstellar medium MNRAS. 2014. 440, 4 3027–3035.

Barrera-Ballesteros, J. K., Falcón-Barroso, J., García-Lorenzo, B., van de Ven, G., Aguerri, J. A. L., Mendez-Abreu, J., Spekkens, K., Lyubenova, M., Sánchez, S. F., Husemann, B., Mast, D., García-Benito, R., Iglesias-Paramo, J., Del Olmo, A., Márquez, I., Masegosa, J., Kehrig, C., Marino, R. A., Verdes-Montenegro, L., Ziegler, B., McIntosh, D. H., Bland-Hawthorn, J., Walcher, C. J., Califa Collaboration, . Kinematic alignment of non-interacting CALIFA galaxies. Quantifying the impact of bars on stellar and ionised gas velocity field orientations A&A. 2014. 568 A70.

Barrera-Ballesteros, J. K., García-Lorenzo, B., Falcón-Barroso, J., van de Ven, G., Lyubenova, M., Wild, V., Méndez-Abreu, J., Sánchez, S. F., Marquez, I., Masegosa, J., Monreal-Ibero, A., Ziegler, B., del Olmo, A., Verdes-Montenegro, L., García-Benito, R., Husemann, B., Mast, D., Kehrig, C., Iglesias-Paramo, J., Marino, R. A., Aguerri, J. A. L., Walcher, C. J., Vílchez, J. M., Bomans, D. J., Cortijo-Ferrero, C., González Delgado, R. M., Bland-Hawthorn, J., McIntosh, D. H., Bekeraitė, S. Tracing kinematic (mis)alignments in CALIFA merging galaxies. Stellar and ionized gas kinematic orientations at every merger stage A&A. 2015. 582 A21.

Begeman, K. G. HI rotation curves of spiral galaxies. 1987.

Begeman, K. G. H I rotation curves of spiral galaxies. I - NGC 3198 A&A. 1989. 223 47–60.

Belfiore, F., Maiolino, R., Maraston, C., Emsellem, E., Bershady, M. A., Masters, K. L., Yan, R., Bizyaev, D., Boquien, M., Brownstein, J. R., Bundy, K., Drory, N., Heckman, T. M., Law, D. R., Roman-Lopes, A., Pan, K., Stanghellini, L., Thomas, D., Weijmans, A.-M., Westfall, K. B. SDSS IV MaNGA - spatially resolved diagnostic diagrams: a proof that many galaxies are LIERs MNRAS. 2016. 461 3111–3134.

Bendo, G. J., Beswick, R. J., D'Cruze, M. J., Dickinson, C., Fuller, G. A., Muxlow, T. W. B. ALMA observations of 99 GHz free-free and H40α line emission from star formation in the centre of NGC 253 MNRAS. 2015. 450, 1 L80–L84.

Bershady, M. A. 3D Spectroscopic Instrumentation arXiv e-prints. 2009. arXiv:0910.0167.

Bershady, M. A., Andersen, D. R., Harker, J., Ramsey, L. W., Verheijen, M. A. W. SparsePak: A Formatted Fiber Field Unit for the WIYN Telescope Bench Spectrograph. I. Design, Construction, and Calibration PASP. 2004. 116, 820 565–590.

Binette, L., Flores-Fajardo, N., Raga, A. C., Drissen, L., Morisset, C. Photoionized Mixing Layer Models of the Diffuse Ionized Gas ApJ. 2009. 695 552–560.

Binney, J. The Cosmological Context of Extra-planar Gas Extra-Planar Gas. 331. 2005. 131. (Astronomical Society of the Pacific Conference Series).

Binney, J., Tremaine, S. Galactic Dynamics: Second Edition. 2008.

Binney, J., Gerhard, O. E., Stark, A. A., Bally, J., Uchida, K. I. Understanding the kinematics of Galactic Centre gas. MNRAS. 1991. 252 210.

Bitsakis, T., Sánchez, S. F., Ciesla, L., Bonfini, P., Charmandaris, V., Cervantes Sodi, B., Maragkoudakis, A., Diaz-Santos, T., Zezas, A. The integrated properties of the CALIFA galaxies: model-derived galaxy parameters and quenching of star formation MNRAS. 2019. 483 370–380.

Bizyaev, D., Walterbos, R. A. M., Yoachim, P., Riffel, R. A., Fernández-Trincado, J. G., Pan, K., Diamond-Stanic, A. M., Jones, A., Thomas, D., Cleary, J., Brinkmann, J. SDSS IV MaNGA — Rotation Velocity Lags in the Extraplanar Ionized Gas from MaNGA Observations of Edge-on Galaxies ApJ. 2017. 839 87.

Blanc, G. A., Heiderman, A., Gebhardt, K., Evans, N. J. II, Adams, J. The Spatially Resolved Star Formation Law From Integral Field Spectroscopy: VIRUS-P Observations of NGC 5194 ApJ. 2009. 704 842–862.

Boettcher, E., Gallagher, J. S. III, Zweibel, E. G. Detection of Extraplanar Diffuse Ionized Gas in M83 ApJ. 2017. 845 155.

Boettcher, E., Zweibel, E. G., Gallagher, J. S. III, Benjamin, R. A. Testing a Dynamical Equilibrium Model of the Extraplanar Diffuse Ionized Gas in NGC 891 ApJ. 2016. 832 118.

Boissier, S., Prantzos, N., Boselli, A., Gavazzi, G. The star formation rate in disc galaxies: thresholds and dependence on gas amount MNRAS. 2003. 346 1215–1230.

Böker, T., Falcón-Barroso, J., Schinnerer, E., Knapen, J. H., Ryder, S. A SINFONI View of Galaxy Centers: Morphology and Kinematics of Five Nuclear Star Formation-Rings AJ. 2008. 135, 2 479–495.

Bolatto, A. D., Warren, S. R., Leroy, A. K., Walter, F., Veilleux, S., Ostriker, E. C., Ott, J., Zwaan, M., Fisher, D. B., Weiss, A., Rosolowsky, E., Hodge, J. Suppression of star formation in the galaxy NGC 253 by a starburst-driven molecular wind Nature. 2013a. 499 450–453.

Bolatto, A. D., Wolfire, M., Leroy, A. K. The CO-to-H_2 Conversion Factor ARA&A. 2013b. 51 207–268.

Bolatto, A. D., Wong, T., Utomo, D., Blitz, L., Vogel, S. N., Sánchez, S. F., Barrera-Ballesteros, J., Cao, Y., Colombo, D., Dannerbauer, H., García-Benito, R., Herrera-Camus, R., Husemann, B., Kalinova, V., Leroy, A. K., Leung, G., Levy, R. C., Mast, D., Ostriker, E., Rosolowsky, E., Sandstrom, K. M., Teuben,

P., van de Ven, G., Walter, F. The EDGE-CALIFA Survey: Interferometric Observations of 126 Galaxies with CARMA ApJ. 2017. 846 159.

Bolatto, A. D., Simon, J. D., Leroy, A., Blitz, L. The Density Profile of the Dark Matter Halo of NGC 4605 ApJ. 2002. 565, 1 238–243.

Bosma, A. The distribution and kinematics of neutral hydrogen in spiral galaxies of various morphological types. 1978.

Bosma, A., Byun, Y., Freeman, K. C., Athanassoula, E. The opacity of spiral disks ApJL. 1992. 400 L21–L24.

Bradley, L., Sipocz, B., Robitaille, T., Tollerud, E., Vinícius, Z., Deil, C., Barbary, K., Wilson, T. J., Busko, I., GÃŒnther, H. M., Cara, M., Conseil, S., Bostroem, A., Droettboom, M., Bray, E. M., Bratholm, L. A., Lim, P. L., Barentsen, G., Craig, M., Rathi, S., Pascual, S., Perren, G., Donath, A., Georgiev, I. Y., Val-Borro, M. de, Kerzendorf, W., Bach, Y. P., Quint, B., Souchereau, H., Weaver, B. A. astropy/photutils: 1.0.2. 2021.

Bregman, J. N. The galactic fountain of high-velocity clouds ApJ. 1980. 236 577–591.

Brinchmann, J., Charlot, S., White, S. D. M., Tremonti, C., Kauffmann, G., Heckman, T., Brinkmann, J. The physical properties of star-forming galaxies in the low-redshift Universe MNRAS. 2004. 351, 4 1151–1179.

Brown, G., Gnedin, O. Y. Radii of Young Star Clusters in Nearby Galaxies MNRAS. 2021. submitted.

Brown, M. J. I., Moustakas, J., Smith, J. D. T., da Cunha, E., Jarrett, T. H., Imanishi, M., Armus, L., Brandl, B. R., Peek, J. E. G. An Atlas of Galaxy Spectral Energy Distributions from the Ultraviolet to the Mid-infrared The Astrophysical Journal Supplement Series. 2014. 212 18.

Bryant, J. J., Owers, M. S., Robotham, A. S. G., Croom, S. M., Driver, S. P., Drinkwater, M. J., Lorente, N. P. F., Cortese, L., Scott, N., Colless, M., Schaefer, A., Taylor, E. N., Konstantopoulos, I. S., Allen, J. T., Baldry, I., Barnes, L., Bauer, A. E., Bland-Hawthorn, J., Bloom, J. V., Brooks, A. M., Brough, S., Cecil, G., Couch, W., Croton, D., Davies, R., Ellis, S., Fogarty, L. M. R., Foster, C., Glazebrook, K., Goodwin, M., Green, A., Gunawardhana, M. L., Hampton, E., Ho, I. T., Hopkins, A. M., Kewley, L., Lawrence, J. S., Leon-Saval, S. G., Leslie, S., McElroy, R., Lewis, G., Liske, J., López-Sánchez, Á. R., Mahajan, S., Medling, A. M., Metcalfe, N., Meyer, M., Mould, J., Obreschkow, D., O'Toole, S., Pracy, M., Richards, S. N., Shanks, T., Sharp, R., Sweet, S. M., Thomas, A. D., Tonini, C., Walcher, C. J. The SAMI Galaxy Survey: instrument specification and target selection MNRAS. 2015. 447, 3 2857–2879.

Bullock, J. S., Boylan-Kolchin, M. Small-Scale Challenges to the ΛCDM Paradigm ARA&A. 2017. 55, 1 343–387.

Bundy, K., Bershady, M. A., Law, D. R., Yan, R., Drory, N., MacDonald, N., Wake, D. A., Cherinka, B., Sánchez-Gallego, J. R., Weijmans, A.-M., Thomas, D., Tremonti, C., Masters, K., Coccato, L., Diamond-Stanic, A. M., Aragón-Salamanca, A., Avila-Reese, V., Badenes, C., Falcón-Barroso, J., Belfiore, F., Bizyaev, D., Blanc, G. A., Bland-Hawthorn, J., Blanton, M. R., Brownstein, J. R., Byler, N., Cappellari, M., Conroy, C., Dutton, A. A., Emsellem, E., Etherington, J., Frinchaboy, P. M., Fu, H., Gunn, J. E., Harding, P., Johnston, E. J., Kauffmann, G., Kinemuchi, K., Klaene, M. A., Knapen, J. H., Leauthaud, A., Li, C., Lin, L., Maiolino, R., Malanushenko, V., Malanushenko, E., Mao, S., Maraston, C., McDermid, R. M., Merrifield, M. R., Nichol, R. C., Oravetz, D., Pan, K., Parejko, J. K., Sanchez, S. F., Schlegel, D., Simmons, A., Steele, O., Steinmetz, M., Thanjavur, K., Thompson, B. A., Tinker, J. L., van den Bosch, R. C. E., Westfall, K. B., Wilkinson, D., Wright, S., Xiao, T., Zhang, K. Overview of the SDSS-IV MaNGA Survey: Mapping nearby Galaxies at Apache Point Observatory ApJ. 2015. 798 7.

Burkert, A., Genzel, R., Bouché, N., Cresci, G., Khochfar, S., Sommer-Larsen, J., Sternberg, A., Naab, T., Förster Schreiber, N., Tacconi, L., Shapiro, K., Hicks, E., Lutz, D., Davies, R., Buschkamp, P., Genel, S. High-redshift Star-forming Galaxies: Angular Momentum and Baryon Fraction, Turbulent Pressure Effects, and the Origin of Turbulence ApJ. 2010. 725 2324–2332.

Buta, R., Combes, F. Galactic Rings Fund. Cosmic Physics. 1996. 17 95–281.

Calura, F., Few, C. G., Romano, D., D'Ercole, A. Feedback from Massive Stars and Gas Expulsion from Proto&ndashGlobular Clusters ApJL. 2015. 814, 1 L14.

Calzetti, D., Armus, L., Bohlin, R. C., Kinney, A. L., Koornneef, J., Storchi-Bergmann, T. The Dust Content and Opacity of Actively Star-forming Galaxies ApJ. 2000. 533 682–695.

Caswell, T. A., Droettboom, M., Lee, A., Hunter, J., Andrade, E. S. de, Firing, E., Hoffmann, T., Klymak, J., Stansby, D., Varoquaux, N., Nielsen, J. H., Root, B., May, R., Elson, P., SeppÃ€nen, J. K., Dale, D., Lee, J.-J., McDougall, D., Straw, A., Hobson, P., Gohlke, C., Yu, T. S., Ma, E., Vincent, A. F., Silvester, S., Moad, C., Kniazev, N., hannah, , Ernest, E., Ivanov, P. matplotlib/matplotlib: REL: v3.3.2. 2020.

Catalán-Torrecilla, C., Gil de Paz, A., Castillo-Morales, A., Iglesias-Páramo, J., Sánchez, S. F., Kennicutt, R. C., Pérez-González, P. G., Marino, R. A., Walcher, C. J., Husemann, B., García-Benito, R., Mast, D., González Delgado, R. M., Muñoz-Mateos, J. C., Bland-Hawthorn, J., Bomans, D. J., Del Olmo, A., Galbany, L., Gomes, J. M., Kehrig, C., López-Sánchez, Á. R., Mendoza, M. A.,

Monreal-Ibero, A., Pérez-Torres, M., Sánchez-Blázquez, P., Vilchez, J. M., Califa Collaboration, . Star formation in the local Universe from the CALIFA sample. I. Calibrating the SFR using integral field spectroscopy data A&A. 2015. 584 A87.

Catinella, B., Schiminovich, D., Kauffmann, G., Fabello, S., Wang, J., Hummels, C., Lemonias, J., Moran, S. M., Wu, R., Giovanelli, R., Haynes, M. P., Heckman, T. M., Basu-Zych, A. R., Blanton, M. R., Brinchmann, J., Budavári, T., Gonçalves, T., Johnson, B. D., Kennicutt, R. C., Madore, B. F., Martin, C. D., Rich, M. R., Tacconi, L. J., Thilker, D. A., Wild, V., Wyder, T. K. The GALEX Arecibo SDSS Survey - I. Gas fraction scaling relations of massive galaxies and first data release MNRAS. 2010. 403, 2 683–708.

Chabrier, G. Galactic Stellar and Substellar Initial Mass Function PASP. 2003. 115, 809 763–795.

Chambers, K. C., Magnier, E. A., Metcalfe, N., Flewelling, H. A., Huber, M. E., Waters, C. Z., Denneau, L., Draper, P. W., Farrow, D., Finkbeiner, D. P., Holmberg, C., Koppenhoefer, J., Price, P. A., Rest, A., Saglia, R. P., Schlafly, E. F., Smartt, S. J., Sweeney, W., Wainscoat, R. J., Burgett, W. S., Chastel, S., Grav, T., Heasley, J. N., Hodapp, K. W., Jedicke, R., Kaiser, N., Kudritzki, R. P., Luppino, G. A., Lupton, R. H., Monet, D. G., Morgan, J. S., Onaka, P. M., Shiao, B., Stubbs, C. W., Tonry, J. L., White, R., Bañados, E., Bell, E. F., Bender, R., Bernard, E. J., Boegner, M., Boffi, F., Botticella, M. T., Calamida, A., Casertano, S., Chen, W. P., Chen, X., Cole, S., Deacon, N., Frenk, C., Fitzsimmons, A., Gezari, S., Gibbs, V., Goessl, C., Goggia, T., Gourgue, R., Goldman, B., Grant, P., Grebel, E. K., Hambly, N. C., Hasinger, G., Heavens, A. F., Heckman, T. M., Henderson, R., Henning, T., Holman, M., Hopp, U., Ip, W. H., Isani, S., Jackson, M., Keyes, C. D., Koekemoer, A. M., Kotak, R., Le, D., Liska, D., Long, K. S., Lucey, J. R., Liu, M., Martin, N. F., Masci, G., McLean, B., Mindel, E., Misra, P., Morganson, E., Murphy, D. N. A., Obaika, A., Narayan, G., Nieto-Santisteban, M. A., Norberg, P., Peacock, J. A., Pier, E. A., Postman, M., Primak, N., Rae, C., Rai, A., Riess, A., Riffeser, A., Rix, H. W., Röser, S., Russel, R., Rutz, L., Schilbach, E., Schultz, A. S. B., Scolnic, D., Strolger, L., Szalay, A., Seitz, S., Small, E., Smith, K. W., Soderblom, D. R., Taylor, P., Thomson, R., Taylor, A. N., Thakar, A. R., Thiel, J., Thilker, D., Unger, D., Urata, Y., Valenti, J., Wagner, J., Walder, T., Walter, F., Watters, S. P., Werner, S., Wood-Vasey, W. M., Wyse, R. The Pan-STARRS1 Surveys arXiv e-prints. 2016. arXiv:1612.05560.

Chan, T. K., Kereš, D., Oñorbe, J., Hopkins, P. F., Muratov, A. L., Faucher-Giguère, C. A., Quataert, E. The impact of baryonic physics on the structure of dark matter haloes: the view from the FIRE cosmological simulations MNRAS. 2015. 454, 3 2981–3001.

Charnley, S. B. Sulfuretted Molecules in Hot Cores ApJ. 1997. 481, 1 396–405.

Chaves, T. A., Irwin, J. A. High-Latitude H I in NGC 2613: Structure and Dynamics ApJ. 2001. 557 646–658.

Cid Fernandes, R., Stasińska, G., Schlickmann, M. S., Mateus, A., Vale Asari, N., Schoenell, W., Sodré, L. Alternative diagnostic diagrams and the 'forgotten' population of weak line galaxies in the SDSS MNRAS. 2010. 403, 2 1036–1053.

Cohen, D. P., Turner, J. L., Consiglio, S. M., Martin, E. C., Beck, S. C. Ionized Gas Motions and the Structure of Feedback near a Forming Globular Cluster in NGC 5253 ApJ. 2018. 860, 1 47.

Collins, J. A., Rand, R. J. Ionization Sources and Physical Conditions in the Diffuse Ionized Gas Halos of Four Edge-On Galaxies ApJ. 2001. 551 57–71.

Collins, J. A., Rand, R. J., Duric, N., Walterbos, R. A. M. Diffuse Ionized Gas in a Sample of Edge-on Galaxies and Comparisons with H I and Radio Continuum Emission ApJ. 2000. 536 645–662.

Collins, M. L. M., Read, J. I., Ibata, R. A., Rich, R. M., Martin, N. F., Peñarrubia, J., Chapman, S. C., Tollerud, E. J., Weisz, D. R. Andromeda XXI - a dwarf galaxy in a low-density dark matter halo MNRAS. 2021. 505, 4 5686–5701.

Colombo, D., Sanchez, S. F., Bolatto, A. D., Kalinova, V., Weiß, A., Wong, T., Rosolowsky, E., Vogel, S. N., Barrera-Ballesteros, J., Dannerbauer, H., Cao, Y., Levy, R. C., Utomo, D., Blitz, L. The EDGE-CALIFA survey: exploring the role of molecular gas on galaxy star formation quenching A&A. 2020. 644 A97.

Colzi, L., Fontani, F., Caselli, P., Ceccarelli, C., Hily-Blant, P., Bizzocchi, L. Nitrogen and hydrogen fractionation in high-mass star-forming cores from observations of HCN and HNC A&A. 2018. 609 A129.

Combes, F. Gas Accretion in Disk Galaxies Structure and Dynamics of Disk Galaxies. 480. 2014. 211. (Astronomical Society of the Pacific Conference Series).

Condon, J. J., Ransom, S. M. Essential Radio Astronomy. 2016.

Consiglio, S. M., Turner, J. L., Beck, S., Meier, D. S. ALMA Reveals Potential Localized Dust Enrichment from Massive Star Clusters in II Zw 40 ApJL. 2016. 833, 1 L6.

Contopoulos, G., Grosbol, P. Orbits in barred galaxies A&ARv. 1989. 1, 3-4 261–289.

Contopoulos, G., Mertzanides, C. Inner Lindblad resonance in galaxies. Nonlinear theory. II. Bars. A&A. 1977. 61, 4 477–485.

Cooke, L. H., Levy, R. C., Bolatto, A. D., Teuben, P., Davey, B. D., Newman, A. B., Simon, J. D., Wright, M., Lenkić, L., Tarantino, E., Villanueva, V. Cuspy Dark Matter Density Profiles in Massive Dwarf Galaxies MNRAS. 2021. submitted.

Cordoni, G., Milone, A. P., Marino, A. F., Da Costa, G. S., Dondoglio, E., Jerjen, H., Lagioia, E. P., Mastrobuono-Battisti, A., Norris, J. E., Tailo, M., Yong, D. Gaia and Hubble Unveil the Kinematics of Stellar Populations in the Type II Globular Clusters ω Centauri and M22 ApJ. 2020. 898, 2 147.

Cornwell, T. J. Multiscale CLEAN Deconvolution of Radio Synthesis Images IEEE Journal of Selected Topics in Signal Processing. 2008. 2, 5 793–801.

Corradi, R. L. M., Grosso, N., Acker, A., Greimel, R., Guillout, P. Gas physical conditions and kinematics of the giant outflow Ou4 A&A. 2014. 570 A105.

Cox, D. P. Structure of the Diffuse Interstellar Medium IAU Colloq. 120: Structure and Dynamics of the Interstellar Medium. 350. 1989. 500. (Lecture Notes in Physics, Berlin Springer Verlag).

Crocker, R. M., Krumholz, M. R., Thompson, T. A., Baumgardt, H., Mackey, D. Radiation pressure limits on the star formation efficiency and surface density of compact stellar systems MNRAS. 2018a. 481, 4 4895–4906.

Crocker, R. M., Krumholz, M. R., Thompson, T. A., Clutterbuck, J. The maximum flux of star-forming galaxies MNRAS. 2018b. 478, 1 81–94.

Croom, S. M., Lawrence, J. S., Bland-Hawthorn, J., Bryant, J. J., Fogarty, L., Richards, S., Goodwin, M., Farrell, T., Miziarski, S., Heald, R., Jones, D. H., Lee, S., Colless, M., Brough, S., Hopkins, A. M., Bauer, A. E., Birchall, M. N., Ellis, S., Horton, A., Leon-Saval, S., Lewis, G., López-Sánchez, Á. R., Min, S.-S., Trinh, C., Trowland, H. The Sydney-AAO Multi-object Integral field spectrograph MNRAS. 2012. 421, 1 872–893.

Cyr-Racine, F.-Y., Sigurdson, K., Zavala, J., Bringmann, T., Vogelsberger, M., Pfrommer, C. ETHOS—an effective theory of structure formation: From dark particle physics to the matter distribution of the Universe Phys. Rev. D.. 2016. 93, 12 123527.

Dabrowski, I. The Lyman and Werner bands of H_2 Canadian Journal of Physics. 1984. 62 1639.

Davidge, T. J. The Compact Star-forming Complex at the Heart of NGC 253 ApJ. 2016. 818, 2 142.

Davidge, T. J., Le Fevre, O., Clark, C. C. Multicolor CCD Imaging of Supergiants in the Disk of NGC 253 ApJ. 1991. 370 559.

Davis, T. A., Bayet, E., Crocker, A., Topal, S., Bureau, M. ISM chemistry in metal-rich environments: molecular tracers of metallicity MNRAS. 2013. 433, 2 1659–1674.

Dettmar, R.-J. The distribution of the diffuse ionized interstellar medium perpendicular to the disk of the edge-on galaxy NGC 891 A&A. 1990. 232 L15–L18.

Di Cintio, A., Brook, C. B., Macciò, A. V., Stinson, G. S., Knebe, A., Dutton, A. A., Wadsley, J. The dependence of dark matter profiles on the stellar-to-halo mass ratio: a prediction for cusps versus cores MNRAS. 2014. 437, 1 415–423.

Di Teodoro, E. M., Fraternali, F., Miller, S. H. Flat rotation curves and low velocity dispersions in KMOS star-forming galaxies at z ˜ 1 A&A. 2016. 594 A77.

Di Valentino, E., Mena, O., Pan, S., Visinelli, L., Yang, W., Melchiorri, A., Mota, D. F., Riess, A. G., Silk, J. In the Realm of the Hubble tension − a Review of Solutions arXiv e-prints. 2021. arXiv:2103.01183.

Dickey, J. M., Lockman, F. J. H I in the galaxy. ARA&A. 1990. 28 215–261.

Dinnbier, F., Walch, S. How fast do young star clusters expel their natal gas? Estimating the upper limit of the gas expulsion time-scale MNRAS. 2020. 499, 1 748–767.

Doi, M., Tanaka, M., Fukugita, M., Gunn, J. E., Yasuda, N., Ivezić, Ž., Brinkmann, J., de Haars, E., Kleinman, S. J., Krzesinski, J., French Leger, R. Photometric Response Functions of the Sloan Digital Sky Survey Imager AJ. 2010. 139 1628–1648.

Domínguez, A., Siana, B., Henry, A. L., Scarlata, C., Bedregal, A. G., Malkan, M., Atek, H., Ross, N. R., Colbert, J. W., Teplitz, H. I., Rafelski, M., McCarthy, P., Bunker, A., Hathi, N. P., Dressler, A., Martin, C. L., Masters, D. Dust Extinction from Balmer Decrements of Star-forming Galaxies at 0.75 <= z <= 1.5 with Hubble Space Telescope/Wide-Field-Camera 3 Spectroscopy from the WFC3 Infrared Spectroscopic Parallel Survey ApJ. 2013. 763 145.

Draine, B. T. Physics of the Interstellar and Intergalactic Medium. 2011.

Dutton, A. A., Macciò, A. V. Cold dark matter haloes in the Planck era: evolution of structural parameters for Einasto and NFW profiles MNRAS. 2014. 441, 4 3359–3374.

Eisenstein, D. J., Weinberg, D. H., Agol, E., Aihara, H., Allende Prieto, C., Anderson, S. F., Arns, J. A., Aubourg, É., Bailey, S., Balbinot, E., al., et. SDSS-III: Massive Spectroscopic Surveys of the Distant Universe, the Milky Way, and Extra-Solar Planetary Systems AJ. 2011. 142 72.

El-Badry, K., Ostriker, E. C., Kim, C.-G., Quataert, E., Weisz, D. R. Evolution of supernovae-driven superbubbles with conduction and cooling MNRAS. 2019. 490, 2 1961–1990.

Elbert, O. D., Bullock, J. S., Garrison-Kimmel, S., Rocha, M., Oñorbe, J., Peter, A. H. G. Core formation in dwarf haloes with self-interacting dark matter: no fine-tuning necessary MNRAS. 2015. 453, 1 29–37.

Emig, K. L. From Star-formation to Recombination: Expanding our View of the Radio Recombination Line Universe. 2021.

Emig, K. L., Bolatto, A. D., Leroy, A. K., Mills, E. A. C., Jiménez Donaire, M. J., Tielens, A. G. G. M., Ginsburg, A., Gorski, M., Krieger, N., Levy, R. C., Meier, D. S., Ott, J., Rosolowsky, E., Thompson, T. A., Veilleux, S. Super Star Clusters in the Central Starburst of NGC 4945 ApJ. 2020. 903, 1 50.

Escoffier, R. P., Comoretto, G., Webber, J. C., Baudry, A., Broadwell, C. M., Greenberg, J. H., Treacy, R. R., Cais, P., Quertier, B., Camino, P., Bos, A., Gunst, A. W. The ALMA correlator A&A. 2007. 462, 2 801–810.

Faber, S. M., Willmer, C. N. A., Wolf, C., Koo, D. C., Weiner, B. J., Newman, J. A., Im, M., Coil, A. L., Conroy, C., Cooper, M. C., Davis, M., Finkbeiner, D. P., Gerke, B. F., Gebhardt, K., Groth, E. J., Guhathakurta, P., Harker, J., Kaiser, N., Kassin, S., Kleinheinrich, M., Konidaris, N. P., Kron, R. G., Lin, L., Luppino, G., Madgwick, D. S., Meisenheimer, K., Noeske, K. G., Phillips, A. C., Sarajedini, V. L., Schiavon, R. P., Simard, L., Szalay, A. S., Vogt, N. P., Yan, R. Galaxy Luminosity Functions to z˜1 from DEEP2 and COMBO-17: Implications for Red Galaxy Formation ApJ. 2007. 665, 1 265–294.

Falcón-Barroso, J., Lyubenova, M., van de Ven, G., Mendez-Abreu, J., Aguerri, J. A. L., García-Lorenzo, B., Bekeraité, S., Sánchez, S. F., Husemann, B., García-Benito, R., Mast, D., Walcher, C. J., Zibetti, S., Barrera-Ballesteros, J. K., Galbany, L., Sánchez-Blázquez, P., Singh, R., van den Bosch, R. C. E., Wild, V., Zhu, L., Bland-Hawthorn, J., Cid Fernandes, R., de Lorenzo-Cáceres, A., Gallazzi, A., González Delgado, R. M., Marino, R. A., Márquez, I., Pérez, E., Pérez, I., Roth, M. M., Rosales-Ortega, F. F., Ruiz-Lara, T., Wisotzki, L., Ziegler, B., Califa Collaboration, . Stellar kinematics across the Hubble sequence in the CALIFA survey: general properties and aperture corrections A&A. 2017. 597 A48.

Fall, S. M., Krumholz, M. R., Matzner, C. D. Stellar Feedback in Molecular Clouds and its Influence on the Mass Function of Young Star Clusters ApJL. 2010. 710, 2 L142–L146.

Field, G. B., Goldsmith, D. W., Habing, H. J. Cosmic-Ray Heating of the Interstellar Gas ApJL. 1969. 155 L149.

Fitts, A., Boylan-Kolchin, M., Elbert, O. D., Bullock, J. S., Hopkins, P. F., Oñorbe, J., Wetzel, A., Wheeler, C., Faucher-Giguère, C.-A., Kereš, D., Skillman, E. D., Weisz, D. R. fire in the field: simulating the threshold of galaxy formation MNRAS. 2017. 471, 3 3547–3562.

Flores-Fajardo, N., Morisset, C., Stasińska, G., Binette, L. Ionization of the diffuse gas in galaxies: hot low-mass evolved stars at work MNRAS. 2011. 415 2182–2192.

Flores, R. A., Primack, J. R. Observational and Theoretical Constraints on Singular Dark Matter Halos ApJL. 1994. 427 L1.

Flores Velázquez, J. A., Gurvich, A. B., Faucher-Giguère, C.-A., Bullock, J. S., Starkenburg, T. K., Moreno, J., Lazar, A., Mercado, F. J., Stern, J., Sparre, M., Hayward, C. C., Wetzel, A., El-Badry, K. The time-scales probed by star formation rate indicators for realistic, bursty star formation histories from the FIRE simulations MNRAS. 2021. 501, 4 4812–4824.

Foreman-Mackey, D., Hogg, D. W., Lang, D., Goodman, J. emcee: The MCMC Hammer PASP. 2013. 125 306.

Foreman-Mackey, D. corner.py: Scatterplot matrices in Python The Journal of Open Source Software. 2016. 1, 2 24.

Frank, B. S., de Blok, W. J. G., Walter, F., Leroy, A., Carignan, C. The Impact of Molecular Gas on Mass Models of Nearby Galaxies AJ. 2016. 151 94.

Fraternali, F., Oosterloo, T., Sancisi, R. Kinematics of the ionised gas in the spiral galaxy NGC 2403 A&A. 2004. 424 485–495.

Fraternali, F., Oosterloo, T. A., Sancisi, R., Swaters, R. The Extra-planar Neutral Gas in the Edge-on Spiral Galaxy NGC 891 Extra-Planar Gas. 331. 2005. 239. (Astronomical Society of the Pacific Conference Series).

Fraternali, F., van Moorsel, G., Sancisi, R., Oosterloo, T. Deep H I Survey of the Spiral Galaxy NGC 2403 AJ. 2002. 123 3124–3140.

Fry, A. B., Governato, F., Pontzen, A., Quinn, T., Tremmel, M., Anderson, L., Menon, H., Brooks, A. M., Wadsley, J. All about baryons: revisiting SIDM predictions at small halo masses MNRAS. 2015. 452, 2 1468–1479.

Gallagher, M. J., Leroy, A. K., Bigiel, F., Cormier, D., Jiménez-Donaire, M. J., Hughes, A., Pety, J., Schinnerer, E., Sun, J., Usero, A., Utomo, D., Bolatto, A., Chevance, M., Faesi, C., Glover, S. C. O., Kepley, A. A., Kruijssen, J. M. D., Krumholz, M. R., Meidt, S. E., Meier, D. S., Murphy, E., Querejeta, M., Rosolowsky, E., Saito, T., Schruba, A. Do Spectroscopic Dense Gas Fractions Track Molecular Cloud Surface Densities? ApJL. 2018a. 868, 2 L38.

Gallagher, M. J., Leroy, A. K., Bigiel, F., Cormier, D., Jiménez-Donaire, M. J., Ostriker, E., Usero, A., Bolatto, A. D., García-Burillo, S., Hughes, A., Kepley, A. A., Krumholz, M., Meidt, S. E., Meier, D. S., Murphy, E. J., Pety, J., Rosolowsky, E., Schinnerer, E., Schruba, A., Walter, F. Dense Gas, Dynamical Equilibrium Pressure, and Star Formation in Nearby Star-forming Galaxies ApJ. 2018b. 858, 2 90.

Gao, Y., Solomon, P. M. The Star Formation Rate and Dense Molecular Gas in Galaxies ApJ. 2004. 606, 1 271–290.

Garcia, A. M. General study of group membership. II. Determination of nearby groups. A&AS. 1993. 100 47–90.

*García-Benito, R., Zibetti, S., Sánchez, S. F., Husemann, B., de Amorim, A. L., Castillo-Morales, A., Cid Fernandes, R., Ellis, S. C., Falcón-Barroso, J., Galbany, L., Gil de Paz, A., González Delgado, R. M., Lacerda, E. A. D., López-Fernandez, R., de Lorenzo-Cáceres, A., Lyubenova, M., Marino, R. A., Mast, D., Mendoza, M. A., Pérez, E., Vale Asari, N., Aguerri, J. A. L., Ascasibar, Y., Bekerait*error*ė, S., Bland-Hawthorn, J., Barrera-Ballesteros, J. K., Bomans, D. J., Cano-Díaz, M., Catalán-Torrecilla, C., Cortijo, C., Delgado-Inglada, G., Demleitner, M., Dettmar, R.-J., Díaz, A. I., Florido, E., Gallazzi, A., García-Lorenzo, B., Gomes, J. M., Holmes, L., Iglesias-Páramo, J., Jahnke, K., Kalinova, V., Kehrig, C., Kennicutt, R. C., López-Sánchez, Á. R., Márquez, I., Masegosa, J., Meidt, S. E., Mendez-Abreu, J., Mollá, M., Monreal-Ibero, A., Morisset, C., del Olmo, A., Papaderos, P., Pérez, I., Quirrenbach, A., Rosales-Ortega, F. F., Roth, M. M., Ruiz-Lara, T., Sánchez-Blázquez, P., Sánchez-Menguiano, L., Singh, R., Spekkens, K., Stanishev, V., Torres-Papaqui, J. P., van de Ven, G., Vilchez, J. M., Walcher, C. J., Wild, V., Wisotzki, L., Ziegler, B., Alves, J., Barrado, D., Quintana, J. M., Aceituno, J.* CALIFA, the Calar Alto Legacy Integral Field Area survey. III. Second public data release A&A. 2015. 576 A135.

García-Lorenzo, B., Márquez, I., Barrera-Ballesteros, J. K., Masegosa, J., Husemann, B., Falcón-Barroso, J., Lyubenova, M., Sánchez, S. F., Walcher, J., Mast, D., García-Benito, R., Méndez-Abreu, J., van de Ven, G., Spekkens, K., Holmes, L., Monreal-Ibero, A., del Olmo, A., Ziegler, B., Bland-Hawthorn, J., Sánchez-Blázquez, P., Iglesias-Páramo, J., Aguerri, J. A. L., Papaderos, P., Gomes, J. M., Marino, R. A., González Delgado, R. M., Cortijo-Ferrero, C., López-Sánchez, A. R., Bekeraitė, S., Wisotzki, L., Bomans, D. Ionized gas kinematics of galaxies in the CALIFA survey. I. Velocity fields, kinematic parameters of the dominant component, and presence of kinematically distinct gaseous systems A&A. 2015. 573 A59.

Geen, S., Bieri, R., Rosdahl, J., de Koter, A. The geometry and dynamical role of stellar wind bubbles in photoionized H II regions MNRAS. 2021. 501, 1 1352–1369.

Geen, S., Hennebelle, P., Tremblin, P., Rosdahl, J. Photoionization feedback in a self-gravitating, magnetized, turbulent cloud MNRAS. 2015. 454, 4 4484–4502.

Geen, S., Pellegrini, E., Bieri, R., Klessen, R. When H II regions are complicated: considering perturbations from winds, radiation pressure, and other effects MNRAS. 2020. 492, 1 915–933.

Gilbert, A. M., Graham, J. R. Feedback in the Antennae Galaxies (NGC 4038/9). I. High-Resolution Infrared Spectroscopy of Winds from Super Star Clusters ApJ. 2007. 668, 1 168–181.

Ginsburg, A., Kruijssen, J. M. D. A High Cluster Formation Efficiency in the Sagittarius B2 Complex ApJ. 2018. 864, 1 L17.

Goad, J. W., Roberts, M. S. Spectroscopic observations of superthin galaxies ApJ. 1981. 250 79–86.

Gomes, J. M., Papaderos, P., Vílchez, J. M., Kehrig, C., Iglesias-Páramo, J., Breda, I., Lehnert, M. D., Sánchez, S. F., Ziegler, B., Dos Reis, S. N., Bland-Hawthorn, J., Galbany, L., Bomans, D. J., Rosales-Ortega, F. F., Walcher, C. J., García-Benito, R., Márquez, I., Del Olmo, A., Mollá, M., Marino, R. A., Catalán-Torrecilla, C., González Delgado, R. M., López-Sánchez, Á. R., Califa Collaboration, . Spectroscopic aperture biases in inside-out evolving early-type galaxies from CALIFA A&A. 2016. 586 A22.

Gorski, M., Ott, J., Rand, R., Meier, D. S., Momjian, E., Schinnerer, E. Survey of Water and Ammonia in Nearby Galaxies (SWAN): Resolved Ammonia Thermometry, and Water and Methanol Masers in the Nuclear Starburst of NGC 253 ApJ. 2017. 842, 2 124.

Gorski, M. D., Ott, J., Rand, R., Meier, D. S., Momjian, E., Schinnerer, E., Ellingsen, S. P. Diagnostics of a nuclear starburst: water and methanol masers MNRAS. 2019. 483, 4 5434–5443.

Governato, F., Zolotov, A., Pontzen, A., Christensen, C., Oh, S. H., Brooks, A. M., Quinn, T., Shen, S., Wadsley, J. Cuspy no more: how outflows affect the central dark matter and baryon distribution in Λ cold dark matter galaxies MNRAS. 2012. 422, 2 1231–1240.

Gray, W. J., Oey, M. S., Silich, S., Scannapieco, E. Catastrophic Cooling in Superwinds: Line Emission and Non-equilibrium Ionization ApJ. 2019. 887, 2 161.

Grenier, I. A., Casandjian, J.-M., Terrier, R. Unveiling Extensive Clouds of Dark Gas in the Solar Neighborhood Science. 2005. 307, 5713 1292–1295.

Grudić, M. Y., Hopkins, P. F., Faucher-Giguère, C.-A., Quataert, E., Murray, N., Kereš, D. When feedback fails: the scaling and saturation of star formation efficiency MNRAS. 2018. 475, 3 3511–3528.

Gunn, J. E., Carr, M., Rockosi, C., Sekiguchi, M., Berry, K., Elms, B., de Haas, E., Ivezić, Ž., Knapp, G., Lupton, R., Pauls, G., Simcoe, R., Hirsch, R., Sanford, D., Wang, S., York, D., Harris, F., Annis, J., Bartozek, L., Boroski, W., Bakken, J., Haldeman, M., Kent, S., Holm, S., Holmgren, D., Petravick, D., Prosapio, A., Rechenmacher, R., Doi, M., Fukugita, M., Shimasaku, K., Okada, N., Hull, C., Siegmund, W., Mannery, E., Blouke, M., Heidtman, D., Schneider, D., Lucinio, R., Brinkman, J. The Sloan Digital Sky Survey Photometric Camera AJ. 1998. 116 3040–3081.

Gunn, J. E., Siegmund, W. A., Mannery, E. J., Owen, R. E., Hull, C. L., Leger, R. F., Carey, L. N., Knapp, G. R., York, D. G., Boroski, W. N., Kent, S. M., Lupton, R. H., Rockosi, C. M., Evans, M. L., Waddell, P., Anderson, J. E., Annis, J., Barentine, J. C., Bartoszek, L. M., Bastian, S., Bracker, S. B., Brewington, H. J., Briegel, C. I., Brinkmann, J., Brown, Y. J., Carr, M. A., Czarapata, P. C., Drennan, C. C., Dombeck, T., Federwitz, G. R., Gillespie, B. A., Gonzales, C., Hansen, S. U., Harvanek, M., Hayes, J., Jordan, W., Kinney, E., Klaene, M., Kleinman, S. J., Kron, R. G., Kresinski, J., Lee, G., Limmongkol, S., Lindenmeyer, C. W., Long, D. C., Loomis, C. L., McGehee, P. M., Mantsch, P. M., Neilsen, E. H. Jr., Neswold, R. M., Newman, P. R., Nitta, A., Peoples, J. Jr., Pier, J. R., Prieto, P. S., Prosapio, A., Rivetta, C., Schneider, D. P., Snedden, S., Wang, S.-i. The 2.5 m Telescope of the Sloan Digital Sky Survey AJ. 2006. 131 2332–2359.

Guszejnov, D., Grudić, M. Y., Hopkins, P. F., Offner, S. S. R., Faucher-Giguère, C.-A. STARFORGE: the effects of protostellar outflows on the IMF MNRAS. 2021. 502, 3 3646–3663.

Haffner, L. M., Dettmar, R.-J., Beckman, J. E., Wood, K., Slavin, J. D., Giammanco, C., Madsen, G. J., Zurita, A., Reynolds, R. J. The warm ionized medium in spiral galaxies Reviews of Modern Physics. 2009. 81 969–997.

Hao, C.-N., Kennicutt, R. C., Johnson, B. D., Calzetti, D., Dale, D. A., Moustakas, J. Dust-corrected Star Formation Rates of Galaxies. II. Combinations of Ultraviolet and Infrared Tracers ApJ. 2011. 741, 2 124.

Harris, C. R., Millman, K. J., Walt, S. J. van der, Gommers, R., Virtanen, P., Cournapeau, D., Wieser, E., Taylor, J., Berg, S., Smith, N. J., Kern, R., Picus, M., Hoyer, S., Kerkwijk, M. H. van, Brett, M., Haldane, A., Río, J. Fernández del, Wiebe, M., Peterson, P., GÃ©rard-Marchant, P., Sheppard, K., Reddy, T., Weckesser, W., Abbasi, H., Gohlke, C., Oliphant, T. E. Array programming with NumPy Nature. 2020. 585 357–362.

He, C.-C., Ricotti, M., Geen, S. Simulating star clusters across cosmic time - I. Initial mass function, star formation rates, and efficiencies MNRAS. 2019. 489, 2 1880–1898.

Heald, G. H., Rand, R. J., Benjamin, R. A., Bershady, M. A. Integral Field Unit Observations of NGC 891: Kinematics of the Diffuse Ionized Gas Halo ApJ. 2006a. 647 1018–1029.

Heald, G. H., Rand, R. J., Benjamin, R. A., Bershady, M. A. Integral Field Unit Observations of NGC 4302: Kinematics of the Diffuse Ionized Gas Halo ApJ. 2007. 663 933–947.

Heald, G. H., Rand, R. J., Benjamin, R. A., Collins, J. A., Bland-Hawthorn, J. Imaging Fabry-Perot Spectroscopy of NGC 5775: Kinematics of the Diffuse Ionized Gas Halo ApJ. 2006b. 636 181–199.

Heiles, C. On the Origin of the Diffuse C + 158 Micron Line Emission ApJ. 1994. 436 720.

Heiles, C., Troland, T. H. The Millennium Arecibo 21 Centimeter Absorption-Line Survey. II. Properties of the Warm and Cold Neutral Media ApJ. 2003. 586, 2 1067–1093.

Henkel, C., Asiri, H., Ao, Y., Aalto, S., Danielson, A. L. R., Papadopoulos, P. P., García-Burillo, S., Aladro, R., Impellizzeri, C. M. V., Mauersberger, R., Martín, S., Harada, N. Carbon and oxygen isotope ratios in starburst galaxies: New data from NGC 253 and Mrk 231 and their implications A&A. 2014. 565 A3.

Henshaw, J. D., Longmore, S. N., Kruijssen, J. M. D., Davies, B., Bally, J., Barnes, A., Battersby, C., Burton, M., Cunningham, M. R., Dale, J. E., Ginsburg, A., Immer, K., Jones, P. A., Kendrew, S., Mills, E. A. C., Molinari, S., Moore, T. J. T., Ott, J., Pillai, T., Rathborne, J., Schilke, P., Schmiedeke, A., Testi, L., Walker, D., Walsh, A., Zhang, Q. Molecular gas kinematics within the central 250 pc of the Milky Way MNRAS. 2016. 457, 3 2675–2702.

Herrera, C. N., Boulanger, F. The impact of a massive star cluster on its surrounding matter in the Antennae overlap region A&A. 2017. 600 A139.

Ho, I. T., Medling, A. M., Bland-Hawthorn, J., Groves, B., Kewley, L. J., Kobayashi, C., Dopita, M. A., Leslie, S. K., Sharp, R., Allen, J. T., Bourne, N., Bryant, J. J., Cortese, L., Croom, S. M., Dunne, L., Fogarty, L. M. R., Goodwin, M., Green, A. W., Konstantopoulos, I. S., Lawrence, J. S., Lorente, N. P. F., Owers, M. S., Richards, S., Sweet, S. M., Tescari, E., Valiante, E. The SAMI Galaxy Survey: extraplanar gas, galactic winds and their association with star formation history MNRAS. 2016. 457, 2 1257–1278.

Hoffmann, T. L., Lieb, S., Pauldrach, A. W. A., Lesch, H., Hultzsch, P. J. N., Birk, G. T. Numerical models for the diffuse ionized gas in galaxies. I. Synthetic spectra of thermally excited gas with turbulent magnetic reconnection as energy source A&A. 2012. 544 A57.

Högbom, J. A. Aperture Synthesis with a Non-Regular Distribution of Interferometer Baselines A&AS. 1974. 15 417.

Hollenbach, D. J., Tielens, A. G. G. M. Dense Photodissociation Regions (PDRs) ARA&A. 1997. 35 179–216.

Hooper, D. The density of dark matter in the Galactic bulge and implications for indirect detection Physics of the Dark Universe. 2017. 15 53–56.

Hoopes, C. G., Walterbos, R. A. M. Optical Spectroscopy and Ionization Models of the Diffuse Ionized Gas in M33, M51/NGC 5195, and M81 ApJ. 2003. 586 902–922.

Hoopes, C. G., Walterbos, R. A. M., Rand, R. J. Diffuse Ionized Gas in Edge-on Spiral Galaxies: Extraplanar and Outer Disk Hα Emission ApJ. 1999. 522 669–685.

Hopkins, P. F., Wetzel, A., Kereš, D., Faucher-Giguère, C.-A., Quataert, E., Boylan-Kolchin, M., Murray, N., Hayward, C. C., Garrison-Kimmel, S., Hummels, C., Feldmann, R., Torrey, P., Ma, X., Anglés-Alcázar, D., Su, K.-Y., Orr, M., Schmitz, D., Escala, I., Sanderson, R., Grudić, M. Y., Hafen, Z., Kim, J.-H., Fitts, A., Bullock, J. S., Wheeler, C., Chan, T. K., Elbert, O. D., Narayanan, D. FIRE-2 simulations: physics versus numerics in galaxy formation MNRAS. 2018. 480, 1 800–863.

Howk, J. C. Extraplanar Dust in Spiral Galaxies: Observations and Implications Ap&SS. 1999. 269 293–300.

Howk, J. C., Savage, B. D. Extraplanar Dust in the Edge-On Spiral NGC 891 AJ. 1997. 114 2463.

Howk, J. C., Savage, B. D. A Search for Extraplanar Dust in Nearby Edge-on Spirals AJ. 1999. 117, 5 2077–2101.

*Husemann, B., Jahnke, K., Sánchez, S. F., Barrado, D., Bekerait*error*ė, S., Bomans, D. J., Castillo-Morales, A., Catalán-Torrecilla, C., Cid Fernandes, R., Falcón-Barroso, J., García-Benito, R., González Delgado, R. M., Iglesias-Páramo, J., Johnson, B. D., Kupko, D., López-Fernandez, R., Lyubenova, M., Marino, R. A., Mast, D., Miskolczi, A., Monreal-Ibero, A., Gil de Paz, A., Pérez, E., Pérez, I., Rosales-Ortega, F. F., Ruiz-Lara, T., Schilling, U., van de Ven, G., Walcher, J., Alves, J., de Amorim, A. L., Backsmann, N., Barrera-Ballesteros, J. K., Bland-Hawthorn, J., Cortijo, C., Dettmar, R.-J., Demleitner, M., Díaz, A. I., Enke, H., Florido, E., Flores, H., Galbany, L., Gallazzi, A., García-Lorenzo, B., Gomes, J. M., Gruel, N., Haines, T., Holmes, L., Jungwiert, B., Kalinova, V., Kehrig, C., Kennicutt, R. C., Klar, J., Lehnert, M. D., López-Sánchez, Á. R., de Lorenzo-Cáceres, A., Mármol-Queraltó, E., Márquez, I., Mendez-Abreu, J., Mollá, M., del Olmo, A., Meidt, S. E., Papaderos, P., Puschnig, J., Quirrenbach, A., Roth, M. M., Sánchez-Blázquez, P., Spekkens, K., Singh, R., Stanishev, V., Trager, S. C., Vilchez, J. M., Wild, V., Wisotzki, L., Zibetti, S., Ziegler, B.* CALIFA, the Calar Alto Legacy Integral Field Area survey. II. First public data release A&A. 2013. 549 A87.

Iorio, G., Fraternali, F., Nipoti, C., Di Teodoro, E., Read, J. I., Battaglia, G. LITTLE THINGS in 3D: robust determination of the circular velocity of dwarf irregular galaxies MNRAS. 2017. 466 4159–4192.

Jarrett, T. H., Chester, T., Cutri, R., Schneider, S. E., Huchra, J. P. The 2MASS Large Galaxy Atlas AJ. 2003. 125, 2 525–554.

Jarrett, T. H., Cohen, M., Masci, F., Wright, E., Stern, D., Benford, D., Blain, A., Carey, S., Cutri, R. M., Eisenhardt, P., Lonsdale, C., Mainzer, A., Marsh,

K., Padgett, D., Petty, S., Ressler, M., Skrutskie, M., Stanford, S., Surace, J., Tsai, C. W., Wheelock, S., Yan, D. L. The Spitzer-WISE Survey of the Ecliptic Poles ApJ. 2011. 735 112.

Jarrett, T. H., Masci, F., Tsai, C. W., Petty, S., Cluver, M. E., Assef, R. J., Benford, D., Blain, A., Bridge, C., Donoso, E., Eisenhardt, P., Koribalski, B., Lake, S., Neill, J. D., Seibert, M., Sheth, K., Stanford, S., Wright, E. Extending the Nearby Galaxy Heritage with WISE: First Results from the WISE Enhanced Resolution Galaxy Atlas AJ. 2013. 145 6.

Johnson, K. E., Leroy, A. K., Indebetouw, R., Brogan, C. L., Whitmore, B. C., Hibbard, J., Sheth, K., Evans, A. S. The Physical Conditions in a Pre-super Star Cluster Molecular Cloud in the Antennae Galaxies ApJ. 2015. 806, 1 35.

Johnson, L. C., Seth, A. C., Dalcanton, J. J., Beerman, L. C., Fouesneau, M., Lewis, A. R., Weisz, D. R., Williams, B. F., Bell, E. F., Dolphin, A. E. Panchromatic Hubble Andromeda Treasury. XVI. Star Cluster Formation Efficiency and the Clustered Fraction of Young Stars ApJ. 2016. 827, 1 33.

Jones, G. C., Carilli, C. L., Shao, Y., Wang, R., Capak, P. L., Pavesi, R., Riechers, D. A., Karim, A., Neeleman, M., Walter, F. Dynamical Characterization of Galaxies at z $\sim$ 4-6 via Tilted Ring Fitting to ALMA [C II] Observations ApJ. 2017. 850 180.

Kalberla, P. M. W., Kerp, J. The Hi Distribution of the Milky Way ARA&A. 2009. 47, 1 27–61.

Kamada, A., Kaplinghat, M., Pace, A. B., Yu, H.-B. Self-Interacting Dark Matter Can Explain Diverse Galactic Rotation Curves Phys. Rev. Lett.. 2017. 119, 11 111102.

Kamann, S., Bastian, N. J., Gieles, M., Balbinot, E., Hénault-Brunet, V. Linking the rotation of a cluster to the spins of its stars: the kinematics of NGC 6791 and NGC 6819 in 3D MNRAS. 2019. 483, 2 2197–2206.

Kamphuis, P., Rand, R. J., Józsa, G. I. G., Zschaechner, L. K., Heald, G. H., Patterson, M. T., Gentile, G., Walterbos, R. A. M., Serra, P., de Blok, W. J. G. HALOGAS observations of NGC 5023 and UGC 2082: modelling of non-cylindrically symmetric gas distributions in edge-on galaxies MNRAS. 2013. 434 2069–2093.

Kaplinghat, M., Ren, T., Yu, H.-B. Dark matter cores and cusps in spiral galaxies and their explanations J. Cosmology Astropart. Phys.. 2020. 2020, 6 027.

Kauffmann, G., Heckman, T. M., Tremonti, C., Brinchmann, J., Charlot, S., White, S. D. M., Ridgway, S. E., Brinkmann, J., Fukugita, M., Hall, P. B., Ivezić, Ž., Richards, G. T., Schneider, D. P. The host galaxies of active galactic nuclei MNRAS. 2003. 346 1055–1077.

Kaufmann, T., Mayer, L., Wadsley, J., Stadel, J., Moore, B. Cooling flows within galactic haloes: the kinematics and properties of infalling multiphase gas MNRAS. 2006. 370 1612–1622.

Kennicutt, R. C., Evans, N. J. Star Formation in the Milky Way and Nearby Galaxies ARA&A. 2012. 50 531–608.

Kennicutt, R. C. Jr. The Global Schmidt Law in Star-forming Galaxies ApJ. 1998. 498 541–552.

Keto, E., Ho, L. C., Lo, K. Y. M82, Starbursts, Star Clusters, and the Formation of Globular Clusters ApJ. 2005. 635, 2 1062–1076.

Kewley, L. J., Dopita, M. A., Sutherland, R. S., Heisler, C. A., Trevena, J. Theoretical Modeling of Starburst Galaxies ApJ. 2001. 556 121–140.

Kim, C.-G., Ostriker, E. C. Momentum Injection by Supernovae in the Interstellar Medium ApJ. 2015. 802, 2 99.

Kim, C.-G., Ostriker, E. C., Raileanu, R. Superbubbles in the Multiphase ISM and the Loading of Galactic Winds ApJ. 2017a. 834, 1 25.

Kim, J.-G., Kim, W.-T., Ostriker, E. C. Disruption of Molecular Clouds by Expansion of Dusty H II Regions ApJ. 2016. 819, 2 137.

Kim, J.-G., Kim, W.-T., Ostriker, E. C. Modeling UV Radiation Feedback from Massive Stars. II. Dispersal of Star-forming Giant Molecular Clouds by Photoionization and Radiation Pressure ApJ. 2018. 859, 1 68.

Kim, J.-G., Kim, W.-T., Ostriker, E. C. Modeling UV Radiation Feedback from Massive Stars. III. Escape of Radiation from Star-forming Giant Molecular Clouds ApJ. 2019. 883, 1 102.

Kim, J.-G., Kim, W.-T., Ostriker, E. C., Skinner, M. A. Modeling UV Radiation Feedback from Massive Stars. I. Implementation of Adaptive Ray-tracing Method and Tests ApJ. 2017b. 851, 2 93.

King, I. The structure of star clusters. I. an empirical density law AJ. 1962. 67 471.

Knapen, J. H. Observations of Barred Galaxies The Evolution of Galaxies on Cosmological Timescales. 187. 1999. 72–87. (Astronomical Society of the Pacific Conference Series).

Koribalski, B. S., Staveley-Smith, L., Kilborn, V. A., Ryder, S. D., Kraan-Korteweg, R. C., Ryan-Weber, E. V., Ekers, R. D., Jerjen, H., Henning, P. A., Putman, M. E., Zwaan, M. A., de Blok, W. J. G., Calabretta, M. R., Disney, M. J., Minchin, R. F., Bhathal, R., Boyce, P. J., Drinkwater, M. J., Freeman, K. C., Gibson, B. K., Green, A. J., Haynes, R. F., Juraszek, S., Kesteven, M. J.,

Knezek, P. M., Mader, S., Marquarding, M., Meyer, M., Mould, J. R., Oosterloo, T., O'Brien, J., Price, R. M., Sadler, E. M., Schröder, A., Stewart, I. M., Stootman, F., Waugh, M., Warren, B. E., Webster, R. L., Wright, A. E. The 1000 Brightest HIPASS Galaxies: H I Properties AJ. 2004. 128, 1 16–46.

Kormendy, J., Kennicutt, J. Robert C. Secular Evolution and the Formation of Pseudobulges in Disk Galaxies ARA&A. 2004. 42, 1 603–683.

Kornei, K. A., McCrady, N. A Young Super Star Cluster in the Nuclear Region of NGC 253 ApJ. 2009. 697, 2 1180–1186.

Kregel, M., van der Kruit, P. C., de Grijs, R. Flattening and truncation of stellar discs in edge-on spiral galaxies MNRAS. 2002. 334, 3 646–668.

Krieger, N., Bolatto, A. D., Koch, E. W., Leroy, A. K., Rosolowsky, E., Walter, F., Weiß, A., Eden, D. J., Levy, R. C., Meier, D. S., Mills, E. A. C., Moore, T., Ott, J., Su, Y., Veilleux, S. The Turbulent Gas Structure in the Centers of NGC 253 and the Milky Way ApJ. 2020a. 899, 2 158.

Krieger, N., Bolatto, A. D., Leroy, A. K., Levy, R. C., Mills, E. A. C., Meier, D. S., Ott, J., Veilleux, S., Walter, F., Weiß, A. The Molecular Interstellar Medium in the Super Star Clusters of the Starburst NGC 253 ApJ. 2020b. 897, 2 176.

Krieger, N., Bolatto, A. D., Walter, F., Leroy, A. K., Zschaechner, L. K., Meier, D. S., Ott, J., Weiss, A., Mills, E. A. C., Levy, R. C., Veilleux, S., Gorski, M. The Molecular Outflow in NGC 253 at a Resolution of Two Parsecs ApJ. 2019. 881, 1 43.

Krishnarao, D., Haffner, L. M., Benjamin, R. A., Hill, A. S., Barger, K. A. Warm Ionized Medium throughout the Sagittarius-Carina Arm ApJ. 2017. 838 43.

Kroupa, P. On the variation of the initial mass function MNRAS. 2001. 322, 2 231–246.

Kruijssen, J. M. D. On the fraction of star formation occurring in bound stellar clusters MNRAS. 2012. 426, 4 3008–3040.

Kruijssen, J. M. D., Dale, J. E., Longmore, S. N. The dynamical evolution of molecular clouds near the Galactic Centre - I. Orbital structure and evolutionary timeline MNRAS. 2015. 447, 2 1059–1079.

Krumholz, M. R., Kruijssen, J. M. D. A dynamical model for the formation of gas rings and episodic starbursts near galactic centres MNRAS. 2015. 453, 1 739–757.

Krumholz, M. R., McKee, C. F., Bland -Hawthorn, J. Star Clusters Across Cosmic Time ARA&A. 2019. 57 227–303.

Kulkarni, S. R., Heiles, C. The atomic component Interstellar Processes. 134. 1987. 87–122. (Astrophysics and Space Science Library).

Lacerda, E. A. D., Cid Fernandes, R., Couto, G. S., Stasińska, G., García-Benito, R., Vale Asari, N., Pérez, E., González Delgado, R. M., Sánchez, S. F., de Amorim, A. L. Diffuse ionized gas in galaxies across the Hubble sequence at the CALIFA resolution MNRAS. 2018. 474 3727–3739.

Lada, C. J., Lada, E. A. Embedded Clusters in Molecular Clouds ARA&A. 2003. 41 57–115.

Lancaster, L., Ostriker, E. C., Kim, J.-G., Kim, C.-G. Efficiently Cooled Stellar Wind Bubbles in Turbulent Clouds. I. Fractal Theory and Application to Star-forming Clouds ApJ. 2021a. 914, 2 89.

Lancaster, L., Ostriker, E. C., Kim, J.-G., Kim, C.-G. Efficiently Cooled Stellar Wind Bubbles in Turbulent Clouds. II. Validation of Theory with Hydrodynamic Simulations ApJ. 2021b. 914, 2 90.

Lang, C. C., Goss, W. M., Wood, O. S. VLA H92α and H115β Recombination Line Observations of the Galactic Center H II Regions: The Sickle (G0.18-0.04) and the Pistol (G0.15-0.05) ApJ. 1997. 474 275–291.

Lazar, A., Bullock, J. S., Boylan-Kolchin, M., Chan, T. K., Hopkins, P. F., Graus, A. S., Wetzel, A., El-Badry, K., Wheeler, C., Straight, M. C., Kereš, D., Faucher-Giguère, C.-A., Fitts, A., Garrison-Kimmel, S. A dark matter profile to model diverse feedback-induced core sizes of ΛCDM haloes MNRAS. 2020. 497, 2 2393–2417.

Lee, S.-W., Irwin, J. A., Dettmar, R.-J., Cunningham, C. T., Golla, G., Wang, Q. D. NGC 5775: Anatomy of a disk-halo interface A&A. 2001. 377 759–777.

Leitherer, C., Schaerer, D., Goldader, J. D., Delgado, R. M. G., Robert, C., Kune, D. F., de Mello, D. F., Devost, D., Heckman, T. M. Starburst99: Synthesis Models for Galaxies with Active Star Formation ApJS. 1999. 123, 1 3–40.

Leroy, A. K., Bolatto, A. D., Ostriker, E. C., Walter, F., Gorski, M., Ginsburg, A., Krieger, N., Levy, R. C., Meier, D. S., Mills, E., Ott, J., Rosolowsky, E., Thompson, T. A., Veilleux, S., Zschaechner, L. K. Forming Super Star Clusters in the Central Starburst of NGC 253 ApJ. 2018. 869 126.

Leroy, A. K., Walter, F., Brinks, E., Bigiel, F., de Blok, W. J. G., Madore, B., Thornley, M. D. The Star Formation Efficiency in Nearby Galaxies: Measuring Where Gas Forms Stars Effectively AJ. 2008. 136 2782–2845.

Leroy, A. K., Bolatto, A. D., Ostriker, E. C., Rosolowsky, E., Walter, F., Warren, S. R., Donovan Meyer, J., Hodge, J., Meier, D. S., Ott, J., Sandstrom, K., Schruba, A., Veilleux, S., Zwaan, M. ALMA Reveals the Molecular Medium Fueling the Nearest Nuclear Starburst ApJ. 2015. 801, 1 25.

Leung, G. Y. C., Leaman, R., van de Ven, G., Lyubenova, M., Zhu, L., Bolatto, A. D., Falcón-Barroso, J., Blitz, L., Dannerbauer, H., Fisher, D. B., Levy, R. C., Sanchez, S. F., Utomo, D., Vogel, S., Wong, T., Ziegler, B. The EDGE-CALIFA survey: validating stellar dynamical mass models with CO kinematics MNRAS. 2018. 477 254–292.

Leung, G. Y. C., Leaman, R., Battaglia, G., van de Ven, G., Brooks, A. M., Peñarrubia, J., Venn, K. A. Joint gas and stellar dynamical models of WLM: an isolated dwarf galaxy within a cored, prolate DM halo MNRAS. 2021. 500, 1 410–429.

Levine, E. S., Heiles, C., Blitz, L. The Milky Way Rotation Curve and Its Vertical Derivatives: Inside the Solar Circle ApJ. 2008. 679 1288–1298.

Levy, R. C., Bolatto, A. D., Leroy, A. K., Emig, K. L., Gorski, M., Krieger, N., Lenkić, L., Meier, D. S., Mills, E. A. C., Ott, J., Rosolowsky, E., Tarantino, E., Veilleux, S., Walter, F., Weiß, A., Zwaan, M. A. Outflows from Super Star Clusters in the Central Starburst of NGC 253 ApJ. 2021. 912, 1 4.

Levy, R. C., Bolatto, A. D., Sánchez, S. F., Blitz, L., Colombo, D., Kalinova, V., López-Cobá, C., Ostriker, E. C., Teuben, P., Utomo, D., Vogel, S. N., Wong, T. The EDGE-CALIFA Survey: Evidence for Pervasive Extraplanar Diffuse Ionized Gas in Nearby Edge-on Galaxies ApJ. 2019. 882, 2 84.

Levy, R. C., Bolatto, A. D., Teuben, P., Sánchez, S. F., Barrera-Ballesteros, J. K., Blitz, L., Colombo, D., García-Benito, R., Herrera-Camus, R., Husemann, B., Kalinova, V., Lan, T., Leung, G. Y. C., Mast, D., Utomo, D., van de Ven, G., Vogel, S. N., Wong, T. The EDGE-CALIFA Survey: Molecular and Ionized Gas Kinematics in Nearby Galaxies ApJ. 2018. 860, 2 92.

Lochhaas, C., Thompson, T. A. Second-generation stars in globular clusters from rapid radiative cooling of pre-supernova massive star winds MNRAS. 2017. 470, 1 977–991.

Löckmann, U., Baumgardt, H., Kroupa, P. Constraining the initial mass function of stars in the Galactic Centre MNRAS. 2010. 402, 1 519–525.

López-Cobá, C., Sánchez, S. F., Bland-Hawthorn, J., Moiseev, A. V., Cruz-González, I., García-Benito, R., Barrera-Ballesteros, J. K., Galbany, L. Systematic study of outflows in the Local Universe using CALIFA: I. Sample selection and main properties MNRAS. 2019. 482 4032–4056.

López-Cobá, C., Sánchez, S. F., Moiseev, A. V., Oparin, D. V., Bitsakis, T., Cruz-González, I., Morisset, C., Galbany, L., Bland-Hawthorn, J., Roth, M. M., Dettmar, R.-J., Bomans, D. J., González Delgado, R. M., Cano-Díaz, M., Marino, R. A., Kehrig, C., Monreal Ibero, A., Abril-Melgarejo, V. Star formation driven galactic winds in UGC 10043 MNRAS. 2017. 467 4951–4964.

Lu, J. R., Do, T., Ghez, A. M., Morris, M. R., Yelda, S., Matthews, K. Stellar Populations in the Central 0.5 pc of the Galaxy. II. The Initial Mass Function ApJ. 2013. 764, 2 155.

Maccarone, T. J., Lehmer, B. D., Leyder, J. C., Antoniou, V., Hornschemeier, A., Ptak, A., Wik, D., Zezas, A. A new candidate Wolf-Rayet X-ray binary in NGC 253 MNRAS. 2014. 439, 3 3064–3072.

Macciò, A. V., Crespi, S., Blank, M., Kang, X. NIHAO - XXIII. Dark matter density shaped by black hole feedback MNRAS. 2020. 495, 1 L46–L50.

Madden, S. C., Geis, N., Genzel, R., Herrmann, F., Jackson, J., Poglitsch, A., Stacey, G. J., Townes, C. H. 158 Micron [C ii] Mapping of NGC 6946: Probing the Atomic Medium ApJ. 1993. 407 579.

Madsen, G. J. An exploration of the heterogeneous nature of the warm ionized medium in the Galaxy. 2004.

Madsen, G. J., Reynolds, R. J., Haffner, L. M. A Multiwavelength Optical Emission Line Survey of Warm Ionized Gas in the Galaxy ApJ. 2006. 652 401–425.

Makarov, D., Prugniel, P., Terekhova, N., Courtois, H., Vauglin, I. HyperLEDA. III. The catalogue of extragalactic distances A&A. 2014. 570 A13.

Mangum, J. G., Shirley, Y. L. How to Calculate Molecular Column Density PASP. 2015. 127, 949 266.

Mapelli, M. Rotation in young massive star clusters MNRAS. 2017. 467, 3 3255–3267.

Marasco, A., Fraternali, F. Modelling the H I halo of the Milky Way A&A. 2011. 525 A134.

Marinacci, F., Fraternali, F., Ciotti, L., Nipoti, C. Stationary models for the extraplanar gas in disc galaxies MNRAS. 2010. 401 2451–2462.

Marinacci, F., Fraternali, F., Nipoti, C., Binney, J., Ciotti, L., Londrillo, P. Galactic fountains and the rotation of disc-galaxy coronae MNRAS. 2011. 415 1534–1542.

Marks, M., Kroupa, P., Dabringhausen, J., Pawlowski, M. S. Evidence for top-heavy stellar initial mass functions with increasing density and decreasing metallicity MNRAS. 2012. 422, 3 2246–2254.

Martín, S., Aladro, R., Martín-Pintado, J., Mauersberger, R. A large $^{12}C/^{13}C$ isotopic ratio in M 82 and NGC 253 A&A. 2010. 522 A62.

Martín, S., Mauersberger, R., Martín-Pintado, J., Henkel, C., García-Burillo, S. A 2 Millimeter Spectral Line Survey of the Starburst Galaxy NGC 253 ApJS. 2006. 164, 2 450–476.

Martín, S., Muller, S., Henkel, C., Meier, D. S., Aladro, R., Sakamoto, K., van der Werf, P. P. Spatially resolved carbon and oxygen isotopic ratios in NGC 253 using optically thin tracers A&A. 2019. 624 A125.

Martini, P., Leroy, A. K., Mangum, J. G., Bolatto, A., Keating, K. M., Sandstrom, K., Walter, F. H I Kinematics along the Minor Axis of M82 ApJ. 2018. 856, 1 61.

Mauersberger, R., Henkel, C., Wielebinski, R., Wiklind, T., Reuter, H. P. Molecular distribution and kinematics in nearby galaxies. I. NGC 253. A&A. 1996. 305 421.

Mazzuca, L. M., Knapen, J. H., Veilleux, S., Regan, M. W. A Connection between Star Formation in Nuclear Rings and Their Host Galaxies ApJS. 2008. 174, 2 337–365.

McKee, C. F. The three phase model of the interstellar medium - Where does it stand now? The Evolution of the Interstellar Medium. 12. 1990. 3–29. (Astronomical Society of the Pacific Conference Series).

McKee, C. F. The Multiphase Interstellar Medium The Physics of the Interstellar Medium and Intergalactic Medium. 80. 1995. 292. (Astronomical Society of the Pacific Conference Series).

McKee, C. F., Ostriker, E. C. Theory of Star Formation ARA&A. 2007. 45, 1 565–687.

McMullin, J. P., Waters, B., Schiebel, D., Young, W., Golap, K. CASA Architecture and Applications Astronomical Data Analysis Software and Systems XVI. 376. 2007. 127. (Astronomical Society of the Pacific Conference Series).

Meier, D. S., Walter, F., Bolatto, A. D., Leroy, A. K., Ott, J., Rosolowsky, E., Veilleux, S., Warren, S. R., Weiß, A., Zwaan, M. A., Zschaechner, L. K. ALMA Multi-line Imaging of the Nearby Starburst NGC 253 ApJ. 2015. 801, 1 63.

Méndez-Abreu, J., Ruiz-Lara, T., Sánchez-Menguiano, L., de Lorenzo-Cáceres, A., Costantin, L., Catalán-Torrecilla, C., Florido, E., Aguerri, J. A. L., Bland-Hawthorn, J., Corsini, E. M., Dettmar, R. J., Galbany, L., García-Benito, R., Marino, R. A., Márquez, I., Ortega-Minakata, R. A., Papaderos, P., Sánchez, S. F., Sánchez-Blazquez, P., Spekkens, K., van de Ven, G., Wild, V., Ziegler, B. Two-dimensional multi-component photometric decomposition of CALIFA galaxies A&A. 2017. 598 A32.

Mestel, L. On the galactic law of rotation MNRAS. 1963. 126 553.

Mezger, P. G., Smith, L. F. Helium in the center of the Galaxy. A&A. 1976. 47, 1 143–151.

Miller, S. T., Veilleux, S. Extraplanar Emission-Line Gas in Edge-On Spiral Galaxies. I. Deep Emission-Line Imaging ApJS. 2003a. 148 383–417.

Miller, S. T., Veilleux, S. Extraplanar Emission-Line Gas in Edge-on Spiral Galaxies. II. Optical Spectroscopy ApJ. 2003b. 592 79–110.

Mills, E. A. C., Gorski, M., Emig, K. L., Bolatto, A. D., Levy, R. C., Leroy, A. K., Ginsburg, A., Henshaw, J. D., Zschaechner, L. K., Veilleux, S., Tanaka, K., Meier, D. S., Walter, F., Krieger, N., Ott, J. Clustered Star Formation in the center of NGC 253 Contributes to Driving the Ionized Nuclear Wind ApJ. 2021. in press.

Miyamoto, M., Nagai, R. Three-dimensional models for the distribution of mass in galaxies PASJ. 1975. 27 533–543.

Mogotsi, K. M., de Blok, W. J. G., Caldú-Primo, A., Walter, F., Ianjamasimanana, R., Leroy, A. K. H I and CO Velocity Dispersions in Nearby Galaxies AJ. 2016. 151 15.

Mok, A., Chandar, R., Fall, S. M. Mass Functions of Giant Molecular Clouds and Young Star Clusters in Six Nearby Galaxies ApJ. 2020. 893, 2 135.

Molinari, S., Bally, J., Noriega-Crespo, A., Compiègne, M., Bernard, J. P., Paradis, D., Martin, P., Testi, L., Barlow, M., Moore, T., Plume, R., Swinyard, B., Zavagno, A., Calzoletti, L., Di Giorgio, A. M., Elia, D., Faustini, F., Natoli, P., Pestalozzi, M., Pezzuto, S., Piacentini, F., Polenta, G., Polychroni, D., Schisano, E., Traficante, A., Veneziani, M., Battersby, C., Burton, M., Carey, S., Fukui, Y., Li, J. Z., Lord, S. D., Morgan, L., Motte, F., Schuller, F., Stringfellow, G. S., Tan, J. C., Thompson, M. A., Ward-Thompson, D., White, G., Umana, G. A 100 pc Elliptical and Twisted Ring of Cold and Dense Molecular Clouds Revealed by Herschel Around the Galactic Center ApJL. 2011. 735, 2 L33.

Moore, B. Evidence against dissipation-less dark matter from observations of galaxy haloes Nature. 1994. 370, 6491 629–631.

Moore, B., Ghigna, S., Governato, F., Lake, G., Quinn, T., Stadel, J., Tozzi, P. Dark Matter Substructure within Galactic Halos ApJL. 1999. 524, 1 L19–L22.

Muñoz-Mateos, J. C., Sheth, K., Gil de Paz, A., Meidt, S., Athanassoula, E., Bosma, A., Comerón, S., Elmegreen, D. M., Elmegreen, B. G., Erroz-Ferrer, S., Gadotti, D. A., Hinz, J. L., Ho, L. C., Holwerda, B., Jarrett, T. H., Kim, T., Knapen, J. H., Laine, J., Laurikainen, E., Madore, B. F., Menendez-Delmestre, K., Mizusawa, T., Regan, M., Salo, H., Schinnerer, E., Seibert, M., Skibba, R., Zaritsky, D. The Impact of Bars on Disk Breaks as Probed by S^4G Imaging ApJ. 2013. 771, 1 59.

Müller-Sánchez, F., González-Martín, O., Fernández-Ontiveros, J. A., Acosta-Pulido, J. A., Prieto, M. A. The Stellar Kinematic Center and the True Galactic Nucleus of NGC 253 ApJ. 2010. 716, 2 1166–1177.

Murphy, E. J., Condon, J. J., Schinnerer, E., Kennicutt, R. C., Calzetti, D., Armus, L., Helou, G., Turner, J. L., Aniano, G., Beirão, P., Bolatto, A. D., Brandl, B. R., Croxall, K. V., Dale, D. A., Donovan Meyer, J. L., Draine, B. T., Engelbracht, C., Hunt, L. K., Hao, C.-N., Koda, J., Roussel, H., Skibba, R., Smith, J.-D. T. Calibrating Extinction-free Star Formation Rate Diagnostics with 33 GHz Free-free Emission in NGC 6946 ApJ. 2011. 737 67.

Murray, N., Quataert, E., Thompson, T. A. The Disruption of Giant Molecular Clouds by Radiation Pressure & the Efficiency of Star Formation in Galaxies ApJ. 2010. 709, 1 191–209.

Navarro, J. F., Eke, V. R., Frenk, C. S. The cores of dwarf galaxy haloes MNRAS. 1996a. 283, 3 L72–L78.

Navarro, J. F., Frenk, C. S., White, S. D. M. The Structure of Cold Dark Matter Halos ApJ. 1996b. 462 563.

Nayak, O., Meixner, M., Sewiło, M., Ochsendorf, B., Bolatto, A., Indebetouw, R., Kawamura, A., Onishi, T., Fukui, Y. ALMA Reveals Kinematics of Super Star Cluster Candidate H72.97-69.39 in LMC-N79 ApJ. 2019. 877, 2 135.

Newman, A. B., Belli, S., Ellis, R. S. Discovery of a Strongly Lensed Massive Quiescent Galaxy at z = 2.636: Spatially Resolved Spectroscopy and Indications of Rotation ApJL. 2015. 813, 1 L7.

Oey, M. S., Herrera, C. N., Silich, S., Reiter, M., James, B. L., Jaskot, A. E., Micheva, G. Dense CO in Mrk 71-A: Superwind Suppressed in a Young Super Star Cluster ApJL. 2017. 849, 1 L1.

Oh, S. H., Kim, W.-T., Lee, H. M., Kim, J. Physical Properties of Tidal Features in Interacting Disk Galaxies ApJ. 2008a. 683, 1 94–113.

Oh, S.-H., Brook, C., Governato, F., Brinks, E., Mayer, L., de Blok, W. J. G., Brooks, A., Walter, F. The Central Slope of Dark Matter Cores in Dwarf Galaxies: Simulations versus THINGS AJ. 2011. 142, 1 24.

Oh, S.-H., Hunter, D. A., Brinks, E., Elmegreen, B. G., Schruba, A., Walter, F., Rupen, M. P., Young, L. M., Simpson, C. E., Johnson, M. C., Herrmann, K. A., Ficut-Vicas, D., Cigan, P., Heesen, V., Ashley, T., Zhang, H.-X. High-resolution Mass Models of Dwarf Galaxies from LITTLE THINGS AJ. 2015. 149, 6 180.

Oh, S.-H., de Blok, W. J. G., Walter, F., Brinks, E., Kennicutt, J. Robert C. High-Resolution Dark Matter Density Profiles of THINGS Dwarf Galaxies: Correcting for Noncircular Motions AJ. 2008b. 136, 6 2761–2781.

Olivier, G. M., Lopez, L. A., Rosen, A. L., Nayak, O., Reiter, M., Krumholz, M. R., Bolatto, A. D. Evolution of Stellar Feedback in H II Regions ApJ. 2021. 908, 1 68.

Oman, K. A., Marasco, A., Navarro, J. F., Frenk, C. S., Schaye, J., Benítez-Llambay, A. Non-circular motions and the diversity of dwarf galaxy rotation curves MNRAS. 2019. 482, 1 821–847.

Oman, K. A., Navarro, J. F., Fattahi, A., Frenk, C. S., Sawala, T., White, S. D. M., Bower, R., Crain, R. A., Furlong, M., Schaller, M., Schaye, J., Theuns, T. The unexpected diversity of dwarf galaxy rotation curves MNRAS. 2015. 452, 4 3650–3665.

Oort, J. H. The formation of galaxies and the origin of the high-velocity hydrogen. A&A. 1970. 7 381–404.

Oosterloo, T. Visualisation of Radio Data PASJ. 1995. 12, 2 215.

Oosterloo, T., Fraternali, F., Sancisi, R. The Cold Gaseous Halo of NGC 891 AJ. 2007. 134 1019.

Orkney, M. D. A., Read, J. I., Rey, M. P., Nasim, I., Pontzen, A., Agertz, O., Kim, S. Y., Delorme, M., Dehnen, W. EDGE: two routes to dark matter core formation in ultra-faint dwarfs MNRAS. 2021. 504, 3 3509–3522.

Ossenkopf, V., Henning, T. Dust opacities for protostellar cores. A&A. 1994. 291 943–959.

Osterbrock, D. E. Astrophysics of gaseous nebulae and active galactic nuclei. 1989.

Otte, B., Reynolds, R. J., Gallagher, I. J. S., Ferguson, A. M. N. Searching for Additional Heating: [O II] Emission in the Diffuse Ionized Gas of NGC 891, NGC 4631, and NGC 3079 ApJ. 2001. 560, 1 207–221.

Pabst, C., Higgins, R., Goicoechea, J. R., Teyssier, D., Berne, O., Chambers, E., Wolfire, M., Suri, S. T., Guesten, R., Stutzki, J., Graf, U. U., Risacher, C., Tielens, A. G. G. M. Disruption of the Orion molecular core 1 by wind from the massive star θ^1 Orionis C Nature. 2019. 565, 7741 618–621.

Paglione, T. A. D., Yam, O., Tosaki, T., Jackson, J. M. The Structure, Kinematics, and Physical Properties of the Molecular Gas in the Starburst Nucleus of NGC 253 ApJ. 2004. 611, 2 835–845.

Palouš, J., Wünsch, R., Tenorio-Tagle, G. On the Onset of Secondary Stellar Generations in Giant Star-forming Regions and Massive Star Clusters ApJ. 2014. 792, 2 105.

Pasetto, S., Grebel, E. K., Zwitter, T., Chiosi, C., Bertelli, G., Bienayme, O., Seabroke, G., Bland-Hawthorn, J., Boeche, C., Gibson, B. K., Gilmore, G., Munari, U., Navarro, J. F., Parker, Q., Reid, W., Silviero, A., Steinmetz, M. Thick disk kinematics from RAVE and the solar motion A&A. 2012. 547 A70.

Peek, J. E. G., Heiles, C., Douglas, K. A., Lee, M.-Y., Grcevich, J., Stanimirović, S., Putman, M. E., Korpela, E. J., Gibson, S. J., Begum, A., Saul, D., Robishaw, T., Krčo, M. The GALFA-HI Survey: Data Release 1 ApJS. 2011. 194, 2 20.

Pence, W. D. A photometric and kinematic study of the barred spiral galaxy NGC 253. I - Detailed surface photometry. ApJ. 1980. 239 54–64.

Pérez-Ramírez, D., Knapen, J. H., Peletier, R. F., Laine, S., Doyon, R., Nadeau, D. Circumnuclear regions in barred spiral galaxies - I. Near-infrared imaging MNRAS. 2000. 317, 2 234–248.

Péroux, C., Zwaan, M. A., Klitsch, A., Augustin, R., Hamanowicz, A., Rahmani, H., Pettini, M., Kulkarni, V., Straka, L. A., Biggs, A. D., York, D. G., Milliard, B. Multiphase circumgalactic medium probed with MUSE and ALMA MNRAS. 2019. 485, 2 1595–1613.

Persic, M., Salucci, P. The universal galaxy rotation curve ApJ. 1991. 368 60–65.

Persic, M., Salucci, P., Stel, F. The universal rotation curve of spiral galaxies - I. The dark matter connection MNRAS. 1996. 281 27–47.

Peter, A. H. G., Rocha, M., Bullock, J. S., Kaplinghat, M. Cosmological simulations with self-interacting dark matter - II. Halo shapes versus observations MNRAS. 2013. 430, 1 105–120.

Pineda, J. L., Langer, W. D., Velusamy, T., Goldsmith, P. F. A Herschel [C ii] Galactic plane survey. I. The global distribution of ISM gas components A&A. 2013. 554 A103.

Plummer, H. C. On the problem of distribution in globular star clusters MNRAS. 1911. 71 460–470.

Plunkett, A. L., Arce, H. G., Mardones, D., van Dokkum, P., Dunham, M. M., Fernández-López, M., Gallardo, J., Corder, S. A. Episodic molecular outflow in the very young protostellar cluster Serpens South Nature. 2015. 527, 7576 70–73.

Poetrodjojo, H., D'Agostino, J. J., Groves, B., Kewley, L., Ho, I., Rich, J., Madore, B. F., Seibert, M. The Effects of Diffuse Ionized Gas and Spatial Resolution on Metallicity Gradients: TYPHOON Two-Dimensional Spectrophotometry of M83 arXiv e-prints. 2019.

Pontzen, A., Governato, F. Cold dark matter heats up Nature. 2014. 506, 7487 171–178.

Portegies Zwart, S. F., McMillan, S. L. W., Gieles, M. Young Massive Star Clusters ARA&A. 2010. 48 431–493.

Pozzetti, L., Bolzonella, M., Zucca, E., Zamorani, G., Lilly, S., Renzini, A., Moresco, M., Mignoli, M., Cassata, P., Tasca, L., Lamareille, F., Maier, C., Meneux, B., Halliday, C., Oesch, P., Vergani, D., Caputi, K., Kovač, K., Cimatti, A., Cucciati, O., Iovino, A., Peng, Y., Carollo, M., Contini, T., Kneib, J. P., Le Févre, O., Mainieri, V., Scodeggio, M., Bardelli, S., Bongiorno, A., Coppa, G., de la Torre, S., de Ravel, L., Franzetti, P., Garilli, B., Kampczyk, P., Knobel, C., Le Borgne, J. F., Le Brun, V., Pellò, R., Perez Montero, E., Ricciardelli, E., Silverman, J. D., Tanaka, M., Tresse, L., Abbas, U., Bottini, D., Cappi, A., Guzzo, L., Koekemoer, A. M., Leauthaud, A., Maccagni, D., Marinoni, C., McCracken, H. J., Memeo, P., Porciani, C., Scaramella, R., Scarlata, C., Scoville, N. zCOSMOS - 10k-bright spectroscopic sample. The bimodality in the galaxy stellar mass function: exploring its evolution with redshift A&A. 2010. 523 A13.

Querejeta, M., Meidt, S. E., Schinnerer, E., Cisternas, M., Muñoz-Mateos, J. C., Sheth, K., Knapen, J., van de Ven, G., Norris, M. A., Peletier, R., Laurikainen, E., Salo, H., Holwerda, B. W., Athanassoula, E., Bosma, A., Groves, B., Ho, L. C., Gadotti, D. A., Zaritsky, D., Regan, M., Hinz, J., Gil de Paz, A., Menendez-Delmestre, K., Seibert, M., Mizusawa, T., Kim, T., Erroz-Ferrer, S., Laine, J., Comerón, S. The Spitzer Survey of Stellar Structure in Galaxies (S^4G): Precise Stellar Mass Distributions from Automated Dust Correction at 3.6 μm ApJS. 2015. 219, 1 5.

Rahner, D., Pellegrini, E. W., Glover, S. C. O., Klessen, R. S. Winds and radiation in unison: a new semi-analytic feedback model for cloud dissolution MNRAS. 2017. 470, 4 4453–4472.

Rahner, D., Pellegrini, E. W., Glover, S. C. O., Klessen, R. S. WARPFIELD 2.0: feedback-regulated minimum star formation efficiencies of giant molecular clouds MNRAS. 2019. 483, 2 2547–2560.

Rand, R. J. Diffuse Ionized Gas in Nine Edge-on Galaxies ApJ. 1996. 462 712.

Rand, R. J. A Very Deep Spectrum of the Diffuse Ionized Gas in NGC 891 ApJ. 1997. 474 129–139.

Rand, R. J. Diffuse ionized gas in edge-on galaxies PASJ. 1998. 15 106–10.

Rand, R. J. Ionization, Kinematics, and Extent of the Diffuse Ionized Gas Halo of NGC 5775 ApJL. 2000. 537 L13–L16.

Rand, R. J., Kulkarni, S. R., Hester, J. J. The distribution of warm ionized gas in NGC 891 ApJL. 1990. 352 L1–L4.

Raskutti, S., Ostriker, E. C., Skinner, M. A. Numerical Simulations of Turbulent Molecular Clouds Regulated by Radiation Feedback Forces. II. Radiation-Gas Interactions and Outflows ApJ. 2017. 850, 2 112.

Reach, W. T., Megeath, S. T., Cohen, M., Hora, J., Carey, S., Surace, J., Willner, S. P., Barmby, P., Wilson, G., Glaccum, W., Lowrance, P., Marengo, M., Fazio, G. G. Absolute Calibration of the Infrared Array Camera on the Spitzer Space Telescope PASP. 2005. 117, 835 978–990.

Read, J. I., Iorio, G., Agertz, O., Fraternali, F. Understanding the shape and diversity of dwarf galaxy rotation curves in ΛCDM MNRAS. 2016. 462, 4 3628–3645.

Reback, J., McKinney, W., jbrockmendel, , Bossche, J. V. den, Augspurger, T., Cloud, P., gfyoung, , Sinhrks, , Hawkins, S., Klein, A., Roeschke, M., Tratner, J., Petersen, T., She, C., Ayd, W., MomIsBestFriend, , Garcia, M., Schendel, J., Hayden, A., Saxton, D., Jancauskas, V., McMaster, A., Battiston, P., Seabold, S., b1, chris, vetinari, h, Dong, K., Hoyer, S., Overmeire, W., Winkel, M. pandas-dev/pandas: Pandas 1.1.3. 2020.

Regan, M. W., Teuben, P. The Formation of Nuclear Rings in Barred Spiral Galaxies ApJ. 2003. 582, 2 723–742.

Rekola, R., Richer, M. G., McCall, M. L., Valtonen, M. J., Kotilainen, J. K., Flynn, C. Distance to NGC 253 based on the planetary nebula luminosity function MNRAS. 2005. 361 330–336.

Relatores, N. C., Newman, A. B., Simon, J. D., Ellis, R., Truong, P., Blitz, L., Bolatto, A., Martin, C., Morrissey, P. The Dark Matter Distributions in Low-mass Disk Galaxies. I. Hα Observations Using the Palomar Cosmic Web Imager ApJ. 2019a. 873, 1 5.

Relatores, N. C., Newman, A. B., Simon, J. D., Ellis, R. S., Truong, P., Blitz, L., Bolatto, A., Martin, C., Matuszewski, M., Morrissey, P., Neill, J. D. The Dark Matter Distributions in Low-mass Disk Galaxies. II. The Inner Density Profiles ApJ. 2019b. 887, 1 94.

Renzini, A., Peng, Y.-j. An Objective Definition for the Main Sequence of Star-forming Galaxies ApJL. 2015. 801, 2 L29.

Reynolds, R. J. An Investigation Into the Optical Fluorescence of Interstellar Hydrogen-I. 1971.

Reynolds, R. J. The Radiative Ionization or the Interstellar Medium–The Warm Ionized Gas Massive Stars: Their Lives in the Interstellar Medium. 35. 1993. 338. (Astronomical Society of the Pacific Conference Series).

Reynolds, R. J., Haffner, L. M., Tufte, S. L. Evidence for an Additional Heat Source in the Warm Ionized Medium of Galaxies ApJL. 1999. 525 L21–L24.

Reynolds, R. J., Scherb, F., Roesler, F. L. Observations of Diffuse Galactic HA and [n II] Emission ApJ. 1973. 185 869–876.

Reynolds, R. J., Sterling, N. C., Haffner, L. M. Detection of a Large Arc of Ionized Hydrogen Far above the Cassiopeia OB6 Association: A Superbubble Blowout into the Galactic Halo? ApJL. 2001. 558 L101–L104.

Rich, J. W., de Blok, W. J. G., Cornwell, T. J., Brinks, E., Walter, F., Bagetakos, I., Kennicutt, J. R. C. Multi-Scale CLEAN: A Comparison of its Performance Against Classical CLEAN on Galaxies Using THINGS AJ. 2008. 136, 6 2897–2920.

Rico-Villas, F., Martín-Pintado, J., González-Alfonso, E., Martín, S., Rivilla, V. M. Super Hot Cores in NGC 253: witnessing the formation and early evolution of super star clusters MNRAS. 2020. 491, 3 4573–4589.

Ridley, M. G. L., Sormani, M. C., Treß, R. G., Magorrian, J., Klessen, R. S. Nuclear spirals in the inner Milky Way MNRAS. 2017. 469, 2 2251–2262.

Riess, A. G., Casertano, S., Yuan, W., Bowers, J. B., Macri, L., Zinn, J. C., Scolnic, D. Cosmic Distances Calibrated to 1% Precision with Gaia EDR3 Parallaxes and Hubble Space Telescope Photometry of 75 Milky Way Cepheids Confirm Tension with ΛCDM ApJL. 2021. 908, 1 L6.

Robitaille, T., Bressert, E. APLpy: Astronomical Plotting Library in Python. 2012.

Roelfsema, P. R., Goss, W. M. High resolution radio recombination line observations A&ARv. 1992. 4, 2 161–214.

Rogstad, D. H., Lockhart, I. A., Wright, M. C. H. Aperture-synthesis observations of H I in the galaxy M83. ApJ. 1974. 193 309–319.

Rosado, M., Gabbasov, R. F., Repetto, P., Fuentes-Carrera, I., Amram, P., Martos, M., Hernandez, O. Two-dimensional Kinematics of the Edge-on Spiral Galaxy ESO 379-006 AJ. 2013. 145 135.

Rossa, J., Dettmar, R.-J. An Hα survey aiming at the detection of extraplanar diffuse ionized gas in halos of edge-on spiral galaxies. I. How common are gaseous halos among non-starburst galaxies? A&A. 2003a. 406 493–503.

Rossa, J., Dettmar, R.-J. An Hα survey aiming at the detection of extraplanar diffuse ionized gas in halos of edge-on spiral galaxies. II. The Hα survey atlas and catalog A&A. 2003b. 406 505–525.

Saintonge, A., Catinella, B., Tacconi, L. J., Kauffmann, G., Genzel, R., Cortese, L., Davé, R., Fletcher, T. J., Graciá-Carpio, J., Kramer, C., Heckman, T. M., Janowiecki, S., Lutz, K., Rosario, D., Schiminovich, D., Schuster, K., Wang, J., Wuyts, S., Borthakur, S., Lamperti, I., Roberts-Borsani, G. W. xCOLD GASS: The Complete IRAM 30 m Legacy Survey of Molecular Gas for Galaxy Evolution Studies ApJS. 2017. 233, 2 22.

Sakamoto, K., Ho, P. T. P., Iono, D., Keto, E. R., Mao, R.-Q., Matsushita, S., Peck, A. B., Wiedner, M. C., Wilner, D. J., Zhao, J.-H. Molecular Superbubbles in the Starburst Galaxy NGC 253 ApJ. 2006. 636, 2 685–697.

Sakamoto, K., Mao, R.-Q., Matsushita, S., Peck, A. B., Sawada, T., Wiedner, M. C. Star-forming Cloud Complexes in the Central Molecular Zone of NGC 253 ApJ. 2011. 735, 1 19.

Salim, S., Rich, R. M., Charlot, S., Brinchmann, J., Johnson, B. D., Schiminovich, D., Seibert, M., Mallery, R., Heckman, T. M., Forster, K., Friedman, P. G., Martin, D. C., Morrissey, P., Neff, S. G., Small, T., Wyder, T. K., Bianchi, L., Donas, J., Lee, Y.-W., Madore, B. F., Milliard, B., Szalay, A. S., Welsh, B. Y., Yi, S. K. UV Star Formation Rates in the Local Universe ApJS. 2007. 173, 2 267–292.

Salpeter, E. E. The Luminosity Function and Stellar Evolution. ApJ. 1955. 121 161.

Sánchez, S. F., García-Benito, R., Zibetti, S., Walcher, C. J., Husemann, B., Mendoza, M. A., Galbany, L., Falcón-Barroso, J., Mast, D., Aceituno, J., Aguerri, J. A. L., Alves, J., Amorim, A. L., Ascasibar, Y., Barrado-Navascues, D., Barrera-Ballesteros, J., Bekeraitè, S., Bland-Hawthorn, J., Cano Díaz, M., Cid Fernandes, R., Cavichia, O., Cortijo, C., Dannerbauer, H., Demleitner, M., Díaz, A., Dettmar, R. J., de Lorenzo-Cáceres, A., del Olmo, A., Galazzi, A., García-Lorenzo, B., Gil de Paz, A., González Delgado, R., Holmes, L., Iglésias-Páramo, J., Kehrig, C., Kelz, A., Kennicutt, R. C., Kleemann, B., Lacerda, E. A. D., López Fernández, R., López Sánchez, A. R., Lyubenova, M., Marino, R., Márquez, I., Mendez-Abreu, J., Mollá, M., Monreal-Ibero, A., Ortega Minakata, R., Torres-Papaqui, J. P., Pérez, E., Rosales-Ortega, F. F., Roth, M. M., Sánchez-Blázquez, P., Schilling, U., Spekkens, K., Vale Asari, N., van den Bosch, R. C. E., van de Ven, G., Vilchez, J. M., Wild, V., Wisotzki, L., Yıldırım, A., Ziegler, B. CALIFA, the Calar Alto Legacy Integral Field Area survey. IV. Third public data release A&A. 2016a. 594 A36.

Sánchez, S. F., Kennicutt, R. C., Gil de Paz, A., van de Ven, G., Vílchez, J. M., Wisotzki, L., Walcher, C. J., Mast, D., Aguerri, J. A. L., Albiol-Pérez, S., Alonso-Herrero, A., Alves, J., Bakos, J., Bartáková, T., Bland-Hawthorn, J., Boselli, A., Bomans, D. J., Castillo-Morales, A., Cortijo-Ferrero, C., de Lorenzo-Cáceres, A., Del Olmo, A., Dettmar, R.-J., Díaz, A., Ellis, S., Falcón-Barroso, J., Flores, H., Gallazzi, A., García-Lorenzo, B., González Delgado, R., Gruel, N., Haines, T., Hao, C., Husemann, B., Iglésias-Páramo, J., Jahnke, K., Johnson, B., Jungwiert, B., Kalinova, V., Kehrig, C., Kupko, D., López-Sánchez, Á. R., Lyubenova, M., Marino, R. A., Mármol-Queraltó, E., Márquez, I., Masegosa, J., Meidt, S., Mendez-Abreu, J., Monreal-Ibero, A., Montijo, C., Mourão, A. M., Palacios-Navarro, G., Papaderos, P., Pasquali, A., Peletier, R., Pérez, E., Pérez, I., Quirrenbach, A., Relaño, M., Rosales-Ortega, F. F., Roth, M. M., Ruiz-Lara,

T., Sánchez-Blázquez, P., Sengupta, C., Singh, R., Stanishev, V., Trager, S. C., Vazdekis, A., Viironen, K., Wild, V., Zibetti, S., Ziegler, B. CALIFA, the Calar Alto Legacy Integral Field Area survey. I. Survey presentation A&A. 2012. 538 A8.

Sánchez, S. F., Pérez, E., Sánchez-Blázquez, P., García-Benito, R., Ibarra-Mede, H. J., González, J. J., Rosales-Ortega, F. F., Sánchez-Menguiano, L., Ascasibar, Y., Bitsakis, T., Law, D., Cano-Díaz, M., López-Cobá, C., Marino, R. A., Gil de Paz, A., López-Sánchez, A. R., Barrera-Ballesteros, J., Galbany, L., Mast, D., Abril-Melgarejo, V., Roman-Lopes, A. Pipe3D, a pipeline to analyze Integral Field Spectroscopy Data: II. Analysis sequence and CALIFA dataproducts RMxAA. 2016b. 52 171–220.

Sánchez, S. F., Pérez, E., Sánchez-Blázquez, P., González, J. J., Rosález-Ortega, F. F., Cano-Dí az, M., López-Cobá, C., Marino, R. A., Gil de Paz, A., Mollá, M., López-Sánchez, A. R., Ascasibar, Y., Barrera-Ballesteros, J. Pipe3D, a pipeline to analyze Integral Field Spectroscopy Data: I. New fitting philosophy of FIT3D RMxAA. 2016c. 52 21–53.

Sánchez, S. F., Rosales-Ortega, F. F., Iglesias-Páramo, J., Mollá, M., Barrera-Ballesteros, J., Marino, R. A., Pérez, E., Sánchez-Blazquez, P., González Delgado, R., Cid Fernandes, R., de Lorenzo-Cáceres, A., Mendez-Abreu, J., Galbany, L., Falcon-Barroso, J., Miralles-Caballero, D., Husemann, B., García-Benito, R., Mast, D., Walcher, C. J., Gil de Paz, A., García-Lorenzo, B., Jungwiert, B., Vílchez, J. M., Jílková, L., Lyubenova, M., Cortijo-Ferrero, C., Díaz, A. I., Wisotzki, L., Márquez, I., Bland-Hawthorn, J., Ellis, S., van de Ven, G., Jahnke, K., Papaderos, P., Gomes, J. M., Mendoza, M. A., López-Sánchez, Á. R. A characteristic oxygen abundance gradient in galaxy disks unveiled with CALIFA A&A. 2014. 563 A49.

Sánchez, S. F. Spatially Resolved Spectroscopic Properties of Low-Redshift Star-Forming Galaxies ARA&A. 2020. 58 99–155.

Sanders, D. B., Mirabel, I. F. Luminous Infrared Galaxies ARA&A. 1996. 34 749.

Santos-Santos, I. M., Di Cintio, A., Brook, C. B., Macciò, A., Dutton, A., Domínguez-Tenreiro, R. NIHAO - XIV. Reproducing the observed diversity of dwarf galaxy rotation curve shapes in ΛCDM MNRAS. 2018. 473, 4 4392–4403.

Santos-Santos, I. M. E., Navarro, J. F., Robertson, A., Benítez-Llambay, A., Oman, K. A., Lovell, M. R., Frenk, C. S., Ludlow, A. D., Fattahi, A., Ritz, A. Baryonic clues to the puzzling diversity of dwarf galaxy rotation curves MNRAS. 2020. 495, 1 58–77.

Sarzi, M., Shields, J. C., Schawinski, K., Jeong, H., Shapiro, K., Bacon, R., Bureau, M., Cappellari, M., Davies, R. L., de Zeeuw, P. T., Emsellem, E., Falcón-Barroso, J., Krajnović, D., Kuntschner, H., McDermid, R. M., Peletier, R. F.,

van den Bosch, R. C. E., van de Ven, G., Yi, S. K. The SAURON project - XVI. On the sources of ionization for the gas in elliptical and lenticular galaxies MNRAS. 2010. 402 2187–2210.

Sault, R. J., Teuben, P. J., Wright, M. C. H. A Retrospective View of MIRIAD Astronomical Data Analysis Software and Systems IV. 77. 1995. 433. (Astronomical Society of the Pacific Conference Series).

Sawada, T., Hasegawa, T., Handa, T., Cohen, R. J. A molecular face-on view of the Galactic Centre region MNRAS. 2004. 349, 4 1167–1178.

Schaap, W. E., Sancisi, R., Swaters, R. A. The vertical extent and kinematics of the HI in NGC 2403 A&A. 2000. 356 L49–L52.

Schneider, F. R. N., Sana, H., Evans, C. J., Bestenlehner, J. M., Castro, N., Fossati, L., Gräfener, G., Langer, N., Ramírez-Agudelo, O. H., Sabín-Sanjulián, C., Simón-Díaz, S., Tramper, F., Crowther, P. A., de Koter, A., de Mink, S. E., Dufton, P. L., Garcia, M., Gieles, M., Hénault-Brunet, V., Herrero, A., Izzard, R. G., Kalari, V., Lennon, D. J., Maíz Apellániz, J., Markova, N., Najarro, F., Podsiadlowski, P., Puls, J., Taylor, W. D., van Loon, J. T., Vink, J. S., Norman, C. An excess of massive stars in the local 30 Doradus starburst Science. 2018. 359, 6371 69–71.

Schoenmakers, R. H. M. Asymmetries in spiral galaxies. 1999.

Schöier, F. L., van der Tak, F. F. S., van Dishoeck, E. F., Black, J. H. An atomic and molecular database for analysis of submillimetre line observations A&A. 2005. 432, 1 369–379.

Scoville, N. Z., Soifer, B. T., Neugebauer, G., Young, J. S., Matthews, K., Yerka, J. The inner disk of NGC 253. ApJ. 1985. 289 129–140.

Semenov, D., Henning, T., Helling, C., Ilgner, M., Sedlmayr, E. Rosseland and Planck mean opacities for protoplanetary discs A&A. 2003. 410 611–621.

Shapiro, P. R., Field, G. B. Consequences of a New Hot Component of the Interstellar Medium ApJ. 1976. 205 762–765.

Sheth, K., Regan, M., Hinz, J. L., Gil de Paz, A., Menéndez-Delmestre, K., Muñoz-Mateos, J.-C., Seibert, M., Kim, T., Laurikainen, E., Salo, H., Gadotti, D. A., Laine, J., Mizusawa, T., Armus, L., Athanassoula, E., Bosma, A., Buta, R. J., Capak, P., Jarrett, T. H., Elmegreen, D. M., Elmegreen, B. G., Knapen, J. H., Koda, J., Helou, G., Ho, L. C., Madore, B. F., Masters, K. L., Mobasher, B., Ogle, P., Peng, C. Y., Schinnerer, E., Surace, J. A., Zaritsky, D., Comerón, S., de Swardt, B., Meidt, S. E., Kasliwal, M., Aravena, M. The Spitzer Survey of Stellar Structure in Galaxies (S4G) PASP. 2010. 122, 898 1397.

Shin, J., Kim, S. S., Baba, J., Saitoh, T. R., Hwang, J.-S., Chun, K., Hozumi, S. Hydrodynamic Simulations of the Central Molecular Zone with a Realistic Galactic Potential ApJ. 2017. 841, 2 74.

Shirley, Y. L. The Critical Density and the Effective Excitation Density of Commonly Observed Molecular Dense Gas Tracers PASP. 2015. 127 299.

Shlosman, I., Begelman, M. C., Frank, J. The fuelling of active galactic nuclei Nature. 1990. 345, 6277 679–686.

Shlosman, I., Frank, J., Begelman, M. C. Bars within bars: a mechanism for fuelling active galactic nuclei Nature. 1989. 338, 6210 45–47.

Silich, S., Tenorio-Tagle, G., Rodríguez-González, A. Winds Driven by Super Star Clusters: The Self-Consistent Radiative Solution ApJ. 2004. 610, 1 226–232.

Simon, J. D., Bolatto, A. D., Leroy, A., Blitz, L., Gates, E. L. High-Resolution Measurements of the Halos of Four Dark Matter-Dominated Galaxies: Deviations from a Universal Density Profile ApJ. 2005. 621 757–776.

Simon, J. D., Bolatto, A. D., Leroy, A., Blitz, L. High-Resolution Measurements of the Dark Matter Halo of NGC 2976: Evidence for a Shallow Density Profile ApJ. 2003. 596, 2 957–981.

Skinner, M. A., Ostriker, E. C. Numerical Simulations of Turbulent Molecular Clouds Regulated by Reprocessed Radiation Feedback from Nascent Super Star Clusters ApJ. 2015. 809, 2 187.

Sofue, Y. Galactic-Center Molecular Arms, Ring, and Expanding Shell. I. Kinematical Structures in Longitude–Velocity Diagrams PASJ. 1995. 47 527–549.

Sokal, K. R., Johnson, K. E., Indebetouw, R., Massey, P. The Prevalence and Impact of Wolf-Rayet Stars in Emerging Massive Star Clusters ApJ. 2016. 826, 2 194.

Sokolowski, J., Bland-Hawthorn, J. Photoionization of high-latitude gas in NGC 891 PASP. 1991. 103 911–915.

Sorai, K., Nakai, N., Kuno, N., Nishiyama, K., Hasegawa, T. Distribution and Kinematics of Molecular Gas in Barred Spiral Galaxies. II. NGC 253 PASJ. 2000. 52 785–802.

Sormani, M. C., Barnes, A. T. Mass inflow rate into the Central Molecular Zone: observational determination and evidence of episodic accretion MNRAS. 2019. 484, 1 1213–1219.

Sormani, M. C., Treß, R. G., Glover, S. C. O., Klessen, R. S., Barnes, A. T., Battersby, C. D., Clark, P. C., Hatchfield, H. P., Smith, R. J. The geometry of the gas surrounding the Central Molecular Zone: on the origin of localized

molecular clouds with extreme velocity dispersions MNRAS. 2019. 488, 4 4663–4673.

Spagna, A., Lattanzi, M. G., Re Fiorentin, P., Smart, R. L. Evidence of a thick disk rotation-metallicity correlation A&A. 2010. 510 L4.

Spergel, D. N., Steinhardt, P. J. Observational Evidence for Self-Interacting Cold Dark Matter Phys. Rev. Lett.. 2000. 84, 17 3760–3763.

Spitzer, L. Jr. The Dynamics of the Interstellar Medium. III. Galactic Distribution. ApJ. 1942. 95 329.

Springob, C. M., Haynes, M. P., Giovanelli, R., Kent, B. R. A Digital Archive of H I 21 Centimeter Line Spectra of Optically Targeted Galaxies ApJS. 2005. 160 149–162.

Stanimirovic, S. Short-Spacings Correction from the Single-Dish Perspective Single-Dish Radio Astronomy: Techniques and Applications. 278. 2002. 375–396. (Astronomical Society of the Pacific Conference Series).

Stasińska, G., Vale Asari, N., Cid Fernandes, R., Gomes, J. M., Schlickmann, M., Mateus, A., Schoenell, W., Sodré, J. L., Seagal Collaboration, . Can retired galaxies mimic active galaxies? Clues from the Sloan Digital Sky Survey MNRAS. 2008. 391, 1 L29–L33.

Swaters, R. A. Dark Matter in Late-type Dwarf Galaxies. 1999.

Swaters, R. A., Sancisi, R., van der Hulst, J. M. The H I Halo of NGC 891 ApJ. 1997. 491 140–145.

Tacconi, L. J., Genzel, R., Sternberg, A. The Evolution of the Star-Forming Interstellar Medium Across Cosmic Time ARA&A. 2020. 58 157–203.

Tang, X. D., Henkel, C., Menten, K. M., Gong, Y., Martín, S., Mühle, S., Aalto, S., Muller, S., García-Burillo, S., Levshakov, S., Aladro, R., Spaans, M., Viti, S., Asiri, H. M., Ao, Y. P., Zhang, J. S., Zheng, X. W., Esimbek, J., Zhou, J. J. ALMA view of the $^{12}C/^{13}C$ isotopic ratio in starburst galaxies A&A. 2019. 629 A6.

Teuben, P. The Stellar Dynamics Toolbox NEMO Astronomical Data Analysis Software and Systems IV. 77. 1995. 398. (Astronomical Society of the Pacific Conference Series).

Teuben, P. J. Velocity Fields of Disk Galaxies Disks of Galaxies: Kinematics, Dynamics and Peturbations. 275. 2002. 217–228. (Astronomical Society of the Pacific Conference Series).

Thompson, A. R., Moran, J. M., Swenson, J. George W. Interferometry and Synthesis in Radio Astronomy, 3rd Edition. 2017.

Thompson, T. A., Krumholz, M. R. Sub-Eddington star-forming regions are super-Eddington: momentum-driven outflows from supersonic turbulence MNRAS. 2016. 455, 1 334–342.

Tielens, A. G. G. M. The Physics and Chemistry of the Interstellar Medium. 2005.

Tollet, E., Macciò, A. V., Dutton, A. A., Stinson, G. S., Wang, L., Penzo, C., Gutcke, T. A., Buck, T., Kang, X., Brook, C., Di Cintio, A., Keller, B. W., Wadsley, J. NIHAO - IV: core creation and destruction in dark matter density profiles across cosmic time MNRAS. 2016. 456, 4 3542–3552.

Tonry, J. L., Stubbs, C. W., Lykke, K. R., Doherty, P., Shivvers, I. S., Burgett, W. S., Chambers, K. C., Hodapp, K. W., Kaiser, N., Kudritzki, R. P., Magnier, E. A., Morgan, J. S., Price, P. A., Wainscoat, R. J. The Pan-STARRS1 Photometric System ApJ. 2012. 750, 2 99.

Tress, R. G., Sormani, M. C., Glover, S. C. O., Klessen, R. S., Battersby, C. D., Clark, P. C., Hatchfield, H. P., Smith, R. J. Simulations of the Milky Way's central molecular zone - I. Gas dynamics MNRAS. 2020. 499, 3 4455–4478.

Truong, P. N., Newman, A. B., Simon, J. D., Blitz, L., Ellis, R., Bolatto, A. High-resolution Velocity Fields of Low-mass Disk Galaxies. I. CO Observations ApJ. 2017. 843, 1 37.

Tully, R. B., Courtois, H. M., Dolphin, A. E., Fisher, J. R., Héraudeau, P., Jacobs, B. A., Karachentsev, I. D., Makarov, D., Makarova, L., Mitronova, S., Rizzi, L., Shaya, E. J., Sorce, J. G., Wu, P.-F. Cosmicflows-2: The Data AJ. 2013. 146, 4 86.

Turner, J. L., Beck, S. C., Benford, D. J., Consiglio, S. M., Ho, P. T. P., Kovács, A., Meier, D. S., Zhao, J. H. Highly efficient star formation in NGC 5253 possibly from stream-fed accretion Nature. 2015. 519, 7543 331–333.

Turner, J. L., Ho, P. T. P. The 1 parsec radio core and possible nuclear ejection in NGC 253. ApJL. 1985. 299 L77–L81.

Turner, J. L., Consiglio, S. M., Beck, S. C., Goss, W. M., Ho, P. T. P., Meier, D. S., Silich, S., Zhao, J.-H. ALMA Detects CO(3-2) within a Super Star Cluster in NGC 5253 ApJ. 2017. 846, 1 73.

Ulvestad, J. S., Antonucci, R. R. J. VLA Observations of NGC 253: Supernova Remnants and H II Regions at 1 Parsec Resolution ApJ. 1997. 488, 2 621–641.

Utomo, D., Bolatto, A. D., Wong, T., Ostriker, E. C., Blitz, L., Sanchez, S. F., Colombo, D., Leroy, A. K., Cao, Y., Dannerbauer, H., Garcia-Benito, R., Husemann, B., Kalinova, V., Levy, R. C., Mast, D., Rosolowsky, E., Vogel, S. N. The EDGE-CALIFA Survey: Variations in the Molecular Gas Depletion Time in Local Galaxies ApJ. 2017. 849 26.

Vargas, C. J., Heald, G., Walterbos, R. A. M., Fraternali, F., Patterson, M. T., Rand, R. J., Józsa, G. I. G., Gentile, G., Serra, P. HALOGAS Observations of NGC 4559: Anomalous and Extraplanar H i and its Relation to Star Formation ApJ. 2017. 839 118.

Vázquez-Semadeni, E., Ryu, D., Passot, T., González, R. F., Gazol, A. Molecular Cloud Evolution. I. Molecular Cloud and Thin Cold Neutral Medium Sheet Formation ApJ. 2006. 643, 1 245–259.

Veilleux, S., Cecil, G., Bland-Hawthorn, J. The interstellar disk-halo connection in the spiral galaxy NGC 3079 ApJ. 1995. 445 152–160.

Veilleux, S., Cecil, G., Bland-Hawthorn, J. Galactic Winds ARA&A. 2005. 43, 1 769–826.

Veilleux, S., Maiolino, R., Bolatto, A. D., Aalto, S. Cool outflows in galaxies and their implications A&ARv. 2020. 28, 1 2.

Vink, J. S., de Koter, A. On the metallicity dependence of Wolf-Rayet winds A&A. 2005. 442, 2 587–596.

Virtanen, P., Gommers, R., Oliphant, T. E., Haberland, M., Reddy, T., Cournapeau, D., Burovski, E., Peterson, P., Weckesser, W., Bright, J., van der Walt, S. J., Brett, M., Wilson, J., Millman, K. J., Mayorov, N., Nelson, A. R. J., Jones, E., Kern, R., Larson, E., Carey, C. J., Polat, İ., Feng, Y., Moore, E. W., VanderPlas, J., Laxalde, D., Perktold, J., Cimrman, R., Henriksen, I., Quintero, E. A., Harris, C. R., Archibald, A. M., Ribeiro, A. H., Pedregosa, F., van Mulbregt, P., SciPy 1.0 Contributors, . SciPy 1.0: Fundamental Algorithms for Scientific Computing in Python Nature Methods. 2020. 17 261–272.

Vogelsberger, M., Zavala, J., Cyr-Racine, F.-Y., Pfrommer, C., Bringmann, T., Sigurdson, K. ETHOS - an effective theory of structure formation: dark matter physics as a possible explanation of the small-scale CDM problems MNRAS. 2016. 460, 2 1399–1416.

Vogelsberger, M., Zavala, J., Loeb, A. Subhaloes in self-interacting galactic dark matter haloes MNRAS. 2012. 423, 4 3740–3752.

Vorontsov-Vel'Yaminov, B. A., Arkhipova, V. P. Morphological catalogue of galaxies. Part 1. Morphological catalogue of galaxies., 1 (1962). 1962.

Walcher, C. J., Wisotzki, L., Bekeraité, S., Husemann, B., Iglesias-Páramo, J., Backsmann, N., Barrera Ballesteros, J., Catalán-Torrecilla, C., Cortijo, C., del Olmo, A., Garcia Lorenzo, B., Falcón-Barroso, J., Jilkova, L., Kalinova, V., Mast, D., Marino, R. A., Méndez-Abreu, J., Pasquali, A., Sánchez, S. F., Trager, S., Zibetti, S., Aguerri, J. A. L., Alves, J., Bland-Hawthorn, J., Boselli, A., Castillo Morales, A., Cid Fernandes, R., Flores, H., Galbany, L., Gallazzi, A.,

García-Benito, R., Gil de Paz, A., González-Delgado, R. M., Jahnke, K., Jungwiert, B., Kehrig, C., Lyubenova, M., Márquez Perez, I., Masegosa, J., Monreal Ibero, A., Pérez, E., Quirrenbach, A., Rosales-Ortega, F. F., Roth, M. M., Sanchez-Blazquez, P., Spekkens, K., Tundo, E., van de Ven, G., Verheijen, M. A. W., Vilchez, J. V., Ziegler, B. CALIFA: a diameter-selected sample for an integral field spectroscopy galaxy survey A&A. 2014. 569 A1.

Walter, F., Bolatto, A. D., Leroy, A. K., Veilleux, S., Warren, S. R., Hodge, J., Levy, R. C., Meier, D. S., Ostriker, E. C., Ott, J. Dense Molecular Gas Tracers in the Outflow of the Starburst Galaxy NGC 253 ApJ. 2017. 835, 2 265.

Walter, F., Brinks, E., de Blok, W. J. G., Bigiel, F., Kennicutt, J. Robert C., Thornley, M. D., Leroy, A. THINGS: The H I Nearby Galaxy Survey AJ. 2008. 136, 6 2563–2647.

Walter, F., Dahlem, M., Lisenfeld, U. The Superwind Galaxy NGC 4666: Gravitational Interactions and the Influence of the Resulting Starburst on the Interstellar Medium ApJ. 2004. 606, 1 258–270.

Wang, J., Heckman, T. M., Lehnert, M. D. On the Dynamical and Physical State of the "Diffuse Ionized Medium" in Nearby Spiral Galaxies ApJ. 1997. 491 114–133.

Warner, P. J., Wright, M. C. H., Baldwin, J. E. High resolution observations of neutral hydrogen in M33 - II. The velocity field. MNRAS. 1973. 163 163.

Waskom, M., Botvinnik, O., Hobson, P., Cole, J. B., Halchenko, Y., Hoyer, S., Miles, A., Augspurger, T., Yarkoni, T., Megies, T., Coelho, L. P., Wehner, D., cynddl, , Ziegler, E., diego0020, , Zaytsev, Y. V., Hoppe, T., Seabold, S., Cloud, P., Koskinen, M., Meyer, K., Qalieh, A., Allan, D. Seaborn: V0.5.0 (November 2014). 2014.

Watson, A. M., Gallagher, I. J. S., Holtzman, J. A., Hester, J. J., Mould, J. R., Ballester, G. E., Burrows, C. J., Casertano, S., Clarke, J. T., Crisp, D., Evans, R., Griffiths, R. E., Hoessel, J. G., Scowen, P. A., Stapelfeldt, K. R., Trauger, J. T., Westphal, J. A. The Discovery of Young, Luminous, Compact Stellar Clusters in the Starburst Galaxy NGC 253 AJ. 1996. 112 534.

Weaver, R., McCray, R., Castor, J., Shapiro, P., Moore, R. Interstellar bubbles. II. Structure and evolution. ApJ. 1977. 218 377–395.

Weber, J. A., Pauldrach, A. W. A., Hoffmann, T. L. Numerical models for the diffuse ionized gas in galaxies. II. Three-dimensional radiative transfer in inhomogeneous interstellar structures as a tool for analyzing the diffuse ionized gas A&A. 2019. 622 A115.

Weedman, D. W., Feldman, F. R., Balzano, V. A., Ramsey, L. W., Sramek, R. A., Wuu, C. C. NGC 7714 - The prototype star-burst galactic nucleus ApJ. 1981. 248 105–112.

Westmoquette, M. S., Smith, L. J., Gallagher, I. J. S. Spatially resolved optical integral field unit spectroscopy of the inner superwind of NGC 253 MNRAS. 2011. 414, 4 3719–3739.

Whitaker, K. E., van Dokkum, P. G., Brammer, G., Franx, M. The Star Formation Mass Sequence Out to z = 2.5 ApJL. 2012. 754, 2 L29.

Wiener, J., Zweibel, E. G., Oh, S. P. Cosmic Ray Heating of the Warm Ionized Medium ApJ. 2013. 767 87.

Willmer, C. N. A. The Absolute Magnitude of the Sun in Several Filters ApJS. 2018. 236, 2 47.

Wilson, R. W., Jefferts, K. B., Penzias, A. A. Carbon Monoxide in the Orion Nebula ApJL. 1970. 161 L43.

Wolfire, M. G., Hollenbach, D., McKee, C. F., Tielens, A. G. G. M., Bakes, E. L. O. The Neutral Atomic Phases of the Interstellar Medium ApJ. 1995. 443 152.

Wong, T., Blitz, L., Bosma, A. A Search for Kinematic Evidence of Radial Gas Flows in Spiral Galaxies ApJ. 2004. 605 183–204.

Wright, E. L., Eisenhardt, P. R. M., Mainzer, A. K., Ressler, M. E., Cutri, R. M., Jarrett, T., Kirkpatrick, J. D., Padgett, D., McMillan, R. S., Skrutskie, M., Stanford, S. A., Cohen, M., Walker, R. G., Mather, J. C., Leisawitz, D., Gautier, T. N. III, McLean, I., Benford, D., Lonsdale, C. J., Blain, A., Mendez, B., Irace, W. R., Duval, V., Liu, F., Royer, D., Heinrichsen, I., Howard, J., Shannon, M., Kendall, M., Walsh, A. L., Larsen, M., Cardon, J. G., Schick, S., Schwalm, M., Abid, M., Fabinsky, B., Naes, L., Tsai, C.-W. The Wide-field Infrared Survey Explorer (WISE): Mission Description and Initial On-orbit Performance AJ. 2010. 140 1868–1881.

Wünsch, R., Palouš, J., Tenorio-Tagle, G., Ehlerová, S. The Formation of Secondary Stellar Generations in Massive Young Star Clusters from Rapidly Cooling Shocked Stellar Winds ApJ. 2017. 835, 1 60.

Yim, K., Wong, T., Xue, R., Rand, R. J., Rosolowsky, E., van der Hulst, J. M., Benjamin, R., Murphy, E. J. The Interstellar Medium and Star Formation in Edge-On Galaxies. II. NGC 4157, 4565, and 5907 AJ. 2014. 148 127.

Zapartas, E., de Mink, S. E., Izzard, R. G., Yoon, S. C., Badenes, C., Götberg, Y., de Koter, A., Neijssel, C. J., Renzo, M., Schootemeijer, A., Shrotriya, T. S. Delay-time distribution of core-collapse supernovae with late events resulting from binary interaction A&A. 2017. 601 A29.

Zhang, D. A Review of the Theory of Galactic Winds Driven by Stellar Feedback Galaxies. 2018. 6, 4 114.

Zhao, H. Analytical models for galactic nuclei MNRAS. 1996. 278, 2 488–496.

Ziurys, L. M., Turner, B. E. Detection of interstellar vibrationally excited HCN ApJL. 1986. 300 L19–L23.

Zschaechner, L. K., Rand, R. J. The H I Kinematics of NGC 4013: A Steep and Radially Shallowing Extra-planar Rotational Lag ApJ. 2015. 808 153.

Zschaechner, L. K., Rand, R. J., Heald, G. H., Gentile, G., Józsa, G. HALOGAS: H I Observations and Modeling of the Nearby Edge-on Spiral Galaxy NGC 4565 ApJ. 2012. 760 37.

Zschaechner, L. K., Rand, R. J., Heald, G. H., Gentile, G., Kamphuis, P. HALOGAS: H I Observations and Modeling of the Nearby Edge-on Spiral Galaxy NGC 4244 ApJ. 2011. 740 35.

Zschaechner, L. K., Rand, R. J., Walterbos, R. Investigating Disk-halo Flows and Accretion: A Kinematic and Morphological Analysis of Extraplanar H I in NGC 3044 and NGC 4302 ApJ. 2015. 799 61.

Zschaechner, L. K., Bolatto, A. D., Walter, F., Leroy, A. K., Herrera, C., Krieger, N., Kruijssen, J. M. D., Meier, D. S., Mills, E. A. C., Ott, J., Veilleux, S., Weiss, A. Spatially Resolved ^{12}CO(2-1)/^{12}CO(1-0) in the Starburst Galaxy NGC 253: Assessing Optical Depth to Constrain the Molecular Mass Outflow Rate ApJ. 2018. 867, 2 111.

Zurita, A., Rozas, M., Beckman, J. E. The origin of the ionization of the diffuse interstellar medium in spiral galaxies. I. Photometric measurements A&A. 2000. 363 9–28.

Zwaan, M. A. Primordial Rain or Galactic Pollution? Science. 2000. 288 822.

de Blok, W. J. G., Bosma, A. High-resolution rotation curves of low surface brightness galaxies A&A. 2002. 385 816–846.

de Blok, W. J. G., McGaugh, S. S., Bosma, A., Rubin, V. C. Mass Density Profiles of Low Surface Brightness Galaxies ApJL. 2001a. 552, 1 L23–L26.

de Blok, W. J. G., McGaugh, S. S., Rubin, V. C. High-Resolution Rotation Curves of Low Surface Brightness Galaxies. II. Mass Models AJ. 2001b. 122, 5 2396–2427.

de Blok, W. J. G., Walter, F., Brinks, E., Trachternach, C., Oh, S.-H., Kennicutt, R. C. Jr. High-Resolution Rotation Curves and Galaxy Mass Models from THINGS AJ. 2008. 136 2648–2719.

de Blok, W. J. G., Walter, F., Smith, J.-D. T., Herrera-Camus, R., Bolatto, A. D., Requena-Torres, M. A., Crocker, A. F., Croxall, K. V., Kennicutt, R. C., Koda, J., Armus, L., Boquien, M., Dale, D., Kreckel, K., Meidt, S. Comparing [C II] , HI, and CO Dynamics of Nearby Galaxies AJ. 2016. 152 51.

de Grijs, R., Peletier, R. F., van der Kruit, P. C. The z-structure of disk galaxies towards the galaxy planes A&A. 1997. 327 966–982.

de Pree, C. G., Gaume, R. A., Goss, W. M., Claussen, M. J. The Sagittarius B2 Star-forming Region. III. High-Resolution H52 alpha and H66 alpha Observations of Sagittarius B2 Main ApJ. 1996. 464 788.

van Dishoeck, E. F., Black, J. H. The Photodissociation and Chemistry of Interstellar CO ApJ. 1988. 334 771.

van Dishoeck, E. F., Blake, G. A. Chemical Evolution of Star-Forming Regions ARA&A. 1998. 36 317–368.

van de Ven, G., Fathi, K. Kinematic Analysis of Nuclear Spirals: Feeding the Black Hole in NGC 1097 ApJ. 2010. 723 767–780.

van der Kruit, P. C. The three-dimensional distribution of light and mass in disks of spiral galaxies A&A. 1988. 192 117–127.